

Wrocław University of Technology
Centre of Advanced Materials and Nanotechnology

Materials Science Poland

**Conference
New Materials for Magnetoelectronics
Będlewo, 2–6 May 2005**

**Guest Editors
Tadeusz Luciński and Stanisław Lipiński**

Vol. 24



No. 3



2006



Oficyna Wydawnicza Politechniki Wrocławskiej

Materials Science is an interdisciplinary journal devoted to experimental and theoretical research into the synthesis, structure, properties and applications of materials.

Among the materials of interest are:

- glasses and ceramics
- sol-gel materials
- photoactive materials (including materials for nonlinear optics)
- laser materials
- photonic crystals
- semiconductor micro- and nanostructures
- piezo-, pyro- and ferroelectric materials
- high- T_c superconductors
- magnetic materials
- molecular materials (including polymers) for use in electronics and photonics
- novel solid phases
- other novel and unconventional materials

The broad spectrum of the areas of interest reflects the interdisciplinary nature of materials research. Papers covering the modelling of materials, their synthesis and characterisation, physicochemical aspects of their fabrication, properties and applications are welcome. In addition to regular papers, the journal features issues containing conference papers, as well as special issues on key topics in materials science.

Materials Science is published under the auspices of the Centre of Advanced Materials and Nanotechnology of the Wrocław University of Technology, in collaboration with the Institute of Low Temperatures and Structural Research of the Polish Academy of Sciences and the Wrocław University of Economics.

All accepted papers are placed on the Web page of the journal and are available at the address:
<http://MaterialsScience.pwr.wroc.pl>

Materials Science is abstracted/indexed in: Chemical Abstracts; Materials Science Citation Index; Science Citation Index Expanded.

Editor-in-Chief

Juliusz Sworakowski

Institute of Physical and Theoretical Chemistry
Wrocław University of Technology
Wybrzeże Wyspiańskiego 27
50-370 Wrocław, Poland
sworakowski@pwr.wroc.pl

Associate Editors

Wiesław Stręk

Institute of Low Temperature
and Structure Research
Polish Academy of Sciences
P. O. Box 1410
50-950 Wrocław 2, Poland
strek@int.pan.wroc.pl

Jerzy Hanuza

Department of Bioorganic Chemistry
Faculty of Industry and Economics
Wrocław University of Economics
Komandorska 118/120
53-345 Wrocław, Poland
hanuza@credit.ae.wroc.pl

Scientific Secretary

Jan Felba

Faculty of Microsystem Electronics and Photonics
Wrocław University of Technology
Wybrzeże Wyspiańskiego 27
50-370 Wrocław, Poland
jan.felba@pwr.wroc.pl

Advisory Editorial Board

Ludwig J. Balk, Wuppertal, Germany
Mikhaylo S. Brodyn, Kyiv, Ukraine
Maciej Bugajski, Warsaw, Poland
Alexander Bulinski, Ottawa, Canada
Roberto M. Faria, São Carlos, Brazil
Reimund Gerhard-Multhaupt, Potsdam, Germany
Paweł Hawrylak, Ottawa, Canada
Wacław Kasprzak, Wrocław, Poland
Andrzej Klonkowski, Gdańsk, Poland
Seiji Kojima, Tsukuba, Japan
Shin-ya Koshihara, Tokyo, Japan
Krzysztof J. Kurzydłowski, Warsaw, Poland
Janina Legendziewicz, Wrocław, Poland
Benedykt Licznernski, Wrocław, Poland

Jerzy Lis, Cracow, Poland
Tadeusz Luty, Wrocław, Poland
Joop H. van der Maas, Utrecht, The Netherlands
Bolesław Mazurek, Wrocław, Poland
Jan Misiewicz, Wrocław, Poland
Jerzy Mroziński, Wrocław, Poland
Robert W. Munn, Manchester, U.K.
Krzysztof Nauka, Palo Alto, CA, U.S.A.
Stanislav Nešpůrek, Prague, Czech Republic
Romek Nowak, San Jose, CA, U.S.A.
Marek Samoć, Canberra, Australia
Jan Stankowski, Poznań, Poland
Jacek Ulański, Łódź, Poland
Vladislav Zolin, Moscow, Russia

The Journal is supported by the State Committee for Scientific Research

Editorial Office

Tomasz Fałat
Karol Langner

Printed in Poland

© Copyright by Oficyna Wydawnicza Politechniki Wrocławskiej, Wrocław 2006

Drukarnia Oficyny Wydawniczej Politechniki Wrocławskiej
Zam. nr 737/2006.

Contents

From the Organizers.....	539
E. Wawrzyńska, A. Szytuła, Magnetic ordering schemes in $R_3T_4X_4$ compounds	543
W. Głogowski, A. Ślebarski, Photoemission study of $CeRh_{1-x}Pd_xAl$. The effect of Pd doping on electronic structure.....	551
A. Szytuła, D. Gomółka, A. Jezierski, B. Penc, E. Wawrzyńska, A. Winiarski, Electronic structures of intermetallic rare earth compounds	557
J. Goraus, A. Ślebarski, J. Deniszczuk, Electronic structure of $Ce_2Rh_3Al_9$	563
M. Gamża, A. Ślebarski, J. Deniszczuk, Electronic structure of $CeRhIn_5$ and $CeIrIn_5$	569
A. Gil, Magnetic interaction in RT_xX_2 ternary compounds	577
R. Troć, Study of the valence state of U ions in quasi-two-dimensional ternary uranium compounds.....	585
G. Grabecki, PbTe constrictions for spin filtering	591
T. Szumiata, K. Brzózka, B. Górka, M. Gawroński, G. Pavlík, P. Sovák, Evolution of hyperfine parameters in Co-doped FINEMET.....	599
B. J. Spisak, A. Paja, Conductivities and transmission coefficients of ultra-thin disordered metallic films	605
M. Samsel-Czekala, G. Kontrym-Sznajd, M. Biasini, Electronic structures of f-electron intermetallic compounds studied by positrons	611
J. Sadowski, J. Z. Domagała, J. Kanski, C. H. Rodriguez, F. Terki, S. Charar, D. Maude, How to make GaMnAs with a high ferromagnetic phase transition temperature?	617
M. Sawicki, K.-Y. Wang, K.W. Edmonds, R.P. Champion, C.R. Staddon, N.R.S. Farley, C.T. Foxon, T. Dietl, B.L. Gallagher, In-plane uniaxial anisotropy rotations in (Ga, Mn)As thin films.....	627
P. Jarguz, A. Paja, Electrical resistivity of disordered monolayer metallic films	633
J. Jaworowicz, Z. Kurant, K. Postava, A. Maziewski, L.T. Baczewski, A. Wawro, Domain structures and magnetization processes in thin Co films with in-plane anisotropy.....	639
T. Błachowicz, M. Wieja, Analysis of magnetisation reversal at the exchange-biased interface using the Ising approach	643
S. Krompiewski, Electronic transport through carbon nanotubes with ferromagnetic electrodes and in magnetic fields	649
A. Stupakiewicz, R. Gieniusz, K. Postava, M. Tekielak, A. Maziewski, I. Szerel, A. Wawro, L.T. Baczewski, Magnetic ordering in ultra-thin Co films grown on vicinal substrates.....	659
P. Przysługowski, A. Tsarou, I. Komissarov, K. Dybko, P. Dłużewski, M. Sawicki, B. Dąbrowski, C. Kimball, Magnetism and superconductivity in oxide ferromagnet/superconductor heterostructures.....	665
V. H. Tran, Hall effect in strongly correlated electron systems	669
A. M. Werpachowska, Z. Wilamowski, RKKY coupling in diluted magnetic semiconductors.....	675
A. Jezierski, A. Szytuła, D. Kaczorowski, Effect of spin-orbit coupling on the electronic structure of bismuthide $YbAuBi$	683
S. Lipiński, Spin and orbital Kondo effect in electrostatically coupled quantum dots.....	689
M. Wawrzyniak, M. Gmitra, J. Barnaś, Resonant tunnelling through a single level quantum dot attached to ferromagnetic leads with non-collinear magnetizations.....	695
I. Staniucha, A. Urbaniak-Kucharczyk, The influence of roughness on the Curie temperature and magnetisation in multilayers	701
M. Wójcik, E. Jędryka, I. Škorvánek, P. Švec, Partitioning of Co upon the nanocrystallisation of soft magnetic $FeCo(Zr, Nb)B$ alloys – a ^{59}Co NMR study.....	707
E. Talik, M. Adamiec, A. Molak, Photoelectron spectroscopy of Ba-doped lead germanate – $Pb_5Ge_3O_{11}$	713
T. Balcerzak, Calculation of the Fermi wave vector for thin films, quantum wires and quantum dots.....	719
A. Wronka, First principles calculations of zinc blende superlattices with ferromagnetic dopants ..	725

K. Warda, L. Wojtczak, D. Baldomir, M. Pereiro, J. Arias, The influence of effective mass on magnetoresistance in ultrathin Fe/Cr/Fe films	731
A. Szytuła, Complex magnetic phenomena in f-electron intermetallic compounds.....	737
K. Szymański, L. Dobrzyński, D. Satuła, E. Voronina, E. P. Yelsukov, Magnetization distribution in nanocrystalline $\text{Fe}_{0.48}\text{Al}_{0.52}$	753
J. Wiśniewska, M. Kowalik, J. Barnaś, Transport characteristics of ferromagnetic single-electron transistors with non-collinear magnetizations.....	761
J. Dajka, E. Zipper, Persistent currents controlled by non-classical electromagnetic fields	769
P. Dziawa, V. Osinniy, W. Dobrowolski, K. Dybko, E. Łusakowska, B. Taliashvili, T. Story, C.J.P. Smits, H.J.M. Swagten, Magnetic properties of (Eu,Gd)Te semiconductor layers.....	777
W. Stefanowicz, M. Tekielak, V. Bucha, A. Maziewski, V. Zablotskii, L.T. Baczewski, A. Wawro, Dendritic domain structures in ultrathin cobalt films	783
T. Toliński, V. Ivanov, A. Kowalczyk, Electrical resistivity of RNi_4Al and RNi_4Cu	789
T. Zajac, L. Folcik, J. Chmista, A. Kołodziejczyk, H. Drulis, K. Krop, G. Gritzner, Magnetisation and electron spin resonance of the colossal magnetoresistive $\text{La}_{0.67}\text{Ca}_{0.33}\text{Mn}_{1-x}\text{Fe}_x\text{O}_3$	795
Z. Wilamowski, A. M. Werpachowska, Spintronics in semiconductors.....	803
L. Kowalczyk, M. Chernyshova, T. Story, A. Yu. Sipatov, Photoluminescence in EuS–PbS–EuS semiconductor structures with a double ferromagnetic barrier	809
M. Kowalik, J. Wiśniewska, J. Barnaś, Torque due to spin-polarized current in ferromagnetic single-electron transistors	815
L. Smardz, K. Smardz, Weak interlayer exchange coupling in Fe–Zr and Fe–Ti layered structures	821
K. Smardz, L. Smardz, Structure and electronic properties of Fe–Ti thin films	827
F. Stobiecki, M. Urbaniak, B. Szymański, T. Luciński, M. Schmidt, J. Aleksiejew, $\text{Ni}_{80}\text{Fe}_{20}/\text{Au}/\text{Co}/\text{Au}$ multilayers as magnetic field sensors	833
A. Szajek, J. A. Morkowski, Calculated magnetic moments and electronic structures of the compounds $\text{R}_{n+1}\text{Co}_{3n+5}\text{B}_{2n}$, R = Gd, Tb, $n = 0, 1, 2, 3$, and ∞	839
A. Szajek, Electronic and magnetic properties of $\text{Nd}_5\text{Co}_{19}\text{B}_6$ and $\text{Nd}_5\text{Co}_{21}\text{B}_4$	843
B. Szymański, F. Stobiecki, M. Urbaniak, Temperature dependence of magnetization reversal in $\text{Ni}_{80}\text{Fe}_{20}/\text{Au}/\text{Co}/\text{Au}$ multilayers.....	849
A. Szajek, S.A. Kostyrya, B. Idzikowski, Electronic and magnetic properties of metastable $\text{Fe}_{22}\text{PdB}_6$ and $\text{Fe}_{22}\text{PtB}_6$ compounds	855
P. Wandziuk, T. Luciński, M. Kopcewicz, Influence of Ge on antiferromagnetic coupling in Fe/Si multilayers	861
A. Bajorek, D. Stysiak, G. Chelkowska, J. Deniszczyk, W. Borgiel, M. Neumann, Magnetic properties and electronic structure of $\text{Y}_x\text{Gd}_{1-x}\text{Ni}_5$ compounds	867

From the Organizers

Recent advances in spin electronics have created a demand for a more structured method of sharing and disseminating information and experience gathered by the leading research groups engaged in the subject. Hence the idea of scientific network *New Materials for Magnetoelectronics* – MAG-EL-MAT which was founded early in 2003 and has soon gained support of a number of research institutes in Poland as well as financial support of the Ministry of Scientific Research and Information Technology, now extended until 2008.

Currently, MAG-EL-MAT network extends on 52 research groups bringing together over 300 scientists investigating the electric and magnetic properties of solids, with particular interest in various applications of the spin degree of freedom. A general theoretical and experimental long-term goal is to research electronic and magnetic properties of nanoscopic materials such as thin layers, multilayers, composites, nanocrystalline alloys, intermetallic compounds, molecular systems (including carbon nanotubes) and quantum dots. Knowledge and new materials developed by network members are the basis for the creation of new magnetoelectronic devices.

The first and second annual MAG-EL-MAT Members Meeting was held in Będlewo on 26–28 October 2003 and 13–16 April 2004, respectively. The venue of the third Members Meeting to be held on 2–6 May, 2005 was again Będlewo which has now become the traditional meeting place of MAG-EL-MAT members. Its convenient and attractive location (40 km from Poznań, amidst lakes and forests, in an old palace and modern buildings offering excellent accommodation and conference facilities) has now become recognized by our regular visitors.

The third meeting took a form of seven sessions chaired by leading scientists selected by the coordinating committee (L. Adamowicz, T. Luciński, W. Nawroćik, A. Paja, B. Bułka, G. Chełkowska, T. Story, D. Kaczorowski, R. Micnas, A. Maziewski, H. Puzkarski, T. Balcerzak, T. Stobiecki, E. Zipper, J. Barnaś). Their task was also to decide upon the topics of the sessions, to invite the key-speakers (Z. Wilamowski, A. Hryniewicz, K. Byczuk, J. Martinek, A. Szytuła, J. Sadowski, J. Spątek, S. Stuligrosz, B. Susła, T. Luciński, S. Krompiewski, G. Grabecki) and to select 25 oral and 34 poster contributions. Finally, the topics selected for the third MAG-EL-MAT Meeting were nanostructured semiconductors, alloys and metals, magnetism in intermetallic compounds and semiconductors, structure and magnetic properties of thin films, electronic transport and spin-polarized transport and quantum coherence in mesoscopic systems.

Many presented papers were prepared for publication and then subjected to regular refereeing procedures by at least one referee. Finally, 50 papers were accepted for publication in the *Materials Science-Poland*. The success of 2005 MAG-EL-MAT Members Meeting was due to the active contribution to the program by 102 participants. Especially we would like to thank the chairmen and referees for their hard work in the scientific program and processing of evaluation of the papers for this special issue of *Materials Science-Poland*.

T. Luciński, S. Lipiński, B. Idzikowski



Participants of the Meeting of the Members of Scientific Network New Materials for Magnetolectronics, MAG-EL-MAT, Będlewo, 2–6 May 2005

Magnetic ordering schemes in $R_3T_4X_4$ compounds

E. WAWRZYŃSKA*, A. SZYTUŁA

M. Smoluchowski Institute of Physics, Jagiellonian University, Reymonta 4, 30-059 Cracow, Poland

This work is an attempt to systematize the magnetic structures of $R_3T_4X_4$ (R – rare earth atom, T – transition metal, X – p-electron element) compounds, investigated by neutron diffraction in the course of a broader research programme. Experiments were performed for twenty samples containing Pr, Nd, Tb, Dy, Ho, and Er. Although the determined structures display a huge variety, some regularities were found. Different approaches are tried in order to elucidate the observed behaviours, and several conclusions are arrived at concerning the factors responsible for the observed magnetic ordering schemes.

Key words: *magnetic ordering; rare earth intermetallics; neutron diffraction*

1. Introduction

The research reported here aims at performing a detailed study of isostructural 3:4:4 compounds crystallizing in the $Gd_3Cu_4Ge_4$ -type structure (space group *Immm*), expected to bring a systematisation in their magnetic properties, including magnetic structures. The most interesting feature of these intermetallics is the fact that rare earth ions occupy two symmetry non-equivalent positions (4e and 2d).

Twenty three compounds such as $R_3Mn_4Sn_4$ (R = La, Pr, Nd), $R_3Cu_4Si_4$ (R = Tb, Dy, Ho, Er), $R_3Cu_4Ge_4$ (R = Nd, Tb, Dy, Ho, Er), $R_3Cu_4Sn_4$ (R = Pr, Nd, Tb, Dy, Ho, Er), $R_3Pd_4Ge_4$ (R = Tb, Ho, Er), and $R_3Ag_4Sn_4$ (R = Pr, Nd) have been investigated by means of neutron powder diffraction. The determined magnetic structures exhibit a huge diversity, however some regularities were found.

2. Experimental results and discussion

The samples were synthesized and examined as described elsewhere [1], where a detailed description of the determined magnetic structures can also be found. Mag-

*Corresponding author, e-mail: e.w@wp.pl

netic data indicate that all the investigated compounds are antiferromagnets at low temperatures. The whole group may be divided into three sub-groups: manganese compounds, light rare earth compounds, and heavy rare earth compounds, which will be described below.

In the compounds containing manganese, i.e. $R_3Mn_4Sn_4$ ($R = La, Pr, Nd$), the manganese moments are the first to order on decreasing temperature. In the La compounds, they are actually the only ones that do order, forming a sine-wave modulated structure described by the propagation vector $\mathbf{k} = (k_x, 0, 0)$, with magnetic moments always lying in the bc plane. The value of k_x increases with temperature. In the Pr and Nd compounds, the rare earth magnetic moments at the 4e sites order as well, in both cases forming collinear structures described by the propagation vector $\mathbf{k} = (1, 1, 1)$; their ordering temperatures, however, are lower than the ordering temperatures of the Mn sublattices. The magnetic moments of Pr and Nd lay in the ab planes for both compounds.

The Néel temperatures corresponding to the Mn sublattice ordering decrease with the increasing Z value of the R element, which corresponds to a decreasing unit cell volume. This is an anomalous result. The Néel temperatures for the rare earth sublattices fulfil the de Gennes relation. The ratio $T_N(Nd)/T_N(Pr)$ is equal to 2.4, whereas the corresponding ratio of de Gennes factors is 2.3.

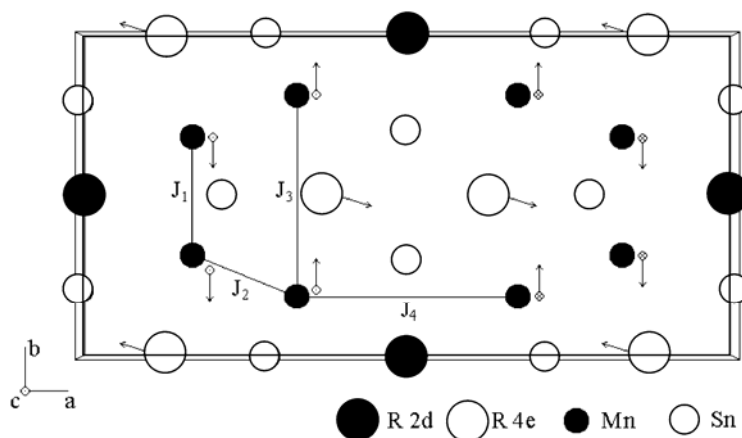


Fig. 1. Crystal structure of the $R_3Mn_4Sn_4$ ($R = La, Pr, Nd$) compounds projected along $[001]$, with four different exchange integrals among the Mn magnetic moments. The vectors show the components of the Mn magnetic moments and the directions of the rare earth magnetic moments in the Pr and Nd compounds

The interaction between Mn moments may be described by four integrals, J_1 , J_2 , J_3 , and J_4 (Fig. 1), related to four Mn–Mn interatomic distances, d_1 , d_2 , d_3 , and d_4 , respectively. The shortest distance, d_1 (smaller than 2.88 \AA), corresponds to the ferromagnetic coupling between moments ($J_1 > 0$). The other distances are larger than

3.21 Å. In $\text{La}_3\text{Mn}_4\text{Sn}_4$, all the other integrals are also positive. In the case of $\text{Pr}_3\text{Mn}_4\text{Sn}_4$ and $\text{Nd}_3\text{Mn}_4\text{Sn}_4$, only J_2 is negative, whereas the other two integrals are positive as well. The idea of a critical Mn–Mn distance of about 2.85 Å, which would govern interionic coupling, applicable to many manganese-transition metal alloys and proposed by Goodenough on the assumption of localised/delocalised 3d electrons [2, 3], does not seem to work in this case.

The dependence of the magnetic moment of Mn on Mn–Mn and Mn–Sn interatomic distances reveals a positive correlation, similar to the one observed for rare earth manganese-germanides [4]. This result indicates a stronger localization of d electrons on manganese atoms. In the Pr and Nd compounds, rare earth magnetic moments in the 4e sublattice become ordered independently on Mn at low temperatures. A similar behaviour is observed in other Pr and Nd compounds [5–7], where the manganese–rare earth interatomic distances are larger than 3 Å, analogously to the compounds studied in this work. These results indicate a weak interaction between the rare earth and manganese sublattices.

The R–Mn coupling is different in various compounds; non-collinear ordering is observed in the majority of cases. Iwata et al. showed that for light rare earths the ferromagnetic coupling between the R and Mn sublattices is dominant [8]. Such a behaviour is observed for NdMn_2Si_2 [9]. In other compounds, antiferromagnetic (for example in PrMnSi_2 [6]) or complex (NdMnSi , NdMnSi_2) coupling is observed, similar to the one appearing in the compounds investigated here. The above results confirm independent magnetic ordering in rare earth sublattices.

In the case of light rare earth compounds, the rare earth magnetic moments were found to order in $\text{Nd}_3\text{Cu}_4\text{Ge}_4$, $\text{Pr}_3\text{Cu}_4\text{Sn}_4$, and $\text{R}_3\text{Ag}_4\text{Sn}_4$ (R = Pr, Nd). The only exception was $\text{Nd}_3\text{Cu}_4\text{Sn}_4$, in which no ordering was detected down to 1.5 K. The predominant arrangements observed in this group are the structures described by the propagation vector $\mathbf{k} = (1, 1, 1)$, with magnetic moments pointing along the a-axis or laying in the a-b plane. Only in $\text{Nd}_3\text{Cu}_4\text{Ge}_4$ do the magnetic moments point along the c-axis, and simultaneously only in this case the 2d sublattice does not order.

The Néel temperatures of the light rare earth compounds do not fulfil the de Gennes relation. The experimental values are larger than those resulting from de Gennes scaling normalized to the Néel temperatures of isostructural $\text{Gd}_3\text{T}_4\text{X}_4$ compounds. The values of $\Delta T_N = T_{N\text{obs}} - T_{N\text{calc}}$ ($T_{N\text{calc}}$ is determined as T_N normalized to the Néel temperature of the isostructural Gd compound) decrease with an increasing number of the 4f electrons. These differences between the observed and calculated values result from the strong influence of the crystalline electric field effect [10] or hybridisation of 4f shells with conduction bands and/or d or p shells of the surrounding atoms [11].

The largest group, in which the magnetic structures were determined, are heavy rare earth compounds, i.e. $R_3Cu_4Si_4$ ($R = Tb, Dy, Ho, Er$), $R_3Cu_4Ge_4$ ($R = Tb, Dy, Ho, Er$), $R_3Cu_4Sn_4$ ($R = Tb, Dy, Ho, Er$), and $R_3Pd_4Ge_4$ ($R = Tb, Ho, Er$), which simultaneously display the largest diversity. Both rare earth sublattices become ordered in all of them. The most distinctive feature in this group is the existence of more than one critical temperature (observed for 12 out of 15 compounds) which indicates changes in magnetic structure with temperature. These changes concern disordering of one of the two rare earth sublattices or involve a transformation of the propagation vector.

The most frequently observed arrangements in this group are the structures described by the vector $\mathbf{k} = (0, 1/2, 0)$ or its derivatives $\mathbf{k} = (0, 1/2 + \delta, 0)$, where $\delta < 0.03$ (in 9 cases out of 15). These structures often coexist with other, modulated arrangements at low temperatures (in 7 cases out of 9). The described ordering type dominates in $R_3Cu_4Si_4$ and $R_3Cu_4Ge_4$ compounds (it appears in all the studied compounds, in fact).

Among the $R_3Cu_4Sn_4$ compounds, two ($R = Tb, Dy$) have structures described by the propagation vector $\mathbf{k} = (0, 0, 1/2 + \delta)$, where $\delta < 0.09$, which do not change with temperature. For one compound ($R = Er$), the propagation vector $\mathbf{k} = (1/2, 1/2, 0)$ is accompanied by another one at low temperatures, and one compound ($R = Ho$) has a very complex structure that changes with temperature, described by different sets of vectors in each range.

Regarding the $R_3Pd_4Ge_4$ compounds, all of them have modulated structures described by propagation vectors with two ($R = Tb, Ho$) or one ($R = Er$) non-zero components. These propagation vectors in two cases ($R = Tb, Er$) are accompanied by the propagation vector $\mathbf{k} = (0, 0, 0)$ at low temperatures.

The reported changes in the propagation vectors, connected with transitions from commensurate structures at low temperatures to modulated, non-commensurate ones in the vicinity of the Néel temperature, are very common among rare earth intermetallics. They may be explained as a result of temperature-dependent free energy for different propagation vectors appearing in the presence of magnetocrystalline anisotropy [12, 13].

The other analysed parameter is the direction of the magnetic moment which may provide information about magnetocrystalline anisotropy and crystalline electric field parameters. Among light rare earth compounds (Pr, Nd), rare earth magnetic moments in the 2d sublattice are parallel to the a -axis, which in general applies to the 4e sublattice magnetic moments as well (except for $Nd_3Cu_4Ge_4$ and $Nd_3Ag_4Ge_4$). It is much more difficult to find any distinct trends among the heavy rare earth compounds (Tb–Er). In the $Tb_3Cu_4X_4$ ($X = Si, Ge, Sn$) series, the Tb 2d magnetic moments are parallel to the a -axis, in the $Ho_3Cu_4X_4$ ($X = Si, Ge, Sn$) compounds the Ho 2d moments are parallel to the b -axis, and in $Er_3Cu_4X_4$ ($X = Si, Ge, Sn$) and $Er_3Pd_4Ge_4$ the Er 2d moments are parallel to the c -axis. Finding the respective regularities for the 4e sublattice is impossible.

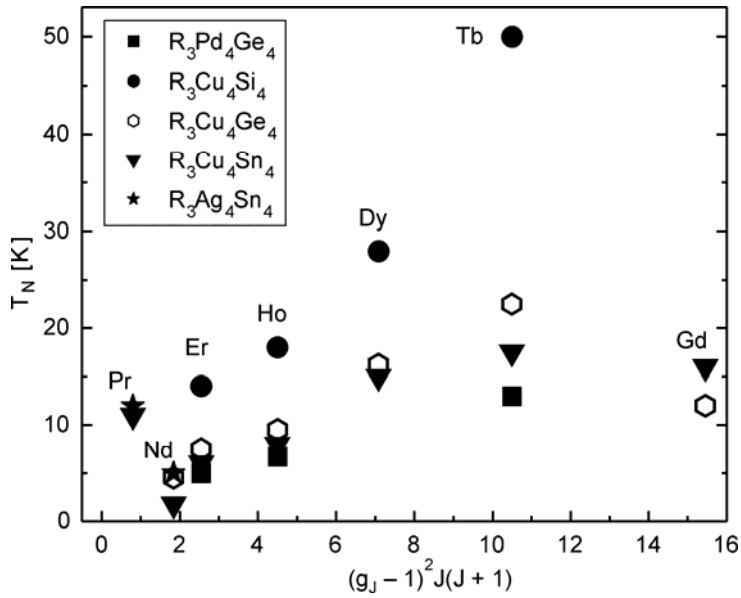


Fig. 2. Néel temperatures of $R_3Ag_4Sn_4$ ($R = Pr, Nd$), $R_3Cu_4Si_4$ ($R = Tb, Dy, Ho, Er$), $R_3Cu_4Ge_4$ ($R = Nd, Tb, Dy, Ho, Er$), $R_3Cu_4Sn_4$ ($R = Pr, Nd, Tb, Dy, Ho, Er$), and $R_3Pd_4Ge_4$ ($R = Tb, Ho, Er$) versus the de Gennes factor. The Néel temperatures of $Gd_3Cu_4Sn_4$ and $Gd_3Cu_4Ge_4$ were taken from [9] and [11], respectively

It is commonly known that the observed magnetic ordering results from exchange interaction transferred via conduction band electrons, as described by the RKKY model. Its adoption here is justified by large spacing between rare earth moments and the fact that the investigated compounds are good conductors [14]. According to this model, the critical temperatures connected with magnetic ordering should be proportional to the above-mentioned de Gennes function, $(g_J - 1)^2 J(J + 1)$ [15, 16]. For the compounds discussed here, this scaling is not fulfilled (Fig. 2), which suggests that additional factors are responsible for the ordering that appears. The first factor that needs to be considered is the influence of the crystalline electric field [10].

The description of the RKKY-type interaction is connected with the interaction integral $J(X)$, which is an oscillatory function of $X = k_F R_{ij}$ ($F(X) = (X \cos X - \sin X) X^{-4}$), where k_F is the Fermi vector and R_{ij} is the distance between the i th and the j th spin. In order to enable an interpretation of the obtained results, the Fermi vector must be calculated. For $Tb_3Cu_4Si_4$, it was evaluated to be 1.672 \AA^{-1} . Taking into account the distances between a singled out Tb atom in the 4e sublattice and the nearest Tb atoms in the 2d sublattice of this compound (equal to 3.663, 5.039 and 5.516 \AA), one obtains the following values of the product $k_F R_{ij}$: 6.120, 8.425 and 9.223. Two of these numbers are close to the zero points of the oscillatory function $F(X)$, equal to 6.425 and 9.530. This result indicates that the interactions originating from the magnetic mo-

ments in the 2d sublattice almost cancel out at the 4e sites and the magnetic moments in this sublattice are ordered independently in consequence. The same explanation can be applied for the other $R_3Cu_4X_4$ ($X = Si, Ge, Sn$) compounds for the sake of the similarity of their (also electronic) structures. Magnetic ordering in two symmetry non-equivalent sublattices also proceeds independently in many of the $RTGe_2$ compounds ($T = Pt, Pd, Ir$) [17–19].

The ^{166}Er Mössbauer spectroscopy performed for $Er_3Cu_4X_4$ ($X = Si, Ge, Sn$) at different temperatures [20] shows that the effective field in the 2d sublattice is larger than in the 4e sublattice, which suggests that a similar relation should appear in the case of magnetic moments. For $Er_3Cu_4Si_4$, a line broadening referring to the 4e sublattice is observed in the spectrum obtained at 2 K, which can be ascribed to the existence of magnetic moment relaxation in this sublattice. Neutron diffraction measurements carried out for this compound reveal a broadening of the magnetic reflexes connected to diffraction on Er magnetic moments in the 4e sublattice, which indicates that the correlation length is of the order of 20 Å [20]. The cited experimental facts suggest that the ordering in the 4e sublattice is induced by the moments in the 2d sublattice.

For $R_3Cu_4X_4$, a distinct regularity is observed: $T_N(X = Si) > T_N(X = Ge) > T_N(X = Sn)$. Additionally, the transition temperatures of the copper compounds are higher than those of the palladium compounds. As already mentioned above, the local symmetries and atomic surroundings of the rare earth atoms occupying two different sublattices differ from each other. In order to investigate the influence of these factors on the crystalline electric field parameters, calculations based on the point charge approximation (described in detail in [1]) were performed for some of the investigated compounds, namely $R_3Cu_4Sn_4$ ($R = Pr, Nd, Tb, Dy, Ho, Er$), $Tb_3Cu_4X_4$ ($X = Si, Ge, Sn$), and $Tb_3Pd_4Ge_4$. It must be clearly stated that the applied method, though very simple, can give only scarce information on the real values of the B_n^m parameters and should rather be treated as the one that gives a very raw estimation.

Concerning copper stannides, while passing from holmium to erbium, the signs of the crystalline electric field parameters change, due to a change in the sign of the Stevens α parameter. The second important result following from these calculations is the observation that the three parameters B_2^0 , B_2^2 and B_4^0 are of a comparable magnitude, which suggests that their participation in the formation of a magnetic structure is evenly important. It seems that for these compounds the complete crystalline electric field Hamiltonian needs to be considered, which contradicts the case of, for example, the RT_4X_4 series [10], for which magnetic structure formation is determined solely by B_2^0 . The calculations aiming at revealing the possible influence of d- or p-electron elements (those performed for $Tb_3Cu_4X_4$ ($X = Si, Ge, Sn$) and $Tb_3Pd_4Ge_4$) did not reveal any evident relationships.

3. Conclusions

It seems that at this stage it is not possible to unambiguously point out one factor, or even a set of factors, to which any vital, decisive role in the formation of a magnetic structure can be ascribed. It appears that only further and broader studies of compounds of this class may yield premises for elaborating a suitable theory or at least for finding some explicit, general regularities.

Acknowledgements

E. W. thanks the Foundation for Polish Science (FNP) for the granted scholarship.

References

- [1] WAWRZYŃSKA E., [in:] *Magnetic structures of $R_3T_4X_4$ compounds*, PhD Thesis, Institute of Physics, Jagiellonian University, Cracow, 2005.
- [2] TEBBLE R.S., CRAIK D.J., [in:] *Magnetic Materials*, Wiley, New York, 1969, p. 61.
- [3] GOODENOUGH J.B., [in:] *Magnetism and the Chemical Bond*, Wiley, New York, 1963, p. 240.
- [4] SZYTULA A., PENC B., JEZERSKI A., HOFMANN M., CAMPBELL S.J., *Acta Phys. Polon. B*, 34 (2003), 1561.
- [5] WELTER R., VENTURINI G., MALAMAN B., *J. Alloys Comp.*, 206 (1994), 55.
- [6] MALAMAN B., VENTURINI G., POUTONNIER L., FRUCHART D., *J. Magn. Magn. Mater.*, 86 (1990), 349.
- [7] WELTER R., VENTURINI G., FRUCHART D., MALAMAN B., *J. Alloys Comp.*, 191 (1993), 263.
- [8] IWATA N., IKEDA T., SHIGEOKA T., FURII H., AKAMOTO T.J., *J. Magn. Magn. Mater.*, 54–57 (1985), 481.
- [9] SINGH S., DHAR S.K., MANFRINETTI P., PALENZONA A., *J. Alloys Comp.*, 298 (2000), 68.
- [10] NOAKES D.R., SHENOY G., *Phys. Lett.*, A 91 (1982), 35.
- [11] OESTERREICHER H., *Phys. Stat. Sol. (a)*, 39 (1977), K75.
- [12] GIGNOUX D., SCHMITT D., *Phys. Rev. B*, 48 (1993), 12682.
- [13] BAK P., *Rep. Prog. Phys.*, 45 (1982), 587.
- [14] SHOLOZDRA R.V., [in:] *Stannides of Rare Earth and Transition Metals*, Svit, Lviv, 1993, p. 200.
- [15] DE GENNES P.G., *J. Phys. Rad.*, 23 (1962), 510.
- [16] DE GENNES P.G., *J. Phys. Rad.*, 23 (1962), 630.
- [17] GIL A., PENC B., HOFMANN M., SZYTULA A., ZYGMUNT A., *J. Alloys Comp.* 322 (2001), 21.
- [18] SCHMITT D., OULADDIAF B., ROUTSI CH.D., YAKINTHOS J.K., *J. Magn. Magn. Mater.*, 234 (2001), 62.
- [19] PAPANASSIOU G.F., YAKINTHOS J.K., SCHÄFER W., *J. Magn. Magn. Mater.*, 269 (2004), 1.
- [20] RYAN D.H., CADOGAN J.M., GAGNON R., SWAINSON I., *J. Phys.: Condens. Matter.*, 16 (2004), 3183.

Received 1 June 2005
Revised 10 October 2005

Photoemission study of $\text{CeRh}_{1-x}\text{Pd}_x\text{Al}$. The effect of Pd doping on electronic structure

W. GŁOGOWSKI, A. ŚLEBARKI*

Institute of Physics, University of Silesia, Uniwersytecka 4, 40-007 Katowice, Poland

In view of a contrasting behaviour of Pd-containing and Rh-containing systems, we investigate solid solutions $\text{CeRh}_{1-x}\text{Pd}_x\text{Al}$ in order to determine the dependence of their electronic properties on the number of the conduction electrons. We present structural and X-ray photoemission spectroscopy (XPS) data for $\text{CeRh}_{1-x}\text{Pd}_x\text{Al}$. We also discuss the influence of the number of free electrons in the conduction band on the stability of the crystallographic structure and the occupation number of the f-shell.

Key words: *strongly correlated electron system; electronic structure*

1. Introduction

Ce-based Kondo-lattice systems exhibit unusual physical, behaviour such as of the heavy-Fermi (HF) liquid (e.g., CeRhSb , CeNiSn for $T > \sim 10$ K, $\text{Ce}(\text{Ni,Pt})\text{Sn}$ [1]) and non-Fermi liquid (NFL) types, in the metallic state (e.g., CeRhSn [2]) or Kondo-lattice insulating type state (CeRhSb [3] and CeNiSn [4]). Recently, we suggested that the NFL behaviour in CeRhSn may be due to the existence of Griffiths phases in the vicinity of the quantum critical point [2], whereas in CeRhAl [5] the disorder leads to an unconventional metallic state, which does not fit within the framework of FL theory [5].

The stability of paramagnetic as a magnetic ground state in the Kondo-lattice limit [6] is strongly dependent on the number of electrons per atom. In the series of compounds, CeRhSb , CeRhSn , and CeRhAl , the number of valence electrons per formula unit is 18, 17, and 16, respectively. In the case of momentum-dependent hybridisation, the gap formed at $T \rightarrow 0$ for CeRhSb may vanish, e.g. in CeRhSn . CeRhAl is expected to be an insulator, this, however, is not the case [7]. For CeRhAl , we have recently observed [5] a coexistence of antiferromagnetic ordering ($T_N = 3.8$ K) and the NFL-like behaviour.

In view of the diverse behaviour of CePdAl with respect to CeRhAl , it is of interest to examine the solid solution $\text{CeRh}_{1-x}\text{Pd}_x\text{Al}$, to see the effect of decreasing the

*Corresponding author, e-mail: slebar@us.edu.pl

number of s -states (conduction states, if one treats d -electrons as almost localized) on the properties ground state. The aim of this work is to investigate the crystallographic and electronic structure of this series of compounds.

2. Experimental details and discussion

The samples of $\text{CeRh}_{1-x}\text{Pd}_x\text{Al}$ were prepared by arc melting, and were then annealed at 800 °C for 3 weeks. The lattice parameters were acquired from diffraction patterns using the Powder-Cell program. X-ray photoelectron spectroscopy spectra (XPS) were obtained with monochromatised Al K_α radiation using a PHI 5700 ESCA spectrometer. The samples were found to be orthorhombic (ϵ -TiNiSi structure, space group $Pnma$) for $0 \leq x \leq 0.8$, whereas CePdAl crystallizes in a hexagonal structure (ZrNiAl-type, space group $P6_2m$). In Figure 1, we compare the X-ray diffraction (XRD) spectra measured and calculated for the orthorhombic samples CeRhAl , $\text{CeRh}_{0.4}\text{Pd}_{0.6}\text{Al}$, and hexagonal CePdAl .

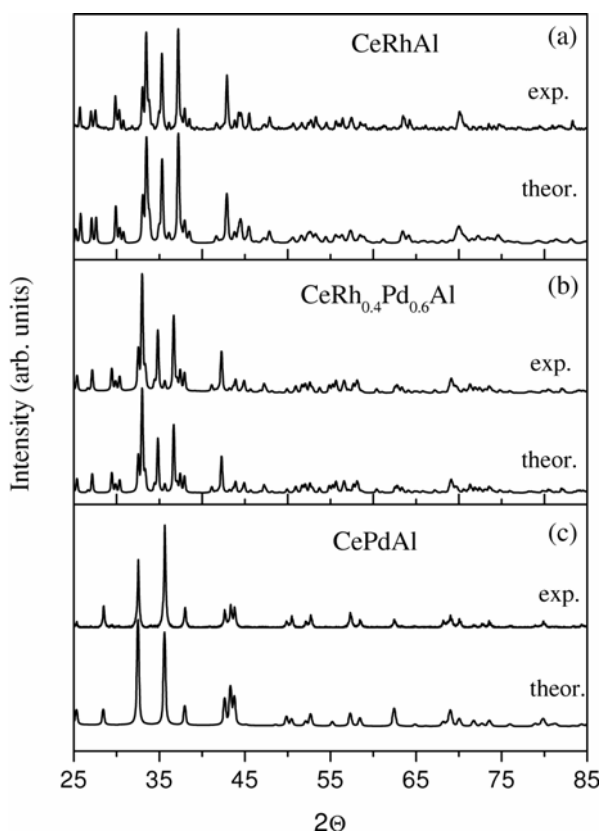


Fig. 1. XRD spectra and their calculated counterparts for CeRhAl , $\text{CeRh}_{0.4}\text{Pd}_{0.6}\text{Al}$, and CePdAl

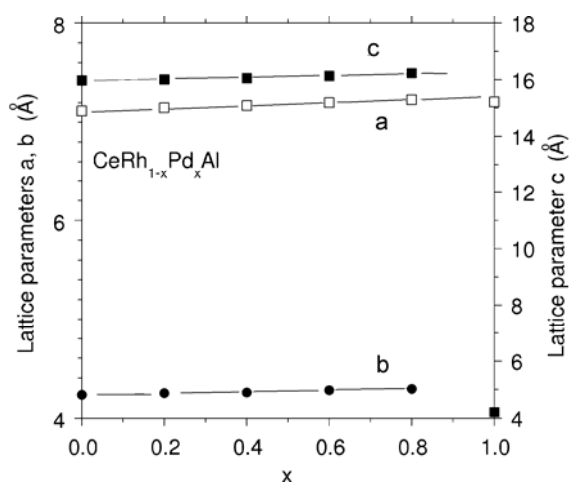
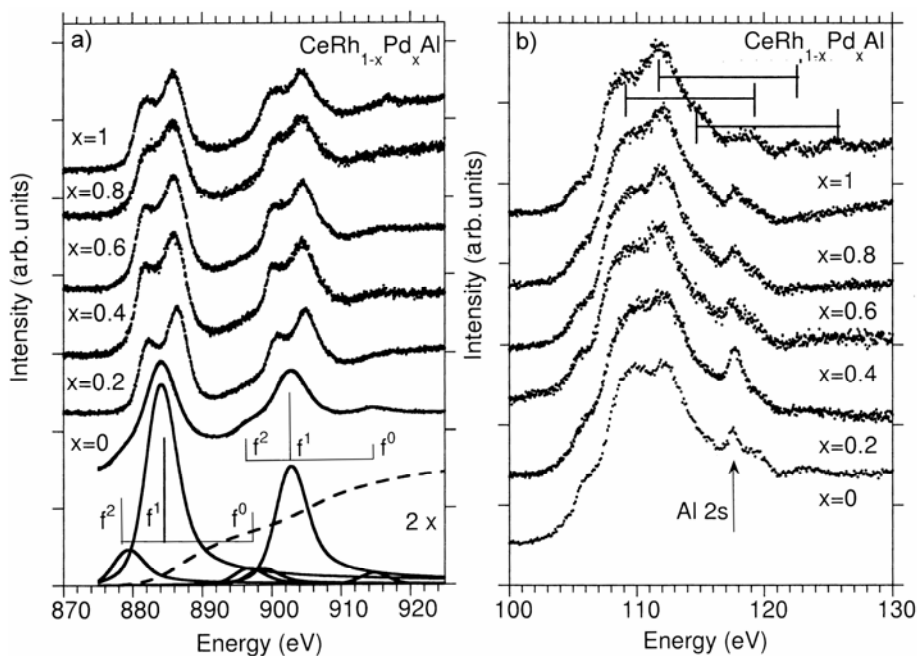
Fig. 2. Lattice parameters of $CeRh_{1-x}Pd_xAl$ 

Fig. 3. Ce 3d XPS (a) and Ce 4d XPS (b) spectra obtained for $CeRh_{1-x}Pd_xAl$. The f^0 , f^1 , and f^2 components in (a) are separated on the basis of Doniach–Šunjić theory. The satellite lines observed in the 3d XPS spectra of $CePdAl$ are interpreted as plasmon losses with an energy of $\hbar\omega_p \approx 11$ eV

Figure 2 shows the lattice parameters for the $CeRh_{1-x}Pd_xAl$ series, determined from the best fit to the XRD spectra obtained experimentally. The volume of the unit cell systematically increases with x , whereas for $CePdAl$ it rapidly decreases. $CeRh_{1-x}Pd_xAl$ samples with $x \leq 0.8$ have an orthorhombic $Pd_2(Mn,Pd)Ge_2$ -type structure,

which is a kind of a mixture of the orthorhombic CeRhSb and hexagonal CeRhSn-type structures [8], whereas the structure of CePdAl is hexagonal of the ZrNiAl-type [9].

Figure 3a shows the Ce 3d XPS spectra obtained for the series of compounds CeRh_{1-x}Pd_xAl. The contributions of the final states f^1 and f^2 are clearly observed, which exhibit a spin-orbit splitting of 18.6 eV. The presence of the f^0 component clearly marks the intermediate valence character of Ce atoms only for CeRhAl. Gunnarsson and Schönhammer (GS) have explained how to determine the properties of the initial f -state from Ce 3d XPS spectra [10] which are related to the final f -states. It is possible to estimate the hybridisation energy Δ from the ratio $r = I(f^2)/[I(f^1)+I(f^2)]$ (for details, see Ref. [10]), when the peaks of the 3d XPS spectra that overlap in Figs. 3 and 4 are separated (the method is described in Refs. [11–13]). The value of Δ is ~ 200 meV for CePdAl, ~ 190 meV for CeRh_{1-x}Pd_xAl samples with $x \leq 0.8$, and for CeRhAl it drastically decreases to ~ 70 meV.

The occupation number n_f of CeRh_{1-x}Pd_xAl is 0.9, whereas for the remaining CeRh_{1-x}Pd_xAl compounds $n_f \rightarrow 1$. We attribute the peak located at ~ 917 eV at the high-energy side of the f^1 component (see Fig. 4) in the 3d XPS spectra of CePdAl to plasmon losses with an energy of $\hbar\omega_p \approx 11$ eV. The same energy plasmons are visible in the Ce 4d XPS spectrum of CePdAl (see Fig. 3b).

There is a further evidence for the fluctuating valence of Ce in CeRhAl, as shown in Fig. 3b. The Ce 4d XPS spectra of CeRhAl exhibit two peaks, at ~ 119 and 123 eV, which can be assigned to the f^0 final state [10]. The indicated splitting of 3.1 eV has almost the same value as the spin-orbit splitting of the La 4d states.

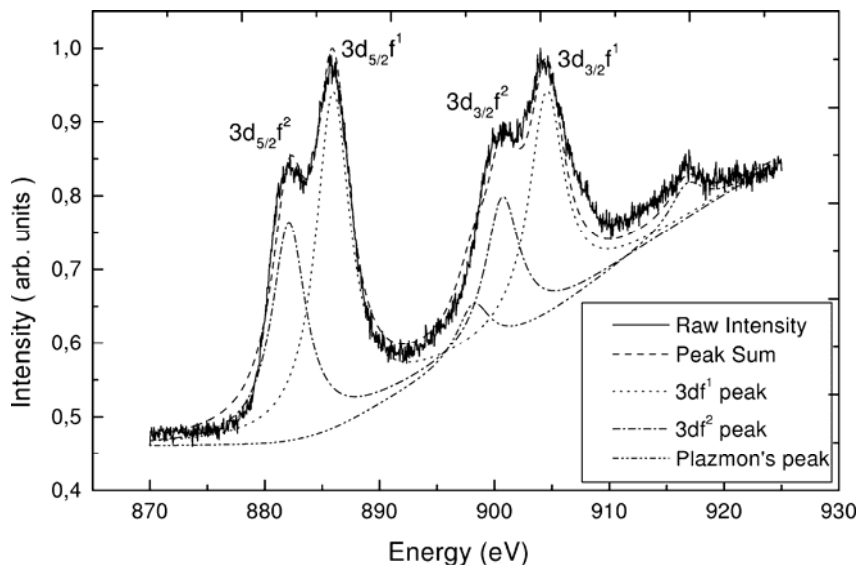


Fig. 4. Deconvolution of 3d Ce XPS spectra for CePdAl. The high-energy peaks located at 898 and 916.5 eV are of plasmon origin

We conclude that the Ce atoms of the components of the series $CeRh_{1-x}Pd_xAl$ containing Pd have stable f-shell configurations ($n_f = 1$), whereas $CeRhAl$ is an MV system. An increasing number of valence electrons (i.e. increasing x value) stabilize the occupation of the f shell ($n_f \rightarrow 0$). It is possible that both the stable configuration of Ce and the increasing number of conduction electrons give rise to the hexagonal structure of $CePdAl$ in the $CeRh_{1-x}Pd_xAl$ series of alloys.

Acknowledgements

The authors acknowledge the support of the State Committee for Scientific Research (KBN), through grant No. 1 P03B 052 28 and for the grant No. N202038 31/1805 of the Ministry of Science and Higher Education.

References

- [1] TAKABATAKE T., NAKAMOTO G., TANAKA H., BANDO Y., FUJI H., NISHIGORI S., GOSHIMA H., SUZUKI T., FUJITA T., OGURO I., HIRAOKA T., MALIK S.K., *Physica B*, 199–200 (1994), 457.
- [2] ŚLEBARSKI A., MAPLE M.B., FREEMAN E.J., SIRVENT C., RADLOWSKA M., JEZIERSKI A., GRANADO E., HUANG Q., LYNN J.W., *Phil. Mag. B*, 82 (2002), 943.
- [3] MALIK S.K., ADROJA D.T., *Phys. Rev. B*, 43 (1991), 6277.
- [4] TAKABATAKE T., FESHIMA F., FUJII H., NISHIGORI S., SUZUKI T., FUJITA T., YAMAGUCHI Y., SAKURAI J., JACCARD D., *Phys. Rev. B*, 41 (1990), 9607.
- [5] ŚLEBARSKI A., GORAUS J., HACKEMER A., SOLYGA M., *Phys. Rev. B*, 70 (2004), 195123.
- [6] DORADZIŃSKI R., SPALEK J., *Phys. Rev. B*, 58 (1998), 3293.
- [7] KUMAR N.H., MALIK S.K., *Phys. Rev. B*, 62 (2000), 127.
- [8] SCHWER H., HULLIGER F., *J. Alloys Comp.*, 259 (1997), 249.
- [9] KELLER L., DÖNNI A., KITAZAWA H., VAN DEN BRANDT B., *Appl. Phys. A* 74 (Suppl.) (2002), S686.
- [10] FAGGLE J.C., HILLEBRECHT F.U., ZOLNIEREK Z., LÄSSER R., FREIBURG CH., GUNNARSSON O., SCHÖNHAMMER K., *Phys. Rev. B*, 27 (1983), 7330.
- [11] DONIACH S., SUNJIC M., *J. Phys. C*, 3 (1970), 286.
- [12] DONIACH S., *Physica B, C*, 91 (1977), 231.
- [13] TOUGAARD S., SIGMUND P., *Phys. Rev. B*, 25 (1982), 4452.

Received 1 June 2005
Revised 10 October 2005

Electronic structures of intermetallic rare earth compounds

A. SZYTUŁA^{1*}, D. GOMÓŁKA¹, A. JEZIERSKI²,
B. PENC¹, E. WAWRZYŃSKA¹, A. WINIARSKI³

¹M. Smoluchowski Institute of Physics, Jagiellonian University, Reymonta 4, 30-059 Cracow, Poland

²Institute of Molecular Physics, Polish Academy of Sciences,
ul. M. Smoluchowskiego 17, 60-179 Poznań, Poland

³A. Chelkowski Institute of Physics, University of Silesia, Uniwersytecka 4, 40-007 Katowice, Poland

The electronic structures of intermetallic rare earth compounds of different compositions: RMn_2Ge_2 ($\text{R} = \text{Nd}, \text{Sm}$), $\text{R}_3\text{Mn}_4\text{Sn}_4$ ($\text{R} = \text{La}, \text{Ce}, \text{Nd}$), $\text{Ce}_3\text{Ag}_4\text{X}_4$ ($\text{X} = \text{Ge}, \text{Sn}$), and Ce_2MnGe_6 , have been investigated. XPS measurements were performed using a commercial LHS10 spectrometer. The valence band and core-level states have been analysed. In Mn compounds, the Mn 3d state forms a broad band near the Fermi level. The analysis of XPS spectra using the Gunnarsson–Schönhammer model gives the coupling parameters (hybridisation energy) between the R 4f states and electrons of the conduction band.

Key words: *rare earth compounds; transition metal compounds; electronic structure; photoelectron spectroscopy*

1. Introduction

The magnetic properties of ternary rare earth transition metal silicides, germanides, and stannides have been intensively studied over the last 30 years. Among these compounds, special attention is drawn by those of the R–Mn–X system in which it is expected that both rare earth and Mn atoms have localized magnetic moments. In this work, the electronic structures of compounds with Mn and isostructural compounds without Mn— RMn_2Ge_2 ($\text{R} = \text{Nd}, \text{Sm}$), RAg_2Ge_2 ($\text{R} = \text{Pr}, \text{Nd}$), $\text{R}_3\text{Mn}_4\text{Ge}_4$ ($\text{R} = \text{La}, \text{Ce}, \text{Nd}$), $\text{Ce}_3\text{Ag}_4\text{X}_4$ ($\text{X} = \text{Ge}, \text{Sn}$), and Ce_2MnGe_6 are investigated in order to determine their electronic structure. The valence band state and core-level states are also analysed.

*Corresponding author, e-mail: szytula@if.uj.edu.pl

RMn_2Ge_2 ($\text{R} = \text{Nd}, \text{Sm}$) and RAg_2Ge_2 compounds crystallize in the tetragonal ThCr_2Si_2 -type structure [1, 2]. In RMn_2Ge_2 compounds, the rare earth magnetic moments (Nd, Sm) order at low temperatures, whereas the Mn moments order close to 300 K [1]. PrAg_2Ge_2 remains paramagnetic down to 1.9 K, NdAg_2Ge_2 is an antiferromagnet at low temperatures [3], and Ce_2MnGe_6 is a ferrimagnet.

$\text{R}_3\text{Mn}_4\text{Sn}_4$ and $\text{Ce}_3\text{Ag}_4\text{X}_4$ compounds crystallize in an orthorhombic crystal structure of the $\text{Gd}_3\text{Cu}_4\text{Ge}_4$ -type [4, 5]. In $\text{R}_3\text{Mn}_4\text{Sn}_4$, the Mn moments order at about room temperature, whereas the rare earth moments order at low temperatures [5]. In $\text{Ce}_3\text{Ag}_4\text{X}_4$ magnetic order is found at low temperatures.

2. Experimental and results

XPS spectra were obtained at room temperature using a Leybold LHS10 electron photoemission spectrometer with MgK_α ($h\nu = 1253.6$ eV) and AlK_α ($h\nu = 1486.6$ eV) radiation. All experiments were performed in vacuum of about 10^{-9} mbar. The total energy resolution of the spectrometer with a hemispherical energy analyzer was about 0.75 eV for $\text{Ag } 3d$. Binding energies are given relative to the Fermi level ($E_F = 0$). The spectrometer was calibrated using $\text{Cu } 2p_{3/2}$ (932.5 eV), $\text{Ag } 3d_{5/2}$ (368.1 eV), and $\text{Au } 4f_{7/2}$ (84.0 eV) core-level photoemission spectra. Measurements were carried out at room temperature. The surfaces of the samples were mechanically cleaned by scraping with a diamond file in a preparation chamber under high vacuum (10^{-9} mbar) and then moved immediately to the analysis chamber. This procedure was repeated several times until the $\text{C } 1s$ and $\text{O } 1s$ core-level peaks became negligibly small or did not change after further scrapings. Such a cleaning procedure was performed before each XPS measurement. The Shirley method [6] was used to subtract background and the experimental spectra prepared in this manner were numerically fitted using the 80% Gaussian and 20% Lorentzian model.

The XPS spectra of the investigated compounds were measured over a wide binding energy range of 0–1100 eV. The binding energies were related to the Fermi level ($E_F = 0$ eV). The XPS valence bands (VB) of some of the investigated compounds are presented in Fig. 1.

The valence bands of all the Mn compounds have a similar character. The $\text{Mn } 3d$ state forms a broad band near the Fermi level. The $\text{R } 4f$ state, where R is a light rare earth element, forms a narrow band at 3 eV below E_F for $\text{R} = \text{Pr}$, and at 5 eV for $\text{R} = \text{Nd}$ and Sm . In RAg_2Ge_2 and $\text{Ce}_3\text{Ag}_4\text{X}_4$, the valence bands are dominated mainly by broad peaks near 5.8 eV, corresponding to $\text{Ag } 4d_{3/2}$ and $\text{Ag } 4d_{5/2}$ sites. A very weak peak near the Fermi level at ca. 1.2 eV, corresponding to the $(5d6s)^3$ state, is present. In $\text{Ce}_3\text{Ag}_4\text{X}_4$, an additional peak near 2.5 eV, corresponding to the $\text{Ce } 4f^1$ state, is observed. In RAg_2Ge_2 compounds, the peaks corresponding to $\text{Pr } 4f$ and $\text{Nd } 4f$ coincide with the $\text{Ag } 4d$ band. In all the investigated germanides the $\text{Ge } 4p$ and $4s$ bands,

and for the stannides the Sn 5p and 5s bands, form broad bands, which coincide with the states of 4f- and nd-electron elements. These results indicate the existence of a direct charge transfer from Ge or Sn to Mn.

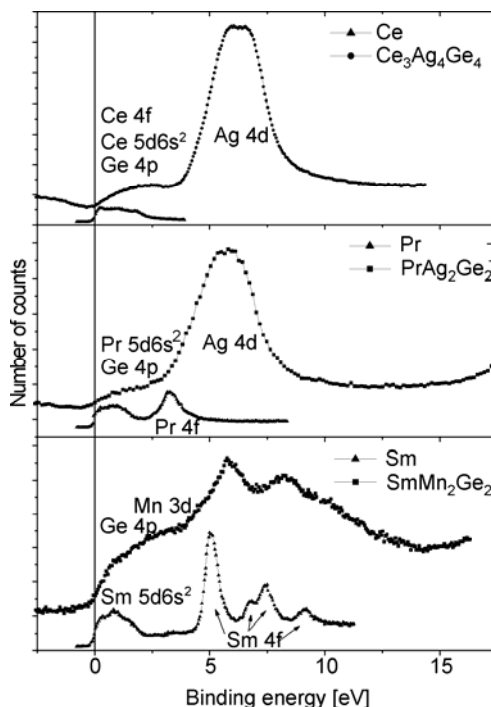


Fig. 1. XPS valence band spectra of $\text{Ce}_3\text{Ag}_4\text{Ge}_4$, PrAg_2Ge_2 , and SmMn_2Ge_2 compared to those of the pure elements [11]

For example, Figure 2 shows the $R 3d_{5/2}$ and $R 3d_{3/2}$ core-levels for $\text{Ce}_3\text{Ag}_4\text{Ge}_4$, PrAg_2Ge_2 , and SmMn_2Ge_2 . Similar patterns are observed for the other investigated compounds. The spin-orbit splitting, Δ_{S-O} , dominates the spectral structure of the 3d peaks. The determined values are listed in Table 1. The obtained values of Δ_{S-O} are independent of composition and increase with the increasing number of 4f electrons.

An analysis of the XPS spectra of $R 3d_{5/2}$ and $R 3d_{3/2}$ states based on the Gunnarsson-Schönhammer model [7] provides information on the hybridisation of 4f orbitals with the conduction band. The separation of the peaks based on Doniach-Šunjić theory [8] gives the ratio of $r = I(f^{n+1})/[I(f^n) + I(f^{n+1})]$. From the ratio r , it is possible to estimate the coupling parameter Δ . The coupling parameter Δ is defined as $\pi V^2 \rho_{\max}$, where ρ_{\max} is the maximum density of states of the conduction electrons and V is the hybridisation matrix. On the basis of the Gunnarsson-Schönhammer model, an estimation of Δ for Pr, Nd, and Sm compounds seems to be possible if one assumes that their calculated intensity ratios r change with Δ in the same way as for Ce [9, 10]. The determined values of the ratio r and adequate values of the coupling parameter Δ are summarized in Table 1.

The coupling parameter Δ has large values for the cerium compounds, particularly for those containing also manganese atoms. In this case, ρ_{\max} attains large values, be-

cause the Mn 3d band is at the Fermi level and the hybridisation energy between the Ce 4f states and conduction band is large. The density of states on the Fermi level for

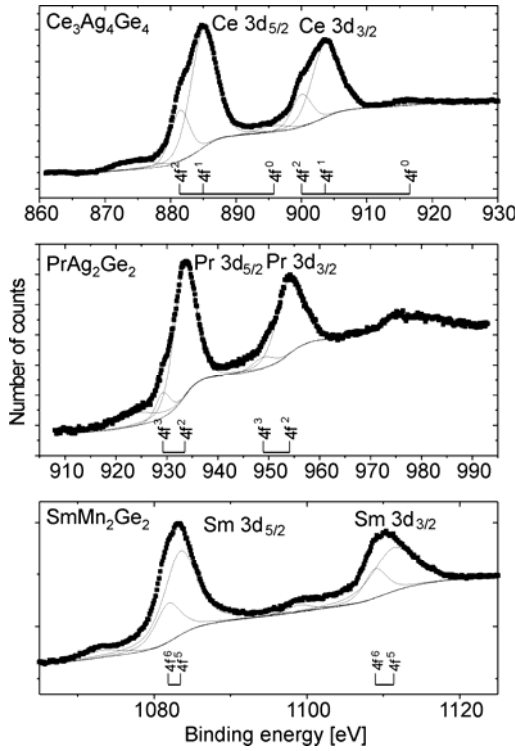


Fig. 2. 3d XPS spectra of $\text{Ce}_3\text{Ag}_4\text{Ge}_4$, PrAg_2Ge_2 , and SmMn_2Ge_2 . The broad, low intensity peaks, observed at 874 and 896 eV for $\text{Ce}_3\text{Ag}_4\text{Ge}_4$, 923 eV for PrAg_2Ge_2 , and 1068 and 1098 eV for SmMn_2Ge_2 , correspond to the $\text{K}\alpha_3$ and $\text{K}\alpha_4$ components of the X-ray radiation

Table 1. The values of r and corresponding hybridisation energy Δ

Compound	Δ_{S-O} (meV)	r	Δ (meV)	μ_{Mn} [μ_{B}]
NdMn_2Ge_2	22.4	0.07	37.5	2.7
SmMn_2Ge_2	27.4	0.18	80.0	3.0
PrAg_2Ge_2	20.5	0.09	58.0	
NdAg_2Ge_2	21.1	0.17	75.0	
Ce_2MnGe_6	18.7	0.25	126.0	2.0
$\text{Ce}_3\text{Mn}_4\text{Sn}_4$	19.0	0.35	186.0	
$\text{Nd}_3\text{Mn}_4\text{Sn}_4$	21.8	0.27	133.0	3.20(6)
$\text{Ce}_3\text{Ag}_4\text{Ge}_4$	18.7	0.33	169.0	
$\text{Ce}_3\text{Ag}_4\text{Sn}_4$	18.6	0.165	82.0	

the isostructural RMn_2Ge_2 ($\text{R} = \text{La}, \text{Y}$) compounds are 2.8 and 1.47 states/eV·atom, respectively [9]. The calculated Mn magnetic moments for these compounds are near $3.0\mu_{\text{B}}$, which is in good agreement with the Mn moment found in the compounds investigated here. The Mn 2p core-level spectra for RMn_2Ge_2 ($\text{R} = \text{Nd}, \text{Sm}$), $\text{R}_3\text{Mn}_4\text{Sn}_4$ ($\text{R} = \text{La}, \text{Ce}, \text{Nd}$), and Ce_2MnGe_6 have a similar character. The spin-orbit splitting of

the Mn 2p levels is between 10.9 and 11.6 eV, typical of Mn compounds. The values for $R\text{Ag}_2\text{Ge}_2$ ($R = \text{Pr}, \text{Nd}$) indicate the weakness of the coupling of 4f electrons and conduction band electrons, which manifests itself in the magnetic properties of these compounds.

In the $\text{Ce}_3\text{Ag}_4\text{X}_4$ ($X = \text{Ge}, \text{Sn}$) compounds an additional peak, corresponding to the $3d^9 4f^0$ configuration of the cerium ion, is observed. Based on the Gunnarsson–Schönhammer model [7], the intensity ratio $I(f^0)/[I(f^0)+I(f^1)+I(f^2)]$ which is directly related to the probability of f-occupation in the final state, reflects the f-occupation number n_f . The occupation number of the f shell, n_f , is equal to 0.95 for $\text{Ce}_3\text{Ag}_4\text{Ge}_4$ and 0.97 for $\text{Ce}_3\text{Ag}_4\text{Sn}_4$, which suggests the intermediate valence behaviour of Ce in these compounds.

The results obtained indicate a strong hybridisation of the 4f and conduction electrons in cerium compounds. This influences the Ce magnetic moment and other properties of the studied compounds. For Mn-compounds, the broad state of Mn 3d determines the magnetic moment and magnetic properties of these compounds.

References

- [1] SZYTULA A., LECIEJEWICZ J., [in:] *Handbook on the Physics and Chemistry of Rare Earths*, Vol.12, K. A. Gschneider Jr., L. Eyring (Eds.), Elsevier, Amsterdam, 1989.
- [2] SALAMAKHA P., ZAPLATYNSKY O., SOLOGUB O., BODAK O., *J. Alloys Comp.*, 239 (1996), 94.
- [3] SZYTULA A., BALANDA M., KACZOROWSKI D., BARAN S., GONDEK L., HERNÁNDEZ-VELASCO J., STÜSSER N., WAWRZYŃSKA E., *Intermetallics*, 14 (2006), 315.
- [4] RIEGER W., *Monatsh. Chem.*, 101 (1970), 449.
- [5] WAWRZYŃSKA E., BARAN S., LECIEJEWICZ J., SIKORA W., STÜBER N., SZYTULA A., *J. Phys.: Condens. Matter*, 15 (2003), 803.
- [6] SHIRLEY D. A., *Phys. Rev. B*, 5 (1972), 4709.
- [7] GUNNARSSON O., SCHÖNHAMMER K., *Phys. Rev. B*, 28 (1982), 4315.
- [8] DONIACH S., ŠUNJIĆ M., *J. Phys. C*, 3 (1970), 285.
- [9] ISHIDA S., ASAN S., ISHIDA J., *J. Phys. Soc. Jpn.*, 55 (1986), 936.
- [10] FUGGLE J. C., HILBRECHT F. U., ŻOLNIEREK Z., LÄSSER R., FREIBURG C., GUNNARSSON O., SCHÖNHAMMER K., *Phys. Rev. B*, 39 (1989), 3380.
- [11] LANG J. K., BAER Y., COX P. A., *J. Phys. F: Metal Phys.*, 11 (1981), 21.

Received 1 June 2005
Revised 10 October 2005

Electronic structure of $\text{Ce}_2\text{Rh}_3\text{Al}_9$

J. GORAUS^{1*}, A. ŚLEBARSKI¹, J. DENISZCZYK²

¹Institute of Physics, University of Silesia, ul. Bankowa 12, 40-007 Katowice, Poland

²Institute of Physics and Chemistry of Metals, University of Silesia,
ul. Bankowa 12, 40-007 Katowice, Poland

We have investigated the XPS spectra of $\text{Ce}_2\text{Rh}_3\text{Al}_9$ and calculated the DOS by using the full potential linear augmented plane wave (FP-LAPW) and tight binding linear muffin tin orbitals (TB-LMTO-ASA) methods. The overall agreement between the calculated and measured XPS valence band spectra is good. The analysis of the 3d XPS (X-ray Photoemission) spectra, using Gunnarson–Schonhammer theory, suggests a mixed valence behaviour of Ce. FP-LAPW calculations show a half-metallic behaviour of $\text{Ce}_2\text{Rh}_3\text{Al}_9$, whereas LMTO calculations result in a semiconducting and nonmagnetic ground state. This result is, however, in contradiction to the experimental observation of resistivity $\rho(T)$, which does not show an activated behaviour. We attribute the possible appearance of a semiconducting/half-metallic gap for $\text{Ce}_2\text{Rh}_3\text{Al}_9$ to atomic disorder.

Key words: strongly correlated electron system; Kondo insulators

1. Introduction

$\text{Ce}_2\text{Rh}_3\text{Al}_9$ is known to be a nonmagnetic heavy fermion (HF) compound [1, 2] which also shows features of mixed valence (MV) Ce-compounds in its magnetic data [3] and non-Fermi liquid behaviour. This rather unconventional behaviour of $\text{Ce}_2\text{Rh}_3\text{Al}_9$, which exhibits characteristics of both intermediate valent and HF compounds, did not, however, allow a coherent description. The temperature dependences of susceptibility and specific heat do not result from the crystalline field and/or Kondo effect, and suggest rather an intermediate valent Ce-state showing additional low energy interactions [4]. The aim of this work is to investigate the electronic structure of $\text{Ce}_2\text{Rh}_3\text{Al}_9$. Our calculations reveal the gap (or pseudogap) in the bands, located at the Fermi energy ε_f . Occurrence of this gap could explain the anomalous behaviour observed in susceptibility and resistivity below 35 K.

*Corresponding author, e-mail: jg@xps2.zfcst.us.edu.pl

2. Experimental details

Polycrystalline ingots were arc-melted using Ce (99.9%), Rh (99.9%), and Al (99.99%) in a high purity argon atmosphere on a water-cooled copper hearth with Zr getter, and annealed for six days at 1100 K. The $\text{Ce}_2\text{Rh}_3\text{Al}_9$ sample was examined by X-ray diffraction (Siemens D-5000) and it was found to consist of a single phase with lattice parameters $a = 13.146\text{\AA}$, $b = 7.688\text{\AA}$ and $c = 9.559\text{\AA}$, and suggested the $\text{Y}_2\text{Co}_3\text{Ga}_9$ structure type and a space group $Cmcm$ [3]. XPS spectra were obtained with a Physical Electronics PHI-5700 XPS spectrometer using monochromatised $\text{Al}_{K\alpha}$. From the survey spectra we found that there was neither carbon nor oxygen contamination. The electronic structure was calculated using the tight binding linear muffin tin orbitals (TB-LMTO-ASA) and full potential linear augmented plane wave (FP-LAPW) methods. In the LMTO method [5, 6] (exchange correlation), the potential was used in the form proposed by von Bart and Hedin [7] with generalized gradient corrections of the Langreth–Mehl–Hu [8] type. The sphere radii were chosen in such a way that the cell volume was equal to the volume of a formula unit, hence the spheres overlapped.

The electronic structure was computed for experimental lattice parameters. For the FP-LAPW method, we used the Wien2K package [9] with the general gradient approximation [10] for electron correlations. Both types of calculations were performed with spin-polarization and relativistic effects taken into account. In order to obtain VB XPS (valence band X-ray photoemission) spectra from DOS (density of states) calculations, we multiplied the partial DOS by the cross sections [11] and convoluted it with 0.4 eV gaussians.

3. Results and discussion

Figure 1 shows the Ce 3d XPS spectra which exhibit different final states depending on the occupation of the f shell: f^0 , f^1 , and f^2 [12, 13]. The f^0 components are clear evidence of the MV of Ce, the f^2 components are located at the low binding energy side, and the f^1 lines are attributed within the Gunnarson–Schonhammer (GS) theoretical model to the hybridisation between the f states and conduction band. The ground state f occupation number n_f (~ 0.8) was obtained from the relative intensity ratio, $I(f^0)/(I(f^0) + I(f^1) + I(f^2))$ (details in [12]). The intermediate valence of Ce, $\nu = 3.2$ ($n_f = 0.8$), seems to be too large due to several reasons, e.g. background subtraction and plasmons with energy $\hbar\omega_p = 12.5$ eV, which are visible in the 4d XPS spectra (see Fig. 2). The f^0 peak is usually located ca. 11 eV above the f^1 line, whereas the f^0 peak in Fig. 1 is very broad and shifted towards higher binding energies by about 3 eV. The correct Doniach–Sunjic analysis of the Ce 3d XPS spectra should also include the plasmon energy peak covered by the f^0 line. The separation of the plasmon intensities and f^0 line is, however, difficult. The hybridisation energy Δ (ca. 30 meV), was also estimated from these spectra on the basis of the GS method.

There is other evidence for the fluctuating valence of Ce ions in $Ce_2Rh_3Al_9$, as shown in Fig. 2. The Ce 4d XPS spectra exhibits two peaks above 120 eV, which are usually assigned to the f^0 final states [12].

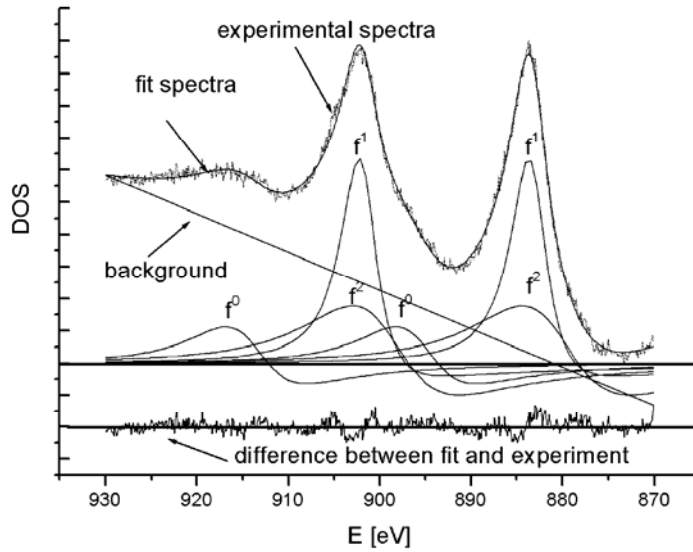


Fig. 1. Deconvolution of 3d Ce-XPS spectra for $Ce_2Rh_3Al_9$

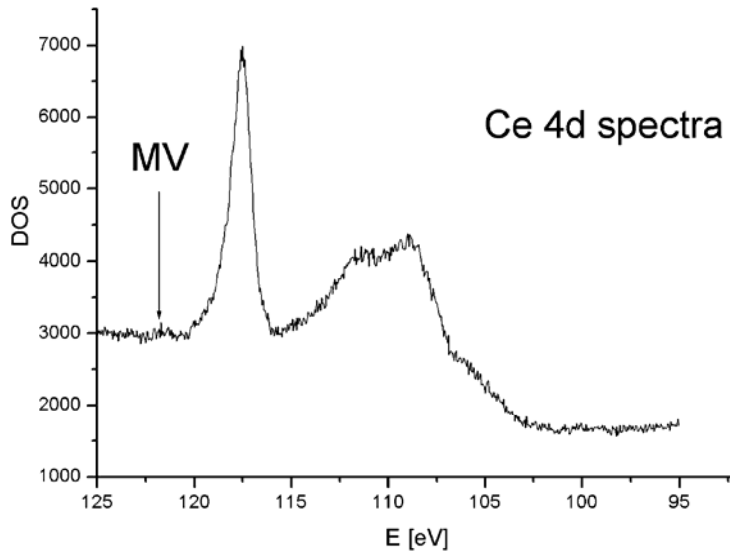


Fig. 2. Ce XPS 4d and Al 2s (sharp peak) spectra for $Ce_2Rh_3Al_9$

The overlapping peaks in Ce-3d spectra were separated using the Doniach–Sunjic approach [14,15] and the Tougaard background [16]. In Figures 3 and 4, the results of total DOS calculations are presented. LMTO results in a non-magnetic ground state

with the gap of ca. 3 meV at the Fermi level, whereas LAPW gives a pseudogap in one spin direction with the DOS of about 1 state/(eV f.u.) at ε_f and 30 state/(eV f.u.) in the opposite spin direction. In Figure 5, we present numerically calculated XPS valence band (VB) spectra and the measured ones. The agreement between the calculated and experimentally obtained bands is reasonably good, excluding the low-binding energies between 0 and 3 eV.

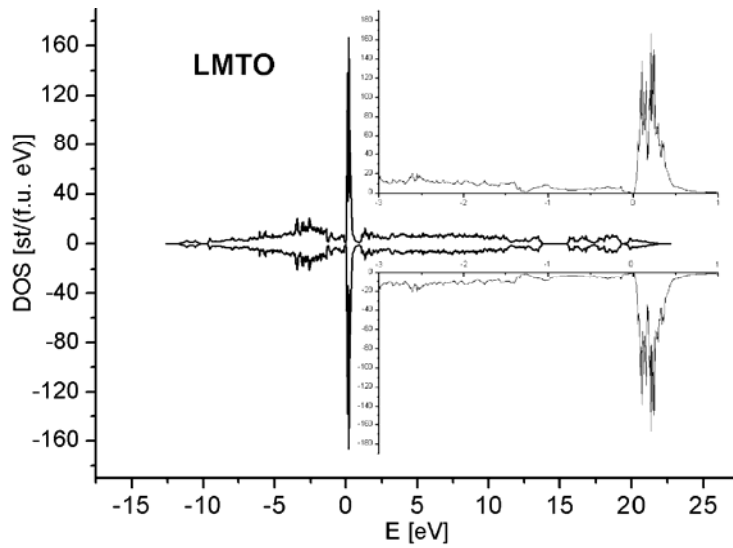


Fig. 3. LMTO calculation results for $\text{Ce}_2\text{Rh}_3\text{Al}_9$

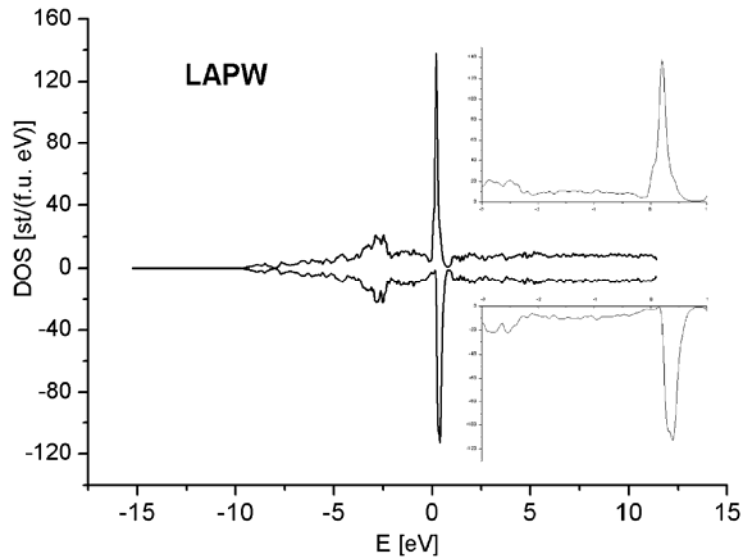
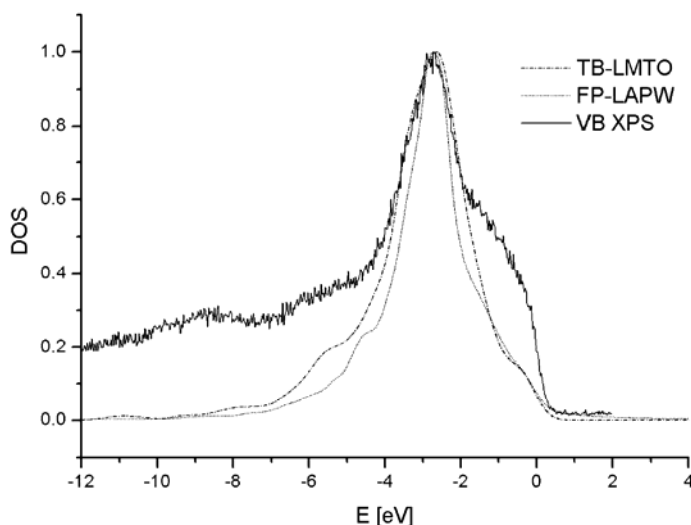


Fig. 4. LAPW calculation results for $\text{Ce}_2\text{Rh}_3\text{Al}_9$

Fig. 5. VB spectra for $Ce_2Rh_3Al_9$

Moreover, the LMTO DOSs are in better agreement with the experimental data between 5 and 10 eV than the LAPW ones. We attribute the low-energy divergence between the calculated and experimentally observed VB spectra to charge transfer and/or the energy shift of Ce 4f and Rh 4d bands due to interatomic hybridisation which is not taken into account by either methods.

The gap ΔE of ca. 3 meV resulting from LMTO calculations corresponds to $T \approx 35$ K. Note that the resistivity $\rho(T)$ data do not exhibit any evidence of activated behaviour (of the $\rho = \rho_0 \exp(\Delta E / (k_B T))$ type), the resistivity $\rho(T)$ curve, however, shows a clear hump at 35 K. One should note that DFT-type calculations assume the ground state at $T = 0$ K, while the DOSs are obtained for the lattice parameters measured at the room temperature. To obtain the unit cell volume, which depends on T , we also calculated the LMTO-DOS taking into account lattice thermal expansion, namely calculations were carried out for hypothetical lattice parameters that were 3.5% smaller and larger than those measured at room temperature. In effect, the gap is still present and its width is 65 meV or 40 meV, respectively. One could therefore expect that an activation behaviour could be observed under high pressure or can result from atomic substitution. Atomic disorder could be the reason why the gap is not observed in $\rho(T)$ data. Disorder usually removes the hybridisation gap, e.g. in the Kondo insulators. LMTO calculations give an occupation number of $n_f \approx 0.9$. This value is roughly comparable with that obtained from the Ce 3d XPS spectra analysis, and indicates the MV character of the $Ce_2Rh_3Al_9$ compound.

4. Conclusion

In this paper, we have discussed gap formation at the Fermi level in the electronic bands of $Ce_2Rh_3Al_9$. The LMTO calculations predict a gap of ca. 3 meV and the non-

magnetic ground state. We also discuss the influence of lattice thermal expansion on the ground state properties, i.e. thermally decreasing the lattice parameters stabilizes the gap at ε_f . We suggest that under pressure the resistivity should exhibit an activated behaviour, like in semiconductors, and a similar behaviour could be obtained by alloying. LAPW calculations predict the magnetic ground state with the magnetic moment of $0.27\mu_B$ on Ce atoms, and the pseudogap in one spin direction band. The LAPW pseudogap corresponds well to the resistivity results, however it is in contradiction to the magnetic results. Both methods give a Sommerfeld coefficient γ (for LAPW we obtained the value of about $2.35 \text{ mJ}/(\text{mol}\cdot\text{K})$ much smaller than the one experimentally obtained from the specific heat measurements [1]).

Acknowledgements

Two of the authors (J.G. and A.Š) acknowledge the support of the State Committee for Scientific Research (KBN), through Grant No. 1 P03B 052 28.

References

- [1] STRYDOM A.M., *Solid State Comm.*, 123 (2002), 343.
- [2] BUSCHINGER B., GEIBEL C., WEIDEN M., DIETRICH C., CORDIER G., OLESCH G., KOHLER J., STEGLICH F., *J. Alloys Comp.*, 260 (1997), 44.
- [3] NIERMANN J., FEHRMANN B., WOLFF M.W., JEITSCHKO W., *J. Sol. State Chem.*, 177 (2004), 2600.
- [4] BUSCHINGER B., TROVARELLI O., WEIDEN M., GEIBEL C., STEGLICH F., *J. Alloys Comp.*, 275–277 (1998), 633.
- [5] ANDERSEN O.K., JEPSEN O., *Phys. Rev. Lett.*, 53 (1984), 2571.
- [6] ANDERSEN O.K., JEPSEN O., *Physica B*, 91 (1977), 317.
- [7] VON BARTH U., HEDIN L., *J. Phys. C*, 5 (1972), 1629.
- [8] HU C.D., LANGRETH D.C., *Phys. Scr.* 32 (1985), 391.
- [9] BLAHA P., SCHWARZ K., MADSEN G., KVASNICKA D., LUITZ J., *WIEN2k, An Augmented Plane Wave + Local Orbitals Program for Calculating Crystal Properties*, Karlheinz Schwarz, Techn. Universität Wien, Austria, 2001.
- [10] PERDEW J.P., BURKE K., ERNZERHOF M., *Phys. Rev. Letters*, 77 (1996), 3865.
- [11] YEH J.J., LINDAU I., *At. Data Nucl. Data Tables* 32, (1985), 1.
- [12] FUGGLE J.C., HILLEBRECHT F.U., ZOLNIEREK Z., LASSER R., FREIBURG CH., GUNNARSON O., SCHONHAMMER K., *Phys. Rev. B*, 27 (1983), 7330.
- [13] GUNNARSSON O., SCHONHAMMER K., *Phys. Rev. B*, 28 (1983), 4315.
- [14] DONIACH S., SUNJIC M., *J. Phys. C*, 3 (1970), 286.
- [15] DONIACH S., *Physica B, C*, 91 (1977), 231.
- [16] TOUGAARD S., SIGMUND P., *Phys. Rev. B*, 25 (1982), 4452.

Received 1 June 2005
Revised 10 October 2005

Electronic structure of CeRhIn₅ and CeIrIn₅

M. GAMŻA^{1*}, A. ŚLEBARSKI¹, J. DENISZCZYK²

¹Institute of Physics, University of Silesia, Uniwersytecka 4, 40-007 Katowice, Poland

²Institute of Physics and Chemistry of Metals,
University of Silesia, Uniwersytecka 4, 40-007 Katowice, Poland

We have performed the full potential linearized augmented plane-wave (FP-LAPW) calculations of the layered cerium compounds CeRhIn₅ and CeIrIn₅, which belong to a novel, intensively investigated family of heavy fermion (HF) materials. The ground states of this compounds can be tuned between antiferromagnetism (AFM) and superconductivity (SC) by external pressure or doping. We have carried out X-ray photoelectron spectroscopy (XPS) experiments to compare recorded valence band spectra with theoretical calculations. We have also analysed the XPS 3d Ce spectra, to estimate the occupation of the Ce 4f shell and the hybridisation between 4f and conduction electrons. We have found and discussed the influence of the lattice parameter a and the df interatomic hybridization effect on the properties of ground state in the series of CeMIn₅ compounds.

Key words: *heavy fermions; electronic structure; XPS; superconductivity*

1. Introduction

Recently, much attention have attracted studies of the relationship between magnetism and superconductivity in HF compounds. In these materials, evolution of ground states as a function of pressure or chemical environment frequently is discussed in terms of Doniach's model [1, 2]. This model considers a subtle competition between the local on-site exchange interaction (Kondo effect) compensating the local magnetic moment, and the long-range magnetic interaction, which can lead to magnetic order through the Ruderman–Kittel–Kasuya–Yoshida (RKKY) mechanism. In few classes of HF compounds, the SC near the boundary between the magnetic and nonmagnetic region can be extorted either by pressure or doping in order to suppress the magnetic order.

CeMIn₅ (M = Co, Rh or Ir) are good examples of such materials. CeCoIn₅ and CeIrIn₅ are HF superconductors at ambient pressure with $T_C = 2.3$ K and 0.4 K, respectively [3, 4], while CeRhIn₅ ordered antiferromagnetically below $T_N = 3.8$ K ex-

*Corresponding author, e-mail: monikag3@o2.pl

hibits a transition to the superconducting state with $T_C \approx 2.2$ K at the pressure 2.5 kbar [5, 6]. All of those compounds are found to be located near the quantum critical point (QCP) in the Doniach phase diagram and are very intensively investigated. However, their unconventional ground states are still somewhat controversial. To understand the ground state properties, we calculated electronic structure of CeRhIn₅ and CeIrIn₅ by the FP-LAPW method. The results of the band structure calculations are compared with the XPS valence band spectra. We also investigated the Ce 3d XPS spectra, from which the occupation number of the Ce 4f shell and the hybridization energy between 4f shell and conducting band were determined. We present the results of GGA + U calculations for different correlation energies U and analyse the f–f correlation effects.

2. Experimental details

Polycrystalline samples of CeRhIn₅ and CeIrIn₅ were prepared by arc melting stoichiometric amounts of the elemental metals (Ce 99.99%, Rh 99.9%, Ir 99.99%, In 99.995% in purity) on a water cooled cooper hearth in an ultra-high purity Ar atmosphere with an Al getter. Each sample was remelted several times to promote homogeneity, and then annealed at 800 °C for 7 days. The samples were examined by X-ray powder diffraction analysis (XRD) and found to consist of a single phase. The lattice parameters (listed in Table 1) were obtained from the XRD patterns analysis using the POWDER-CELL program, and are in good agreement with those previously reported [7–10]. The XPS spectra were obtained with monochromatized Al K _{α} radiation at room temperature using a PHI 5700 ESCA spectrometer.

Table 1. Lattice parameters for CeCoIn₅, CeRhIn₅ and CeIrIn₅ (space group $P4/mmm$)

Lattice parameter	Compound		
	CeCoIn ₅ [21]	CeRhIn ₅	CeIrIn ₅
a [Å]	4.601	4.652	4.668
c [Å]	7.54	7.542	7.515

The electronic structure was studied by the full potential linearized augmented plane-wave (FP-LAPW) method [11] using the experimental lattice parameters. The gradient corrected local spin density exchange (LSD XC) potential in the form proposed by Perdew, Burke and Ernzerhof [12] was included. In the calculations, the core levels were treated completely relativistically, while for valence states relativistic effects were included either in a scalar relativistic treatment [13] or with the second variational method using the scalar-relativistic eigenfunctions as basis, including spin-orbit coupling [14]. CeMIn₅ compounds are strongly correlated systems, we therefore go beyond the standard generalized gradient approximation (GGA) and include orbital

dependent potentials in methods GGA + U, introduced by Anisimov et al. [15], with an approximate correction for the self-interaction correction.

3. Results and discussion

Figure 1 shows the results of numerical calculations of the total electronic density of states (DOS) for paramagnetic $CeRhIn_5$ and $CeIrIn_5$. The DOSs were convoluted by

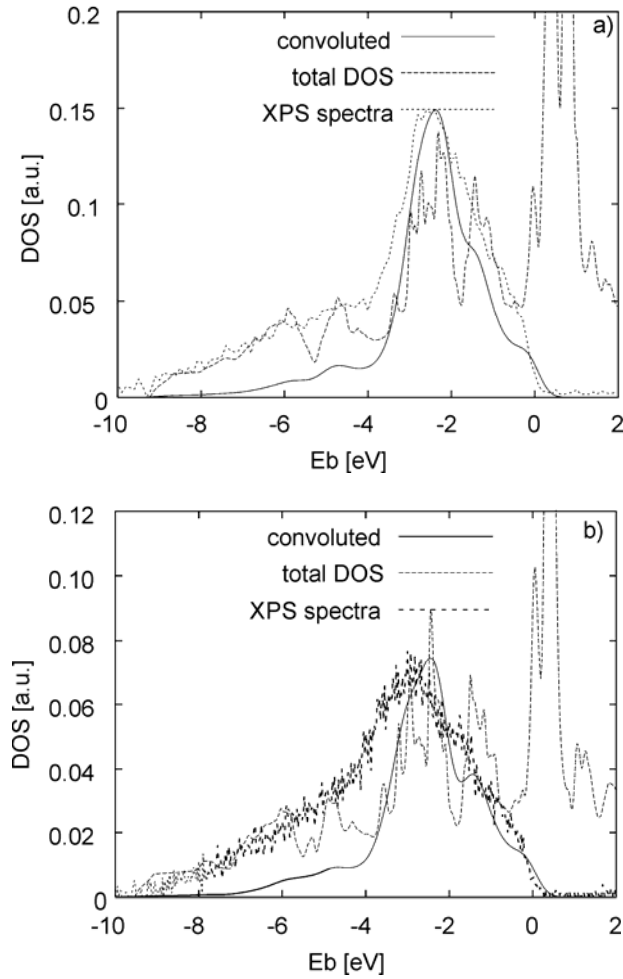


Fig. 1. XPS valence band spectra for paramagnetic $CeRhIn_5$ (a) and $CeIrIn_5$ (b)

Lorentzians with a half-width of 0.35 eV to account for the instrumental resolution. The partial DOSs were multiplied by the corresponding cross sections [16]. A background, calculated by means of the Tougaard algorithm [17], was subtracted from the

XPS data. The agreement between the calculated and measured XPS valence band spectra is good. The spectra reveal that the valence bands of CeRhIn_5 and CeIrIn_5 have a major peak mainly due to the d states of Rh or Ir located near the Fermi level. The second peak centred at about 5 eV is mainly due to the In states. The Ce 4f states give only negligible contribution to the total XPS spectra of CeRhIn_5 and CeIrIn_5 .

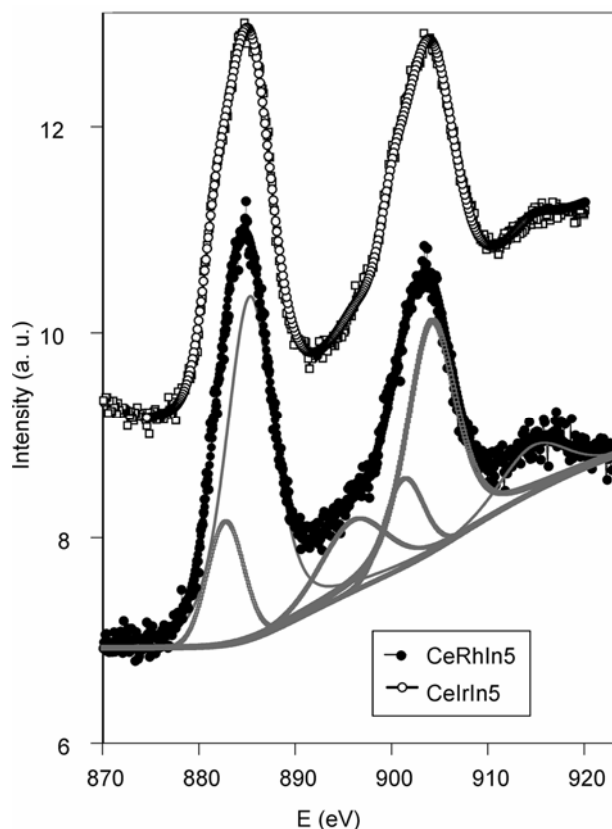


Fig. 2. Ce 3d XPS spectra for CeRhIn_5 and CeIrIn_5 . For CeRhIn_5 , separated and overlapping peaks attributed to the $4d^9f^2$, $4d^9f^1$ and $4d^0f^0$ final states are also shown

Figure 2 shows the Ce 3d XPS spectra for CeRhIn_5 and CeIrIn_5 . Three final-state contributions f^0 , f^1 and f^2 exhibit a spin-orbit splitting $\Delta_{\text{so}} = 18.6$ eV. The separation of the overlapping peaks in the Ce 3d XPS spectra was made on the basis of the Doniach–Šunjić theory [18]. The appearance of the f^0 components suggest the mixed valence behavior of Ce, while the f^2 peaks located at the low-binding energy side of the f^1 components are attributed to the hybridization between the f states and the conduction band. Based on the Gunnarson–Schönhammer (GS) theoretical model [19, 20], we have estimated the f-occupation number n_f and the hybridization energy Δ for the both compounds. The n_f value is 0.89 for CeRhIn_5 and 0.95 for CeIrIn_5 . Our

FP-LAPW calculations as well as the FP-LMTO [21] indicate that Ce is nearly trivalent in $CeRhIn_5$ and in $CeIrIn_5$, which is in contradiction to the results obtained from the Ce 3d XPS spectra. The hybridization energy Δ is ca. 89 meV for $CeRhIn_5$, while for $CeIrIn_5$ Δ is slightly higher (92 meV) which could be explained by the following: the SC ground state of $CeIrIn_5$ is equivalent to that of $CeRhIn_5$ under external pressure, which usually increases hybridization effect (see also discussion of the resonant df XPS spectra in Ref. [22]).

The spin-polarized calculations make preference for the magnetic ground state in both compounds and the magnetic moment is calculated only for Ce (considering for simplicity the ferromagnetic order and magnetic moments along the c axis). The electronic structures of $CeRhIn_5$ and $CeIrIn_5$ are similar (compare Figs. 3 and 4). For $CeRhIn_5$ we have also performed antiferromagnetic (AF) calculations, an AF order, however, has a very small effect on the magnitude of magnetic moments and the shape of DOSs.

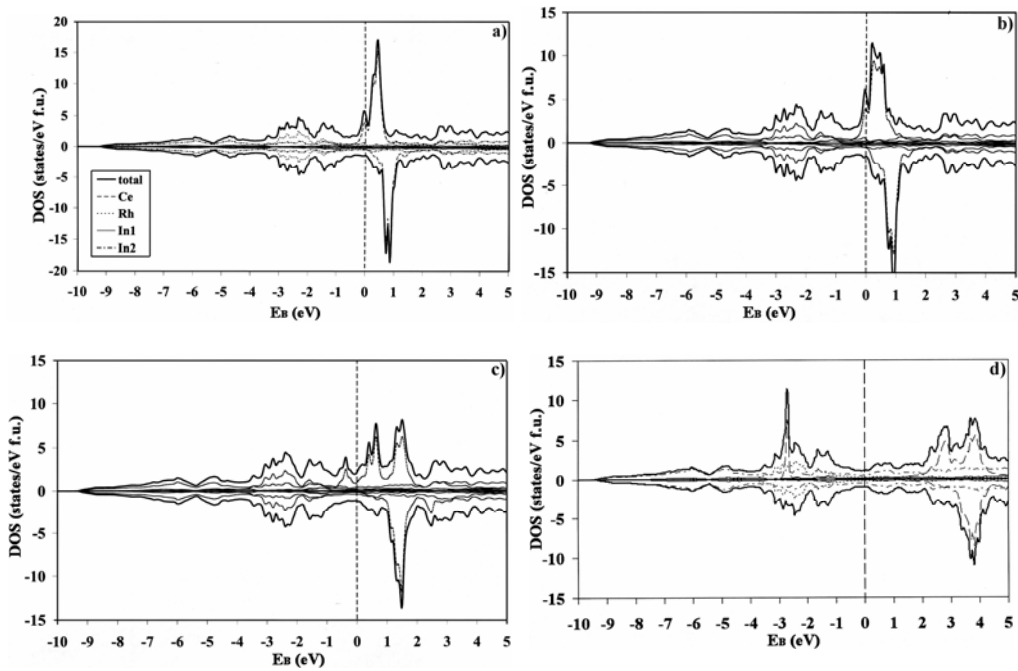


Fig. 3. Total and partial spin up and spin down DOSs for $CeRhIn_5$ calculated by the following methods: GGA (a), GGA + SO (b), GGA + SO + U (1.65 eV) (c) and GGA + SO + U (6.8 eV) (d)

The FP-LAPW calculations beyond the GGA allowed us to investigate the strength of the correlation effects of the Ce 4f electrons in $CeRhIn_5$. The GGA + U calculations give the best agreement of the calculated magnetic moment to the experimental value of ca. $0.37\mu_B$ [23] for the correlation energy $U = 1.65$ eV. This U -value is slightly larger than that of ca. 1.5 eV, acquired from FP-LMTO [21].

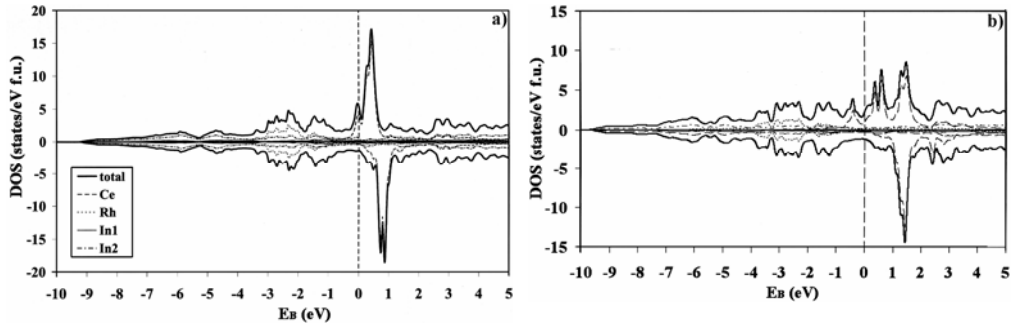


Fig. 4. Total and partial spin up and spin down DOSs for CeIrIn₅ calculated by: GGA (a) and by GGA + SO + U (1.75 eV) (b)

In Figure 3, we have shown for comparison the total and partial DOSs for CeRhIn₅ calculated by GGA, GGA + SO and GGA + SO + U method with $U = 1.65$ eV and $U = 6.8$ eV, respectively (typical value of Ce compounds). The correlation energy in the GGA + U calculations causes progressive localization of the 4f states and leads to a change of the ground state from itinerant to localized, while the GGA calculations suggest the itinerant magnetism. In our opinion the Ce 4f states are on the border between localization and itinerancy.

Table 2. Density of states at the Fermi level DOS (E_F), calculated (M_c) and experimental (M_{exp}) values of the total magnetic moment on Ce atom in CeRhIn₅ and in CeIrIn₅

Parameter	CeRhIn ₅				CeIrIn ₅			
	GGA	GGA + SO	GGA + SO + U (1.65 eV)	GGA + SO + U (6.8 eV)	GGA	GGA + SO	GGA + SO + U (1.65 eV)	GGA + SO + U (6.8 eV)
M_c [μB]	–	0.201	0.37	0.444	–	0.195	0.364	0.435
M_{exp} [μB]	0.37 [23]				–			
DOS [E_F]	6.79	7.19	3.33	2.1	6.56	7.26	3.3	2.03

The nature of the ground state of CeMT₅, discussed here on the basis of the Doniach model [1, 2], depends both on the exchange $J(\text{f-s})$ coupling and the DOS (E_F). However, the DOS (E_F) of the CeMIn₅ series are almost the same (Table 2), therefore in framework of this model, the magnetic or nonmagnetic behaviour results from the strength of $J \sim 1/V$, where V is a unit cell volume. Increasing the pressure or chemical substitution, which both lead to decreasing of the lattice parameters a , could provoke the magnetic–nonmagnetic phase transition due to the change of J coupling. Another reason of the magnetic/nonmagnetic ground state is a hybridization between Ce 4f and M 3d states along c axis, which could delocalize the f states and in consequence form the nonmagnetic ground state, too.

Table 3. The pf and df hybridization parameter for Ce–In1 (0.5, 0.5, 0), Ce–In2 (0, 0.5, 0.3103(6)) and Ce–M interactions, calculated by FP-LMTO method and the total fp (V_{pf}) and fd (V_{df}) hybridization energies estimated by Kumar et al. [24] using parameters from the tight binding approximation of Harrison, summing the values over all nearest neighbours

Compound	pf and df hybridization parameter $\times 10^3$ [eV ²]			Hybridization energy [eV]	
	Ce–In1	Ce–In2	Ce–M	V_{df}	V_{pf}
CeCoIn ₅	6.08	14.36	0.19	0.307	2.066
CeRhIn ₅	5.88	15.27	0.58	0.572	2.03
CeIrIn ₅	6.16	17.04	0.77	0.627	2.031

Nonmagnetic CeCoIn₅ and AF CeRhIn₅ are good examples of the situation (i), their lattice parameters a are distinctly different (Table 1), whereas the fd hybridization strengths are very similar (see Table 3). Moreover, a transition to the SC state observed under a pressure of ~ 1.6 kbar in the magnetic CeRhIn₅ [5, 6] could be attributed to strong lattice contraction (i.e., increasing of J), experimentally observed [24].

The second reason (ii) is clearly documented when one compares the properties of CeRhIn₅ and CeIrIn₅; their unit cell volumes are very similar (Table 1), while the fd hybridization energies are different. On the base of (ii), we can understand the magnetic or nonmagnetic properties of the respective compounds at $T = 0$.

Note, that the interatomic hybridization between Ce 4f and In 5p states is dominant in the CeMIn₅ series (Table 3), however, this energy is the same in CeRhIn₅ and in CeIrIn₅, therefore it cannot decide about the ground state behaviour. The most important effect, we believe, is attributed to the fd hybridization strength, nevertheless, this energy is about one order in magnitude weaker than the fp interaction.

4. Conclusions

The magnetic/nonmagnetic character of the ground state of the CeMIn₅ is the result of the competition between effect of pressure exerted in the direction parallel to the basal plane of the unit cell and the hybridization between Ce 4f and the transition metal d-states. Both, strong fd hybridization and contraction of the lattice parameter a cause delocalization of the 4f states and, in consequence, lead to demagnetization and probably to a superconducting ground state.

We have found, that Ce in CeRhIn₅ and CeIrIn₅ are nearly trivalent, and the hybridization between the f states and the conduction electrons is stronger in CeIrIn₅. This suggests that f electrons in the superconducting CeIrIn₅ are more delocalized than those in AF CeRhIn₅, but generally the electronic structure of the both compounds is very similar. When strong correlation effects between the f electrons were taken into account by the GGA + U approach ($U \approx 1.65$ eV), the calculated total magnetic moment on the cerium atom in CeRhIn₅ is well compared to that obtained from neutron diffraction. The GGA + U calculations show that the 4f electrons both in

CeRhIn₅ and CeIrIn₅ are closed to the border which separates the localized and delocalized (itinerant) states.

Acknowledgements

The support of KBN through Grant No. 1 PO3B 052 28 is acknowledged.

References

- [1] DONIACH S., *Valence Instability and Related Narrow Band Phenomena*, Plenum Press, New York, 1977.
- [2] DONIACH S., *Physica B*, 23 (1977), 231.
- [3] PETROVIC C., MOVSHOVICH R., JAIME M., PAGLIUSO P.G., HUNDLEY M.F., SARRAO J.L., FISK Z., THOMPSON J.D., *Europhys. Lett.*, 53 (2001), 354.
- [4] PETROVIC C., PAGLIUSO P.G., HUNDLEY M.F., MOVSHOVICH R., SARRAO J.L., THOMPSON J.D., FISK Z., *J. Phys.: Condens. Mater.*, 13 (2001), L337.
- [5] HEGGER H., PETROVIC C., MOSHOPOULOU E.G., HUNDLEY M.F., SARRAO J.L., FISK Z., THOMPSON J.D., *Phys. Rev. Lett.*, 84 (2000), 4986.
- [6] THOMPSON J.D., MOVSHOVICH R., FISK Z., BOUGUET F., CURRO N.J., FISHER R.A., HAMMEL P.C., HEGGER H., HUNDLEY M.F., JAIME M., PAGLIUSO P.G., PETROVIC C., PHILLIPS N.E., SARRAO J.L., *J. Magn. Magn. Mater.*, 226 (2001), 5.
- [7] PAGLIUSO P.G., PETROVIC C., MOVSHOVICH R., HALL D., HUNDLEY M.F., SARRAO J.L., THOMPSON J.D., FISK Z., *Phys. Rev. B*, 64 (2001), 100503.
- [8] KALYCHAK YA.M., ZAREMBA V.I., BARANYAK V.M., BRUSKOV V.A., ZAVALII P.Y., *Izv. Akad. Nauk SSSR, Metally*, (1989), 213–215.
- [9] PAGLIUSO P.G., MOVSHOVICH R., BIANCHI A.D., NICKLAS M., MORENO N.O., THOMPSON J.D., HUNDLEY M.F., SARRAO J.L., FISK Z., *Physica B*, 312–313 (2002), 129.
- [10] ZAPF V.S., FREEMAN E.J., BAUER E.D., PETRICKA J., SIRVENT C., FREDERICK N.A., DICKEY R.P., MAPLE M.B., *Phys. Rev. B*, 65 (2001), 014506.
- [11] BLAHA P., SCHWARZ K., MADSEN G.K.H., KVASNICKA D., LUITZ J., *An Augmented Plane Wave + Local Orbitals Program for Calculating Crystal Properties*, Karlheinz Schwarz, Techn. Universität Wien, 2001.
- [12] PERDEW J.P., BURKE S., ERNZERHOF M., *Phys. Rev. Lett.*, 77 (1996), 3865.
- [13] KOELLING D.D., HARMON B.N., *J. Phys. C: Sol. St. Phys.*, 10 (1977), 3107.
- [14] MACDONALD A.H., PICKETT W.E., KOELLING D.D., *J. Phys. C: Sol. St. Phys.*, 13 (1980), 2675.
- [15] ANISIMOV V.I., SOLOVYEV I.V., KOROTIN M.A., CZYZYK M.T., SAWATZKY G.A., *Phys. Rev. B*, 48 (1993), 16929.
- [16] YEH J.J.L LINDAU I., *At. Data Nucl. Data Tables*, 32 (1985), 1.
- [17] TOUGAARD S.L SIGMUND P., *Phys. Rev. B*, 25 (1982), 4452.
- [18] DONIACH S.L ŠUNJIĆ M., *Phys. C*, 3 (1970), 286.
- [19] GUNNARSON O., SCHONHAMMER K., *Phys. Rev. B*, 28 (1983), 4315.
- [20] FUGGLE J.C., HILLEBRECHT F.U., ŹOLNIEREK Z., LÄSSER R., FREIBURG CH., GUNNARSON O., SCHÖNHAMMER K., *Phys. Rev. B*, 27 (1983), 7330.
- [21] WANG J.L., ZENG Z., ZHENG Q.Q., LIN H.Q., *J. Appl. Phys.*, 93 (2003), 10.
- [22] FUJIMORI S., OKANE T., OKAMOTO J., MAMIYA K., MURAMATSU Y., FUJIMORI A., HARIMA H., AOKI D., IKEDA S., SHISHIDO H., TIKIWA Y., HAGA Y., ONUKI Y., *Phys. Rev B*, 67 (2003), 144507.
- [23] BAO W., PAGLIUSO P.G., SARRAO I.L., THOMPSON I.D., FISK Z., LYNN J.W., ERWIN R.W., *Phys. Rev. B*, 62 (2000), R14621.
- [24] KUMAR R.S., CORNELIUS A.L., SARRAO J.L., *Phys. Rev. B*, 70 (2004), 214526.

Received 1 June 2005
Revised 10 October 2005

Magnetic interaction in RT_xX_2 ternary compounds

A. GIL*

Department of Mathematical and Natural Sciences, Jan Długosz University,
Armii Krajowej 13/15, 42-200 Częstochowa, Poland

This work is an attempt to systematize the magnetic properties of RT_xX_2 (R – rare earth, T – transition metal, X – Si, Ge, Sn) compounds crystallizing in the orthorhombic CeNiSi₂-type structure. All silicides crystallize in the stoichiometric structure RTX_2 , while germanides and stannides form mainly defected RT_xX_2 structures ($0 < x < 1$). This family of compounds exhibits a complex magnetic behaviour. Two factors influencing stability of various magnetic structures are considered with the purpose of finding the magnetic ordering scheme: magnetic interactions of the RKKY type and crystal electric field effect.

Key words: *rare earth compounds; magnetic structure; RKKY model; crystal electric field effect*

1. Introduction

RT_xX_2 -type metallic compounds, where R is a rare-earth element, T is a 3d-electron element, and X is a p-electron element ($X = \text{Si, Ge, Sn}$) have been intensively investigated. The majority of these compounds crystallize in the orthorhombic CeNiSi₂-type structure [1].

The research is partially motivated by the possibility of obtaining novel, promising magnetic materials. The atoms in these structures: Ce (R), Ni (T), Si1 (X1), and Si2 (X2) occupy the 4(c) positions – $(0, y, 1/4)$, $(0, -y, 3/4)$, $(1/2, 1/2 + y, 1/4)$, $(1/2, 1/2 - y, 3/4)$ with different values of the y parameter.

All silicides crystallize in the stoichiometric structure, while germanides and stannides form mainly defected RT_xX_2 structures ($0 < x \leq 1$) with vacancies in the transition metal sublattice [2]. The stability of the crystal structure is determined by the radius of the X atoms (Si, Ge, Sn) and the degree in which the 3d band of the T element is filled up [3].

*E-mail: a.gil@ajd.czest.pl

2. Magnetic properties

Magnetic properties of RT_xX_2 compounds were studied by means of magnetic susceptibility and neutron diffraction measurements. All the magnetic data for RT_xX_2 compounds can be found in Refs. [4–37]. The measurements indicate that the majority of these compounds order antiferromagnetically at low temperatures. Above their Néel temperatures, their effective magnetic moments are close to free R^{3+} ion values $g(J(J+1))^{1/2}$. Only for compounds with $T = \text{Mn}$, the magnetic moment localized on Mn is observed.

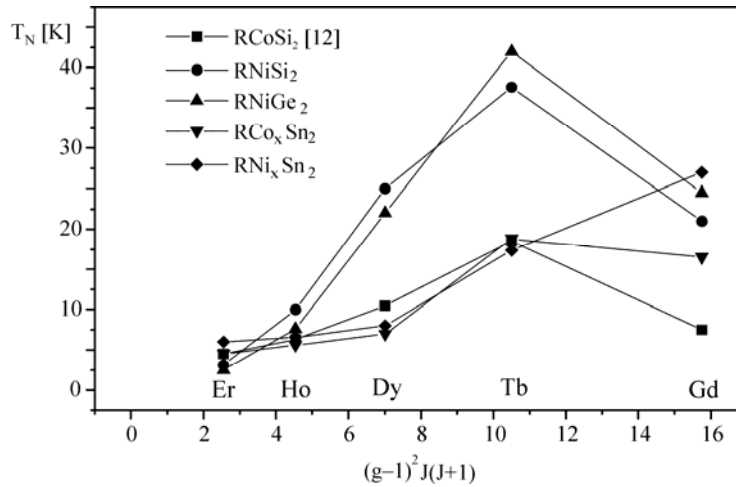


Fig. 1. Observed Néel temperatures in some RT_xX_2 intermetallics versus the de Gennes function $(g-1)^2J(J+1)$

Crystal structure of the compounds under investigation has a distinct layer character. Rare-earth atoms occupy layers perpendicular to the b -axis and are separated by layers of other atoms. In the majority of the compounds, the magnetic moments located on the same planes are coupled ferromagnetically, while the coupling between moments on adjacent planes is antiferromagnetic. The $R^{3+}-R^{3+}$ distances are large (in TbNiSi_2 $d_{R-R} = 4.012 \text{ \AA}$, in TbNiGe_2 $d_{R-R} = 4.086 \text{ \AA}$, and in TbNiSn_2 $d_{R-R} = 4.021 \text{ \AA}$), suggesting that direct magnetic interactions are highly improbable. The stability of the observed magnetic ordering schemes may be considered as being due to interactions via conduction electrons as described by the RKKY model [38–40]. RKKY interactions are long-range, which should in general lead to modulated magnetic structures. In the case of the studied series, one can observe a wide variety of orderings: collinear and non-collinear.

In this mechanism, the ordering temperature T_N should be proportional to the de Gennes factor [41]: $G = (g-1)^2J(J+1)$, where g is the Landé factor and J the total angular momentum of the considered rare-earth ion, which is highest for Gd-containing compounds. For the majority of systems, the maximum appears at $R = \text{Tb}$

(Fig. 1). The $T_{c,N}$ shift may result from the crystalline electric field effect (CEF). Thus, CEF terms should be added to the exchange Hamiltonian. The rare-earth ions are in the $4(c)$ sites of low mm symmetry. Neither experimental nor calculated data concerning CEF parameters for RTX_2 are available.

A comparison of structural and magnetic properties for the stoichiometric $TbNiGe_2$ compound and non-stoichiometric $TbNi_xGe_2$ compounds indicates that the lattice parameter b decreases from 16.681 Å to 16.142 Å with decreasing concentration x of Ni, and the ordering temperature T_N also decreases linearly from 42 K to 16 K. The antiferromagnetic structures are similar, whereas the magnetic moments are different. Increasing the number of defects in the Ni sublattice decreases the distances between the Tb planes, which should lead to an increase in the Néel temperature, but this is not observed.

According to RKKY theory, the exchange integral $J(R_{ij})$ between i -th and j -th magnetic ions is proportional to the conduction electron density of states at the Fermi surface for one spin direction $N(E_F)$ and to the oscillating function $F(x)$ of the distance R_{ij} and Fermi vector \mathbf{k}_F : $J(R_{ij}) \sim N(E_F)F(x)$, where $F(x) = (x\cos x - \sin x)x^{-4}$, and $x = 2k_F R_{ij}$. The function $F(x)$ depends on the Fermi vector, which is connected to the concentration of conduction electrons. XPS measurements of intermetallic compounds $RNiX$ [42] have shown that the 3d band of Ni is close to the Fermi level. A change in the Ni concentration leads to a reduction of the number of states at the Fermi level and influences the strength of ordering.

One can also describe the magnetic ordering in RTX_2 compounds by five exchange integrals: J_1 and J_2 within the same (010) plane, which are strongly ferromagnetic, and J_3 – J_5 describing the coupling between planes (Fig. 2).

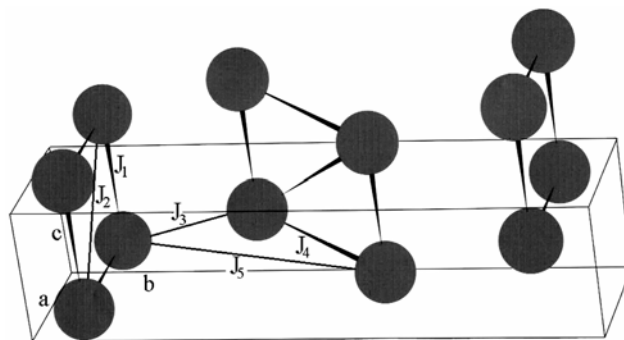


Fig. 2. Exchange integrals describing the ordering between magnetic ions in the crystal structure of $CeNiSi_2$

In the G-type antiferromagnetic structure [43], most often observed in RTX_2 compounds with the $CeNiSi_2$ -type crystal structure, the exchange integral J_5 is positive, while J_3 and J_4 are negative. In the A-type antiferromagnetic structure, observed in $HoNiSi_2$, J_3 is positive while J_4 and J_5 are negative; in the C-type structure observed in $CeCu_{0.86}Ge_2$, J_4 is positive while J_3 and J_5 are negative.

In compounds with a complex magnetic structure, where the magnetic cell is either commensurate or incommensurate with the crystal structure, the magnetic ordering is compatible with one of the above-mentioned models. The appearance of complex magnetic structures suggests that long-range magnetic ordering, probably realized by conduction electrons, plays a dominant role in forming the magnetic ordering.

Ferromagnetic ordering is observed in the compounds with Pr and Nd. The majority of compounds with Si and Ge order antiferromagnetically, and the magnetic structure is of the G (+ - + -) type but compounds with Sn are antiferromagnetics of the A (+ - - +) or C (+ + - -) type.

The ordering described by the J_3 exchange integral is realized through the layer with T and X elements, and J_4 is realized through p-electron atoms, but J_5 is described by long-range ordering probably realized by conduction electrons. J_5 is negative for compounds with Sn (A, C structure types), while for compounds with Si and Ge it is positive. The unit cell volume for Sn compounds is larger than for Si, Ge compounds and suggests the differences in interatomic distances. According to RKKY theory, the exchange integral oscillates with the distance R_{ij} and Fermi vector \mathbf{k}_F , a change in the sign of the integral is therefore possible.

Another feature, which mainly determines the magnetic properties of rare-earth compounds, is the interaction of 4f electrons with the electric charges of the surrounding ions [44], as described by the Hamiltonian:

$$H_{CF} = \sum_{n=0}^{n'} \sum_{m=-n}^{+n} B_n^m O_n^m(J)$$

where B_n^m are the crystal field parameters and $O_n^m(J)$ represent polynomials of the the angular momentum operators J_z , J^2 , J_+ , and J_- . Crystal electric field effects are responsible for the observed decrease of the rare-earth magnetic moments as compared to the free ion values gJ .

The rare-earth site in RTX_2 compounds has the point symmetry mm . In such a symmetry, the CEF Hamiltonian can be written as:

$$H_{CF} = B_2^0 O_2^0 + B_2^2 O_2^2 + B_4^0 O_4^0 + B_4^2 O_4^2 + B_4^4 O_4^4 + B_6^0 O_6^0 + B_6^2 O_6^2 + B_6^4 O_6^4$$

The B_n^m parameters were determined for RTX_2 compounds using the so-called point-charge model [45]. Computations were performed for the nearest neighbours. The results of calculations are shown in the table (the sixth-order parameters were omitted, because they are very small).

The results of calculations suggest that the fact that the preferred alignment of the magnetic moment is in the (010) plane, as well as B_2^0 , B_2^2 , and B_4^0 , play an important role in the CEF Hamiltonian.

In most of the studied compounds with the $CeNiSi_2$ -type crystal structure, the orientation of magnetic moments agrees with the positive sign of the B_2^0 parameter

(along the c -axis) but for the compounds with Er, a negative sign of the parameter B_2^0 suggests that the b -axis is the preferred direction, but this is not obeyed.

Table 1. Crystal electric field parameters for $RNiSi_2$ compounds calculated using the so-called point-charge model.

R	B_2^0 [meV]	B_2^2 [meV]	B_4^0 [meV]	B_4^2 [meV]	B_4^4 [meV]
Ce	2.741	9.445	6.979	-0.229	-0.257
Pr	0.907	3.126	-0.656	0.022	0.024
Nd	0.256	0.882	-0.222	0.007	0.008
Tb	0.307	1.058	0.055	-0.002	-0.002
Dy	0.184	0.634	-0.025	0.001	0.001
Ho	0.061	0.209	-0.012	0.0004	0.0004
Er	-0.067	-0.231	0.014	-0.0005	-0.0005

3. Conclusions

The discussed compounds crystallize in an orthorhombic crystal structure of the $CeNiSi_2$ type. They exhibit complex magnetic behaviour. It is well established that in these compounds (except those with $T = Mn$) the magnetic moment is localized only on rare-earth atoms. Their magnetism arises from the interaction of the magnetic moments localized on rare-earth ions.

Large interatomic R–R distances (about 4 Å) suggest that the stability of the observed magnetic ordering scheme is due to interactions via conduction electrons (RKKY model).

The Néel and Curie temperatures determined for the presented families only in part follow the de Gennes scaling. This effect suggests that the main interaction leading to magnetic ordering in these systems is not purely of the RKKY-type but is modified by the crystalline electric field effect which can significantly influence the Néel temperature. CEF effects are also responsible for the observed decrease in rare-earth magnetic moments as compared to free ion values.

The conclusion may thus be drawn that the CEF plays a significant role in stabilizing magnetic ordering schemes, so that determining the CEF parameters is of great importance in understanding the nature of the magnetic properties of intermetallic compounds.

The magnetic structures of the investigated stannides are different than those reported for isostructural stoichiometric RTX_2 silicides and germanides, which have simple antiferromagnetic structures with a magnetic unit cell being the same as the crystallographic one. The sequence of magnetic moments corresponds to the G-mode (+ – + –). In the silicides and germanides, the magnetic moments are aligned along the c -axis. In the stannides investigated in this work, the rare-earth magnetic moments form an angle with the c -axis. These results indicate that changing the X element (p-

electron element) from Si, Ge to Sn influences magnetic interactions and leads to a change in the direction of the magnetic moments.

References

- [1] BODAK O.I., GLADYSHEVSKY E.I., *Sov. Phys. Cryst.*, 14 (1970), 859.
- [2] PARTHÉ E., CHABOT B., *Handbook on the Physics and Chemistry of Rare Earth*, K.A. Gschneidner Jr., L. Eyring (Eds.), Elsevier, Amsterdam, 1984, Chap. 48, p. 113.
- [3] PECHARSKY V.K., MRUZ O.YA., KONYK M.B., SALAMAKHA P.S., STARODUB P.K., FEDYNA M. F., BODAK O.I., *Zhur. Strukt. Khim.*, 30 (1989), 96.
- [4] VENTURINI G., MALAMAN B., MEOT-MEYER M., FRUCHART D., G. LE CAER, MALTERRE D., ROQUES B., *Rev. Chim. Minerale* 23 (1986), 162.
- [5] MALAMAN B., VENTURINI G., PONTONNIER L., FRUCHART D., *J. Magn. Magn. Mater.*, 86 (1990), 349.
- [6] GIL A., LECIEJEWICZ J., MALETKA K., SZYTULA A., TOMKOWICZ Z., WOJCIECHOWSKI K., *J. Magn. Magn. Mater.*, 129 (1994), L155.
- [7] WEITZER F., HIEBEL K., ROGL P., *Solid State Commun.*, 82 (1992), 353.
- [8] GIL A., OLEŚ A., SIKORA W., SZYTULA A., *J. Alloys Comp.*, 360 (2003), 21.
- [9] MALAMAN B., VENTURINI G., LECAËR G., PONTONNIER L., FRUCHART D., TOMALA K., SANCHEZ J.P., *Phys. Rev. B*, 41 (1990), 4700.
- [10] DAS I., SAMPATHKUMARAN E.V., *Solid State Commun.*, 83 (1992), 765.
- [11] BODAK O.I., GLADYSHEVSKY E.I., LEVIN E.M., LUTSIV R.V., *Dopov. Akad. Nauk Ukr. RSR, Ser. A12* (1977), 1129.
- [12] PELLIZIONE M., BRAUN H.F., MULLER J., *J. Magn. Magn. Mater.*, 30 (1982), 33.
- [13] ANDRÉ G., OLEŚ A., SZYTULA A., *Phys. Stat. Solidi (a)*, 116 (1989), K29.
- [14] PENC B., SZYTULA A., WAWRZYŃSKA E., HERNANDEZ-VELASCO J., *J. Alloys Comp.*, 366 (2004), 120.
- [15] SZYTULA A., PTASIEWICZ-BAK H., LECIEJEWICZ J., BAŻELA W., *J. Magn. Magn. Mater.*, 80 (1989), 189.
- [16] ANDRÉ G., BOURÉE F., OLEŚ A., SIKORA W., KOLENDA M., SZYTULA A., *J. Magn. Magn. Mater.*, 124 (1993), 69.
- [17] SKOLOZDRA R.V., [in:] *Handbook on the Physics and Chemistry of Rare Earths*, K.A. Gschneidner, L. Eyring (Eds.), Elsevier, Amsterdam, 1997, Vol. 24, p. 399.
- [18] GIL A., PENC B., WAWRZYŃSKA E., HERNANDEZ-VELASCO J., SZYTULA A., ZYGMUNT A., *J. Alloys Comp.*, 365 (2004), 31.
- [19] PENC B., WAWRZYŃSKA E., SZYTULA A., GIL A., HERNANDEZ-VELASCO J., ZYGMUNT A., *J. Alloys Comp.* 375 (2004), L1.
- [20] PELLIZIONE M., BRAUN H.F., MULLER J., *J. Magn. Magn. Mater.*, 30 (1982), 33.
- [21] SCHOBINGER-PAPAMANTELOS P., BUSCHOW K.H.J., *J. Alloys Comp.*, 185 (1992), 51.
- [22] GIL A., SZYTULA A., TOMKOWICZ Z., WOJCIECHOWSKI K., ZYGMUNT A., *J. Magn. Magn. Mater.*, 129 (1994), 271.
- [23] SCHOBINGER-PAPAMANTELOS P., BUSCHOW K.H.J., *J. Less-Common Met.*, 171 (1991), 321.
- [24] SCHOBINGER-PAPAMANTELOS P., RITTER C., BUSCHOW K.H.J., *J. Alloys Comp.*, 264 (1998), 89.
- [25] SCHOBINGER-PAPAMANTELOS P., FAUTH F., BUSCHOW K.H.J., *J. Alloys Comp.*, 252 (1997), 50.
- [26] SCHOBINGER-PAPAMANTELOS P., BUSCHOW K.H.J., WILKINSON C., FAUTH F., RITTER C., *J. Magn. Magn. Mater.*, 189 (1998), 214.
- [27] SCHOBINGER-PAPAMANTELOS P., KRIMMEL A., GRAUEL A., BUSCHOW K.H.J., *J. Magn. Magn. Mater.*, 125 (1993), 151.
- [28] BAŻELA W., LECIEJEWICZ J., MALETKA K., SZYTULA A., *J. Magn. Magn. Mater.*, 109 (1992), 305.
- [29] SCHOBINGER-PAPAMANTELOS P., BUSCHOW K.H.J., RITTER C., *J. Alloys Comp.*, 287 (1999), 51.
- [30] SCHOBINGER-PAPAMANTELOS P., RODRIGUEZ-CARVAJAL J., BUSCHOW K.H.J., *J. Alloys Comp.*, 240 (1996), 85.

- [31] GIL A., PENC B., BARAN S., HERNANDEZ-VELASCO J., SZYTULA A., ZYGMUNT A., *J. Alloys Comp.*, 361 (2003), 32.
- [32] GIL A., PENC B., BARAN S., WAWRZYŃSKA E., SZYTULA A., HERNANDEZ-VELASCO J., ZYGMUNT A., *Neutron Scattering and Complementary Methods in Investigations of Condensed Phase*, Vol. 1, University of Podlasie Publishing House, 2003, Monograph No. 45, p. 103.
- [33] GIL A., PENC B., HERNANDEZ-VELASCO J., SZYTULA A., ZYGMUNT A., *Physica B*, 350 (2004), e119.
- [34] GIL A., PENC B., GONDEK Ł., SZYTULA A., HERNANDEZ-VELASCO J., *J. Alloys Comp.*, 346 (2002), 43.
- [35] RAWAT R., DAS I., *Phys. Rev.*, B64 (2001), 052407.
- [36] SCHOBINGER-PAPAMENTELLOS P., BUSCHOW K.H.J., *J. Alloys Comp.*, 187 (1992), 73.
- [37] GIL A., KACZOROWSKI D., HERNANDEZ-VELASCO J., PENC B., WAWRZYŃSKA E., SZYTULA A., *J. Alloys Comp.*, 384 (2004), L4.
- [38] RUDERMAN M.A., KITTEL C., *Phys. Rev.*, 96 (1954), 99.
- [39] KASUYA T., *Prog. Theor. Phys. (Kyoto)*, 16 (1956), 45.
- [40] YOSHIDA K., *Phys. Rev.*, 106 (1957), 893.
- [41] DE GENNES P.G., *J. Phys. Radium*, 23 (1962), 510, 630.
- [42] SZYTULA A., JEZERSKI A., PENC B., *Physica B*, 237 (2003), 171.
- [43] BERTAUT E.F., *Acta Crystallogr.*, A 24 (1968), 217.
- [44] STEVENS K.W.H., *Proc. Phys. Soc. (Londyn)*, A65 (1952), 209.
- [45] HUTCHINGS M.T., [in:] *Solid State Physics*, Vol. 16, F. Seitz, D. Turnbull (Eds.), Academic Press, New York, 1964.

Received 1 June 2005

Revised 10 October 2005

Study of the valence state of U ions in quasi-two-dimensional ternary uranium compounds

R. TROĆ*

W. Trzebiatowski Institute of Low Temperature and Structure Research,
Polish Academy of Sciences, P.O. Box 1410, 50-950 Wrocław 2, Poland

The valence states and thermoelectric properties of two Ru-based uranium ternaries, namely U_2Ru_2Sn and U_2RuGa_8 , have been studied. Intermediate-valence behaviour manifests itself in broad peaks in the susceptibility, largely negative values of the paramagnetic Curie temperature, and in the occurrence of maxima in the thermoelectric power. At the same time, specific heat data show no transition at low temperatures for both studied compounds. Experimental results are fitted to equations given in the literature relevant to valence fluctuating states. The studied compounds are unique examples of such a state, found for the first time among the huge family of uranium compounds known to be magnetically ordered at low temperatures.

Key words: *mixed valence; magnetic susceptibility; thermoelectric power; actinide intermetallic compounds*

1. Introduction

A fairly large number of Ce, Eu (Sm), and Yb intermetallics have been known for many years to exhibit an intermediate valence (IV) state. Such a state, however, has not been reported up to now for uranium-based intermetallic compounds despite intensive studies of their magnetism and electronic structures for over 50 years. The first example, published recently, turned out to be tetragonal U_2Ru_2Sn , crystallizing in the tetragonal U_3Si_2 type. Its susceptibility was found to exhibit a maximum at about $T_{max} \approx 170$ K and electrical resistivity (ρ) revealed the formation of a hybridisation gap (or so called pseudo-gap) at the Fermi level (E_F) [1–4]. At higher temperatures, the $d\rho/dT$ derivative becomes negative as for Kondo-like behaviour. These features, among others, classify this compound as a Kondo semiconductor with a narrow gap. U_2Ru_2Sn is so far the only representative of this class in the actinide family. Recent inelastic neutron

*E-mail: R.Troc@int.pan.wroc.pl

scattering measurements have shown that the observed magnetic response is nearly q -independent, indicating that single-ion type interactions are responsible for the spin gap formation in U_2Ru_2Sn , confirming the presence of a spin gap of the order of 60–70 meV in the electronic structure of this compound [5].

The layered compound $UCoGa_5$ was considered a second candidate exhibiting the IV state among uranium-based ternary intermetallics. The compound crystallizes in a tetragonal $HoCoGa_5$ type structure. The susceptibility of this compound, however, exhibits a maximum at the temperature as high as 650 K [6].

Very recently, we have discovered [7] a third candidate, namely U_2RuGa_8 , which joins the still very short list of uranium(IV) compounds. U_2RuGa_8 has also a layered tetragonal structure of the Ho_2CoGa_8 type with the stacking sequence of two layers of UGa_3 and one layer of $RuGa_2$. It is interesting to note that in both types of tetragonal crystal structures, i.e. U_3Si_2 and Ho_2CoGa_8 , the closest U–U distances along the a and c axes are almost the same, although their values in each compound are different, i.e. 0.35 and 0.42 nm, respectively. Nevertheless, the magnetic behaviours of both compounds are very similar.

2. Experiment

The tin compound U_2Ru_2Sn and gallides $UCoGa_5$ and U_2RuGa_8 were grown as single crystals by the Czochralski method [2] and so-called self-flux method [7], respectively. Their susceptibility was measured by means of SQUID along two main directions of the tetragonal unit cell, i.e. parallel and perpendicular to the c axis. Thermoelectric power (4.2–300 K) was measured with a steady-state method, also in the two crystallographic directions.

3. Experimental results and fitting procedures

The temperature dependences of magnetic susceptibility measured for U_2Ru_2Sn and U_2RuGa_8 along the two main crystallographic axes a and c are shown in Fig.1. The susceptibility is distinctly anisotropic in both directions and in each case goes through broad maxima at temperatures around 170 and 190 K (U_2Ru_2Sn), and 200 and 220 K (U_2RuGa_8). The upturns in the $\chi(T)$ curves visible at low temperatures are caused by impurities. The susceptibilities measured in these two directions can be fairly well fitted by the interconfiguration fluctuation (ICF) model of Sales and Wohlleben [8] in which a valence fluctuation system is characterized by two energy parameters: E_{ex} , the interconfigurational excitation energy, and by $k_B T_{sf}^*$, where k_B is the Boltzmann constant and T_{sf}^* is the so-called valence fluctuation temperature. This model results in $T_{sf}^* = 180$ K and 500 K for U_2Ru_2Sn , and 320 K and 460 K for U_2RuGa_8 in the two crystallographic directions mentioned above. The energy difference between

the corresponding two closest fluctuating states, namely the hybridised $5f^2$ ($6d^1$) and $5f^3$ states (i.e. related to U^{4+} and U^{3+} , respectively), $\Delta E_{ex}/k_B$, is for these two directions less or over 1000 K. In Figure 1, the solid lines are a least squares fit to the expressions given in Ref. [8]. The most important finding characterizing the mixed-valence behaviour is that the susceptibility measured along both directions follows the Curie–Weiss law at temperatures above ~ 500 K, with the effective magnetic moments of uranium being close to the free ion values for U^{4+} ($5f^2$) and U^{3+} ($5f^3$).

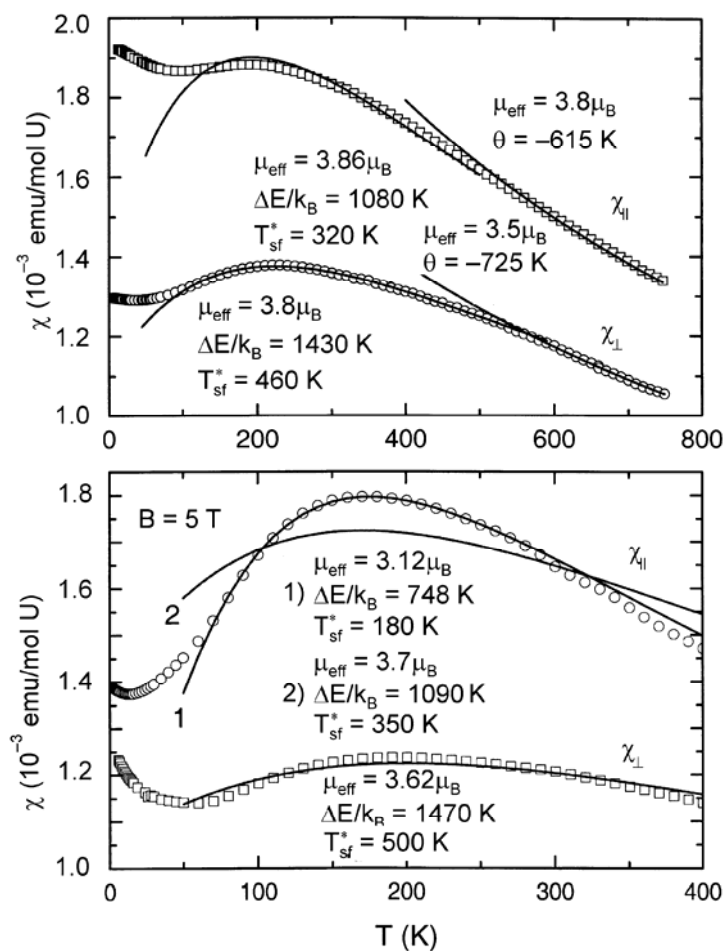


Fig. 1. The Sales–Wohleben model of intermediate configuration fluctuation (ICF) applied to fitting the experimental temperature dependences of the susceptibilities of U_2Ru_2Sn (a) and U_2RuGa_8 (b), measured parallel and perpendicular to the c axis.

The obtained energy parameters E_{ex} and $k_B T_{sf}^*$ are given in the figure

Lawrence et al. [9] have shown that only a single function of a scaled variable T/T_{sf}^* is needed to describe the susceptibility for a broad temperature range, i.e. the

squared effective moment $\mu_{\text{eff}}^2 \equiv T\chi(T)/C$, where C is the Curie constant of U^{3+} , which satisfies the $\mu_{\text{eff}}^2(T) = f(T/T_s)$ function shown in Fig. 2. T_s^* is defined as the temperature at which the squared effective moment μ_{eff}^2 reaches half of the free ion value ($\mu^2(T_s^*) = 1/2$). Thus, it is possible to scale the mixed-valence behaviour of many rare earth compounds on one curve (see, for example, Ref. [10]), including the studied properties of the two uranium representatives along the two main axes of the tetragonal unit cell.

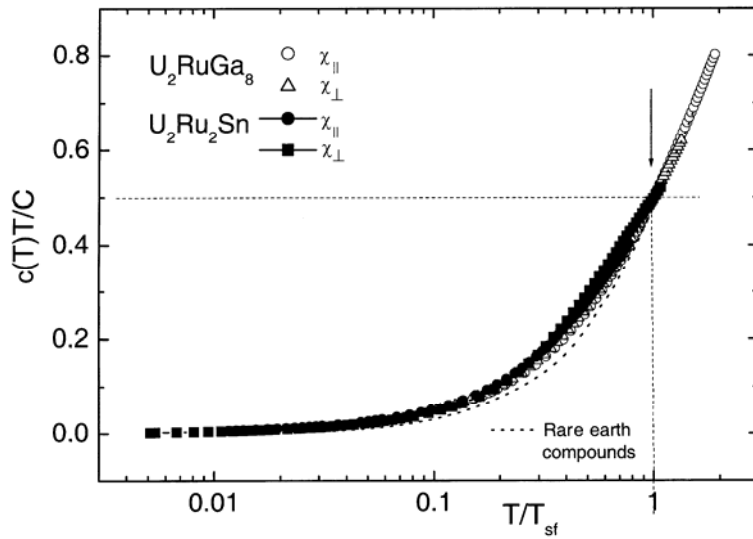


Fig. 2. The scaling scenario in a semi-logarithmic plot for MV rare earths and for the uranium compounds studied in this work

The temperature dependences of electrical resistivity for the current j flowing parallel to the a and c axes are displayed in Refs. [2, 3] and [7] for single crystalline samples of $\text{U}_2\text{Ru}_2\text{Sn}$ and U_2RuGa_8 , respectively. Their behaviour confirms once again the mixed valence state of the uranium ions in these compounds. If for the former compound gap formation in the electronic structure is reflected by a low temperature rise in resistivity [2, 3], then for the latter compound a Fermi liquid state at low temperatures is reminiscent to that of many well-known mixed valence lanthanide systems.

The temperature dependences of thermopower S for both considered compounds with temperature gradients ∇T , applied along the a and c axes, have also been studied. For $\text{U}_2\text{Ru}_2\text{Sn}$, the $S(T)$ curves go through two maxima for both main axes: negative ones at about 20 K and positive ones at high temperatures, where they have different shapes, however, depending on the measured direction. It appears that a fairly sharp maximum occurs at 75 K for the ∇T parallel to c axis ($\nabla T \parallel c$), and a very broad one with a maximum at 150 K for the ∇T parallel to a axis ($\nabla T \parallel a$). All these data could be

fairly well fitted by means of the two-band model [11]. On this basis, energy parameters such as the difference between the electronic levels ($E_f - E_F$) and the width of the 5f electron bands Δ , could be determined. In turn, for U_2RuGa_8 , $S(T)$ curves measured along the a and c axes at first increase with increasing temperature. The curve for $\nabla T||a$ then goes through a broad maximum at 170 K and the curve for $\nabla T||c$ saturates at room temperature. The high temperature variation of $S(T)$, taken as T/S vs. T^2 straight lines for both compounds and for both crystallographic directions, has in turn been fitted by the one band model [12], which has been well-applied in the past to intermediate valence cases of many lanthanide compounds. All these features enabled determination of the energy parameters, which again gives some support for the idea of mixed-valence properties occurring in uranium compounds, until now a phenomenon unknown in this class of materials.

4. Conclusions

Simple intermediate models allowed description of the temperature dependences of magnetic susceptibility and thermoelectric power. Thus, these have provided sufficient proof that both studied ternary compounds can be considered as the first mixed-valence representatives of the family of intermetallic uranium compounds.

References

- [1] DU PLESSIS P. DE V., STRYDOM A.M., TROĆ R., MENON L., *J. Phys. Cond. Matt.*, 13 (2001), 8375.
- [2] STRYDOM A.M., TROĆ R., *Solid State Comm.*, 126 (2003), 207.
- [3] TRAN V.H., PASCHEN S., RABIS A., SENTHILKUMARAN N., BAENITZ M., STEGLICH F., DU PLESSIS P. DE V., STRYDOM A.M., *Physica B*, 312–313 (2002), 215.
- [4] PASCHEN S., BAENITZ M., TRAN V.H., RABIS A., STEGLICH F., CARRILO-CABRERA W., GRIN YU., STRYDOM A., DU PLESSIS P. DE V., *J. Phys. Chem. Solid*, 63 (2002), 1183.
- [5] MCEVEN K. A., ADROJA D.T., HILLIER A.D., PARK J.-G., BEWLEY B.I., [in:] Abstract WE-ACT-4, SCES-04, July 26–30, 2004, Karlsruhe.
- [6] TROĆ R., BUKOWSKI Z., SUŁKOWSKI C., MISIOREK H., MORKOWSKI J.A., SZAJEK A., CHEŁKOWSKA G., *Phys. Rev. B*, 70 (2004), 184443.
- [7] TROĆ R., BUKOWSKI Z., SUŁKOWSKI C., MORKOWSKI J.A., SZAJEK A., CHEŁKOWSKA G., *Physica B*, 359–361 (2005), 1375.
- [8] SALES B.C., WOHLLEBEN D.K., *Phys. Rev. Lett.*, 35 (1975), 1240.
- [9] LAWRENCE J.M., RISEBOROUGH P.S., PARKS R.D., *Rep. Prog. Phys.*, 44 (1981), 1.
- [10] KISHIMOTO Y., KAWASAKI YU., OHNO T., HIHARA T., SUMIYAMA K., GUPTA L.C., GHOSH G., *J. Magn. Magn. Mat.*, 272–276 (2004), 509.
- [11] BANDO Y., SUEMITSU T., TAKAGI K., TOKUSHIMA H., ECHIZEN Y., KATOH K., UMEO K., MAEDA Y., TAKABATAKE T., *J. Alloys Comp.*, 313 (2000), 1.
- [12] GOTTSWICK U., GLOOS K., HORN S., STEGLICH F., GREWE N., *J. Magn. Mat.*, 47–48 (1985), 536.

Received 1 June 2005

Revised 10 October 2005

PbTe constrictions for spin filtering

G. GRABECKI *

Institute of Physics, Polish Academy of Sciences, 02-668 Warsaw, Poland
and ERATO Semiconductor Spintronics Project, Japan Science and Technology Agency

The present article is a review of our experimental work performed on PbTe nanostructures. The uniqueness of lead telluride lies in a combination of excellent semiconducting properties, such as high electron mobility and tuneable carrier concentration, and piezoelectric behaviour leading to a huge dielectric constant at low temperatures. For nanostructured constrictions of PbTe, we have observed 1-dimensional quantization of electron motion at much more impure conditions than in any other system studied so far. This is possibly due to the dielectric screening of Coulomb potential fluctuations produced by various defects usually existing in the solid-state environment. In an external magnetic field, this quantization exhibits a very pronounced spin splitting, already discernible at several kilogauss. This indicates that PbTe nanostructures are very promising as local spin-filtering devices.

Key words: *PbTe; nanostructures; quantum ballistic transport; spin filter*

1. Introduction

Recent progress in semiconductor technology allowed the reduction of sample dimensions both below the electron mean free path l_e and Fermi wavelength λ_F . This is the so-called quantum ballistic regime, where electronic quantum states can be tuned at will. Currently, these studies attract much attention, because quantum ballistic devices are regarded as the basis of future applications of sensing, information processing, and quantum computation [1]. One-dimensional (1D) conductance quantization in narrow constrictions is a canonical example of these effects [2]. A necessary condition for its observation is the reduction of random potential fluctuations arising from charged defects that exist in the device surroundings [3]. In most constrictions studied so far, such as those patterned from two-dimensional electron gas (2DEG) adjacent to a AlGaAs/GaAs heterostructure, spatial separation of charged donors from mobile carriers has been achieved by modulation doping. Remote charges, however, still produce small potential fluctuations in the 2DEG plane. They cause low-angle scattering

*E-mail: grabec@ifpan.edu.pl

of electron waves, precluding 1D quantization in devices larger than $0.5 \mu\text{m}$ [4, 5]. Since then, the future development of quantum ballistic devices relies heavily on the further minimization of the influence of background defect potentials. This is continuously realized by improving material purity and refined fabrication procedures.

In the present work, we propose an entirely new way of reducing long-range Coulomb potentials in quantum ballistic devices, namely by using a background material with a huge dielectric constant. We have examined such a possibility experimentally, developing fabrication methods and performing transport measurements in nanostructures of PbTe. This paper is an update for two previously published works [6, 7]. In the following sections, we review the basic properties of PbTe, nanostructure fabrication methods, experimental results of conductance quantization, and finally the application of PbTe constrictions as spin-filters.

2. Basic properties of PbTe

PbTe is a narrow gap semiconductor crystallizing in the rock-salt structure [8]. It has an inversion symmetry and the conduction band is formed of four ellipsoids of revolution with energy minima at the L points of the Brillouin zone. Since this material is at the borderline of the ferroelectric phase transition due to a cubic-rhombohedral distortion, it is characterized by strong paraelectric behaviour [9]. The static electric permittivity ϵ increases with increasing temperature and reaches the value as high as 1350 at 4.2 K. It has already been noted more than 30 years ago [10] that in bulk PbTe electron mobilities exceed $10^6 \text{ cm}^2/(\text{V}\cdot\text{s})$ at low temperatures. Indeed, this observation was interpreted in terms of the suppression of the Coulomb potentials of ionised defects by dielectric screening. For the purpose of nanofabrication, however, material in form of thin layers or quantum wells (QW) is necessary. Unfortunately, in such cases various misfits usually reduce carrier mobility by about one order of magnitude. Worse still, the best available QWs of PbTe are grown on barium fluoride, BaF_2 , and this material combination is characterized by a large thermal misfit arising at cryogenic temperatures. This causes a tensile strain of about 0.0016, giving rise to dislocations [7, 11]. Obviously, in any usual semiconductor such prerequisites would preclude any possibility of observing quantum ballistic effects. Nevertheless, as we will show below, they are still possible in the case of PbTe.

3. Preparation of PbTe nanostructures

As the initial material we have used 50 nm thick PbTe n-type quantum wells (QW) placed between 100 nm Bi-doped $\text{Pb}_{1-x}\text{Eu}_x\text{Te}$ barriers ($x = 0.08$). They were grown by MBE on a (111)-oriented BaF_2 substrate through a $2.5 \mu\text{m}$ thick buffer layer of $\text{Pb}_{1-x}\text{Eu}_x\text{Te}$, with the same x . Typical values of electron concentration and Hall mobil-

ity in the QW are $4 \times 10^{12} \text{ cm}^{-2}$ and $0.9 \times 10^5 \text{ cm}^2/(\text{V}\cdot\text{s})$, respectively. Because of relatively large thickness, there are up to 7 partially occupied electric subbands in the unperturbed QW, so it can be regarded as 3-dimensional. We have estimated that l_e at helium temperatures is about $2 \text{ }\mu\text{m}$. This value was also confirmed by observations of magneto-size effects on Hall bridges of various widths [7]. It should be noted that the fourfold valley degeneracy in PbTe QWs is lifted due to quantum confinement. The conduction band minimum is formed by a single valley with its long axis parallel to the growth direction, whereas three obliquely oriented valleys are shifted upward with respect to it [12]. This fact significantly simplifies the complex band structure of the material, since for sufficiently low carrier concentrations only one valley contributes to the conductance.

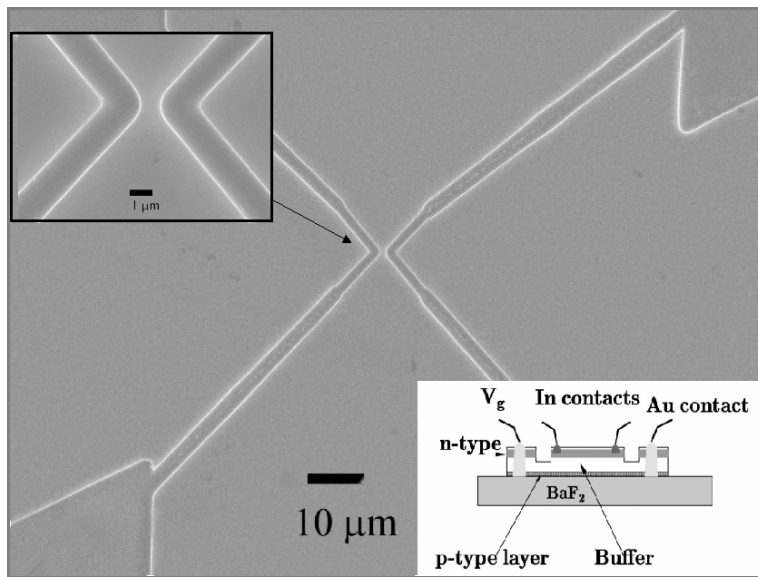


Fig. 1. Scanning electron microscopy profile of a $1 \text{ }\mu\text{m}$ wide constriction made of PbTe/PbEuTe. Inset: schematic view of the device cross-section, illustrating the gate in contact with the interfacial p-type layer

To fabricate narrow constrictions (Fig. 1), we have employed single-level electron-beam lithography followed by wet chemical etching. The trenches defining the nanostructures were about $0.7 \text{ }\mu\text{m}$ deep. Since they do not reach BaF_2 , the thermal stress is quite uniform and does not impair the device quality too much, even after multiple coolings down to helium temperatures [7]. To make the gate electrode necessary for tuning the device, we employ a p-n junction between the n-type PbTe QW and p-type interface layer existing at the BaF_2 substrate [13]. In such an arrangement, the gate electrode extends under the entire structure, including the macroscopic contact pads. When the negative gate voltage V_g is applied, however, the narrow constrictions are depleted first due to the large contribution of edge effects to the constriction

capacitance [14]. Due to a huge dielectric constant, the values of V_g necessary for fully depleting the constriction are quite small, of the order of a hundred millivolts. Electric contacts to the p-type gate have been made using gold chloride brown liquid. For the n-type QW, pure indium spots are soldered (Fig. 1 inset). At helium temperature, the gate resistance reaches the values above $10^9 \Omega$ for near-zero bias and for larger biases it exhibits diode type I - V characteristics.

4. Conductance quantization in PbTe nanostructures

When a negative V_g was applied to the constriction, the conductance was gradually reduced, showing a sequence of steps as represented in Fig. 2. The presence of steps indicates the 1D quantization of the electron gas in the channel, squeezed by the electric field applied to the gate. Interestingly, we are able to resolve only steps ($G = i(2e^2/h)$) corresponding to $i = 1, 3, 6, \dots$, for other intermediate values of i the steps are absent. This

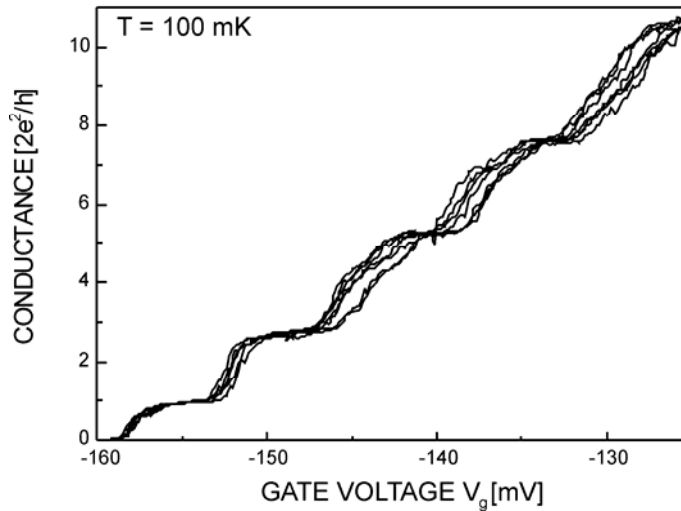


Fig. 2. Zero field conductance quantization in one of the PbTe quantum point contacts.

Multiple traces were taken during long-time subsequent sweeps of V_g .

The quantised values at the steps are slightly reduced due to the contribution of serial resistance from contact regions

demonstrates the presence of an additional orbital degeneracy of the 1D subbands. Such degeneracy stems from the oval shape of the constriction cross-section, whose two transverse directions contribute equally to the quantum confinement [15]. This is a consequence of the large thickness of the initial QW. The multiple curves presented in Fig. 2 were obtained by many slow sweeps of V_g performed during a period of 12 hours. The positions of the conductance steps are always the same despite some changes visible in the intermediate regions. They probably reflect the temporal evolu-

tion of the potential near the constriction, however the quantization remains almost unaltered. This is a result of smoothing out the potential relief due to the huge ϵ and its constant value over the whole constriction volume. Any changes in the potential caused by some defect redistribution or their re-charging simply add to V_g and do not affect the electron transmission through the constriction.

It should also be reminded that the concentration of background defects in PbTe is not smaller than 10^{17} cm^{-3} due to material non-stoichiometry [16]. Therefore, for a constriction diameter equal to the initial QW width, i.e. 50 nm, one still expects about 100 defects inside the conducting channel. For comparison, in AlGaAs/GaAs constrictions even a single defect would destroy the conductance quantization [3]. In contrast to this, in a PbTe device the transmission coefficient for step $i = 1$ (Fig. 2) exceeds 90%. This is also the effect of the huge ϵ , which converts the defects within the channel into short-range centres. According to recent theoretical predictions [17], in such a case the quantization will not be destroyed.

5. Spin-splitting in PbTe nanostructures

There has been a great deal of interest in the concept of spintronics, according to which the control and manipulation of electron spins in solids provides the basis for novel quantum technology. As a first step towards the practical realization of such ideas, the efficient generation of spin-polarized currents, preferably by electrical means and at a small spatial scales, should be mastered [18]. It is well known that narrow constrictions in a magnetic field act as spin dependent barriers for electrons and can be used for constructing local spin filters [6, 19]. In standard semiconductors such as GaAs, however, the electronic Landé factor is rather small and, thus, a high magnetic field must be employed to operate the device. One possible solution circumventing this problem is to exploit materials with a large g -factor. This is the case of narrow-gap semiconductors, in which Zeeman splitting can compete with the separation between 1D energy levels. PbTe constrictions seem to be an ideal candidate for this purpose.

The effect of the magnetic field B on the conductance quantization is illustrated in Fig. 3. Here, we show the conductance quantization for a device of “quantum dot” geometry (see inset). In fact, this can be regarded as two quantum point contacts connected in series [20]. For such a system, the resistances are not additive and we observe conductance quantization as for a single constriction. The visible reduction in step height may be explained by some backscattering from the boundaries in the central “dot” region. In a perpendicular magnetic field, already well below 1 T the half integer step, $i=1/2$, is resolved, indicating the development of spin splitting in the 1D subbands. Surprisingly, however, the *plateau* $i = 1$ disappears at the same field range. Instead, a step with $i = 3/2$ becomes resolved. In order to visualize the energy spectrum, we present in Fig. 4 a contour plot of the transconductance dG/dV_g as a function of V_g and B . The black shadow stripes indicate the occupation thresholds of the sub-

sequent 1D subbands. One can see that the disappearance of the step at $i = 1$ is the result of a crossing between two spin sublevels, which belong to two different 1D

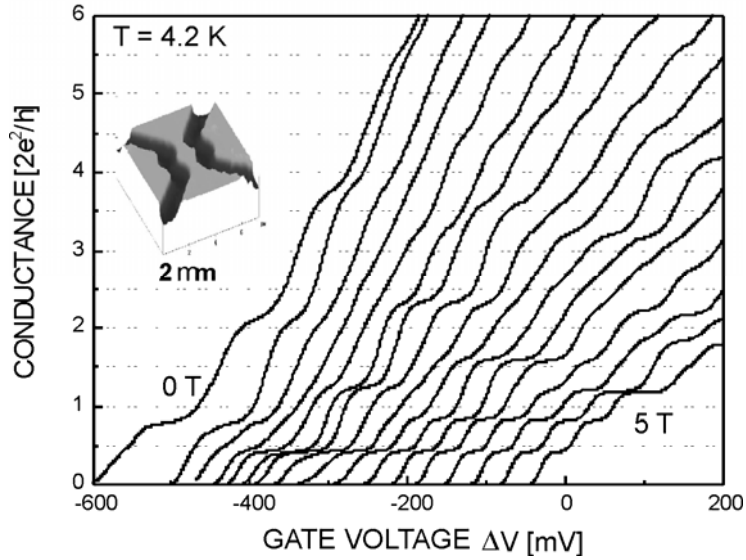


Fig. 3. Evolution of conductance quantization induced by a magnetic field in two serially connected PbTe quantum point contacts. The magnetic field varies from 0 to 5 T with 0.25 T increments. The curves were shifted horizontally to prevent overlap. Inset: atomic-force microscopy image of the device

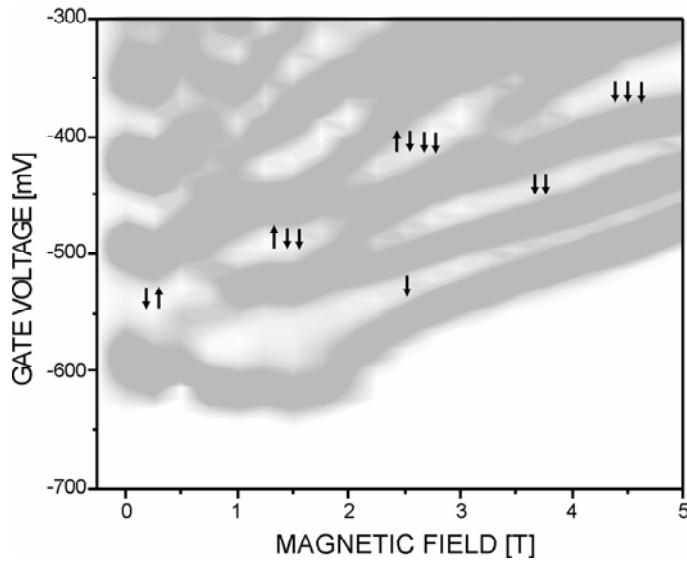


Fig. 4. Shadow contour plot of transconductance dG/dV_g for the data presented in Fig. 3, as a function of gate voltage and the perpendicular magnetic field. Dark stripes represent thresholds of subsequently occupied 1D subbands, and arrows indicate their number and spin polarization

subbands: the “spin up” sublevel of the ground subband and the “spin down” sublevel of the first excited subband. The crossing takes place slightly above $B = 1$ T, indicating that already at this field Zeeman splitting is equal to the energy separation between the lowest 1D subbands.

For larger fields, the step at $i = 1$ appears again, but corresponds to the occupation of two 1D subbands with the same ‘spin down’ orientation. Furthermore, at about 2.5 T the ground “spin up” subband crosses the second excited “spin down” subband, and the spin polarized current is carried by three 1D subbands. In this way, we have a unique situation where the totally spin polarized current is carried by many 1D subbands.

6. Conclusions

We have fabricated nanostructures of PbTe and demonstrated the effect of conductance quantization. It is possible, even though our system contained background charged defects up to a level as high as 10^{17} cm⁻³ and a significant amount of strain-induced dislocations. The origin of such an unusual situation is the huge static dielectric constant suppressing the Coulomb potentials of the defects. Our observations prove that PbTe should be considered as a serious candidate for fabricating future quantum devices. In our opinion, this may be an interesting alternative for the most explored system of AlGaAs/GaAs. An additional advantage of PbTe is a large g^* -factor and spin-filtering capability. Since spin splitting in moderately strong magnetic fields is larger than the 1D level quantization energy, we can obtain a totally spin polarized 1D gas with several partially occupied subbands. Finally, it has to be stressed that since the initial substrate layers used in this work were not optimised (for example, the initial mobility was much lower than the records of bulk PbTe), there is still much room for improving the devices.

Acknowledgements

This work was supported by KBN Grant No. PBZ-KBN-044/P03/2001. The author would like to thank T. Dietl, J. Wróbel, E. Papis, E. Kamińska, A. Piotrowska, G. Springholz, and G. Bauer for their essential contributions and helpful discussions.

References

- [1] BURKARD G., LOSS D., DIVINCENZO D.P., Phys. Rev. B, 59 (1998), 2070.
- [2] VAN WEES B.J., VAN HOUTEN H., BEENAKKER C.W.J., WILLIAMSON J.G., KOUVENHOVEN L.P., VAN DER MAREL D., FOXTON C.T., Phys. Rev. Lett., 60 (1988), 848; WHARAM D.A., THORNTON T.J., NEWBURY R., PEPPER M., AHMED H., FROST J.E.F., HASKO D.G., PEACOCK D.C., RITCHIE D.A., JONES G.A.C., J. Phys C, 21 (1988), L209.
- [3] NIXON J.A., DAVIES J.H., BARANGER H.U., Phys. Rev. B, 43 (1991), 12638.
- [4] TIMP G., [in:] *Semiconductors and Semimetals* Vol. 13, Chapt. 3, R.K. Willardson, A.C. Beer, E.R. Weber (Eds.), Academic Press, San Diego, 1992.
- [5] GLAZMAN L.I., JONSON M., Phys. Rev. B, 44 (1991), 3810.

- [6] GRABECKI G., WROBEL J., DIETL T., PAPIS E., KAMINSKA E., PIOTROWSKA A., SPRINGHOLTZ G., BAUER G., *Physica E*, 13 (2002), 649.
- [7] GRABECKI G., WROBEL J., DIETL T., PAPIS E., KAMINSKA E., PIOTROWSKA A., RATUSZNA A., SPRINGHOLTZ G., BAUER G., *Physica E*, 20 (2004), 236.
- [8] for properties of PbTe, see e.g., *Lead Chalcogenides, Physics and Applications*, D. Khokhlov (Ed.), Taylor and Francis Books, New York, 2003.
- [9] BATE R.T., CARTER D.L., WROBEL J.S., *Phys. Rev. Lett.*, 25 (1970), 159.
- [10] RAVICH J.I., EFIMOVA B.A., SMIRNOV I.A., *Semiconducting Lead Compounds*, Plenum, New York, 1968.
- [11] ZOGG H., BLUNIER S., FACH A., MAISSEN C., MUELLER P., TEODOROPOL S., MEYER V., KOSTORZ G., DOMMANN A., RICHMOND T., *Phys. Rev. B*, 50 (1994), 10801.
- [12] ABRAMOF E., ANDRADA E SILVA E.A., FERREIRA S.O., MOTISUKE P., RAPPL P.H.O., UETA A.Y., *Phys. Rev. B*, 63 (2001), 085304.
- [13] TRANTA B., CLEMENS H., *Lecture Notes in Physics*, Vol. 301, G. Ferenzi, F. Beleznyay (Eds.), Springer-Verlag, Berlin.
- [14] DE VRIES D.K., STELMASZYK P., WIECK A.D., *J. Appl. Phys.*, 79 (1996), 8087.
- [15] SCHERBAKOV A.G., BOGACHEK E.N., LANDMAN U., *Phys. Rev B*, 53 (1996), 4054.
- [16] SPRINGHOLTZ G., [in:] *Lead Chalcogenides, Physics and Applications*, Chapt. 3, D. Khokhlov (Ed.), Taylor and Francis Books, New York, 2003.
- [17] VARGIAMIDIS V., POLATOGLUO H.M., *Phys. Rev B*, 71 (2005), 075301.
- [18] GILBERT M.J., BIRD J.P., *Appl. Phys. Lett.*, 77 (2000), 1050.
- [19] WROBEL J., DIETL T., ŁUSAKOWSKI A., GRABECKI G., FRONC K., HEY R., PLOOG K.H., SHTRIKMAN H., *Phys. Rev. Lett.*, 93 (2004), 246601.
- [20] WHARAM D.A., PEPPER M., AHMED H., FROST J.E.F., HASKO D.G., PEACOCK D.C., RITCHIE D.A., JONES G.A.C., *J. Phys. C*, 21 (1988), L887.

Received 1 June 2005
Revised 10 October 2005

Evolution of hyperfine parameters in Co-doped FINEMET

T. SZUMIATA^{1*}, K. BRZÓZKA¹, B. GÓRKA¹, M. GAWROŃSKI¹, G. PAVLÍK², P. SOVÁK²

¹Department of Physics, Technical University of Radom, Krasickiego 54, 26-600 Radom, Poland

²Institute of Physics, P.J. Šafárik University, Park Angelinum 9, 04001 Košice, Slovakia

The influence of Co addition on the microstructure and hyperfine parameters of $(\text{Fe}_{1-x}\text{Co}_x)_{73.5}\text{Cu}_1\text{Nb}_3\text{Si}_{13.5}\text{B}_9$ alloys was studied by the ^{57}Fe Mössbauer spectrometry. In amorphous ribbons fabricated by melt-spinning technique, the mean hyperfine field and isomer shift changed systematically with cobalt content. In annealed, nanocrystalline samples, the DO_3 -type structure of $\text{Fe}(\text{Co})\text{-Si}$ grains evolves into a *bcc* $(\text{Fe},\text{Co})\text{Si}$ substitutional solid solution when increasing x . Simultaneously, the amorphous matrix is depleted in iron and cobalt. The observed increase in the mean hyperfine field is attributed to the enrichment of nanocrystallites in magnetic elements as well as the segregation of iron.

Key words: *nanocrystalline alloys; Co-doped FINEMET; Mössbauer spectroscopy; hyperfine interactions*

1. Introduction

Two-phase Fe-Cu-Nb-Si-B alloys, known as FINEMET [1], exhibit excellent soft magnetic properties attributed to the presence of Fe-Si nanocrystallites, magnetically coupled via the amorphous matrix [2]. The addition of other metals (e.g., Cr, Al, Co) modifies the magnetic properties of these materials [3–7]. The aim of this work is to analyse the influence of Co admixtures on FINEMET microstructure and hyperfine parameters, investigated with the transmission Mössbauer spectrometry based on ^{57}Fe . Systematic alterations of the composition are particularly important in considering the complex evolution of magnetic characteristics.

2. Experimental

Samples of thin amorphous ribbons with compositions $(\text{Fe}_{1-x}\text{Co}_x)_{73.5}\text{Cu}_1\text{Nb}_3\text{Si}_{13.5}\text{B}_9$ ($x = 0, 0.1, 0.2, 0.3, 0.4, 0.5, 0.7, 0.9$) were prepared by the melt-spinning technique. Nanocryst-

*Corresponding author. e-mail: t.szumiata@pr.radom.pl

talline specimens were obtained after heat treatment in a vacuum furnace at 570 °C for 1 hour. Room temperature ^{57}Fe Mössbauer measurements were performed using a transmission spectrometer with a $^{57}\text{Co}(\text{Rh})$ source of gamma radiation. The drive system was working in a constant acceleration mode and the velocity scale was divided into 256 channels.

3. Results and discussion

Mössbauer spectra of the as-quenched alloys were fitted using a histogram-like hyperfine field (HF) distribution, linearly correlated with the isomer shift (IS) distribution. Several local peaks or bulges can be distinguished in the hyperfine field distribution (at about 10 T, 20 T, and 24 T), reflecting the preferential environments of iron atoms. As a general tendency, increasing mean values of HF with Co increasing concentration are observed in the range $x \leq 0.5$, although for higher Co contents the average HF slowly decreases. Simultaneously, a monotonic growth of the mean isomer shift is noticed (Table 1), indicating a decreasing charge density on iron nuclei.

Table 1. Mean value of hyperfine field and isomer shift (with respect to α -Fe foil) for the as-quenched, amorphous $(\text{Fe}_{1-x}\text{Co}_x)_{73.5}\text{Cu}_1\text{Nb}_3\text{Si}_{13.5}\text{B}_9$ samples as function of cobalt content

$x(\text{Co})$	0	0.1	0.2	0.3	0.4	0.5	0.7	0.9
$\langle B \rangle$ [T]	21.29	21.85	21.85	22.26	22.33	22.79	22.56	22.42
$\langle \text{IS} \rangle$ [mm/s]	0.103	0.114	0.117	0.123	0.139	0.146	0.153	0.156

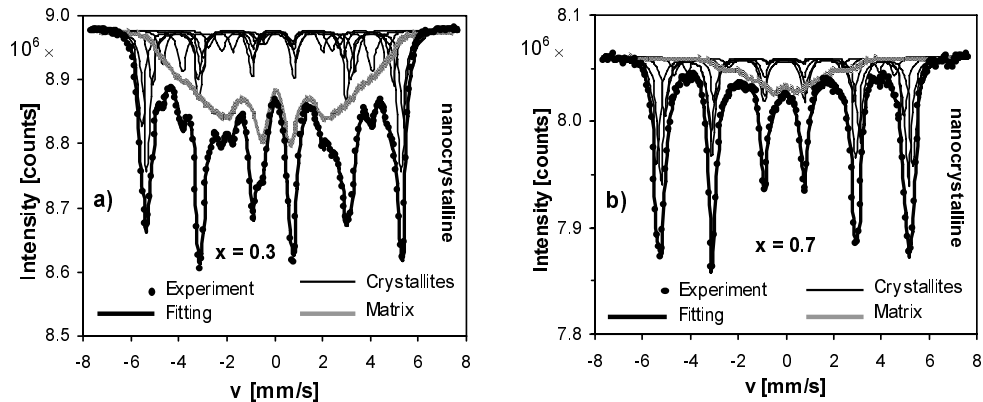


Fig. 1. Mössbauer spectra for annealed, nanocrystalline $(\text{Fe}_{1-x}\text{Co}_x)_{73.5}\text{Cu}_1\text{Nb}_3\text{Si}_{13.5}\text{B}_9$ samples with a) $x = 0.3$ and b) $x = 0.7$

The spectra with complex shapes, collected for nanocrystalline samples (Fig. 1), were fitted with a set of several (up to six) sharp Zeeman sextets attributed to the

nanocrystalline phase, and with a broad HF distribution originating from the amorphous matrix. The relative intensities of the sextets and their hyperfine parameters give information about the structure of the grains. The compositional evolution of the above-mentioned values (Fig. 2) points to a significant contribution of Co atoms to the crystalline phase. Additionally, a new component with the highest hyperfine field (above 33 T) appears in the spectra for $x \geq 0.2$, attributed to iron atoms that have a few Co atoms as near neighbours. For $x \leq 0.3$, we observed a significant intensity of the A4 sextet (with the lowest HF value being about 19.3 T), characteristic of the DO₃ structure (Fig. 2a). It is known that in pure FINEMET the crystallites comprise a DO₃-type Fe-Si alloy. Assuming that cobalt atoms substitute iron in the crystalline lattice, we can evaluate the silicon percentage inside grains, which is equal to about 16–20%. For higher Co contents, the A4 sextet decreases and eventually disappears. Collaterally, sextets with hyperfine fields above 30 T grow up to 90% of the discrete component. Such proportions between the intensities of individual sextets can give evidence of a *bcc* (Fe,Co)Si substitutional solid solution with about 5% of silicon.

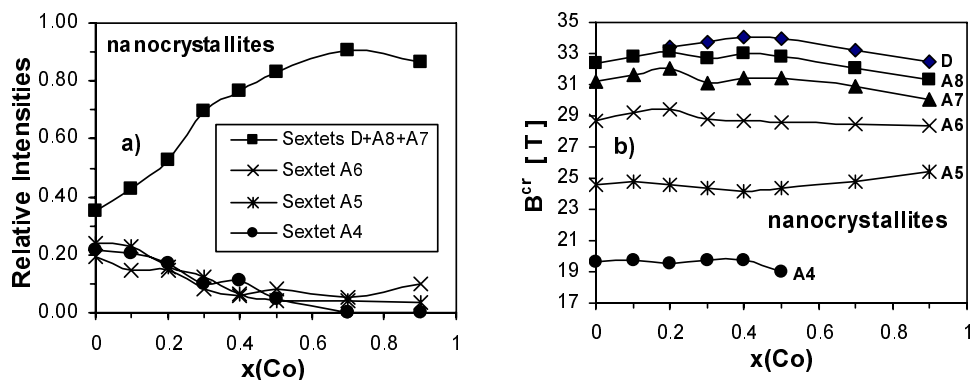


Fig. 2. Relative intensities of the sextets (a) and their hyperfine fields (b) for nanocrystallites in annealed $(\text{Fe}_{1-x}\text{Co}_x)_{73.5}\text{Cu}_1\text{Nb}_3\text{Si}_{13.5}\text{B}_9$ samples as a function of cobalt content x

The relative content of iron atoms belonging to the crystalline phase, p , has been derived from the relation between the intensities of the discrete and continuous components. It decreases from 72% for $x = 0$ to 51% for $x = 0.3$, and then increases up to 86%. In the range $x > 0.7$, p has a nearly constant value. Taking into account the similar heat treatment of all samples, these results point to some differences in the crystallization procedure in the ranges $0 < x < 0.3$ and $0.4 < x < 1$. The real volumetric fraction of the crystalline phase has been evaluated, considering that the concentrations of iron atoms in nanocrystallites and in the amorphous matrix are different due to the different contents of metalloids. For simplicity, we assume similar proportions between iron and cobalt concentrations in the nanocrystalline and amorphous phase. Evaluations (based on the method described, e.g., in [8]) show that the volumetric fraction of nanocrystallites does not differ significantly for minimal and maximal Co

contents, being however clearly lower for intermediate values of x (Fig. 3a). The percentage of iron inside the amorphous matrix diminishes considerably with increasing x . Therefore, the distribution of iron atoms becomes more inhomogeneous.

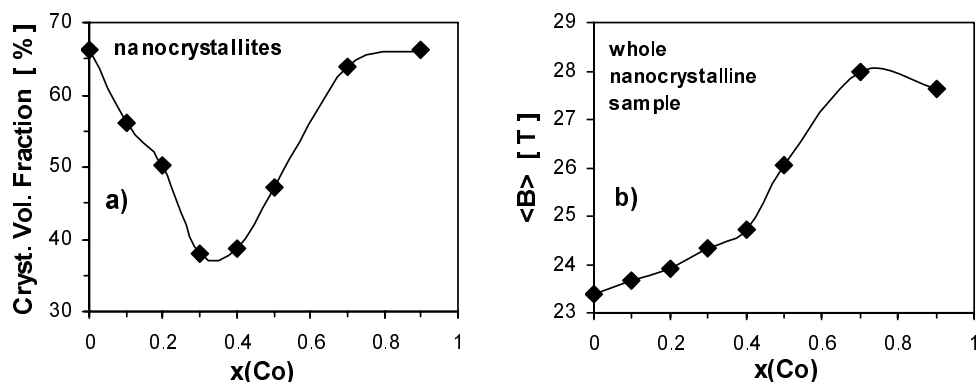


Fig. 3. The volumetric fraction of the nanocrystalline phase (a) and mean hyperfine field (b) in annealed $(\text{Fe}_{1-x}\text{Co}_x)_{73.5}\text{Cu}_1\text{Nb}_3\text{Si}_{13.5}\text{B}_9$ samples as a function of cobalt content x

The mean hyperfine field in general increases with Co concentration, except for the highest Co contents (Fig. 3b). The effect is caused by an increasing hyperfine field in crystallites, owing to larger $(\text{Fe} + \text{Co})$ concentration. This is accompanied by a depletion of iron in the amorphous matrix, resulting in a distinct drop of its mean hyperfine field, observed for $x > 0.4$. Simultaneous segregation of iron atoms inside grains causes the observed mean values of the magnetic hyperfine field not to reflect areas without iron or with very small iron concentration. Thus, the mean hyperfine field calculated for a whole sample is overestimated. This is probably the main reason that the compositional evolution of the mean hyperfine field is not well correlated with changes in magnetization (derived from magnetic measurements).

4. Conclusions

A non-monotonic dependence of the mean hyperfine field of as-quenched alloys on cobalt concentration was detected. In the case of annealed ribbons, the structural evolution of the crystalline phase was found accompanied with the substitution of iron by cobalt. Moreover, a growing chemical inhomogeneity was observed, manifesting itself by a depletion of iron in the amorphous matrix and, consequently, the alteration of the hyperfine parameters.

References

- [1] YOSHIKAWA Y., OGUMA S., YAMAUCHI K., J. Appl. Phys., 64 (1988), 6044.
- [2] HERZER G., IEEE Trans. Magn., 26 (1990), 1397.

- [3] MÜLLER M., GRAHL H., MATTERN N., KÜHN U., SCHNELL B., *Magn. Magn. Mater.*, 160 (1996), 284.
- [4] SOVÁK P., PAVLÍK G., TAUŠ M., ZORKOVSKÁ A., GOŚCIAŃSKA I., BALCERSKI J., *Czech. J. Phys.*, 54, Suppl. D (2004), D261.
- [5] SZUMIATA T., GÓRKA B., ZORKOVSKÁ A., SOVÁK P., *J. Magn. Magn. Mater.*, 288 (2005), 37.
- [6] BORREGO J.M., CONDE C.F., CONDE A., GRENÈCHE J.M., *J. Non-Crys. Sol.*, 287 (2001), 120.
- [7] BORREGO J.M., CONDE C.F., CONDE A., GRENÈCHE J.M., *J. Phys: Cond. Mat.*, 14 (2002), 883.
- [8] SZUMIATA T., BRZÓZKA K., GAWROŃSKI M., GÓRKA B., JEZUITA K., BLÁZQUEZ-GÁMEZ J.S., KULIK T., ŻUBEREK R., ŚLAWSKA-WANIEWSKA A., GRENÈCHE J.M., *J. Magn. Magn. Mater.*, 250 (2002), 83.

Received 1 June 2005

Revised 10 October 2005

Conductivities and transmission coefficients of ultra-thin disordered metallic films

B. J. SPISAK*, A. PAJA

Faculty of Physics and Applied Computer Science, AGH University of Science and Technology,
al. Mickiewicza 30, 30-059 Cracow, Poland

The diffusive motion of quasi-two-dimensional electron gas through an ultra-thin system of disordered potentials is considered. In such a system, the Fermi sphere splits into a set of independent sheets due to a small thickness of the system. Each sheet can be seen as an electron subband. Electron transport goes through these subbands independently. The sum of electrical conductivities over the subbands determines the total current, which is calculated for ultra-thin films of cesium. We also present the relation between our approach and the Landauer formalism based on the notion of the transmission coefficient.

Key words: *electron transport; disorder; relaxation time; thin film; transmission coefficient*

1. Introduction

Low-dimensional systems are artificial structures very interesting for fundamental research, and on the other hand their potential applications in nanoscale technology bring about the rapid development of experimental techniques strongly supported by theoretical methods of analysing their electronic properties. One of the simplest examples of such a system is a thin film. In these structures, the motion of electrons is confined to a thin layer of metal or semiconductor. Motion perpendicular to the layer surface is frozen and the electrons compose a quasi-two-dimensional gas [1]. Size effects in the conductivity of ultra-thin films have been discussed by Fedorov et al. [2]. They considered crystalline films of Cu, composed of 1 to 32 monolayers. They took into account surface and impurity scattering, and assumed a random δ -type impurity potential.

In our paper, we calculate the conductance of a totally disordered thin metallic film. We consider the scattering from all ionic potentials using the diffraction model for quasi-two-dimensional systems [3]. We neglect surface scattering, because we

*Corresponding author, e-mail: spisak@novell.fj.agh.edu.pl

assume a planar motion of charge carriers. Moreover, we assume a realistic, Coulomb-screened potential, located at positions given by the structure factor. Our results are very close to those of Fedorov et al. [2].

2. Theoretical approaches to transport

As is well established, a proper quantum mechanical description of electron transport in disordered systems is based on the linearised von Neumann equation for the density matrix. In the lowest order of perturbation theory, the diagonal elements of the density matrix satisfy a Boltzmann-type equation [4]. This derivation is given for the case of randomly located potentials in metal. Additionally, it is assumed that atomic potentials have no internal structures, therefore electrons scatter from them elastically. The interaction between electrons and potentials is given by the collision integral $I[f]$, which can be modelled by the relaxation time approximation [5]

$$I[f] = -\frac{f(k) - f_0(k)}{\tau_{tr}} \quad (1)$$

where $f(k)$ is a distribution function corresponding to small deviations from equilibrium as described by the Fermi–Dirac distribution function $f_0(k)$, and τ_{tr}^{-1} is the inverse transport relaxation time.

Here we use the diffraction model proposed in our previous paper [3], where we put forward a scheme for calculating the inverse transport relaxation time in thin films. In this model, real atomic potentials are replaced by equivalent pseudopotentials that should give the same effect. In the considered case, the disorder in a thin film is characterized by a two-dimensional structure factor, $S(q)$, approximated by a parabola. Finally, the inverse transport relaxation time is given by the formula

$$\tau_{tr}^{-1} = \frac{1}{(2\pi)^2} \frac{m^*}{\hbar^3} \alpha u_0^2 \int_0^\pi d\varphi \frac{\sin^4 \frac{\varphi}{2}}{\frac{1}{\pi \alpha k_F} + \sin^2 \frac{\varphi}{2} \left(1 - \left(\frac{\pi m}{L_z k_F}\right)^2\right)} \quad (2)$$

where α is the prefactor of the parabola, u_0 is the strength of the pseudopotential, L_z is the width of the layer in the z -direction, the number $m = 1, 2, \dots$ is a subband index, and the remaining symbols have their usual meaning.

The formula given by Eq. (2) depends on the quantum number m . This can be simply explained, namely the finite thickness of the layer causes the Fermi sphere

split into a set of independent sheets. The electronic transport properties of each sheet are characterized by individual inverse transport relaxation times, $[\tau_{tr}^{-1}]_m$, and the number of electrons per unit area, n_m . The knowledge of these quantities allows us to calculate the inverse of resistivity or conductivity, which is given by the following formula [5]:

$$\sigma_m = \frac{1}{L_z} \frac{n_m e^2 \tau_m}{m^*} \quad (3)$$

where τ_m is defined as the inverse of $[\tau_{tr}^{-1}]_m$.

As is well known, the Drude formula for the conductivity given by Eq. (3) can be derived from the semiclassical Boltzmann equation [6]. This expression, however, properly describes systems as far as $k_F \ell \gg 1$, where ℓ is the mean free path. On the other hand, this condition determines the metallic regime, where the motion of electrons is diffusive. The total conductivity of a thin disordered metallic film in the present model is given by the formula

$$\sigma = \sum_{m=1}^{m_{\max}} \sigma_m \quad (4)$$

where m_{\max} is defined by condition (20) in Ref. [3].

Conductivity can be extracted from the conductance G as a function of layer thickness L_z , namely for a very thin stripe the conductance is given by the formula

$$G = \sigma(L_z) L_z \quad (5)$$

An alternative approach to the problem of electron transport in solids is based on the scattering properties of the system. Conductance in the linear transport regime is given by the formula [1,7]

$$G = \frac{2e^2}{h} \frac{T}{1-T} \quad (6)$$

where T is the total transmission coefficient.

If we substitute Eq. (3) into Eq. (4) and compare Eqs. (5) and (6), we obtain the total transmission coefficient in the following form:

$$T = \frac{\sum_{m=1}^{m_{\max}} \frac{n_m e^2 \tau_m}{m^*}}{\frac{2e^2}{h} + \sum_{m=1}^{m_{\max}} \frac{n_m e^2 \tau_m}{m^*}} \quad (7)$$

3. Numerical results

We performed calculations of total conductivity for a thin disordered film of cesium as a function of its thickness L_z using Eq. (4). The values of L_z taken for calculations corresponded to multiples of the atomic diameter of cesium. The Fermi vector for Cs was taken as $k_F = 0.65 \times 10^{10} \text{ m}^{-1}$, and the coefficient α in the two-dimensional structure factor $S(q)$ we equal to 0.28 after Ref. [8]. The results are presented in Fig. 1.

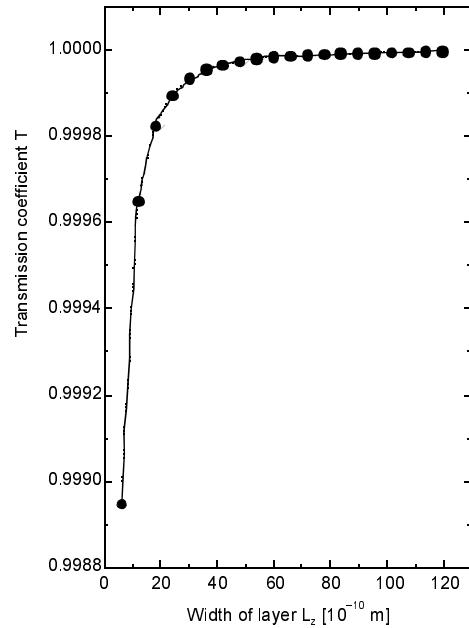
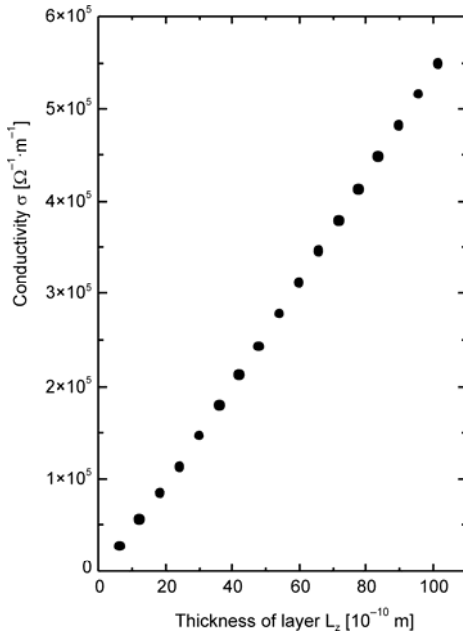


Fig. 1. Electrical conductivity of an ultra-thin film of Cs, calculated as a function of its thickness L_z

Fig. 2. Transmission coefficient of an ultra-thin film of Cs, calculated as a function of its thickness L_z . The solid line is a guide to the eye

The calculated conductivity σ increases almost linearly with increasing film thickness L_z . This is somewhat surprising, because σ is a material constant and should not depend on the size of the sample. In our model of quasi-two-dimensional electron gas, however, an increase of L_z gives rise to an increase of the number of open channels for electron transport. This is true if we neglect the transition between different electron subbands. If we take them into account, the inverse transport relaxation times become smaller and conductivity saturates. We can see that the transmission coefficient T actually saturates for L_z less than 100, which confirms our hypothesis about the conductivity.

4. Conclusions

We have used a diffraction model to investigate the electrical properties of a thin disordered metallic film, taking cesium as an example. We calculated the total con-

ductivity of a stripe with structural disorder for 1 to 17 monolayers as a function of its thickness. The dependence is monotonously increasing. The quantum size effect should be seen when integer multiples of half the Fermi wavelength fit exactly into the film thickness [9]. We calculated the conductivity for discrete values of the thickness (corresponding to full monolayers), and the deviations from monotonous behaviour occur between the points and cannot be seen.

Additionally, we find the relation between our model and a formalism based on the notion of the total transmission coefficient. The saturation observed in the transmission coefficient shows that electrical conductivity should also saturate in films that are thick enough.

In our approach, we do not discuss quantum interference effects between scattered electron waves, which lead to weak localization [9]. This is quite an important problem in two-dimensional systems, but on this level of approximation it can be justified, because only higher orders of perturbation theory for the density matrix include these effects [4, 10], and here we neglect these. We intend to incorporate these effects in future work.

References

- [1] DATTA S., *Electronic Transport in Mesoscopic Systems*, Cambridge University Press, Cambridge, 1999.
- [2] FEDOROV D., ZAHN P., MERTIG I., *Thin Solid Films*, 473 (2005), 346.
- [3] SPISAK B.J., PAJA A., *Mol. Phys. Rep.*, 40 (2004), 144.
- [4] LUTTINGER J.M., KOHN W., *Phys. Rev.*, 108 (1957), 590.
- [5] ASHCROFT N.W., MERMIN N.D., *Solid State Physics*, PWN, Warszawa, 1980 (in Polish).
- [6] ZIMAN J.M., *Electrons and Phonons*, Clarendon Press, Oxford, 2001.
- [7] LANDAUER R., *Phil. Mag.*, 21 (1970), 863.
- [8] KHAN N.Q., TOAN N.M., *Solid State Commun.*, 125 (2003), 133.
- [9] PFENNIGSTORF O., PETKOVA A., KALLASSY Z., HENZLER M., *Eur. Phys. J. B*, 30 (2005), 111.
- [10] KRAMER B., MACKINNON A., *Rep. Prog. Phys.*, 56, (1993), 1469.
- [11] ABRAHAMS E., ANDERSON P.W., LICCIARDELLO D.C., RAMAKRISHNAN T.V., *Phys. Rev. Lett.* 42, (1979) 673.

Received 1 June 2005
Revised 10 October 2005

Electronic structures of f-electron intermetallic compounds studied by positrons

M. SAMSEL-CZEKAŁA^{1*}, G. KONTRYM-SZNAJD¹, M. BIASINI^{2,3}

¹W. Trzebiatowski Institute of Low Temperature and Structure Research,
Polish Academy of Sciences, P.O. Box 1410, 50-950 Wrocław 2, Poland

²ENEA, via don Fiammelli 2, 40129, Bologna, Italy

³Department of Physics, University of California at Riverside, Riverside, California 92521, USA

Electronic structures of the isostructural rare-earth intermetallic compounds TmGa₃, ErGa₃ and CeIn₃ have recently been studied by measurements of two-dimensional angular correlations of annihilation radiation (2D ACAR) spectra. On the example of these systems, we show which kind of information can be exploited from such spectra, i.e. from line projections of the electron-positron momentum density $\rho(\mathbf{p})$. By applying various tomographic techniques, we check how these algorithms can affect reconstructed 3D momentum densities and Fermi surfaces (FS). We confirm that for all these systems in the paramagnetic phase the f-electrons are fully localized and their FSs are similar. TmGa₃ and ErGa₃ exhibit the FS nesting feature, in agreement with their magnetic structure, which is not the case for CeIn₃.

Key words: *electronic structure; positron annihilation; intermetallic compounds*

1. Introduction

The isostructural (AuCu₃-type) rare-earth compounds TmGa₃, ErGa₃, and CeIn₃ are interesting due to their magnetic properties, and CeIn₃ for its intriguing interplay of antiferromagnetism, heavy-fermion behaviour, and superconductivity when under pressure [1]. Their electronic structures have recently been probed by measurements of 2D ACAR spectra, yielding line projections of the electron-positron (e-p) momentum density $\rho(\mathbf{p})$ in the extended zone \mathbf{p} [2, 3].

Previous studies of TmGa₃, ErGa₃, and CeIn₃ (from three, four, and five 2D ACAR spectra, respectively) point out to the similarity of their electronic structures, both Fermi surface (FS) and f-electrons being localized in the paramagnetic phase

*Corresponding author, e-mail: m.samsel@int.pan.wroc.pl

[4, 5]. TmGa_3 and ErGa_3 exhibit the FS nesting feature that fits to the observed magnetic structure, which does not occur in CeIn_3 .

In this work, we discuss the results of reconstructing $\rho(\mathbf{p})$ in these systems by employing different reconstruction algorithms: the modified filtered back projection technique (MFBP) [6], the Cormack method (CM) [7], and new lattice harmonics expansion (LHE) [8] – to the same spectra as in Ref. [4]. Next, we perform Lock–Crisp–West (LCW) folding [9], i.e. conversion from the extended \mathbf{p} to reduced \mathbf{k} space, in order to map the FS. The reason for such investigations was that in the case of LaB_6 LHE gave a slightly different FS than other reconstruction algorithms [8].

2. Results and discussion

In this paper, we limit our analysis of densities $\rho(\mathbf{p})$ to their isotropic average $\rho_0(p)$. Due to the similarity of the reconstructed densities after using different algorithms, in Fig. 1 we show only $\rho_0(p)$ reconstructed by LHE. In order to compare the results for various metals, we present them in units of p/p_F and normalized to

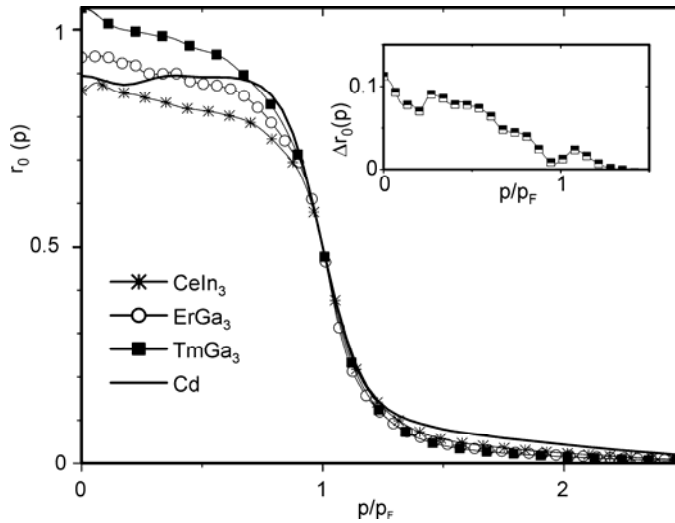


Fig. 1. The isotropic average of momentum densities, $\rho_0(p)$, reconstructed from 2D ACAR spectra of various metals. Inset: the difference between $\rho_0(p)$ in TmGa_3 and ErGa_3

$\rho_0(p/p_F = 1) = 0.5$. The results for rare-earth compounds are compared with densities reconstructed from 2D ACAR data [10] for Cd for the following reason. According to theoretical calculations [11], $4d^{10}$ electrons in Cd are very close to the conduction band minimum, i.e. they are not as strongly localized as typical core states. It is seen in Fig. 1 (inset) that $\rho_0(p/p_F)$ for rare-earth compounds is lower than for Cd for momenta $p/p_F > 1$. Therefore, knowing that the more localized states there are the

smaller the probability of e-p annihilation (positrons as positive particles are repelled from positive ions), we can conclude that the *f*-electrons of the considered systems are strongly localized (below the conduction band minimum). A big discrepancy between ρ_0 in these compounds observed for momenta $p/p_F < 1$ comes, most likely, from differences in the compositions of their cores. TmGa₃ has twelve 4*f* electrons per unit cell, i.e. one more than ErGa₃. Hence, $\rho_0(p)$ for TmGa₃ should be higher than for ErGa₃ (as observed), with the difference similar to a typical core contribution (inset of Fig. 1). CeIn₃, in turn, has only one 4*f* electron per unit cell but three atoms of In provide additional (comparing to Ga) $3 \times (4s^2 + 4p^6 + 4d^{10})$ core electrons. It is therefore somewhat surprising that $\rho_0(p)$ in CeIn₃ is smaller than in ErGa₃. This indicates that localized *f*-electrons are relatively close to the bottom of the conduction band minimum.

Obviously, it is impossible to obtain the shape of the FS from the density $\rho(\mathbf{p})$ itself due to the fact that $\rho(\mathbf{p})$ is not constant on the FS and represents a sum of contributions from all occupied bands, not only those crossing the Fermi energy. Thus, in order to map the FS, LCW conversion [9] is usually performed, $\rho(\mathbf{k}) = \sum_{\mathbf{G}} \rho(\mathbf{p} = \mathbf{k} + \mathbf{G})$, providing momentum densities in reduced \mathbf{k} space (\mathbf{G} are the reciprocal lattice vectors). If the influence of the positron wave function and many-body effects are ignored, $\rho(\mathbf{k})$ depends only on the electron occupation numbers ($n_j(\mathbf{k}) = 0$ or 1) in the *j*-th band. The total contribution of all bands is then equal to $\sum_j n_j(\mathbf{k}) = n(\mathbf{k})$, where $n(\mathbf{k})$ denotes the number of occupied bands at the point \mathbf{k} . In the case of e-p densities, $\rho_j(\mathbf{k}) = n_j(\mathbf{k})g_j(\mathbf{k})$, where the function $g_j(\mathbf{k})$ depends on the electron state $|\mathbf{k}_j\rangle$, even after neglecting e-e and e-p correlations [12,13]. Particularly, small values of g are expected for localized *d*-like states, because an increase of electron state localization decreases the probability of e-p annihilation. Therefore, if the character of various states $|\mathbf{k}_j\rangle$ varies strongly, their relative contributions to $\rho_j(\mathbf{k})$ may be essentially different. Nevertheless, the values of $g_j(\mathbf{k})$ are usually high enough to reproduce an observable jump in $\rho_j(\mathbf{k})$ if this quantity passes from one band to another [12, 13].

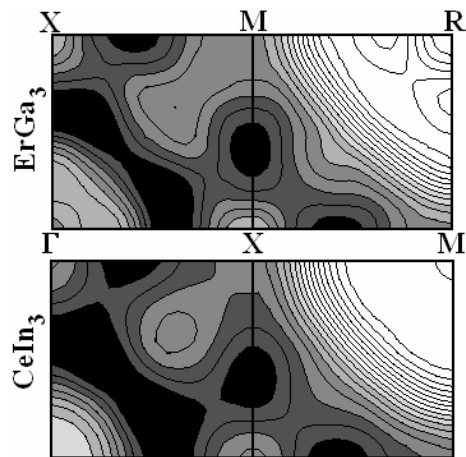


Fig. 2. Densities $\rho(\mathbf{k})$ in ErGa₃ and CeIn₃ on high symmetry planes, reconstructed using LHE. The white region centred at *R* contains the occupied states of the 7th valence band, and the dark region corresponds to the unoccupied states of the 6th band

According to theoretical calculations [4] (with f electrons as core states), the FS sheets of TmGa_3 , ErGa_3 , and CeIn_3 exist in the 6th and 7th valence bands. In Figure 2, we display densities $\rho(\mathbf{k})$ in ErGa_3 and CeIn_3 on high symmetry planes in the Brillouin zone (BZ), reconstructed by the LHE. It is visible that the general shapes of these densities and thus also of the FSs are similar. The nesting of the FS centred around R (Fig. 2) on the planes perpendicular to the XR line (the $[110]$ direction) is in agreement with the propagation vector of the magnetic structure of ErGa_3 . If the FS nesting were present in CeIn_3 , consistent with its antiferromagnetic structure, it would be observed along the $[111]$ direction. No experimental evidence of nesting, however, can be observed. Obviously, even if the electronic structure is in fair agreement with experiment, only a full calculation of Q-dependent magnetic susceptibility can reveal to what extent the adopted band structure calculation is able to account for the magnetic structure of CeIn_3 .

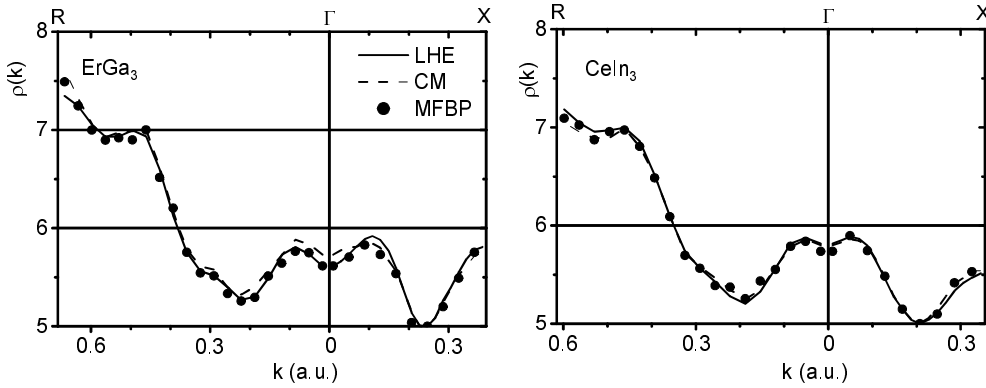


Fig. 3. Densities $\rho(k)$ in ErGa_3 and CeIn_3 along Γ_X and Γ_R , reconstructed using LHE, CM, and MFBP

In order to show more details, in Fig. 3 we present $\rho(\mathbf{k})$ for ErGa_3 and CeIn_3 along some high symmetry directions in the BZ, reconstructed by LHE, CM, and MFBP, and normalized to the number of occupied bands in points \mathbf{k} . It is seen that $\rho(\mathbf{k})$, very similar for both compounds (the same for TmGa_3 not shown here), differs mainly around the R and X points. Around R , where 7 bands are fully occupied, the electron occupation number $n(\mathbf{k})$ is equal to 7. Along the ΓX line and around $k = 0.25$ a.u. (5 bands fully occupied), $n(\mathbf{k}) = 5$ and $n(\mathbf{k}) = 6$ around the Γ and X points. Differences between the occupation numbers $n(\mathbf{k})$ and $\rho(\mathbf{k})$ point out that electrons around R are more free than others and that this effect is more pronounced for ErGa_3 than for CeIn_3 .

3. Conclusions

We presented e-p momentum densities in TmGa_3 , ErGa_3 , and CeIn_3 as reconstructed by various techniques, showing how a positron annihilation experiment en-

ables the character of electrons to be examined. We confirm that *f*-electrons in these compounds are strongly localized in the paramagnetic phase and their FSs are similar to one another. The FS nesting feature in TmGa₃ and ErGa₃ is consistent with the magnetic structure observed by neutrons [14, 15], which is not the case for CeIn₃.

Acknowledgements

We are very grateful to the Polish State Committee for Scientific Research (Grant No. 2 P03B 012 25) and the network MAG-EL-MAT in Poznań (Poland) for financial support.

References

- [1] GROSCHE F.M., WALKER I.R., JULIAN S.R., MATHUR N.D., FREYE D.M., STEINER M.J., LONZARICH G.G., *J. Phys.: Condens. Matter*, 13 (2001), 2845 and references therein.
- [2] BERKO U.P., [in:] W. Brandt, A. Dupasquier (Eds.), *Int. School Phys. Enrico Fermi Course LXXXIII*, North-Holland, Amsterdam, 1983, p. 64.
- [3] WEST R.N., *Adv. Phys.*, 22 (1973), 263; [in:] A. Dupasquier, A.P. Mills Jr. (Eds.), *Positron Spectroscopy of Solids*, IOS Press, Amsterdam, 1995.
- [4] BIASINI M., KONTRYM-SZNAJD G., MONGE M.A., GEMMI M., CZOPNIK A., JURA A., *Phys. Rev. Lett.*, 86 (2001), 4616; BIASINI M., FERRO G., KONTRYM-SZNAJD G., CZOPNIK A., *Phys. Rev. B*, 66 (2002), 075126; BIASINI M., FERRO G., CZOPNIK A., *Phys. Rev. B*, 68 (2003), 094513.
- [5] RUSZ J., BIASINI M., *Phys. Rev. B*, 71 (2005), 233103.
- [6] BROOKS R.A., DI CHIRO G., *Phys. Med. Biol.*, 21 (1976), 689; KONTRYM-SZNAJD G., JÓZEF CZUK E., *Mat. Sci. Forum*, 255–257 (1997), 754.
- [7] CORMACK A.M., *J. Appl. Phys.*, 34 (1963), 2722; 35 (1964), 2908; KONTRYM-SZNAJD G., *Phys. Stat. Sol. (a)*, 117 (1990), 227.
- [8] KONTRYM-SZNAJD G., SAMSEL-CZEKALA M., BIASINI M., KUBO Y., *Phys. Rev. B*, 70 (2004), 125103.
- [9] LOCK D.G., CRISP V.H.C., WEST R.N., *J. Phys. F: Met. Phys.*, 3 (1973), 561.
- [10] WALTERS P.A., MAYERS J., WEST R.N., [in:] *Positron Annihilation*, Proc. 6th Int. Conference *Positron Annihilation*, The University of Texas at Arlington, April 3–7, 1982, P.G. Coleman, S.C. Sharma, L.M. Diana (Eds.), North-Holland, Amsterdam, 1982, p. 334.
- [11] DANIUK S., JARLBORG T., KONTRYM-SZNAJD G., MAJSNEROWSKI J., STACHOWIAK H., *J. Phys. Condens. Matter*, 1 (1989), 8397.
- [12] RABOU L.P.L.M., MIJNARENS P.E., *Solid State Commun.*, 52 (1984), 933.
- [13] KAISER J.H., WEST R.N., SHIOTANI N., *J. Phys. F: Met. Phys.*, 16 (1986), 1307.
- [14] MORIN P., GIRAUD M., BURLET P., CZOPNIK A., *J. Magn. Magn. Mater.*, 68 (1987), 107.
- [15] MURASIK A., CZOPNIK A., KELLER L., FISCHER P., *J. Magn. Magn. Mater.*, 213 (2000), 101.

Received 1 June 2005

How to make GaMnAs with a high ferromagnetic phase transition temperature?

J. SADOWSKI^{1,2*}, J. Z. DOMAGAŁA¹, J. KANSKI³,
C. H. RODRIGUEZ⁴, F. TERKI⁴, S. CHARAR⁴, D. MAUDE⁵

¹Institute of Physics, Polish Academy of Sciences, al. Lotników 32/46, 02-668 Warszawa, Poland

²Institut für Angewandte und Experimentelle Physik, Universität Regensburg,
93040 Regensburg, Germany

³Department of Applied Physics, Chalmers University of Technology, SE-41296 Göteborg, Sweden

⁴Groupe d'Etude des Semiconducteurs CC074, Université Montpellier II, Montpellier, France

⁵High Magnetic Field Laboratory, CNRS-MPI, 25 Avenue des Martyrs, 38042 Grenoble, France

We analyse the role of structural defects in GaMnAs and demonstrate how their density can be drastically reduced by *in situ* post-growth annealing under As capping. Modifications of the magnetic, transport, and structural properties of annealed GaMnAs layers are presented. The main result is that Curie temperatures are strongly increased relative to those of as-grown layers, typically from 70–80 K to 150–160 K. The annealed layers exhibit well-ordered smooth surfaces, suitable for further epitaxial overgrowth.

Key words: *ferromagnetic semiconductor; molecular beam epitaxy; defect, annealing*

1. Introduction

GaMnAs is a model semiconductor with carrier-induced ferromagnetism. It is currently being used to test prototype spintronic devices, such as spin-diodes [1] and giant magnetoresistance structures [2]. Since the first report on ferromagnetism in GaMnAs by Ohno et al. [3], a lot of interesting, spin-related phenomena have been observed in this material. The remarkable magnetotransport properties of GaMnAs enabled the observation of the giant planar Hall effect [4], current driven magnetization reversal [5], and the dependence of magnetic anisotropy on the concentration of carriers [6]. In spite of these results associated with the magnetic properties of GaMnAs, it is still desirable to improve its quality and obtain a material with the ferromagnetic phase transition temperature (T_c) significantly higher than the present record value of 173 K. The mean field Zener model of carrier-

*Corresponding author, e-mail: sadow@ifpan.edu.pl

mediated ferromagnetism in transition metal doped semiconductors developed by Dietl et al. [7] predicts that T_c will reach room temperature for GaMnAs containing 10% of Mn [8] and correspondingly high concentrations of carriers (valence band holes).

The presence of valence band holes is indeed underlined by recently reported extraordinarily high T_c values (250 K) in delta-doped AlGaAs/GaAs quantum well structures [9]. This is also the underlying reason for the markedly increased T_c values accompanying post-growth annealing discussed here. The direct effect of annealing is the efficient removal of Mn atoms from interstitial positions (Mn_i). As shown both theoretically [10, 11] and experimentally, these defects are always present in as-grown GaMnAs, with concentrations of up to about 20% of total Mn content, and they act as double donors. Thus, by reducing the density of Mn interstitials, the density of valence band holes is expected to increase. This was first demonstrated by Edmonds et al. [12], who found that Mn_i defects can be removed by low temperature post-growth annealing of samples exposed to the air after MBE growth. Since GaMnAs with Mn concentrations in the range of a few at. % is intrinsically metastable, the annealing temperature should be kept low. At temperatures above 300 °C, GaMnAs starts to decompose to MnAs inclusions in a GaAs matrix. These inclusions, if sufficiently large, are also ferromagnetic, since MnAs is a ferromagnetic metal with $T_c = 40$ °C, but the GaAs:MnAs system is usually highly resistive, and the main advantage of GaMnAs, namely ferromagnetism mediated by carriers in a semiconductor, is lost. The best results achieved so far are thus obtained after very long annealing periods (~100 hours) at temperatures well below the growth temperature [12]. Higher annealing temperatures and short annealing times (0.5–3 hrs) have also been successfully applied [13–15].

In this paper, we present a modification of the low-temperature annealing method, which uses amorphous As layers deposited on the GaMnAs surface directly after MBE growth as a passivating medium for out-diffused Mn interstitials. We show that our method is more efficient in terms of shorter annealing times and lower annealing temperatures than annealing in air. Moreover, it leaves the GaMnAs surface suitable for further epitaxy, either in the same MBE system which was used for GaMnAs layer growth, or in another MBE system, since As capping forms a protective layer inhibiting surface oxidation and preserving a clean, atomically flat, as-grown surface.

2. Sample preparation

GaMnAs samples were grown in a KRYOVAK MBE system, located at MAX-Lab, Lund University, Sweden. Arsenic was supplied from a valved cracker source. The epitaxially grown GaAs(100) substrates were attached to molybdenum holders with liquid In. After thermal desorption of the native oxide, a standard high temperature GaAs buffer was deposited. The substrate temperature was then decreased to 230–240 °C for growing the GaMnAs layer. During this growth, the As_2 to Ga flux ratio was about 2, and the growth rate about 0.2 molecular layers (ML) per second. The growth was

monitored by reflection high-energy electron diffraction (RHEED). The diffraction showed a 2-dimensional monocrystalline GaMnAs surface, with (1×2) surface reconstruction, and no admixture of other phases (such as MnAs inclusions). Intensity oscillations of the specular beam were used to measure GaMnAs composition *in-situ*, by measuring the growth rate increase of GaMnAs with respect to GaAs. The thicknesses of the GaMnAs layers were chosen between 100 and 1000 Å (thicker layers usually exhibit worse magnetic properties). After completing GaMnAs growth, the As flux was cut by closing the As shutter as well as the As-cracker valve. The substrate heater was then turned off, and when the temperature fell below 150 °C, the As valve and shutter were open again for depositing a thick amorphous As layer. The thickness of this capping layer was in the range 1000 – 2000 Å, as measured by SIMS.

3. Defects in GaMnAs

The most abundant defects present in GaMnAs are As antisites (As_{Ga}) and Mn interstitials. Both defects are double donors, effectively compensating the p-doping provided by Mn atoms in Ga sites (Mn_{Ga}). In the Zener mean field model [7], T_c depends on the density of local moments and the density of charge carriers according to the relation

$$T_c \sim [Mn_{Ga}]p^{1/3} \quad (1)$$

Due to the compensating effect of As_{Ga} and Mn_I defects, the net density of holes p is

$$p = [Mn_{Ga}] - 2([As_{Ga}] + [Mn_I]) \quad (2)$$

According to (1) and (2), maximising T_c requires both a maximum concentration of Mn_{Ga} and minimum concentration of As_{Ga} and Mn_I defects. These two demands are in effect contradictory, since increasing Mn content in GaMnAs requires a reduced growth temperature [16, 17]. Low growth temperature, however, promotes the formation of As antisite defects [18]. Thus, there exists a Mn concentration that provides compromise between these two tendencies. Experimental evidence suggests that this optimum Mn content is in the range 6–8 at. %. The maximum Mn content achieved so far in uniform GaMnAs is 10% [19], however growing $Ga_{0.9}Mn_{0.1}As$ requires very low growth temperatures (about 150 °C) and special growth procedures. The concentrations of two compensating defects (As_{Ga} and Mn_I) can attain levels [20, 21] of ca. 0.5 and 1.7 at. %, respectively, which means that the compensation degree in GaMnAs can be as high as 50–70%. Indeed, such high compensation levels are observed in the as-grown material. As an example we show in Fig. 1 the results of the Hall effect measurements for a 300 Å thick $Ga_{0.94}Mn_{0.06}As$ layer. A general problem in extracting carrier concentration in GaMnAs from the Hall effect measurements is negative magnetoresistance, which can be quite large, up to 20–30%. In the case of the sample shown in Fig. 1, the negative magnetoresistance is rather small, only about 2%. In this case, the value of p can be taken from the R_{xy} vs. B slope without the necessity of sub-

tracting the negative magnetoresistance, and we thus find $p = 6.5 \times 10^{20} \text{ cm}^{-3}$. Mn content of 6% should provide a hole density of $1.32 \times 10^{21} \text{ cm}^{-3}$, which means that the compensation of Mn_{Ga} in this sample is on the level of 50%. This compensation is due to both As_{Ga} and Mn_{I} , and it is not possible to estimate their individual contributions without additional measurements.

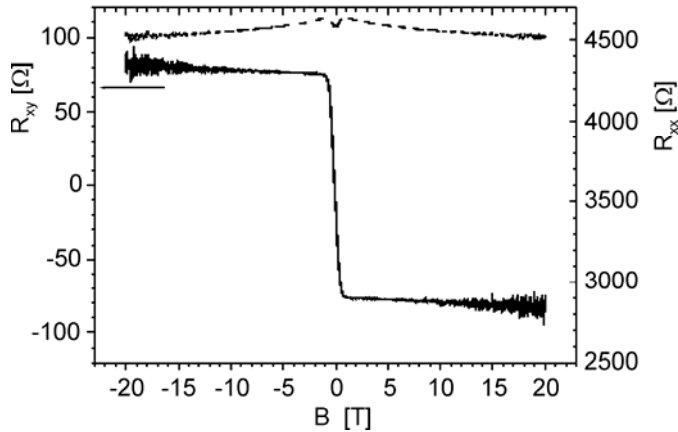


Fig. 1. Results of Hall effect measurements for an as-grown 300 Å thick $\text{Ga}_{0.94}\text{Mn}_{0.06}\text{As}$ layer. Solid curve – Hall resistance R_{xy} , dashed curve – longitudinal resistance R_{xx} . The concentration of holes in the sample – $6.5 \times 10^{20} \text{ cm}^{-3}$ (50% compensation of Mn_{Ga} acceptors)

The concentration of Mn_{I} can be obtained from Rutherford back-scattering (RBS) and particle-induced X-ray emission (PIXE) measurements [21] but the density of As_{Ga} in GaMnAs is more difficult to assess. Since the density of As antisites is mainly related to the growth temperature, and it is independent of the presence of Mn interstitials [22], one can expect that the concentration of As_{Ga} in GaMnAs should be the same as in GaAs grown at the same low temperature. In the case of LT GaAs, the density of As_{Ga} defects can be determined by X-ray diffraction (XRD), since these defects cause a crystal lattice expansion proportional to their content [18, 23] (in the case of GaMnAs the situation is more complicated, since both As_{Ga} and Mn_{I} cause lattice expansion). Thus, by measuring XRD on the LT-GaAs buffer layers grown prior to GaMnAs, we can estimate the density of As antisites. Fig. 2 shows the results of XRD measurements for three 500 Å thick $\text{Ga}_{0.96}\text{Mn}_{0.04}\text{As}$ samples grown at conditions that change the concentration of As_{Ga} , namely at different As_2/Ga flux ratios (2, 5, and 9). The inset shows a comparison between the measured and calculated XRD spectra for the sample with the lowest As_2/Ga flux ratio. The presence of X-ray interference fringes in the measured curve and a very good correspondence between the measured and calculated spectra prove a high quality of the GaMnAs layers – the broadening of the GaMnAs peaks is due to small film thickness. In these curves, the contribution from the LT-GaAs buffer layer is seen as a shoulder on the low-angle

side of the main (004) peak of the GaAs substrate. It is clear that the sample grown at the lowest As_2/Ga flux ratio has also the lowest As_{Ga} concentration, since the shoulder is least pronounced in this case.

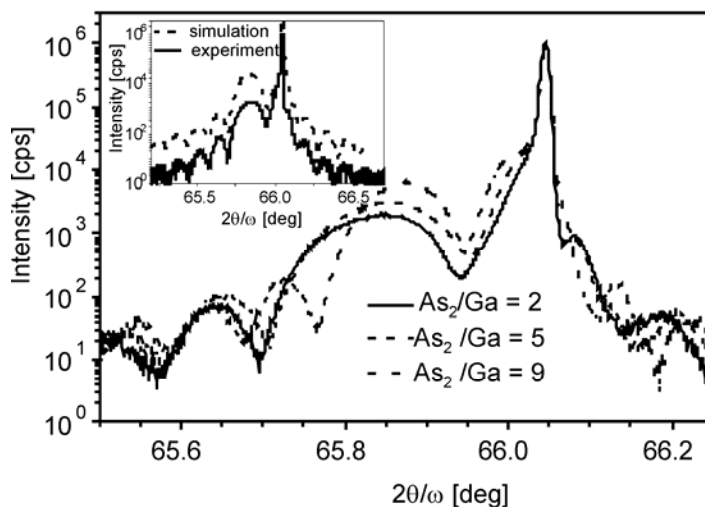


Fig. 2. (004) X-ray Bragg reflections for three 500 Å thick $\text{Ga}_{0.96}\text{Mn}_{0.04}\text{As}$ samples grown at different As_2/Ga flux ratios. The highest intensity peak on the right side results from diffraction on the GaAs(001) substrate. Broad peaks at lower angles are due to diffraction on GaMnAs layers. The inset shows a comparison between simulated and measured spectra for the sample grown at the lowest As_2/Ga flux ratio

For samples grown at higher As_2/Ga flux ratios, the peaks from LT-GaAs are shifted further towards lower diffraction angles, reflecting a lattice expansion caused by the As_{Ga} defects. In contrast, the diffraction peaks from the GaMnAs layers shift towards higher angles for increasing As_2/Ga flux ratios. This suggests that the concentration of Mn_I decreases with an increasing concentration of As_{Ga} in GaMnAs. The quantitative analysis of this process has been presented elsewhere [23].

4. Defect removal by post-growth annealing

From the two defects considered above, namely As antisites and Mn interstitials, the latter is only weakly bound, and can be effectively removed from the GaMnAs bulk by post-growth annealing [12–15, 24]. It has been also shown [24, 25–28] that the essential factor in post-growth annealing is the surface passivation of the out-diffused Mn_I atoms. The annealing of GaMnAs layers capped with even very thin LT GaAs films was found to be ineffective [25]. Moreover, the annealing efficiency of GaMnAs layers with rough surfaces was found to be enhanced compared to smooth layers [28]. All these results suggest that post-growth annealing is associated with pas-

sivating the diffusing Mn_I defects at the GaMnAs surface. Passivation can be due to chemical bonding with oxygen or nitrogen when the GaMnAs surface is exposed to air, or with another reactive element that can be deposited on the GaMnAs surface after MBE growth. We have recently proposed to use an amorphous As capping as a passivating species [24], and all the annealing results presented here concern this situation.

Figure 3 presents the results of the Hall effect measurements for the same sample as in Fig. 1, but after post growth annealing performed at 180 °C for 3 hours. The removal efficiency of Mn interstitials is close to 100%, since the concentration of holes increased from $6.5 \times 10^{21} \text{ cm}^{-3}$ to $1.3 \times 10^{21} \text{ cm}^{-3}$, which corresponds almost exactly to the content of Mn_{Ga} . The ferromagnetic phase transition temperature for this sample is 150 K.

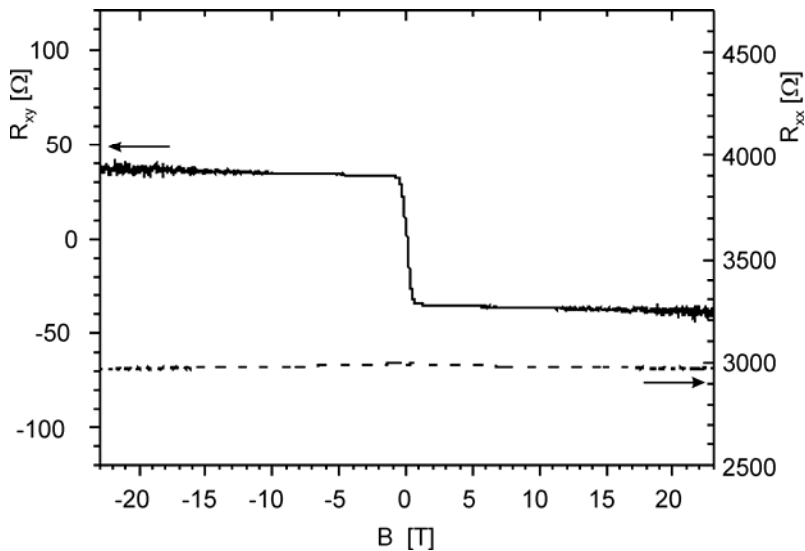


Fig. 3. Results of Hall effect measurements for a 300 Å thick $Ga_{0.94}Mn_{0.06}As$ layer annealed for 3h at 180 °C. Solid curve – hall resistance R_{xy} , dashed curve – longitudinal resistance R_{xx} . The concentration of holes in the sample is $1.3 \times 10^{21} \text{ cm}^{-3}$, corresponding almost exactly to the content of Mn at Ga sites (Mn interstitial defects effectively removed by post-growth annealing). The scales for R_{xx} and R_{xy} are the same as in Fig. 1

Figure 4 shows the temperature dependence of magnetization, measured by a SQUID magnetometer for a 400 Å thick $Ga_{0.94}Mn_{0.06}As$ layer with amorphous As capping, before and after annealing at 180 °C for 2h. This sample is very similar to the one in Fig. 3, but somewhat thicker. The remarkable increase of T_c from about 70 K to about 150 K can also be seen for this sample. The T_c increase is correlated with the increased saturation magnetisation observed at low temperatures. This is due to the removal of antiferromagnetically coupled pairs of $Mn_{Ga}-Mn_I$, which are excluded from participating in the FM phase of the non-annealed sample.

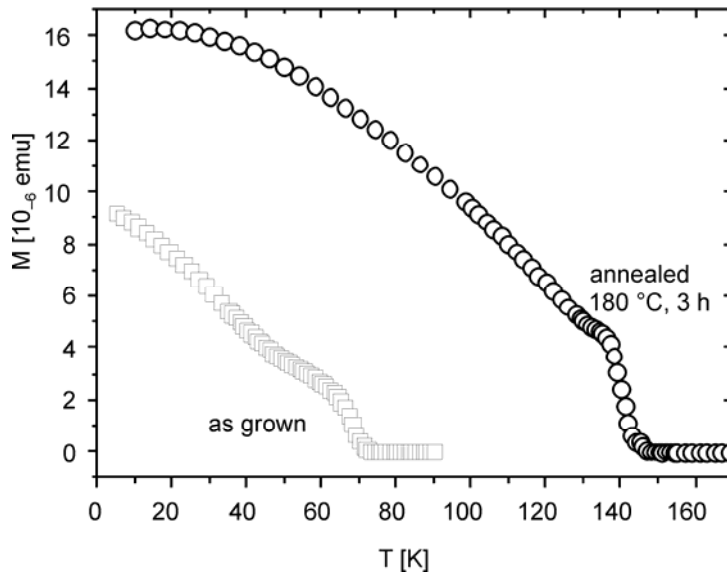


Fig. 4. Temperature dependence of magnetization for a 400 Å thick $\text{Ga}_{0.94}\text{Mn}_{0.06}\text{As}$ layer with an amorphous As capping surface layer, before and after post-growth annealing at 180 °C for 3h. Post-growth annealing increases both T_c and the saturation magnetization

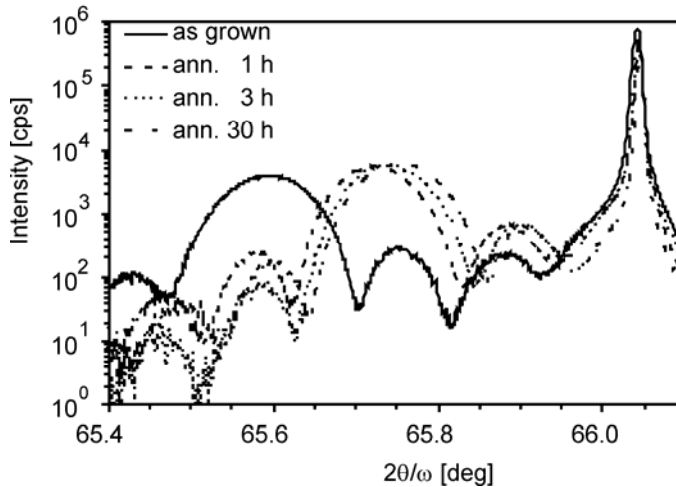


Fig. 5. (004) X-ray Bragg reflections for not annealed (solid curve) and annealed pieces of As-capped 700 Å thick $\text{Ga}_{0.94}\text{Mn}_{0.06}\text{As}$ layers. The shifts in the GaMnAs diffraction peaks to higher angles upon annealing are due to the annealing-induced reduction of the GaMnAs lattice parameter

The efficiency of removing Mn_i defects by annealing As-capped samples is also confirmed by XRD measurements (see Fig. 5). As already discussed, Mn interstitials cause lattice expansion, so that the lattice constant is expected to decrease upon removing these defects. Figure 5 shows significant shifts of (004) Bragg reflections

from a 700 Å thick Ga_{0.94}Mn_{0.06}As layer after consecutive annealings lasting 1, 2, 3, and 30 hrs at 180 °C. Already after 1 hour of annealing the GaMnAs lattice parameter is significantly reduced, annealing for 2 and 3 hours induce only small further reductions, and annealing for further 30 hours has no effect.

5. Conclusions

An efficient method for eliminating Mn interstitials from GaMnAs by post-growth annealing under As capping has been demonstrated. The efficiency of the process is proved by a significant increase of T_c , up to 150 K, for Ga_{0.94}Mn_{0.06}As, as well as by an increase in the concentration of holes to the range of 10^{21} cm⁻³. An additional advantage of our method is that the treatment is carried out *in situ*, and that the surfaces of the annealed layers are smooth and well-ordered. This provides possibility of performing further epitaxial growth on top of the high quality, Mn interstitial-defect-free GaMnAs layers.

Acknowledgements

The present work is part of a project supported by the Swedish Research Council VR. One of the authors (J.S.) acknowledges the financial support from the Polish State Committee for Scientific Research (KBN) through Grant No. PBZ-KBN-044/P03/2001. Measurements at high magnetic fields were supported by the European Community within the *Access to Research Infrastructure action of the Improving Human Potential Programme*.

References

- [1] FLATTÉ M.E., VIGNALE G., Appl. Phys. Lett., 78 (2001), 1273.
- [2] MATTANA R., ELSÉN M., GEORGE J.-M., JAFFRÈS H., NGUYEN VAN DAU F., FERT A., WYCZISK M.F., OLIVIER J., GALTIER P., LÉPINE B., GUIVARC'H A., JÉZÉQUEL G., Phys. Rev. B, 71 (2005), 075206.
- [3] OHNO H., SHEN A., MATSUKURA F., OIWA A., ENDO A., KATSUMOTO S., IYE Y., Appl. Phys. Lett., 69 (1996), 363.
- [4] TANG H.X., KAWAKAMI R.K., AWSCHALOM D.D., ROUKES M.L., Phys. Rev. Lett. 90 (2003), 107201.
- [5] CHIBA D., SATO Y., KITA T., MATSUKURA F., OHNO H., Phys. Rev. Lett., 93 (2004), 216602.
- [6] SAWICKI M., WANG K.-Y., EDMONDS K.W., CAMPION R.P., STADDON C.R., FARLEY N.R.S., FOXON C.T., PAPIŚ E., KAMINSKA E., PIOTROWSKA A., DIETL T., GALLAGHER B.L., Phys. Rev. B, 71 (2005), 121302.
- [7] DIETL T., OHNO H., MATSUKURA F., Phys. Rev. B, 63 (2001), 195205.
- [8] DIETL T., Semicond. Sci. Technol., 17 (2002), 377.
- [9] NAZMUL A.M., AMEMIYA T., SHUTO Y., SUGAHARA S., TANAKA M., Phys. Rev. Lett., 95 (2005), 017201.
- [10] MASEK J., MACA F., Acta Phys. Polon. A, 100 (2001), 319.
- [11] BLINOWSKI J., KACMAN P., Phys. Rev. B, 67 (2003), 121204.
- [12] EDMONDS K.W., BOGUSŁAWSKI P., WANG K.Y., CAMPION R.P., NOVIKOV S.N., FARLEY N.R.S., GALLAGHER B.L., FOXON C.T., SAWICKI M., DIETL T., BUONGIORNO NARDELLI M., BERNHOLC J., Phys. Rev. Lett., 92 (2004), 037201.
- [13] CHIBA D., TAKAMURA K., MATSUKURA F., OHNO H., Appl. Phys. Lett., 82 (2003), 3020.

- [14] KU K.C., POTASHNIK S.J., WANG R.F., CHUN S.H., SCHIFFER P., SAMARTH N., SEONG M.J., MASCARENHAS A., JOHNSTON-HALPERIN E., MYERS R.C., GOSSARD A.C., AWSCHALOM D.D., *Appl. Phys. Lett.*, **82** (2003), 2302.
- [15] KIRBY B.J., BORCHERS J.A., RHYNE J.J., TE VELTHUIS S.G.E., HOFFMANN A., O'DONOVAN K.V., WOJCIWICZ T., LIU X., LIM W.L., FURDYNA J.K., *Phys. Rev. B*, **69** (2004), 081307.
- [16] OHNO H., *Science*, **281** (1998), 951.
- [17] SADOWSKI J., DOMAGALA J.Z., BAK-MISIUK J., KOLESNIK S., SAWICKI M., SWIATEK K., KANSKI J., ILVER L., STRÖM V., *J. Vac. Sci. Technol. B*, **18** (2000), 1697.
- [18] LIU X., PRASAD A., NISHIO J., WEBER E.R., LILIENTAL-WEBER Z., WALUKIEWICZ W., *Appl. Phys. Lett.*, **67** (1995), 279.
- [19] SADOWSKI J., MATHIEU R., SVEDLINDH P., DOMAGALA J.Z., BAK-MISIUK J., SWIATEK K., KARLSTEEN M., KANSKI J., ILVER L., ÅSKLUND H., SÖDERVALL U., *Appl. Phys. Lett.*, **78** (2001), 3271.
- [20] STAAB T.E.M., NIEMINEN R.M., GEBAUER J., KRAUSE-REHBERG R., LUYSBERG M., HAUGK, M., FRAUENHEIM TH., *Phys. Rev. Lett.*, **87** (2001), 045504.
- [21] YU K.M., WALUKIEWICZ W., WOJCIWICZ T., KURYLISZYN I., LIU X., SASAKI Y., FURDYNA J.K., *Phys. Rev. B*, **65** (2002), 201303.
- [22] WOLOS A., KAMINSKA M., PALCZEWSKA M., TWARDOWSKI A., LIU X., WOJCIWICZ T., FURDYNA J.K., *J. Appl. Phys.* **96**, 530 (2004).
- [23] SADOWSKI J., DOMAGALA J.Z., *Phys. Rev. B*, **69** (2004), 075206.
- [24] ADELL M., ILVER L., KANSKI J., STANCIU V., SVEDLINDH P., SADOWSKI J., DOMAGALA J.Z., TERKI F., HERNANDEZ C., CHARAR S., *Appl. Phys. Lett.*, **86** (2005), 112501.
- [25] STONE M.B., KU K.C., POTASHNIK S.J., SHEU B.L., SAMARTH N., SCHIFFER P., *Appl. Phys. Lett.*, **83** (2003), 4568.
- [26] KIRBY B.J., BORCHERS J.A., RHYNE J.J., O'DONOVAN K.V., WOJCIWICZ T., LIU X., GE Z., SHEN S., FURDYNA J.K., *Appl. Phys. Lett.*, **86** (2005), 072506.
- [27] MALFAIT M., VANACKEN J., MOSHCHALOV V.V., VAN ROY W., BORGHS G. *Appl. Phys. Lett.*, **86** (2005), 132501.
- [28] MAKSIMOV O., SHEU B.L., XIANG G., KEIM N., SCHIFFER P., SAMARTH N., *J. Crystal Growth*, **269** (2004), 298.

Received 1 June 2005

In-plane uniaxial anisotropy rotations in (Ga, Mn)As thin films

M. SAWICKI^{1*}, K.-Y. WANG², K.W. EDMONDS², R.P. CAMPION², C.R. STADDON²,
N.R.S. FARLEY², C.T. FOXON², T. DIETL^{1,3,4}, B.L. GALLAGHER²

¹Institute of Physics, Polish Academy of Sciences, al. Lotników 32/46, PL-02668 Warszawa, Poland

²School of Physics and Astronomy, University of Nottingham, Nottingham NG7 2RD, UK

³ERATO Semiconductor Spintronics Project, al. Lotników 32/46, Warszawa, Poland

⁴Institute of Theoretical Physics, Warsaw University, Warszawa, Poland

Using SQUID magnetometry we have found that in (Ga, Mn)As films the in-plane uniaxial magnetic easy axis is consistently associated with particular crystallographic directions. It can be rotated from the $[\bar{1}10]$ direction to the $[110]$ direction by low temperature annealing and we show that this change is hole density-related. We demonstrate that the magnitude of uniaxial anisotropy as well its dependence on hole-concentration and temperature can be explained in terms of the p-d Zener model of ferromagnetism assuming a small trigonal-like distortion.

Key words: *GaMnAs*; magnetic anisotropy; ferromagnetic semiconductor

1. Introduction

Diluted magnetic semiconductors (DMS) in general and (Ga, Mn)As in particular are semiconducting materials for which a few percent of a magnetic element is added to a magnetically inert host. The discovery of carrier-mediated ferromagnetism in (III, Mn)V and (II, Mn)VI DMS grown by molecular beam epitaxy makes it possible to examine the interplay between the physical properties of semiconductor quantum structures and ferromagnetic materials [1] and opens the door for their application in spintronics, where electron spin is used to carry information [2]. It has been known since the early works in the field that (Ga, Mn)As films show strong magnetic anisotropy, which is largely controlled by epitaxial strain. The magnetic easy axis orients out-of-plane and in-plane under tensile and compressive biaxial strains, respectively

*Corresponding author, e-mail: mikes@ifpan.edu.pl

[3-5], which is well understood within the framework of the p-d Zener model of hole-mediated ferromagnetism [6-8]. More recent works have shown that these systems also exhibit a strong in-plane uniaxial magnetic anisotropy [5, 8-10], pointing to the existence of a symmetry breaking mechanism, whose microscopic origin has not been identified yet. Since magnetic anisotropy will have a marked influence on spin injection and magnetotunnelling devices, it is important to develop a greater understanding of this property, and methods for its control. In this paper, we summarise the results of a study of in-plane magnetic anisotropy in a series of 50 nm thick (Ga, Mn)As thin films with Mn concentration x ranging from 1.7 to 9%.

2. Experimental

The crystallographic orientation of the wafer was determined from RHEED measurements during growth. For magnetometry studies, the material was typically cleft into 4×5 mm² rectangles, whose precise crystallographic orientation was reconfirmed by Laue back-reflection X-ray diffraction. Hole concentration was altered by low-temperature annealing. This procedure promotes the out-diffusion of compensating Mn interstitials from the layers [11], thus leading to an increased hole concentration and a higher Curie temperature [12]. Magnetic anisotropy was assessed in a custom-built low-field SQUID magnetometer. Detailed information about magnetic anisotropy was obtained from $M(H)$ curves recorded for various crystallographic orientations [13] and from the temperature dependence of the remnant magnetization M_{REM} [14].

3. Results and discussion

Magnetization loops for two representative samples with Mn concentrations of 2.2% and 5.6% are shown in Fig. 1a-d. It is well established that for typical hole densities (Ga, Mn)As/GaAs exhibits an in-plane magnetic anisotropy, determined by the superposition of two components, a biaxial, cubic-like anisotropy with [100] being the easy axes, and an uniaxial anisotropy with [110] being the easy axes [5, 8-10]. The former is a direct consequence of the spin anisotropy of the hole liquid, originating from strong spin-orbit coupling in the valence band. This coupling transfers all the complexities of valence band physics into the Mn ion subsystem. The second in-plane anisotropy component, the uniaxial term, is not expected from the above model, since its presence is precluded by general symmetry considerations in the biaxially strained zinc blende structure of (Ga, Mn)As. It has been suggested that these uniaxial properties may originate from symmetry lowering ($D_{2d} \Rightarrow C_{2v}$) due to either (i) a lack of top-bottom symmetry in (Ga, Mn)As epilayers [8] or (ii) anisotropic GaAs surface reconstruction during growth [11]. Importantly, it is usually found that the cubic term is dominant only at low temperatures. At elevated temperatures, the uniaxial term becomes larger than the cubic one. In such a case, the magnetic anisotropy of the layers

is solely determined by the uniaxial term. Therefore, we focus on this high temperature regime which allows an unambiguous determination of the easy magnetic axis. We note (see Fig. 1a, b) that for both as-grown samples a clear uniaxial behaviour with $[\bar{1}10]$ being the easy axis is indeed observed.

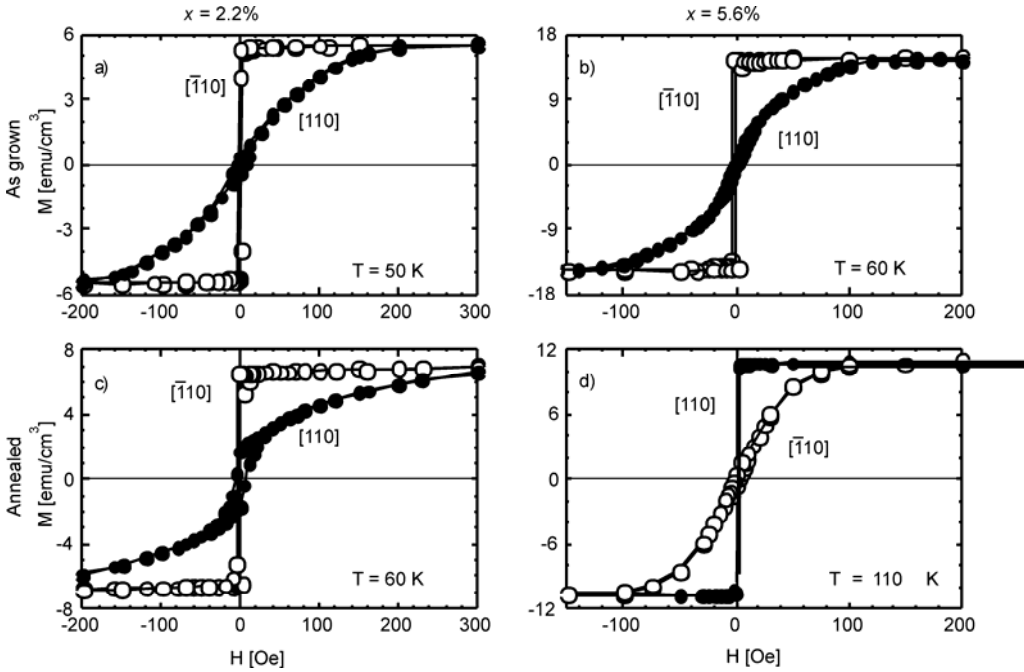


Fig. 1. Magnetization curves at temperatures close to T_C measured for $[110]$ and $[\bar{1}10]$ orientations before a), b) and after annealing c), d) for $\text{Ga}_{0.978}\text{Mn}_{0.022}\text{As}$ and $\text{Ga}_{0.944}\text{Mn}_{0.056}\text{As}$. Note the switch of the magnetic easy axis from $[\bar{1}10]$ to $[110]$ upon annealing for the latter sample

A similar behaviour is observed in all studied as-grown samples. At low Mn concentrations, annealing results in a relatively small increase in T_C and has no qualitative effect on magnetic anisotropy, as indicated in Fig. 1a, c for $x = 2.2\%$. A very different behaviour is observed at higher concentrations. As shown in Fig. 1b, d for $x = 5.6\%$, after annealing the easy axis rotates to the $[110]$ direction. Before annealing, the $M(H)$ curves are square along the $[\bar{1}10]$ direction and elongated along the $[110]$ direction, and this situation is reversed after annealing. Interestingly, some annealed samples also exhibit a temperature-induced reorientation of the easy axis [14]. In this case, the uniaxial easy axis points in the $[\bar{1}10]$ direction at low temperatures, but assumes the $[110]$ direction at higher temperatures.

Since the annealing-induced increase of hole density is larger for the 5.6% sample, we ascribe the rotation of the easy magnetic axis to the increasing hole concentration. This modifies the relative occupancies of the valence sub-bands of the GaAs host,

which (at least in the case of cubic anisotropy) makes competing contributions to the magnetic anisotropy [7]. Figure 2a shows the measured hole concentration in function of Mn concentration for the series of studied samples. By a close inspection of the figure, we can assign a threshold value of p of approximately $6 \times 10^{20} \text{ cm}^{-3}$, above which the easy axis orients along [110]. An independent study showed that the uniaxial anisotropy field is thickness-independent in the range 0.2 to $6.8 \mu\text{m}$ [15]. Both findings strongly indicate that the in-plane uniaxial anisotropy depends on the bulk film parameters. Thus, this anisotropy can be caused by a symmetry lowering mechanism existing inside the film.

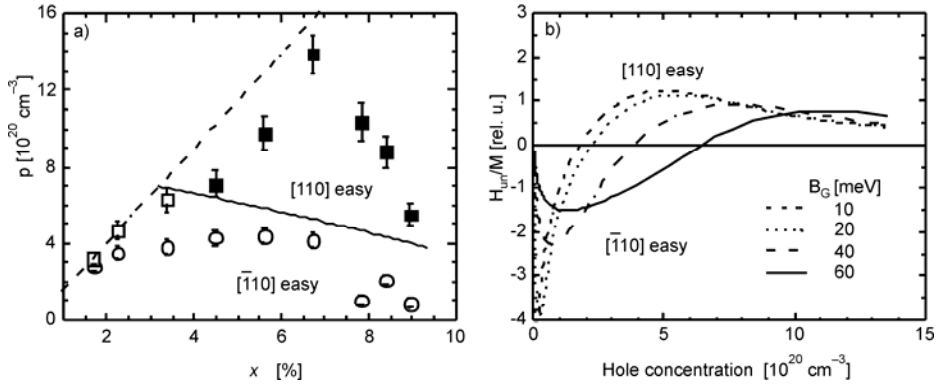


Fig. 2. The uniaxial easy axis fan chart for (Ga, Mn)As. Circles – as grown, squares – after annealing.

Open symbols mark samples with the uniaxial easy axis oriented along the $[\bar{1}10]$ direction,

full symbols denote samples exhibiting the easy axis along [110]. The dashed line marks

the compensation-free p-type Mn doping level in (Ga, Mn)As. The solid line separates two regions of hole densities where, independently of being annealed or not, at elevated temperatures the layers consistently show the same crystallographic alignment of the uniaxial easy axis (a). In-plane uniaxial anisotropy field (normalized to sample saturation magnetization) versus hole density computed for various valence-band spin-splitting in (Ga, Mn)As assuming a non-zero trigonal distortion (b)

In order to find out the magnitude of the symmetry lowering perturbation that would explain our findings, we incorporate a trigonal distortion in the p-d Zener theory of ferromagnetism in tetrahedrally coordinated semiconductors [6, 7] described by the deformation tensor component $\varepsilon_{xy} \neq 0$. The computed anisotropy field corresponding to the in-plane uniaxial anisotropy H_{un} is shown in Fig. 2b as a function of hole concentration and parameterised by the valence-band spin-splitting parameter $B_G = A_F \beta M(T) / 6g\mu_B$, where $g = 2.0$, $A_F = 1.2$ is the Fermi liquid parameter, and $\beta = -0.054 \text{ eV} \cdot \text{nm}^3$ is the p-d exchange integral. In the relevant region of hole concentrations and for $\varepsilon_{xy} = 0.05\%$, H_{un} attains experimentally observed values $\leq 0.1 \text{ T}$. Moreover, for a given value of x , our calculations confirm the possibility of the easy axis rotating from $[\bar{1}10]$ to [110] with increasing hole density. Additionally, since M and B_G are decreasing functions of T , the experimentally reported uniaxial easy axis reorientation transition ($[\bar{1}10] \Rightarrow [110]$) with increasing T is also well explained. Therefore, the $\varepsilon_{xy} \neq 0$ model qualitatively reproduces the observed change in the

easy axis direction as a function of both hole concentration and temperature. The distortion required by the model may be associated with magnetostriction, or may result from a non-isotropic Mn distribution, caused for instance by the presence of surface dimers oriented along the $[\bar{1}10]$ direction during epitaxy. Since it has not yet been seen in other experiments, we conclude that the decisive microscopic mechanism that breaks the D_{2d} symmetry of (Ga, Mn)As epitaxial films is still to be found.

Acknowledgement

The support of UK EPSRC, EU FENIKS (G5RD-CT-2001-0535), and Polish PBZ/KBN/044/PO3/2001 projects is gratefully acknowledged.

References

- [1] MATSUKURA F., OHNO H., DIETL T., *III-V Ferromagnetic Semiconductors*, [in:] *Handbook of Magnetic Materials*, Vol. 14, K.H.J. Buschow (Ed.), Elsevier, Amsterdam, 2002, p. 1–87; DIETL T., *Semicond. Sci. Technol.*, 17 (2002), 377.
- [2] OHNO H., MATSUKURA F., OHNO Y., *JSAP International*, No. 5, January 2002, p. 4; WOLF S.A., AWSCHALOM D.D., BUHRMAN R.A., DAUGHTON J.M., VON MOLNAR S., ROUKES M.L., CHTCHELKANOVA A.Y., TREGGER D.M., *Science* 294 (2001), 1488; DIETL T., *Acta Phys. Polon. A*, 100 (suppl.), (2001), 139.
- [3] MUNEKATA H., ZASLAVSKY A., FUMAGALLI P., GAMBINO R.J., *Appl. Phys. Lett.*, 63 (1993), 2929.
- [4] SHEN A., OHNO H., MATSUKURA F., SUGAWARA Y., AKIBA N., KUROIWA T., OIWA A., ENDO A., KATSUMOTO S., IYE Y., *J. Cryst. Growth*, 175/176 (1997), 1069.
- [5] LIU X., SASAKI Y., FURDYNA J.K., *Phys. Rev. B*, 67 (2003), 205204.
- [6] DIETL T., OHNO H., MATSUKURA F., CIBERT J., FERRAND D., *Science*, 287 (2000), 1019.
- [7] DIETL T., OHNO H., MATSUKURA F., *Phys. Rev. B*, 63 (2001), 195205; ABOLFATH M., JUNGWIRTH T., BRUM J., MACDONALD A.H., *Phys. Rev. B*, 63 (2001), 054418.
- [8] SAWICKI M., MATSUKURA F., IDZIASZEK A., DIETL T., SCHOTT G.M., RUESTER C., KARCZEWSKI G., SCHMIDT G., MOLENKAMP L.W., *Phys. Rev. B*, 70 (2004), 245325.
- [9] TANG H.X., KAWAKAMI R.K., AWSCHALOM D.D., ROUKES M.L., *Phys. Rev. Lett.*, 90 (2003), 107201; HRABOVSKY D., VANELLE E., FERT A.R., YEE D.S., REDOULES J.P., SADOWSKI J., KANSKI J., ILVER L., *Appl. Phys. Lett.*, 81 (2002), 2806.
- [10] WELP U., VLASKO-VLASOV V.K., LIU X., FURDYNA J. K., WOJTIWICZ T., *Phys. Rev. Lett.*, 90 (2003), 167206.
- [11] EDMONDS K.W., BOGUSLAWSKI P., GALLAGHER B.L., CAMPION R.P., WANG K.Y., FARLEY N.R.S., FOXON C.T., SAWICKI M., DIETL T., NARDELLI M.B., BERNHOLC J., *Phys. Rev. Lett.*, 92 (2004), 037201.
- [12] WANG K.Y., EDMONDS K.W., CAMPION R.P., GALLAGHER B.L., FARLEY N.R.S., FOXON C.T., SAWICKI M., BOGUSLAWSKI P., DIETL T., *J. Appl. Phys.* 95 (2004), 6512.
- [13] WANG K.Y., SAWICKI M., EDMONDS K.W., CAMPION R.P., GALLAGHER B.L., FARLEY N.R.L., FOXON C.T., DIETL T., in preparation.
- [14] SAWICKI M., WANG K.-Y., EDMONDS K.W., CAMPION R. P., STADDON C. R., FARLEY N.R.S., FOXON C.T., PAPIŚ E., KAMIŃSKA E., PIOTROWSKA A., DIETL T., GALLAGHER B. L., *Phys. Rev. B*, 71 (2005) 121302(R).
- [15] WELP U., VLASKO-VLASOV V.K., LIU X., FURDYNA J.K., WOJTIWICZ T., *Appl. Phys. Lett.*, 85 (2004), 260.

Received 1 June 2005

Revised 10 October 2005

Electrical resistivity of disordered monolayer metallic films

P. JARGUZ*, A. PAJA

Faculty of Physics and Applied Computer Science, AGH University of Science and Technology,
al. Mickiewicza 30, 30-059 Cracow, Poland

Electron transport through a disordered two-dimensional array of potentials has been investigated. The resistivity was calculated according to the Faber–Ziman diffraction model, suitably modified for a two-dimensional electron gas. The structure factor is obtained by means of numerical simulations. The pseudopotentials are assumed to be Shaw potentials with appropriate screening. The resistivities of disordered monolayers of alkali metals have been calculated in this model using parameters that allowed us to explain the experimental data for bulk materials.

Key words: *electrical resistivity; disordered system; two-dimensional electron gas*

1. Introduction

Rapid development of nanoelectronics that has been recently observed generates the need for a theoretical description of electron transport properties of nanoscale systems. Such systems have at least one size small enough that the electron wave function essentially differs from that in a bulk material. This, in turn, influences physical properties of the system.

In this work, we consider a disordered monolayer metallic film. Such films can now be obtained by the MBE technique [1, 2]. We assume that their transport properties, electrical resistivity in particular, can be described by the behaviour of a two-dimensional electron gas placed in a superposition of a static electric field and a disordered array of ionic potentials. The scattering of conduction electrons is described within the diffraction model [3]. The calculated resistivities of monolayers of alkali metals will be compared with available experimental data for corresponding bulk materials.

*Corresponding author, e-mail: jarguz@uci.agh.edu.pl

2. Theoretical model

The electrical resistivity ρ of a disordered array of ions can be calculated in a Boltzmann-type approximation using the formula

$$\rho = \frac{m}{ne^2\tau_{tr}} \quad (1)$$

where m and e are the electron mass and charge, respectively, n is electron concentration, and τ_{tr} is the transport relaxation time. In a two-dimensional picture, n is of course the area density, i.e. the density of carriers per unit area. Ziman's formula for τ_{tr} [3] should also be appropriately modified [4]:

$$\tau_{tr}^{-1} = 2 \frac{v_F}{A} \int_0^\pi d\varphi \frac{d\sigma}{d\varphi} (1 - \cos\varphi) \quad (2)$$

where v_F is the Fermi velocity and A is the area of the system. Here, $d\sigma/d\varphi$ is the differential cross section for two dimensions [4]:

$$\frac{d\sigma}{d\varphi} = \frac{1}{8\pi k_F} \left(\frac{m}{2\pi\hbar^2} \right)^2 NS(q) |u_a(q)|^2 \quad (3)$$

where k_F is the Fermi wave vector in the xy plane, N is the total number of atoms in the system, $S(q)$ is a two-dimensional structure factor, $u_a(q)$ is a two-dimensional Fourier transform of the atomic potential $u_a(\mathbf{r})$, and

$$q = 2k_F \sin \frac{\varphi}{2} \quad (4)$$

The structure factor $S(q)$ defined as

$$S(q) = \frac{1}{N} \left\langle \sum_j \sum_k \exp[-i\mathbf{q} \cdot (\mathbf{r}_j - \mathbf{r}_k)] \right\rangle - N\delta_{\mathbf{q},0} \quad (5)$$

has been calculated by means of numerical simulations. We placed circles of a given diameter σ in a rectangle of a given size at random, so that they filled up the whole area but did not overlap each other, after which we computed the sum in Eq. (5). This is equivalent to using the random closely packed hard sphere model. The rectangles used in our calculations contained at least a thousand of these artificial atoms. We took the average over an ensemble of at least a thousand random configurations.

To calculate the differential cross-section, we also need an analytical form of the scattering potential. We assumed the Shaw pseudopotential, modified by screening [6]:

$$u_a(r) = \begin{cases} -\frac{Z}{r} \exp(-\lambda r), & r \geq R_c \\ -\frac{Z}{R_c} \exp(-\lambda R_c), & r \leq R_c \end{cases} \quad (6)$$

where R_c is the core radius, λ is the screening parameter, and $Z=e^2/(4\pi\epsilon_0)$ in SI units. Such a form gave good agreement with the experimental results for bulk alkali metals in our previous work [6].

Unfortunately, the Fourier transform of this potential in two dimensions

$$u_a(\mathbf{q}) = \iint u_a(\mathbf{r}) \exp(-i\mathbf{q} \cdot \mathbf{r}) d^2\mathbf{r} \quad (7)$$

cannot be expressed by elementary functions. We converted it into a real integral

$$u_a(q) = 4 \int_0^\infty dr u_a(r) \int_0^{\frac{\pi}{2}} d\varphi \cos(qr \cos\varphi) \quad (8)$$

and calculated it numerically.

3. Results of calculations

We calculated the structure factors $S(q)$ given by Eq. (5) for five alkali metals: Li, Na, K, Rb, and Cs using atomic diameters taken from [7], which reproduced well the experimental structure factors for bulk samples. These values are given in Table 1. The structure factors for all five elements are shown in Fig. 1.

Table 1. Input parameters for numerical calculations and the resulting resistivities

Element	σ [10^{-10} m]	λ [10^{10} m]	R_c [10^{-10} m]	ρ_m [Ω]	ρ_b [$\mu\Omega \cdot \text{cm}$]	ρ_{exp} [$\mu\Omega \cdot \text{cm}$]
Li	2.70	1.36	0.66	55.4	1.68	25
Na	3.28	1.23	1.25	19.7	0.73	9.6
K	4.07	1.11	1.53	22.2	1.01	13
Ru	4.30	1.08	1.47	31.8	1.57	22
Cs	4.73	1.03	1.36	57.0	3.04	36

The pseudopotential depends on two parameters: R_c and λ . The screening parameter λ is closely related to the Fermi wave vector k_F [8]:

$$\lambda^2 = \frac{4k_F}{\pi a_0} \quad (9)$$

where a_0 is the Bohr radius. The core radii R_c for alkali metals were estimated in [6] from fitting the experimental resistivities of liquid metals. We assume that they are

the same the two-dimensional systems. The values of these parameters are also given in Table 1.

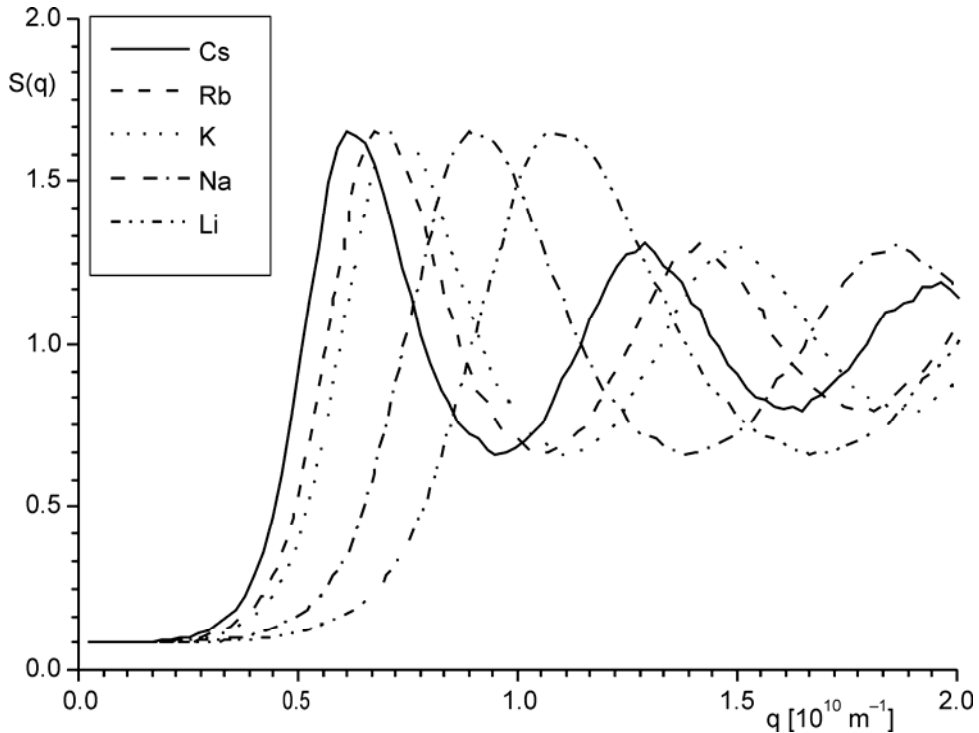


Fig. 1. Structure factors of alkali metals obtained from numerical simulations

The resistivities of the monolayer films of the considered metals, ρ_m , have been calculated by numerical integration and are shown in Table 1. It is interesting to compare the obtained values of ρ_m with the resistivities of the corresponding bulk materials, ρ_b . These quantities are measured in different units, so that when compare them we have to extrapolate our results to bulk values simply by multiplying them by the thickness of the layer, i. e. the atomic diameter. These results are also presented in Table 1, together with the experimental values for liquid metals.

4. Conclusions

We calculated the electrical resistivities of monatomic metallic layers, considering the transport of a two-dimensional electron gas through a disordered array of screened Shaw potentials. The resistivities obtained for alkali metals, after suitable extrapolation, are one order of magnitude smaller than the corresponding values for liquid metals. They are substantially lower because the electron in a two-dimensional system

can be scattered only in a plane, whereas in a bulk material it has an additional degree of freedom. This means that these results can be viewed as reasonable, and could be confirmed by a suitable experiment.

References

- [1] FARROW R.C., IBM J. Res. Develop., 42 (1998), 43.
- [2] ŚLĘZAK T., KARAŚ W., KROP K., KUBIK M., WILGOCKA-ŚLĘZAK D., SPIRIDIS N., KORECKI J., J. Magn. Magn. Mater., 240 (2002), 362.
- [3] ZIMAN J.M., Phil. Mag., 6 (1961), 1013.
- [4] SPISAK B.J., PAJA A., Mol. Phys. Rep., 40 (2004), 144.
- [5] SHAW Jr. R.W., Phys. Rev., 174 (1968), 769.
- [6] JARGUZ P., PAJA A., to be published.
- [7] ASHCROFT N.W., LEKNER J., Phys. Rev. 145 (1966), 83.
- [8] ASHCROFT N.W., MERMIN N. D., Holt, Rinehart and Winston, New York, 1976.

Received 1 June 2005
Revised 10 October 2005

Domain structures and magnetization processes in thin Co films with in-plane anisotropy

J. JAWOROWICZ^{1*}, Z. KURANT², K. POSTAVA³, A. MAZIEWSKI¹,
L.T. BACZEWSKI², A. WAWRO²

¹Institute of Experimental Physics, University of Białystok, Lipowa 41, 15-424 Białystok, Poland

²Institute of Physics, Polish Academy of Sciences, al. Lotników 32/46, 02-668 Warsaw, Poland

³Department of Physics, Technical University of Ostrava, 17. listopadu 15,
70833 Ostrava-Poruba, Czech Republic

Magnetization reversal and domain structures in thin Co films in the thickness range $2 < d < 100$ nm with in-plane magnetic anisotropy were studied. Both magneto-optical (MO) vector magnetometry and MO microscopy were used. A crossover of in-plane anisotropy symmetry from two-fold to six-fold was observed with increasing thickness of the Co layer from 2 nm to 100 nm. The evolution of the domain structure during magnetization reversal was studied for various orientations of the magnetic field relative to the anisotropy easy axis using a longitudinal Kerr MO microscope.

Key words: magnetization reversal; domain structure; Kerr effect; magneto-optic vector magnetometry

1. Introduction

Studies of magnetic domain structures and magnetisation processes occurring in nanostructures are attractive for both scientific and technological interests. Magneto-optical MO vector magnetometry combined with MO microscopy are powerful techniques for flexible anisotropy analysis with high sensitivity. Such a magneto-optical study of ultrathin Co films with in-plane anisotropy was the purpose of this work.

2. Experimental details

Sample preparation. The Au/Co(*d*)/Au sandwiches were grown in a molecular beam epitaxy system Riber EVA 32 in the low range of 10^{-10} Torr vacuum. Al₂O₃

*Corresponding author, e-mail: jawor@uwb.edu.pl

(11–20) substrates buffered with a 20 nm thick Mo layer were used. Co and Mo were evaporated from electron guns and Au from an effusion cell at the rates lower than 0.05 nm/s. The bottom 20 nm Au layer, deposited directly on the Mo buffer, was annealed at 200 °C to minimize its surface roughness. A cobalt layer with a selected thickness d from the range 2–100 nm was then grown at 300 K. Finally, the whole structure was covered with an 8 nm thick gold layer. The growth process of the samples was monitored in-situ by RHEED. A more detailed description of sample preparation and structural characterization is provided elsewhere [1].

MO vector magnetometry. Measurements based on the MO Kerr effect were performed at room temperature with the laser light wavelength of 640 nm and spot diameter of 0.5 mm. Three components of the magnetization vector were separated using an adjustable in-plane magnetic field produced by a computer-controlled electromagnet and using a precise sample rotation system. The polar (perpendicular to the film) magnetization component was measured using the polar MO Kerr effect. The longitudinal and transversal in-plane components (parallel and perpendicular to the applied magnetic field) were measured using the longitudinal MO Kerr effect.

3. Results and discussion

The transition from the out-of-plane easy magnetization axis state to the in-plane state occurs at a Co film thickness of about 1.8 nm [2]. MO vector magnetometry shows the existence of easy magnetization axes oriented in the plane of the film for the Co layer thickness $d > 2$ nm. A two-fold symmetry of the magnetization reversal process was observed for the values of d smaller than 10 nm. This is probably related to a small, unintentional (less than 0.5 deg) miscut of the Al_2O_3 substrate. A similar behaviour was reported in other papers (see Refs. [4, 5]). Six-fold symmetry was found for thicker ($d > 10$ nm) Co films. The analysis presented below is based on the results obtained for the sample with a 31 nm thick Co film.

The hard magnetization axis normal to the film plane can be deduced from the hysteresis loops shown in Figs. 1a–c. The lack of remanent magnetization (Fig. 1a) is evidence for magnetization alignment in the plane of the sample. Two different shape loops recorded for various orientations of the in-plane applied field are shown in Figs 1b, c. They suggest the occurrence of in-plane anisotropy depending on the azimuthal orientation. The six-fold symmetry is visible in the angular dependence of the longitudinal remanence of ellipticity (Fig. 2a), with a weak transverse component (compared to the longitudinal effect). Six-fold symmetry is also present in the angular dependence of the transversal remanence (Fig. 2b).

The magnetization reversal processes, with the resulting multi-domain structure, can be deduced from the shape analysis of the low field longitudinal loops shown in Figs. 1b, c. Observations of domain structures (DS) were performed with a longitudinal Kerr effect micro-magnetometer equipped with a home-made polarizing optical microscope. Both high-sensitivity and high-resolution micro-magnetometer configura-

tions [3] were applied. The former setup was used to obtain an overview of the domain pattern on a large scale. The advantage is the lack of optical elements other than the sample between the polarizer and analyzer, making contrast conditions optimal. Images with a light inclination angle of 50° are presented in Figs 3a-c. The evolution

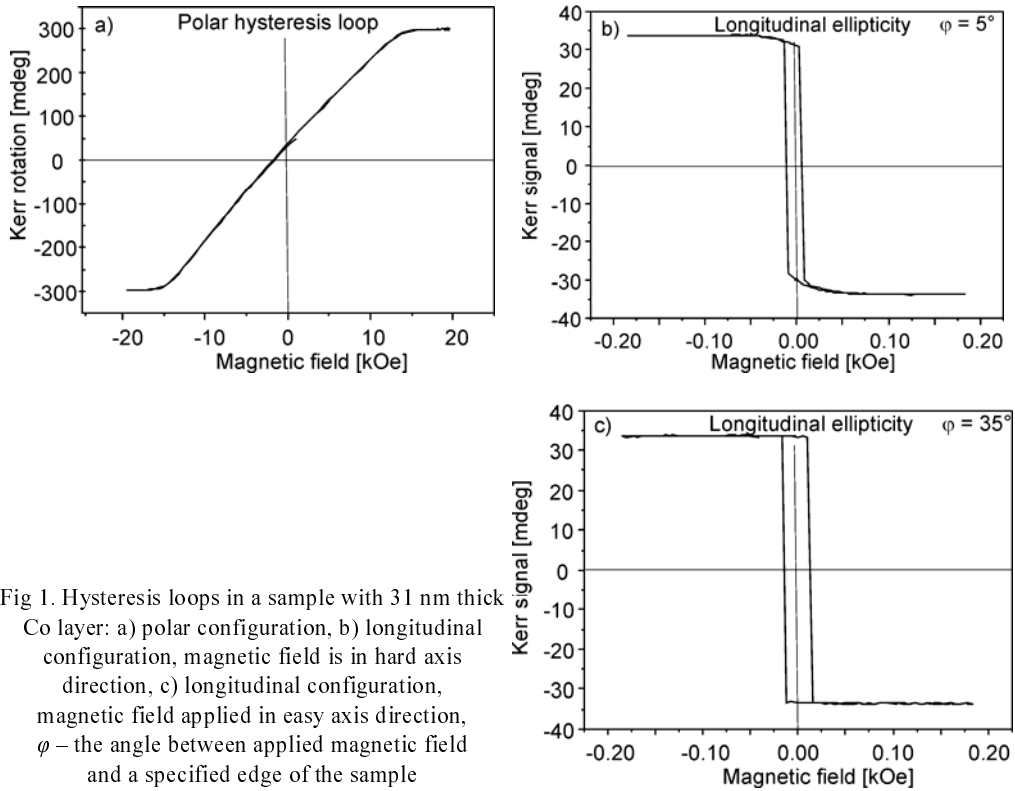


Fig 1. Hysteresis loops in a sample with 31 nm thick Co layer: a) polar configuration, b) longitudinal configuration, magnetic field is in hard axis direction, c) longitudinal configuration, magnetic field applied in easy axis direction, φ – the angle between applied magnetic field and a specified edge of the sample

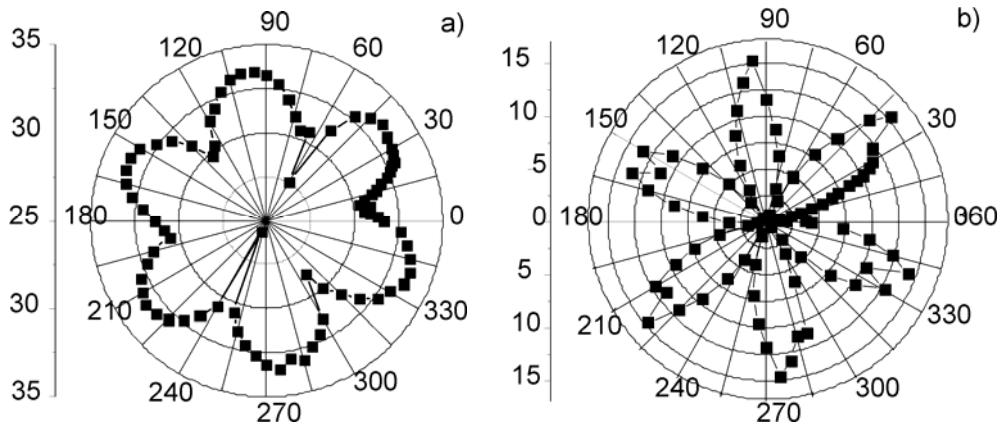


Fig. 2. Polar plot of ellipticity remanence: a) longitudinal, b) transversal. Measurements were performed for the sample with 31 nm thick Co layer

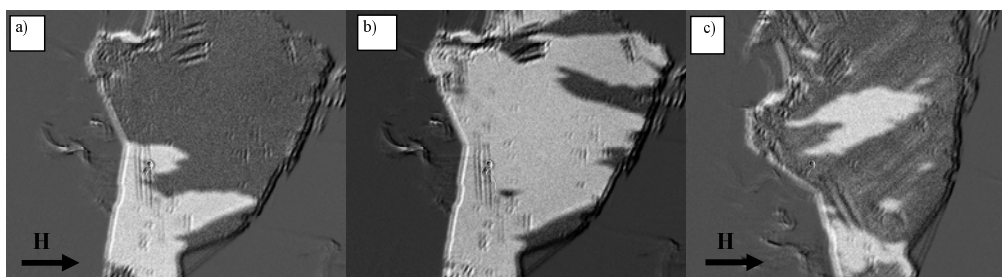


Fig. 3. Domain structures in the sample with 31 nm thick Co layer: a, b) magnetic field applied in the easy axis direction $\varphi = 35^\circ$, c) magnetic field applied in the hard axis direction, $\varphi = 5^\circ$. Size of the pictures – 8 mm \times 10 mm. Remanence images DS obtained by magnetic field impulses; amplitude 20 Oe, time 600 ms

of domain structure during magnetization reversal was studied for various orientations of the applied magnetic field. The magnetisation reversal for the magnetic field applied along the easy axis is shown in Figs. 3a, b. The domain wall propagation mechanism is dominant here. A higher density of nucleation centres was observed when the magnetic field was applied in the direction of the hard axis (Fig. 3c).

4. Conclusions

MO magnetometry studies carried out for samples with Co layer thickness of $d > 2$ nm reveal the thickness dependence of in-plane magnetic anisotropy. The two-fold symmetry of in-plane anisotropy changes to six-fold symmetry with increasing Co layer thickness above $d = 10$ nm. Most probably, the two-fold symmetry is due to the small unintentional substrate being miscut, and the six-fold one is caused by the magnetocrystalline anisotropy of the dominating cobalt hcp phase in thick layers [6].

Acknowledgements

This work was supported by the Polish State Committee for Scientific Research, Grant No. 4 T11B 006 24 and Marie Curie Fellowships for *Transfer of Knowledge*, Nanomag-Lab, No. 2004-003177.

References

- [1] WAWRO A., BACZEWSKI L.T., KISIELEWSKI M., SVEKLO I., MAZIEWSKI A., *Thin Solid Films*, 412 (2002), 34.
- [2] KISIELEWSKI M., MAZIEWSKI A., TEKIELAK M., WAWRO A., BACZEWSKI L.T., *Phys. Rev. Lett.*, 89 (2002), 087203.
- [3] HUBERT A., SCHÄFER R., *Magnetic Domains*, Springer-Verlag, Berlin, 1998.
- [4] FRUCHT O., JUBERT P.-O., MEYER C., KLAUA M., BARTHEL J., KIRSCHNER J., *J. Magn. Magn. Mater.*, 239 (2002), 224.
- [5] JUBERT P.O., FRUCHT O., MEYER C., *Phys. Rev. B*, 64, 115419.
- [6] CHAPPERT C., BRUNO P., *J. Appl. Phys.*, 64 (1988), 5736.

Received 1 June 2005
Revised 10 October 2005

Analysis of magnetization reversal at the exchange-biased interface using the Ising approach

T. BŁACHOWICZ*, M. WIEJA

Department of Electron Technology, Institute of Physics, Silesian University of Technology,
Krzywoustego 2, 44-100 Gliwice, Poland

The paper provides the results of exchange-biased simulations of a single ferromagnetic (FM) layer coupled to a quenched antiferromagnetic (AFM) region using the Random field Ising model (RFIM). From the RFIM algorithm, the shapes of exchange-biased hysteresis loops and featuring perpendicular magnetic anisotropies were obtained. Providing a possible explanation for this effect, the recognized stable part of an interface magnetization, represented by unreversed spins at the interface, was evidently simulated. The obtained results are consistent with the domain state model (DSM) model, in which a part of the AFM interface magnetization is stable during hysteresis loop creation.

Key words: *spintronics; exchange-bias; magnetization reversal*

1. Introduction

The simulation of exchange-biased phenomena is important for intensive theoretical and experimental research whose results have already been applied to magnetoelectronics and will soon be used in novel devices where electron-spin plays an important role [1–4]. One of the most important components of spintronic devices are exchange-biased magnetic thin layers. The phenomenon of importance can be described as shift of the hysteresis loop of a ferromagnetic material along the field axis and as enhancement of the coercive field, observed in coupled ferromagnetic (FM) and antiferromagnetic (AFM) thin films after being deposited in a magnetic field or field cooling below the Néel temperature of the AFM. This effect, which exists at the ferromagnetic/antiferromagnetic (FM/AFM) interface, can be tailored on the atomic scale by structural modifications in the AFM bulk [5–6]. Such efforts have been adequately described within the domain state model (DSM) of exchange-bias [7, 8] and experimentally confirmed by crystal structure dilution [5] and ion irradiation [9]. The DSM approach is based on Monte Carlo calculations using the

*Corresponding author, e-mail: Tomasz.Blachowicz@polsl.pl

heat-bath algorithm [10]. Apart from the DSM, other numerical methods can be applied. One of them is based on the random field Ising model (RFIM) [11–13]. Presented here are the results obtained from numerical simulations using the RFIM algorithm. In particular spin reversibility influenced by atomic roughness at the interface was analysed.

2. Simulations

The RFIM approach can be used to simulate the bias of the FM layer by the AFM region. It has been applied by Illa [14] who intended to reproduce the properties of a single layer of ferromagnetic spins placed on a totally quenched AFM. We propose a similar approach, our results, however, can be interpreted in the scope of perpendicular magnetic anisotropies.

In the current simulation, in order to block spins, the exchange constant between neighbouring FM spins was enhanced at randomly distributed positions from its normal value of 1 to a larger value, for example 10. Thus, the complete magnetic field at a given lattice point i was calculated as

$$H_i = \sum_{j=1}^{j=4} (J_{ij} S_j) + h_i^G + H_{\text{ext}} \quad (1)$$

where J_{ij} is the exchange constant (coupling constant) randomly enhanced to $J_E > J_{ij} = 1$, S_j is the spin with the value of +1 or -1, h_i^G is the Gaussian distributed field representing atomic roughness at the interface, and H_{ext} is the externally applied magnetic field. During simulations, when the total field changed its algebraic sign at a given point, the spin flipped into the opposite orientation. Further, the magnetization of the system was calculated as the ratio of the algebraic sum of spins and the total system square dimension. All simulations started from a saturation state, in which all spins were at +1 positions. The simulation was carried out using one-dimensional periodic conditions of the Born-Karman type. Additionally, numerical experiments were carried out with 2-dimensional periodic conditions, and even with no periodic conditions, but this did not change the obtained results. The results were averaged over many trails, the averages attaining constant values after about 20 replications. Details of the influence of boundary conditions, the dimensions of the investigated system, and the number of disorder realizations on the performance of the RFIM can be found in the author's other work [15]. Calculations were carried out on a computer cluster consisting of 16 PCs to increase numerical performance. The time needed to make and to average 10^3 trails was about 40 minutes for a 50×50 spin system.

3. Results and discussion

Figure 1a and its inset provide the results of simulation carried out for a 50×50 lattice, the standard deviation of the random fields being $\sigma = 1.65$, the enhanced ex-

change constant $J_E = 20$, the fraction of enhanced bounds $f = 0.03$, and the external magnetic field intensity ranging from -2.7 to 8 . Figure 2a and its inset provide results

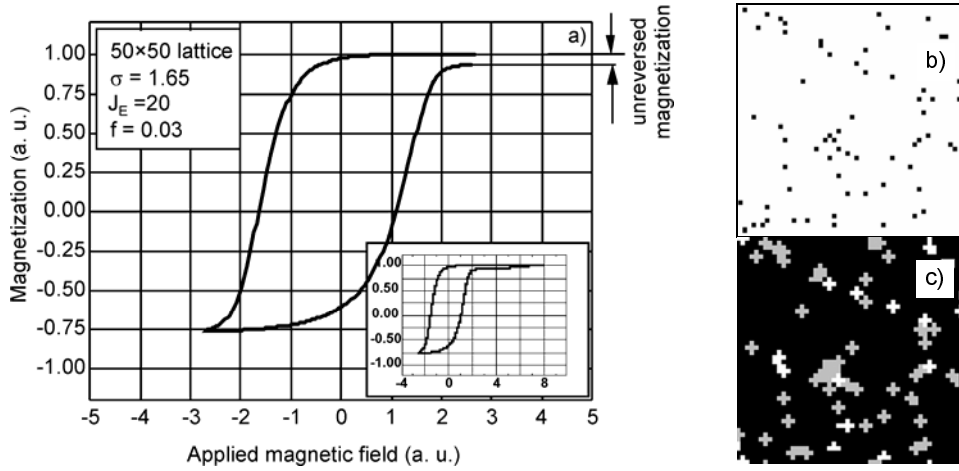


Fig. 1. Simulation of exchange-bias for a system with $\sigma = 1.65$. The simulation starts from saturation under the applied magnetic field 8 a. u. ranging between 8 a. u. and -2.7 a. u. Other input data are given in the figure: a) hysteresis loop with unreversed part of magnetization (Inset: the whole loop), b) randomly distributed locations for the enhanced exchange constants J_E , c) completely unreversed spins in $+1$ positions (grey squares), spins not reversed from -1 orientations for a field intensity of 2.7 (white squares), and fully reversed spins (black region)

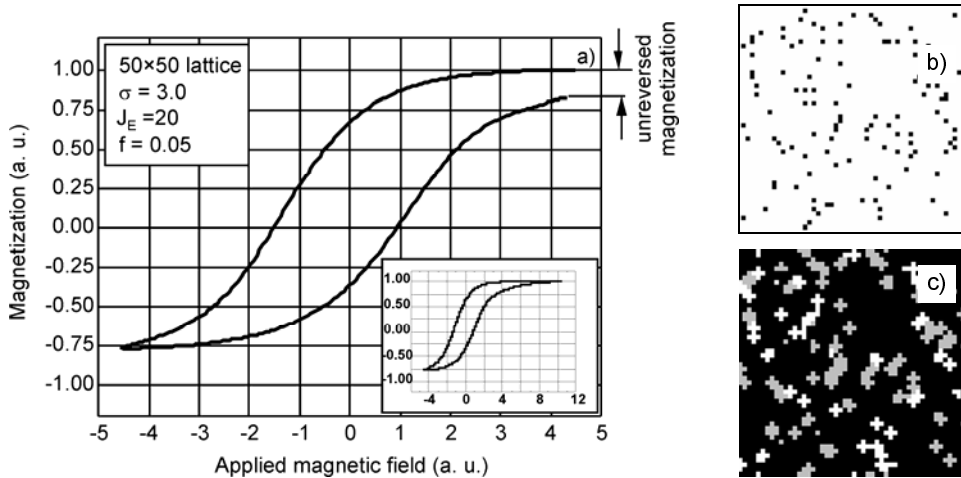


Fig. 2. Simulation of exchange-bias for a system with $\sigma = 3.0$. The simulation starts from saturation under the applied magnetic field 10.5 a. u. ranging between 10.5 a. u. and -2.7 a. u. Other input data are given in the figure: a) hysteresis loop with unreversed part of magnetization (Inset: the whole loop), b) randomly distributed locations for the enhanced exchange constants J_E , c) completely unreversed spins in $+1$ positions (grey squares), spins not reversed from -1 orientations for a field intensity of 4.5 (white squares), and fully reversed spins (black region)

for a standard deviation of the random fields $\sigma = 3$, the fraction of enhanced bounds $f = 0.05$, and the external magnetic field intensity ranging from -4.5 to 10.5 .

The obtained asymmetrical minor loops (Figs. 1a, 2a) point to the existence of unreversed spins during loop creation. What should be emphasized is that these spins can be divided into two parts. The first set of spins can be distinguished as the field decreases from its maximum to minimum value, and where some spins are unreversed (grey squares in Figs. 1c, 2c). The other part can be recognized when the field increases back to its maximum value – these spins were reversed when the field decreased, but some of them were not reversed back (white squares in Fig. 1c, 2c). Obviously, the spins that are unreversed during this first period of the hysteresis loop remain unreversed until the end of a given simulation of the hysteresis loop. In this way, the current effects differ from those provided by X. Illa, where under the same assumptions and applied algorithm, FM spins seem to be completely reversible from their -1 orientations. For clarity, the black regions in Figs. 1c, 2c represent $+1$ orientation of spins – these spins are completely reversible from $+1$ to -1 and back to $+1$. Figs. 1b, 2b provide information on the randomly distributed locations of the enhanced exchange constants J_E .

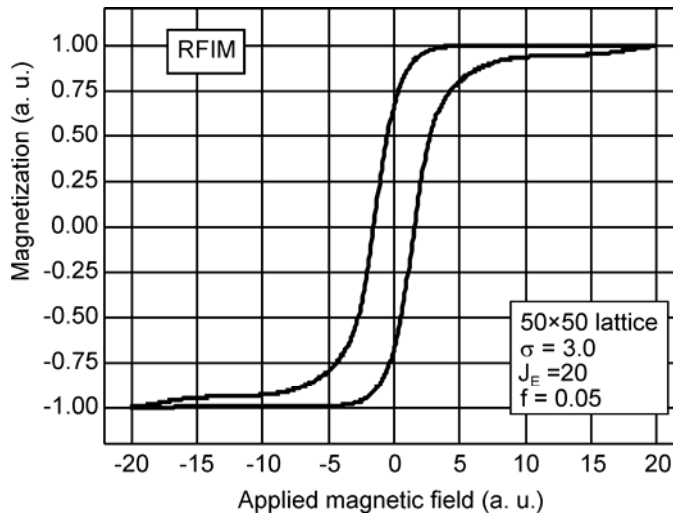


Fig. 3. Simulation of the total loop for the external magnetic field ranging from -20 to 20

The results reported here are consistent with the DSM model [16, 17], where a part of the AFM interface magnetization is stable during creation of the hysteresis loop and leads to the up-shift of the AFM hysteresis loop with open ends. In the DSM model which recognizes this phenomenon, the irreversible part of the interface magnetization of the AFM acts as an additional effective field influencing the FM, and is a source of exchange bias and unidirectional in-plane magnetic anisotropy. Thus, the RFIM results provided here and the DSM results provide information about the stable part of AFM/FM interface magnetization. Furthermore, the results provided here pos-

sess equivalents in experimental reality. The AFM crystal lattice dilution, using different atom substitutions, and exchange-bias in the AFM/FM system, were realized technologically in CoO/Co bilayers – the AFM CoO structure was modified by inserting non-magnetic substitutions of the $\text{Co}_{1-x}\text{Mg}_x\text{O}$ type [18].

Figure 3 provides results of a total loop, for which the external magnetic field intensity ranges from -20 to 20 , the standard deviation of the random fields being $\sigma = 3$, the enhanced exchange constant $J_E = 20$, and the fraction of enhanced bounds $f = 0.05$. This proves that the effects observed in these simulation correspond to minor loops.

4. Conclusions

What can be concluded from the RFIM results shown here, is the existence of unreversed spins of two types: unreversed from the $+1$ orientation and unreversed from the -1 orientation. Importantly, the examination of the data provided here indicates a correlation with results obtained within the DSM model of exchange-bias for the AFM layer at the AFM/FM interface.

Despite this consistency with the DSM model, however, we have tested several types of boundary conditions imposed on the 2D structure. The results were not sensitive to these in-plane features. We can conclude that we simulated perpendicular out-of-plane magnetization reversal. The observed pinning of ferromagnetic spins was influenced by the AFM. It seems realistic that the obtained unreversed part of interface magnetization can be transferred into another perpendicular direction, a third dimension. Importantly, layered structures with perpendicular magnetic anisotropies have been experimentally realized [19] with IrMn applied to exchange-biased Co/Pt multilayers. The model presented in the present paper can be easily extended onto the 3D type to simulate perpendicularly exchange-biased structures as well.

The authors hope that these results will contribute, at least partially, to full understanding of the exchange bias phenomenon [20]. It seems that much work in this area, however, still remains to be done.

Acknowledgements

The paper is associated with the activities related to Grant No. 3 T11F 015 26 received from the Polish State Committee for Scientific Research.

References

- [1] KANAI H., YAMADA K., AOSHIMA K., OHTSUKA Y., KANE J., KANAMINE M., TODA J., MIZOSHITA Y., IEEE Trans. Magn., 32 (1996), 3368.
- [2] KANAI H., KANE J., YAMADA K., AOSHIMA K., KANAMINE M., TODA J., MIZOSHITA Y., IEEE Trans. Magn., 33 (1997), 2872.
- [3] KANAI H., KANAMINE M., HASHIMOTO A., AOSHIMA K., NOMA K., YAMAGISHI M., UENO H., UEHARA Y., UEMATSU Y., IEEE Trans. Magn., 35 (1999), 2580.

- [4] KAKA S., NIBARGER J.P., RUSSEK S.E., STUTZKE N.A., BURKETT S.L., *J. Appl. Phys.*, 93 (2003), 7539.
- [5] BESCHOTEN B., TILLMANN S., KELLER J., GÜNTHERODT G., NOWAK U., USADEL K.D., *Adv. Solid State Phys.*, 42 (2002), 419.
- [6] KELLER J., MILTÉNYI P., BESCHOTEN B., GÜNTHERODT G., NOWAK U., USADEL K.U., *Phys. Rev. B*, 66 (2002), 14431.
- [7] NOWAK U., USADEL K.D., *Phys. Rev. B*, 44 (1991), 7426.
- [8] NOWAK U., USADEL K.U., KELLER J., MILTÉNYI P., BESCHOTEN B., GÜNTHERODT G., *Phys. Rev. B*, 66 (2002), 14430.
- [9] MEWES T., LOPUSNIK R., FASSBENDER J., HILLEBRANDS B., JUNG M., ENGEL D., EHRESMANN A., SCHMORANZER H., *Appl. Phys. Lett.*, 76 (2000), 1057.
- [10] BINDER K., *The Monte Carlo Method in Condensed Matter Physics*, Springer-Verlag, Berlin, 1995.
- [11] SETHNA J.P., DAHMEN K., KARTHA S., KRUMHANSL J.A., ROBERTS B.W., SHORE J.D., *Phys. Rev. Lett.*, 70 (1993), 3347.
- [12] BLOSSEY R., KINOSHITA T., DUPONT-ROC J., *Physica A*, 248 (1998), 247.
- [13] NOWAK U., USADEL K.D., ESSER J., *Physica A*, 250 (1998), 1.
- [14] ILLA X., VIVES E., PLANES A., *Phys. Rev. B*, 66 (2002), 224422.
- [15] BLACHOWICZ T., *Cent. Eur. J. Phys.*, 3 (2005), 147.
- [16] NOWAK U., MISRA A., USADEL K.D., *J. Appl. Phys.*, 89 (2001), 7269.
- [17] NOWAK U., MISRA A., USADEL K.D., *J. Magn. Magn. Mater.*, 240 (2002), 243.
- [18] MILTÉNYI P., GIERLINGS M., KELLER J., BESCHOTEN B., GÜNTHERODT G., NOWAK U., USADEL K.D., *Phys. Rev. Lett.*, 84 (2000), 4224.
- [19] SORT J., GARCIA F., RODMACQ B., AUFFRET S., DIENY B., *J. Magn. Magn. Mater.*, 272–276 (2004) 355.
- [20] MEIKLEJOHN W.H., BEAN C.B., *Phys. Rev.*, 102 (1956), 1413.

Received 1 June 2005
Revised 10 October 2005

Electronic transport through carbon nanotubes with ferromagnetic electrodes or in magnetic fields

S. KROMPIEWSKI*

Institute of Molecular Physics, Polish Academy of Sciences,
M. Smoluchowskiego 17, 60-179 Poznań, Poland

Spin-dependent electronic transport through carbon nanotubes (CNTs) was studied, either sandwiched between ferromagnetic contacts or in external magnetic fields. Attention was paid to the conductance dependence on geometrical size (the length and diameter) of the CNTs, chirality, and conditions at CNT/contact interface. The CNTs are end-contacted to *fcc* (111) metallic leads, and the relative atomic positions at the interfaces are determined by the relaxation procedure. Additionally, a charge neutrality condition is imposed on the extended molecule (i.e., CNT with a few atomic layers of the leads) in order to fix the band line-up of the whole system. Using a single-band tight-binding model and a Green's function technique, it is shown that if the electrodes are ferromagnetic, quite a considerable giant magnetoresistance effect can occur. For paramagnetic electrodes in a parallel magnetic field, clear Aharonov-Bohm oscillations are observed, with distinct minima in the conductance. The depth of the dips depends on the diameters of the CNTs, most likely due to some unintentional doping from the contacts. In the case of perpendicular geometry, pronounced conductance oscillations appear whenever the magnetic length becomes smaller than the perimeter of a CNT.

Key words: *carbon nanotube; electronic transport; magnetoresistance*

1. Introduction

Carbon nanotubes (CNTs) are tubular structures made of graphene (two-dimensional graphite) by rolling it up along the so-called wrapping vector [1]. The wrapping (or chiral) vector, \mathbf{C}_h , is fully defined in terms of its components (n, m) in the basis vectors $\mathbf{a}_1 = (0.5a\sqrt{3}, 0.5a)$ and $\mathbf{a}_2 = (0.5a\sqrt{3}, -0.5a)$, where $a = 2.46 \text{ \AA}$ is the lattice constant of graphene. Typically, the length of CNTs ranges from several hundred nanometers up to a few micrometers, whereas their cross-sections are quite small and amount only to several nanometers for single-wall (SW) CNTs, and roughly 10 times more for multi-wall (MW) CNTs. Remarkably, the physical properties of the CNTs depend critically on their chirality, that is, on the manner in which they fold up

*E-mail: stefan.krompiewski@ifmpan.poznan.pl

from the pristine graphene plane. CNTs whose chiral vector components fulfil the condition that $n-m$ is divisible by 3 are metallic, otherwise they are semiconducting. Metallicity (or lack thereof) is fully related to the electronic structure of nanotubes and the absence (presence) of energy gaps. To see how the so-called zone folding proceeds, let us start with a graphene energy spectrum:

$$E(\vec{k}) = \pm t \sqrt{1 + 4 \cos \frac{3k_x a}{2} \cos \frac{k_y a}{2} + 4 \cos^2 \frac{k_y a}{2}} \quad (1)$$

where t is the nearest neighbour transfer (hopping) integral, regarded hereafter as the energy unit. Now, in order to obtain the band structure of a CNT, one simply imposes cyclic boundary conditions on the chiral vector C_h , and the \mathbf{k} vector becomes quantised according to $C_h \mathbf{k} = 2\pi j$, $j = 1, 2, \dots$. Specifically, in the case of the armchair SWCNT, $C_h = (n, n)$, one finds:

$$E(k_y, j) = \pm t \sqrt{1 + 4 \cos \frac{k_y a}{2} \cos \frac{j\pi}{n} + 4 \cos^2 \frac{k_y a}{2}} \quad (2)$$

Similarly, for another most fundamental symmetry, the zigzag with $C_h = (n, 0)$, the results reads:

$$E(k_x, j) = \pm t \sqrt{1 + 4 \cos \frac{3k_x a}{2} \cos \frac{j\pi}{2} + 4 \cos^2 \frac{j\pi}{2}} \quad (3)$$

It can be easily seen that, in agreement with what has been stated before, armchair CNTs are always metallic, in contrast to zigzag ones, which have a gap unless n is a multiple* of 3. Undoped CNTs have a Fermi energy at $E = 0$ (charge neutrality point), and the valence (lower) bands cross the conduction (upper) bands in metallic CNTs exclusively at $k = \pm 2\pi/3a$ and 0 for the wrapping vectors (n, n) and $(3i, 0)$, respectively. This observation suggests that metallic CNTs can be easily driven to a semiconducting state upon applying external disturbances such as mechanical strain or magnetic field. Both theoretical and experimental studies fully confirm this suggestion [2–5]. In this paper, attention is directed to the physical properties of CNTs, which might be utilized in emerging spin electronics – spintronics. Attention is therefore directed to the effect of magnetic field on electronic transport through CNTs, as well as to so-called giant magnetoresistance (GR) observed when CNTs are sandwiched between ferromagnetic electrodes. The paper is organized in the following way. In Sec. 2 the mathematical apparatus and simulation method of the devices of interest are described, followed by results elucidating size and chirality effects. Sec. 3 is devoted to the GMR effect and Sec. 4 shows results on the conductance of CNTs in

*Incidentally, even for zigzag CNTs with modulo $(n, 3) = 0$ it is straightforward to show that in the case of anisotropic hopping integrals, $t_{\perp} \neq t_{\parallel}$, a narrow gap does open.

the presence of either parallel or perpendicular magnetic fields. Finally, Sec. 5 summarizes the main results of the paper.

2. The method and geometrical aspects

The method is based on a single-band tight-binding model and is applied to both $p_z(\pi)$ electrons in CNTs and s electrons in metal-electrodes. In general, computations are performed within the non-equilibrium Green's function method (see e.g. [6] and references therein), using the following relations for the Green's function (g), electron density matrix (ρ), and current (I), with L , R , and C referring to the left and right electrodes and the CNT itself, respectively:

$$g = (E - H_C - \Sigma_L - \Sigma_R)^{-1} \quad (4)$$

$$\rho = \frac{1}{2\pi} \int dE g (f_L \Gamma_L + f_R \Gamma_R) g^\dagger \quad (5)$$

$$I = \frac{e}{h} \int dE (f_L - f_R) \text{Tr}(\Gamma_L g \Gamma_R g^\dagger) \quad (6)$$

where $\Gamma_\alpha = i(\Sigma_\alpha - \Sigma_\alpha^\dagger)$, $\Sigma_\alpha = T_{C\alpha} g_\alpha T_{C\alpha}^\dagger$, and f_α is the Fermi function with the chemical potential $\mu_\alpha = \mu \pm eV/2$ for $\alpha = L, R$. Additionally, $T_{C\alpha}$ is the matrix that couples the CNT to the α -th electrode, V stands for the voltage, and g_α is the surface Green's function of the infinite lead, E denotes energy, and H_C – Hamiltonian of an isolated CNT. The electric current I yields a differential conductance $G = dI/dV$, which in the equilibrium case, $V = 0$, reduces to the well-known Landauer–Büttiker formula

$$G = \frac{e^2}{h} \text{Tr}(\Gamma_L g \Gamma_R g^\dagger) \quad (7)$$

The devices of interest here are CNTs end-contacted to metal electrodes. They are simulated as described in [7]. It is noteworthy that the structures in question are relaxed using the Lennard–Jones potential in order to find energetically favourable positions of carbon atoms with respect to electrode atoms. During the relaxation process, the external electrodes are allowed to rotate and shift independently of each other, and in the case of double-wall (DW) CNTs the inner carbon tube is also free to rotate. The nearest neighbour hopping integrals are kept constant (equal to t) within the cut-off radii throughout the whole system, whereas inter-tube hopping is set to

$$t_{\text{int}} = -\frac{t}{8} \cos\theta_{ij} \exp\left(\frac{d_{ij} - b}{\delta}\right) \quad (8)$$

where θ_{ij} stands for the angle between the π orbitals, d_{ij} is the relative distance, and the two remaining constants are $\delta = 0.45 \text{ \AA}$ and $b = 3.34 \text{ \AA}$ [8]. In order to line up the

Fermi energies of the CNTs and the model electrodes, the charge neutrality requirement has been imposed on the so-called extended molecule consisting of the CNT and two closest atomic planes from each electrode. The charge has been calculated from Eq. (5) in a self-consistent way by shifting all the on-site potentials of the extended molecule so as to ensure global charge neutrality at $E_F = 0$.

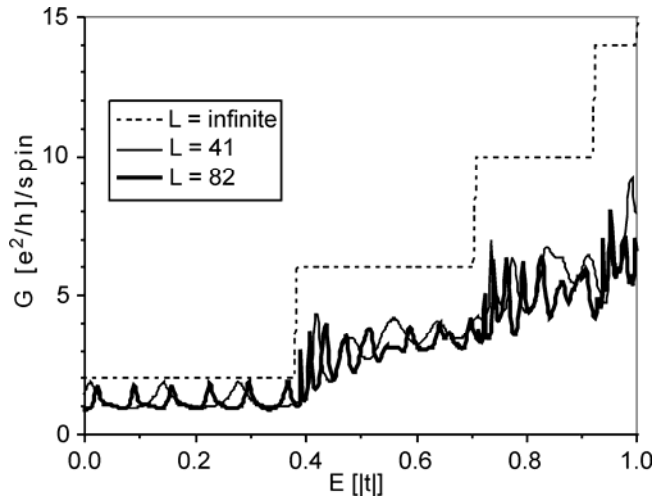


Fig. 1. Conductance of the armchair SWCNT (8,8) as a function of energy. The dashed line corresponds to a pristine (ideal infinite) CNT, whereas the thin (thick) curve to one with finite length, and $L = 41$ carbon rings ($L = 82$ carbon rings). Note a periodic behaviour below $E \approx 0.4$, and a halving of the period as the length doubles

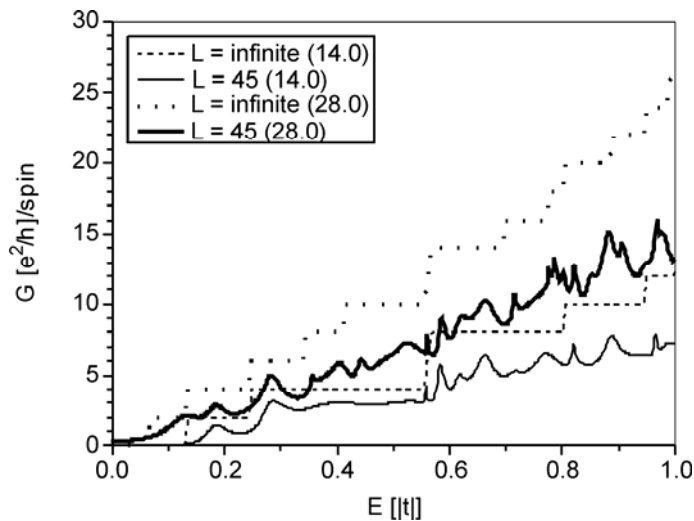


Fig. 2. Conductance spectra for 2 zigzag tubes with different diameters. The stepped curves represent pristine tubes, and the others correspond to $L = 45$ carbon rings. Thick (thin) lines apply to the larger (smaller) diameters

Figures 1 and 2 present the effect of length, diameter, and chirality on the electrical conductance of SWCNTs. As a reference, pristine nanotubes infinite in length are also shown, and they are purely ballistic conductors quantised in integer multiples of the fundamental conductance unit e^2/h (per spin). It is readily seen from Fig. 1 that in the vicinity of the charge neutrality point ($E_F = 0$) the conductance is a periodic function of energy, with a period inversely proportional to the length. Otherwise, the conductance is strongly reduced when compared to that of an infinite CNT. They are also quite irregular, but still reveal some extra features at energies corresponding to van Hove singularities (or steps) of the latter. Figure 2 shows that in the case of semiconducting zigzag nanotubes the “memory” about van Hove singularities seems to be lost rather quickly as the diameter increases. Another observation is that the region of small conductance narrows with increasing diameter due to the onset of new subbands. In fact, these results show that nominally semiconducting CNTs can become slightly metallic due to doping by the electrodes. The doping depends in general on the work functions of the involved materials (carbon vs. the electrode metal) and on the area of the contact region, so it is the most effective for ultra-short CNTs with a high percentage of atoms at the interface.

3. Giant magnetoresistance

If electrodes are ferromagnetic and the spin-diffusion length is long enough, the giant magnetoresistance effect can occur (for an excellent review on spin-transport in nanoscopic systems see Ref. [9]). Here, it is defined as $GMR = (G_{\uparrow\uparrow} - G_{\uparrow\downarrow})/G_{\uparrow\uparrow}$, where the arrows $\uparrow\uparrow$ and $\uparrow\downarrow$ denote aligned and anti-aligned magnetization orientations of the electrodes.

Motivated by recent experimental findings [10–12] which show that the magnetoresistance of ferromagnetically contacted carbon nanotubes reveals a peculiar behaviour, including the appearance of the so-called inverse GMR for some samples, the present author has studied such systems for several years [6, 7, 13, 14]. The studies were carried out in the quasi-ballistic regime, although most of the hitherto existing experiments concern the diffusive regime and highly resistive devices. It turns out, however, that the ferromagnetic electrodes can also form low resistive junctions with CNTs. This was demonstrated in [15], where MWCNTs were sandwiched between electrodes made of the ferromagnetic alloy $Pd_{1-x}Ni_x$ ($x \approx 0.7$), and shown to have resistances below 100 k Ω at room temperature.

Figure 3 presents the conductance and GMR for a double-wall carbon nanotube, which consists of 45 zigzag rings and 39 armchair rings (45–(5, 0)@39–(8, 8)). The corresponding lengths are then roughly the same (ca. 5 nm each), so both the inner and outer tubes can be regarded as being contacted to the magnetic electrodes. Quantum oscillations are inherent in quantum transport phenomena, yet in the case of MWCNT they are often reported to be washed-out by disorder coming from inter-wall interactions [16, 17]. To mimic a possible effect of disorder, conductance curves have

been energy-averaged. The averaged curves, along with the resultant GMR (dashed), are drawn with solid lines. The averaging was made over the energy-level spacing, which is the most obvious energy-scale in this context.

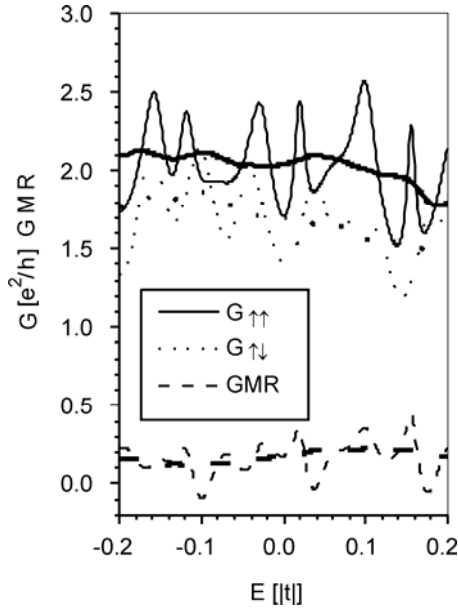


Fig. 3. Conductance and GMR for a double-wall carbon nanotube, which consists of 45 zigzag rings and 39 armchair rings (45-(5,0)@39-(8,8)). The energy averaged conductance (over energy bins equal to the energy-level spacing) and resulting GMR are depicted by thick lines. The averaging mimics the anticipated effect of disorder

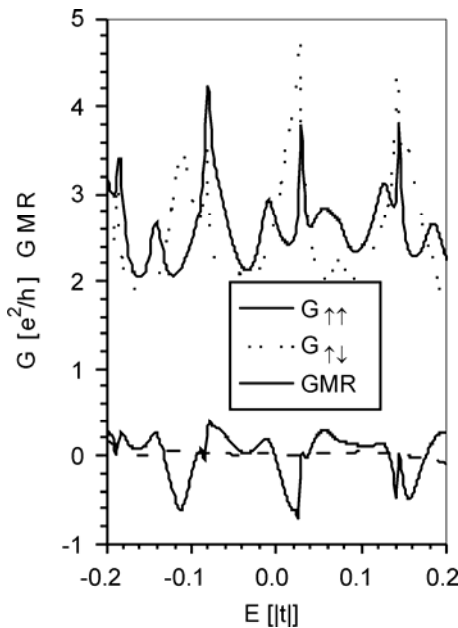


Fig. 4. Conductance and GMR for an armchair DWCNT (3,3)@ (8,8). There are 39 (38) carbon rings in the outer (inner) tube, so that the inner tube is out of contact with the drain. The thick dashed line is defined as in Fig. 3

In order to gain deeper insight into the role of the inner tube, Fig. 4 depicts the results for the pure armchair DWCNT (38-(3, 3)@39-(8, 8)). The inner tube in this

case is by one inter-ring spacing (half the lattice constant) shorter than the outer tube and is out of contact with the drain electrode. Hence, the systems presented in Figs. 3 and 4 are similar, since the zigzag nanotube (5, 0), as a semiconductor, also does not conduct (due to the energy gap in the interval $|E/t| < 0.2$). The most important conclusion to be drawn from this comparison is that the former DWCNT has a much larger and more robust GMR at the neutrality point than the latter one, which happens to change the sign at E_F and reveals large conductance fluctuations. A more detailed analysis [7] shows that these peculiarities originate from inter-tube quantum interference effects and would be suppressed if t_{int} were allowed to vanish.

4. Carbon nanotubes in magnetic fields

Recently, two seminal papers have been published on the magnetoconductance of CNT-based devices [4, 5]. The papers were motivated by theoretical predictions that a magnetic field can drastically modify the electronic band structure [1, 3], including periodic opening (closing) of energy gaps and a splitting of van Hove singularities in the density of states. In this section, an attempt is made to generalize the hitherto existing theoretical studies (restricted to free CNTs) by taking into account the presence of electrodes and accompanying charge transfer processes. Within the tight-binding method, a magnetic field can be most conveniently implemented by the well-known Peierls substitution, $t \rightarrow t \exp[i(2\pi/\Phi_0)\xi]$, where the phase factor is given by [1]:

$$\xi = \frac{\Delta x}{C_h} \Phi \quad (9)$$

$$\xi = \left(\frac{C_h}{2\pi} \right)^2 \frac{B\Delta y}{\Delta x} \left[\cos \frac{2\pi x}{C_h} - \cos \frac{2\pi(x + \Delta x)}{C_h} \right] \quad (10)$$

and for the parallel and axial magnetic field orientations. Above, Φ is a magnetic flux penetrating the cross-section of the CNT, Φ_0 is the magnetic flux quantum, B denotes a uniform static magnetic field, whereas x (Δx) and y (Δy) stand for circumferential and axial coordinates (increments), respectively. Figure 5 presents magnetoconductance spectra computed from Eq. (7) at the global charge neutrality point for 3 armchair nanotubes with different diameters. At a perpendicular field (Fig. 3a), there are conductance oscillations that show an interesting structure with the number of peaks increasing regularly with the diameter. Since on one hand for the increasing diameter the curvature of CNTs decreases, and on the other hand in strong magnetic fields the magnetic length $l = [\Phi_0/(2\pi B)]^{1/2}$ becomes smaller than the perimeter C_h , the CNT electron band structure approaches roughly that of graphene. The observed features can be identified as typical interference patterns (the first sharp peak in Fig. 5a always appears for $l < C_h/2$). For the parallel configuration, Aharonov–Bohm oscillations are clearly visible, with a constant period of Φ_0 . The presence of external electrodes manifests

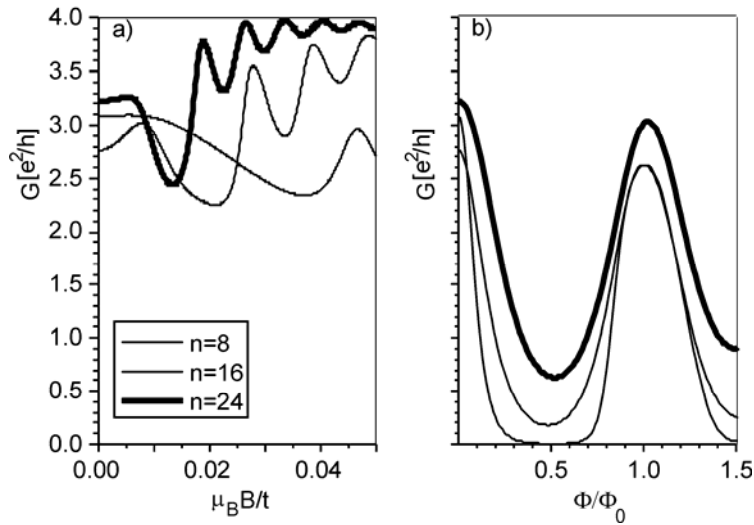


Fig. 5. Magnetoconductance of single-wall CNTs versus dimensionless magnetic field and flux for perpendicular (a) and parallel (b) orientations. B is normalized to the hopping parameter, and Φ to the magnetic flux quantum

itself by doping and broadening of the energy levels which make a complete opening of the gap no longer possible.

5. Conclusions

In this work, the effect of external leads (electrodes) on quantum transport through carbon nanotubes was analysed. The studies included both geometrical aspects (length, diameter, and chirality of CNTs) and those essential for spintronic applications, i.e. the use of ferromagnetic electrodes and the application of magnetic fields. In general, the GMR effect is quite considerable and may reach several tens of percent. It is, however, very sensitive to the internal structure of the MWCNT and depends on the chirality of the inner tubes and inter-tube interactions. This applies even to the case when the current flows mainly through the outer tube and the inner tubes are either decoupled from one of the electrodes or have a gap in the transport energy window. Regarding the influence of magnetic fields, it was shown that electrode-induced doping modifies magnetoconductance spectra for parallel fields without changing the period of Aharonov-Bohm oscillations. The magnetoconductance spectra of CNTs at perpendicular fields, in turn, reveal pronounced oscillations with a period that scales with the diameter of the CNT.

Acknowledgements

Discussions with G. Cuniberti and N. Nemeč are acknowledged, and I thank the Poznan Supercomputing and Networking Center for the computing time.

References

- [1] SAITO R., DRESSELHAUS M.S., DRESSELHAUS G., *Physical Properties of Carbon Nanotubes*, Imperial College Press, London, 1998.
- [2] MINOT D.E., YAISH Y., SAZONOVA V., PARK J.-Y., DRINK M., MCEUEN P.L., *Phys Rev. Lett.*, 90 (2003), 156401.
- [3] AJIKI H., ANDO T., *J. Phys. Soc. Jpn.*, 62 (1993), 1255.
- [4] ZARIC S., OSTOLIC G.N., KONO J., SHAVER J., MOORE V.C., STRANO M.S., HAUGE R.H., SMALLEY R.E., WEI X., *Science*, 304 (2004), 1129.
- [5] COSKUN U.C., WEI T.-C., VISHVESHWARA S., GOLDBART P.M., BEZRYADIN A., *Science*, 304 (2004), 1132.
- [6] KROMPIEWSKI S., *J. Magn. Magn. Mater.*, 272–276 (2004), 1645.
- [7] KROMPIEWSKI S., *Phys. Stat. Sol. (b)*, 242 (2005), 226.
- [8] ROCHE S., TRIOZON F., RUBIO A., MAYOU D., *Phys. Rev. B*, 64 (2001), 121401.
- [9] SANVITO S., *Handbook of Computational Nanotechnology*, American Scientific Publ. (Stevenson Ranch, CA, 2005); also cond-mat/0503445.
- [10] TSUKAGOSHI K., ALPHENAAR B.A., AGO H., *Nature (London)*, 401 (1999), 572.
- [11] ZHAO B., MÖNCH I., MÜHL T., SCHNEIDER C.M., *Appl. Phys. Lett.*, 80 (2002), 3144.
- [12] JENSEN A., NYGÅRD J., BORGGREEN J., [in:] *Toward the Controllable Quantum States*, Proc. Internat. Symp. Mesoscopic Superconductivity and Spintronics, H. Takayanagi, J. Nitta (Eds.), World Scientific, Singapore, 2003, 33–37.
- [13] KROMPIEWSKI S., *J. Phys.: Condens. Matter*, 16 (2004), 2981.
- [14] KROMPIEWSKI S., GUTIERREZ R., CUNIBERTI G., *Phys Rev. B*, 69 (2004), 155423.
- [15] SAHOO S., KONTOS T., SCHÖNENBERGER C., SÜRGENS C., *Appl. Phys. Lett.*, 86 (2005), 112109.
- [16] TRIOZON F., ROCHE S., RUBIO A., MAYOU D., *Phys. Rev. B*, 69 (2004), 121410.
- [17] STOJETZ B., MIKO C., FERRÓL., STRUNK C., *Phys Rev. Lett.*, 94 (2005), 186802.

Received 1 June 2005

Revised 10 October 2005

Magnetic ordering in ultra-thin Co films grown on vicinal substrates

A. STUPAKIEWICZ^{1*}, R. GIENIUSZ¹, K. POSTAVA¹, M. TEKIELAK¹,
A. MAZIEWSKI¹, I. SZEREL¹, A. WAWRO², L.T. BACZEWSKI²

¹Institute of Experimental Physics, University of Białystok, Lipowa 41, 15-424 Białystok, Poland

²Institute of Physics, Polish Academy of Sciences, al. Lotników 32/46, 02-668 Warsaw, Poland

The magnetic anisotropy of ultra-thin Au/Co/Au magnetic films epitaxially grown on vicinal monocrystalline (11–20) sapphire substrates with different miscut angles, covered with a Mo buffer, are investigated by means of ferromagnetic resonance and magneto-optical techniques. Changes in in-plane magnetic anisotropy symmetry were deduced from the shape analysis of magnetization curves and the angular dependence of the resonance field measured in the sample plane. Two-fold and four-fold symmetry was observed for different miscut angles. The preference of the domain wall orientation was observed. The experimental data are discussed taking into account the shape anisotropy, perpendicular uniaxial anisotropy, and step-induced uniaxial anisotropy.

Key words: *magnetic anisotropy; ultra-thin film; cobalt*

1. Introduction

Ultra-thin magnetic multilayers have been intensively investigated due to their interesting physical properties and possible applications for magnetic storage media. Magnetic anisotropy, spin-reorientation transition and self-organization in ultra-thin magnetic films grown on vicinal surfaces, i.e. substrates with ordered monatomic steps, are the properties that attract general attention. Magnetic films grown on vicinal surfaces have shown a strong correlation between the structure of the substrate surface and magnetic properties. In addition to magnetocrystalline anisotropy, an in-plane uniaxial anisotropy is induced when the film is grown on a stepped surface [1–3]. It can favour a magnetic moment alignment perpendicular to the steps [3] as well as parallel to the step edges [4, 5]. For Co layers, magnetic anisotropy strongly depends on thickness, with the spins flipping from the perpendicular to the in-plane orientation [6, 7]. In the

*Corresponding author: and@uwb.edu.pl

present work, we report on magnetic anisotropy, magnetisation reversal, and domain structures in ultra-thin Co films grown by molecular beam epitaxy on vicinal sapphire substrates with miscut angles of 1° and 5° .

2. Experimental

Samples grown on sapphire single-crystal (11–20) wafers have the following structure: (i) a buffer layer of 20 nm Mo(110) deposited at $T = 1000^\circ\text{C}$, (ii) a 10 nm Au(111) under-layer deposited at room temperature and annealed at $T = 200^\circ\text{C}$ for 30 minutes, (iii) a 2.4 nm Co layer, (iv) a 10 nm thick Au overlayer. The structures of the samples were monitored in-situ by RHEED and Auger spectroscopy.

Measurements were performed at room temperature by means of a magnetometer based on the magneto-optical Kerr effect (MOKE), a polarizing Kerr microscope in the polar configuration, and an FMR X-band spectrometer. Magnetization processes were studied in both longitudinal (L-MOKE) and polar (P-MOKE) configurations. A MOKE magnetometer with laser light with $\lambda = 640$ nm enabled the Kerr rotation and ellipticity to be determined. The laser beam was focused to a spot 0.5 mm in diameter.

3. Results and discussion

The measured resonance field (H_r) is related to magnetic anisotropy constants and enables the determination of the easy magnetization axes. An external magnetic field H was applied to the sample in different directions, defined by polar θ_H and azimuthal φ_H angles measured from the film normal and substrate miscut direction in the sample plane, respectively. By sweeping the amplitude of H , the resonance field H_r was determined for a selected direction defined by the angles θ_H and φ_H . The experimental dependence of H_r on the angle θ_H for samples with different miscut angles is shown in Figs. 1a, b.

An inclination of the easy magnetization axis of about 90° and 70° from the plane normal of samples with miscut angles of 1° and 5° , respectively, was deduced (see Figs. 1a, b). Figures 1c, d depict the dependences of in-plane $H_A(\varphi_H)$ with two-fold and four-fold symmetries for samples with miscut angles of 1° and 5° , respectively.

P-MOKE hysteresis loops for different miscut angles are shown in Fig. 2. The loops measured for 1° and 5° miscut angles correspond to in-plane and out-of-plane magnetization orientations, respectively. For the monodomain sample, the magnetization inclination angle θ_{inc} (measured from the film normal) could be determined from the relation $\cos\theta_{\text{inc}} = \theta_K(H_z = 0)/\theta_{K\text{max}}$, where $\theta_{K\text{max}}$ is the maximum polar Kerr rotation, and H_z is the magnetic field applied in the direction perpendicular to the film plane. The value of θ_{inc} close to 90° and about 70° could be calculated from Figs. 2a and 2b, respectively. The shape of the loops is strong evidence of magnetic anisotropy with a canted axis (by

about 70° from the normal) for the sample grown on a substrate with a higher miscut. These results are consistent with FMR experiments (Fig. 1).

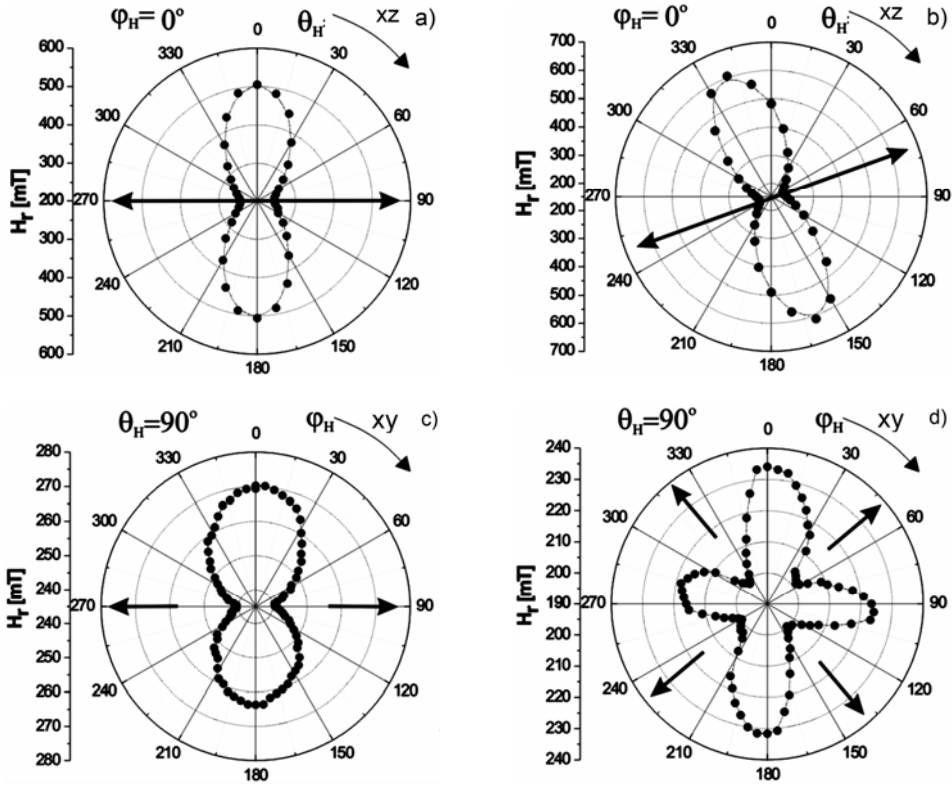


Fig. 1. The dependences of $H_T(\theta_H)$ for the samples with miscut angles of 1° (a) and 5° (b), and for the in-plane samples with miscut angles of 1° (c) and 5° (d)

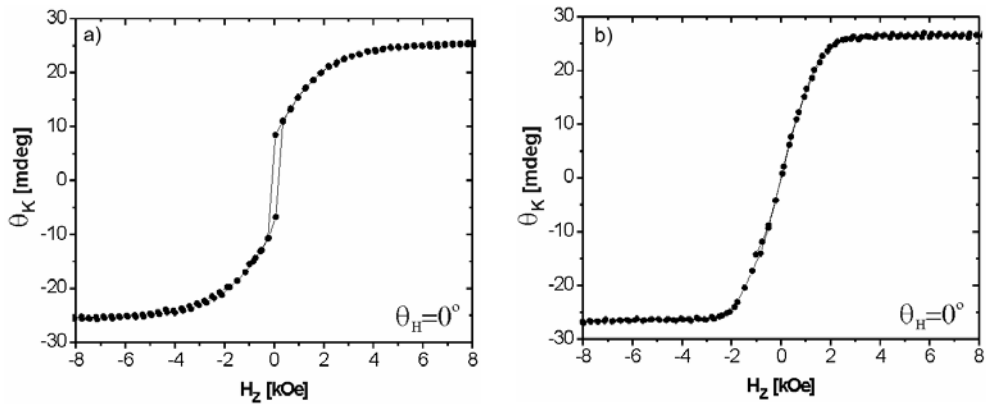


Fig. 2. Hysteresis loops measured as polar Kerr rotations for different miscut angles: a) 1° , b) 5° ; for 1° , $\arccos(\theta_K(H_z = 0)/\theta_{Kmax}) = 90^\circ$, and for 5° , $\arccos(\theta_K(H_z = 0)/\theta_{Kmax}) = 70^\circ$

L-MOKE hysteresis loops measured in-plane magnetic fields H_x oriented at various directions with respect to the miscut direction are plotted in Fig. 3. Curves illustrating the magnetization process when the field is applied along the hard and easy directions, respectively, are shown in Figs. 3a, c for the sample with a 1° miscut angle. The L-MOKE magnetization curves are related to the in-plane two-fold symmetry observed in FMR measurements. In the case of a 5° miscut, a complex form of the hysteresis loops is observed (Figs. 3b, d). This can be explained by the presence of the two easy magnetization axes as found in the FMR experiment.

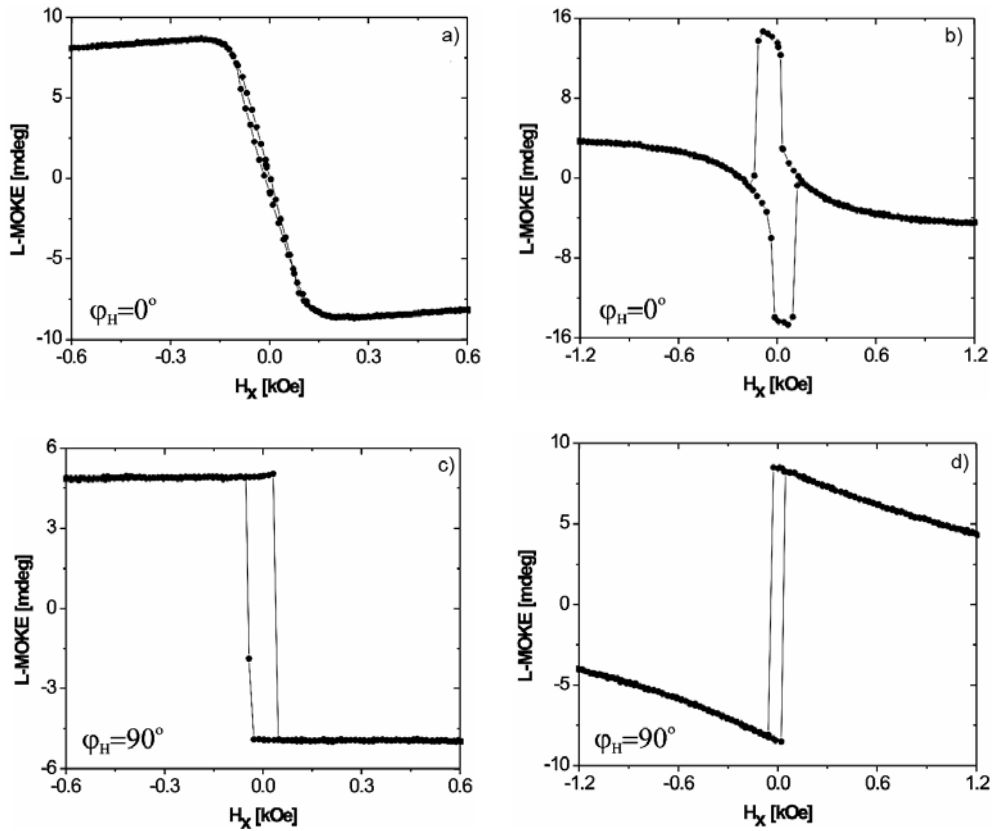


Fig. 3. Hysteresis loops measured as longitudinal Kerr rotations for miscut angles of 1° (a, c) and 5° (b, d) and various angles $\varphi_H = 0^\circ, 90^\circ$

The evolution of magnetic domain structure in the sample with a 5° miscut angle is presented for two steps of magnetization reversal in Fig. 4. The black and grey areas correspond to the change in domain structure after applying magnetic field pulses perpendicular to the film direction. The preference of domain wall orientation could be found in Fig. 4. A similar effect is observed in Ref. [8].

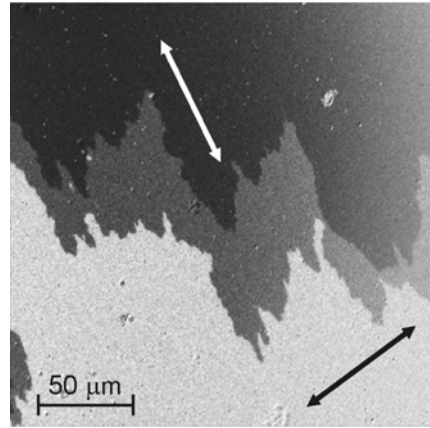
To analyse the experimental data, the following energy contributions were taken into account: (i) uniaxial anisotropy related to the miscut direction defined by the unit

vector $\mathbf{v}_{\text{mis}} = (\sin\theta_{\text{mis}}, 0, \cos\theta_{\text{mis}})$, (ii) shape anisotropy, and (iii) step-induced uniaxial in-plane anisotropy in the direction $\mathbf{v}_{\text{step}}=(0, 1, 0)$:

$$E_A(\mathbf{m}, \mathbf{v}_{\text{mis}}, \mathbf{v}_{\text{step}}) = \left(K_{1v} + \frac{2K_{1s}}{d} \right) \left[1 - (\mathbf{m} \cdot \mathbf{v}_{\text{mis}})^2 \right] - 2\pi M_s^2 \sin^2 \theta \\ + K_{\text{step}}^{(2)} \left[1 - (\mathbf{m} \cdot \mathbf{v}_{\text{step}})^2 \right] + K_{\text{step}}^{(4)} \left[1 - (\mathbf{m} \cdot \mathbf{v}_{\text{step}})^2 \right]^2$$

where $\mathbf{m} = (\sin\theta \cos\varphi, \sin\theta \sin\varphi, \cos\theta)$ is a unit magnetization vector, and K_{1v} and K_{1s} are the volume and surface anisotropy coefficients [7] determined for a film with thickness d . The proposed formula well describes the magnetic anisotropy of the investigated samples.

Fig. 4. Magnetic domain structure evolution in the sample with a 5° miscut angle (the black arrow shows the miscut direction); the sample initially saturated by a perpendicular magnetic field $H > 0$. The black and grey areas illustrate the change in the structure induced by $H < 0$ pulses. The white arrow illustrates preferential domain wall orientation



In conclusion, we suggest that the magnetic anisotropy of the Co layer can be tuned between (i) the easy out-of-plane axis, (ii) the two easy out-of-plane axes, and (iii) the easy in-plane axis, by changing the miscut angle of the vicinal substrates and Co thickness. Magnetic anisotropy induces a preference of domain wall orientation.

Acknowledgement

This work was supported by the Polish State Committee for Scientific Research (Grant No. 4 T08A02523) and Marie Curie Fellowships for “Transfer of Knowledge” (“NANOMAG-LAB” N 2004-003177).

References

- [1] HILLEBRANDS B., BAUMGART P., GÜNTHERODT G., Phys. Rev. B, 36 (1987), 2450.
- [2] BERGER A., LINKE U., OEPEN H.P., Phys. Rev. Lett., 68 (1992), 839.
- [3] CHEN J., ERSKINE J.L., Phys. Rev. Lett., 68 (1992), 1212.
- [4] KAWAKAMI R.K., ESCORCIA-APARICIO E.J., QIU Z.Q., Phys. Rev. Lett., 77 (1996), 2570.
- [5] CHEIKH-ROUHO W., SAMPAIO L.C., BARTENLIAN B., BEAUVILLAIN P., BRUN A., FERRE J., GEORGES P., JAMET J.P., MATHET V., STUPAKIEWICZ A., Appl. Phys. B, 74 (2002), 665.

- [6] QIU Z.Q., PEARSON J., BADER S.D., Phys. Rev. Lett., 70 (1993), 1006.
- [7] KISIELEWSKI M., MAZIEWSKI A., TEKIELAK M., WAWRO A., BACZEWSKI T., Phys. Rev. Lett., 89 (2002), 087203.
- [8] HAIBACH P., HUTH M., ADRIAN H., Phys. Rev. Lett., 84 (2000), 1312.

Received 1 June 2005
Revised 10 October 2005

Magnetism and superconductivity in oxide ferromagnet/superconductor heterostructures

P. PRZYŚLUPSKI^{1*}, A. TSAROU¹, I. KOMISSAROV¹, K. DYBKO¹,
P. DŁUŻEWSKI¹, M. SAWICKI¹, B. DĄBROWSKI², C. KIMBALL²

¹Institute of Physics, Polish Academy of Sciences, 02-668 Warszawa, Poland

²Department of Physics, Northern Illinois University, DeKalb, IL, 60115, U.S.A.

We report on transport and magnetic properties of $\text{La}_{0.67}\text{Sr}_{0.33}\text{MnO}_3/\text{YBa}_2\text{Cu}_3\text{O}_7/\text{La}_{0.67}\text{Sr}_{0.33}\text{MnO}_3$ (LSMO/YBCO/LSMO) trilayer structures. The onset of the superconducting transition temperature in trilayer structures starts from the sample with a 6 nm (5 unit cells) thick YBCO layer. The $M(H)$ hysteresis loop indicates an indirect exchange coupling between LSMO layers across the YBCO layer. Magnetoresistance studies demonstrate a change in the magnetoconductance of the trilayer structure with magnetic field variation, indicating an indirect exchange coupling between LSMO layers across the non-superconducting YBCO layer.

Key words: *trilayer structure; superconducting transition; exchange coupling; magnetoresistance*

1. Introduction

Studies of oxide ferromagnet/superconductor (F/S) heterostructures have attracted much attention. Using such structures, it is possible to probe the interplay between superconductivity and ferromagnetism on the nanometer length scale. Superconducting and magnetic orders are generally incompatible with each other: it is known that the exchange field of magnetic systems reduces the superconducting order parameter. A possibility of indirect exchange coupling between F layers across S layers in manganese/cuprate heterostructures has been predicted theoretically [1]. A signature of this effect has been recently demonstrated experimentally in LSMO/YBCO superlattices [2, 3]. The interplay between spin-polarized materials also has potential applications.

*Corresponding author, e-mail: przys@ifpan.edu.pl

2. Experimental

$\text{La}_{0.67}\text{Sr}_{0.33}\text{MnO}_3/\text{YBa}_2\text{Cu}_3\text{O}_7/\text{La}_{0.67}\text{Sr}_{0.33}\text{MnO}_3$ (LSMO/YBCO/LSMO) trilayer structures were deposited on (100) $[(\text{LaAlO}_3)_{0.3}(\text{Sr}_2\text{TaAlO}_6)_{0.7}]$ (LSAT) substrates by high pressure sputtering [2, 3]. Magnetic measurements were performed in a SQUID magnetometer in the temperature range 5–300 K. Transport measurements were carried out with the four-point probe method. For tunnelling magnetoconductance (TMC) measurements, we have synthesized the trilayer heterostructure using a shadow mask, with the bottom electrode 2 mm in width and separated by a YBCO spacer layer (7.2 nm thick) from the upper electrode of the same width and perpendicular to the bottom electrode. Differential conductance dI/dV was measured using a lock-in amplifier with an amplitude of 10 μV . The measurements were performed with a magnetic field parallel to the trilayer, with a DC bias voltage of 0.15 mV in a current perpendicular to the plane configuration (CPP).

3. Results and discussion

In this report, we present the measurements of LSMO/YBCO/LSMO trilayer structures, with YBCO layer thickness varying from 5 to 7 unit cells (u.c.) and LSMO layer thickness kept at 10 nm (25 u.c.). Figure 1 shows the temperature dependence of the resistance of trilayers with 5 (LaY114), 6 (LaY115), and 7 (LaY116) u.c. thick YBCO layers. It can be seen that the onset of the transition to the superconducting state is observed beginning from the sample with a 5 u.c. thick YBCO layer. In all measured samples, the Curie temperature was higher than 300 K. The in-plane M - H

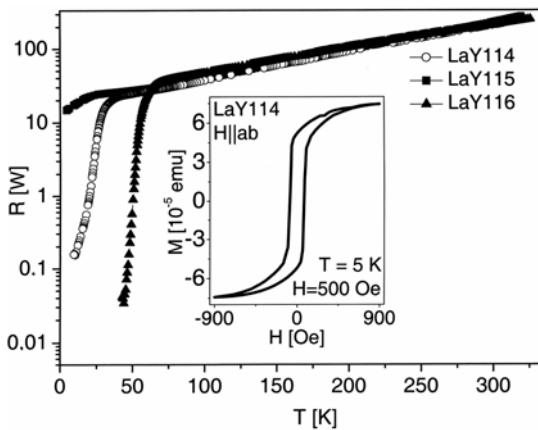


Fig. 1. Temperature dependences of resistance in trilayers with 6 nm (LaY114), 7.2 nm (LaY115) and 8.4 nm (LaY116) thick YBCO layer. Inset: hysteresis loop measured at $T = 5$ K in the sample LaY114

loop recorded at 5 K represents two magnetic contributions (see the inset in Fig. 1). At relatively small magnetic fields (below 100 Oe), the soft part of ferromagnetic LSMO

layers is observed, whereas the reversal of magnetic moments takes place at higher fields and saturates at about 650 Oe. This observation can be interpreted as a signature of indirect exchange coupling between LSMO layers across the YBCO superconducting layer. According to the theoretical model [1], there is a possibility of such a coupling, both above and below the superconducting transition. To confirm this

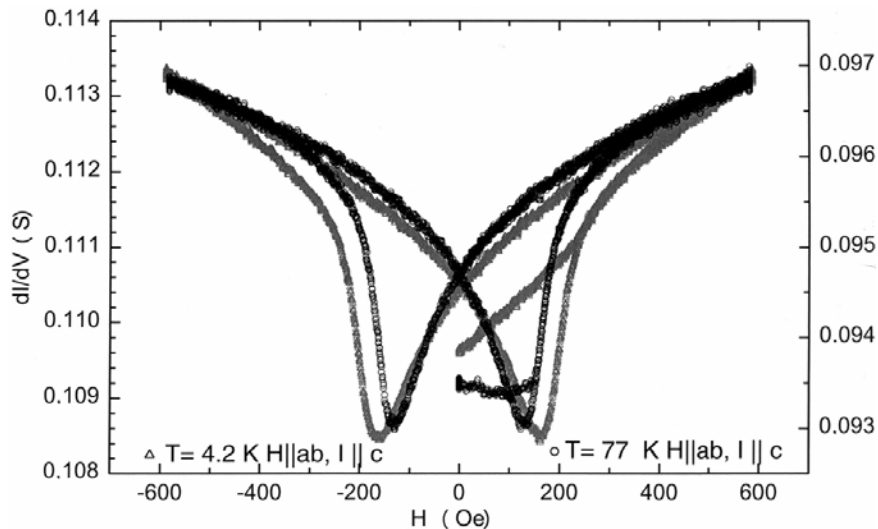


Fig. 2. Dynamical conductivity vs. applied magnetic field of LSMO (100 nm)/YBCO (7.2 nm)/LSMO (100 nm) trilayer measured at $T = 4.2$ and 77 K

effect, we measured the magnetoresistance (MR) effect in the LSMO (100 nm)/YBCO (7.2 nm)/LSMO (100 nm) trilayer. Our preliminary results are shown in Fig. 2. As in tunnel junctions [4], MR demonstrates conductivity variation when the magnetic configuration of magnetization changes from parallel to antiparallel, and back to parallel. Maximum conductivity is observed when the magnetic moments in LSMO layers are parallel, and conductivity decreases when the magnetic moments in LSMO layers are oriented antiparallel. For this particular sample, however, the YBCO layer is not superconducting, because of the suppression of superconductivity due to the exchange field of the thick LSMO ferromagnetic layer. The tunnelling effect observed in the magnetic field indicates the existence of indirect exchange coupling between LSMO layers through YBCO being in normal state. This indicates that the suppression of T_{c0} in the YBCO layer can be attributed to the injection of polarized spins from the highly polarized LSMO layer to the YBCO layer. Due to the d -wave symmetry of the order parameter in YBCO [1], there is a large population of quasi-particle excitations. The effect of MR is larger for quasi-particles with spins parallel to LSMO layers.

M - H hysteresis loops for superlattices [2, 3] with YBCO layers 1, 4, 6, and 8 unit cells thick demonstrate the antiparallel orientation of magnetic moments in consecu-

tive LSMO layers at low temperatures. On the other hand, superlattices with YBCO layers 2, 3, and 5 unit cells thick demonstrate only parallel alignment. This observation suggests an oscillating nature of the coupling. Recent experimental results also demonstrate a change from antiparallel to parallel alignment of the magnetic moments of LCMO layers in LCMO/YBCO/LCMO trilayers [5]. On the other hand, measurements on LSMO/YBCO/LSMO trilayer structures [6] suggest only an antiparallel alignment of magnetic moments in LSMO layers. More work is necessary to explain the nature of indirect exchange coupling between LSMO layers across YBCO layers.

Acknowledgements

The partial support of NSF-DMR-0302617 and the U.S. Dept. of education is gratefully acknowledged.

References

- [1] SA DE MELO C.A.R., *Physica C*, 387,17 (2003).
- [2] PRZYSLUPSKI P., KOMISSAROV I., PASZKOWICZ W., DLUZEWski P., MINIKAYEV R., SAWICKI M., *J. Appl. Phys.*, 95 (2004), 2906.
- [3] PRZYSLUPSKI P., KOMISSAROV I., PASZKOWICZ W., DLUZEWski P., MINIKAYEV R., SAWICKI M., *Phys. Rev B*, 69 (2004), 134428.
- [4] DE TERESA J.M., BARTHELEMY A.A., FERT A., CONTOUR J.P., LYONNET R., MONTAIGNE F., SENEOR P., VAURES A., *Phys. Rev. Lett.*, 82 (1999), 4288.
- [5] PENA V., SEFRIQUI Z., ARIAS D., LEON C., SANTAMARIA J., MARTINEZ J.M., TE VELTHUIS S.G.E., HOFFMAN A., *Phys. Rev. Lett.*, 94 (2005), 057002.
- [6] SENAPATI K., BUDHANI R.C., *Phys. Rev. B*, 71 (2005), 224507.

Received 1 June 2005

Revised 10 October 2006

Hall effect in strongly correlated electron systems

V. H. TRAN*

Institute of Low Temperature and Structure Research, Polish Academy of Sciences,
P. O. Box 1014, 50-950 Wrocław, Poland

This work provides a brief survey of the Hall effect data collected for some strongly correlated electron systems. The experimental results illustrate the behaviour of the heavy-fermion system UCu_5Al , heavy-fermion semiconductor $\text{U}_2\text{Ru}_2\text{Sn}$, ferromagnetic superconductor under pressure UGe_2 , and the ferromagnet with a weak 2D localization effect $\text{UCo}_{0.5}\text{Sb}_2$.

Key words: Hall effect; strongly correlated electron system; heavy fermion system

1. Introduction

Over the last three decades, strongly correlated electron systems (SCES) have attracted an increased attention of many experimental and theoretical solid-state scientists around the world. The essential property of f-electron SCES is the instability of the f-electron shell and, in consequence, f-electrons in compounds with sp- and d-elements easily hybridise with conduction electrons. It is well known that the Hall resistivity of magnetic materials consists of normal R_0 (OHE) and anomalous R_s (AHE) contributions. While the normal Hall effect results from the Lorenz force, the AHE is related to an asymmetric probability of electron scattering on magnetic centres. This means that the Hall effect could be a good probe for both electronic and magnetic properties in SCES. Recently, we have reported the Hall effect measurements on some U-based SCES, such as the heavy-fermion (HF) antiferromagnet UCu_5Al [1], HF semiconductor $\text{U}_2\text{Ru}_2\text{Sn}$ [2], ferromagnetic superconductor under pressure UGe_2 [3], and low-carrier density ferromagnet with a weak 2-dimensional localisation effect $\text{UCo}_{0.5}\text{Sb}_2$ [4]. In this contribution, some outstanding and interesting features of these investigations will be outlined and highlighted.

*E-mail: V.H.Tran@int.pan.wroc.pl

2. Results

The temperature dependences of the Hall coefficient R_H for the studied compounds are shown in Fig. 1. At high temperatures R_H is proportional to the magnetic susceptibility (M/B). For UCu_5Al and $\text{U}_2\text{Ru}_2\text{Sn}$, the Hall effect data can be described based on skew scattering theory [5]. The R_H data for UGe_2 and $\text{UCo}_{0.5}\text{Sb}_2$ can also be decomposed into negative R_0 and positive R_s components. In all the samples, the extraordinary contribution (Table 1) was found to be dominant, indicating that the $R_H(T)$ dependence is mainly due to incoherent skew scattering by U 5f moments. Carrier concentration at room temperature, estimated in a one-band model from R_0 values, ranges from 0.4 for UGe_2 , 0.8 for $\text{UCo}_{0.5}\text{Sb}_2$, 1.2 for $\text{U}_2\text{Ru}_2\text{Sn}$ to 4.9 e/f.u. for UCu_5Al .

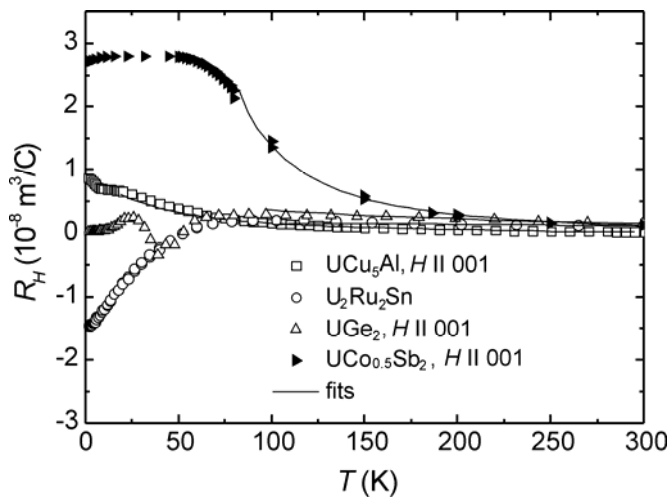


Fig. 1. Temperature dependence of the Hall coefficients of UCu_5Al , $\text{U}_2\text{Ru}_2\text{Sn}$, UGe_2 , and $\text{UCo}_{0.5}\text{Sb}_2$. The solid lines represent fits (see text)

Table 1. Hall parameters derived from the fit of the experimental data

Compound	R_s [m^3/C]	γ_1 [K/T]	R_0 [m^3/C]	n [f.u.]	m^* [m.e.]
UCu_5Al , $H \parallel c$		0.08	-6.44×10^{-10}	0.9	105
$\text{U}_2\text{Ru}_2\text{Sn}$		0.38	-5×10^{-10}	0.04	48
UGe_2 , $H \parallel c$	3.7×10^{-6}		-9.4×10^{-10}	3.1	15
$\text{UCo}_{0.5}\text{Sb}_2$, $H \parallel c$	1.3×10^{-5}		-1.96×10^{-10}	0.02	70

Fit to the equations $R_H = R_0 + R_s \mu_0 M/B$ and $R_H = R_0 + \gamma_1 \rho M/B$, where γ_1 is a parameter related to the phase shift, M is magnetisation, B – magnetic induction, n – is charge carrier concentration at 2 K, and m^ – the effective mass at 2 K.

A different behaviour of the investigated compounds is observed at low temperatures. A remarkable feature is the increase in R_H for UCu_5Al below 50 K. At 2 K, R_H achieves the value of $9 \times 10^{-9} \text{ m}^3/\text{C}$, corresponding to 0.9 carriers per f.u. Taking $\gamma = 210 \text{ mJ}/(\text{K}^2 \cdot \text{mol U})$ [1], one can estimate the electron effective mass $m^* = 105 m_e$.

This enhancement of the electron mass points out that a development of the heavy-fermion state occurs in this compound at low temperatures.

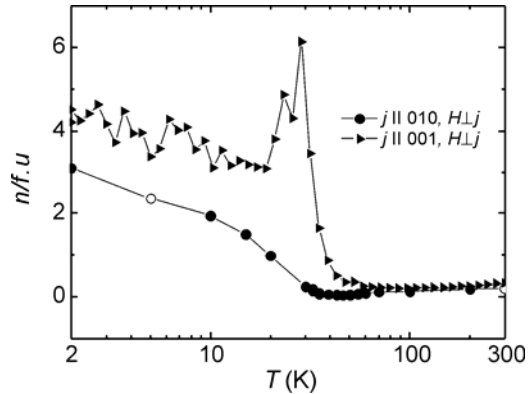


Fig. 2. Temperature dependence of the charge carrier concentration n of UGe_2 , measured with a field applied perpendicular to the 010 and 001 directions

For $\text{U}_2\text{Ru}_2\text{Sn}$, the $R_H(T)$ dependence shows a broad positive maximum at about 80 K and changes its sign below 50 K. At 2 K, R_H reaches the value of $-1.5 \times 10^{-8} \text{ m}^3/\text{C}$, which corresponds to a single-band concentration of $n = 0.04 \text{ e/f.u.}$ In the temperature range 15–80 K, the $n(T)$ dependence can be described with the help of an exponential law with the energy gap of about 60 K. The latter value is comparable with those derived from the specific heat and NMR studies at 70 and 80 K, respectively [2]. All these features point to a gap opening in $\text{U}_2\text{Ru}_2\text{Sn}$.

Physical properties of UGe_2 are very unusual. Under the pressure of $\sim 12 \text{ kbar}$, superconductivity with $T_{SC} = 0.8 \text{ K}$ coexists with ferromagnetism [6]. It has also been pointed out that there exists a close relation between T_{SC} and T^* . The latter temperature is a characteristic temperature, visible in the temperature dependence of resistivity and tending to T_{SC} on increasing pressure. In the ordered state, the coefficients R_0 and R_s of UGe_2 have been separated using $R_H(B)$ and $M(B)$ data simultaneously. Interestingly, the R_0 coefficient displays a distinct anomaly at T^* . In consequence, the charge carrier concentration calculated within the single-band model has an upturn with decreasing temperature below T^* (Fig. 2). This phenomenon can be understood in terms of the so-called “dual nature” of 5f-electrons. Assuming that a hybridisation between the 5f and conduction electrons takes place below T^* , one can explain not only the carrier concentration, but also the enhancement of the density of states, and the itinerant behaviour of 5f electrons at low temperatures.

The Hall coefficient of $\text{UCo}_{0.5}\text{Sb}_2$ increases rapidly with decreasing temperature below 100 K. This behaviour is associated with a decrease in the carrier concentration. At 2 K, n falls to 0.024 e/f.u. (Fig. 3), making $\text{UCo}_{0.5}\text{Sb}_2$ a low carrier system. It should be emphasised that the Hall mobility in $\text{UCo}_{0.5}\text{Sb}_2$ changes sharply with temperature. It passes through a maximum of $450 \text{ cm}^2/(\text{V}\cdot\text{s})$ at 20 K and decreases by as

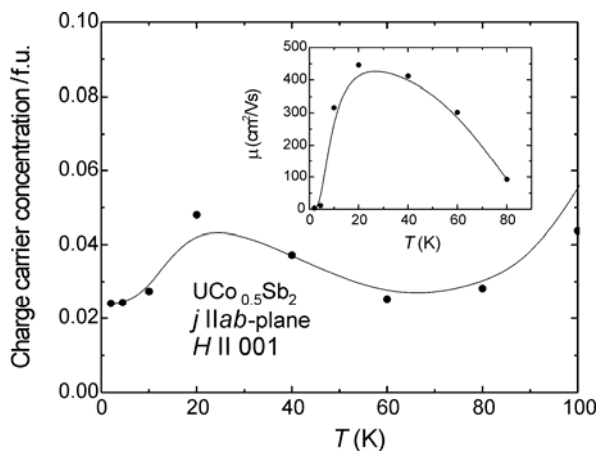


Fig. 3. Temperature dependence of the charge carrier concentration of $\text{UCo}_{0.5}\text{Sb}_2$. The inset shows mobility as a function of temperature

many as two orders of magnitude, i.e. to $3.7 \text{ cm}^2/(\text{V}\cdot\text{s})$ at $T = 2 \text{ K}$ (see the inset in Fig. 3). This change is probably related to a decrease in the carrier collision time. The Hall mean free path λ , estimated from $R_H(T)$ and resistivity, also shows a dramatic drop, falling from about 350 \AA at 20 K to 12 \AA at 2 K . The temperature dependences of μ and λ may support the weak localization effect suggested previously [4].

3. Summary

This work is an attempt to show some important results obtained by the measurements of the Hall coefficient on four 5f electron-based compounds (UCu_5Al , $\text{U}_2\text{Ru}_2\text{Sn}$, UGe_2 , $\text{UCo}_{0.5}\text{Sb}_2$). Though these materials have different ground states, they belong to the so-called SCES family. The Hall effect data provided evidence of the enhancement of electron effective masses in all the studied compounds and shed new light on the behaviour associated with electron correlations.

Acknowledgements

The author is indebted to M. Baenitz, E. Bauer, Z. Bukowski, T. Komatsubara, S. Paschen, F. Steglich, and R. Troć for their collaboration and discussion on this subject. This work was supported by the KBN Grant No. 2 PO3B 109 24.

References

- [1] TRAN V. H., TROĆ R., STĘPIEŃ-DAMM J., KOMATSUBARA T., STEGLICH F., HAUSER R., BAUER E., Phys. Rev. B, 66 (2002), 54421.
- [2] TRAN V. H., PASCHEN S., RABIS A., SENTHILKUMARAN N., BAENITZ M., STEGLICH F., DU PLESSIS P., DE V., STRYDOM A.M., Phys. Rev. B, 67 (2003), 75111; TRAN V.H., PASCHEN S., RABIS A., BAENITZ M., STEGLICH F., DU PLESSIS P. DE V., STRYDOM A.M., Physica B, 312–313 (2002), 215.

- [3] TRAN V. H., PASCHEN S., TROĆ R., BAENITZ M., STEGLICH F., Phys. Rev. B, 69 (2004), 195314.
- [4] TRAN V. H., TROĆ R., BUKOWSKI Z., BADURSKI D., SULKOWSKI C., Phys. Rev. B, 71 (2005), 94428;
TRAN V.H., PASCHEN S., STEGLICH F., TROĆ R., BUKOWSKI Z., phys. stat. sol B, 243 (2006), 94.
- [5] FERT A., LEVY P.M., Phys. Rev. B, 36 (1987), 1907.
- [6] SAXENA S.S., AGARVAL P., AHILAN K., GROSCHE F.M., HASSELWIMMER R.K.W., STEINER M.J., PUGH E.,
WALKER I.R., JULIAN S.R., MONTHOUX P., LONZARICH G.G., HUXLEY A., SHEIKIN I., BRAITHWAITE D.,
FLOUQUET J., Nature, 406 (2000), 587.

Received 1 June 2005

RKKY coupling in diluted magnetic semiconductors

A. M. WERPACHOWSKA*, Z. WILAMOWSKI

Institute of Physics, Polish Academy of Sciences, al. Lotników 32/46, 02-668 Warsaw, Poland

This paper is an attempt to modify the classic Ruderman–Kittel–Kasuya–Yosida (RKKY) model to allow the analysis of the experimental data of the magnetic resonance measurements. In our calculations, we follow the treatment of the original authors of the RKKY model but include the finite band splitting, Δ , as a phenomenological parameter. The RKKY exchange is not anymore of the Heisenberg type and an anisotropy induced by the direction of carrier magnetization occurs.

Key words: *RKKY coupling; ferromagnetic semiconductor; magnetic resonance*

1. Introduction

The Ruderman–Kittel–Kasuya–Yosida (RKKY) coupling [1, 2], the exchange interaction between localized core spins mediated by metallic electron gas, has been known for 50 years as the basic interaction in metallic ferromagnets. The oscillatory character of the RKKY coupling causes a spin glass behaviour in diluted magnetic metals. It rules the interlayer coupling in magnetic layered structures. As has been shown for the last few years, the RKKY interaction is also the dominant spin interaction in diluted ferromagnetic semiconductors [3, 4]. However, in the case of semiconductors (strictly speaking, of semi-metallic phases of semiconductors), the Fermi energy, E_F , is small as compared to classical metals and comparable to the exchange spin splitting of the conduction band, Δ . The small Fermi energy causes the saturation of the spin polarization of the carrier spins and some other new effects [5].

In this paper, we discuss the consequences of the spin splitting on the RKKY coupling. The investigation of analytical expressions for the distance dependence of the exchange coupling shows that in the presence of spin splitting the RKKY exchange is not anymore of Heisenberg type but leads to magnetization-induced anisotropy. With the increase of Δ , which we treat as a phenomenological parameter, the RKKY coupling evolves from the classical Heisenberg coupling, via anisotropic interaction, to

*Corresponding author, e-mail: awer@student.ifpan.edu.pl

the Ising coupling. Moreover, the spin splitting leads to the occurrence of various contributions to the RKKY coupling which are characterized by different distance dependencies and various characteristic lengths.

2. Magnetic resonance in (Ga, Mn)As

The formation of magnetic order in semi-metallic (Ga, Mn)As is well described by the mean field approach (MFA) models [6]. It is now commonly accepted that the p-d exchange is responsible for the hole mediated exchange. Within the MFA, the Zener [7], RKKY [1, 2] and Dietl [3, 4] models are equivalent. All of them enable a good estimation of the critical temperature. The Dietl model, which attributes the p-d energy to the carrier spins and takes into consideration the details of the valence band structure, additionally allows the estimation of the magnetic anisotropy. Unfortunately, the aforementioned models calculate the energy of the ground state of the system but they do not analyse the elementary excitations. Therefore, they cannot be directly applied to the discussion of the magnetic resonance.

Studies of the magnetic resonance show that there are two types of the magnetic resonance observed in (Ga, Mn)As [8, 9]. None of them, however, can be attributed to any magnetic resonance already observed in similar systems [10–12], and none of them has been satisfactorily explained. In particular, ferromagnetic resonance in the semi-insulating (Ga, Mn)As is characterized by the resonance frequency which matches precisely the manganese spin resonance frequency. The absence of any influence of the hole spins remains unexplained. The resonance in the semi-metallic (Ga, Mn)As is of a very different character. It is characterized by a large anisotropy, a complex structure which can be attributed to the spin wave resonance and g -factor considerably different from that corresponding to the g -factor of the Mn spins. These properties allow us to conclude that the resonance corresponds to the ferromagnetic mode of the ferrimagnetic resonance [8, 9]. This suggests that the carrier spins are ordered and form a macroscopic magnetic moment. Till now, the problem has not been considered by any theoretical model. The exchange correction within the Fermi liquid approach is the only effect discussed by Dietl et al. [3, 4]. All of the approaches discussed postulate paramagnetic properties of the carrier spins.

A quantitative description of the ferrimagnetic resonance requires the solution of the equation of motion of two interacting spin subsystems. The precise definition of the tensor components describing spin coupling is of crucial importance. In particular, the two cases: the Heisenberg exchange and the effective field lead to very different types of precession. For example, according to the RKKY model, which treats the carriers as a paramagnetic medium and postulates a Heisenberg coupling between the localized spins, the resonance in the magnetically ordered semi-metallic (Ga, Mn)As should correspond to the isotropic resonance with $g = 2$. On the other hand, according to the Zener model, which predicts a huge mean p-d exchange field affecting each spin subsystem, the two resonances corresponding to Mn and hole spins are expected

at very high frequencies. None of the models corresponds to the experimental observations.

3. Effect of band splitting on RKKY interaction

The aim of this paper is a critical study of the RKKY interaction and an attempt to modify the classic RKKY model to allow the analysis of the experimental data of the magnetic resonance measurements. In our calculations, we follow the treatment of the original authors of the RKKY model, the difference being that we assume a finite band splitting, Δ . We do not specify whether this splitting comes from the spontaneous magnetization of the local spin subsystem, if the giant spin splitting is typical of DMSs, $\Delta = (N_0\beta)x_{\text{Mn}}\langle S \rangle$, or finally, whether it is caused by the external magnetic field, $\Delta = g\mu_B B$. We obtain the analytical formula for the direction-dependent RKKY range functions which are presented in the Appendix.

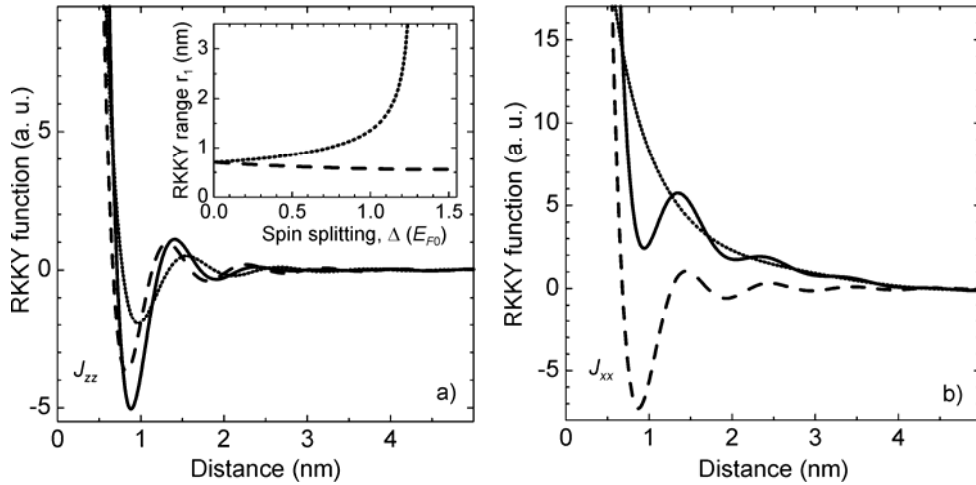


Fig. 1. The components of the RKKY function as a function of the distance calculated for a simple parabolic band with $n_c = 10^{27} \text{ m}^{-3}$: a) the solid line represents the $J_{zz}(r)$ component, the dashed and the dotted lines stand for the contributions from the spin up and spin down subbands. The insert shows the dependence of the characteristic RKKY range on the spin splitting, Δ , by plotting r_1 (the positions of the first zeros of two $J_{zz}(r)$ contributions) for changing Δ , b) the transverse component $J_{xx}(r)$ is plotted as the solid line. The dashed and the dotted line correspond to the two contributions. The long-range contribution (dotted line) oscillates in the range of large distances beyond the figure frame

Figure 1 shows an example of the dependence of the exchange integrals on the distance for $\Delta = 0.25E_{F0}$, here E_{F0} is the Fermi energy in the absence of the spin splitting. All of them are of oscillating character but their amplitudes and oscillation frequencies are different. As a consequence of one direction being privileged by the splitting Δ , a magnetization-induced anisotropy arises. As opposed to the classic RKKY cou-

pling, which has the form of a strictly Heisenberg-like interaction, the RKKY tensor (J_{RKKY}) diagonal components are not all equal in our calculations. The J_{zz} component corresponds to the direction parallel to the conduction band magnetization and the components $J_{xx} = J_{yy}$ correspond to the perpendicular direction.

The $J_{zz}(r)$ component is a sum of two components (Eq. (1) in the Appendix). Each of them is the classic RKKY function for different Fermi vectors $k_{F\uparrow}$ and $k_{F\downarrow}$. (corresponding to the spin up and spin down subbands). Due to differing frequencies, the exchange interaction range $\lambda = \pi/4k_F$ is different for each of the two contributions. The insert of Fig. 1a shows the dependence of the distance r_1 (for which the two components of J_{zz} reach zero value for the first time) on Δ . The distance for the majority spin subband systematically decreases, while the distance to the first zero increases and diverges for a complete polarization.

It is notable that the J_{zz} component (Fig. 1a) does not vanish for the half-metal case, when only one of the spin subbands is occupied (for Δ larger than the Fermi energy). In this regime, the exchange interaction is carried by the total polarized charge density of the electron gas (Friedel oscillations). Generally, we can treat the classic RKKY interaction as a sum of two Friedel contributions. In the $\Delta \rightarrow 0$ limit, the contributions are precisely equal and the total-charge density oscillations vanish, while the spin polarization (RKKY) oscillations remain. For a non-zero spin splitting, the contributions are not equal anymore. Finally for $\Delta > E_{F0}$, when only the majority spin subband is occupied, the exchange is mediated by the Friedel oscillations only.

The $J_{xx}(r)$ component (Eq. (2) in the Appendix) can be expressed as the sum of two qualitatively different contributions (Fig. 1b). One of them, shown in Fig. 1b by the dashed line, is the modified RKKY function with the oscillations corresponding to the sum of the Fermi vectors. The amplitude of this contribution gets smaller as Δ increases and vanishes in the half-metal regime. The second contribution, shown in Fig. 1b by the dotted line, oscillates with the frequency corresponding to the difference of the Fermi vectors, $k_{F\uparrow}$ and $k_{F\downarrow}$. It is therefore characterized by the long characteristic range. The amplitude of this contribution grows with Δ and in the half-metal regime decreases with the further increase of Δ .

The amplitudes of particular contributions are better seen in Fig. 2, where the mean exchange field, $\bar{\mathcal{E}}$, proportional to the volume integral of the $J(r)$ function is plotted as a function of Δ . For the whole range of Δ the longitudinal component of the exchange field, $\bar{\mathcal{E}}_{zz}$, is bigger than the transverse one, $\bar{\mathcal{E}}_{xx}$. This means that the magnetization of the local spin has the tendency to be oriented parallel to the z direction, as defined by the magnetization of the carrier spins. This tendency vanishes with vanishing Δ . Apart from the listed dependencies of the contributions on the spin splitting, we see the onset of a magnetization-induced anisotropy. The difference, $D = \bar{\mathcal{E}}_{zz} - \bar{\mathcal{E}}_{xx}$, corresponds to the magnetization-induced anisotropy. The coupling between the local spins evolves with Δ , from the pure Heisenberg coupling for $\Delta = 0$, via anisotropic, to the Ising coupling in the large Δ limit where the transverse component vanishes. In this regime, the exchange field, as seen by a random local spin, is parallel to the electron gas magnetiza-

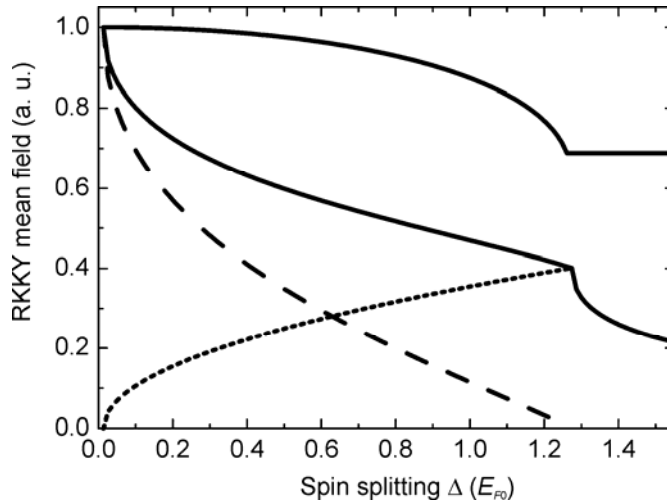


Fig. 2. The dependence of the two RKKY mean field components, Ξ_{zz} and Ξ_{xx} , on the spin splitting Δ (solid lines). The two contributions to the transverse component Ξ_{xx} are marked by the dotted and the dashed line

tion. In this sense, the Ising form of the exchange coupling between the localized spins corresponds to the Zener model, where the p-d coupling between both spin subsystems also has only the component parallel to the z axis. Both models, Zener and RKKY, neglect the transverse components. However, the Zener approach explains the lack of influence of the perpendicular components by the postulated averaging of the perpendicular spin components (random phases of spin precession), while the lack of the transverse component of RKKY exchange is the consequence of the half-metal character and the large spin splitting of the carrier band.

4. Conclusions

Contrary to the intuition given by the Zener model, which suggests an anti-parallel orientation of both magnetic moments, tilting of the directions of magnetizations is not that energetically expensive. Only in the limit of large Δ , within the range of the Ising exchange, the energy of the magnetization deviation as predicted by the RKKY coupling and that estimated by the Zener model are similar. For a small value of Δ , however, the energy gain for the collinear magnetizations is not as significant as suggested by the Zener model.

The anisotropic part of the RKKY interaction, which results from the band spin splitting, is not very important when discussing the ground state of the system, i.e., when the directions of the Mn and the carrier spins are parallel. Its importance increases, e.g., when the carrier magnetization is tilted by an anisotropy field, or in an external field when the precession angles of both magnetizations are different. It may be

a possible explanation of the shapes of the hysteresis loops. Magnetic anisotropy parameters evaluated from the magnetic resonance studies cannot describe the hysteresis loops observed in the transport, Kerr and SQUID measurements.

The described character of the exchange integrals should also lead to a peculiar spin wave dispersion and domain wall structure. The appearance of several contributions to the range functions components with the different characteristic ranges results in the non-parabolic spin wave dispersion. The occurrence of the long-range component of the RKKY coupling may lead to a big magnetic stiffness and consequently to a high energy of the domain wall. However, this kind of anisotropy has no direct influence on the observed anisotropy of the spin wave dispersion.

Appendix

The function J_{zz} is given by the analytical formula

$$J_{zz}(r) = (N_0\alpha)^2 \left(\frac{m^* (\sin(2k_{F\uparrow}r) - 2k_{F\uparrow}r \cos(2k_{F\uparrow}r))}{4\hbar^2\pi^3 r^4} + \frac{m^* (\sin(2k_{F\downarrow}r) - 2k_{F\downarrow}r \cos(2k_{F\downarrow}r))}{4\hbar^2\pi^3 r^4} \right) \quad (1)$$

where m^* is the effective mass, $\hbar = h/2\pi$, h being the Planck constant, and $(N_0\alpha)$ is the exchange constant. The formula for $J_{xx} = J_{yy}$ function is

$$\begin{aligned} J_{xx}(r) = & \frac{m^* (N_0\alpha)^2}{8\hbar^2\pi^3 r^4} \left((k_{F\uparrow} + k_{F\downarrow})r \left((k_{F\uparrow} - k_{F\downarrow})^2 r^2 - 2 \right) \cos((k_{F\uparrow} + k_{F\downarrow})r) \right. \\ & + \sqrt{(k_{F\uparrow}^2 - k_{F\downarrow}^2)}r \left(2 - (k_{F\uparrow}^2 - k_{F\downarrow}^2)r^2 \right) \cos(\sqrt{k_{F\uparrow}^2 - k_{F\downarrow}^2}r) \\ & + \left(2 + (k_{F\uparrow} - k_{F\downarrow})^2 r^2 \right) \sin((k_{F\uparrow} + k_{F\downarrow})r) - \left(2 + (k_{F\uparrow}^2 - k_{F\downarrow}^2)r^2 \right) \sin(\sqrt{k_{F\uparrow}^2 - k_{F\downarrow}^2}r) \\ & + (k_{F\uparrow}^2 - k_{F\downarrow}^2)r^4 \left(Si((k_{F\uparrow} + k_{F\downarrow})r) - Si(\sqrt{k_{F\uparrow}^2 - k_{F\downarrow}^2}r) \right) \Big) \\ & + \frac{m^* (N_0\alpha)^2}{4\hbar^2\pi^2 r^3} \left(\begin{aligned} & (k_{F\uparrow}^2 - k_{F\downarrow}^2)r H_0(\sqrt{2}\sqrt{k_{F\uparrow}^2 - k_{F\downarrow}^2}r) \\ & - \sqrt{2}\sqrt{k_{F\uparrow}^2 - k_{F\downarrow}^2} H_1(\sqrt{2}\sqrt{k_{F\uparrow}^2 - k_{F\downarrow}^2}r) \end{aligned} \right) \end{aligned} \quad (2)$$

where

$$Si(z) = \int_0^z \frac{\sin t}{t} dt$$

and the Struve function $Hn(z)$ ([13], p. 496) for integer n satisfies the differential equation

$$z^2 y'' + zy' + (z^2 - n^2)y = \frac{2}{\pi} \frac{z^{n+1}}{(2n-1)!!}$$

Acknowledgement

This work supported by PBZ-KBN-044/P03/2001.

References

- [1] RUDERMAN M.A., KITTEL C., Phys. Rev., 96 (1954), 99.
- [2] YOSIDA K., Phys. Rev., 106 (1957), 893.
- [3] DIETL T., OHNO H., MATSUKURA F., CIBERT J., FERRAND D., Science, 287 (2000), 1019.
- [4] DIETL T., OHNO H., MATSUKURA F., Phys. Rev. B, 63 (2001), 195205.
- [5] NAGAEV E.L., Phys. Rev. B, 54 (1996), 16608.
- [6] KÖNIG J., SCHLIEMANN J., JUNGWIRTH T., MACDONALD A.H., *Ferromagnetism in (III,Mn)V Semiconductors* (2001), <http://arxiv.org/abs/cond-mat/0111314>.
- [7] ZENER C., Phys. Rev., 82 (1951), 403.
- [8] FEDORYCH O.M., Ph. Thesis, Institute of Physics, Polish Academy of Sciences, Warsaw, 2004.
- [9] FEDORYCH O.M., WILAMOWSKI Z., POTEMSKI M., BYSZEWSKI M., SADOWSKI J., J. Supercond., 16 (2003), 51.
- [10] TERRAN F.J., POTEMSKI M., MAUDE D.K., WILAMOWSKI Z., HASSAN A.K., PLANTIER T.D., ANDREARCZYK T., JAROSIŃSKI J., WOJTOWICZ T., KARCZEWSKI G., Phys. Rev. Lett., 91 (2003), 077201.
- [11] STORY T., GAŁĄZKA R.R., FRANKEL R.B., WOLFF P.A., Phys. Rev. Lett., 56 (1986), 777.
- [12] BARNES S.E., Adv. Phys., 30 (1981), 801.
- [13] ABRAMOVITZ M., STEGUN I.A., *Handbook of Mathematical Functions*, Dower, New York, 1970.

Received 1 June 2005

Revised 10 October 2005

Effect of spin-orbit coupling on the electronic structure of bismuthide YbAuBi

A. JEZIERSKI^{1*}, A. SZYTUŁA², D. KACZOROWSKI³

¹Institute of Molecular Physics, Polish Academy of Sciences,
M. Smoluchowskiego 17, 60-179 Poznań, Poland

²M. Smoluchowski Institute of Physics, Jagiellonian University,
30-059 Cracow, Reymonta 4, Poland

³W. Trzebiatowski Institute of Low Temperatures and Structure Research,
50-950 Wrocław, Okólna 2, Poland

The electronic structures of ternary ytterbium YbAuBi and YbAuSn compounds were studied by X-ray photoemission spectroscopy (XPS) and *ab initio* methods (LMTO-ASA, FP LMTO, FPLO). The results showed that the valence bands in these compounds are formed by the 4f orbitals of ytterbium and 5d orbitals of transition metals. Full relativistic band calculations (FP LMTO and FPLO) with spin-orbit coupling have shown that the 4f peak consists of two peaks that correspond to the Yb 4f_{7/2} and 4f_{5/2} doublet.

Key words: *rare earth compounds; electronic structure; photoelectron spectroscopy; ab initio methods; FPLO; FP LMTO*

1. Introduction

Ternary YbTM (T – transition metal, M – Sn, Bi) compounds crystallise into different crystallographic structures (MgAgAs, LiGaGe, Fe₂P, CaLiSn, TiNiSn). The magnetic, thermodynamic, and transport properties of this series of ytterbium compounds were studied by Kaczorowski et al. [1]. They found that the compounds YbTBi, with T = Cu, Ag, and Au, and YbTSn, with T = Ag, Au, and Zn, are nonmagnetic with divalent ytterbium ions [1]. In YbPdBi, YbRhSn, and YbPtSn, however, they observed localised magnetism with trivalent Yb ions.

Recently, Szytula et al. [2] studied their electronic structure by X-ray photoemission spectroscopy. The XPS measurements indicated that YbAuSn and YbAuBi are divalent, while YbRhSn and YbPtSn are trivalent. The band structure of Yb compounds was calculated in the past by various *ab initio* methods [4–10], within the

*Corresponding author, e-mail:jeziersk@ifmpan.poznan.pl

local spin density (LSD) approximation using various contributions to the exchange potentials [4–9]. The divalent, trivalent, or intermediate valence of Yb depends on the type of elements in the ytterbium compounds.

2. Experimental and theoretical methods

The electronic structures of YbTX compounds were obtained by X-ray photoemission spectroscopy (XPS) and by *ab initio* calculations. Measurements were carried out on polycrystalline samples [1]. The XPS spectra were measured at room temperature using a Multipurpose Electron Spectrometer PHI5700/600 with AlK_α monochromatised radiation ($h\nu = 1486.6$ eV) and a Leybold LHS10 Electron Photoemission Spectrometer with MgK_α radiation ($h\nu = 1253.6$ eV) [2]. The experimental procedure is described in Ref. [2].

The electronic densities of states (DOS) of YbTM have been calculated by the spin-polarised self-consistent tight binding linear muffin tin orbital (TB LMTO) method in the atomic sphere approximation (ASA) [11, 12] for experimental lattice parameters [1]. The scalar-relativistic approximation for band electrons and the full relativistic treatment of frozen core electrons were applied. The exchange correlation potential was assumed in the form of von Barth and Hedin [13], and gradient corrections were also included [14]. The results of calculations are presented in [2] and [3]. Scalar-relativistic (without spin orbit coupling) LMTO-ASA calculations gave a single, large peak due to the 4f electrons of Yb near the Fermi level. The position of Au was close to that observed in XPS spectra [2].

In this paper, we present the electronic structure of YbAuBi calculated by the FP LMTO (LmtArt) [15, 16] and FPLO [17] methods. The band structure was calculated for the experimental lattice parameter (structure type MgAgAs, $a = 0.6848$ nm). In both methods, we applied spin-orbit coupling. In the FPLO scheme, the calculations were performed using the full relativistic version of the full potential local orbital minimum basis. For the site-centre potentials and densities, expansions into spherical harmonics were used up to $l_{\text{max}} = 12$. The number of k points in the irreducible part of the Brillouin zone was 484. The parameterisation of the exchange-correlation potential in the framework of the local spin density approximation was used in the form proposed by Perdew–Wang [18].

3. Results

The electronic structure was measured for YbAuBi and YbAuSn, and we calculated the band structure for YbAuBi including the spin-orbit coupling. In Figure 1, we present the XPS spectra of the valence bands of YbAuSn, YbAuBi, and of metallic Yb. We observed two peaks below the Fermi level, corresponding to the Yb $4f_{7/2}$ and $4f_{5/2}$ doublet, similar to that in metallic Yb. In the region of higher binding energies, 5

$< E < 10$ eV, the peaks correspond to the 5d states of Au and p-electron states of Sn and Bi.

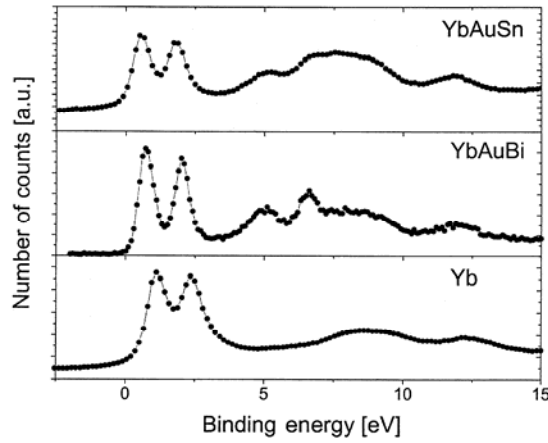


Fig. 1. XPS spectra of the valence bands of YbAuBi, YbAuSn, and metallic Yb

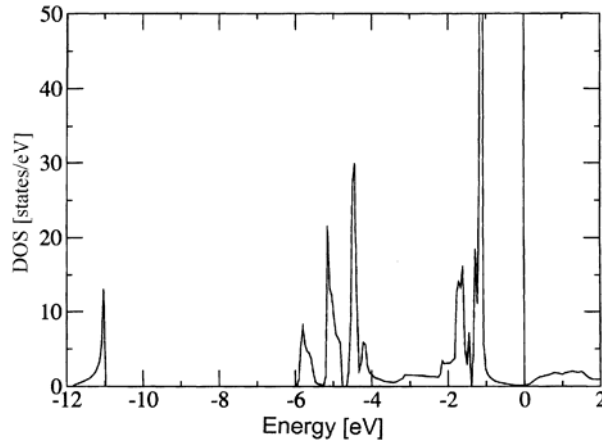


Fig. 2. The total density of states of YbAuBi (scalar-relativistic FPLO)

Recently, we presented the electronic structures of YbAuSn and YbAuBi [2] calculated by the TB LMTO–ASA method [11, 12]. We observed one main peak below the Fermi level as well as contributions from the 5d electron states of Au and p-electron states of Sn and Bi for higher binding energies. In this work, we present fully relativistic full potential band calculations including spin-orbit coupling. Scalar relativistic full potential calculations (FPLO and FP LMTO) give similar shapes of the densities of states (only one main peak below the Fermi level, see Fig. 2.) to those seen in TB LMTO-ASA results [2]. The number of 4f electrons obtained from scalar relativistic FPLO and LMTO-ASA methods are 13.94 and 13.91, respectively.

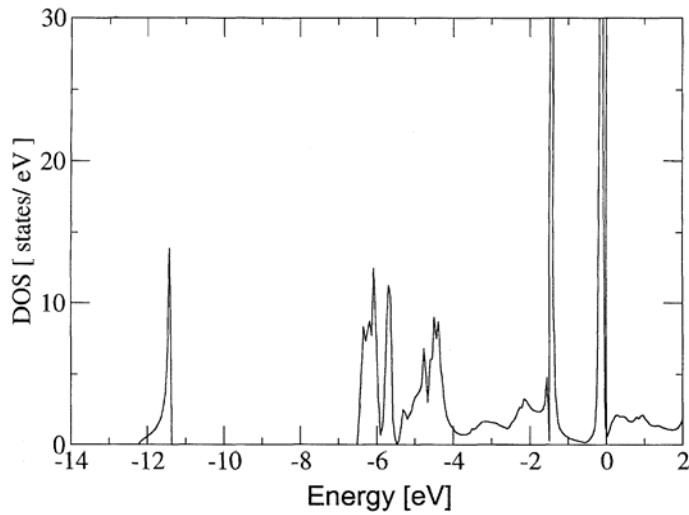


Fig. 3. The total density of states of YbAuBi (full relativistic FPLO)

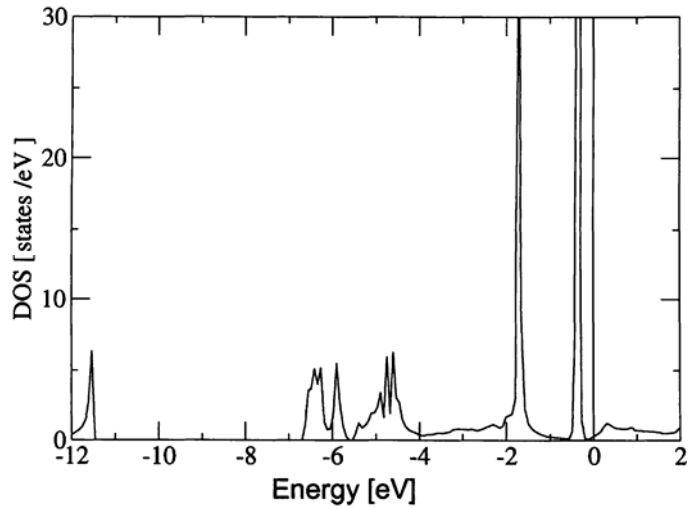


Fig. 4. The total density of states of YbAuBi (FP LMTO)

In Figures 3 and 4, we present the total density of states (DOS) for YbAuBi, obtained by the FPLO [17] and FP LMTO [15,16] methods. The total DOS in Fig. 3 is plotted for two spin directions, however the DOS obtained from the FP LMTO method is for only one spin direction. We observe a 4f feature below the Fermi level, consisting of two peaks, one corresponding to Yb $4f_{7/2}$ and the other to the $4f_{5/2}$ doublet. The splitting of the peaks is about 1.5 eV, close to that of the XPS spectra [2]. The number of 4f electrons of Yb obtained from the FPLO and FP LMTO methods are 13.61 and 13.76, respectively.

4. Conclusions

We present the XPS spectra of YbAuSn and YbAuBi compounds and *ab initio* fully relativistic full potential (FPLO and FP LMTO) calculations of the electronic structure of YbAuBi. FP LMTO and FPLO calculations (including S-O) give a splitting of the 4f states of Yb similar to that from photoemission measurements. Both methods give very similar results. The scalar relativistic (TB LMTO and FPLO) methods also give similar shapes of the densities of states – one main 4f peak below the Fermi energy. Our *ab initio* calculations confirmed that the ytterbium ion is divalent in YbAuBi as well as YbAuSn (not discussed here).

Acknowledgements

One of the authors (A. J.) thanks the State Committee for Scientific Research for financial support (Project No. 4T11F 014 24).

References

- [1] KACZOROWSKI D., LEITHE-JASPER A., ROGL P., FLANDORFER H., CICHOREK T., PIETRI R., ANDRAKA B., Phys. Rev. B, 60 (1999), 422.
- [2] SZYTULA A., JEZIERSKI A., PENC B., WINIARSKI A., LEITHE-JASPER A., KACZOROWSKI D., J. Alloys Comp., 360 (2003), 41.
- [3] JEZIERSKI A., SZYTULA A., Mol. Phys. Rep., 40 (2004), 84.
- [4] SVANE A., TEMMERMAN W.M., SZOTEK Z., LÆGSGAARD J., WINTER H., J. Phys. Cond. Matter., 10 (1998), 5309.
- [5] SVANE A., TEMMERMAN W.M., SZOTEK Z., LÆGSGAARD J., WINTER H., Int. J. Quantum Chem., 77 (2000), 799.
- [6] TEMMERMAN W.M., SZOTEK Z., SVANE A., STRANGE P., WINTER H., DELIN A., JOHANSSON B., ERIKSSON O., FAST L., WILLS J.M., Phys. Rev. Lett., 83 (1999), 3900.
- [7] LUNDIN U., SANDALOV I., ERIKSSON O., JOHANSSON B., Solid State Commun., 115 (2000), 7.
- [8] TEMMERMAN W.M., SVANE A., STRANGE P., SZOTEK Z., WINTER H., Phil. Mag. B, 80 (2000), 1179.
- [9] PETIT L., SVANE A., TEMMERMAN W.M., SZOTEK Z., Solid State Commun., 116 (2000), 379.
- [10] MC MULLAN G.J., RAY M.P., J.Phys.: Condens. Matter., 4 (1992), 7095.
- [11] ANDERSEN O.K., JEPSEN O., SOB M., [in:] *Electronic Structure and Its Applications*, M. Yussouff, (Ed.), Springer-Verlag, Berlin, 1987 (p. 2).
- [12] ANDERSEN O.K., JEPSEN O., Phys. Rev. Lett., 53 (1984), 2571.
- [13] VON BARTH U., HEDIN L., J. Phys. C, 5 (1972), 1629.
- [14] HU D., LANGRETH D.C., Phys. Scripta, 32 (1985), 391.
- [15] SAVRASOV S.Y., SAVRASOV D.Y., Phys. Rev. B, 46 (1992), 12181.
- [16] SAVRASOV S.Y., Phys. Rev. B, 54 (1996), 16470.
- [17] KOEPERNIK K., ESCHRIG H., Phys. Rev. B, 59 (1999), 1743.
- [18] PERDEW J.P., BURKE K., ERNZERHOF M., Phys. Rev. Lett., 77 (1996), 3865.

Received 1 June 2005

Spin and orbital Kondo effect in electrostatically coupled quantum dots

S. LIPIŃSKI*

Institute of Molecular Physics, Polish Academy of Sciences, M. Smoluchowskiego 17, 60-179 Poznań, Poland

The spin polarization of conductance in a system of two capacitively coupled quantum dots is studied in the Kondo regime by the equation of motion method. In the case of orbital degeneracy in one spin channel, the system can operate as a spin filter.

Key words: *spin-polarized transport; nanoscopic system; Kondo effect*

1. Introduction

Spin-dependent coherent electronic transport recently attracts great interest due to its potential applications in reprogrammable logic devices [1] and quantum computers [2]. One of the challenging problems for such applications is to obtain sufficient control over spin dynamics in nanostructures. In the following, we address this issue and propose a double dot setup that can operate as a spin filter. Our proposal utilizes spin-dependent orbital degeneracy and the resulting orbital Kondo effect as a mechanism for spin filtering. In this case, the orbital quantum number is conserved during tunnelling and orbital degrees of freedom come into play as pseudo-spins [3]. The orbital Kondo effect has been observed in semiconductor double quantum dots [4, 5] and carbon nanotubes [6].

2. Model

We discuss a system of two capacitively coupled quantum dots (DQD) placed in a magnetic field. Each of the dots is coupled to a separate pair of leads. The corresponding Hamiltonian reads:

$$H = \sum_{kri\sigma} \varepsilon_{kri\sigma} c_{kri\sigma}^{\dagger} c_{kri\sigma} + \sum_{i\sigma} \varepsilon_{i\sigma} c_{i\sigma}^{\dagger} c_{i\sigma} + \sum_i U_i n_{i+} n_{i-} + U \sum_{\sigma\sigma'} n_{1\sigma} n_{2\sigma'} + \sum_{kri\sigma} t_{ri} (c_{kri\sigma}^{\dagger} c_{i\sigma} + cc) \quad (1)$$

*E-mail: lipinski@ifmpan.poznan.pl

where $\varepsilon_{i\sigma} = \varepsilon_i + g\sigma\hbar$ (we set $|e| = \mu_B = k_B = 1$). The first term describes the electrons in the electrodes ($i = 1, 2, r = L, R$), the second represents field-dependent site energies, the third and fourth – account for intra and inter-Coulomb interactions, and the last one describes tunnelling. Assuming quasi-elastic transport, for which the current conservation rule is fulfilled for any ω , one obtains an expression for the current $I = \sum_{i\sigma} I_{i\sigma}$, within the Keldysh formalism, in the form [7] :

$$I_{i\sigma} = \frac{e}{\hbar} \int d\omega \frac{\Gamma_{iL\sigma}(\omega)\Gamma_{iR\sigma}(\omega)}{\Gamma_{iL\sigma}(\omega) + \Gamma_{iR\sigma}(\omega)} [f_{iL}(\omega) - f_{iR}(\omega)] \rho_{i\sigma}(\omega) \quad (2)$$

where $\rho_{i\sigma}(\omega) = (-1/\pi)\text{Im} G_{i\sigma}^r(\omega)$, $G_{i\sigma}$ denotes Green's function of the dot, and f_{ir} are the Fermi distribution functions of the electrodes. We restrict ourselves here to the case of equal couplings to the dots, i.e. $t_{i\bar{n}} \equiv t$. Bare Green's functions of the electrodes,

$$g_{r\sigma} = \sum_k g_{kr\sigma} = \sum_k \frac{1}{\omega - \varepsilon_{kr\sigma}} \equiv g, \quad \text{are taken in the form } g = -i\pi\rho_0, \quad \text{where } \rho_0 = 1/2D \text{ is the}$$

assumed constant density of states for $|\varepsilon| < D$, and D is the half of the bandwidth of electrons in the electrodes. Consequently, the elastic couplings to the electrodes are energy independent, $\Gamma_{ir\sigma}(\omega) \equiv \pi t^2 \rho_0 \equiv \Gamma$ (we set $\Gamma = 1$).

In order to determine the Green's function, we use the equation of motion method (EOM). To truncate higher order Green's functions, the self-consistent decoupling procedure proposed by Lacroix is used [8]. In the limit $(U, U_i) \rightarrow \infty$ one gets

$$G_{i\sigma, i\sigma}^r(\omega) = \frac{1 - \sum_{l \in \Omega} (n_l - H_l(\omega))}{\omega - E_{i\sigma} - \Sigma_0 + \sum_{l \in \Omega} (F_l(\omega) - 2\Sigma_0 H_l(\omega))} \quad (3)$$

where $\Sigma_0 = -i\Gamma$ is the self-energy for the non-interacting QD due to tunnelling of the $i\sigma$ electron, $\Omega = \{(\bar{i}, \sigma), (i, -\sigma), (\bar{i}, -\sigma)\}$, $(\bar{1} = 2, \bar{2} = 1)$, $n_l = (n_{lL} + n_{lR})/2$, and

$$F_l(\omega) = \Gamma \sum_{\alpha} \int_{-D}^D \frac{d\omega'}{\pi} \frac{f_{\alpha}(\omega')}{\omega' - \omega - i0^+}, \quad H_l(\omega) = \Gamma \sum_{\alpha} \int_{-D}^D \frac{d\omega'}{\pi} \frac{f_{\alpha}(\omega') G_{i,l}^a(\omega')}{\omega' - \omega - i0^+} \quad (4)$$

3. Numerical results and discussion

For the considered strong inter and intra-dot interactions, the Kondo effect has two possible sources, spin and orbital degeneracies. For $h = 0$ and $\Delta E = \varepsilon_2 - \varepsilon_1 = 0$, the spin and charge degrees of freedom of the DQD are totally entangled and the state possesses $SU(4)$ symmetry. This corresponds to the highest conductance (DC) in Fig. 1 (VSD, $h \approx 0$), where VSD denotes bias voltage.

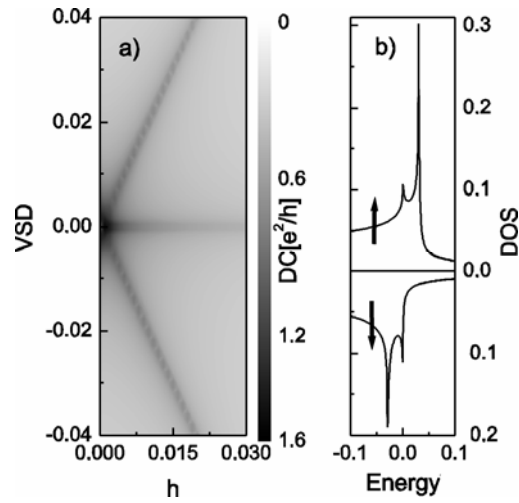


Fig. 1. Differential conductance vs. voltage bias and magnetic field for $\varepsilon_1 = -4$, $\Delta E = 0$ and $g_1 = g_2 = 1$ (a) and many-body structure of the DOS for zero bias voltage and $h = 0.015$ (b)

A magnetic field lifts the spin degeneracy. The observed high conductance line for zero bias ($VSD = 0$) is due to orbital Kondo effects occurring in both spin channels separately ($\varepsilon_{1\sigma} = \varepsilon_{2\sigma}$, $2^*SU(2)$). In the many-body structure of the density of states (DOS), apart from the Kondo peaks there are also satellite peaks, located above and below the Fermi level at positions determined by the magnetic field (Fig. 1b). They result from the tunnelling processes, which link non-degenerate states. The satellites are responsible for the occurrence of high conductance lines with $VSD = \pm 2h$. Figure 2 presents the polarization of conductance in the considered case. The polarization of conductance is defined as $PC = (\sigma_+ - \sigma_-) / (\sigma_+ + \sigma_-)$, where σ denotes the differential conductance.

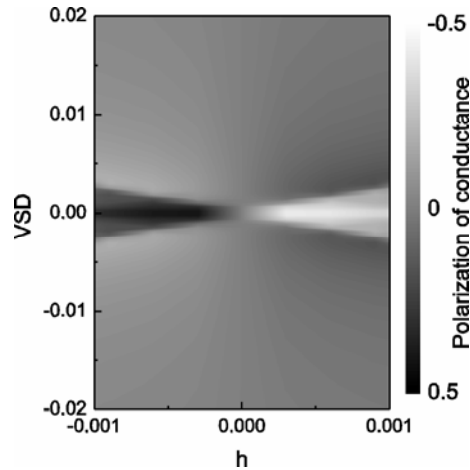


Fig. 2. Polarization of conductance vs. voltage bias and magnetic field for the same parameters as in Fig. 1

Opposite polarizations are observed close to the zero bias line for opposite field orientations. This can be used for spin filtering, what has been discussed earlier by Borda et al. [8]. The spin asymmetry of the current results from the Zeeman splitting of the bare energy levels. In the following, we discuss a different spin-filtering scenario. By an appropriate tuning of gate voltages, orbital degeneracy can be recovered for only one spin channel.

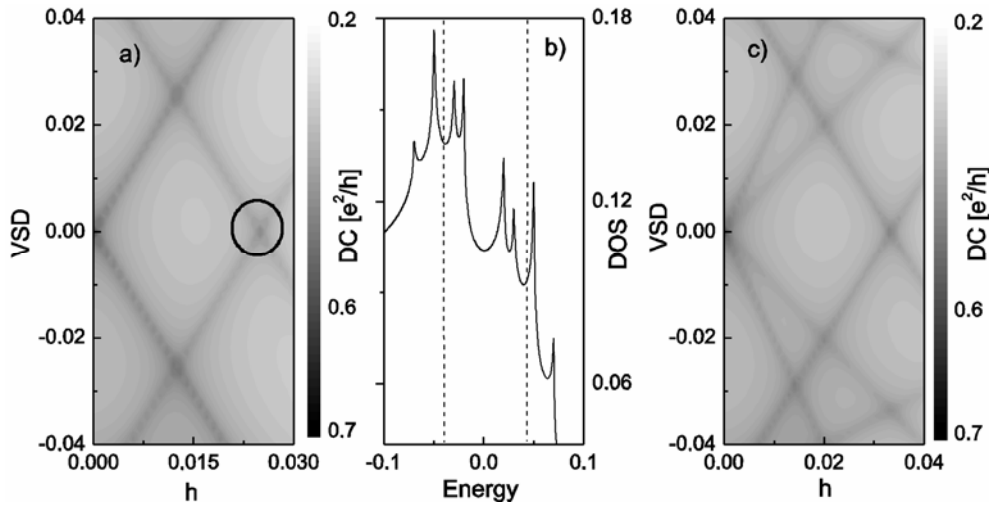


Fig. 3. Differential conductance for $\Delta E = 0.05$, $g_1 = \pm g_2 = 1$ (a) and $g_1 = 1$, $g_2 = 0.5$ (c). Fig. 3b presents the many-body structure for zero bias and $h = 0.01$

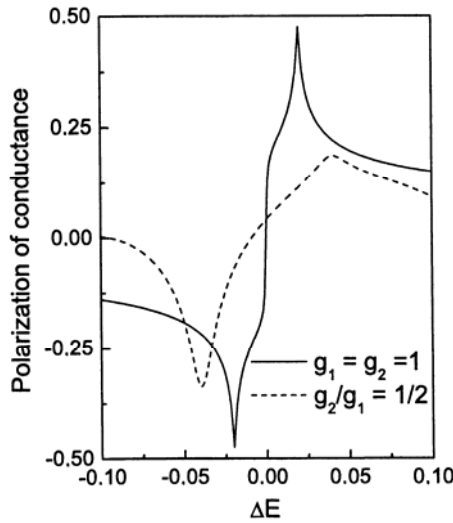


Fig. 4. Polarization of conductance vs. gate voltage (ΔE) for $g_1 = -g_2 = 1$ (solid line) and $g_1 = 1$, $g_2 = 0.5$ (dashed line), with $\varepsilon_1 = -4$, $h = 0.01$

Figure 3a presents the differential conductance of a DQD for $\Delta E \neq 0$. The high transparency region (VSD, $h \approx 0$) corresponds to the spin Kondo effect at the dots ($\varepsilon_{i+} = \varepsilon_{i-}$, $2^*SU(2)$). The enhanced conductance in this region, marked by the dark circle, is due to the orbital Kondo effect ($\varepsilon_{1+} = \varepsilon_{2-}$ for $g_1 = g_2$, or $\varepsilon_{1+} = \varepsilon_{2+}$ for $g_1 = -g_2$). The orbital degeneracy for the same spin orientation can be used for spin filtering. Reversing the spin polarization of conductance can be induced either by a change in gate voltage or by reversing the magnetic field (Fig. 4). For $g_1 = -g_2$, an antisymmetric change in polarization is evident (bipolar spin filter). The four high-conductance lines visible in Fig. 3a occur in regions where the satellite peaks of the DOS, located at $E = \pm 2h \pm \Delta E$, enter the region between the Fermi levels of the leads from opposite sides (Fig. 3b). This happens for bias voltages equal to the positions of the satellite peaks. The peaks in the DOS outside the energy region marked by the dashed vertical lines in Fig 3b do not play any role in the conductance for the voltage range of Fig 3a. DC for a more general case ($g_1 \neq g_2$) is presented in Fig. 3c. The number of high transparency lines increases due to the lack of dot spin symmetry or antisymmetry. The tunnelling processes within the $\{\varepsilon_{i\sigma}\}$ manifold are specified in this case by a larger number of characteristic energies.

Acknowledgements

The author thanks Mr. D. Krychowski for the help with numerical calculations. The work was supported by the Polish State Committee for Scientific Research through project PBZ/KBN/044/P03/2001 and the MAG-EL-MAT network.

References

- [1] PRINZ G., *Science* 282 (1998), 1660.
- [2] DI VINCENZO D.P., *Science* 270 (1995), 255.
- [3] POHJOLA T., SCHOELLER H., SCHOEN G., *Europhys. Lett.*, 54 (2001), 241.
- [4] WILHELM U., SCHMIDT J., WEIS J., V. KLITZING K., *Physica E*, 14 (2002), 385.
- [5] HOLLEITNER A.W., CHUDNOVSKY A., PFANNKUCHE D., EBERL K., BLICK R.H., *Phys. Rev. B*, 70 (2004), 075204.
- [6] JARILLO-HERRERO P., KONG J., VAN DER ZANT H.S.J., DEKKER C., KOUVENHOVEN L.P., DE FRANCESCHI S., *Nature*, 434 (2005), 484.
- [7] HAUG H., JAUHO A.P., *Quantum Kinetics in Transport and Optics of Semiconductors*, Springer-Verlag, Berlin, 1998.
- [8] LACROIX C., *J. Phys. F: Metal Phys.*, 11 (1981) 2389.
- [9] BORDA L., ZARAND G., HEFSETTER W., HALPERIN B.L., VON DELFT J., *Phys. Rev. B*, 90 (2003) 026602.

Received 1 June 2005

Resonant tunnelling through a single level quantum dot attached to ferromagnetic leads with non-collinear magnetizations

M. WAWRZY尼亚K^{1*}, M. GMITRA¹, J. BARNAŚ^{1,2}

¹Department of Physics, Adam Mickiewicz University, Umultowska 85, 61-614 Poznań, Poland

²Institute of Molecular Physics, Polish Academy of Sciences,
M. Smoluchowskiego 17, 60-179 Poznań, Poland

Resonant tunnelling through a non-interacting single-level quantum dot attached to ferromagnetic leads is analysed theoretically. The magnetic moments of the leads are assumed to be non-collinear. Apart from this, an external magnetic field is applied to the system, which is non-collinear with the magnetizations. The magnetic moments of the leads and the external magnetic field are, however, in a common plane. Basic transport characteristics, including current-voltage curves, differential conductance, and tunnel magnetoresistance associated with magnetization rotation, are calculated using the non-equilibrium Green function technique. The dependence of transport characteristics on the bias voltage has been calculated numerically.

Key words: *spin dependent transport; tunnel magnetoresistance; quantum dot*

1. Introduction

Transport of spin-polarized electrons through quantum dots coupled to ferromagnetic leads is currently of interest due to possible applications in magnetoelectronic and spintronic devices [1–3]. This applies especially to spin valve structures, where the transition from parallel to antiparallel magnetic configuration leads to a large magnetoresistance effect. Additional interesting effects, such as the precession of the dot spin, can arise in structures with a non-collinear orientation of the magnetic moments of external leads [4, 5]. Such a precession results from an effective exchange field exerted on the dot by the ferromagnetic electrodes.

The magnetism of the electrodes can also lead to some other phenomena, for instance the zero bias anomaly in the cotunneling regime [6]. Additional interesting

*Corresponding author, e-mail: lauraphy@spin.amu.edu.pl

effects may arise when an external magnetic field is applied to the dot, leading to a spin splitting of a discrete level and modification of transport properties [7]. In this paper, we consider transport through a non-interacting ($U = 0$) single-level dot (impurity) with non-collinear magnetic moments of the leads. The dot is assumed to be in an external magnetic field, whose orientation is non-collinear with the magnetic moments of the leads. Thus, the results generalize those obtained in Ref. [5].

2. The model

The structure under consideration is a non-interacting single-level quantum dot attached to ferromagnetic leads with non-collinear magnetizations. Spin degeneration of the discrete level is removed by an external magnetic field, which is non-collinear with the magnetizations of the electrodes. The field and magnetizations, however, are assumed to be in a common plane. The axis z of the reference frame is assumed to be along the field, whereas the spin moments of the leads are in the (x, z) plane and form angles ϕ_R (right lead) and ϕ_L (left lead) with axis z , as shown in Fig. 1.

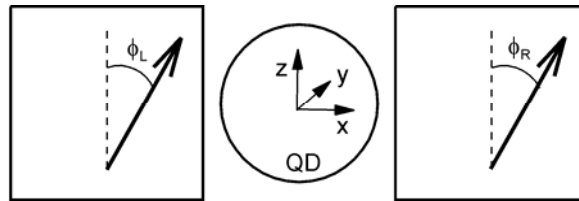


Fig. 1. Schematic illustration of the considered system

The whole system is described by the Hamiltonian of a general form

$$H = \sum_{\alpha} H_{\alpha} + H_D + H_T \quad (1)$$

where H_{α} describes the electrodes

$$H_{\alpha} = \sum_k \sum_{\beta=\pm} \varepsilon_{\alpha k \beta} a_{\alpha k \beta}^{\dagger} a_{\alpha k \beta} \quad (2)$$

for $\alpha = L, R$ (left and right electrode, respectively). Here, $\varepsilon_{\alpha k \beta}$ is the energy of an electron with a wave vector \mathbf{k} and spin β in electrode α , whereas $a_{\alpha k \beta}^{\dagger}$ and $a_{\alpha k \beta}$ are creation and annihilation operators, respectively. The electrostatic energy is included in $\varepsilon_{\alpha k \beta}$, i.e. $\varepsilon_{\alpha k \beta} = \varepsilon_{\alpha k \beta}^0 + eU_c^{\alpha}$, where e ($e < 0$) stands for the electron charge, $\varepsilon_{\alpha k \beta}^0$ is the single-particle energy for the unbiased system, and the electrostatic potentials $U_c^L = V_l/2$ and $U_c^R = -V_l/2$ are applied to the system, with V_l being the transport voltage.

The dot is described by the Hamiltonian

$$H_D = \sum_{\sigma} \varepsilon_d^{\sigma} c_{\sigma}^{\dagger} c_{\sigma} \quad (3)$$

where c_{σ}^{\dagger} and c_{σ} are creation and annihilation operators for spin σ , whereas ε_d^{σ} is the energy level of the dot for $\sigma = \uparrow$ or $\sigma = \downarrow$. The Zeeman splitting of the dot level is $\Delta_Z = \varepsilon_d^{\uparrow} - \varepsilon_d^{\downarrow}$. Finally, the tunnelling term H_T in the Hamiltonian in (1) has the form

$$H_T = \sum_{\alpha} \sum_{\mathbf{k}} \left\{ \left[T_{\alpha\mathbf{k}+} a_{\alpha\mathbf{k}+}^{\dagger} \cos \frac{\phi_{\alpha}}{2} - T_{\alpha\mathbf{k}-} a_{\alpha\mathbf{k}-}^{\dagger} \sin \frac{\phi_{\alpha}}{2} \right] c_{\uparrow} \right. \\ \left. + \left[T_{\alpha\mathbf{k}+} a_{\alpha\mathbf{k}+}^{\dagger} \sin \frac{\phi_{\alpha}}{2} + T_{\alpha\mathbf{k}-} a_{\alpha\mathbf{k}-}^{\dagger} \cos \frac{\phi_{\alpha}}{2} \right] c_{\downarrow} + h.c. \right\} \quad (4)$$

where $T_{\alpha\mathbf{k}\beta}$ stands for the appropriate tunnelling matrix element. According to our definition, the spin projection on the local quantisation axis in the leads is denoted by $\beta = +$ and $\beta = -$ for spin-majority and spin-minority electrons, respectively, whereas spin projection on the global quantization axis (axis z in this case) is denoted by $\sigma = \uparrow$ and $\sigma = \downarrow$.

3. The method

In order to calculate the current and other transport characteristics, we have applied the equation of motion technique for the Green function of the dot, $G_{\sigma\sigma'} = \langle\langle c_{\sigma} | c_{\sigma'}^{\dagger} \rangle\rangle$ and calculated the retarded (advanced) Green functions $G_{\sigma\sigma'}^{r(a)}(\varepsilon) = G_{\sigma\sigma'}(\varepsilon \pm i\eta)$

$$\mathbf{G}^r(\varepsilon) = \left[\mathbf{1} - \mathbf{g}^r(\varepsilon) \mathbf{\Sigma}^r(\varepsilon) \right]^{-1} \mathbf{g}^r(\varepsilon) \quad (5)$$

where

$$\mathbf{g}^r(\varepsilon) = \begin{pmatrix} (\varepsilon - \varepsilon_d^{\uparrow} + i\eta)^{-1} & 0 \\ 0 & (\varepsilon - \varepsilon_d^{\downarrow} + i\eta)^{-1} \end{pmatrix} \quad (6)$$

and

$$\mathbf{\Sigma}^r(\varepsilon) = \begin{pmatrix} \Sigma_{0+}^r(\varepsilon) & \Sigma_1^r(\varepsilon) \\ \Sigma_1^r(\varepsilon) & \Sigma_{0-}^r(\varepsilon) \end{pmatrix} \quad (7)$$

The self energies are given by the formulae

$$\Sigma_{0\pm}^r(\varepsilon) = -\sum_{\alpha} \frac{\Gamma_{\alpha}^r}{2} (1 \pm p_{\alpha} \cos \phi_{\alpha}) \left[\frac{1}{\pi} \ln \left(\frac{B + eU_{\alpha}^r - \varepsilon}{B - eU_{\alpha}^r + \varepsilon} \right) + i \right] \quad (8)$$

$$\Sigma_1^r(\varepsilon) = -\sum_{\alpha} \frac{\Gamma_0^{\alpha}}{2} (p_{\alpha} \sin \phi_{\alpha}) \left[\frac{1}{\pi} \ln \left(\frac{B + eU_e^{\alpha} - \varepsilon}{B - eU_e^{\alpha} + \varepsilon} \right) + i \right] \quad (9)$$

where the electron band is assumed to extend from $-B$ to B , p_{α} is the spin polarization of the α -th electrode, and Γ_0^{α} is a constant defined via the relation $\Gamma_{\pm}^{\alpha}(\varepsilon) = \Gamma_{\pm}^{\alpha} = \Gamma_0^{\alpha}(1 \pm p_{\alpha})$, where $\Gamma_{\pm}^{\alpha}(\varepsilon) = 2\pi \sum_{\mathbf{k}} |T_{\alpha\mathbf{k}\pm}|^2 \delta(\varepsilon - \varepsilon_{\alpha\mathbf{k}\pm})$ is assumed to be independent of the energy within the electron band. In the following, we assume that $\Gamma_0^L = \Gamma_0^R = \Gamma_0$.

The next step is to obtain the lesser Green function from the formula $\mathbf{G}^<(\varepsilon) = \mathbf{G}^r(\varepsilon)\Sigma^<(\varepsilon)\mathbf{G}^a(\varepsilon)$. Here, $\Sigma^<(\varepsilon) = -\sum_{\alpha} [\Sigma_{\alpha}^r(\varepsilon) - \Sigma_{\alpha}^a(\varepsilon)]f_{\alpha}(\varepsilon)$ and $f_{\alpha}(\varepsilon)$ is the Fermi-Dirac distribution function for lead α , $f_{\alpha}(\varepsilon) = 1/\{1 + \exp[(\varepsilon - eU_e^{\alpha})/k_B T]\}$.

The average occupation numbers can be calculated from the formula [5]

$$\langle n_{\sigma} \rangle = \langle c_{\sigma}^{\dagger} c_{\sigma} \rangle = \text{Im} \int_{-\infty}^{+\infty} \frac{d\varepsilon}{2\pi} G_{\sigma\sigma}^<(\varepsilon) \quad (10)$$

and

$$\langle n_{\sigma-\sigma} \rangle = \langle c_{\sigma}^{\dagger} c_{-\sigma} \rangle = -i \int_{-\infty}^{+\infty} \frac{d\varepsilon}{2\pi} G_{-\sigma\sigma}^<(\varepsilon), \quad (11)$$

whereas the electric current flowing from the α -th electrode to the dot is given by the general expression

$$J_{\alpha} = \frac{ie}{\hbar} \int_{-\infty}^{+\infty} \frac{d\varepsilon}{2\pi} \text{Tr} \left\{ \Gamma_{\alpha} \left[\mathbf{G}^<(\varepsilon) + f_{\alpha}(\varepsilon) (\mathbf{G}^r(\varepsilon) - \mathbf{G}^a(\varepsilon)) \right] \right\} \quad (12)$$

with

$$\Gamma_{\alpha} = \Gamma_0 \begin{pmatrix} 1 + p_{\alpha} \cos \phi_{\alpha} & p_{\alpha} \sin \phi_{\alpha} \\ p_{\alpha} \sin \phi_{\alpha} & 1 - p_{\alpha} \cos \phi_{\alpha} \end{pmatrix} \quad (13)$$

The current J flowing through the system must be conserved, $J_L = -J_R$, so one can also calculate J as $J = (1/2)(J_L - J_R)$.

4. Numerical results and discussion

In this section, we discuss some numerical results for non-linear transport, assuming an empty dot level at equilibrium, $\varepsilon_d = 0.25$ eV. The electric current for the paral-

lel configuration, $\phi_L - \phi_R = 0$, is shown in Fig. 2a. The dashed line represents the total current in the absence of a magnetic field, $\Delta_Z = 0$. The solid line corresponds to the case with Zeeman splitting $\Delta_Z = 0.05$ eV, while the dotted and dashed-dotted lines represent the corresponding contributions from two spin channels. The inset in Fig. 2a describes the case with $\Delta_Z = 0.05$ eV, and shows the suppression of current with increasing angle between the spin polarizations of the electrodes.

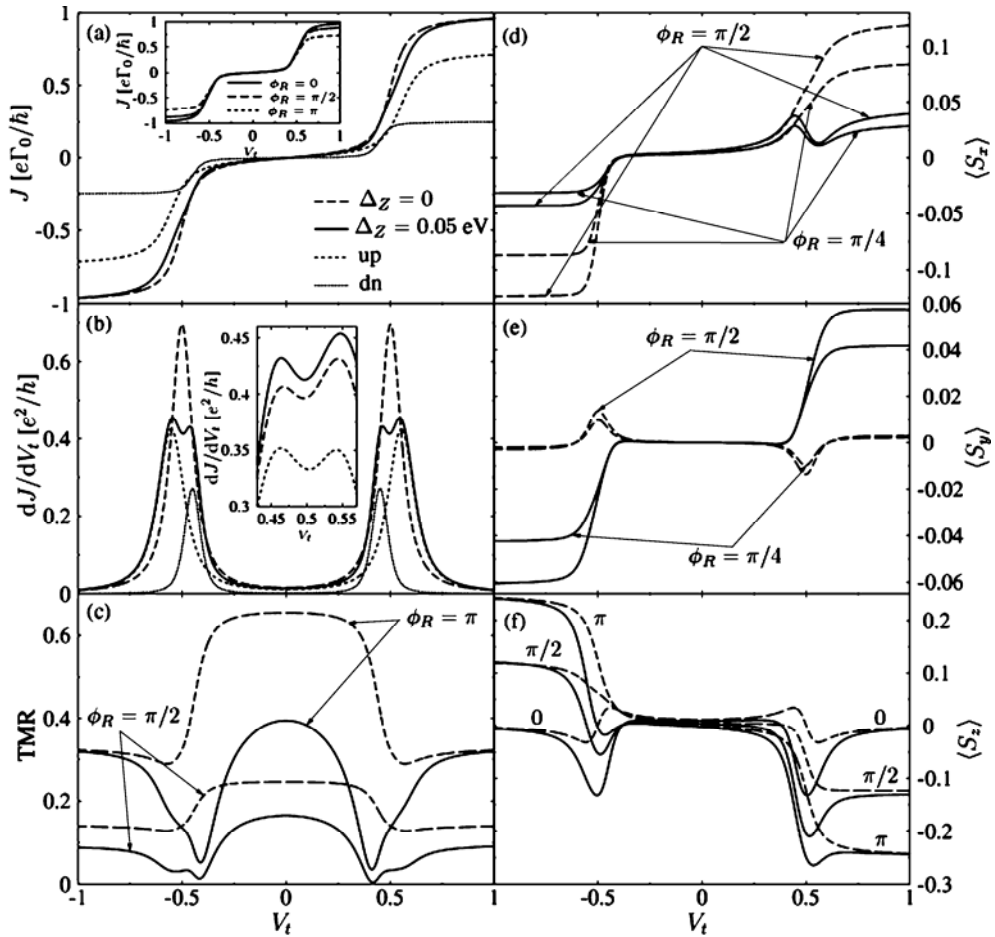


Fig. 2. Transport characteristics versus bias voltage V_t for $\phi_L = 0$. The other parameters are $T = 100$ K, $\Gamma_0 = 0.02$ eV, $\varepsilon_d = 0.25$ eV, and the electron band extends from -3.3 to 3.3 eV: a) the bias dependence of electric current in the parallel configuration, $\phi_R = 0$. The dashed line corresponds to the case with no Zeeman splitting, $\Delta_Z = 0$. The solid line refers to $\Delta_Z = 0.05$ eV, with the corresponding contributions of the two spin channels represented by the dotted and dashed-dotted lines. The inset shows current–voltage curves for $\Delta_Z = 0.05$ eV and for $\phi_R = 0$, $\phi_R = \pi/2$ and $\phi_R = \pi$; b) differential conductance corresponding to the current–voltage curves shown in a. The inset shows the differential conductance for the same values of ϕ_R as in the inset in a; c) the magnitude of TMR for $\Delta_Z = 0.05$ eV (solid lines) and $\Delta_Z = 0$ (dashed lines); parts (d), (e), and (f) present the bias dependences of the average spin components, $\langle S_x \rangle$, $\langle S_y \rangle$ and $\langle S_z \rangle$, for $\Delta_Z = 0.05$ eV (solid lines) and $\Delta_Z = 0$ (dashed lines)

In all cases, a significant current starts to flow when the discrete level of the dot crosses the Fermi level of the source electrode. The steps in the electric current lead to peaks in differential conductance, as shown in Fig. 1b for the same situations as in Fig. 1a. The peaks in external magnetic field (solid line) are spin-split and their amplitude becomes smaller compared to that for $\Delta_z = 0$ (dashed line). This splitting is a consequence of the Zeeman splitting of the discrete dot level. The inset in Fig. 1b shows that conductance decreases with increasing angle between the spin polarizations of the electrodes.

The magnitude of the tunnel magnetoresistance (TMR) effect, defined as $[J(\phi_R = 0, \phi_L = 0) - J(\phi_R, \phi_L)]/J(\phi_R = 0, \phi_L = 0)$, is shown in Fig. 2c for $\phi_L = 0$ and two values of the angle ϕ_R . In general, the TMR effect increases with increasing angle between spin polarizations. We also notice that the TMR effect is larger below the threshold voltage, where current flows mainly due to higher-order tunnelling processes [6].

The right column of Fig. 2 (parts d–f) shows the bias dependence of the average dot spin components. The components are derived from Eqs. (10) and (11) and are given in units of \hbar by the formulas $\langle S_x \rangle = \text{Re}\{n_{\uparrow\downarrow}\}$, $\langle S_y \rangle = \text{Im}\{n_{\uparrow\downarrow}\}$, and $\langle S_z \rangle = (n_{\uparrow} - n_{\downarrow})/2$. The average values $\langle S_x \rangle$ and $\langle S_y \rangle$ are zero for any bias voltage in the parallel and antiparallel configurations, and are not plotted in Fig. 2. It is worth noting that an external magnetic field removes the antisymmetrical behaviour of $\langle S_z \rangle$ for the antiparallel configuration. The $\langle S_z \rangle$ component is symmetrical with respect to the bias voltage only in the parallel configuration. Figure 2e shows the y -component of the average spin. A nonzero value of this component indicates spin precession due to interaction between the dot and electrodes.

Acknowledgements

We thank Dr W. Rudziński for useful discussions. The work was supported by the Polish State Committee for Scientific Research through the project PBZ/KBN/044/P03/2001, as well as RTN Spintronics (contract HPRN-CT-2002-00302) and the MAG-ELMAT network.

References

- [1] RUDZIŃSKI W., BARNAŚ J., Phys. Rev. B, 64 (2001), 085318.
- [2] BULKA B.R., Phys. Rev. B, 62 (2000), 1186.
- [3] ŚWIRKOWICZ R., BARNAŚ J., WILCZYŃSKI M., J. Phys.: Condens. Matter, 14 (2002), 2011.
- [4] KÖNIG J., MARTINEK J., Phys. Rev. Lett., 90 (2003), 166602.
- [5] RUDZIŃSKI W., ŚWIRKOWICZ R., BARNAŚ J., WILCZYŃSKI M., J. Magn. Magn. Mater., 294 (2005), 1.
- [6] WEYMANN I., BARNAŚ J., KÖNIG J., MARTINEK J., SCHÖN G., Phys. Rev. B, 72 (2005), 113301.
- [7] PEDERSEN J.N., THOMASSEN J.Q., FLENSBERG K., Phys. Rev. B, 72 (2005), 045341.

Received 1 June 2005
Revised 10 October 2005

The influence of roughness on the Curie temperature and magnetisation in multilayers

I. STANIUCHA*, A. URBANIAK-KUCHARCZYK

Department of Solid State Physics, University of Łódź, ul. Pomorska 149/153, 90-236 Łódź, Poland

A system of three magnetic (M) layers divided by nonmagnetic (N) spacers is considered. The existence of roughness on the interfaces, described by the model proposed by Bruno and Chappert, leads to a modification of interlayer exchange coupling (IEC). The Curie temperature and magnetisation are calculated using the Green function formalism for the system of layers with Fe standing for M and Cu or Au standing for N. The parameters characterising this system are taken into account for the GaAs substrate. The results obtained show a decreasing Curie temperature with the increasing roughness parameter as compared to the Curie temperature of the sample with an ideal interface. The magnetisation curves are shifted as a result of roughness in the interface region.

Key words: *multilayer; Curie temperature; magnetisation*

1. Introduction

Since the discovery of interlayer exchange coupling (IEC) between magnetic layers separated by nonmagnetic metallic spacers, great interest has been paid to the magnetic properties of exchange-coupled multilayers [1, 2]. The properties of systems such as Fe/Cu/Fe, Fe/Au/Fe, and Co/Cu/Co have been extensively investigated [3–6]. The number of papers in which the problem of magnetic characteristics such as magnetisation and Curie temperature are discussed [7, 8], is however, much smaller than the number of papers devoted to other properties of multilayers [9–11].

We consider a system consisting of three magnetic (M) layers divided by nonmagnetic (N) spacers, described by a Heisenberg-type Hamiltonian with a nearest-neighbour interaction of the form [12]:

$$H = -\frac{1}{2} \sum_{vj, v'j'} J_{vj, v'j'} \vec{S}_{vj} \cdot \vec{S}_{v'j'} - g\mu_B H_{\text{eff}} \sum S_{vj}^z - \frac{1}{2} \sum_{vj, v'j'} A_{vj, v'j'} S_{vj}^z S_{v'j'}^z \quad (1)$$

*Corresponding author, e-mail: staniuch@uni.lodz.pl

where ν denotes the number of monatomic planes and j the position of a lattice point on the plane, respectively. The parameter $J_{\nu j, \nu j'}$ is taken as J for the homogenous medium of internal layers, and as J_{12} for the interaction between spins belonging to interfaces. $A_{\nu j, \nu j'}$ is the anisotropy parameter, consisting of a uniaxial volume anisotropy along the z -axis as the preferred axis and a surface and interfacial anisotropy, H_{eff} is the sum of the external field oriented perpendicular to the surface and the demagnetising field.

In our considerations, we take into account a generalisation of the Ruderman–Kittel theory for oscillatory interlayer exchange coupling [13]. The roughness of the interface, represented by the parameter r , changing from 0 (a flat interface) to 0.25 (a rough interface), was introduced by a model proposed by Bruno and Chappert, leading to the modification of the IEC [14, 15]. The parameter r has the meaning of the probability of appearing of monolayer step up or down interfaces.

2. Results

Applying the standard Green function formalism to the considered system, we calculate the Curie temperature and magnetisation [12]. In this section, we discuss numerical results obtained on the basis of this model. All the characteristics presented have been obtained for the thickness of 5 magnetic layers (MLs). An example of the dependence of Curie temperature on the roughness parameter is shown in Fig. 1a, for the system Fe/Cu/Fe/Cu/Fe/GaAs with spacers of the same thickness and the surface anisotropy parameter taken from [4]. One can see that the Curie temperature decreases with increasing roughness and is smaller for larger spacer thickness.

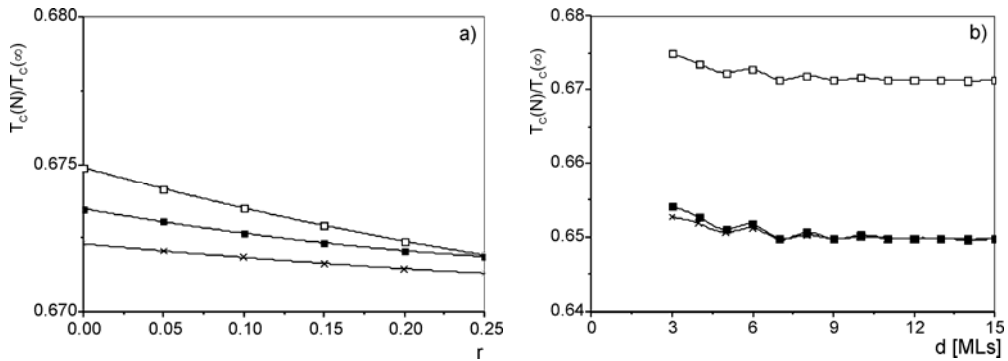


Fig. 1. The Curie temperature as function of a) the roughness parameter r for a constant spacer thickness of 3 MLs (open squares), 4 MLs (full squares), 5 MLs (crosses), b) spacer thickness for different roughness parameters: $r = 0$ for one of the spacer interfaces, $r = 0$ (open squares), $r = 0.15$ (full squares), and $r = 0.25$ (crosses) for the others. The results are obtained for the system Fe/Cu/Fe/Cu/Fe/GaAs, where the orientation of the spacer is (111). The thickness is 5 MLs and $T_c(\infty)$ denotes the Curie temperature for the bulk magnetic materials

Figure 1b presents the Curie temperature as a function of the spacer thickness for various roughness parameters. The upper curve in Fig. 1b is obtained for interfaces with the same level of roughness. As one can expect, the Curie temperature is an oscillating function of the spacer thickness and decreases with the increasing roughness parameter. The period of oscillation is equal to half of the period of oscillation of IEC. A similar behaviour of T_C can be observed for the systems Fe/Au/Fe/Au/Fe/GaAs, Fe/Au/Fe/Au/Fe/InAs and Co/Cu/Co/Cu/Co.

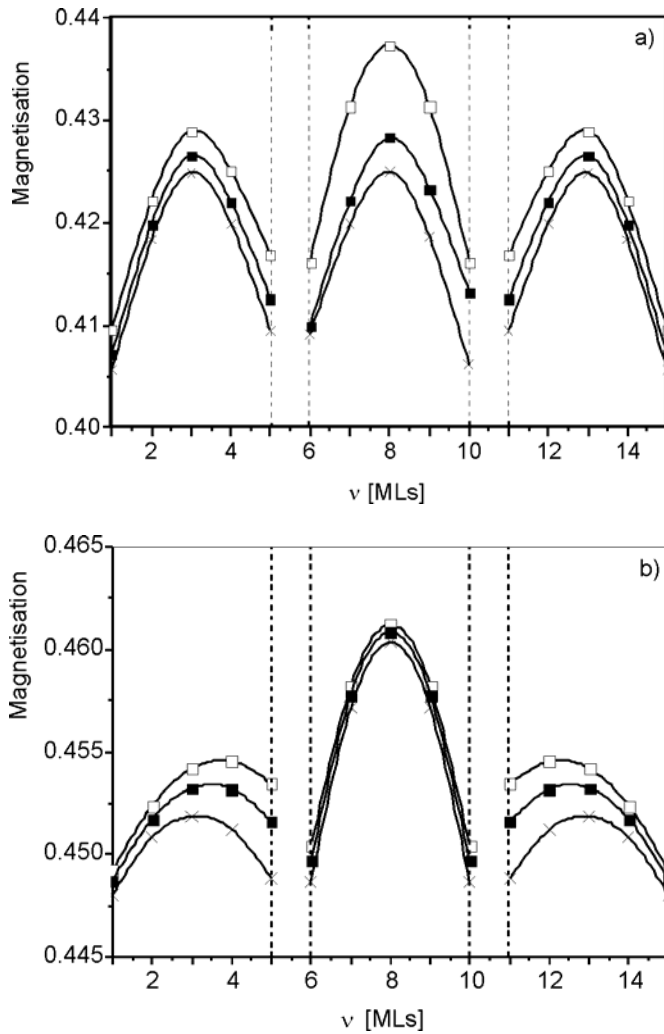


Fig. 2. Magnetisation profiles as a function of the number of layers for: a) the roughness of one respective interface equal to $r = 0$, and of the other equal to 0 (open squares), 0.15 (full squares), and 0.25 (crosses); the spacer thickness 3 MLs, b) for the same spacer thickness of 3 MLs (open squares), 5 MLs (full squares), and 7 MLs (crosses) in the structure Fe/Cu/Fe/Cu/Fe/GaAs. The width of the “gap” between the magnetic layers is not related to the spacer thickness

In view of the fact that the presence of roughness results in a change in the magnitude and phase of IEC, one can expect that the roughness influences the magnetisation distribution across magnetic layers.

The influence of roughness on magnetisation distribution is very weak for Cu(111) and Au(111), and a little stronger for other orientations of the spacer. More significant are the shifts in the profiles induced by the difference parameters describing both spacers. The profiles have been obtained for the temperature of 300 K (Figs. 2a, b). In addition, different values of the roughness parameter of the interfaces are the reason for the asymmetric magnetisation profiles visible in Fig. 2a.

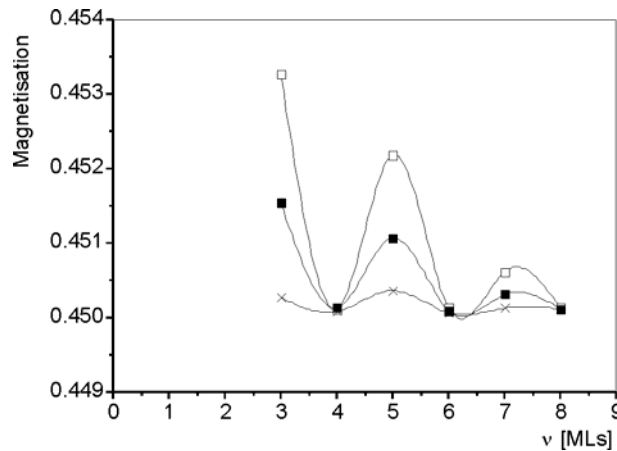


Fig. 3. The magnetisation profile for one of the chosen numbers of layers and for $T = 300\text{K}$ in the system Fe/Cu/Fe/Cu/Fe/GaAs as a function of spacer thickness and for different roughness parameters

It is interesting to see the cross-section of the magnetisation profile for one chosen magnetic layer. Figure 3 presents the magnetisation as a function of the spacer thickness for the central layer of the system. Roughness is the reason for decreasing magnetisation but the period of oscillation is the same as for the oscillation of Curie temperature, and twice smaller than for IEC.

3. Conclusions

Although the presented results are obtained in the framework of a very simple model and have rather a qualitative character, it seems that some information is important from the experimental point of view. In order to apply multilayers, it is necessary to work out methods for obtaining layered structures with well-defined layer thicknesses and surfaces that are as flat as possible. Small differences between spacers or roughness parameters caused magnetisation and the Curie temperature to change in the coupled systems.

References

- [1] PAJDA M., KUDRNOVSKÝ J., TUREK I., DRCHAL V., BRUNO P., *Phys. Rev. B*, 64 (2001), 174402.
- [2] UNGURIS J., CELOTTA R.J., PIERCE D.T., *J. Magn. Magn. Mater.*, 127 (1993), 205.
- [3] KUDRNOVSKÝ J., DRCHAL V., TUREK I., BRUNO P., *Surf. Sci.*, 507–510 (2002) 567.
- [4] MCPHAIL S., GÜRTLER C.M., MONTAIGNE F., XU Y.B., TSELEPI M., BLAND J.A.C., *Phys. Rev. B*, 67 (2003), 024409.
- [5] BRUNO P., *J. Magn. Magn. Mater.*, 148 (1995) 202.
- [6] LAIDLER H., HICKEY B.J., *J. Phys.: Condens. Matter.*, 12 (2000) 8401.
- [7] LINDNER J., BABERSCHKE K., *J. Phys. Condens. Matter.*, 15, (2003), R193.
- [8] BAYREUTHER G., BENSCH F., KOTTLER V., *J. Appl. Phys.*, 79 (1996), 4509.
- [9] KUDRNOVSKÝ J., DRCHAL V., BLAAS C., WEINBERGER P., TUREK I., BRUNO P., *Phys. Rev. B*, 62 (2000), 15084.
- [10] MONCHESKY T.L., URBAN R., HEINRICH B., KLAUE M., KIRSCHNER J., *J. Appl. Phys.*, 87 (2000), 5167.
- [11] COSTA A.T.JR., MUNIZ R.B., MILLS D.L., *Phys. Rev. B*, 69 (2004), 064413.
- [12] URBANIAK-KUCHARCZYK A., *Phys. Stat. Sol. (b)*, 203, (1997), 195.
- [13] BRUNO P., CHAPPERT C., *Phys. Rev. B*, 46 (1992), 261.
- [14] BRUNO P., CHAPPERT C., *Phys. Rev. Lett.*, 67 (1991), 1602.
- [15] WANG Y., LEVY P.M., FRY J.L., *Phys. Rev. Lett.*, 65 (1990), 2732.

Received 1 June 2005

Revised 10 October 2005

Partitioning of Co upon the nanocrystallisation of soft magnetic FeCo(Zr, Nb)B alloys – a ^{59}Co NMR study

M. WÓJCIK^{1*}, E. JĘDRYKA¹, I. ŠKORVÁNEK², P. ŠVEC³

¹Institute of Physics, Polish Academy of Sciences, 02-668 Warszawa, Poland

²Institute of Experimental Physics, Slovak Academy of Sciences, 043 53 Košice, Slovakia

³Institute of Physics, Slovak Academy of Sciences, 842 28 Bratislava, Slovakia

^{59}Co NMR spectroscopy has been used to monitor structural modifications of $(\text{Fe}_{0.5}\text{Co}_{0.5})_{89}\text{Zr}_7\text{B}_4$ and $(\text{Fe}_{0.25}\text{Co}_{0.75})_{81}\text{Nb}_7\text{B}_{12}$ amorphous ribbons subject to different heat treatments. The characteristic features of ^{59}Co NMR spectra in the as-cast samples indicate a compositional modulation of $(\text{Fe}_{0.25}\text{Co}_{0.75})_{81}\text{Nb}_7\text{B}_{12}$, whereas $(\text{Fe}_{0.5}\text{Co}_{0.5})_{89}\text{Zr}_7\text{B}_4$ ribbon is more homogenous, indicating, however, a slight preference to form $\text{Co}_{78}\text{Zr}_{22}$ -like environments. Upon heat treatment, a precipitation of an ordered (B2) CoFe crystalline phase is observed in both systems.

Key words: *nanocrystalline material; NMR; hyperfine field*

1. Introduction

Nanocrystalline FeCo(Zr, Nb)B(Cu) alloys (better known under their technical name HITPERM), prepared by devitrifying melt-spun amorphous precursors, have been the subject of intense research during the last few years [1–5]. This interest is driven by a technological demand for soft magnetic materials offering large magnetic induction, and at the same time being capable of operating at elevated temperatures.

The microstructure of these materials consists of nanocrystalline FeCo grains embedded in a surrounding amorphous matrix. Among the most significant structural parameters determining the magnetic behaviour of these two-phase systems are the size and volume fraction of crystalline grains as well as the structural and compositional nature of the remaining intergranular phase. In addition, it is well known that the magnetic properties of crystalline Fe-Co, such as magnetization and magnetocrystalline anisotropy, vary with composition and also depend on the degree of ordering

*Corresponding author, e-mail: Marek.Wojcik@ifpan.edu.pl

[6]. Therefore, in order to optimise the properties of HITPERM materials, it is important to study in detail the development of the nanocrystalline structure during annealing, and especially the partitioning of different atomic species between the constituent phases, as well as the degree of ordering in FeCo nanocrystals.

This kind of structural information can be obtained by studying the distribution of hyperfine fields, which are extremely sensitive to local atomic configuration, and thus reflect the structural and chemical order in alloys. In this paper, we present the results of a ^{59}Co nuclear magnetic resonance (NMR) experiment that enables the partitioning of Co atoms in the FeCo(Zr,Nb)B system to be followed as it varies with increasing annealing temperature.

2. Experimental

Amorphous ribbons with a composition $(\text{Fe}_{0.5}\text{Co}_{0.5})_{89}\text{Zr}_7\text{B}_4$ (sample A) and $(\text{Co}_{0.75}\text{Fe}_{0.25})_{81}\text{Nb}_7\text{B}_{12}$ (sample B) have been obtained in vacuum by the planar flow casting technique. Pieces of amorphous ribbons were subsequently annealed under high vacuum for 1 hour, at 510 °C and 560 °C in the case of sample A and at 450 °C and 600 °C in the case of sample B, in order to prepare samples with different volume fractions of nanocrystalline particles.

The ^{59}Co NMR experiment was performed at 4.2 K in a zero magnetic field using a coherent, phase sensitive spin echo spectrometer. Several sets of NMR spectra were recorded, every 1 MHz in the frequency range 20–320 MHz, at varying excitations of the r.f. field amplitude. The ^{59}Co NMR frequency can be readily interpreted as fingerprints of different structural components (nanocrystalline precipitates, amorphous remainder) – the structural information can thus be extracted in a straightforward way. On the other hand, the applied experimental procedure provides the value of the local restoring field acting on the magnetization in different structural components of the sample. In this way, microscopic magnetic information is added to structural information.

3. Results

We have previously reported a detailed NMR study of nanocrystallisation in $(\text{Fe}_{0.5}\text{Co}_{0.5})_{89}\text{Zr}_7\text{B}_4$ ribbon [7, 8]. It was shown that the ^{59}Co spectrum recorded for the as-quenched sample represents a broad distribution of different atomic environments, typical of a disordered amorphous material (Fig. 1). The lack of any peaks and spectral features confirms that the atoms are intermixed and there are no crystalline precipitates in the specimen. The maximum of spectrum intensity, located around 200 MHz, is mainly determined by the average proportion of transition metal (Co, Fe) and nonmagnetic elements (Zr, B), whereas a broad line width reflects a predominantly random distribution of magnetic and nonmagnetic elements [7]. This was also supported by an almost flat

frequency dependence of the restoring field, reflecting an effective averaging of local anisotropies, which have a random character in the amorphous state [8].

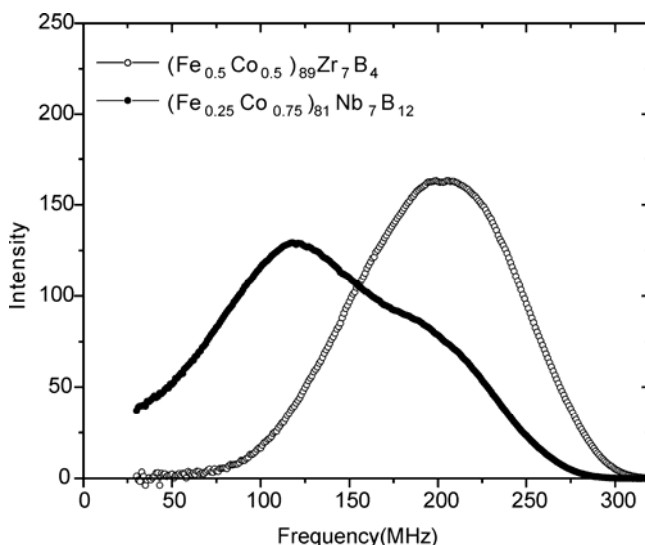


Fig. 1. ^{59}Co NMR spectra of as-cast $(\text{Fe}_{0.5}\text{Co}_{0.5})_{89}\text{Zr}_7\text{B}_4$ and $(\text{Co}_{0.75}\text{Fe}_{0.25})_{81}\text{Nb}_7\text{B}_{12}$ amorphous ribbons recorded at 4.2 K

In contrast to this, the ^{59}Co hyperfine field distribution for the as-cast amorphous ribbon of $(\text{Fe}_{0.25}\text{Co}_{0.75})_{81}\text{Nb}_7\text{B}_{12}$ (also shown in Fig. 1) exhibits a bimodal shape with two broad maxima. This kind of hyperfine field distribution reveals the presence of two types of Co local environments in the Nb-containing alloy. The two maxima of spectrum intensity at around 120 MHz and 200 MHz are assigned to Co atoms located in Nb-rich and Nb-poor regions, respectively.

After annealing, NMR spectra recorded from both types of ribbons display a characteristic split into two components (Fig. 2a). The spectrum component representing the amorphous matrix is downshifted in frequency with respect to the line from the as-quenched precursor, reflecting a higher proportion of nonmagnetic elements. The frequency shift is especially drastic in the case of $(\text{Co}_{0.75}\text{Fe}_{0.25})_{81}\text{Nb}_7\text{B}_{12}$ (about 30 MHz). In the case of $(\text{Fe}_{0.5}\text{Co}_{0.5})_{89}\text{Zr}_7\text{B}_4$, the line position was found to be only partly due to the depletion of Co and Fe. An additional, important factor is compositional modulation due to the tendency of Co and Zr to cluster. This tendency is driven by a negative heat of mixing of Co and Zr, resulting in the preferential formation of environments that have a composition close to $\text{Co}_{78}\text{Zr}_{22}$ [7]. This was clearly evidenced by the development of a two component structure after annealing at 560 °C, although such a tendency was already hinted at by certain features in the NMR spectrum of the as-quenched $\text{Fe}_{44.5}\text{Co}_{44.5}\text{Zr}_7\text{B}_4$ ribbon [8].

The high-frequency component of the NMR spectra in the annealed samples corresponds to the crystalline CoFe part (Fig. 2b). Short-range order present in the sam-

ples can be studied by comparing these spectral components with selected reference spectra from well-characterized samples of known composition. Such an analysis has been performed for $(\text{Fe}_{0.5}\text{Co}_{0.5})_{89}\text{Zr}_7\text{B}_4$ alloys and shows that the crystalline phase has the composition close to that of the highly ordered B2 phase ($\text{Co}_{50}\text{Fe}_{50}$ alloy) [7]. Two characteristic features of the NMR spectrum in $(\text{Fe}_{0.5}\text{Co}_{0.5})_{89}\text{Zr}_7\text{B}_4$ show that the nanocrystallites are enriched in Fe with respect to the nominal 50:50 composition. One of them is a slight frequency up-shift (to 291 MHz) with respect to 287 MHz, the latter being characteristic of a perfectly ordered B2 phase with a composition of $\text{Co}_{50}\text{Fe}_{50}$. Another is the presence of high frequency satellites spaced by +7 MHz, which are due to antisite Fe atoms on the Co sublattice.

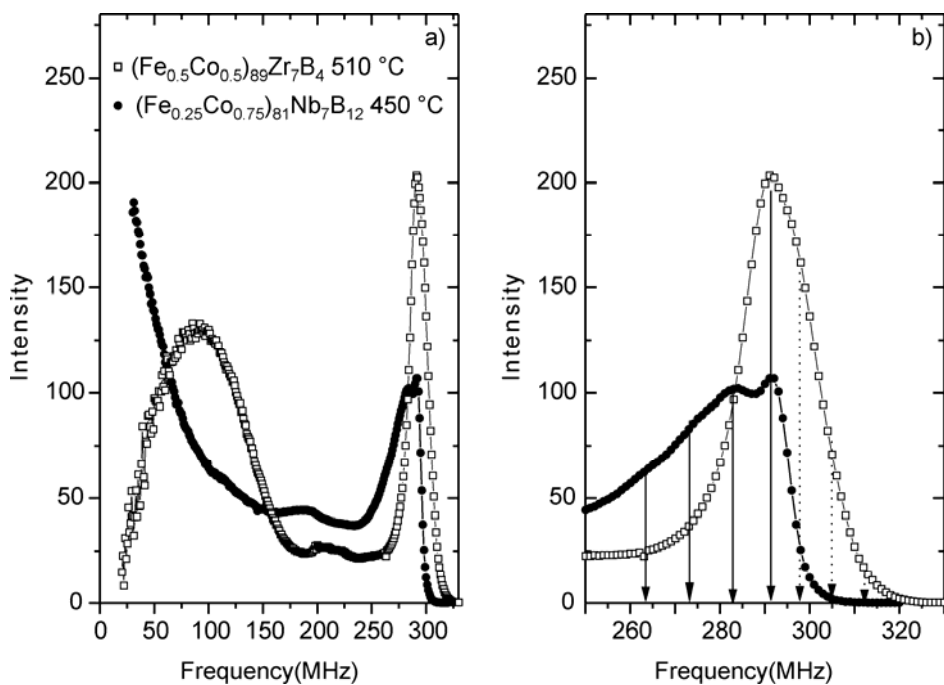


Fig. 2. ^{59}Co NMR spectra of $(\text{Fe}_{0.5}\text{Co}_{0.5})_{89}\text{Zr}_7\text{B}_4$ ribbon annealed at 510 °C and $(\text{Co}_{0.75}\text{Fe}_{0.25})_{81}\text{Nb}_7\text{B}_{12}$ annealed at 450 °C (a) and the high frequency part of the spectrum in greater detail (b); the arrows indicate the positions of satellite lines due to Co and Fe atoms located in antisite positions of the B2 structure of $\text{Co}_{50}\text{Fe}_{50}$

The analysis of the satellite intensity in terms of the hyperfine field model developed for B2 ordered CoFe alloys [9] allowed estimation of the crystal composition as $\text{Co}_{45}\text{Fe}_{55}$ [7]. A similar tendency to preferentially crystallize in the B2 phase is also displayed by $(\text{Co}_{0.75}\text{Fe}_{0.25})_{81}\text{Nb}_7\text{B}_{12}$ samples, as evidenced by the characteristic peak in the NMR spectrum in Fig. 2b. This is interesting, considering that the composition of the matrix of departure is considerably Co-enriched compared to $(\text{Fe}_{0.5}\text{Co}_{0.5})_{89}\text{Zr}_7\text{B}_4$. The presence of surplus Co in the highly ordered B2 sublattice manifests itself in the

long tail of this spectral component, extending down to 150 MHz, with a characteristic satellite structure due to different nearest neighbour environments of Co.

These results clearly demonstrate that unique nanoscopic structural information can be obtained from studying ^{59}Co hyperfine field distribution using nuclear magnetic resonance. Further studies, including the correlation of observed spectral features with the variation of the restoring field, are currently underway.

Acknowledgement

This work was supported in part by NATO Grant No. PST.EAP.CLG.981072 and the international network MAG-EL-MAT.

References

- [1] WILLARD M.A., LAUGHLIN D.E., MCHENRY M.E., THOMA D., SICKAFUS K., CROSS J.O., HARIS V.G., *J. Appl. Phys.*, 84 (1998), 6773.
- [2] PING D.H., WU Y.Q., HONO K., WILLARD M.A., MCHENRY M.E., LAUGHLIN D.E., *Scr. Mater.*, 45, (2001), 781.
- [3] KEMENY T., KAPTAS D., KISS L.F., BALOGH J., BUJDOSO L., GUBICZA J., UNGAR T., VINCZE I., *Appl. Phys. Lett.*, 76 (2000), 2110.
- [4] KOPCEWICZ M., GRABIAS A., WILLARD M.A., LAUGHLIN D.E., MCHENRY M.E., *IEEE Trans. Magn.*, 37 (2001), 2226.
- [5] ŠKORVÁNEK I., ŠVEC P., MARCIN J., KOVÁČ J., KRENICKÝ T., DEANKO M., *Phys. Stat. Sol. (a)*, 196 (2003), 217.
- [6] O'HANDLEY R.C., *Modern Magnetic Materials: Principles and Applications*, Wiley, New York, 1999.
- [7] JĘDRYKA E., WÓJCIK M., ŠVEC P., ŠKORVÁNEK I., *Appl. Phys. Lett.*, 85 (2004), 2884.
- [8] WÓJCIK M., JĘDRYKA E., ŠKORVÁNEK I., ŠVEC P., *J. Magn. Magn. Mat.*, 290–291 (2005), 1433.
- [9] JAY J.P.H., WÓJCIK M., PANISSOD P., *Z. Phys. B*, 101 (1996), 471.

Received 1 June 2005
Revised 10 October 2005

Photoelectron spectroscopy of Ba-doped lead germanate – $\text{Pb}_5\text{Ge}_3\text{O}_{11}$

E. TALIK*, M. ADAMIEC, A. MOLAK

Institute of Physics, University of Silesia, Uniwersytecka 4, 40-007 Katowice, Poland

XPS electronic structure measurements of barium-doped lead germanate ($\text{Pb}_5\text{Ge}_3\text{O}_{11}$) single crystals along the principal directions revealed a deviation of stoichiometry, which was the reason for the structural disorder and broadening of the core level lines.

Key words: *lead germanate; single crystal; photoelectron spectroscopy*

1. Introduction

Lead germanate ($\text{Pb}_5\text{Ge}_3\text{O}_{11}$) is a ferroelectric crystal, which attracts attention due to its applicability in electro-optical devices related to its pyroelectric and photorefractive effects [1–3]. The influence of dopant elements – Ba, Ca, Sr, Cu, Mn, La, Nd, Gd – on the electro-optical properties of lead germanate was investigated. Doping affects e.g., the pyroelectric coefficient as well as spontaneous polarisation and causes a distinct shift in the temperature of the para-ferroelectric phase transition. Its crystal structure consists of layers arranged alternately along the c axis within a Pb frame. These layers consist of germanate groups: GeO_4 tetrahedra and Ge_2O_7 double tetrahedra (Fig. 1) [4]. The properties of lead germanate show a marked anisotropy due to the uniaxial structure, e.g. in electric permittivity, piezoelectric and electrostrictive constants, refractive index, electro-optic coefficients, and elastic constants. The electric conduction of undoped lead germanate crystals is thermally activated, with the activation energy E_a varying from 0.64 to 0.83 eV. Barium ions influence the electric conduction, lowering the activation energy to 0.35–0.51 eV, depending on concentration. Moreover, Ba-doping enhances the pyroelectric coefficient, decreases spontaneous polarisation, and increases coercive field values [5].

The aim of this work is to examine the influence of barium doping on the electronic structure of lead germanate. $\text{Pb}_5\text{Ge}_3\text{O}_{11}$ single crystals, pure and doped with Ba,

*Corresponding author, e-mail: talik@us.edu.pl

were measured by XPS. Changes in the full width at half maximum with increasing Ba content were observed. The core levels are sensitive to chemical surroundings,

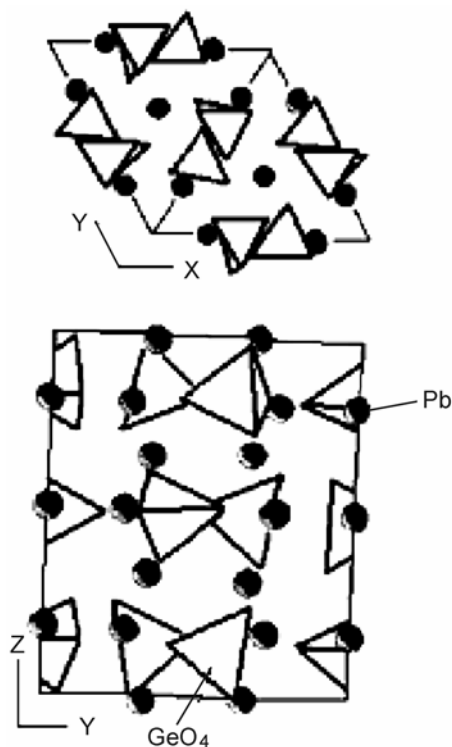


Fig. 1. Projection of the crystal structure on the basal plane after [4]

therefore XPS spectroscopy is very useful for characterising the chemical environment of elements, especially in the case of disordered materials. According to Lewis et al. [6], core-level X-ray photoelectron spectroscopy probes the local potentials at lattice sites in a solid and hence it should be able to provide information both on averaged site potentials in a disordered alloy and on fluctuations around those averages.

2. Experimental

Pure lead germanate, $\text{Pb}_5\text{Ge}_3\text{O}_{11}$, and the barium-doped, $\text{Pb}_5\text{Ge}_3\text{O}_{11}:\text{Ba}$, single crystals were grown from a melt using the Czochralski technique. The monocrystalline samples were prepared from a boule, transparent light yellow in colour, grown along the [001] direction. The orientation was verified using the standard Laue technique [7–9]. Three $\text{Pb}_5\text{Ge}_3\text{O}_{11}$ single crystals, pure and doped with 10% and 25% of barium, were cut along the b and c principal directions. The a direction is not a principal one but is perpendicular to the b and c axes (Fig. 2). XPS spectra were obtained

using a PHI 5700/660 Physical Electronics Photoelectron Spectrometer with monochromatised Al K_{α} X-ray radiation (1486.6 eV). A hemispherical mirror analyser was used to analyse the energy of electrons, with the energy resolution of about 0.3 eV. All measurements were performed for monocrystalline samples broken perpendicular to the a , b , and c directions under UHV conditions at 10^{-8} Pa. In each case, a neutraliser was used due to the charge effect that occurs for non-conducting dielectric

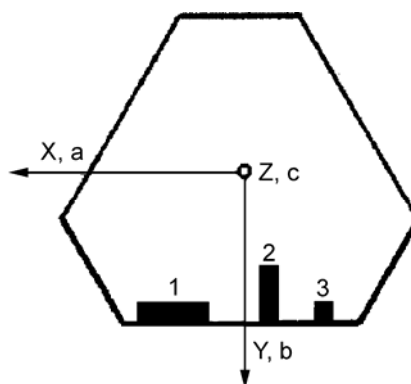


Fig. 2. The crystal habit of a boule pulled along the c axis and a sketch of the samples cut for XPS measurements along the: a axis – sample 1, b axis – sample 2, c axis sample 3

samples. The binding energy was determined by reference to the C 1s component set at 285 eV. Each peak of the recorded spectrum is characteristic of a certain electron energy level of a certain element. The electron binding energies are characteristic of each element. The measured binding energies, however, are not absolutely constant, but depend on the chemical environments of functional groups due to the modification of the valence electron distribution. These differences in the electron binding energies in relation to pure elements are called chemical shifts. For XPS investigations it is important to determine the relative concentrations of various constituents. The Multi-pak Physical Electronics programme enables the quantification of XPS spectra, utilising the peak area and peak height sensitivity factor [10]. The calculation of the standard atomic concentration provides the ratio of each component to the sum of the other elements considered in the data. Only those elements, for which the specific lines were clearly visible in the spectrum, were considered. For these lines, the Shirley background was subtracted, the limit of the region of the lines was individually selected, and the integration was then done. The area following sensitivity factors were used: 9.000 for Pb 4f, 7.343 for Ba $3d_{5/2}$ and 0.733 for O 1s. The accuracy of this method is $\pm 10\%$.

3. Results and discussion

The XPS spectra of the single crystals recorded in the energy range of 0–1400 eV show some contamination with carbon (Fig. 3). The chemical compositions of the pure crystal and the ones doped with 10% and 25% Ba, calculated using the XPS

spectra, are collected in Table 1. For all the measured crystals, a lower than nominal concentration of oxygen is observed, indicating the presence of oxygen vacancies. Moreover, an enhanced concentration of germanium, which has the smallest ionic radius in the compound, is observed. This suggests the presence of some germanium as an interstitial atom.

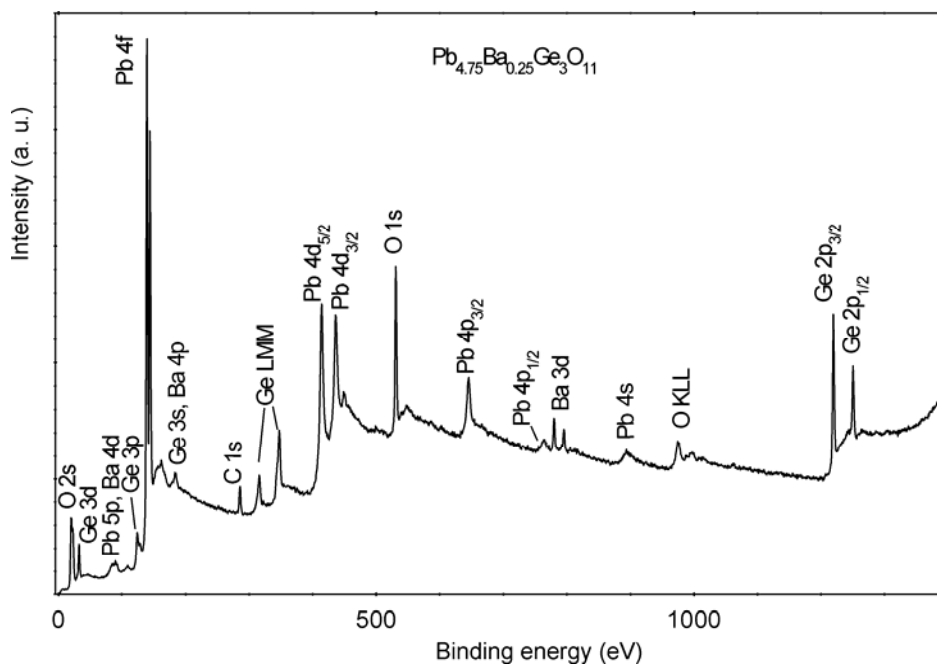


Fig. 3. XPS spectrum of $\text{Pb}_5\text{Ge}_3\text{O}_{11}$: 25% Ba in a wide energy range

Table 1. Chemical compositions of pure and Ba-doped $\text{Pb}_5\text{Ge}_3\text{O}_{11}$

Element	Ba content [wt. %]								
	0			10			25		
	<i>a</i> axis	<i>b</i> axis	<i>c</i> axis	<i>a</i> axis	<i>b</i> axis	<i>c</i> axis	<i>a</i> axis	<i>b</i> axis	<i>c</i> axis
Pb	5.00	4.86	5.00	5.01	5.00	4.69	5.00	4.86	4.76
Ge	3.28	3.48	3.53	3.30	3.50	3.22	3.21	3.39	3.57
O	10.73	10.66	10.47	10.55	10.43	10.98	10.55	10.50	10.45
Ba	–	–	–	0.14	0.07	0.11	0.24	0.25	0.22

For the pure crystals broken perpendicular to the *a* and *c* directions, the nominal concentration of lead was found. A decrease in the concentration of lead, however, was observed for the crystal broken perpendicularly to the *b* axis. For the crystal doped with 10% of barium, which has the ionic radii similar to lead and the same

oxidation state, the concentrations of oxygen and germanium were similar as for the pure crystal. In the planes (b,c) and (a,c) , the lead concentration is nominal. This indicates that barium is in the interstitial positions. For the (a,b) plane, lead concentration is lower than the nominal one and in this plane probably only barium atoms are in the Pb sites.

A similar effect is observed for the crystal doped with 25% Ba. Narrow and almost symmetric lines are observed for the planes (a,c) and (a,b) where barium probably replaced Pb ions. For the (b,c) plane, where the concentration of Ba and Pb ions is enhanced, a broadening of the line occurs due to structural disorder. An example is shown in Fig. 4.

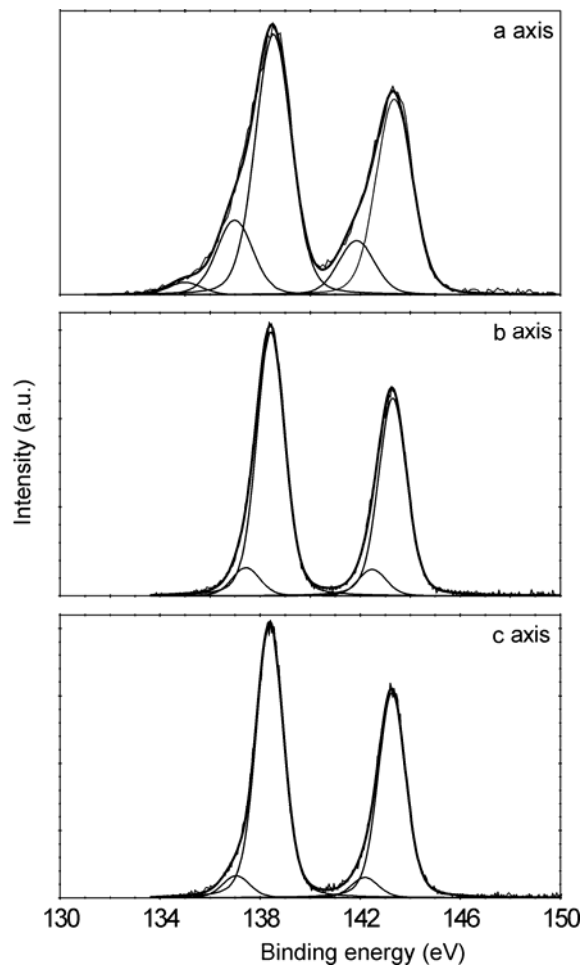


Fig. 4. Pb 4f lines for crystals broken perpendicularly to the a , b , and c directions

The XPS lines are much narrower for these planes (see Table 1) which exhibit the chemical composition in agreement with the nominal one, suggesting a better struc-

tural order. It is worthwhile to notice that these directions are the principal ones. For the a direction (not principal), all measured lines are broadened due to a more random arrangement of atoms. Moreover, barium ions are probably located not exactly in the lead sites in this direction. These two effects influence the electrostatic charges on the crystal lattice sites. The satellite lines at lower binding energies may be partly related to a not fully neutralized surface and/or partly to disorder, corresponding to the distortion of germanate groups. It is known that variations in bond length and bond angles, such as in amorphous silicon, cause static charge fluctuations in the network [11]. Local variations of valence charge affect electronic structure and lead to a homogeneous broadening of the Si 2p core level, similar to the obtained results.

4. Conclusions

XPS electronic structure measurements of barium-doped lead germanate crystals along perpendicular directions revealed variations in crystal stoichiometry, related to structural disorder and a broadening of the core level lines.

Acknowledgements

The authors are thankful to Dr. M. Koralewski and Prof. G.A. Saunders for kindly supplying lead germanate crystals.

References

- [1] OTTO H.H., LOSTER P., *Ferroelectrics Lett.*, 16 (1993), 81.
- [2] STRUKOV B.A., SINIAKOV YE.V., MAISHTCHIK YE.P., MINAIEVA K.A., MONIA V.G., VLOKH O.G., *Izv. AN SSSR, ser. Fiz.*, 41 (1977), 692.
- [3] BURNS G., DACOL F.H., TAYLOR W., *Phys. Rev. B*, 28 (1983), 253.
- [4] IWATA Y., *J. Phys. Soc. Japan*, 43 (1977), 961.
- [5] Landolt-Börnstein, New Series, Group III, Vol. 16a, *Ferroelectrics and Related Substances: Oxides*, Springer-Verlag, Berlin, 1982.
- [6] LEWIS D., COLE R.J., WEIGHTMAN P., *J. Phys.: Condens. Matter*, 11 (1999), 8431.
- [7] SUGII K., IWASAKI H., MIYAZAWA S., *Mat. Res. Bull.*, 6 (1971), 503.
- [8] AL-MUMAR I.J., SAUNDERS G.A., *Phys. Rev. B*, 34 (1986), 4304.
- [9] KORALEWSKI M., MOLAK A., *J. Phys.: Condens. Matter*, 11 (1999), 1341.
- [10] MOULDER J.F., STICKLE W.F., SOBOL P.E., BOMBEN K.D., *Handbook of X-ray Photoelectron Spectroscopy – Physical Electronics*, Physical Electronics, Inc., Eden Prairie, Minnesota, USA, 1995.
- [11] LEY L., REICHARDT J., JOHNSON R.L., *Phys. Rev. Lett.*, 49 (1982), 1664.

Received 1 June 2005
Revised 10 October 2005

Calculation of the Fermi wave vector for thin films, quantum wires and quantum dots

T. BALCERZAK*

Department of Solid State Physics, University of Łódź, Pomorska 149/153, 90-236 Łódź, Poland

A comparison of the construction of the Fermi surface for thin films, quantum wires and quantum dots has been made within the framework of the free-electron model. The dependence of the Fermi wave vector on the confined size of low-dimensional systems has been numerically obtained for the model, with some experimental parameters corresponding to Cu structure.

Key words: *thin film; quantum wire; quantum dot; Fermi surface*

1. Introduction

Various physical properties of bulk materials can be illustratively and relatively simply discussed within the framework of the free-electron model [1, 2]. On the other hand, low-dimensional systems (LDS) play an important and continuously growing role in contemporary science and technology [3–6]. Therefore, in order to discuss the physical properties of LDS, i.e. thin films (TF), quantum wires (QWr), and quantum dots (QD), it is important in the first approximation to have an extension of the free-electron model for confined structures. In such considerations, the quantum-mechanical description, and in particular the concept of a quantum well, plays a crucial role [4, 7].

The aim of this paper is to perform some model calculations of the Fermi wave vector in the framework of the free-electron approximation for the low-dimensional systems (TF, QWr, and QD). In the theoretical section, the formulae suitable for numerical calculation of the Fermi wave vector k_F for TF, QWr, and QD are given. In the final section, some tentative numerical results are presented for the model LDS with the electronic density corresponding to Cu and (100)-type surface orientation. A wider presentation of the results for TF has been given elsewhere [8].

*E-mail: t_balcerzak@uni.lodz.pl

2. Theoretical model

A thin film is considered to be a set of n monoatomic planes, perpendicular to the z axis, with each plane having its own thickness d dependent on crystallographic orientation. As a result, the total thickness of the film is given by $L_z = nd$. The lateral dimensions of the film in the x and y directions are denoted by L_x and L_y , respectively, and it is assumed that these dimensions tend to infinity. Thus, the model corresponds to a 1-dimensional quantum well, in which one-electron states are described by the normalized wave function:

$$\varphi_{k_x, k_y, \tau_z}(x, y, z) = \frac{1}{\sqrt{L_x L_y}} e^{i(k_x x + k_y y)} \sqrt{\frac{2}{L_z}} \sin\left(\frac{\pi \tau_z z}{L_z}\right) \quad (1)$$

The function represents a plane wave propagating in the (x, y) plane, with quasi-continuous wave vector components k_x, k_y and periodic boundary conditions as well as a standing wave in the z -direction that vanishes at the film surface and has a discrete wave vector $k_z = \pi \tau_z / L_z$, where $\tau_z = 1, 2, \dots$ is a mode number.

In the case of quantum wires, we deal with a 2-dimensional quantum well with lateral dimensions of $L_y = md$ and $L_z = nd$, and L_x tending to infinity. Thus, in such a case two components of the wave vector (k_y and k_z) are quantised, with corresponding $\tau_y, \tau_z = 1, 2, \dots$ and the pairs (τ_y, τ_z) numbering the 2-dimensional standing modes. Simultaneously, in a QWr the plane wave is propagating in the x -direction.

For a quantum dot we assume a 3-dimensional quantum well model represented by a box, having the lateral dimensions $L_x = pd$, $L_y = md$, and $L_z = nd$, in which only standing waves exist. A triple of natural numbers (τ_x, τ_y, τ_z) unambiguously describes a 3-dimensional standing wave mode in the quantum well.

The construction of the Fermi surface and the Fermi wave vector k_F is schematically shown in Fig. 1. In Figure 1a, the occupied electronic states for TF are shown, forming circular cross-sections from a bulk Fermi sphere, perpendicular to the k_z axis and separated by distances of π/L_z . In Figure 1b, the occupied electronic states for a QWr are presented by the bold segments, oriented parallel to the k_x axis and separated in the k_y and k_z dimensions by π/L_y and π/L_z , respectively. Finally, in Figure 1c the occupied electronic states for a QD are depicted by the bold points with the coordinates (τ_x, τ_y, τ_z) . The points are separated by distances of $\pi/L_x, \pi/L_y$, and π/L_z , in the k_x, k_y , and k_z directions, respectively. All the electronic states are contained within a sphere possessing a k_F radius. The surface of the sphere has a constant energy, whereas the quantization of the wave vector and the Pauli exclusion principle are taken into account in the occupation scheme.

For a TF, the analytical formula can be derived for the Fermi wave vector k_F [8] :

$$(k_F d)^2 = 2\pi\rho \frac{n}{\tau_F} + \frac{\pi^2}{6n^2} (\tau_F + 1)(2\tau_F + 1) \quad (2)$$

where n corresponds to the thickness of the film and ρ is a dimensionless electronic density defined by the formula $\rho = N_e d^3 / L_x L_y L_z$, where N_e is the total number of electrons in the sample. By τ_F in Eq. (2) we denote the largest natural number satisfying the inequality:

$$\rho \geq \pi \tau_F (\tau_F - 1) \frac{\left(2\tau_F + \frac{1}{2}\right)}{6n^3}$$

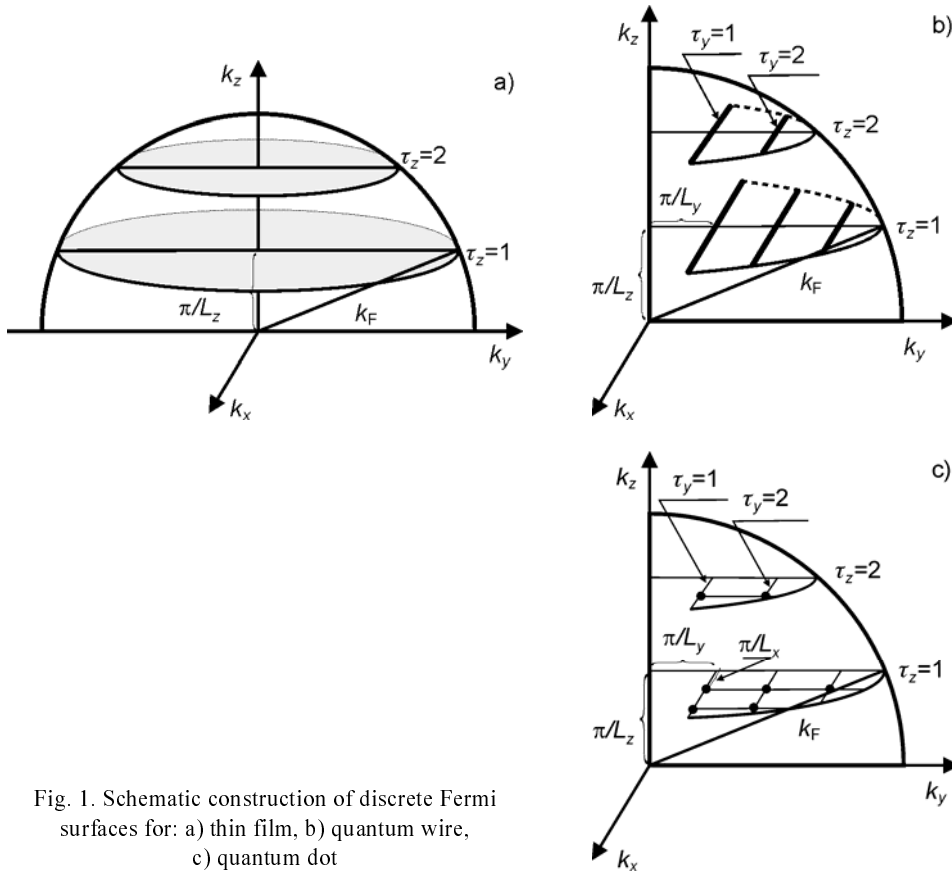


Fig. 1. Schematic construction of discrete Fermi surfaces for: a) thin film, b) quantum wire, c) quantum dot

In the case of a QWr, the Fermi wave vector is found to be of the form:

$$\pi \rho m n = 2 \sum_{\tau_y} \sum_{\tau_z} \sqrt{(k_F d)^2 - \left(\frac{\pi \tau_y}{m}\right)^2 - \left(\frac{\pi \tau_z}{n}\right)^2} \quad (3)$$

where summation over the natural numbers τ_y and τ_z should be done numerically. When performing the summation, the upper limits for τ_y and τ_z are imposed by a simple requirement that the expression under the square root in Eq. (3) must not be negative.

For a QD, the formula for k_F is the following :

$$\rho p m n = 2 \sum_{\tau_x} \sum_{\tau_y} \sum_{\tau_z} 1 \quad (4)$$

where summation over the natural numbers τ_x , τ_y , and τ_z should be performed numerically with the boundary condition: $(k_F d)^2 \geq (\pi \tau_x / p)^2 + (\pi \tau_y / m)^2 + (\pi \tau_z / n)^2$, determining the radius of summation.

3. Numerical results and discussion

Numerical results have been obtained for a prototype crystalline structure and electron density corresponding to Cu, i.e. $N_e / L_x L_y L_z = 0.085 / \text{\AA}^3$, and a (100)-type LDS surfaces. Thus, the interplanar distance is equal to $d = a/2 = 1.805 \text{ \AA}$, whereas the dimensionless electronic density ρ is 0.5. The choice of copper is connected to the view that the Fermi surface for this metal is quite similar to a spherical surface [9], therefore our model is more realistic than for other metals.

The results of calculation of the Fermi wave vector k_F are shown in Fig. 2. In Figure 2a, a decreasing tendency of k_F with increasing thickness of the film n is seen (n is the number of atomic planes). The bulk value of k_F for Cu is 1.360 \AA^{-1} , being the limit for k_F when $n \rightarrow \infty$. The results of calculation of k_F for a QWr are presented in Fig. 2b, versus the wire width m for three selected thicknesses: $n = 1$, $n = 2$, and $n = 5$. It can be seen in Fig. 2b that the most rapid changes occur for the smallest values of m and n . In Figure 2b, the limiting values of k_F for $m \rightarrow \infty$ are also depicted by the values corresponding to the results for thin films for a given n (compare with Fig. 2a).

In turn, the Fermi wave vector k_F is plotted in Fig. 2c versus the length of the QD p . Two cases are illustrated – the upper curve (for $m = n = 1$) at the $p \rightarrow \infty$ limit corresponds to the QWr result (compare with Fig. 2b for $m = 1$ and $n = 1$), and the lower curve (for $m = n = p$) describes a cubic QD. The limit for the lower curve when $p \rightarrow \infty$ corresponds to the bulk material and has the same value as in Fig. 2a.

It follows from the calculations that this simple extension of the free electron model for LDSs leads to interesting and important results, induced only by size quantization. It has been checked that by increasing the sizes of the confined structures the results for k_F become convergent. For instance, when tending with successive sizes to infinity, the results for a QD at first approach the QWr results, which in turn tend to TF results in the limit of the next infinite size. Calculations of the Fermi wave vector should be regarded as useful, since they are necessary for obtaining information about the density of states at the Fermi level, which in turn determines the electronic properties of LDSs.

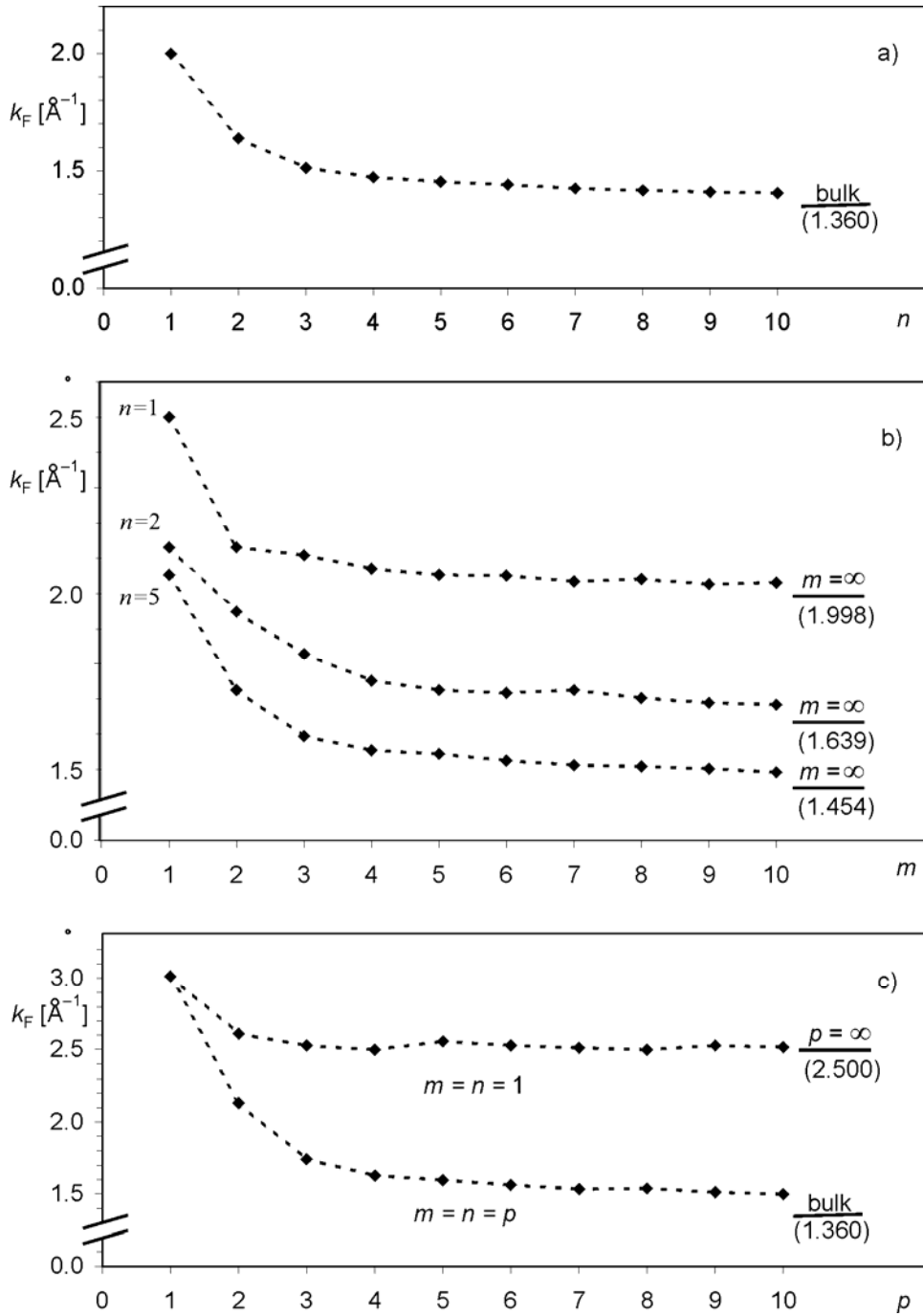


Fig. 2. The Fermi wave vector, k_F , calculated for experimental parameters corresponding to the electronic density and (100) interplanar distances of Cu: a) k_F for a TF vs. thickness n , b) k_F for a QWr vs. the wire width m , c) k_F for a QD vs. the dot length p

Acknowledgements

The author is indebted to Mrs. Teresa Rychtelska for her valuable help in the preparation of the figures.

References

- [1] BLATT F.J., *Physics of Electronic Conduction in Solids*, McGraw-Hill, New York, 1968.
- [2] KITTEL C., *Introduction to Solid State Physics*, Wiley, New York, 1996.
- [3] WEISBUCH C., BENISTY H., HOUDRÉ R., *J. Lum.*, 85 (2000), 271.
- [4] DAVIES J.H., *The Physics of Low-Dimensional Systems*, Cambridge University Press, Cambridge, 2000.
- [5] LEE E.-H., PARK K., *Mater. Sci. Eng. B*, 74 (2000), 1.
- [6] SAKAKI H., *J. Cryst. Growth*, 251 (2003), 9.
- [7] HIMPEL F.J., *J. Phys.: Condens. Matter*, 11 (1999), 9483.
- [8] BALCERZAK T., *Thin Solid Films*, 500 (2006), 341..
- [9] MERTIG I., *Rep. Prog. Phys.*, 62 (1999), 273.

Received 1 June 2005
Revised 10 October 2005

First principles calculations of zinc blende superlattices with ferromagnetic dopants

A. WRONKA*

Department of Solid State Physics, University of Łódź, Pomorska 149/153, 90-236 Łódź, Poland

Technological advances in device micro- and nano-fabrication over the past decade have enabled a variety of novel heterojunction device structures to be made in various spintronic device applications [1]. Among these, diluted and digital ferromagnetic half-metallic heterostructures and multilayers with ferromagnetic dopants exhibit a rich variety of features, with the potential for future generations of electronic devices with improved sensitivity and higher packing density. We investigate the electronic and magnetic structure of three-component Fe/MnAs/AsGa(0,0,1) thin superlattices in various supercell geometries. Calculations are performed by means of density functional theory (DFT) within the general gradient approximation with ultrasoft pseudopotentials, a plane-wave basis, and non-collinear magnetism. In our DFT calculations, we have found that the half-metallicity (HM) of MnAs/AsGa digital alloys can be destroyed by embedding Fe submonolayers.

Key words: *digital ferromagnetic heterostructure; density functional theory; half-metals*

1. Introduction

Ferromagnetic III–Mn–V semiconductors, such as (Ga, Mn)As random alloys, MnAs/GaAs digital alloys with Mn and GaAs layers grown alternately by molecular beam epitaxy, and zinc blende ferromagnetic heterostructures (FH) based on them are very promising candidates for materials that may be useful in spin electronic devices. There is evidence that the distance of spin diffusion in these semiconductors is long, with values of many microns being reported for GaAs. Mn-doped GaAs is a tetrahedrally bonded, half-metallic material that has been successfully used for spin-polarized injection into GaAs, III–V [2], and II–VI [3] semiconductors, opening the prospect of combining spin electronics and opto-electronics. Inspired by new possibilities of spin-dependent transport properties, the concept of a spin transistor has been put forward by Datta and Das [4], in which spin-polarized electrons are injected from a magnetic source, manipulated and controlled before they are collected at the mag-

*E-mail: awronka@uni.lodz.pl

netic drain. In these types of devices, not only the charge properties of the electrons are used, but also the fact that the electron has a spin degree of freedom.

The suggested applications include, e.g. “spin-field-effect-transistors” [4] which could allow software re-programming of microprocessor hardware during run-time, semiconductor-based “spin-valves” [5] which would result in high density, non-volatile semiconductor memory chips, and even “spin qubits” [6] to be used as basic building blocks for quantum computing.

Mn/GaAs superlattices [7] have remarkable properties in comparison to random (Ga,Mn) alloys. The Curie temperature of the alloy system is a linear function of Mn concentration, what can be described in the first approximation by the Zener model [8]. The solubility limit of Mn in GaAs is rather low, but large Mn concentrations, up to 50%, can be obtained in the MnAs/GaAs superlattice with MnAs submonolayers embedded into GaAs. The Curie temperature decays for increasing GaAs interlayer thickness for these structures, but saturates at thicknesses above ~ 50 GaAs monolayers (ML) [7], which is unexpected in the three dimensional Zener model and suggests that digital ferromagnetic heterostructures behave like planar systems [9] and magnetic interactions are confined to the MnAs layers. Theoretical *ab initio* calculations of thin superlattices of zinc blende compounds have been performed in the framework of density functional theory (DFT) by several authors [10, 11].

2. Method of calculation

In this paper, we intended to extend first-principle calculations to describe the magnetic moment distribution of a zinc blende multilayer and heterostructure with Mn and Fe dopants. Non-collinear magnetism and augmented plane wave (APW) methods [12], based on the total energy calculations implemented in the PWscf *ab initio* package [13], were used. The energies and atomic magnetic moments were calculated by total energy minimisation, using plane wave, Vanderbilt-type ultrasoft pseudopotentials (US-PPs) [14] as an approximation to the core-valence interaction based on DFT [15] in the general gradient approximation (GGA) [16]. Spin polarized calculations were carried out to account for different spin channels. A kinetic energy cut-off of 30 Ry was used for the plane waves included in the basis set. A $16 \times 16 \times 1$ Monkhorst-Pack [17] plane k -point mesh was used for the wave vector summation to the multilayer slab, and for the digital alloy MnAs/(GaAs) heterostructure a $8 \times 8 \times 6$ k -mesh was implemented. We used a supercell model, with a zinc blende (ZB) tetragonal unit cell with $a_0/(2)^{1/2}$ in the a and b directions. The GGA-optimised lattice constant of GaAs ($a_0 = 5.722 \text{ \AA}$) was used for all calculations. We have performed non-collinear magnetism calculations to evaluate the influence of the alloy electronic structure on the magnetization of ferromagnetic impurities (Mn and Fe monolayers).

We study the magnetic and electronic properties of zinc blende digital heterostructures with Mn and Fe planar impurities in DFT calculations. We consider three supercell geometries for DFT, with the relative atomic positions described in Table 1: a 14-atom super-

cell (1–14) for the Fe/Ga_{0.5}Mn_{0.5}As/AsGa/Ga_{0.5}Mn_{0.5}As/Fe multilayer (slab) with 3 AsGa ML of vacuum to isolate this supercell from others; a 13-atom supercell (2–14) for the heterostructure Ga_{0.5}Mn_{0.5}As/AsGa/Ga_{0.5}Mn_{0.5}As/Fe; a 12-atom supercell (2–13) for the heterostructure Ga_{0.5}Mn_{0.5}As/AsGa/Ga_{0.5}Mn_{0.5}As with no Fe submonolayers. By Ga_{0.5}Mn_{0.5}As we denote a 4-atom region of a GaAs unit with a MnAs monolayer. We use 0.5 ML, with Mn substituting Ga (because only 0.5 ML of Mn can be deposited by the MBE technique) and 0.5 ML of Fe atoms placed on As/Ga positions.

3. Results

In the first step, we obtained the atomic magnetic moment and electron charge distributions for the thin ZB superlattice and multilayer by means of non-collinear DFT calculations, as displayed in Table 1.

Table 1. The supercell relative atomic positions, magnetization distribution, and charge for the Fe/Ga_{0.5}Mn_{0.5}As/AsGa/Ga_{0.5}Mn_{0.5}As/Fe multilayer (upper values of magnetization and charge for atomic positions 1–14), and the Ga_{0.5}Mn_{0.5}As/AsGa/Ga_{0.5}Mn_{0.5}As/Fe superlattice (positions 2–14)

Atom number	Element	Relative position			Magnetization [μ_B]			Charge [a. u.]
		x	y	z	M_x	M_y	M_z	
1	Fe	0.0	0.0	-0.3536	1.007	0.000	0.001	4.345
2	As	0.0	0.0	0.0	-0.007	0.000	0.000	0.549
3	Mn	0.5	0.5	0.3536	3.879	0.000	0.000	10.091
					3.791	0.000	-0.006	10.079
4	As	0.5	0.5	0.7071	-0.020	0.000	0.000	0.587
					-0.021	0.000	0.000	0.585
5	Ga	1.0	1.0	1.0607	0.003	0.000	0.001	8.708
					-0.001	0.000	0.001	8.708
6	As	0.0	0.0	1.4142	0.003	0.000	0.000	0.564
					-0.001	0.000	0.001	0.567
7	Ga	0.5	0.5	1.7678	0.003	0.000	0.000	8.712
					0.001	0.000	0.000	8.711
8	As	0.5	0.5	2.1213	0.003	0.000	0.000	0.564
					0.000	0.000	0.000	0.565
9	Ga	1.0	1.0	2.4749	0.006	0.000	0.000	8.710
					0.004	0.000	0.000	8.710
10	As	0.0	0.0	2.8284	0.004	0.000	0.000	0.563
					0.003	0.000	0.000	0.562
11	Mn	0.5	0.5	3.1820	4.038	0.000	-0.002	10.090
					3.814	0.000	0.003	10.100
12	As	0.5	0.5	3.5355	-0.013	0.000	0.000	0.583
					-0.017	0.000	0.000	0.582
13	Ga	1.0	1.0	3.8891	0.018	0.000	0.000	8.696
					0.002	0.000	0.000	8.692
14	Fe	1.0	1.0	4.2426	1.531	0.000	0.008	4.363
					0.711	0.000	0.008	4.602

The calculated local magnetic moment lies on the x -axis and is ca. $4.0\mu_B$ for the multilayer and ca. $3.8\mu_B$ for the heterostructure. These results are in good agreement with the magnetic moment of $5\mu_B$ for free Mn atoms, which is reduced in the lattice since Mn acts as an acceptor. Larger differences appear for the magnetic moments of Fe atoms, which are surface atoms for the multilayer (ca. 1.0 and $1.5\mu_B$) and submonolayers for the superlattice (ca. $0.7\mu_B$). The atomic charges are very close for both structures. These results suggest that Mn dopants dominate the magnetic properties of the studied systems, but Fe atomic planes can be considered to be good metallic contacts in the case of multilayers.

In the next step, we performed spin polarized GGA calculations to evaluate the influence of Fe impurities on the electronic structure of the $\text{Ga}_{0.5}\text{Mn}_{0.5}\text{As}/\text{AsGa}/\text{Ga}_{0.5}\text{Mn}_{0.5}\text{As}/\text{Fe}$ heterostructure as compared to the $\text{Ga}_{0.5}\text{Mn}_{0.5}\text{As}/\text{AsGa}/\text{Ga}_{0.5}\text{Mn}_{0.5}\text{As}$ superlattice. The band structure calculated for that heterostructure seems to confirm the results described in Ref. [11], and the band dispersion in the direction perpendicular to the MnAs plane normal is very narrow, suggesting a two-dimensional electron transport system with small hopping between MnAs planes. The main results of the calculations are the densities of states (DOS) in the total and partial figure, projected onto ferromagnetic Mn and Fe atoms and 3d states for majority and minority spins.

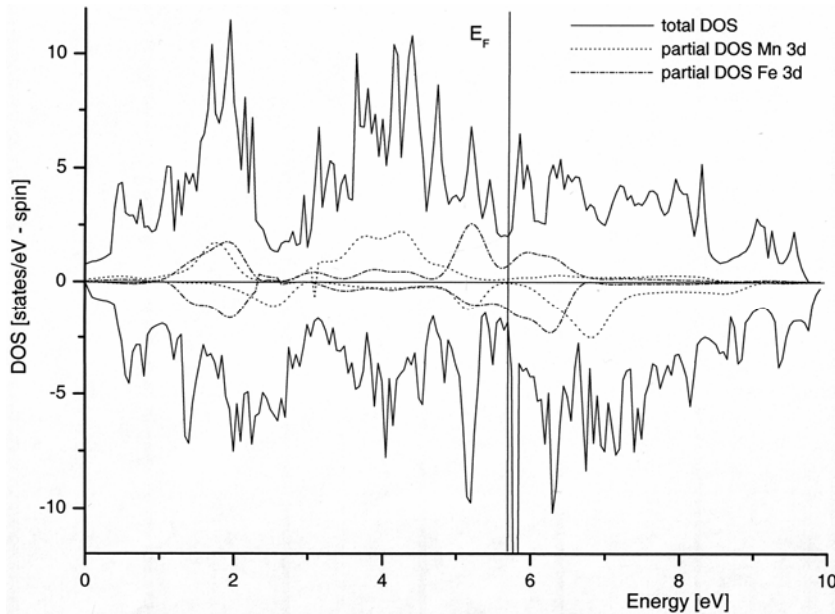


Fig. 1. Total DOS and partial DOS projected onto the Mn/Fe 3d states of the $\text{Ga}_{0.5}\text{Mn}_{0.5}\text{As}/\text{AsGa}/\text{Ga}_{0.5}\text{Mn}_{0.5}\text{As}/\text{Fe}$ heterostructure for the majority and minority spin channel

In the $\text{Ga}_{0.5}\text{Mn}_{0.5}\text{As}/\text{AsGa}/\text{Ga}_{0.5}\text{Mn}_{0.5}\text{As}/\text{Fe}$ superlattice (Fig. 1), both majority and minority total DOSs are nonzero at the Fermi energy level and the system has DOS features typical of ferromagnetic metals. Although the minority partial DOS for Mn

3d states is zero at the Fermi level, half-metallicity is destroyed by Fe 3d states at the Fermi level.

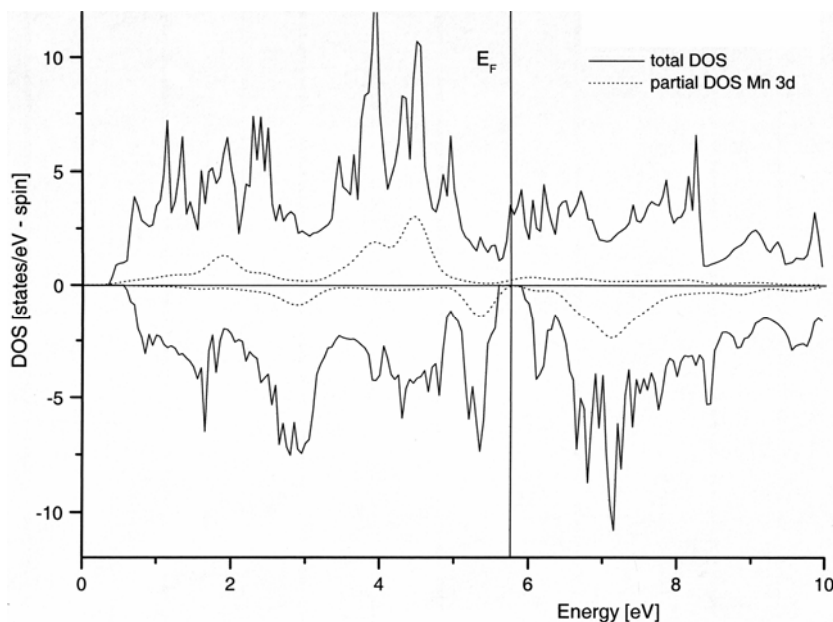


Fig. 2. Total DOS and partial DOS projected onto the Mn 3d states of the $\text{Ga}_{0.5}\text{Mn}_{0.5}\text{As}/\text{AsGa}/\text{Ga}_{0.5}\text{Mn}_{0.5}\text{As}$ superlattice for both majority and minority spin

It can be seen in Fig. 2 that the minority spin DOS at E_F has a small semiconductor gap of ca. 0.3 eV, but no such gap exists in the majority spin channel in the case of the $\text{Ga}_{0.5}\text{Mn}_{0.5}\text{As}/\text{AsGa}/\text{Ga}_{0.5}\text{Mn}_{0.5}\text{As}$ digital alloy. The mechanism of ferromagnetism for MnAs/GaAs digital alloys remains unclear in general [9], partly because of the large range of hole concentrations and the complexity of Mn/carrier interactions [18]. The metallic majority spin DOS at E_F is composed largely of As p states, suggesting that hole doping at the top of the valence band by Mn^{2+} 3d ions, and subsequent polarization of mobile charge carriers by interaction with exchange split energy levels Mn 3d, is responsible for the half-metallicity in this case.

4. Summary

In this article we have studied the electronic and magnetic properties of thin zinc blende superlattices with ferromagnetic dopants by DFT methods based on ultrasoft pseudopotentials. These fast DFT ultrasoft pseudopotential calculations can be competitive and complementary to relatively slow all-electron DFT calculations [19]. The DFT non-collinear magnetism technique exactly shows the magnetization localized on supercell atoms in Fe/MnAs/AsGa(0,0,1) multilayers and MnAs/AsGa(0,0,1) super-

lattices. These calculations are in good agreement with spin polarized GGA calculations for the studied zinc blende heterostructures. We suggest that Fe submonolayers in these systems can destroy the half-metallicity of MnAs/AsGa digital alloys.

In summary, we have shown that DFT *ab initio* calculations lead to a correct description of the magnetic and electronic properties and can be used to theoretically identify half-metallicity in zinc blende superlattices with ferromagnetic dopants and other spintronic materials.

References

- [1] ŽUTIĆ I., FABIAN J., DAS SARMA S., Rev. Mod. Phys., 76 (2004), 323.
- [2] OHNO Y., YOUNG D.K., BESCHOTEN B., MATSKURA F., OHNO H., AWSCHALOM D.D., Nature, 402 (1999), 790.
- [3] FIEDERLING R., KEIM M., REUSCHER G., OSSAU W., SCHMIDT G., WANG A., MOLENKAMP L.W., Nature, 402 (1999), 787.
- [4] DATA S., DAS B., Appl. Phys. Lett., 56 (1990), 665.
- [5] PRINZ G., Science, 282 (1998), 1660.
- [6] BURKARD G., LOSS D., DIVINCENZO D.P., Phys. Rev. B, 59 (1999), 2070.
- [7] KAWAKAMI R.K., JOHNSON-HALPERIN E., CHEN L.F., HANSON M., GUEBELS N., SPECK J.S., GOSSARD A.C., AWSCHALOM D.D., App. Phys. Lett., 77 (2000), 2379.
- [8] DIETL T., OHNO H., MATSUKURA F., CIBERT J., FERRAN D., Science, 287 (2000), 1019.
- [9] SANVITO S., HILL N.A., Phys. Rev. Lett., 87 (2001), 267202.
- [10] QIAN M.C., FONG C.Y., PICKETT W.E., PASK J.E., YANG L.H., DAG S., Phys. Rev. B, 71 (2005), 012414.
- [11] SANVITO S., Phys. Rev. B, 68 (2003), 054425.
- [12] GEBAUER R., BARONI S., Phys. Rev. B, 61 (2000), R6459.
- [13] BARONI S., DE GIRONNOLI S., DAL CORSO A., GIANNOZI P., Rev. Mod. Phys., 73 (2001), 515.
- [14] VANDERBILT D., Phys. Rev. B, 41 (1990), 7892.
- [15] HOHENBERG P., KOHN W., Phys. Rev., 136 (1964), B864.
- [16] PERDEW J.P., BURKE K., ERNZERHOF M., Phys. Rev. Lett., 77 (1996), 3865.
- [17] MONKHORST H.J., PACK J.D., Phys. Rev. B, 13 (1976), 5188.
- [18] KAMINSKI A., DAS SARMA S., Phys. Rev. Lett., 88 (2002), 247202.
- [19] WRONKA A., Acta Physicae Superficierum, 7 (2004), 111.

Received 1 June 2005

Revised 10 October 2005

The influence of effective mass on magnetoresistance in ultrathin Fe/Cr/Fe films

K. WARDA^{1*}, L. WOJTCZAK¹, D. BALDOMIR², M. PEREIRO², J. ARIAS²

¹Solid State Physics Department, University of Łódź, Pomorska 149/153, 90-236 Łódź, Poland

²Departamento de Física Aplicada, Universidad Santiago de Compostela,
15782 Santiago de Compostela, Spain

The transport properties of ultrathin metallic sandwich structures of Fe/Cr/Fe are studied as a function of magnetic layer thickness for the current in plane geometry (CIP). Taking into account the band structure obtained from density functional theory (DFT), we calculate basic physical properties such as Fermi energy and relaxation time for each magnetic and spacer layer. Next, using the Boltzmann formalism in its extended form, we obtain results for magnetoresistance (MR). In particular, we analyse the influence of effective mass parameterisation.

Key words: *magnetoresistance; multilayer; Boltzmann equation; effective mass of electrons*

1. Introduction

Progress in the fabrication of very thin magnetic layers separated by non-magnetic films has led to the discovery of giant magnetoresistance (GMR). This effect was originally discovered in Fe/Cr/Fe multilayers [1, 2]. GMR is the change of electrical resistance observed when rotating from an antiparallel to parallel alignment of film magnetizations. For its description, two different approaches are usually used: the quasi-classical method based on the Boltzmann equation [3–5] or the quantum-mechanical Kubo formalism [6].

Most of models are idealized and do not take into account the details of the materials or the finite sample size. It is a well known fact that for a very thin layer the basic physical quantities connected with transport, such as the Fermi energy, effective mass, and relaxation time of electrons, depend on the boundary conditions at the surface. A precise description of transport in such a system is very important from the technological point of view, but requires a proper set of parameters describing the multilayered structure to be determined.

*Corresponding author, e-mail: Kwarda@mvii.uni.lodz.pl

In our earlier work [7], we have determined the electronic structure and layer potentials in a Fe/Cr/Fe trilayer, as well as the Fermi energy characterizing the system. These data are used in the present paper to determine the effective mass of electrons and to analyse its influence on GMR.

2. Model description

A proper choice of potentials for the trilayer plays a very important role in GMR calculations. The electronic structure, as well as the magnetic properties of the $\text{Fe}_N/\text{Cr}/\text{Fe}_N$ trilayer (N is the number of atomic layers) have been widely studied using density functional theory (DFT) in the local spin approximation [7]. We consider the transport properties in magnetic multilayers for electronic current in the layers parallel to the surface of the sample.

GMR is then determined by the relation $MR = (\sigma_{\uparrow\uparrow} - \sigma_{\uparrow\downarrow}) / \sigma_{\uparrow\uparrow}$, where the conductivity of the trilayer sample is given by the formula

$$\sigma_{\uparrow,\uparrow(\downarrow)} = \frac{1}{d} \sum_{\sigma\nu} \int_{(\nu-1)a}^{\nu a} \sigma_{\uparrow,\uparrow(\downarrow)}^{\nu\sigma}(z) dz \quad (1)$$

for the parallel $\sigma_{\uparrow\uparrow}$ or antiparallel $\sigma_{\uparrow\downarrow}$ configurations of magnetization in iron layers, while in terms of the Hood and Falicov approach the local conductivity can be introduced in the form

$$\sigma_{\uparrow,\uparrow(\downarrow)}^{\nu\sigma}(z) = -e^2 \left(\frac{m_\sigma^*}{h} \right)^3 \tau_{\nu\sigma} \int d^3\nu (\nu^x)^2 \frac{\partial f_{\nu\sigma}^0}{\partial E_{\sigma}^{\uparrow,\uparrow(\downarrow)}} \left(1 + F_{\sigma}^{\uparrow,\uparrow(\downarrow)}(\nu) e^{\mp \frac{z}{\tau_{\nu\sigma} |\nu^z|}} \right) \quad (2)$$

where the symbols have their usual meanings as described in [8].

Besides fundamental quantities such as electron charge and Planck's constant, we need to determine the effective mass of the electron m_σ and the relaxation time $\tau_{\nu\sigma}$ considered in each monatomic layer. DFT calculations allow us to obtain these constants on the basis of the electronic structure of a sample by means of the density of states and the Fermi level, which determines the effective potentials for electrons with oriented spins.

The conductivity given by (2) is derived using the semi-classical Boltzmann equation for the distribution function $f_{\nu\sigma} = f_{\nu\sigma}^0 + g_{\nu\sigma}$, where $f_{\nu\sigma}^0$ is the equilibrium distribution function for electrons with spin σ appearing in the layer ν in the absence of any electric field E , while $g_{i\sigma}$ contributes to the Boltzmann distribution by the influence of the electric field. Next, we can see that we should determine the integral constants $F_{\sigma}^{\uparrow,\uparrow(\downarrow)}$ appearing in Eq. (2) in a way that allows us to satisfy the matching conditions for the Boltzmann functions $f_{\nu\sigma}$ at the interfaces between ferromagnetic and

spacer films. The construction of these matching conditions is presented in [9]. The results depend on the specular factors P_σ , considered at the outer surfaces and connected to surface roughness. In order to extend our considerations to a more realistic case from the physical point of view, we define the specular factor P_σ using the physical pictures of electrons moving through a potential barrier. In this case, the value of P_σ corresponds to the specular factor in the Fuchs–Sondheimer [9] conductivity theory of thin films and can be expressed by the effective result

$$P_\sigma = \left(1 - \frac{(\chi_F^\sigma)^2 \cos^4 \theta + 2}{1 + (\chi_F^\sigma)^2 \cos^4 \theta} \right) \left(1 - \frac{(\chi_F^\sigma)^2 \cos^4 \theta + 2}{1 + (\chi_F^\sigma)^2 \cos^4 \theta} \exp \left(-\frac{\frac{d}{\tau_\sigma v^2}}{\cos \theta} \right) \right)^{-1} \quad (3)$$

which is an alternative to other models, assuming that the coefficients for coherent transmission and specular reflections are determined in quantum mechanics by matching free electron wave functions at each interface [10]. The constant χ_F^σ is defined in terms of the Fermi velocity v_F , where m_σ is the effective mass of electrons and the relaxation time τ_σ is taken for electrons at the surface, i.e. $\tau_\sigma = \tau_{1\sigma}$ or $\tau_\sigma = \tau_{N\sigma}$. This parameter is determined from DFT. From the physical point of view, the constant χ_F^σ represents the ratio of the electron free path and de Broglie wavelength, and is related to the angle of incidence of electrons with respect to the z -axis as $\chi_F^\sigma = (2m_\sigma \tau_\sigma v_F^2)/\hbar$. The relaxation time can be evaluated in terms of DFT calculations by means of the Fermi golden rule. The relaxation time can be expressed as follows [11]:

$$(\tau_{v\sigma})^{-1} = 2\pi c \rho(E_F) (V_{v\sigma})^2 \quad (4)$$

i.e., it is determined by the parameters of the potential barrier, in particular by the shape of the density of states at the Fermi level. In Eq. (4), c is the number of scattering centres and plays the role of a calibration factor when comparing the obtained relaxation time with the average values discussed in literature [8, 11].

3. Results

The dependence of GMR on the number of ferromagnetic monatomic layers N in a trilayer $\text{Fe}_N/\text{Cr}/\text{Fe}_N$ with a fixed spacer thickness of $d_s = 4.32 \text{ \AA}$ is shown in Fig.1 for various effective electron masses. The calculations were performed using the matching conditions $V_M = -8.23 \text{ eV}$, $V_m = -5.73 \text{ eV}$, $V_S = -5.77 \text{ eV}$; V_M , V_m , V_S corresponding to the potential barriers for majority and minority spins in the ferromagnetic layer and the spacer, respectively, and the relaxation time for electrons $\tau = 5 \times 10^{-13} \text{ s}$ in the case of the Hood–Falicov approach [8] to describe GMR.

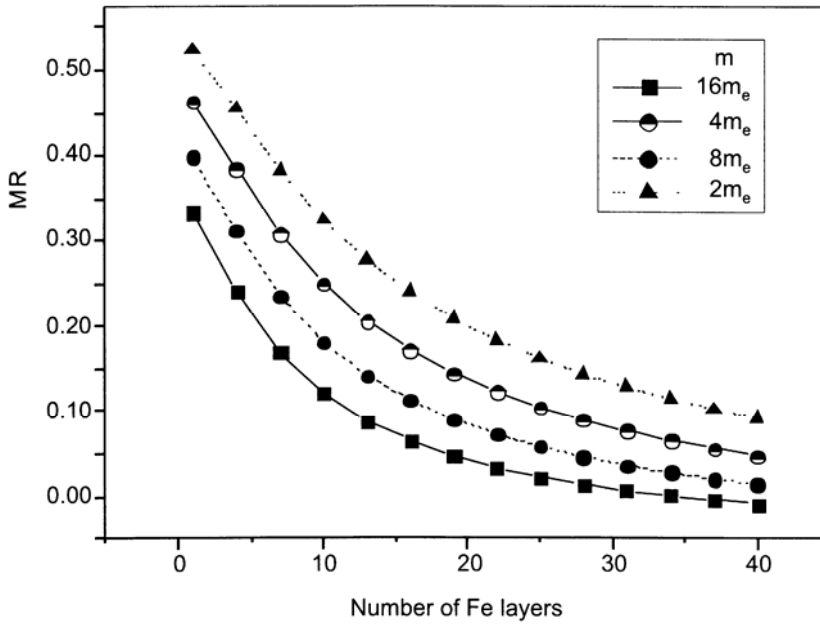


Fig. 1. Ratio of GMR and the number of ferromagnetic monolayers for four effective electron masses. The calculations are based on the theoretical model described in [9], with the following parameterisation: potentials: $V_M = -8.23$ eV, $V_m = -5.73$ eV, and $V_S = -5.77$ eV, relaxation time $\tau = 5 \times 10^{-13}$ s

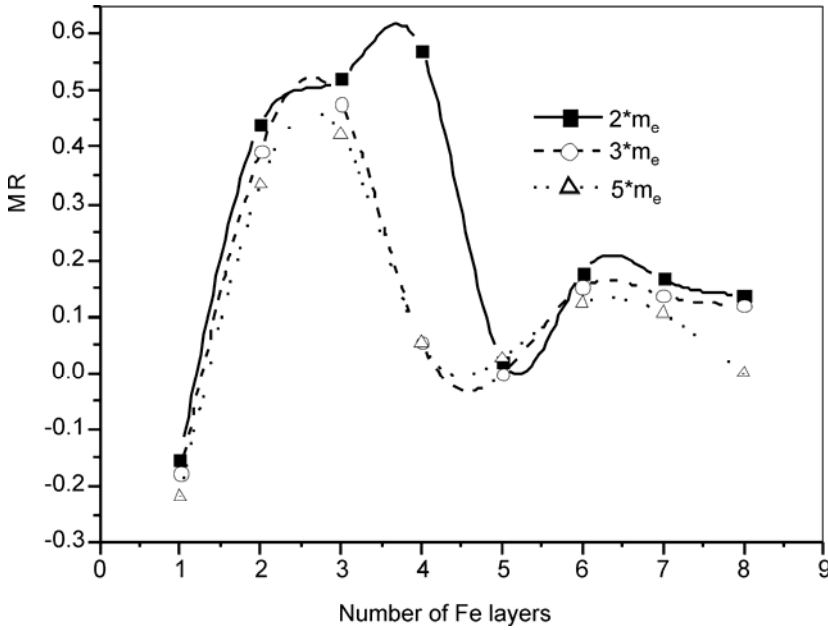


Fig. 2. GMR ratio as a function of the number of ferromagnetic layers for three effective electron masses in the Fe/Cr/Fe trilayer. All the parameters used in calculations were determined from DFT [7]

The GMR results shown in Fig. 2 are obtained for three different effective masses and parameters taken from the DFT calculations. It is worthwhile to notice that the DFT parametrisation curves oscillate with varying amplitude, while the character of these oscillations depends on the effective mass. In particular, when we compare the upper curve in Fig. 1 (dotted line), obtained by means of the Hood–Falicov approach ($m^* = 2m_e$), with the curve in Fig. 2 (solid line) for the same effective mass ($m^* = 2m_e$), we can see that the appearance of oscillations is connected to the fact that DFT calculations are used. From the physical point of view, these calculations include band parameterisation as well as the geometry of the considered system. The band structure departs from its quasi-free particle behaviour and the method conserves the shape of the dispersion law, while the effective mass parameterisation now depends on the wave vector distribution, effectively leading to a change in the dispersion law. Thus, the effective mass m^* applied in the case of the Hood–Falicov approach is equivalent to the coefficient m^* ($k = 0$) appearing in the DFT representation.

In the above context, we can conclude that the most important results obtained in the present paper are the oscillatory character of GMR in $\text{Fe}_N/\text{Cr}/\text{Fe}_N$ with respect to the number of Fe layers and that the source of these oscillations is connected to the shape of the energetic bands, which are described by boundary conditions directly related to the geometry of the considered sample and included immanently in DFT calculations.

References

- [1] BAIBICH M., BROTO N.J.M., FERT A.F., VAN DAU N., PETROFF F., ETIENNE P., CREUZET G., FRIEDERICH A., CHAZELAS J., *Phys. Rev. Lett.*, 61 (1988), 2472.
- [2] BINASCH G., GRUNBERG P., SZAURENBACH F., ZINN W., *Phys. Rev. B*, 39 (1989), 4828.
- [3] BARNAŚ J., FUSS A., CAMLEY R., GRUMBERG P., ZINN W., *Phys. Rev. B*, 42 (1990), 8110.
- [4] CAMLEY R., BARNAŚ J., *Phys. Rev. Lett.*, 63 (1989), 664.
- [5] HOOD R., FALICOV L., *Phys. Rev. B*, 46 (1992), 8287.
- [6] LEVY P., ZHANG S., FERT A., *Phys. Rev. Lett.*, 65 (1990), 1643.
- [7] PEREIRO M., BALDOMIR D., MANKOVSKY S., WARDA K., ARIAS J., WOJTCZAK L., BOTANA J., submitted to *J. Phys. Cond. Matt.*
- [8] HOOD R.Q., FALICOV L.M., *Phys. Rev. B*, 46 (1990), 8287.
- [9] WARDA K., WOJTCZAK L., WIATROWSKI G., BALDOMIR D., PEREIRO M., ARIAS J.E., *Acta Phys. Superfic.*, 7 (2004), 171.
- [10] FUCHS K., *Proc. Cambridge Philos. Soc.*, 34 (1938), 100; SONDEHEIMER E.H., *Adv. Phys.*, 1 (1952) 1.
- [11] KUBLER J., *Theory of Itinerant Electron Magnetism*, Clarendon Press, Oxford, 2000.

Received 1 June 2005
Revised 10 October 2005

Complex magnetic phenomena in f-electron intermetallic compounds

A. SZYTUŁA*

M. Smoluchowski Institute of Physics, Jagiellonian University, Reymonta 4, 30-059 Cracow, Poland

Various aspects of the magnetic properties of lanthanide and actinide intermetallic compounds are discussed. The first part deals with 1:2:2 stoichiometry compounds. The temperature dependence of magnetic ordering type is discussed. The electronic structures of the investigated compounds are then presented. The third part of the paper concentrates on magnetically hard intermetallics.

Key words: *f-electron intermetallic; magnetic properties; electronic structure*

1. Introduction

During last 25 years, the properties of lanthanide and actinide intermetallics have been extensively investigated from the point of view of both applications and fundamental research. Lanthanides and actinides are representatives of two families that develop the f-electron shell. The physical properties of these compounds deserve vast interest, because of their intriguing fundamental properties resulting from electronic structure and wide applications. The latter reason obviously concerns only lanthanides.

Investigations of lanthanide intermetallics started about four decades ago when lanthanide elements were separated. Neutron diffraction experiments for pure elements indicate complex magnetic structures [1]. Those experimental data led to the development of theoretical models of magnetic interactions in lanthanide metals [2]. Systematic investigations of binary and ternary lanthanide compounds have been performed. These investigations provided lots of new results that were interesting for the fundamental aspects of magnetism, such as crystalline electric field, exchange interactions, magnetoelastic and quadrupolar coupling, etc.

The impact for starting fundamental research on 5f electron materials was doubtlessly the determination of the ferromagnetic properties of UH_3 and UD_3 [3] and the detection of the superconducting state in UBe_{12} [4]. Special attention has been given

*E-mail: szytula@if.uj.edu.pl

to ternary compounds. For example, ternary compounds based on transition metals show physical properties different than binary compounds. The synthesis performed using the Pauli paramagnetic compounds CoTi and CoSi results in the strongly ferromagnetic compound Co_2TiSn , with T_C close to room temperature [5].

In the course of investigating the physical properties of binary and ternary lanthanide and uranium phases, a number of new effects have been either discovered or confirmed. Effects such as mixed valence, Kondo lattice spin fluctuations, heavy fermions, and the coexistence of magnetism and superconductivity were found to depend on the electronic structure of lanthanide and uranium ions, in particular they are strongly related to the position of the 4f or 5f electron levels with respect to the Fermi energy. Rare earth intermetallics play an important role in a large part of current research that concerns new magnetostrictive and permanent magnetic materials, spin glass, and random anisotropy systems.

This work concentrates on the magnetic properties of ternary compounds containing 4f electron (rare earth) or 5f electron (actinides) elements (denoted as M), transition metals (denoted as T), and fourth or fifth group elements (denoted as X).

2. Ternary intermetallic

Intermetallic compounds are formed according to the thermodynamic stability of a certain type of crystal structure but quantum chemistry is unable to predict their existence. Phase equilibrium has been investigated only for a small number of possible ternary combinations M–T–X [6]. A typical ternary phase diagram for M–Rh–Si systems (where R is a rare earth element) is shown in Fig. 1. It contains seven phases

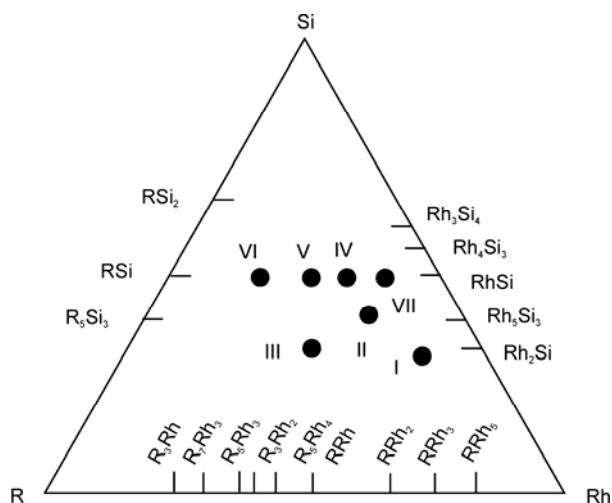


Fig. 1. Ternary rare earth–rhodium–silicon phase diagram [6]:

I – RRh_3Si_2 , II – RRh_2Si_2 , III – RRhSi , IV – $\text{R}_2\text{Rh}_3\text{Si}_5$,

V – RRhSi_2 , VI – R_2RhSi_3 , VII – $\text{R}_5\text{Rh}_4\text{Si}_{10}$

with different compositions and crystal structures. The structural, magnetic, and superconducting properties of these systems are summarized in Table 1.

Table 1. Crystallographic, magnetic, and superconductive data of ternary silicides in R–Rh–Si systems¹

Element	I	II	III	IV	V	VI
	RRh ₃ Si ₂	RRh ₂ Si ₂	RRhSi	R ₂ Rh ₃ Si ₅	RRhSi ₂	R ₂ RhSi ₃
	Structure type					
	hexagonal	tetragonal	orthorhombic			hexagonal
CeCo ₃ B ₂ (<i>P6/mmm</i>)	ThCr ₂ Si ₂ (<i>I4/mmm</i>)	NiTiSi (<i>Pnma</i>) or cubic ZrOS (<i>P2₁3</i>)	Sc ₂ Co ₃ Si ₅ (<i>Ibam</i>)	CeNiSi ₂ (<i>Cmcm</i>)	(<i>P62c</i>)	
La		S $T_s = 7.4$ K	S $T_s = 4.4$ K	S $T_s = 4.5$ K	S $T_s = 3.4$ K	
Ce		AF $T_N = 36$ K				AF $T_N = 6$ K
Nd	P	AF $T_N = 56$ K		AF $T_N = 2.7$ K		F $T_C = 15$ K
Sm	F $T_C = 34$ K	AF $T_N = 46$ K		P		
Eu		AF $T_N = 25$ K				
Gd	F $T_C = 31$ K	AF $T_N = 98$ K	F $T_C = 18.5$	AF $T_N = 8.4$ K	AF $T_N = 20.5$ K	AF $T_N = 14$ K
Tb	F $T_C = 37$ K	AF $T_N = 94$ K	AF $T_N = 28$ K	AF $T_N = 7.8$		AF $T_N = 11$ K
Dy	F $T_C = 29$ K	AF $T_N = 55$ K	AF $T_N = 14.6$ K	AF $T_N = 4.5$ K		AF $T_N = 6.3$ K
Ho	AF $T_N = 10$ K	AF $T_N = 27$ K	AF $T_N = 8.5$ K	AF $T_N = 2.8$ K		AF $T_N = 5.2$ K
Er	F $T_C = 24$ K	AF $T_N = 12.8$ K	AF $T_N = 8.1$ K	AF $T_N = 2.6$ K		AF $T_N = 5.0$ K

¹S – superconductor, P – paramagnetic, F – ferromagnetic, AF – antiferromagnetic.

These data and data for other systems indicate that the intermetallic $M_nT_mX_p$ phases have been found to exhibit not only a wide composition range ($n:m:p$), but also a large variety of crystal structures. The structural characteristics of ternary intermetallic rare-earth compounds were presented in a review paper [7]. Among $M_nT_mX_p$ compounds, only the phases with a 1:2:2 ratio were systematically studied. Based on the data for these systems, the magnetic properties of intermetallic compounds are discussed here. The lanthanide and actinides compounds with a 1:2:2 stoichiometry crystallize in two variants, in a body-centred tetragonal structure (space group *I4/mmm*, ThCr₂Si₂ type) or in a primitive tetragonal structure (space group *P4/nmm*, CaBe₂Ge₂ type). Both crystal structures are shown in Fig. 2. The atomic framework of both structures can be alternatively displayed as a monatomic sequence perpendicular to the *c*-axis:

- for the ThCr_2Si_2 -type structure:



- and for the CaBe_2Ge_2 -type structure:



The layered character and anisotropy ($c/a \approx 2.5$) of the crystal structure of these compounds is strongly reflected in their magnetic properties.

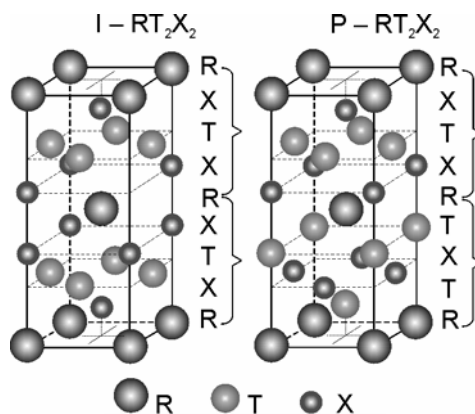


Fig. 2. Crystal structures of MT_2X_2 compounds of the ThCr_2Si_2 - and CaBe_2Ge_2 -type

The results of investigations indicate that the T component carries no magnetic moment in most compounds, except for those with Mn. In MMn_2X_2 ($\text{X} = \text{Si}, \text{Ge}$) compounds, the Mn moments order at high temperatures, while the rare earth moments usually order antiferromagnetically or ferromagnetically at low temperatures.

Data on the magnetic properties, including magnetic structure, are presented in Refs. [8–11]. In this work, only some data concerning the magnetic ordering of rare earths are presented. The results of neutron diffraction measurements indicate that rare earth sublattices exhibit a large variety of magnetic ordering schemes, including collinear ferro- and antiferromagnetic structures, as well as a number of different non-collinear modulated structures (see Fig. 23 in Ref. [8]). In this work, these structures are briefly discussed as functions of temperature, magnetic field, and pressure.

In some RT_2X_2 compounds, similarly to other rare earth intermetallics, a change in magnetic structure with temperature is observed [12]. For example, in RCO_2X_2 ($\text{R} = \text{Pr}, \text{Nd}, \text{Tb}, \text{Dy}, \text{Ho}$; $\text{X} = \text{Si}, \text{Ge}$) the rare earth moments form a collinear antiferromagnetic structure of the AFI type [8]. On increasing temperature, a change in the magnetic structure to a long-period modulated structure is observed (see Table 2). The occurrence of incommensurate phases results from competition between the indirect RKKY exchange, responsible for long-range magnetic ordering, and the crystalline

field anisotropy that might promote uniaxial arrangements. Magnetization as a function of the applied magnetic field gives evidence of phase transitions and new magnetic data. On the basis of these data, the magnetic phase diagram of these compounds is presented (see Fig. 3).

Table 2. Magnetic data for $M_2T_2X_2$ compounds

Compound	Magnetic ordering	Reference
PrCo ₂ Si ₂	1.5 K < T < 9 K AFI, 9 K < T < 17 K LSWI ($k_z = 0.074$) 17 K < T < 30 K LSWI ($k_z = 0.223$)	[a]
PrCo ₂ Ge ₂	1.5 K < T < 28 K, LSWI ($k_z = 0.27$)	[b]
NdCo ₂ Si ₂	1.5 K < T < 15 K AFI, 15 K < T < 24 K, LSWI ($k_z = 0.07$), 24 K < T < 32 K LSWI ($k_z = 0.20$)	[c]
NdCo ₂ Ge ₂	1.5 K < T < 12 K AFI, 12 K < T < 28 K LSWI ($k_z = 0.261$)	[d]
TbCo ₂ Si ₂	1.5 K < T < 43.5 K AFI, 43.5 K < T < 45.5 K LSWI ($k_z = 0.042$)	[e]
TbCo ₂ Ge ₂	1.5 K < T < 29.1 K AFI, 29.1 K < T < 34 K LSWI ($k_z = 0.055$)	[f]
DyCo ₂ Si ₂	1.5 K < T < 20.3 K AFI, 20.3 K < T < 21.4 K LSWI ($k_z = 0.05$)	[e]
DyCo ₂ Ge ₂	1.5 K < T < 11.5 K AFI, 11.5 K < T < 19.6 K LSWI ($k_z = 0.08$)	[g]
HoCo ₂ Si ₂	1.5 K < T < 14 K AFI	[g]
HoCo ₂ Ge ₂	1.5 K < T < 6.7 K AFI, 6.7 K < T < 10.6 K LSWI ($k_z = 0.08$)	[g]
UNi ₂ Si ₂	1.5 K < T < 53 K LSWI ($k_z = 1/3$), 53 K < T < 103 K AFI, 103 K < T < 124 K LSWI ($k_z = 0.255$)	[h]
UNi ₂ Ge ₂	1.5 K < T < 80 K AFI	[i]

AFI – antiferromagnetic collinear structure described by the propagation vector $\mathbf{k} = (0, 0, 1)$; LSWI – modulated structure described by the propagation vector $\mathbf{k} = (0, 0, 1 - k_z)$ (see Ref. [9]); [a] Shigeoka T. et al., *Physica* 156–157 (1989), 741; [b] Pinto H. et al., *Acta Cryst. A*, 35 (1979), 533. [c] Shigeoka T. et al., *J. Phys. (Paris)* 49 (1988), C8-431; [d] André G. et al., *J. Magn. Magn. Mater.*, 86 (1990) 387; [e] Szytuła A. et al., *J. Phys.: Cond. Matter*, 12 (2000), 7455; [f] Penc B. et al., *J. Phys.: Cond. Matter*, 11 (1999), 7579; [g] Schobinger-Papamantellos P. et al., *J. Magn. Magn. Mater.*, 264 (2003), 130; [h] Rebersky L. et al., *Physica B*, 180–181 (1992), 43; [i] Chelmicki L. et al., *J. Phys. Chem. Solids*, 46 (1985), 528.

The interpretation of such magnetic behaviour is possible on the basis of various theoretical models: the ANNNI (anisotropic-next-nearest-neighbour-Ising) model [16], Date's incommensurate mean field model [17], or self-consistent periodic field model [18]. All these models reproduce the observed change in magnetic structure as a function of temperature or magnetic field.

The PrNi₂Si₂ system exhibits the most original behaviour. Pr magnetic moments form an amplitude-modulated structure down to 0 K. At low temperature, squaring to the antiphase structure was detected. The external magnetic field causes a change in the ferromagnetic state. The above results indicate that the ground state is non-magnetic [11].

Anomalous properties are observed in some 1:2:2 compounds with R = Ce, Eu, Yb. The temperature dependence of specific heat indicates that CeCu₂Si₂ is a superconductor below 0.5 K. The large value of the electric specific heat ($\gamma = 1.1 \text{ J}/(\text{mol}\cdot\text{K}^2)$) suggests that CeCu₂Si₂ is a heavy fermion system with an effective mass of approximately $100m_0$

[19]. The external magnetic field causes the superconducting state to disappear and induces an antiferromagnetic one [20]. The phase diagram of CeCu_2Si_2 is presented in Fig. 4a. A different effect is observed in CePb_3 , in which the external magnetic field induces the superconducting state (see Fig. 4b) [21].

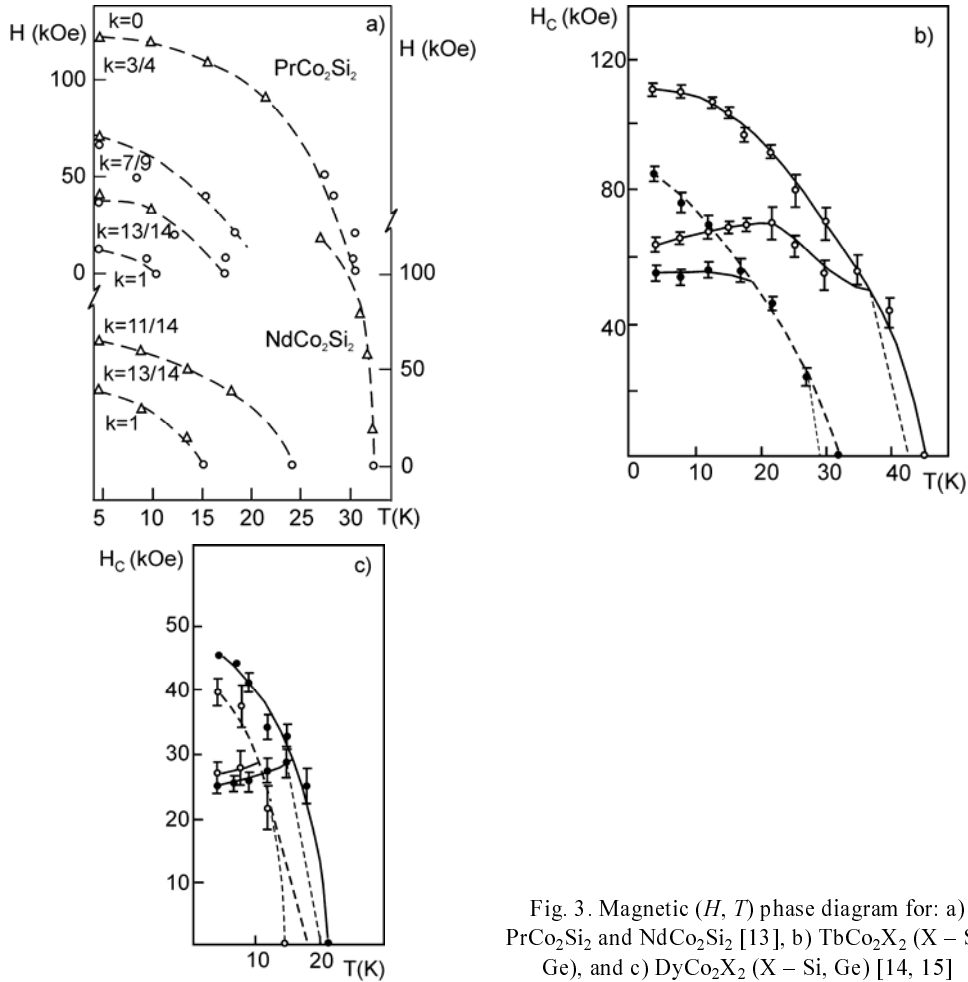


Fig. 3. Magnetic (H , T) phase diagram for: a) PrCo_2Si_2 and NdCo_2Si_2 [13], b) TbCo_2X_2 (X – Si, Ge), and c) DyCo_2X_2 (X – Si, Ge) [14, 15]

CePd_2Si_2 is an antiferromagnet with the Néel temperature T_N equal to 10 K and collinear magnetic structure described by the propagation vector $\mathbf{k} = (1/2, 1/2, 0)$ [22]. The temperature dependence of electrical resistivity ρ as a function of external pressure, summarized in Fig. 5a, indicates the following:

- the Néel temperature T_N decreases slowly and monotonically with increasing pressure,
- at a critical pressure P_c of ~ 26 kbar, the phase transition to the superconducting state takes place.

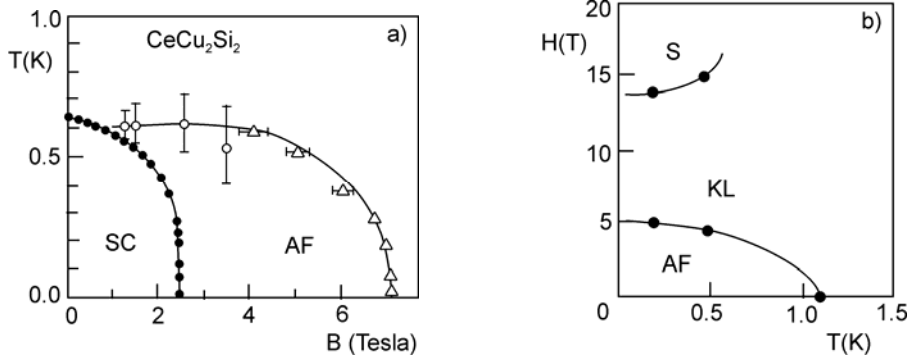


Fig. 4. Magnetic (*H*, *T*) phase diagram of: a) CeCu₂Si₂ [20], b) CePb₃ [21]

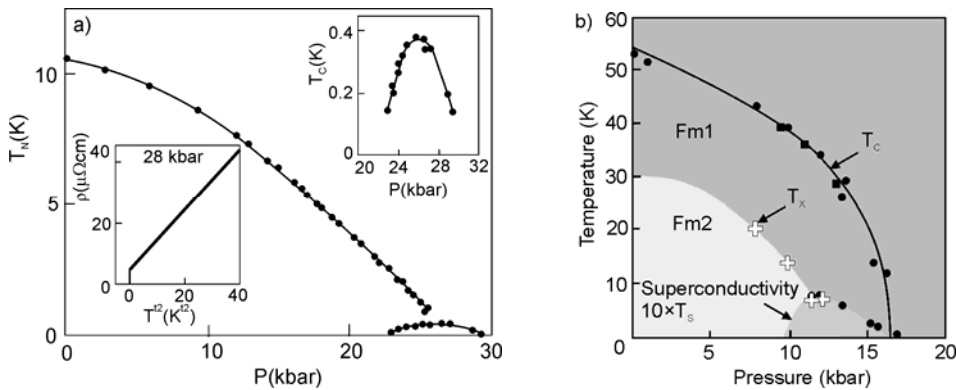


Fig. 5. *T*, *p* phase diagrams of: a) CePd₂Si₂ [23, 24], b) UGa₂ [28]

It was observed that ρ changes as $T^{1.2(1)}$ near P_c , which is indicative of non-Fermi behaviour. The behaviour of $\rho(T)$ and $T_N(P)$ near P_c suggests that spin fluctuations have a 2D character [19, 20].

The 1:2:2 uranium compounds show similar properties to those of isostructural rare earth compounds. The most interesting discovery for these compounds, however, was their heavy-fermion behaviour, at first in URu₂Si₂ ($\gamma = 180 \text{ mJ}/(\text{mol}\cdot\text{K}^2)$) [25]. Neutron diffraction studies confirmed that URu₂Si₂ exhibits an AFI-type magnetic structure below 17 K, with a very small magnetic moment of $0.04(1)\mu_B$ at $T = 0.57 \text{ K}$ [26]. At low temperatures, below 1 K, a transition to a superconducting state was detected [27].

UGe₂ compounds are ferromagnets with the Curie temperature T_C of 52 K for which an external pressure P causes monotonical decrease of T_C , and at about $P = 1 \text{ GPa}$ induces the superconducting state (Fig. 5b) [28].

EuT₂X₂ compounds are the most suitable for studying valence fluctuations, for example by ¹⁵¹Eu Mössbauer spectroscopy, because the isomer shift has significantly different values for Eu²⁺ ($\delta_{IS} = -10.6 \text{ mm/s}$) and Eu³⁺ ($\delta_{IS} = 0.6 \text{ mm/s}$) ions. Figure 6 shows the classification of silicides and germanides based on the isomer shift and

atomic volumes at room temperature. In germanides Eu ions are trivalent which is associated with the large volume available for Eu^{3+} ions in the unit cell. The case of silicides is much more complex: depending on the volume of the unit cell, Eu^{2+} , Eu^{3+} ions or mixed-valence states are present. It was estimated that the fluctuation time between the two valence states is shorter (10^{-13} s) than the Mössbauer probe time (10^{-11} s). Germanides (EuT_2Ge_2 for $T = \text{Co}, \text{Ni}, \text{Cu}, \text{Ru}$ and Rh) are antiferromagnets, while only silicides, EuT_2Si_2 , with $T = \text{Ru}, \text{Rh}, \text{Ag}$, and Au are antiferromagnets [10, 28].

Mn	156 Fe 2 0.3 2	152 Co 2 0.5 2	155 Ni 2 0.7 2	163 Cu -3.4
	168 Ru 0.6 2	173 Rh -8.3 3	Pd -7.0	Ag -10.4 3
	Os	Ir -5.6	Pt -8.1 3	Au -10.4 3

193.6 Mn -102.3 3	170.3 Fe 3 -9.5 3	174.3 Co 3 -9.1 3	180.9 Ni 3 -9.9 3	Cu
	185.1 Ru -102.3 3	183.6 Rh -102.3 3	Pd 3	Ag
	Os	Ir	Pt	Au

Fig. 6. Parameters of EuT_2Si_2 (left panel) and EuT_2Ge_2 (right panel) at 300 K: the unit cell volume in \AA^3 (upper right), isomer shift in mm/s of the ^{151}Eu Mössbauer absorption (bottom left) and valence (bottom right) for various T elements

Magnetic data have been published only for some YbT_2X_2 phases (see Ref. [10]). The majority of these compounds exhibit an unstable 4f shell intermediate valence effect. In contrast to the compounds with Ce and Eu, in the case of Yb the mixed-valence state is observed for both silicides and germanides. Lately, the magnetic properties of YbRh_2Si_2 , which is a weak antiferromagnet below $T_N = 70$ mK [30] have been determined. The magnetic phase diagram (see Fig. 5 in Ref. [30]) indicates complex magnetic and electronic properties. In this diagram, antiferromagnetic (AF), non-Fermi liquid (NFL) and Landau-Fermi liquid phases exist.

RMn_2X_2 ($X = \text{Si}, \text{Ge}$) compounds exhibit two critical temperatures [31]:

- at low temperatures the magnetic moments are localized on the R atoms and become ordered,
- at high temperatures only magnetic moments on Mn atoms show either ferro- or antiferromagnetic ordering.

The type of magnetic ordering in the Mn sublattice depends on the interatomic Mn–Mn distance. The coupling between Mn–Mn moments is antiferromagnetic when $R_{\text{Mn-Mn}}^a < 0.285$ nm and becomes ferromagnetic for $R_{\text{Mn-Mn}}^a > 0.285$ nm [32]. Similar critical distances were observed in many other alloys with transition metals [33]. The localization-delocalisation effect of 3d electrons occurs when the critical distance in Mn compounds reaches 0.285 nm [34].

SmMn_2Ge_2 has interesting magnetic properties – in the temperature range $341 \text{ K} < T < 385 \text{ K}$ it is antiferromagnetic, but ferromagnetic in the range $153 \text{ K} < T < 341 \text{ K}$. It becomes a re-entrant antiferro- (106.5–153 K) and ferromagnetic below 106.5 K [35, 36]. External pressure changes these magnetic phase transitions [30]. The fact that

in the antiferromagnetic state the resistance is higher than in the ferromagnetic state suggests the giant magnetoresistance in this compound [37]. Extraordinary large changes of magnetoresistance during metamagnetic phase transitions in TbNiSn single crystals at 4.2 K were observed [38].

3. Frustration systems

Geometrically frustrated systems are ubiquitous and interesting because their behaviour is difficult to predict as frustration can lead to a macroscopic degeneracy and qualitatively new states of matter.

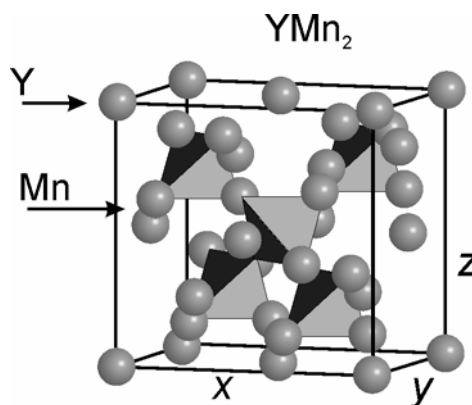


Fig. 7. The cubic corner-sharing tetrahedron lattice and crystal structure of YMn_2

The fundamental unit of frustration is a system of three antiferromagnetically interacting spins on a regular triangle. A regular tetrahedron composed of four triangles serves as a unit of three-dimensional frustrated lattices. Geometrically frustrated lattices are formed by joining their edges or corners. The triangular lattice and face-centered cubic lattice are edge-sharing lattices of triangles and tetrahedrons, respectively. Corner-sharing triangles yield the kagomé lattice while tetrahedrons form the lattice presented in Fig. 7. A number of magnetic materials crystallize in the last type of structure which belong to different classes of crystal symmetries, such as normal spinel, pyrochlores ($Y_2Mo_2O_7$), and *C15* Laves phase intermetallic compounds such as $Y(Sc)Mn_2$. In all these systems, the Mn magnetic ions form corner-shared tetrahedrons as depicted in Fig. 7. As in the case of the two-dimensional triangular lattice, this topology leads to a highly frustrated lattice, in which magnetic interactions between Mn moments are negative. Moreover, Mn moments in the RMn_2 series are very close to the magnetic-nonmagnetic instability as a function of distance. The critical distance is $d_c = 2.66 \text{ \AA}$. It has been determined that a complex magnetic structure arises as a result of frustration in YMn_2 , with a long wavelength distorted helical component [39].

A large group of the rare earth intermetallics crystallize in the hexagonal $ZrNiAl$ -type structure (space group $P\bar{6}2m$). The distribution of rare earth atoms in the basal

plane is similar to that in the kagomé lattice (Fig. 8). The results of neutron diffraction measurements indicate the existence of complex magnetic structures in these compounds. For example, in TbAuIn the Tb moments in the ab plane form a typical triangle structure (Fig. 9) [40]. A similar magnetic ordering is observed in a large number of isostructural compounds [41].

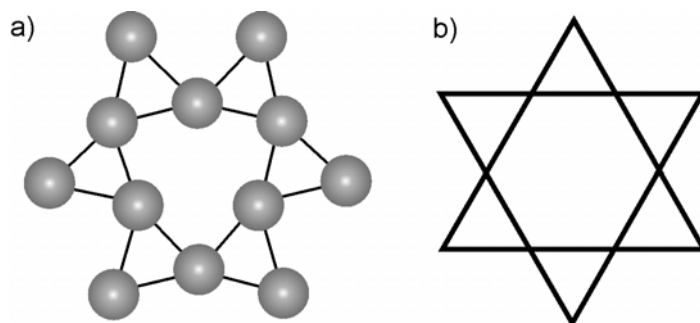


Fig. 8. Projection of the hexagonal ZrNiAl-type structure on the basal plane (a). Only rare earth atoms are shown, kagomé lattice (b)

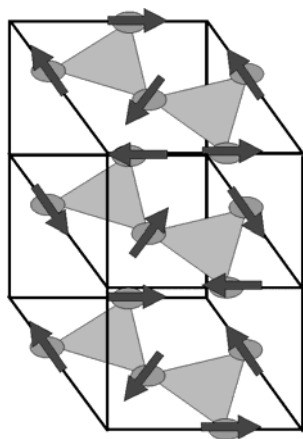


Fig. 9. Typical magnetic structure observed in RTX compounds with a ZrNiAl-type crystal structure

4. Electronic structure

Knowledge of the band structure of MT_2X_2 should lead to a better understanding of their magnetic properties. Results of X-ray absorption spectroscopy and XPS studies carried out on CeT_2Si_2 compounds ($T = 3d$ metal) indicate that with an increasing number of 3d electrons per atom the maximum of the 3d band moves below the Fermi level (Fig. 10) [42, 43]. For Mn compounds the Mn 3d states are at the Fermi level. With an increasing number of 3d electrons, the peak corresponding to the T 3d state moves away from the Fermi level. Calculations performed for YMn_2Ge_2 , $LaMn_2Ge_2$, $LaCo_2Ge_2$

[44], YMn_2Si_2 , LaMn_2Si_2 [45] and YbMn_2Si_2 and YbMn_2Ge_2 [46] indicate that the Fermi level crosses the 3d band. The calculated density of states at the Fermi level $N(E_F)$ is equal to 1.47 states/(eV·atom) for YMn_2Si_2 , 1.78 for LaMn_2Si_2 [45], 1.47 for YMn_2Ge_2 and 2.13 for LaMn_2Ge_2 [44], 4.10 for YbMn_2Si_2 and 2.97 for YbMn_2Ge_2 [46], and 0.6 for LaCo_2Ge_2 . The last value implies that the Co 3d band in LaCo_2Ge_2 is located below the Fermi level [44]. XPS spectra of the valence band of HoFe_2Ge_2 (see Fig. 11) indicate that the valence band is dominated by the multiplet structure of Ho^{3+} . Near the Fermi level, a broad maximum corresponding to Fe 3d states is observed.

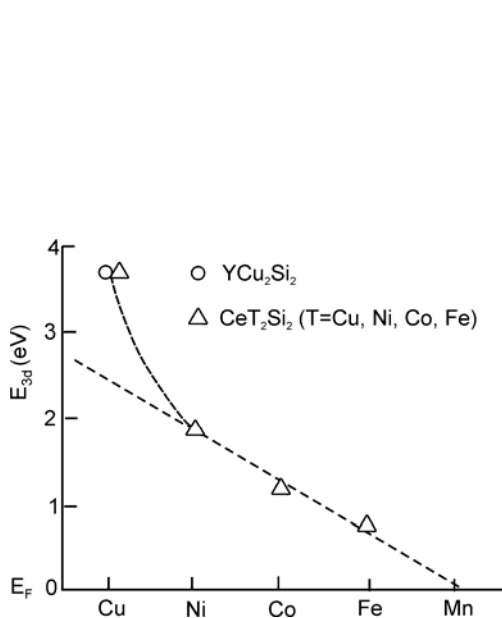


Fig. 10. Position of the 3d band relative to the Fermi level in CeT_2Si_2 ($T = \text{Cu, Ni, Co, Fe}$) [42] and YCu_2Si_2 [43]

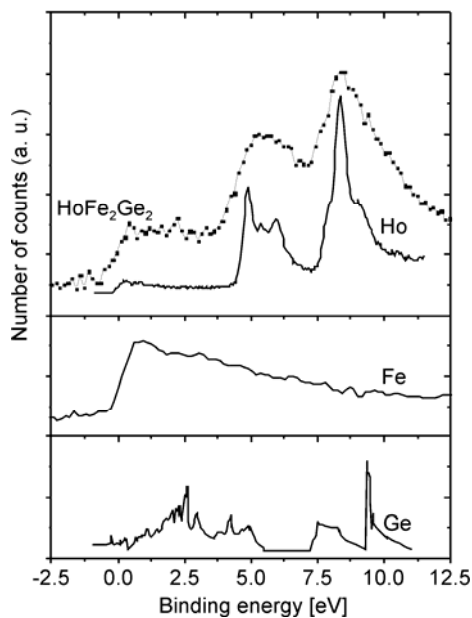


Fig. 11. XPS spectra of the valence band of HoFe_2Ge_2 and pure Ho, Fe, and Ge elements

The calculated band structures of CeCu_2Si_2 and LaCu_2Si_2 show that the 4f levels of Ce are located mainly above E_F . The density of states at E_F is large. The XPS spectra obtained for CeT_2Si_2 ($T = \text{Cu, Ag, Au, Pd}$) suggest that the hybridisation of the 4f electrons of Ce with the d-states of T ions takes place [47].

An analysis of the XPS spectra of Ce $3d_{5/2}$ and Ce $3d_{3/2}$ states based on the Gunnarsson–Schönhammer model determined the hybridisation energy of the Ce 4f orbital with the conduction band to be 59 meV [48] for CeCu_2Si_2 and 220 meV for CeT_2X_2 ($T = \text{Ni, Cu; X = Sb, Sn}$) [49].

The electronic structure of UT_2Si_2 ($T = \text{Ru, Rh, Pd, Ir}$) was determined by means of XPS measurements [50] and calculation of the density of states [51]. The situation in the valence band of uranium intermetallic compounds can be characterized by a more or less narrow 5f band intersected at the Fermi level. The XPS spectra of

UT_2Si_2 ($T = Ru, Rh, Pd, Ir$) [50] indicate that the structure of the Fermi surface is formed by the 5f states of uranium. For the 4d states of the transition metal a shift of the centre of the d-band from 1.9 eV for Ru to 3.9 eV for Pd is observed. These data indicate that for URu_2Si_2 a strong hybridisation of the U 5f and Ru 4d states appears to be very close to nonmagnetic-magnetic instability.

5. Magnetic hard materials

Historically, the trend in the development of permanent magnets is to rapidly increase $(BH)_{\max}$ (Fig. 11). Impressive progress in these materials was observed during the 20th century. Progress in new hard materials with large $(BH)_{\max}$ values, which gives the maximum energy product of the magnet, was obtained for rare earth–3d intermetallics. The interesting magnetic properties of these materials result from different microscopic magnetic properties of the elements. The rare earth atoms, with 4f electrons, display localized magnetic moments. On the contrary, the 3d-electrons of the transition metals are considered to be itinerant. On the basis these materials, new materials for permanent magnets are obtained, first the system R–Co with 1:5 and 2:17 stoichiometries [52], and next the $Nd_2Fe_{14}B$ compound with a relatively large T_C equal to 589 K and very large value of $(BH)_{\max}$ (50 MGOe) [53, 54].

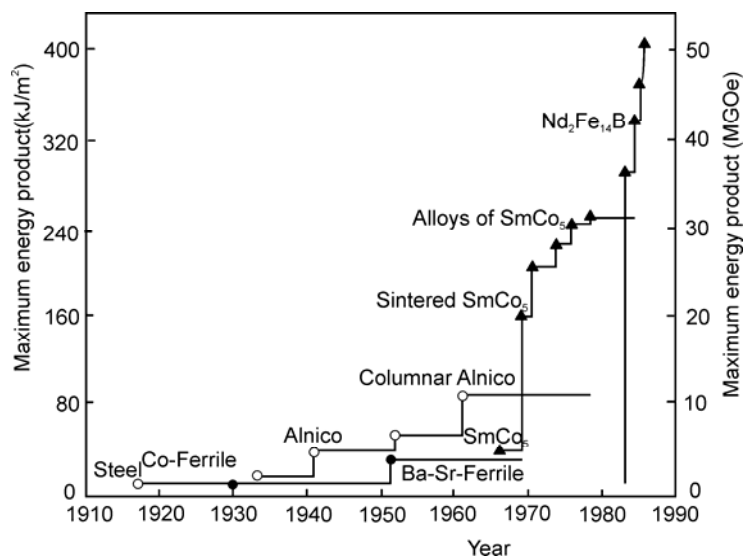


Fig. 12. Evolution of the maximum energy product of permanent magnets during the 20th century

The next group of compounds, which have been proposed as cheap alternative materials for the production of permanent magnets, are $RT_{12-x}T'_x$ compounds, where R is a rare earth element, T is a 3d electron element, T' is Ti, V, Cr, Mn, Mo, W, Al, or Si, and x is in the range $1 < x < 4$ [55]. These compounds have Curie temperatures ranging

from 260 to 650 K, with the highest values for Gd compounds in each series, except for the Mo-containing series, for which the maximum occurs for the Sm compound. $RFe_{12-x}M_x$ compounds are characterized by high Curie temperatures and high uniaxial anisotropy, and are good materials for the production of permanent magnets. In order to obtain the best parameters of these compounds, light elements such as H, C, and N are used and they have a dramatic effect on the magnetic properties (see Table 3).

Table 3. Main characteristics as observed after interstitial charging of hard magnetic compounds*

Quantity	Compound			
	R_2Fe_{17}		$RFe_{12-x}M_x$	
Interstitial	H	C, N	H	C, N
Curie temperature T_C	ii	iii	ii	iii
Saturation magnetization M_s	i or c	i	ii	
Anisotropy fields H_A	d or c	iii	i or c	

* d – decrease, c – constant, i – increase, ii – large increase, iii – very large increase.

6. Conclusions

The analysis of the structural and magnetic ternary intermetallic phases enables a number of general conclusions to be drawn. The first characteristic feature is the existence of many phases in each of these ternary systems, having different magnetic properties. The magnetic properties of the different intermetallics presented in this work indicate that these properties are strongly correlated with the electronic states of atoms. In the discussed compounds, the “normal” lanthanide and uranium atoms have localized magnetic moments. The localization of magnetic moments on 3d-electron atoms depends on the concentration of these atoms in the compound. For high concentrations of iron, the magnetic moment is localized, while for low concentrations (except for Mn) the magnetic moments of 3d-electron atoms disappear. The magnitude of the magnetic moment μ of 3d-electron atoms is proportional to the distribution of the bands of spin up and spin down electrons.

In 1:2:2 type intermetallic compounds, the magnetism arises from the interaction of magnetic moments localized on *f*-electron ions. The magnetic order observed in these compounds results from a compromise between different interactions and thermal effects. These interactions are of two types. The first, the bilinear exchange interaction of the RKKY type, is long range, oscillates with distance, and leads to different magnetic structures. It is also incommensurate with the crystallographic lattice. The second interaction to be taken into account is the crystalline electric field (CEF). In an uniaxial structure, CEF favours Ising and X–Y systems, with magnetic moments parallel and perpendicular to the tetragonal *c*-axis, respectively.

References

- [1] KOEHLER W.C., [in:] *Magnetic Properties of Rare Earth Metals*, R.J. Elliott (Ed.), Plenum Press, New York, 1972.
- [2] KASUYA T. *Prog. Theor. Phys.*, (Kyoto) 16 (1956), 45; RUDERMAN M.A., KITTEL C., *Phys. Rev.*, 96 (1954), 93.
- [3] TRZEBIATOWSKI W., ŚLIWA A., STALIŃSKI B., *Roczn. Chemii*, 26 (1952), 110; *ibid* 28 (1954), 12.
- [4] MAPLE M.B., CHEN J.W., LAMBERT S.E., FISK Z., SMITH J.L., OTT H.R., BROOKS J.S., NAUGHTON M.J., *Phys. Rev. Lett.*, 54 (1985), 477.
- [5] FUJITA Y., ENDO K., TERADA M., KIMURA R., *J. Phys. Chem. Solids*, 33 (1972), 1443.
- [6] CHEVALIER B., LEYAY P., ETOURNEAU J., HAGENMULLER P., *Matter. Res. Bull.*, 18 (1983), 315.
- [7] BODAK O.I., GLADYSHEVSKY E.I., [in:] *Handbook on the Physics and Chemistry of Rare Earths*, Vol. 13, K.A. Gschneidner Jr., L. Eyring (Eds.), North Holland, Amsterdam 1990, 1.
- [8] SZYTULA A., LECIEJEWICZ J., [in:] *Handbook on the Physics and Chemistry of Rare Earths*, Vol. 12, K.A. Gschneidner Jr., L. Eyring (Eds.), Elsevier Science Publ. B.V., 1989, p. 133.
- [9] SZYTULA A., [in:] *Handbook of Magnetic Materials*, Vol. 6, H.H.J. Buschow (Ed.), Elsevier, 1991, p. 85.
- [10] SZYTULA A., LECIEJEWICZ J., *Handbook of Crystal Structures and Magnetic Properties of Rare Earth Intermetallics*, CRC Press, Boca Raton, 1994.
- [11] GIGNOUX D., SCHMITT D., [in:] *Handbook on the Physics and Chemistry of Rare Earths*, Vol. 20, K.A. Gschneidner Jr., L. Eyring (Eds.), Elsevier, p. 293.
- [12] GIGNOUX D., SCHMITT D., *Phys. Rev. B*, 48 (1993), 12682.
- [13] VINOKUROVA L., IVANOV V., SZYTULA A., *J. Magn. Magn. Mater.*, 99 (1991), 193.
- [14] VINOKUROVA L., IVANOV V., SZYTULA A., *J. Alloys Comp.*, 190 (1992), L23.
- [15] SHIGEOKA I., GARNIER A., GIGNOUX D., SCHMITT D., ZHANG F.Y., BURLT P., *J. Phys. Soc., Japan*, 63 (1994), 2731.
- [16] BAK P., VON BOEHM J., *Phys. Rev. B*, 21 (1980), 5297.
- [17] DATE M., *J. Phys. Soc., Japan*, 57 (1988), 3682.
- [18] IWATA N., *J. Magn. Magn. Mater.*, 86 (1990), 225.
- [19] STEWART G.R., *Rev. Mod. Phys.*, 56 (1984), 755.
- [20] NAKAMURA H., KITAOKA Y., YAMADA H., ASAYAMA K., *J. Magn. Magn. Mater.*, 76–77 (1988), 517.
- [21] LIN C.L., TETER J., CROW J.E., MIHALISIN T., BROOKS J., ABOU-ALY A.I., STEWART G.R., *Phys. Rev. Lett.*, 54 (1985), 2541.
- [22] STEEMAN R.A., FRIKKEE E., HELMHOLDTR B., MENOVSKY J., VANDENBERG J., NIEUWENHUYNS G.J., MYDOSH J.A., *Solid State Commun.*, 66 (1988), 103.
- [23] JULIAN S.R., CARTER F.V., GROSCHE F.M., HASELWIMMER R.K.W., LISTER S.J., MATHUR N.D., MCMULLAN G.J., PFELEIDERER C., SAXENA S.S., WALKER I.R., WILSON N.J.W., LONZARICH G.G., *J. Magn. Magn. Mater.*, 177–181 (1998), 265.
- [24] MATHUR N.D., GROSCHE F.M., JULIAN S.R., WALKER I.R., FREYE D.M., HASELWIMMER R.K.W., LONZARICH G.G., *Nature*, 394 (1998), 39.
- [25] SCHLABITZ W., BAUMAN J., POLLIT B., RAUCHSCHWELBE U., MAYER H.M., AHLEHEIM U., BREDL C.D., *Z. Phys. B*, 62 (1986), 171.
- [26] BROHOLM C., KJEMS J.K., BUYERS W.J.L., MATTHEW P., PALSTRA T.T.M., MENOVSKY A.A., MYDOSH J.A., *Phys. Rev. Lett.*, 58 (1987), 1467.
- [27] LOPEZ DE LA TORRE M.A., VISANI P., DALICHAOUCH Y., LEE B.W., MAPLE M.B., *Physica B*, 179 (1992), 208.
- [28] SAXENA S.S., AGARVAL P., AHILAN K., GROSCHE F.M., HASELWIMMER R.K.W., STEINER M.J., PUGH E., WALKER L.B., JULIAN S.R., MONTHOUX P., LONZARICH G.G., HUXLEY A., SHELKIN L., BRAITHWAITE D., FLOUQUET J., *Nature*, 106 (2000), 587.
- [29] GÖRLICH E.A., Ph. D. Thesis, Jagiellonian Univeristy, Cracow, 1997.

- [30] GEGENWART P., CUSTERS J., TAYAMA T., TENYA K., GEIBEL C., TROVARELLI O., STEGLICH F., *Acta Phys. Polon.*, **34** (2003), 323.
- [31] SZYTULA A., SZOTT I., *Solid State Commun.*, **40** (1981), 199.
- [32] SZYTULA A., SIEK S., *J. Magn. Magn. Mater.*, **27** (1982), 49.
- [33] FORRER R., *Ann. Phys.*, **7** (1952), 605.
- [34] GOODENOUGH J.B., *Magnetism and Chemical Bond*, Wiley, New York, 1963, p. 240.
- [35] DURAJ M., DURAJ R., SZYTULA A., TOMKOWICZ Z., *J. Magn. Magn. Mater.*, **73** (1988), 240.
- [36] GYORGY E.M., BATLOGG B., REMEIK A.J.P., VAN DOVER R.B., FLEMING R.M., BAIR H.E., ESPINOSA G.P., COOPER A.S., MAINES R.G., *J. Appl. Phys.*, **61** (1987), 4237.
- [37] BRABERS J.H.V.J., NOLTEN A.J., KAYZEL F., LENZOWSKI S.H.J., BUSCHOW K.H.J., DEBOER F.R., *Phys. Rev. B*, **50** (1994), 16410.
- [38] HORI H., OKI A., KURISU M., FURUSAWA M., ANDOH Y., KINDO K., *Phys. Lett. A*, **224** (1997), 293.
- [39] BALLOU R., DEPORTES J., LEMAIRE R., NAKAMURA Y., OULADDIAF B., *J. Magn. Magn. Mater.*, **70** (1987), 129.
- [40] SZYTULA A., BAŻELA W., GONDEK Ł., JAWORSKA-GOŁĄB T., PENC B., STÜSSER N., ZYGMUNT A., *J. Alloys Comp.*, **336** (2002), 11-17.
- [41] GONDEK Ł., Ph. D. Thesis, Jagiellonian University, Cracow, 2004.
- [42] SAMPATHKUMARAN E.V., KALKOWSKI G., LAUBSCHAT C., KAINDL G., DOMKE M., SCHMIESTER G., WORTMANN G., *J. Magn. Magn. Mater.*, **47-48** (1985), 212.
- [43] BUSCHOW K.H.J., CAMPAGNA M., WARTHEIM S.K., *Solid State Commun.*, **24** (1977), 253.
- [44] ISHIDA S., ASANO S., ISHIDA J., *J. Phys. Soc. Jpn.*, **55** (1986), 93.
- [45] KULATOV E., VESELAGO V., VINOKUROVA L., *Acta Phys. Polon.*, **A 77** (1990), 709.
- [46] SZYTULA A., JEZERSKI A., PENC B., HOFMANN M., CAMPBELL S.J., *J. Alloys Comp.*, **366** (2004), 313.
- [47] PARKS R.D., REHL B., MERTENSSON N., STEGLICH F., *Phys. Rev. B*, **27** (1983), 6052.
- [48] KANG J.S., ALLEN J.W., GUNARSSON O., CHRISTENSEN N.E., ANDERSEN O.K., LASSAILLY Y., MAPLE M.B., TORIKACHVILI M.S., *Phys. Rev. B*, **41** (1990), 6610.
- [49] ŚLEBARKI A., JEZERSKI A., ZYGMUNT A., NEUMANN M., MÄHL S., BORSTEL G., *J. Magn. Magn. Mater.*, **159** (1996), 179.
- [50] GRASSMANN A., *Physica B*, **163** (1990), 547.
- [51] SANDRATSKII L.M., KUBLER J., *Solid State Commun.*, **91** (1994), 183.
- [52] STRNAT K.J., HOFFER G., OLSON J., OSTERTAG W., BECKER J.J., *J. Appl. Phys.*, **38** (1967), 1001.
- [53] SAGAWA M., FUJIMURA S., TOGAWA N., YAMAMOTO H., MASUURA Y., *J. Appl. Phys.*, **55** (1984), 2083.
- [54] CROAT J.J., HERBST J.F., LEE R.W., PINKERTON F.E., *Appl. Phys. Lett.*, **44** (1984), 148.
- [55] SUSKI W., [in:] *Handbook on the Physics and Chemistry of Rare Earths*, Vol. 22, K.A. Gschneidner Jr., L. Eyring (Eds.), Elsevier, Amsterdam, 1996.

Received 1 June 2005
Revised 10 October 2005

Magnetization distribution in nanocrystalline $\text{Fe}_{0.48}\text{Al}_{0.52}$

K. SZYMAŃSKI^{1*}, L. DOBRZYŃSKI^{1,2}, D. SATUŁA¹,
E. VORONINA³, E. P. YELSUKOV³

¹Institute of Experimental Physics, University of Białystok, 15-424 Białystok, Poland

²The Sołtan Institute for Nuclear Studies, 05-400 Otwock-Świerk, Poland

³Physical-Technical Institute of the Ural Division of Russian Academy of Sciences, Izhevsk 426000, Russia

Mössbauer polarimetry is used for investigating the orientation of Fe magnetic moments in the nanocrystalline $\text{Fe}_{0.48}\text{Al}_{0.52}$ disordered alloy prepared by mechanical grinding. Local Fe magnetic moments and their contributions to the net magnetization at selected external fields and temperatures were estimated. It was found that the components of the Fe magnetic moments parallel to the net magnetizations reduce their values much faster with an increasing number of neighbouring Al atoms than the total iron moments.

Key words: *Mössbauer polarimetry; magnetic moment; nanocrystalline $\text{Fe}_{0.48}\text{Al}_{0.52}$*

1. Introduction

Structurally ordered alloys with Al concentrations between 35% and 43% and with equiatomic composition have been suspected of the presence of antiferromagnetic order [1–5]. Quite recent neutron diffraction data for *bcc*-ordered Fe–Al with Al concentrations of 34–43 at. % [6] showed the presence of incommensurate spin density waves. It has been found earlier that ferromagnetic order can exist close to FeAl composition [7], and that supposedly antiferromagnetic or paramagnetic configurations can change to ferromagnetic upon simple filing [1, 8–11]. Ferromagnetism has also been detected in alloys with Al concentrations larger than 50 at. % [8, 12] and in the concentration range 40–60 at. % [13].

The ratio of hyperfine fields and magnetic moments (or magnetization) in many Fe-based ferromagnetic systems is in the range 10.0–15.0 T/ μ_{B} [14–16]. Magnetization data for disordered Fe–Al alloys [11, 17], can be compared with the average hyperfine magnetic field (h.m.f.) obtained from Mössbauer experiments [8, 12, 17]. The ratio is an

*Corresponding author, e-mail: kszym@alpha.uwb.edu.pl

omalously high, about $30 \text{ T}/\mu_{\text{B}}$ for concentrations close to equiatomic, while it is about $12.0\text{--}13.5 \text{ T}/\mu_{\text{B}}$ in ferromagnetic alloys with Al concentrations less than 40 at. %.

For systems with atomic and spin disorders – in particular for non-ordered metal systems with RKKY interaction – Mattis has considered a model in which spin–spin interactions were random in sign but did not result in frustrations [18]. The spin system was considered to be composed of two subsystems with randomly distributed antiparallel spins, which form the so-called Mattis phase. The magnetisation behaviour of the Fe–Al system and the ideas found in Refs. [18–20] indicate that concentrated Fe–Al alloys could exhibit the Mattis phase, no experimental support, however, has been reported so far.

Studies of Fe–Al alloys by the Monte Carlo techniques [21] in the Al concentration range $0.25 < x < 0.50$ showed that it was possible to qualitatively account for the transformation of the magnetic state from a ferromagnetic one to a certain spin glass state at about 34% Al using the indirect exchange model [1]. A peculiar feature of this spin-glass is the fact that frustrations arise from the positional disorder of Fe and Al atoms.

These controversial findings, and the apparent impact of various defects and inhomogeneities on the magnetic structure of bulk and nanocrystalline alloys, require more detailed investigations that will elucidate the nature of magnetism in this system. This paper reports the studies of nanocrystalline Fe–Al alloys in the concentration range close to the onset of ferromagnetism by the Mössbauer technique with circularly polarized monochromatic radiation. Polarized radiation has been widely used in investigating magnetically ordered systems, for an extended review see Ref. [22]. Circularly polarized radiation has the advantage of being sensitive to the sign of the h.m.f. Our observations strongly suggest that a non-collinear magnetic order must exist in the sample studied.

2. Sample

Fe–Al ingot was synthesized from high-purity components (99.99 % Fe and 99.99% Al) in an induction furnace in Ar atmosphere, then homogenized in a vacuum furnace at 1400 K for 6 h. The chemical analysis showed that the Al concentration was 52.0 ± 0.5 at. %. The ingots were milled and a fraction with particle sizes lower than $300 \mu\text{m}$ was used for further mechanical treatment in a planetary ball mill with vials and balls made of tungsten carbide. Mechanical grinding was performed in an inert gas atmosphere. The milling time was adjusted to provide a disordered state in the Fe–Al alloys [17]. The obtained sample exhibited a single *bcc* phase with the lattice parameter $0.2918(4)$ nm. The X-ray diffraction pattern consists of the broadened peaks (110), (200), (211), and (220) of the *bcc* structure. The analysis of the shape of the diffraction lines using the harmonic analysis [23] lead to the conclusion that the mean grain size of the alloy is $4.0(3)$ nm.

3. Mössbauer polarimetric measurements

The absorbers were placed inside one of the rare earth magnets, producing an axially symmetric field perpendicular to the absorber surface and parallel to the gamma rays. The measurements were performed at temperatures of 13, 50, and 298 K and external fields between 0 and 1.1 T, see the example in Fig. 1.

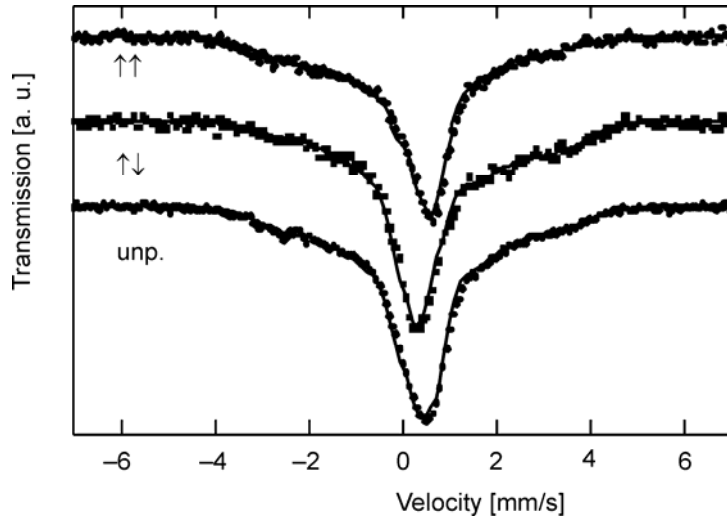


Fig. 1. An example of the Mössbauer spectra recorded at $T = 13$ K with polarized and unpolarized radiation in an axial, externally applied magnetic field of 1.1 T. The arrows $\uparrow\uparrow$ and $\uparrow\downarrow$ indicate two opposite circular polarizations. Solid lines represent the results of the simultaneous fitting the h.m.f.s to all the recorded spectra

A full Hamiltonian was used for treating the mixed magnetic dipole and electric quadrupole interaction. The transmission integral was used to treat thickness effects, and the temperature dependence of the f -factor was taken into account. To analyse the low-temperature data, we assumed the same isomer shift and electric field gradient, as well as their probabilities determined at room temperature. We allowed only the second order Doppler shift and the appearance of the h.m.f. distribution. The principles of the adopted polarimetric method are given in Ref. [24], while details of the construction of the source of circularly polarized radiation in Refs. [25, 26].

An experiment with circularly polarized radiation is sensitive to the angular average $\langle \gamma_r \cdot \mathbf{m} \rangle$, where \mathbf{m} is a unit vector parallel to the local h.m.f., \mathbf{B}_{hf} , γ_r is the Cartesian vector ($r = x, y, z$) and the brackets $\langle \rangle$ denote angular averaging with the magnetic texture function $P(\Omega)$:

$$\langle \gamma_r \cdot \mathbf{m} \rangle = \int_{4\pi} \gamma_r \cdot \mathbf{m} P(\Omega) d\Omega \quad (1)$$

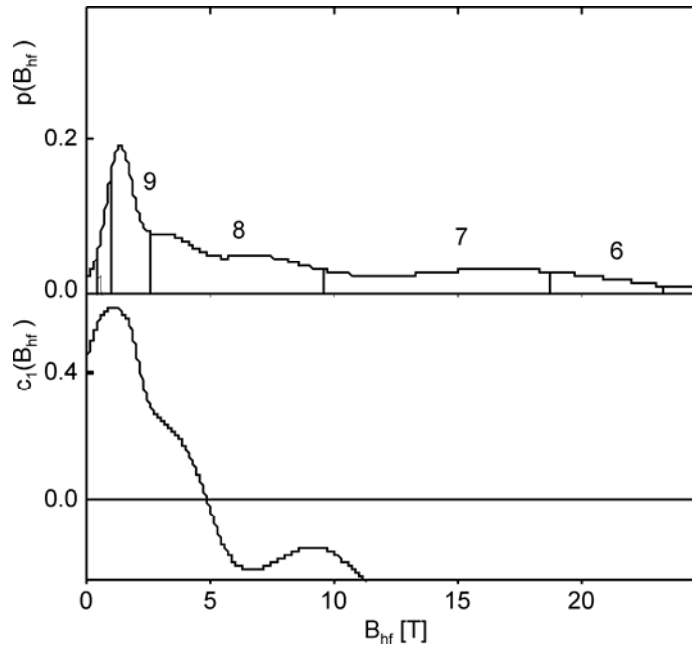


Fig. 2. An example of the distribution of h.m.f. obtained from experiment (up) and the h.m.f. dependence of the average cosine between the h.m.f. vector and magnetization (down) measured at $T = 13$ K and $B_{\text{ext}} = 1.1$ T. The vertical bars split the $p(B_{hf})$ distribution into sectors numbered by $k = \dots, 9, 8, 7, \dots$, for which the two first coordination shells are taken into account (cf. Eq. (2))

In particular, one can obtain the value of $c_1 B_{hf}$, which is an average component of the h.m.f. along photon directions. In the case of α -Fe, the h.m.f. is antiparallel to the direction of the magnetic moment of iron atoms [27], so the c_1 parameter is negative. Negative values of c_1 for our sample are observed only for hyperfine fields larger than about 5 T (Fig. 2). Figure 2 also shows that a relatively large probability $p(B_{hf})$ is observed in the region close to $B_{hf} = 5$ T, much above the intensity of the external field. It is thus reasonable to suppose that B_{hf} in this region corresponds to the Fe atoms with nonzero magnetic moments. If this is so, then a nearly zero value of the c_1 parameter in Fig. 2 indicates that these moments, on average, do not contribute to the total magnetization.

4. Discussion and conclusions

A considerable enhancement of the experimental value B_{hf}/σ_{Fe} (attaining values close to 30 T/ μ_B) in the studied Fe–Al system with respect to the values calculated for collinear systems can be explained by a transformation from ferromagnetic to non-ferromagnetic order. One should expect that the magnetization should be correlated with the z -th component of the h.m.f., B_z . This is indeed observed in our alloy $\text{Fe}_{0.48}\text{Al}_{0.52}$ (Fig. 3).

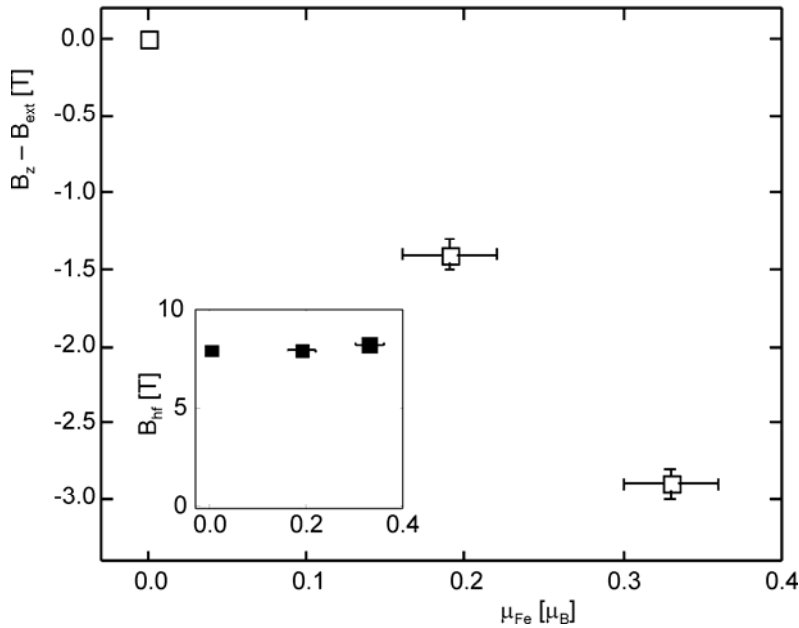


Fig. 3. Correlation between the average z -component of the h.m.f. (corrected to the external field) and the Fe magnetic moment (the inset shows a lack of correlation between the average h.m.f. and magnetic moment). Open and full symbols correspond to the z -component of the h.m.f. and the h.m.f. itself, respectively

It is reasonable to assume that the larger number of Fe atoms, the larger the observed B_{hf} . Next, it follows from EXAFS results [28] that the probabilities of finding the Fe atom in the first (I) and the second (II) coordination shells are given by $x_I = 0.10$ and $x_{II} = 0.883$, respectively. Assuming random distributions within the shells, the probability $P(k)$ that an iron atom is surrounded by $(14 - k)$ Fe and k Al atoms in the two first coordination shells is:

$$P(k) = \sum_{\substack{i,j \\ i+j=k}} \binom{8}{j} \binom{6}{i} x_I^{8-j} (1-x_I)^j x_{II}^{6-i} (1-x_{II})^i \quad (2)$$

These assumptions allow one to divide $p(B_{hf})$ into a few sections, each having the area proportional to the probability $P(k)$. The sectioning is displayed in Fig. 2 by vertical lines. The average fields estimated for each section are displayed in Fig. 4 by full symbols, while the z -components of the fields by open symbols. As expected, an increase of the field from $B_{ext} = 0.2$ T to $B_{ext} = 1.1$ T results in an increase of B_z and not B_{hf} (see the open and the overlapping full points in Fig. 4). The average $\bar{B}(k)$ for $k = 6$ (Fig. 4) is slightly above the value k related to ordered Fe_3Al at low temperature [29].

It should be noted that Eq. (2) is valid under the assumption that the contributions of neighbouring atoms from the I and II coordination shells are the same, which is an approximation. The opposite approximation, in which the influence of the II coordination shell is neglected, can be made by using the binomial distribution instead of Eq. (2). The results of such treatment exhibit similar features and are not shown here (average $\bar{B}(k)$ for $k = 4$ is slightly below the value related to ordered Fe_3Al reported in [29]).

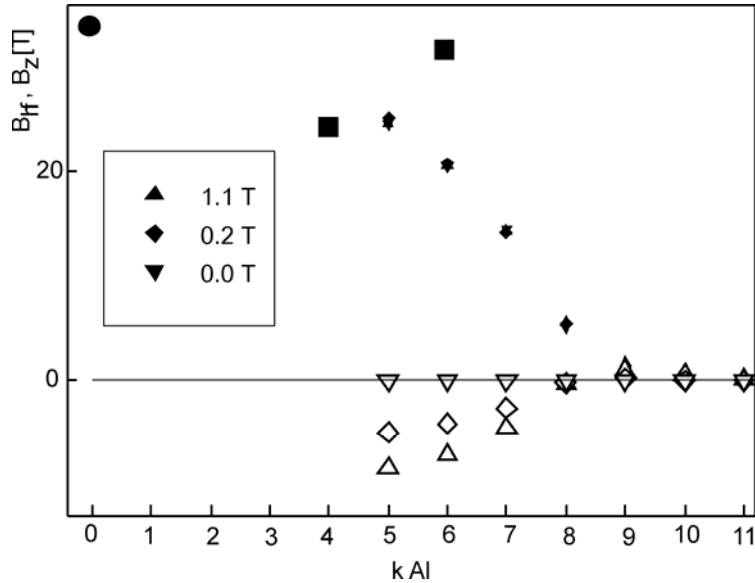


Fig. 4 Average h.m.f. and average z -th component of the field (not corrected for the external field) related to the sectors from Fig. 2, under the assumption that contributions from the first and the second coordination shells to the h.m.f. are the same. Full symbols correspond to the h.m.f., open symbols to the z -component of the h.m.f., \bullet – Ref [16], \blacksquare – Ref. [29]

The magnetization and Mössbauer data can be combined to obtain the local magnetic moments of Fe. To estimate the z -th component of the magnetic moment in the external magnetic field, we assume that it is proportional to $\bar{B}_z(k)$ and that the total contribution to the magnetization of all Fe atoms is equal to the measured magnetization. The two most important results are as follows.

An increase of the number of Al atoms in the two first coordination shells (*bcc* structure) causes a decrease of the magnetic moments and a much faster decrease of the z -component of the magnetic moments (local contribution to magnetization). Configuration (7, 1) was found as the most suitable for forming a non-collinear structure, where (k_1, k_2) denotes a Fe atom surrounded by k_1 Al atoms in the I coordination shell and k_2 Al atoms in the II coordination shell. It should be stressed that such a detailed description of the magnetic moment arrangement would hardly be possible if not for the extensive combination of experimental methods used in the present studies.

References

- [1] ARROTT A., SATO H., Phys. Rev., 114 (1959), 1420.
- [2] SATO H., ARROTT A., Phys. Rev., 114 (1959), 1427.
- [3] DANAN H., GENGNAGEL H., J. Appl. Phys., 39 (1968), 678.
- [4] HUFFMAN G.P., J. Appl. Phys., 42 (1971), 1606.
- [5] SHIGA M., NAKAMURA Y., J. Phys., Soc. Japan, 40 (1976), 1295.
- [6] NOAKES D.R., ARROTT A.S., BELK M.G., DEEVI S.C., HUANG Q.Z., LYNNJ W., SHULL R.D., WU, D., Phys. Rev. Lett., 91 (2003), 217201.
- [7] SHIGA M., NAKAMURA Y., J. Phys. Soc. Japan, 40 (1976), 1295.
- [8] BESNUS M.J., HERR A., MEYER A.J.P., J. Phys. F5, (1975), 2138.
- [9] TAYLOR A., JONES R.M., J. Phys. Chem. Solids, 6 (1958), 16.
- [10] FRIEDMAN E.A., NICHOLSON W.J., J. Appl. Phys., 34 (1963), 1048.
- [11] HUFFMAN G.P., FISHER R.M., J. Appl. Phys., 38 (1967), 735.
- [12] SHIGA M., KIKAWA T., SUMIYAMA K., NAKAMURA Y., J. Magn. Soc. Japan, 9 (1985), 187.
- [13] KULIKOV N.I., POSTNIKOV A.V., BORSTEL G., BRAUN J., Phys. Rev. B, 59 (1999), 6824.
- [14] YELSUKOV E.P., VOROBYOV YU.N., ARBUSOVA T.I., SMOLYAK, I.B., J. Magn. Magn. Mater., 130 (1994), 44.
- [15] PANISSOD P., DURAND J., BUDNICK J.I., Nucl. Instr. Meth., 199 (1982), 99.
- [16] VIOLET C.E., PIPKORN D.N., J., Appl. Phys., 42, (1971), 4339.
- [17] YELSUKOV E.P., VORONINA E.V., BARINOV V.A., J. Magn. Magn. Mater., 115 (1992), 271.
- [18] MATTIS D.C., Phys. Lett., 56A (1976), 421.
- [19] ARZHNIKOV A.K., DOBYSHEVA L.V., J. Magn. Magn. Mater., 117 (1992), 87.
- [20] ARZHNIKOV A.K., DOBYSHEVA L.V., Phys. Lett., A, 195 (1994), 176.
- [21] GREST G.S., Phys. Rev. B, 21 (1980), 165.
- [22] GONSER U., FISCHER H., [in:] *Mössbauer Spectroscopy II*, Springer-Verlag, Berlin, 1981.
- [23] WARREN B.E., B.L.AVERBACH B.L., J. Appl. Phys., 21 (1950), 595.
- [24] SZYMAŃSKI K., SATULA D., DOBRZYŃSKI L., Hyp. Int., 156/157 (2004), 21.
- [25] SZYMAŃSKI K., DOBRZYŃSKI L., PRUS B., COOPER M.J., Nucl. Instr. Meth. B, 119 (1996), 438.
- [26] SZYMAŃSKI K., Nucl. Instr. Meth. B, 134 (1998), 405.
- [27] HANNA S.S., HEBERLE J., LITTLEJOHN C., PERLOW G.J., PRESTON R.S., VINCENT D.H., Phys. Rev. Lett., 4 (1960), 513.
- [28] SZYMAŃSKI K., DOBRZYŃSKI L., SATULA D., VORONINA E., YELSUKOV E.P., MIYANAGA T., Phys. Rev. B, 72 (2005), 104409.
- [29] JOHNSON C.E., RIDOUT M.S., CRANSHAW T.E., Proc. Phys. Soc., 81 (1963), 1079.

Received 1 June 2005
Revised 10 October 2005

Transport characteristics of ferromagnetic single-electron transistors with non-collinear magnetizations

J. WIŚNIEWSKA^{1*}, M. KOWALIK¹, J. BARNAS^{1,2}

¹Institute of Physics, Adam Mickiewicz University, Umultowska 85, 61-614 Poznań, Poland

²Institute of Molecular Physics, Polish Academy of Sciences,
M. Smoluchowskiego 17, 60-179 Poznań, Poland

Theoretical analysis of spin-polarized transport through a ferromagnetic single-electron transistor (FM SET) has been carried out in the sequential tunnelling regime. Two external electrodes and the central part (island) of the device are assumed to be ferromagnetic, with the corresponding magnetizations being generally non-collinear. The transport properties of the FM SET are analysed within the master equation approach with the respective transition rates determined from the Fermi golden rule. It is assumed that spin relaxation processes on the island are sufficiently fast to neglect spin accumulation. It is shown that electric current and tunnel magnetoresistance strongly depend on the magnetic configuration of the device. Transport characteristics of symmetrical and asymmetrical structures have been calculated as a function of bias and gate voltages.

Key words: *ferromagnetic single-electron transistor; spin-polarized transport; tunnel magnetoresistance*

1. Introduction

There is a general need to produce smaller and faster processors, smaller and more voluminous memories, and smaller and more sensitive sensors. It seems that spintronics fulfils such expectations and demands. Moreover, in the nanometer scale we have to consider the increasing importance of interactions between electrons, so that the role of electron spin becomes important as well. The problem of spin-polarized transport in ferromagnetic single-electron transistors (FM SETs) with quantum dots or metallic grains [1–4] has been addressed only recently, particularly for non-collinear magnetic moments of the external electrodes [5]. In Ref. [5], a situation with one nonmagnetic and one magnetic electrode was considered, and it was shown that transport characteristics strongly depend on the angle between the magnetic moments of the lead and island.

* Corresponding author, e-mail address: justyw@amu.edu.pl

In this paper, we present the results of our theoretical analysis of spin-polarized electronic transport in a ferromagnetic single-electron transistor, whose all three electrodes, i.e. two external leads and the central part (island), are ferromagnetic, with the corresponding magnetizations being generally non-collinear, but oriented in a common plane. The angle α (β) between the angular spin moments of the right (left) lead and the island is arbitrary (see Fig. 1). Apart from this, we assume that an external gate voltage is applied to the island. Our objective is to analyse the dependence of electric current, differential conductance, and tunnel magnetoresistance (TMR) on the angles between magnetizations and on the transport and gate voltages.

Transport properties are analysed within the master equation approach, with the corresponding transition rates determined from the Fermi golden rule. In this analysis, we take into account only sequential tunnelling processes – with lowest-order perturbation theory [6]. It is also assumed that the spin relaxation on the island is sufficiently fast to neglect spin accumulation. We have analysed numerically the electric current flowing through the device, the corresponding differential conductance, and the resulting tunnel magnetoresistance for different magnetic configurations of the device. From this analysis it follows that all transport characteristics strongly depend on the angles α and β .

2. Model and theoretical description

A schematic diagram of the analysed ferromagnetic single-electron transistor is shown in Fig. 1. The device under consideration consists of three electrodes made of the same ferromagnetic material. When a sufficiently high bias voltage is applied to the device, electrons can tunnel through the barriers sequentially one by one, giving rise to electric current. When the charging energy is considerably larger than the thermal energy, charging effects become observable and the current–voltage characteristics display a typical Coulomb staircase with a Coulomb blockade in the small bias regime. Apart from this, Coulomb oscillations in the electric current occur with increasing gate voltage. These effects lead to an oscillatory behaviour of TMR with increasing bias voltage.

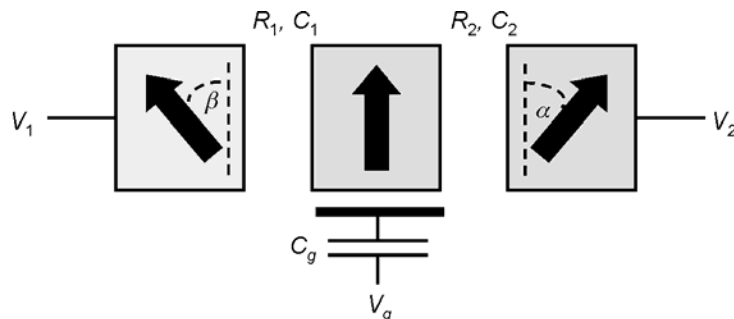


Fig. 1. A schematic diagram of the ferromagnetic single-electron transistor. The arrows indicate the spin moments of the island and the two external electrodes

In our considerations, we take into account only sequential tunnelling processes and assume that the contributions of higher-order processes are small compared to the first-order ones. This is justifiable when the barrier resistances significantly exceed quantum resistance, $R_j \gg R_q = h/e^2$, $j = 1, 2$, which implies that the charge on the island is well localized and that orthodox tunnelling theory is applicable [6]. The resistances of the tunnel junctions depend on the tunnel matrix elements between the corresponding states of the left (labelled with 1) and right (labelled with 2) electrodes and the island, which in turn depend on the angle between magnetizations. Furthermore, we take into account only tunnelling processes that conserve electron spin when the magnetic moments of the leads are collinear. Apart from this, we assume that spin relaxation time on the island is shorter than the time between the two successive tunnelling events. This means that a non-equilibrium magnetic moment (spin accumulation) cannot build up on the island. Moreover, the island is assumed to be relatively large, so that quantization effects of the corresponding energy levels can be neglected.

The rate of electron tunnelling from the spin majority/minority (+/-) electron bands of the first (left) electrode to the spin majority/minority (+/-) electron channels of the island can be expressed in terms of the Fermi golden rule as:

$$\Gamma_{1 \rightarrow i}^{\pm\pm} = \frac{2\pi}{\hbar} |\langle \Psi_{i\pm} | H_T | \Psi_{1\pm} \rangle|^2 \delta(E_f - E_i) \quad (1)$$

where $|\Psi_{1\pm}\rangle$ and $|\Psi_{i\pm}\rangle$ are the wave functions of spin-majority (spin-minority) electrons in the first electrode and island, respectively, E_i and E_f are the initial and final energies of the whole system, and H_T is the tunnelling Hamiltonian. These wave functions are written in the respective local reference systems (with the local quantization axes determined by local spin moments). When a bias voltage V is applied to the device, the tunnelling rate from the first electrode to the island, already occupied by n excess electrons, can be written in the form:

$$\Gamma_{1 \rightarrow i}^{++(-)}(n, V) = \Gamma_{1 \rightarrow i}^{p,+(-)}(n, V) \cos^2 \frac{\beta}{2} \quad (2a)$$

$$\Gamma_{1 \rightarrow i}^{+-(+)}(n, V) = \Gamma_{1 \rightarrow i}^{ap}(n, V) \sin^2 \frac{\beta}{2} \quad (2b)$$

with $\Gamma_{1 \rightarrow i}^{p,+(-)}(n, V)$ denoting the tunnelling rate of spin majority (+) and spin minority (-) electrons in the parallel magnetic configuration. Similarly, $\Gamma_{1 \rightarrow i}^{ap}(n, V)$ is the corresponding tunnelling rate in the antiparallel configuration. Note that $\Gamma_{1 \rightarrow i}^{+-}(n, V) = \Gamma_{1 \rightarrow i}^{-+}(n, V)$, which is a consequence of the assumption that all electrodes and the island are made of the same ferromagnetic material.

The rate $\Gamma_{1 \rightarrow i}^{p,+(-)}(n, V)$ is given by the formula:

$$\Gamma_{1 \rightarrow i}^{p,+(-)}(n, V) = \frac{1}{e^2 R_1^{p,+(-)}} \frac{\Delta E_1(n, V)}{\exp[\Delta E_1(n, V)/k_B T] - 1} \quad (3)$$

where e is the electron charge ($e > 0$), $R_1^{p,+(-)}$ denotes the spin-dependent resistance of the left junction in the parallel configuration, and $k_B T$ is the thermal energy. Here, $\Delta E_1(n, V)$ describes a change in the electrostatic energy of the system caused by the respective tunnelling event. A similar expression also holds for $\Gamma_{1 \rightarrow i}^{op}(n, V)$, but with $R_1^{p,+(-)}$ replaced by R_1^{op} . Since both ferromagnetic electrodes and the island are assumed to be made of the same material, the resistance R_1^{op} is independent of electron spin. The rates of tunnelling from the island back to the first electrode and also of tunnelling through the second junction can be derived in a similar way.

In order to calculate the electric current flowing through the system in a stationary state, we take into account the fact that in a steady-state the net transition rate between charge states with n and $n+1$ excess electrons on the island is equal to zero [7]

$$\begin{aligned} & P(n, V) \left[\sum_{\sigma=+,-} \sum_{\sigma'=+,-} \left[\Gamma_{1 \rightarrow i}^{\sigma' \sigma}(n, V) + \Gamma_{2 \rightarrow i}^{\sigma' \sigma}(n, V) \right] \right] \\ &= P(n+1, V) \left[\sum_{\sigma=+,-} \sum_{\sigma'=+,-} \left[\Gamma_{i \rightarrow 1}^{\sigma \sigma'}(n+1, V) + \Gamma_{i \rightarrow 2}^{\sigma \sigma'}(n+1, V) \right] \right] \end{aligned} \quad (4)$$

From this, one can determine the probability $P(n, V)$ of finding the island in a state with n excess electrons when a bias voltage V is applied to the system.

Finally, the electric current flowing through the system from left to right can be calculated from the following formula:

$$I(V) = -e \sum_{\sigma=+,-} \sum_{\sigma'=+,-} \sum_{n=-\infty}^{\infty} \left[\Gamma_{1 \rightarrow i}^{\sigma' \sigma}(n, V) - \Gamma_{i \rightarrow 1}^{\sigma \sigma'}(n, V) \right] P(n, V) \quad (5)$$

Equation (5) corresponds to the current flowing through the first junction, which in the stationary limit is equal to the current flowing through the second junction, and thus through the device.

3. Numerical results and discussion

Equation (5) can be used to calculate the tunnelling current for any magnetic configuration. The tunnel magnetoresistance can be described by the ratio [8]

$$TMR = \frac{I(\alpha = 0, \beta = 0)}{I(\alpha, \beta)} - 1 \quad (6)$$

where $I(\alpha, \beta)$ is the current flowing when the angle between angular spin moments of the right electrode and island is equal to α and the angle between angular spin moments of the left electrode and island is β ($\alpha = 0$ and $\beta = 0$ corresponds to the parallel

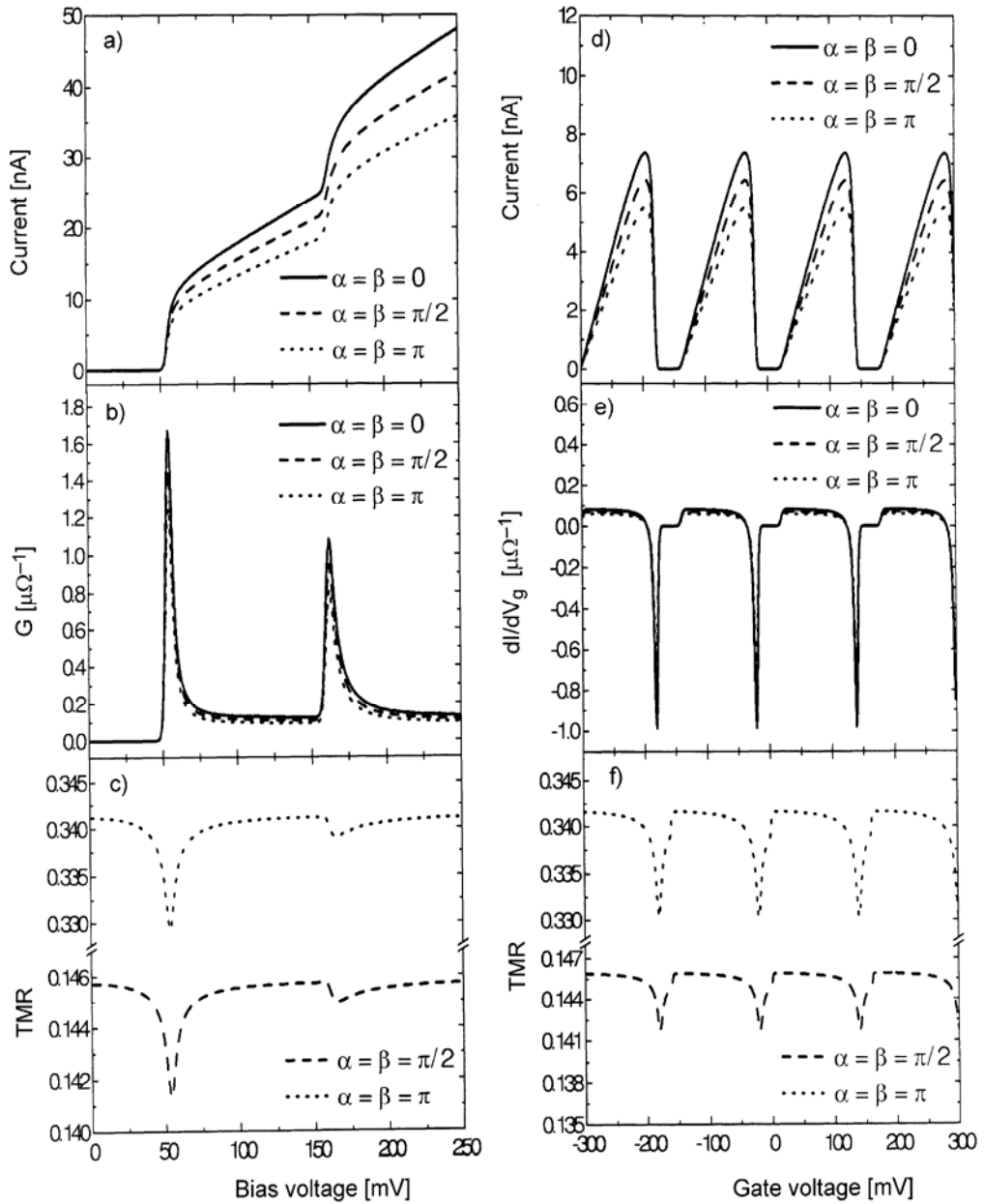


Fig. 2. The bias dependence of electric current (a), differential conductance (b), and TMR (c) in a FM SET with non-collinear magnetizations for indicated values of the angles between angular spin moments. The parameters used for numerical calculations: $T = 4.2$ K, $C_1 = C_2 = C_g = 1$ aF, $V_g = 0$. Bias voltage applied symmetrically, the following resistances assumed: $R_1^{p,+} = 0.5$ M Ω , $R_1^{p,-} = 0.1$ M Ω , $R_2^{p,+} = 25$ M Ω , $R_2^{p,-} = 5$ M Ω and $R_i^{pp} = \sqrt{R_i^{p,+} R_i^{p,-}}$, $i = 1, 2$.

The gate voltage dependences of electric current (d), the derivative dI/dV_g (e), and TMR (f) have been calculated for the indicated values of the angles α and β and for $V = 40$ mV

configuration). In Figure 2, we present the results of our numerical calculations of electric current flowing through the system and TMR as a function of the bias and gate voltages for several values of the angles ($\alpha = \beta$) between magnetizations. We have also calculated differential conductance as a function of the bias voltage and current sensitivity to the gate voltage, dI/dV_g , as a function of V_g .

For all magnetic configurations, the dependence of the electric current on the bias voltage is non-linear and presents characteristic Coulomb staircases, as is shown explicitly in Fig. 2a for three values of the angle between magnetic moments. The dependence of differential conductance on the bias voltage shows peaks corresponding to Coulomb steps in the current-voltage curves (Fig. 2b). In turn, the difference in currents flowing in two magnetic configurations – parallel ($\alpha = \beta = 0$) and non-collinear ($\alpha, \beta \neq 0$) – gives rise to a nonzero tunnel magnetoresistance, as shown in Fig. 2c. For an arbitrary magnetic configuration, TMR is modulated by charging effects which leads to characteristic dips (Fig. 2c) at bias voltages corresponding to Coulomb steps in the current-voltage characteristics of Fig. 2a. The amplitude of these dips decreases with increasing bias voltage. The gate voltage dependence of the electric current presents characteristic Coulomb oscillations (Fig. 2d). The corresponding derivative of electric current with respect to the gate voltage is shown in Fig. 2e. Finally, the Coulomb oscillations in electric current lead to the periodic behaviour of TMR with increasing gate voltage, as shown in Fig. 2f. Thus, the electric current and TMR effect strongly depend on the angles between the magnetic moments of the leads and island.

4. Conclusions

We have studied the transport characteristics of a ferromagnetic single-electron transistor. The device consists of a ferromagnetic island and two ferromagnetic external electrodes, whose magnetic moments can be oriented arbitrarily. We have calculated the current flowing through such a device, differential conductance, and the corresponding tunnel magnetoresistance. The bias dependence of electric current reveals characteristic Coulomb staircases, while the TMR effect shows characteristic dips. Furthermore, the current flowing through the system as well as the tunnel magnetoresistance also strongly depend on the gate voltage.

References

- [1] BARNAŚ J., FERT A., *Phys. Rev. Lett.*, 80 (1998), 1058.
- [2] TAKAHASHI S., MAEKAWA S., *Phys. Rev. Lett.*, 80 (1998), 1758.
- [3] BARNAŚ J., DUGAEV V., KROMPIEWSKI S., MARTINEK J., RUDZIŃSKI W., ŚWIRKOWICZ R., WEYMANN I., WILCZYŃSKI M., *Phys. Stat. Sol. (b)*, 236 (2003), 246.
- [4] WEYMANN I., BARNAŚ J., *Phys. Stat. Sol. (b)*, 236 (2003), 651.
- [5] WIŚNIEWSKA J., WEYMANN I., BARNAŚ J., *Mater. Sci.-Poland*, 22 (2004), 461.

- [6] GRABERT H., DEVORET M.H., *Single Charge Tunneling*, NATO ASI Series, Vol. 294, Plenum Press, New York, 1992.
- [7] AMMAN M., WILKINS R., BEN-JACOB E., MAKER P.D., JAKLEVIC R.C., *Phys. Rev. B*, 43 (1991), 1146.
- [8] JULLIERE M., *Phys. Lett. A*, 54 (1975), 225.

Received 1 June 2005
Revised 10 October 2005

Persistent currents controlled by non-classical electromagnetic fields

J. DAJKA*, E. ZIPPER

Institute of Physics, University of Silesia, 40-007 Katowice, Poland

Mesoscopic systems and non-classical electromagnetic fields are of central importance to quantum information processing. Our aim is to present the significant influence of non-classical radiation on the properties of persistent currents. We study mesoscopic rings subject to both classical and non-classical electromagnetic fields. Our discussion is limited to one- and two-mode fields prepared in a given quantum state. We show that non-classical fields with a definite phase can induce persistent currents even in the absence of classical driving. There are two qualitatively distinct classes of two-mode electromagnetic fields: separable and entangled. This is reflected in the properties of the current, which becomes time-dependent for fields in an entangled state. We extend our earlier work and investigate the effect of entanglement for a family of various states with various amounts of entanglement: from separable states to Bell states quantified by concurrence.

Key words: *persistent current; non-classical electromagnetic field; entangled state*

Mesoscopic devices operating at temperatures 0.1–1 K exhibit interesting quantum phenomena. Most work involves the interaction of these devices with classical microwaves and static magnetic fields. In our recent papers [1, 2], we have investigated the properties of persistent currents [3] in mesoscopic normal metal rings or cylinders subject to both classical and non-classical electromagnetic fields prepared in a given quantum state. The emphasis in these studies is on the properties arising from the quantum nature of the electromagnetic field and cannot be understood classically. The present work shows how one- and two-mode electromagnetic fields prepared in some special quantum states influence persistent currents. Persistent currents in mesoscopic metallic and semiconducting rings at low temperature are a signature of electron phase coherence [3]. They can be induced by a static magnetic flux φ_e at $T < T^*$, where $T^* = \Delta/(2\pi^2)$ and Δ is the quantum size energy gap. The formula for the persistent current is ($\hbar = c = k_B = 1$) [4]:

*Corresponding author, e-mail: dajka@server.phys.us.edu.pl

$$I_e \left(\frac{\varphi_e}{\varphi_0}, T \right) = I_0 \sum_{n=1}^{\infty} A_n(T) \sin \frac{2\pi n \varphi_e}{\varphi_0} \quad (1)$$

$$A_n(T) = \frac{4T}{\pi T^*} \frac{\exp(-nT/T^*)}{1 - \exp(-2nT/T^*)} \cos(nk_F l_x)$$

where $\varphi_0 = 2\pi/e$ is the flux quantum, I_0 is the current amplitude, and k_F is the Fermi wave vector. The currents are periodic functions of φ_e/φ_0 and depend on certain parameters (e.g. radius of the ring). They can be paramagnetic or diamagnetic at small φ_e . The following discussion is limited to the case of paramagnetic currents flowing in quasi 1D rings with an even number of coherent electrons. The result for diamagnetic currents can be obtained if one replaces φ_e by $\varphi_e + \varphi_0/2$ [1]. For quantum electromagnetic fields, the electric and magnetic fields are the well-known dual quantum variables [6]. One can also associate them, by simple integration around the circumference of the ring, with variables representing electromotive force and the magnetic flux. The operator of magnetic flux evolves in the Heisenberg picture, and after suitable renormalization, in the following way (for details see [5]):

$$\varphi(t) = \frac{1}{\sqrt{2}} \left[\exp(i\omega t) a^+ + \text{h.c.} \right]$$

In further considerations, we assume that the energy scales $T < \omega < \Delta$ are well separated in order to satisfy ‘‘adiabatic’’ conditions [1] and avoid various non-linear effects. Since the coherent current depends on the ratio of the flux and flux quantum φ_0 rather than the flux itself, we introduce the re-scaled flux operator

$$x = \frac{\varphi_e}{\varphi_0} + \frac{\varphi}{\varphi_0} \equiv \lambda + x_q \quad (2)$$

where λ is the classical magnetic flux (c -number) and x_q is the operator of the non-classical flux (both in φ_0 units). As a result of the presence of non-classical fields, the current itself is no longer a c -number, but becomes a quantum mechanical operator. This current operator, rescaled with respect to the current unit I_0 , reads after rearrangement (for details see Ref. [1]):

$$I_c := \sum_{n=1}^{\infty} A_n(T) \exp(i2\pi n x) = \sum_{n=1}^{\infty} A_n(T) \exp(i2\pi n \lambda) \exp(i2\pi n x_q) \quad (3)$$

$$= \sum_{n=1}^{\infty} A_n(T) \exp(i2\pi n \lambda) D(n\xi e^{i\omega t})$$

where $D(A) := \exp(Aa^+ - A^*a)$ is the displacement operator [6], $\xi = \sqrt{2}\pi/\varphi_0$, and ρ is the density operator of the electromagnetic field. The observable quantity is the imaginary part of the expectation value of the current operator:

$$I(x, T) = \Im m \langle I_c \rangle = \Im m \text{Tr}(I_c \rho) = \sum_{n=1}^{\infty} A_n(T) \exp(i2\pi n \lambda) W(\zeta_n) \tag{4}$$

and the calculation of the expectation value of the current reduces to the calculation of the Weyl function $W(\zeta_n) = \text{Tr}(\rho D(n\xi \exp(i\omega t)))$, with $\zeta_n = n\xi \exp(i\omega t)$. We see that persistent currents calculated from Eq. (4) are influenced by the features of non-classical radiation contained in the Weyl function.

The most popular “object” of quantum computing is the qubit described by:

$$\rho = |\psi\rangle\langle\psi|; |\psi\rangle = \frac{1}{\sqrt{2}}|0\rangle + \frac{e^{i\delta}}{\sqrt{2}}|1\rangle \tag{5}$$

where the phase $\delta \in \langle 0, 2\pi \rangle$ reflects the different superpositions of the two lowest number eigenstates of the non-classical field. The qubit is a quantum mechanical analogue of the bit and is subject to intensive research itself. In our case, it is the most general state of the electromagnetic field, involving only the two lowest energy eigenstates. In the state described by Eq. (5), the number of photons is not definite and therefore the state has a definite phase (the phase and the number of photons are dual variables [7]). We have already found [1] that the persistent current calculated in a state with a phase is time dependent.

In order to take into account the noise present in every real experiment, we assume that the qubit, before reaching the ring, is transmitted via the depolarizing channel [8]:

$$\rho' = \Pi(\rho) = \frac{I_d}{2} + (1-p)\rho \tag{6}$$

where $I_d/2$ (given by the identity matrix I_d [8]) is the maximally mixed state of the two-state system, and p describes a classical probability.

The behaviour of the current calculated with ρ given by Eq. (5) is plotted in Figs. 1 and 2, for which two important effects can be seen. The first is the lowering of the overall amplitude of the current with increasing p . It is shown in Fig. 1, where the current, being a function of the classical flux λ , is plotted for several values of p for $\delta=0$ and $t=0$. This effect does not kill the current even for $p=1$.

The second effect is connected to the phase δ . We find that a choice of the phase leads to a finite value of the current, even in the absence of the classical flux ($\lambda=0$). This is shown in Fig. 2, where, in the main graph, the current $I(\lambda=0)$ vs. δ is plotted at $t=0$. We see that non-classical electromagnetic fields with different values of δ can produce, in contrast to the classical flux, both diamagnetic and paramagnetic currents. Note that for the state with $p=1$, the current $I(\lambda=0)=0$. The inset in Fig. 2 shows the time dependence of the current $I(\lambda=0)$ for two values of δ . A similar effect has already been discovered for coherent states in Ref. [1].

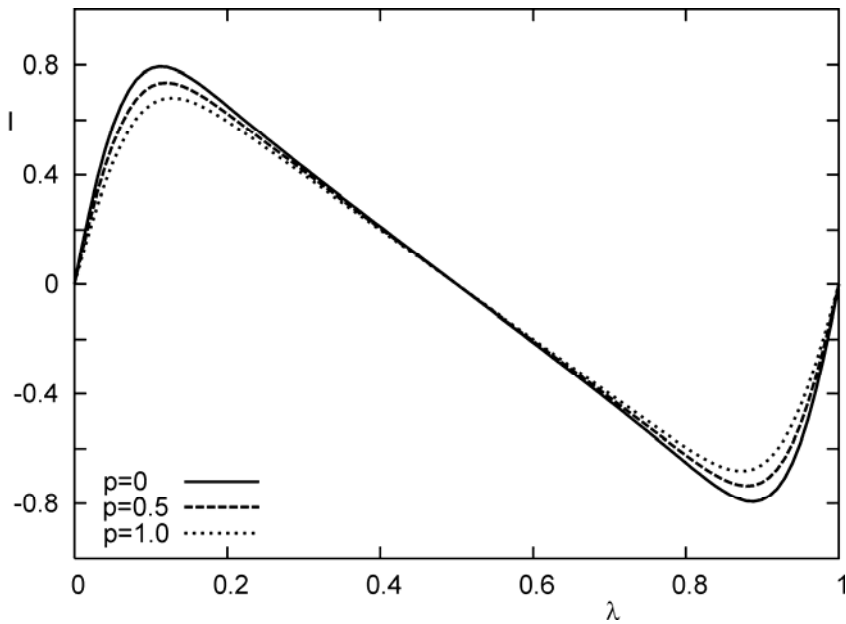


Fig. 1. Persistent current vs. classical flux in the presence of a depolarised qubit for three values of p and $\delta = t = 0$

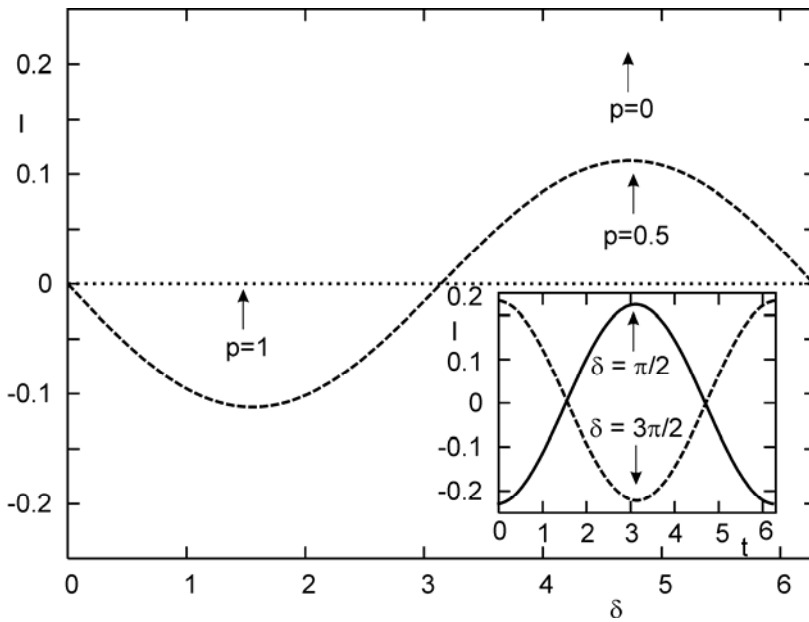


Fig. 2. Current in the presence of a depolarised qubit vs. the phase δ in the absence of classical flux $\lambda = 0$ for different values of p and $t = 0$ (main graph). The inset shows the time dependence of the current $I(\lambda = 0)$ for two values of δ and $p = 0$

Entangled states of photons are of central interest in quantum communication and quantum information. Their “classically unusual” properties allow one to expect that the current in the presence of such states will also become “unusual”. The expectation value of the complex current in the mesoscopic ring in the presence of two-mode fields with frequencies ω_1 and ω_2 is given by [1]

$$\langle I_c \rangle = \sum_{n=1}^{\infty} A_n(T) \exp(i2\pi n\lambda) W(\zeta_{1n}, \zeta_{2n}) \tag{7}$$

where the two-mode Weyl function is

$$W(\zeta_{1n}, \zeta_{2n}) = \text{Tr} \left(\rho D_1(n\xi \exp(i\omega_1 t)) D_2(n\xi \exp(i\omega_2 t)) \right)$$

with $\zeta_{in} = n\xi \exp(i\omega_i t)$.

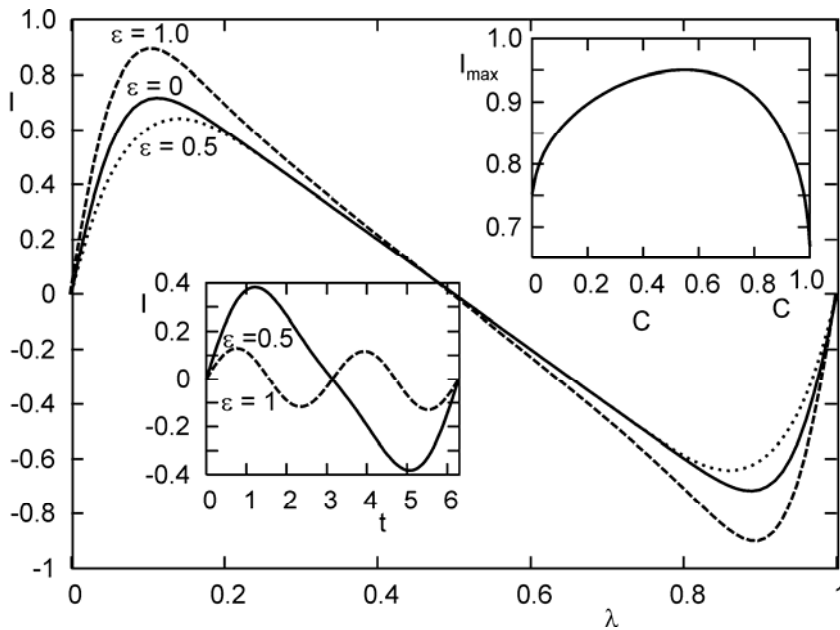


Fig. 3. Persistent currents in the presence of two-mode fields with different amounts of entanglement at $t = 0$. Inset 1 (bottom): time dependence of the current for $\lambda = 0$. Inset 2 (top): amplitude of the current as a function of concurrence C

In the following, we investigate the properties of the currents in the presence of the following family of states

$$|\psi\rangle = \frac{1}{\sqrt{2}}(a(\epsilon)|00\rangle + b(\epsilon)|01\rangle + c(\epsilon)|10\rangle + d(\epsilon)|11\rangle) \tag{8}$$

with

$$a(\varepsilon) = \sqrt{2 - \varepsilon(1 - \sqrt{2})}, \quad d(\varepsilon) = \varepsilon, \\ b(\varepsilon) = \sqrt{2 - a^2(\varepsilon) + d^2(\varepsilon)} \quad \text{and} \quad c(\varepsilon) = 0 \quad \text{for} \quad 0 \leq \varepsilon \leq 1$$

The amount of entanglement in this family of states increases with ε and can be measured by the concurrence $C = |ab|$ [9]. The problem of time-dependence has already been discussed in Ref. [2]. Here, we focus on the amplitude of the current. The plot of the resulting current vs. λ for $\omega_1 \approx \omega_2$ is given in Fig. 3. Notice that both the overall amplitude (main graph) and the current in the absence of classical flux ($\lambda = 0$) approach their maxima for non-extremum values of ε , namely $\varepsilon \approx 0.5$ (the upper inset in Fig. 3). Furthermore, the presence of entangled light also changes the period of the time dependence of the current (the lower inset in Fig. 3).

It is well known that persistent currents can be driven by static magnetic fluxes [3]. In this paper, we show that they can also be induced by non-classical electromagnetic fields. The purpose of these considerations is to present some interdisciplinary research that exploits the quantum nature of the non-classical fields, which are studied in optics in order to control the behaviour of mesoscopic quantum devices. Persistent currents flowing in mesoscopic rings or cylinders are placed on the border of the classical and quantum worlds. Hence, as expected, they can be controlled by both classical and quantum parameters. In this paper, we have investigated the possibility of quantum-like control. We have shown that one obtains the time-dependence of the current, provided that the non-classical field is in a state with a well-defined phase (indefinite number of photons). Such a field can produce a current even in the absence of classical driving. Further, the effect of entanglement in a two-mode electromagnetic field was considered. We have studied fields with different amounts of entanglement as measured by concurrence, and found that a moderate (non-extremum) amount of entanglement can enhance the current amplitude relative to the case of separable ($\varepsilon = 0$) fields. The work belongs to the general context of studying fully quantum mechanical devices comprising mesoscopic devices and non-classical electromagnetic fields. Such devices are potentially useful for quantum technologies and quantum information processing. The presented results show that persistent currents can serve as detectors of non-classical properties of radiation or as efficient tools in quantum-driving mesoscopic systems.

Acknowledgements

J. D. acknowledges the support of the Foundation for Polish Science under Grant No. SN-302-934/2005 and of the Polish State Committee for Scientific Research (KBN) via grant PBZ-MIN 008/P03/2003. The authors acknowledge the joint support of the Ministry of Scientific Research and Information Technology of Poland and the British Council under the British-Polish Research Partnership Programme WAR/341/256.

References

- [1] DAJKA J., SZOPA M., VOURDAS A., ZIPPER E., Phys. Rev. B, 69 (2004), 045305.
- [2] DAJKA J., SZOPA M., VOURDAS A., ZIPPER E., Phys. Stat. Sol. (b), 242 (2005), 296.
- [3] BUTTIKER M., IMRY Y., LANDAUER R., Phys. Lett. A, 96 (1983), 365; ECKERN U., SCHWAB P., J. Low Temp. Phys., 126 (2002), 1291.
- [4] CHEUNG H.F., GEFEN Y., RIEDEL E.K., SHIH W.H., Phys. Rev. B, 37 (1988), 6050.
- [5] VOURDAS A., Phys. Rev. B, 49 (1994), 12040.
- [6] LUISELL W.H., *Quantum Statistical Properties of Radiation*, Wiley, New York, 1973.
- [7] PERINA J., HRADIL Z., JURCO B., *Quantum Optics and Fundamentals of Physics*, Kluwer, Dordrecht, 1994.
- [8] NIELSEN M.A., CHUANG I.L., *Quantum Computation and Quantum Information*, Cambridge University Press, Cambridge, 2000.
- [9] WOOTERS W.K., Phys. Rev. Lett., 78 (1998), 5022; LEVAY P., quant-ph/0306115v1 (2003).

Received 1 June 2005
Revised 10 October 2005

Magnetic properties of (Eu,Gd)Te semiconductor layers

P. DZIAWA^{1*}, V. OSINNIY¹, W. DOBROWOLSKI¹, K. DYBKO¹, E. ŁUSAKOWSKA¹,
B. TALIASHVILI¹, T. STORY¹, C.J.P. SMITS², H.J.M. SWAGTEN²

¹Institute of Physics, Polish Academy of Sciences, al. Lotników 32/46, 02-668 Warsaw, Poland

²Eindhoven University of Technology, P.O. Box 513, 5600 MB Eindhoven, The Netherlands

In (Eu,Gd)Te semiconductor alloys, a well known antiferromagnetic semiconductor compound EuTe is transformed into an n-type ferromagnetic alloy. This effect is driven by the RKKY interaction via conducting electrons, created due to the substitution of Gd³⁺ for Eu²⁺ ions. It is expected that due to the high degree of electron spin polarization, (Eu,Gd)Te can be exploited in new semiconductor spintronic heterostructures as a model injector of spin-polarized carriers. (Eu,Gd)Te monocrystalline layers with Gd content up to 5 at. % were grown by MBE on BaF₂ (111) substrates with either PbTe or EuTe buffer layers. Measurements of magnetic susceptibility and magnetization revealed that the ferromagnetic transition with the Curie temperature of $T_C = 11\text{--}15$ K is observed in (Eu,Gd)Te layers with n-type metallic conductivity. The analysis of the magnetization of (Eu,Gd)Te was carried out in a broad range of magnetic fields applied along various crystal directions, both in- and out of the layer plane. It revealed, in particular, that a rapid low-field ferromagnetic response of the (Eu,Gd)Te layer is followed by a paramagnetic-like further increase towards a full saturation.

Key words: *spintronics; ferromagnetic semiconductor; rare earth compound*

1. Introduction

Europium telluride belongs to a well know family of magnetic semiconductors and is a model type II antiferromagnetic material. This material offers the unique possibility to transform it from an insulating antiferromagnetic to an n-type ferromagnetic by substituting Gd³⁺ ions for Eu²⁺ in the crystal matrix. The mechanism responsible for such a transformation is attributed to Ruderman–Kittel–Kasuya–Yosida interactions, i.e. the coupling between strongly localized Eu $S = 7/2$ spins mediated by quasi-free carriers. In early studies of bulk materials, it was shown [1–4] that for concentrations of Gd up to 60 at. %, (Eu,Gd)Te crystals exhibit a ferromagnetic transition, whereas for higher concentrations of Gd the type of magnetism again changes to antiferromag-

*Corresponding author, e-mail: dziawa@ifpan.edu.pl

netic (resulting from the oscillating behaviour of RKKY interactions). According to the above-described mechanism, all europium-gadolinium chalcogenides with Gd contents below about 60 at. % were found to be ferromagnetic semiconductors with the maximum Curie temperature $T_C = 150$ K for oxides and about $T_C = 10$ K for tellurides [1–4]. The terminal alloys (gadolinium chalcogenides) are antiferromagnetic compounds with metallic-type conductivity. In the n-type ferromagnetic state, (Eu,Gd)Te exhibits high electron-spin polarization related to the large splitting of 5d6s conduction band states. This feature, together with the expected epitaxial compatibility of (Eu,Gd)Te with well-known nonmagnetic semiconductor materials such as PbTe or CdTe, makes (Eu,Gd)Te an intriguing key-element of new all-semiconductor spin injection spintronic heterostructures. In this work, we experimentally study the magnetic properties of epitaxial layers of (Eu,Gd)Te in which both metallic and insulating electrical properties are observed, depending on Gd content and the crystal stoichiometry of the alloy.

2. Growth and characterization of layers

The (Eu,Gd)Te layers were grown in a home-built MBE system equipped with effusions cells for Eu, Gd, Te₂, and PbTe solid sources. Either a EuTe layer or a EuTe/PbTe bilayer, deposited on a freshly cleaved (111) surface of BaF₂ monocrystals at about 270 °C, was used as a buffer. Next, a (Eu,Gd)Te layer from 0.25 up to 1 μm thick was grown. Reflection high-energy electron diffraction (RHEED) was used to monitor the growth process in situ, showing well-defined streaky patterns indicating the two-dimensional mode of growth. A more detailed description of the MBE growth process for (Eu,Gd)Te layers is given in Ref. [5]. Structural studies of epilayers were carried out using standard X-ray diffraction (XRD). The θ -2 θ diffraction spectra clearly revealed the peaks due to the BaF₂ substrate, the buffer layer, and (Eu,Gd)Te layer with lattice parameters depending on Gd content. All the layers are monocrystalline (rock salt structure) with the [111] growth direction. FWHM parameters of the rocking curves in the range 200–400 arcsec confirmed the good crystalline quality of our samples. Additionally, epilayers were examined by atomic force microscopy (AFM). The root mean square parameter describing the roughness of the layer surface was 0.6 nm (corresponding to two atomic monolayers) over a 10×10 μm² area for the best layers. The concentration of gadolinium in the layers was obtained from energy dispersive X-ray fluorescence and electron micro-probe analysis. (Eu,Gd)Te layers with a maximum content of Gd up to 5 at. % were obtained.

3. Experimental

AC magnetic susceptibility (χ) measurements were applied to investigate the influence of quasi-free carriers on the type of magnetic ordering in (Eu,Gd)Te layers. The measurements were carried out in the temperature range $T = 4.5$ –80 K using

a LakeShore susceptometer and applying an AC magnetic field of 5 Oe at the frequency of 625 Hz. We obtained two dramatically different $\chi(T)$ curves, depending on the type of conductivity (Fig. 1).

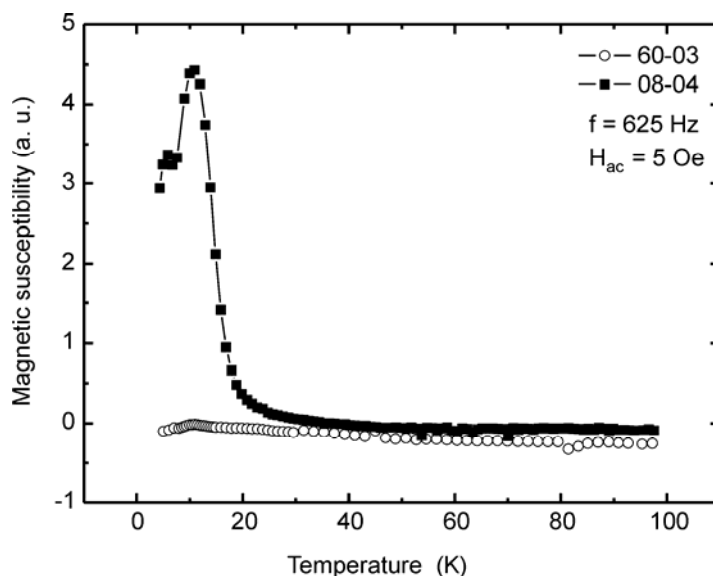


Fig. 1. AC magnetic susceptibility vs. temperature: insulating antiferromagnetic (open dots) and n-type ferromagnetic (squares) layer

For all n-type (Eu,Gd)Te layers, a ferromagnetic transition was observed (squares) at $T_C = 11\text{--}15$ K, while insulating (Eu,Gd)Te layers exhibited an antiferromagnetic transition (open dots) at $T_N \approx 10$ K. In the latter case, in spite of incorporating Gd into the EuTe matrix (therefore supplying it with carriers), we destroyed n-type conductivity using excess Te in the molecular beam flux, resulting in an insulating (Eu,Gd)Te material similar to undoped EuTe. These experimental observations give strong evidence of carrier-induced ferromagnetic ordering in (Eu,Gd)Te alloys. The magnetic effects discussed above were also reflected in electron transport studies. The Hall effect measurements, carried out in the temperature range 4.2–300 K, revealed n-type conductivity with a very high concentration of quasi-free carriers $n \approx 10^{20} \text{ cm}^{-3}$. Moreover, the resistivity dependence on temperature demonstrates behaviour correlated with the magnetic transition. Lowering T_C results in an increase of resistance due to the scattering on spin moments. Over 90% negative magnetoresistance was observed at magnetic fields of about 0.6 T. The ferromagnetic properties of n-(Eu,Gd)Te were also studied by SQUID magnetometry. Measurements of magnetization hysteresis loops were carried out in various crystal directions, both in-plane and out of plane (Fig. 2). In (Eu,Gd)Te layers, the in-plane magnetocrystalline anisotropy is very weak, with an estimated anisotropy field below 2 mT. The dominant anisotropy effect is the strong ($H_A \approx 1$ T) shape anisotropy expected in a ferromagnetic layer.

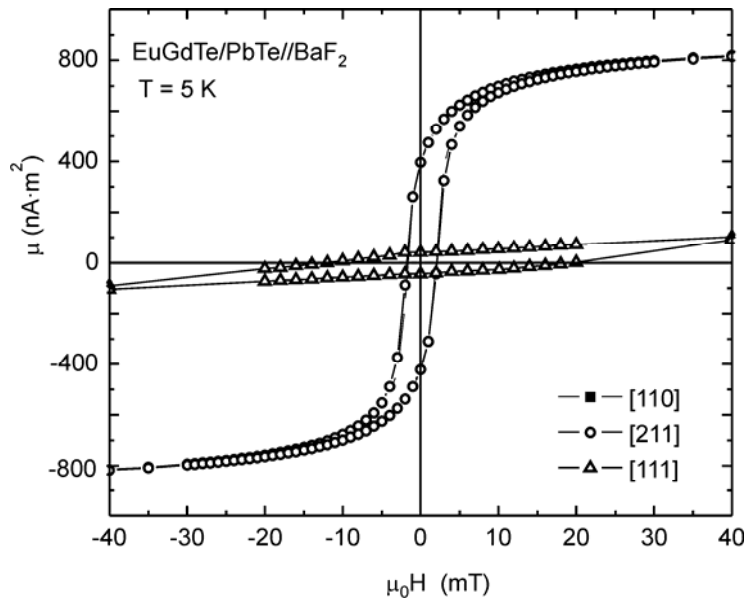


Fig. 2. Hysteresis loops for various crystalline directions: out-of-plane [111] as well as in-plane ([110] and [211])

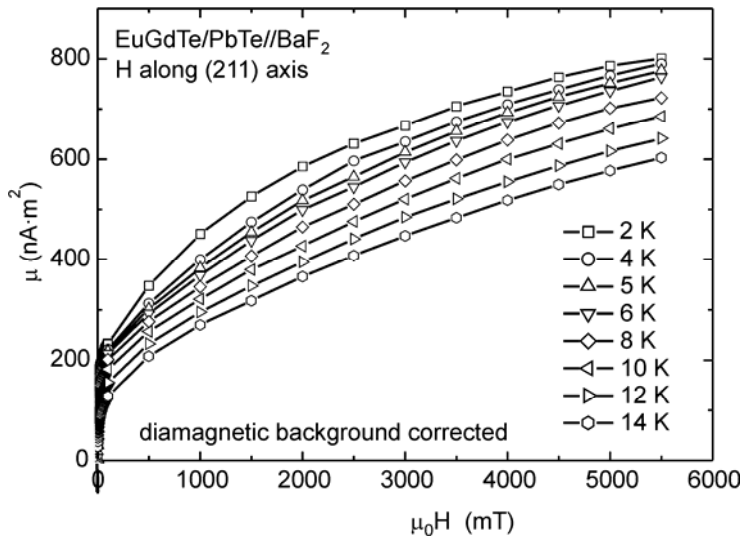


Fig. 3. High-field magnetization of n-(Eu,Gd)Te layers (SQUID measurements)

SQUID high-field measurements of magnetization for n-(Eu,Gd)Te (see Fig. 3) showed that the low-field rapid ferromagnetic response is followed by a much slower approach to full magnetic saturation, still not reached at fields of 5.5 T. Recent MOKE magnetometry studies of high-field (up to 20 T) magnetization of n-(Eu,Gd)Te layers showed full saturation (at $T = 5$ K) for fields above 10 T. Although this behaviour is not yet fully un-

derstood, we consider in particular the competition between ferromagnetic and anti-ferromagnetic exchange interactions when discussing this experimental finding. We also consider possible electronic separation effects, resulting in the co-existence of n-type ferromagnetic and insulating antiferromagnetic regions in the layer.

4. Conclusions

Heterostructures incorporating (Eu,Gd)Te semiconductor ferromagnetic layers were grown on BaF₂ (111) substrates exploiting the MBE technique. Structural characterization performed by RHEED, XRD, and AFM methods revealed good surface morphology and crystal quality of the layers. The Hall effect and resistivity measurements showed the dependence of electrical properties of (Eu,Gd)Te on stoichiometry (controlled by tellurium content), resulting in either a metallic n-type or insulating material. The ferromagnetic transition with the Curie temperature of $T_C = 11\text{--}15$ K was observed only in metallic n-(Eu,Gd)Te layers.

Acknowledgements

This work was supported by KBN research project PBZ-KBN-044/P03/2001.

References

- [1] WATCHER P., *Handbook on the Physics and Chemistry of the Rare Earth*, North Holland, Amsterdam, 1979.
- [2] MAUGER A., GODART C., *Phys. Rep.*, 141 (1986), 51.
- [3] VON MOLNAR S., *J. Supercond.*, 16 (2003), 1.
- [4] HOLTZBERG F., MCGUIRE T.R. AND METHFESSEL S., *J. Appl. Phys.*, 37 (1966), 976.
- [5] DZIAWA P., TALIAHVILI B., DOMUCHOWSKI W., ŁUSAKOWSKA E., ARCISZEWSKA M., DEMCHENKO I., DOBROWOLSKI W., DYBKO K., FEDORYCH O.M., NADOLNY A.J., OSINNIY V., PETROUCHYK A. AND STORY T., *Acta Phys. Polon. A*, 106 (2004), 215.

Received 1 June 2005

Revised 10 October 2005

Dendritic domain structures in ultrathin cobalt films

W. STEFANOWICZ¹, M. TEKIELAK¹, V. BUCHA², A. MAZIEWSKI¹,
V. ZABLOTSKI^{1,3*}, L.T. BACZEWSKI⁴, A. WAWRO⁴

¹Institute of Experimental Physics, University of Białystok, Lipowa 41, 15-424 Białystok, Poland

²United Institute of Informatics Problems, Minsk, Belarus

³Institute of Physics, Czech Academy of Sciences, 18221 Prague 8, Czech Republic

⁴Institute of Physics, Polish Academy of Sciences, Lotników 32/46, 02-668 Warsaw, Poland

We report on the study of dendritic domain structures in gold-enveloped cobalt ultrathin films of thicknesses slightly below the thickness at which the reorientation from a perpendicular magnetization state to the in-plane state takes place. In these films, magnetization reversal proceeds through the dendritic growth of domains. A magnetic after-effect was observed. We reveal the mechanism and key parameters controlling the dendritic growth of magnetic domains.

Key words: *magnetic domains; ultrathin film; cobalt*

1. Introduction

Dendrite growth is a phenomenon well known in the physics of crystals. Up to now, however, this phenomenon has puzzled in many aspects. The main question of the general dendrite growth problem is how the nanoscale short-ranged interatomic interaction can drive structure growth on mesoscopic length scales. Previously, dendritic domain structures were observed in Co/Pt multilayers (0.4 nm Co/1.1 nm Pt)₁₀ [1, 2]. In these works, dendritic domain growth was explained by the difference in the activation volumes of the domain wall-motion and nucleation processes. Here, we report on the studies of dendrite domains in Co-monolayer ultrathin films (Au/Co/Au) and put forward another possible explanation of the phenomenon observed in our samples.

Cobalt ultrathin films of nominal thickness, $d = 1.5\text{--}1.6$ nm were studied. The thicknesses of our samples were slightly below the critical thickness $d_1 = 1.79$ nm [3] defining the reorientation phase transition (RPT) from the perpendicular to in-plane magnetization state.

*Corresponding author, e-mail: zablot@fzu.cz

2. Experimental

Samples of the structure $\text{Al}_2\text{O}_3/\text{Mo}$ (20 nm)/ Au (20 nm)/ Co (1.5 nm)/ Au (8 nm) were grown in a molecular beam epitaxy system under the pressure of 10^{-10} Torr. In samples with thicknesses inferior to d_1 , perpendicular anisotropy favours the out-of-plane magnetization orientation and domain formation. Domain structure visualization was performed by an optical polarization microscope. A magnetic field H perpendicular to the sample plane was applied and the magnetization changes were recorded. A special software was developed to extract the domain parameters. Remnant dendritic domain structure (DDS) images were recorded during magnetization reversal induced by magnetic field pulses with (i) increasing numbers of pulses or (ii) increasing pulse amplitude.

3. Results and discussion

The studied samples are characterized by square-like magnetic hysteresis loops as shown in Fig. 1a. To study the dynamics of magnetization reversal, we measured the normal component of film magnetization as a function of time after applying $H > 0$ to a sample initially saturated by $H < 0$ (Fig. 1b). As is seen in Fig. 1b, a magnetic after-effect takes place. From this figure, one can see that in relatively low applied magnetic fields ($H < 100$ Oe) the magnetization reversal rate is rather low and film magnetization does not reach saturation ($M/M_S = 1$) during the observation time.

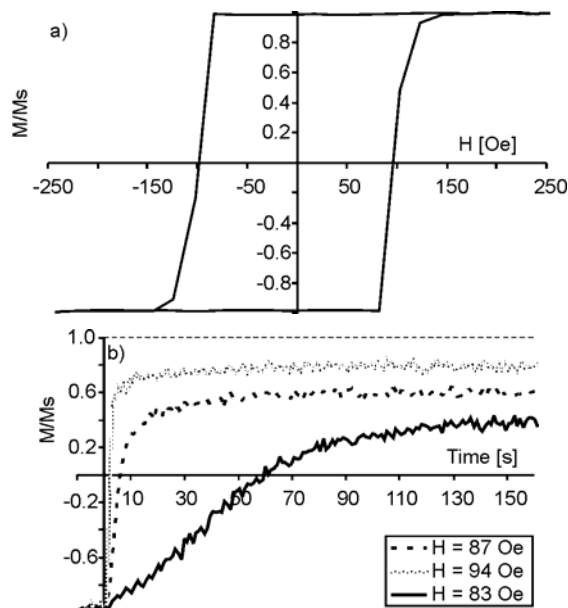


Fig. 1. Magnetic hysteresis loop for a cobalt film with a thickness of $d = 1.5$ nm (a) and time dependences of film magnetization for different strengths of the applied magnetic field (b)

Domain structure images were recorded for a remnant state after magnetic field pulses. Starting from the saturated state ($H < 0$, “black” field), we applied a sequence of reverse field pulses ($H > 0$, “white” field) of different durations and amplitudes.

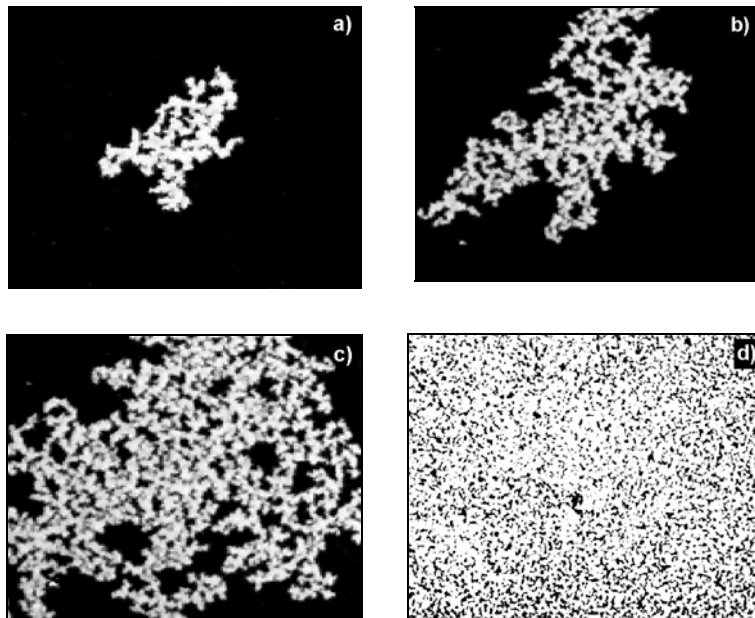


Fig. 2. Evolution of the dendritic domain structure in a cobalt film with a thickness of 1.5 nm. The sample was initially saturated by a field $H < 0$ favouring “black” domains. Images after: a) $H = 87$ Oe, $\Delta t = 1$ s, b) $H = 87$ Oe, $\Delta t = 2$ s, c) $H = 87$ Oe, $\Delta t = 3$ s, d) $H = 87$ Oe, $\Delta t = 200$ s. The image sizes are 0.11×0.10 mm²

Figure 2a–d shows a typical dendrite domain growth during magnetization reversal. Initially, the reversal domain nuclei appear in the selected films and they subsequently grow by domain wall propagation in different directions. Such directions are “easy roads” for the motion of domain walls constituting many branches (fingers) to a dendrite. The total dendrite area significantly increases with time (or with the number of field pulses), while dendrite branch width practically does not change. We have found that dendrite branch width w is typically about 6 μm . Note that dendrite-like domain geometry differs from the so-called “swiss cheese” domain structure observed in Au/Co(d)/Au ultrathin films with $d = 0.8$ nm [4]. The latter has irregularities in its spatial hole distribution and their sizes, while in the DDS “black holes” are regularly distributed and have a characteristic size of about 1 μm . The dendritic character of magnetic flux penetration was recently observed in superconducting films [5, 6]. The final stage of DDS evolution is a barely saturated magnetization state, in which “hard” non-reversed magnetic domains (small black regions in Fig. 2d) still exist up to higher magnetic fields, $H \approx H_{\text{col}} = 140$ Oe. Such an unexpected phenomenon – an incompletely saturated state – is related to the contributions of the spatial distribution of

local coercive fields, H_c , and domain magnetostatic forces that keep isolated domains metastable.

Making use of an elaborated image processing software, we found the time dependences of the total area fraction of dendritic domains (Fig. 3a). The plots indicate that avalanches – jumps of the derivative of dendrite surface area (Fig. 3b) – are present in the evolution of dendritic domain structure. Such avalanches are the result of domain structure instabilities with respect to small variations in the applied field.

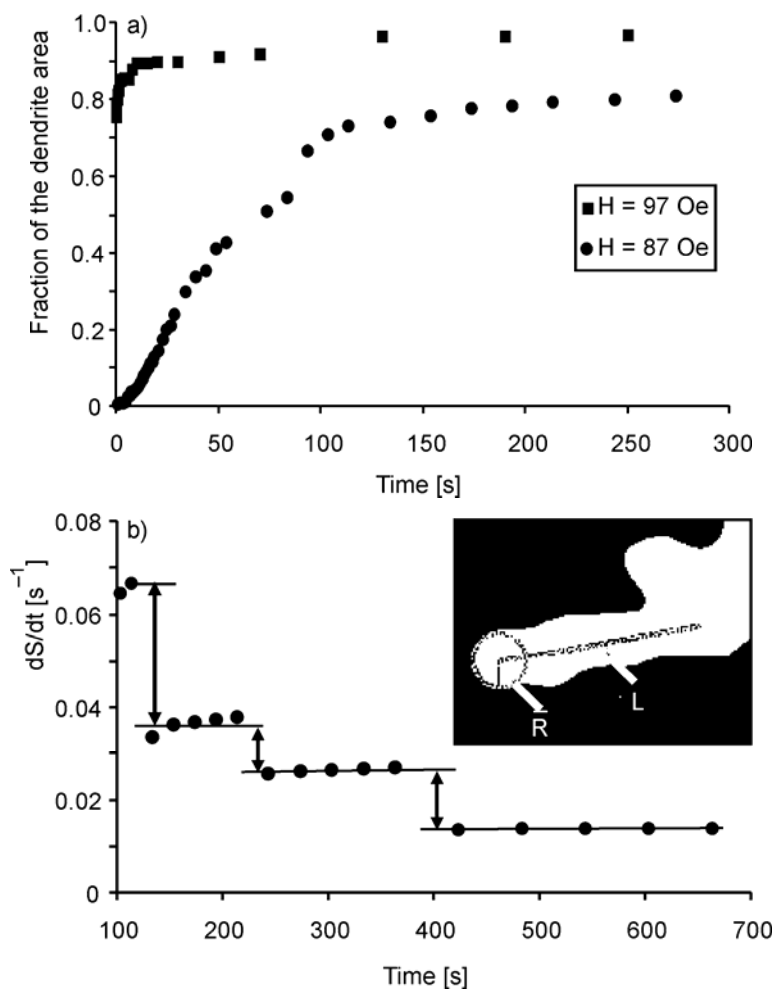


Fig. 3. Time dependence of the total reversed area fraction of domains for two amplitudes of the magnetic field (a) and time derivative of dendrite area (b), $H = 87$ Oe. The inset shows the geometry of a dendrite finger

Now we describe the dendrite growth mechanism in ultrathin Co films. Initially, some domain nucleation centres (stripe-like domains with magnetization parallel to the applied field) appear in areas where the film morphology favours nucleation proc-

esses. It could be possible, for example, that areas with a locally lowered anisotropy constant are caused by variations in film composition or thickness.

Further, nucleation centres grow through fingers. Finger geometry is described by: width w , length L and finger tip radius R (see the inset in Fig. 3). This growth is determined by a balance between magnetic (Zeeman) and magnetostatic forces for transversal and longitudinal directions, respectively,

$$F'_{MS} = -\frac{\partial E_{MS}}{\partial w} \quad \text{and} \quad F^l_{MS} = -\frac{\partial E_{MS}}{\partial L}$$

which tend to increase both domain length and width, and the coercive force and domain wall tension preventing it. Local equilibrium requires a balance of all these forces per unit length of the finger contour. A force per unit contour length represents a 2D-pressure acting on the finger walls. Let us denote the 2D-pressures on the lateral finger wall and tip wall as $f_L = F^l/L$ and $f_{tip} = F^l/\pi R$, respectively. In these terms, the coercive pressure is $f_c = 2M_s H_c d$ and it is the same for transversal and longitudinal directions. The domain wall pressure is given by the Laplace formula $f_w = \sigma d/R$ (σ is the surface density the domain wall energy).

The curvature radius of a lateral finger surface is infinite, and the wall tension there is zero. Therefore, the condition for transversal domain growth is $f'_{MS} + f_H \geq f_c$. In the case of $L \gg w$, one can neglect the lateral magnetostatic force and rewrite the transversal growth condition as

$$2M_s H d \geq f_c \quad (1)$$

Due to domain wall tension at the domain tip, however, the longitudinal growth is determined by the condition

$$\frac{1}{\pi R} \left[\left| \frac{\partial E_{MS}}{\partial L} \right| - \pi \sigma d \right] + 2M_s H d \geq f_c \quad (2)$$

There is an inequivalence between the growth conditions in the longitudinal and transversal directions. Equation 2 shows that the possibility of longitudinal domain growth is strongly determined by the tip radius and domain wall energy density, σ . Comparing the longitudinal growth condition (Eq. (2)) with the transversal condition (Eq. (1)), one can conclude that the former one is softer, especially in the case of small values of R and σ . The wall tension is small near the RPT, because here the effective anisotropy constant tends to zero ($K_{\text{eff}}(d_1) = 0$), hence $\sigma \propto K_{\text{eff}}^{1/2}$ is low enough. In this case, the first term in Eq. (2) is positive, which promotes the longitudinal growth. This explains the fact that longitudinal growth dominates during dendrite formation in films with d close to the RPT thickness. The mechanism of dendritic domain growth can be explained with the help of Eqs. (1) and (2) as follows. From the nucleation area, the domains initially grow in both directions, transversal and longitudinal. Dur-

ing their growth, however, the domain tip radius increases and it causes the longitudinal growth of a given finger to stop, because of a decreasing driving force according to Eq. (2). After that, the second finger nucleates somewhere on the finger's side surface and the process repeats again until reaching $R \approx w/2$. In the next step, a new nucleation starts and a new finger appears, and so forth. Therefore, domains can only grow in directions where the tip curvature is high enough. As is known, a typical feature of any dendritic growth is a fast decay of tip velocity with time (see Ref. [7] and the references therein). In our case, this phenomenon has a natural explanation – lateral finger expansion increases the tip radius and consequently, in accord with Eq. (2), decreases both the driving force and tip velocity.

4. Conclusion

We have studied some aspects of dendrite growth in the magnetic domains of ultrathin cobalt films. The domain tip radius and wall surface energy density are the key parameters that control the dendrite growth of magnetic domains. We have demonstrated that dendritic domain structures exhibit the general features of dendrite pattern formation: avalanches and finger propagation dependent on tip curvature.

Acknowledgements

This work was supported by the Polish State Committee for Scientific Research (Grant No. 4 T11B 006 24) and Marie Curie Fellowships for “Transfer of Knowledge” (“NANOMAG-LAB”, No. 2004-003177).

References

- [1] CHO Y.C., CHOE S.B., SHIN S.C., J. Appl. Phys., 90 (2001), 1419.
- [2] CHO Y.C., CHOE S.B., SHIN S.C., Appl. Phys. Lett., 80 (2002), 452.
- [3] KISIELEWSKI M., MAZIEWSKI A., POLYAKOVA T., AND ZABLOTSKII V., Phys. Rev. B, 69 (2004), 184419.
- [4] FERRÉ J., GROLIER V., MEYER P., LEMERLE S., MAZIEWSKI A., STEFANOWICZ E., TARASENKO S.V., TARASENKO V.V., KISIELEWSKI M., RENARD D., Phys. Rev B, 55, 22 (1997), 15092.
- [5] JOHANSEN T.H., BAZILJEVICH M., SHANTSEV D.V., GOA P.E., GALPERIN Y.M., KANG W.N., KIM H.J., CHOI E.M., KIM M.-S., LEE S.I., Europhys. Lett., 59 (2002), 599.
- [6] RAKHMANOV A.L., SHANTSEV D.V., GALPERIN Y.M. AND JOHANSEN T.H., Phys. Rev B, 70 (2004), 224502.
- [7] GRÁNÁSY L., PUSZTAI T., BÖRZSÖNYI T., WARREN J.A., DOUGLAS J.F., Nature Mater., 3 (2004), 645.

Received 1 June 2005

Revised 10 October 2005

Electrical resistivity of RNi_4Al and RNi_4Cu

T. TOLIŃSKI^{1*}, V. IVANOV², A. KOWALCZYK¹

¹Institute of Molecular Physics, Polish Academy of Sciences,
Smoluchowskiego 17, 60-179 Poznań, Poland

²General Physics Institute, Russian Academy of Sciences, Vavilov 38, Moscow 119991, Russia

Comparative studies of the temperature dependence of resistivity for RNi_4X ($\text{X} = \text{Al}, \text{Cu}$; $\text{R} = \text{Y}$ or rare earth) compounds are presented. These results are also compared to the previously obtained for RNi_4B . The ordering temperatures are well identified on the $\rho(T)$ curves. The residual resistivity ρ_0 of RNi_4Al is several times higher than those of RNi_4Cu and RNi_4B . The YNi_4X compounds are included in these studies as the nonmagnetic isostructural reference materials. The phonon contribution has been determined for both Y-based compounds employing the Bloch–Grüneisen formula. The CeNi_4X compounds show a shallow minimum in $\rho(T)$ at low temperatures (about 15 K). This anomaly has been ascribed to the Kondo impurity-like behaviour. For the other rare earths, the $\rho(T)$ dependences below T_C have been analyzed assuming the scattering on magnons as the predominant mechanism.

Key words: *rare earth compound; electrical resistivity*

1. Introduction

The analysis of the temperature dependence of the electrical resistivity in the intermetallic compounds is a powerful tool to get information on the intrinsic properties of these materials. Depending on the temperature range considered, one can conclude on the scattering of electrons on the thermal excitations of the lattice or on magnons.

In this paper, we present the analysis of the $\rho(T)$ curves for RNi_4Cu and RNi_4Al compounds ($\text{R} = \text{Y}$ or rare earth), both crystallizing in the hexagonal CaCu_5 -type of structure. For the sake of comparison, our previous studies on the RNi_4B series (CeCo_4B -type of structure) [1] are recalled within this paper.

*Corresponding author, e-mail: tomtol@ifmpan.poznan.pl

2. Results and discussion

We assume that the Matthiessen rule is fulfilled, i.e., the temperature dependence of resistivity can be treated as a sum of the involved contributions:

$$\rho(T) = \rho_0 + \rho_{ph}(T) + \rho_m(T) \quad (1)$$

where ρ_0 is the residual resistivity, $\rho_{ph}(T)$ represents the phonon term and $\rho_m(T)$ is the magnetic contribution.

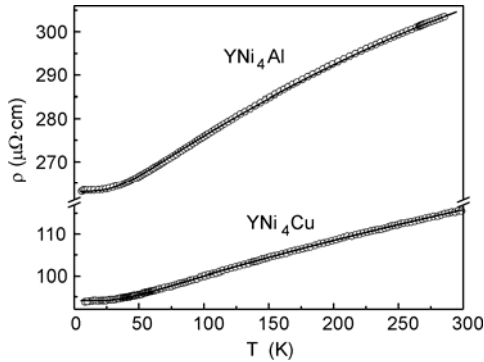


Fig. 1. The $\rho(T)$ curves of the nonmagnetic YNi_4Cu and YNi_4Al compounds. The solid lines represent fits with Eq. (2)

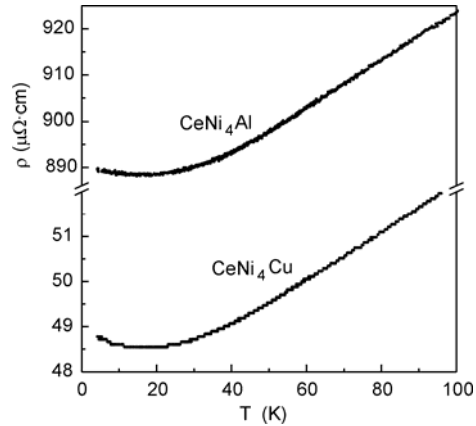


Fig. 2. The $\rho(T)$ dependences for CeNi_4Cu and CeNi_4Al . Shallow minima due to the Kondo impurity like behaviour are visible at low temperatures

Figure 1 shows the $\rho(T)$ curves measured for the nonmagnetic YNi_4Cu and YNi_4Al compounds. The solid line is a fit to the formula:

$$\rho(T) = \rho_0 + 4R\Theta_D \left(\frac{T}{\Theta_D} \right)^5 \int_0^{\Theta_D/T} \frac{x^5 dx}{(e^x - 1)(1 - e^{-x})} - KT^3 \quad (2)$$

where the second right-hand term is the Bloch–Grüneisen relation and the last term denotes the Mott scattering. This term is mainly reflected in the curvature visible in the range from about 50 K up to room temperature. For YNi_4Al we have obtained the Debye temperature $\Theta_D = 204$ K, the constants $R = 0.165 \mu\Omega\cdot\text{cm}/\text{K}$ and $K = 2.25 \times 10^{-7} \mu\Omega\cdot\text{cm}/\text{K}^3$. In the case of YNi_4Cu , the parameters are: $\Theta_D = 235$ K, $R = 0.08 \mu\Omega\cdot\text{cm}/\text{K}$ and $K = 0.5 \times 10^{-7} \mu\Omega\cdot\text{cm}/\text{K}^3$. In the previous studies on YNi_4B , we have determined $\Theta_D = 240$ K, $R = 0.109 \mu\Omega\cdot\text{cm}/\text{K}$ and $K = 0$ [1]. These values of the Debye temperature suggest that the shortest phonon wavelength occurs for YNi_4B . It seems to correlate well with the structural features, namely the lattice constant a is similar for all the RNi_4X ($X = \text{Al}, \text{Cu}, \text{B}$) series ($a \approx 5 \text{ \AA}$), whereas in the c direction the R–R separation is in average 4 Å, 3.98 Å and 3.42 Å for $X = \text{Al}, \text{Cu}$ and B , respectively.

The $\rho(T)$ dependences of the $CeNi_4Cu$ and $CeNi_4Al$ compounds are plotted in Fig. 2. The Cu-based compound exhibits a shallow minimum at low temperatures, which resembles the case of the Al- [2] and B-based [3] samples. It is ascribed to the Kondo impurity-like effect, developed by a very small amount of Ce precipitates with well localized magnetic moment. In general, it is also possible that the $CeNi_4X$ ($X = B, Al, Cu$) compounds are intermediate between the mixed valence and the Kondo lattice systems.

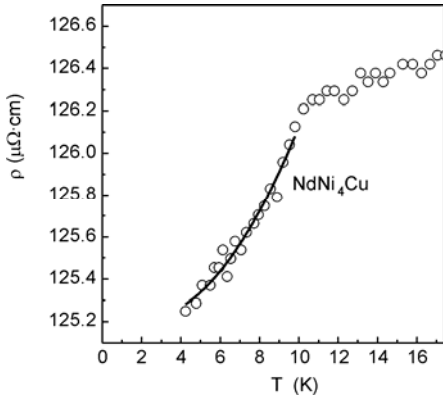


Fig. 3. The magnetic contribution $\rho_m(T)$ for $NdNi_4Cu$ fitted with Eq. (3). T_C is visible at ca. 11 K

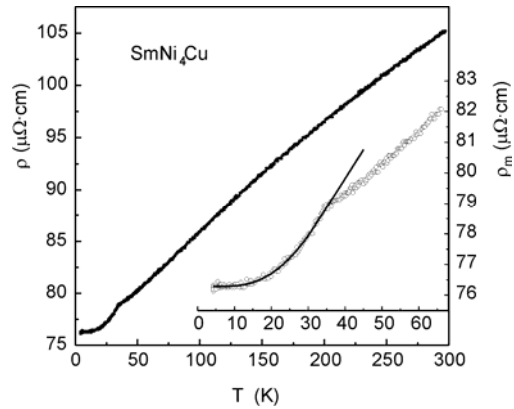


Fig. 4. The $\rho(T)$ curve of $SmNi_4Cu$ in the full temperature range. Inset: the magnetic part $\rho_m(T)$ fitted with Eq. (3) below the phase transition

$NdNi_4Al$ and $NdNi_4Cu$ exhibit transitions to the ferromagnetic order at 6 K and 11 K, respectively. These temperatures are well visible in the resistivity (Fig. 3) and coincide well with the previous magnetometric findings [4]. Below T_C the main contribution to the resistivity comes from the scattering on the spin wave excitations and is usually represented by a $\rho_m \sim T^2$ dependence. However, in the presence of a strong magnetic anisotropy a gap Δ can be developed in the magnon spectrum ($E_k = \Delta + Dk^2$) and $\rho_m(T)$ takes the form [5]:

$$\rho_m(T) = \rho_0 + m\Delta T e^{-\Delta/T} \left(1 + 2\frac{T}{\Delta} \right) \quad (3)$$

where m is a material constant. The fit below T_C (Fig. 3) provides $\Delta = 7.7$ K for $NdNi_4Cu$, it was 19 K for $NdNi_4B$ [1] and the spread of the experimental points does not allow a reasonable fit in the case of $NdNi_4Al$. Figure 4 demonstrates that Eq. (3) operates perfectly in the case of $SmNi_4Cu$ providing $\Delta = 40$ K. Sm-based compounds are usually characterized by a strong magnetic anisotropy. We have observed the coercive field of 2.8 T for $SmNi_4Cu$ and 7 T for $SmNi_4B$ [6]. The latter compound has shown the energy gap $\Delta = 42$ K. Hence, it is evident that there is a correlation between the parameter Δ and the coercive field. The $NdNi_4X$ compounds have shown

H_C of the order of 10^{-3} T. In the case of GdNi_4X the magnetic anisotropy is negligible because Gd is in the S state (orbital number $L = 0$). It is corroborated by the resistivity measurements, which reveal that the temperature variation below T_C fulfils the ‘gap-free’ $\rho_m \sim T^2$ dependence (Fig. 5).

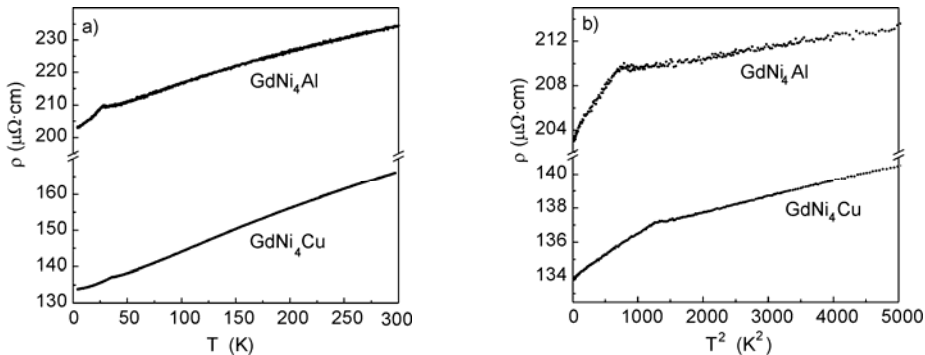


Fig. 5. (a) The $\rho(T)$ curves of the GdNi_4X ($X = \text{Al}, \text{Cu}$) compounds as a function of: a) T , b) T^2 ; the curve b) reflects the scattering on magnons below T_C and the spin fluctuations in a narrow range above the ordering temperature

For all the magnetic RNi_4X compounds the temperature dependence of resistivity in the paramagnetic region – but near T_C – is also quadratic, which is typical of the spin fluctuations ρ_{sf} .

Finally, one can notice that the RNi_4Al , RNi_4Cu and RNi_4B compounds differ dramatically in the value of the residual resistivity ρ_0 . For RNi_4Al it is several times higher than for RNi_4Cu but the latter one still has ρ_0 twice the values of the previously studied RNi_4B [1]. It can be explained by the increased disorder in RNi_4Al and RNi_4Cu (CaCu_5 -type of structure) characterized by a random occupation of the 3g site by the Ni and Al(Cu) atoms [4]. A similar tendency occurs for the spin-disorder resistivity defined as a difference between $\rho_{sf}(T \rightarrow 0)$ and ρ_0 . The difference in the transport properties of the isostructural RNi_4Al and RNi_4Cu compounds stems probably from the presence of the $\text{Cu}(3d)$ states in the valence band region.

3. Conclusions

Based on the Bloch–Grüneisen formula the phonon contribution to $\rho(T)$ has been determined for YNi_4X compounds with the Debye temperatures equal to 204 K, 235 K and 240 K for $X = \text{Al}, \text{Cu}$ and B , respectively. These values appeared to reflect well the differences in the Y–Y separation in the direction of the hexagonal axis. For the ferromagnetic rare earths the energy gap in the magnon spectrum has been estimated, with the largest value in the case of the SmNi_4X compounds. The $\rho(T)$ dependences of the CeNi_4X compounds show a shallow minimum at low temperatures, which has been ascribed to the Kondo impurity-like effect.

Acknowledgements

This research was supported by the Polish State Committee for Scientific Research (KBN), grant No. 1 PB03 077 28).

References

- [1] TOLIŃSKI T., KOWALCZYK A., IVANOV V., Phys. Stat. Sol. (b), 240 (2003), 153.
- [2] TOLIŃSKI T., KOWALCZYK A., CHELKOWSKA G., PUGACZOWA-MICHALSKA M., ANDRZEJEWSKI B., IVANOV V., SZEWCZYK A., GUTOWSKA M., Phys. Rev. B, 70 (2004), 064413.
- [3] TOLIŃSKI T., KOWALCZYK A., PUGACZOWA-MICHALSKA M., CHELKOWSKA G., J. Phys.: Condens. Matter, 15 (2003), 1397.
- [4] TOLIŃSKI T., SCHÄFER W., KOCKELMANN W., KOWALCZYK A., HOSER A., Phys. Rev. B, 68 (2003), 144403.
- [5] ANDERSEN N.H., SMITH H., Phys. Rev. B, 19 (1979), 384.
- [6] TOLIŃSKI T., KOWALCZYK A., SZLAFEREK A., ANDRZEJEWSKI B., KOVÁČ J., TIMKO M., J. Alloys Comp., 347 (2002), 31.

Received 1 June 2005
Revised 10 October 2005

Magnetisation and electron spin resonance of the colossal magnetoresistive $\text{La}_{0.67}\text{Ca}_{0.33}\text{Mn}_{1-x}\text{Fe}_x\text{O}_3$

T. ZAJĄC¹, L. FOLCIK², J. CHMIST¹, A. KOŁODZIEJCZYK^{1*},
H. DRULIS², K. KROP¹, G. GRITZNER³

¹Faculty of Physics and Applied Computer Science, AGH University of Science and Technology,
30-059 Cracow, Poland

²Institute of Low Temperature and Structure Research, Polish Academy of Sciences,
50-950 Wrocław, Poland

³Institut für Chemische Technologie Anorganischer Stoffe, Johannes Kepler Universität,
A-4040 Linz, Austria

We report magnetisation and electron spin resonance (ESR) measurements on the colossal magnetoresistive manganites $\text{La}_{0.67}\text{Ca}_{0.33}\text{Mn}_{1-x}\text{Fe}_x\text{O}_3$, with $x = 0, 0.01, 0.03, 0.06, 0.10,$ and 0.15 , in the vicinity of their magnetic (T_C) and metal-insulator (T_{MI}) transition temperatures. Above T_C , the resonance lines with $g \approx 2$ are caused by ferromagnetic metallic clusters exhibiting a double exchange interaction between Mn^{3+} – Mn^{4+} ions. The lines were observed with cooling far below both T_C and T_{MI} , and were fitted by the Dysonian line-shape. The temperature dependences of the line-widths exhibited a minimum value at $T_{\min} \approx 1.25T_C$, followed by an increase with further cooling toward T_C . The anomalous behaviour of the line-width below T_{\min} is due to the appearance of a ferromagnetic metallic phase within the paramagnetic matrix. The role of phase segregation, in which the compounds are phase-separated into a mixture of ferromagnetic and paramagnetic regions, is discussed.

Key words: *iron substituted manganite; electron spin resonance; ESR; phase segregation*

1. Introduction

The system $\text{Ln}_{2/3}\text{B}_{1/3}\text{MnO}_3$, where Ln is a rare earth ion and B a divalent alkali metal, has been the most widely studied among all ABO_3 -type perovskite manganites [1]. In the manganites, the doping concentration introduces a mixed valence (Mn^{3+} , Mn^{4+}), which governs the magnetic and electric properties of the compounds. The system undergoes a transition from a paramagnetic insulating (PMI) to a ferromagnetic metallic (FMM) state when temperature is decreased. Around that transition,

* Corresponding author, e-mail: akolo@uci.agh.edu.pl

a resistance maximum is observed, which is largely suppressed by magnetic field, leading to an observation of the colossal magnetoresistance effect (CMR). The metal-to-insulator transition temperature T_{MI} is sometimes significantly different from the Curie temperature T_C . Various mechanisms have been proposed to explain the CMR effect, nonetheless the physical origin of the transition is still a matter of controversy [1–3]. Most frequently, the Zener double-exchange model (DE) [4] is proposed to understand the magnetic and electrical properties of the materials. Electronic phase separation into conducting ferromagnetic clusters, coupled via DE interaction between Mn^{3+} and Mn^{4+} ions with a characteristic lifetime τ exceeding 10^{-5} s [5], has recently been considered responsible for their CMR.

We have performed ESR studies on iron-substituted manganites to search for the dynamic properties of the mechanism of double exchange interaction between itinerant e_g electrons and localised t_{2g} electrons forming the $S = 3/2$ spins of Mn^{4+} ions. The magnetic moments of these clusters and their concentrations are responsible for the ESR signal.

2. Experimental results and analysis

Polycrystalline samples of $La_{0.67}Ca_{0.33}Mn_{1-x}Fe_xO_{3+\delta}$, with $x = 0, 0.01, 0.03, 0.06, 0.10,$ and 0.15 , were prepared by the wet sol-gel method and solid-state reaction with $\delta \approx 0$, which were performed by the same procedure as in [6]. The overall stoichiometry was determined by a thermogravimetric method. The crystal structure and exact stoichiometry were determined from precise the X-ray diffraction by a Siemens 5050 diffractometer, using the Rietveld procedure and Full-prof fitting programme. The lattice parameters were calculated from the XRD data. Each of the investigated compounds was found to consist of a single phase.

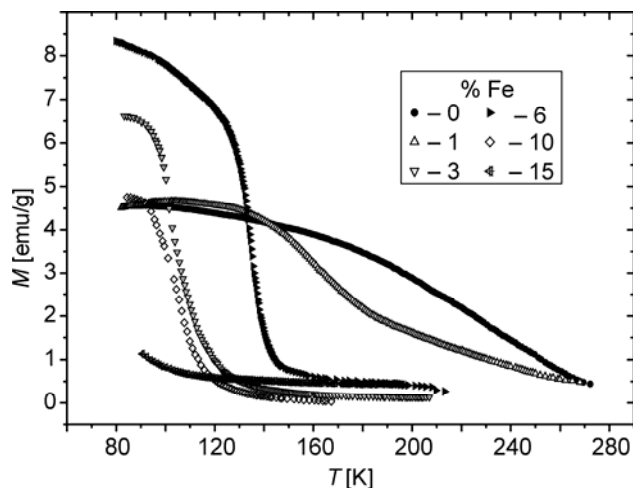


Fig. 1. Temperature dependence of magnetisation for $La_{0.67}Ca_{0.33}Mn_{1-x}Fe_xO_3$ with a given x in a magnetic field of 100 Oe

The susceptibilities and specific heats of some of the compounds have been described previously [7]. Specifically, for the present study all samples were magnetically characterized with the help of a standard vibrating sample magnetometer (VSM), in a magnetic field of 100 Oe, and as a function of temperature from 77 K up to room temperature (Fig. 1). DC magnetization was recorded during heating in the applied DC field after zero-field cooling (ZFC) down to 77 K. Magnetisation was measured for powdered specimens.

Curie temperatures were determined from the temperature dependence of magnetisation as the inflection point of the $M(T)$ curve at 100 Oe (Fig. 1), i.e. the temperature corresponding to the minimum of the dM/dT curve. T_C decreases from 262 K for $x = 0$, through 166 K for $x = 0.01$, 102 K for $x = 0.03$, 126 K for $x = 0.06$, and to 104 K for $x = 0.1$. The error of T_C is about 2 K. The Curie temperature $T_C \approx 80 \pm 5$ K for $x = 0.15$ was estimated from extrapolation of the experimental points in Fig. 1 to lower temperatures by a fifth order polynomial fit followed by differentiation. ESR spectra were carried out at X-band microwave radiation ($\nu = 9.5$ GHz) in the temperature range 4.2–300 K in magnetic fields up to 0.7 T by a microwave spectrometer equipped with a continuous gas-flow cryostat for He (Oxford Instruments). Bulk or powder samples were placed into quartz tubes in the cylindrical resonant cavity. Selected spectra are shown in Figs. 2 and 3 as examples.

From the spectra in Fig. 2 for the sample with $x = 0$, the single asymmetric, rather narrow line in the paramagnetic region above T_C undergoes a transition to the very broad single line in the low-temperature ferromagnetic region. The same behaviour is observed in Fig. 3 for the sample with $x = 0.1$, but the paramagnetic line exists far below the paramagnetic-ferromagnetic transition at T_C . In the intermediate region around the magnetic phase transition, both lines are visible. These are characteristic observations of all investigated samples. In our previous paper [8], more spectra were presented. Therein, the qualitative analysis of these spectra was restricted to ESR above the Curie temperature T_C .

In the frame of the present paper, quantitative analysis of ESR spectra above and below T_C was performed in according to the approach presented previously [9, 10]. As one can see from Figs. 2 and 3, far below T_C a very broad ferromagnetic resonant line (FMR) was detected in addition to the ESR line. The FMR line gradually disappears below T_C , because when temperature is decreased the sample enters the unsaturated magnetisation state at the given applied magnetic fields and the resonant condition is not further fulfilled. We leave the analysis of the FMR lines for future studies. Here, our analysis is restricted to the ESR lines above and below T_C . It has already been established [8–11] that the ESR lines come from ferromagnetic and metallic clusters of Mn^{3+} – Mn^{4+} ions coupled via double exchange interactions. These clusters are embedded in a paramagnetic matrix above T_C and in a ferromagnetic matrix below T_C due to the phase-separation phenomenon [5, 8–11].

The single, rather broad asymmetric lines detected in the paramagnetic region (see Figs. 2 and 3) are usually fitted with the Dysonian line shape [8–12]. From the first derivative of the microwave absorbed power P with respect to the applied magnetic field B , the

line-widths ΔB and resonance fields B_{res} were derived by fitting with a proper combination of absorptive and dispersive Lorentzian terms, following the method proposed in [12]:

$$\frac{dP}{dB} \propto \frac{d}{dB} \left(\frac{\Delta B + \alpha(B - B_{\text{res}})}{(B - B_{\text{res}})^2 + \Delta B^2} + \frac{\Delta B + \alpha(B - B_{\text{res}})}{(B + B_{\text{res}})^2 + \Delta B^2} \right) \quad (1)$$

where α is the ratio of the dispersion to the absorption line components.

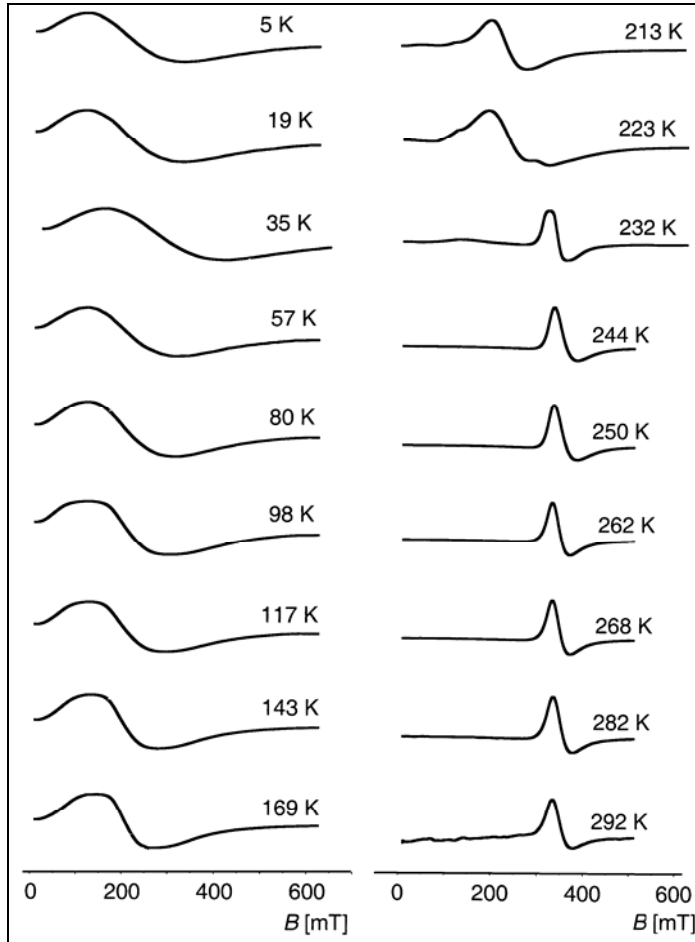


Fig. 2. Temperature dependence of the ESR spectra of $\text{La}_{0.67}\text{Ca}_{0.33}\text{Mn}_{1-x}\text{Fe}_x\text{O}_3$ for $x = 0$

The resonance field of all investigated compounds in the paramagnetic region yields the g -factor value of 1.98–2.00, slightly below the free electron value. For a single run of measurements for bulk $\text{La}_{0.67}\text{Ca}_{0.33}\text{MnO}_3$, we detected the asymmetric two-component resonant and anti-resonant structure of the line due to the sufficiently high conductivity of the compound [11]. The ratio α changes from nearly zero to

about 2 as x increases, and obeys a very similar temperature dependence as the absorption line width. All recorded paramagnetic Dysonian-like shaped spectra were successfully decomposed into absorption and dispersive components. The temperature dependences of the absorption line-width are shown in Fig. 4.

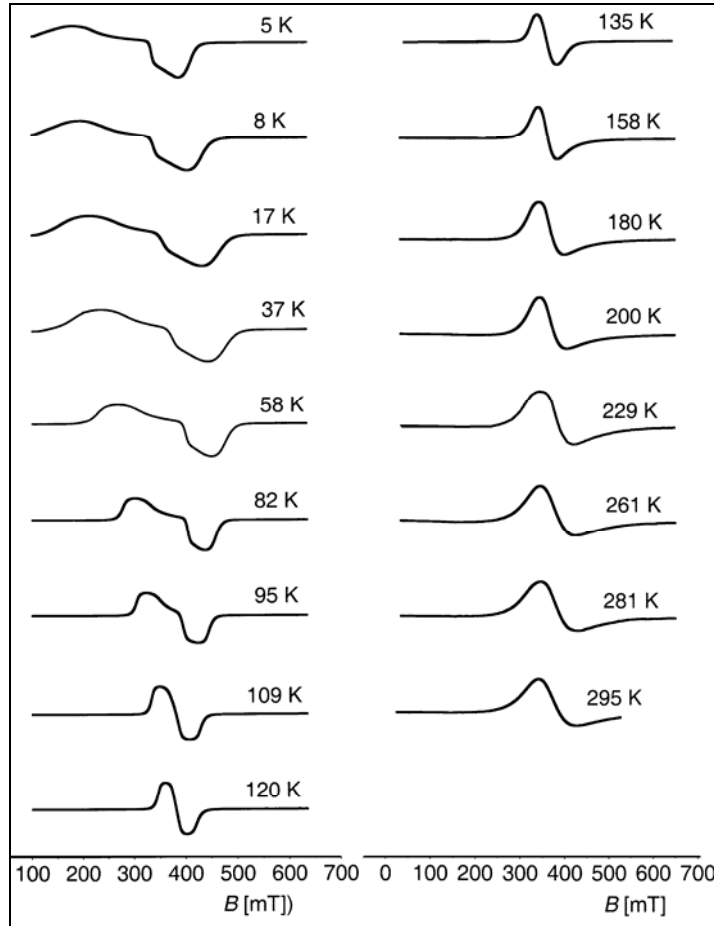


Fig. 3. Temperature dependence of the ESR spectra of $\text{La}_{0.67}\text{Ca}_{0.33}\text{Mn}_{1-x}\text{Fe}_x\text{O}_3$ for $x = 0.1$

The dependences exhibit minima at $T_{\min} \approx 1.2T_C$. Above the minimum, the line-widths increase with temperature due to the spin lattice relaxation of clusters of Mn^{3+} – Mn^{4+} ions coupled via double exchange interactions. We assumed that the temperature dependence of the line-width $\Delta B(T)$ above T_{\min} might be described by the saturation Boltzmann curve:

$$\Delta B(T) = \Delta B_{\max} + \frac{\Delta B_{\min} - \Delta B_{\max}}{1 + e^{(T-T_0)/\delta T}} \quad (2)$$

The line-width reaches a minimum ΔB_{\min} at T_{\min} and a maximum ΔB_{\max} for $T \rightarrow \infty$. The function $\Delta B(T)$ possesses an inflection point at T_0 . Figure 4 shows the fitting of Eq. (2) above T_{\min} . The values of parameters ΔB_{\min} and ΔB_{\max} are listed in Table 1.

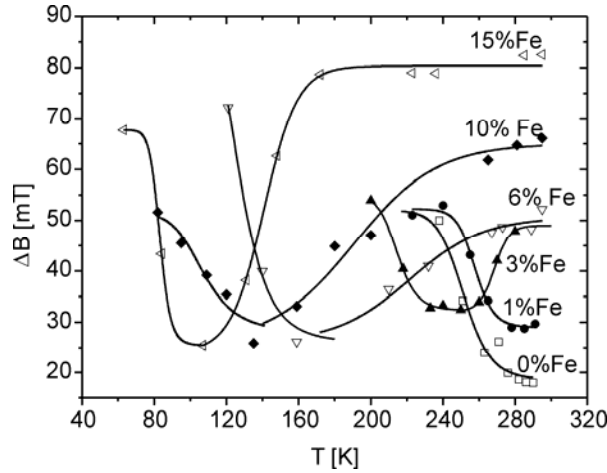


Fig. 4. Temperature dependence of the resonance line width for the indicated compounds

Table 1. Fitting parameters of the temperature dependence of resonance line widths for $\text{La}_{0.67}\text{Ca}_{0.33}\text{Mn}_{1-x}\text{Fe}_x\text{O}_3$ (shown in Fig. 4) according to Eqs (2) and (3)

x	ΔB_{\min} [mT]	ΔB [mT]	U/k_B [K]	ΔB_{\max} [mT]	T_0 [K]	δT [K]
0	18.6	33.4	8445	—	—	—
0.01	29	23.3	12860	—	—	—
0.03	32.4	22.8	8345	48.9	268	4.1
0.06	26	71.6	1910	50.6	221.6	20.4
0.10	18	34.6	1824	66.3	181	30.7
0.15	25.4	42.3	2360	80.3	140	9.3

The temperature dependence of the line width below T_{\min} obeys the temperature dependence of magnetisation (Figs. 1 and 4), as well as magnetoresistance [1, 7]. In Ref. [9], it is described by the equation:

$$\Delta B(t) = \Delta B_{\min} + \frac{\Delta B_0 - \Delta B_{\min}}{1 + e^{-U(1-t)/k_B T}} \quad (3)$$

where ΔB_0 is the line width at $T = 0$, $t = T/T_C$, and U is the activation energy. We followed the approach, and the fitted curves below T_{\min} are shown in Fig. 4. The values of U/k_B and $\Delta B = \Delta B_0 - \Delta B_{\min}$ are listed in Table 1.

From the quantitative analysis we can conclude that the ESR line comes entirely from $\text{Mn}^{3+}\text{-Mn}^{4+}$ clusters, because ESR measures an average state due to the jumping

of electrons between these two manganese valence states. With an increasing concentration of Fe, which is in the Fe^{3+} ionic state [1], the concentration of Mn^{3+} ions decreases mainly within the clusters. Since the ESR line width increases (Fig. 4), i.e. the cluster spin-lattice relaxation time decreases with the concentration of Fe at $T \rightarrow \infty$, as well as with temperature above T_{min} , we conclude that substitution by iron weakens the double exchange interaction within $Mn^{3+}-Mn^{4+}$ clusters.

3. Conclusions

We concluded that ferromagnetic metallic clusters, exhibiting double exchange interactions between $Mn^{3+}-Mn^{4+}$ ions, play a dominant role in resonant absorption. The temperature dependences of absorption line width exhibit a minimum value at $T_{min} \cong 1.2T_C$ and in the region below T_{min} follow the temperature dependences of magnetisation and magnetoresistance (Eq. (3)). Above T_{min} , the line width increases and reaches ΔB_{max} at high temperatures. In this region, the temperature dependence of line width obeys the saturation curve (Eq. (2)).

Acknowledgements

This work was financially supported by the Faculty of Physics and Applied Computer Science, AGH University of Science and Technology, Cracow, Poland and by the Polish–Austria Co-operation project.

References

- [1] DAGOTTO E., HOTTA T., MOREO A., Phys. Rep., 344 (2001), 1.
- [2] YUAN S.L., LI J.Q., JIANG Y., YANG Y.P., ZENG X.Y., LI G., TU F., ZHANG G.Q., TANG C.Q., JIN S.Z., Phys. Rev. B, 62 (2000), 5313.
- [3] RETTORI C., RAO D., SINGLEY J., KIDWELL D., OSEROFF S.B., CAUSA M.T., NEUMEIER J.J., MCCLELLAN K.J., CHEONG S-W., SCHULTZ, Phys. Rev. B 55 (1997), 3083.
- [4] ZENER C., Phys. Rev., 82 (1951), 403.
- [5] KAPUSTA C., RIEDI P., J. Mag. Mag. Mater., 196–197 (1999), 446.
- [6] PRZEWOŹNIK J., CHMIST J., KOLWICZ-CHODAK L., TARNAWSKI Z., KOŁODZIEJCZYK A., KROP K., KELLNER K., GRITZNER G., Acta Phys. Polon. A, 106 (2004), 665.
- [7] TARNAWSKI Z., WAŚNIEWSKA M., CHMIST J., SECHOVSKY V., KOŁODZIEJCZYK A., KOZŁOWSKI A., KROP K., GRITZNER G., Physica B, 329–333 (2003), 721.
- [8] ZAJĄC T., FOLCIK L., KOŁODZIEJCZYK A., DRULIS H., KROP K., GRITZNER G., J. Mag. Mag. Mater., 272–276 (2004), 120.
- [9] YUAN S.L., ZHAO W.Y., ZHANG G.Q., TU F., PENG G., LIU J., YANG P.Y., LI G., JIANG Y., ZENG X.Y., TANG C.Q., Appl. Phys. Lett., 77 (2000), 4398.
- [10] LI J.Q., YUAN S.L., Solid State Commun., 129 (2004), 431.
- [11] DE BRION S., DUPONT F., REINKE D., G. CHOUTEAU, Appl. Magn. Res., 19 (2000), 547.
- [12] PETER M., SHALTIEL D., WERNICK J.H., WILLIAMS H.J., MOCK J.B., SHERWOOD R.C., Phys. Rev., 126 (1962), 1395.

Received 1 June 2005

Revised 10 October 2005

Spintronics in semiconductors

Z. WILAMOWSKI*, A. M. WERPACHOWSKA

Institute of Physics, Polish Academy of Sciences, al. Lotników 32/46, 02-668 Warsaw, Poland

In the last years, spin effects in semiconductors have been of great interest not only in the context of solid state physics, but also for their potential use in technology. In this paper, we give a short review of spintronic materials, in which electron spin is exploited as an additional degree of freedom. Afterwards, we discuss the properties of classic, non-magnetic semiconductors, where efforts are put into enriching traditional semiconductor technology by engaging the electrical effects of spin effects. Various phenomena and scientific state of the art is highlighted.

Key words: *spintronics, semiconductor; spin-orbit coupling; spin current*

1. Introduction

Next to the electron charge, the electron spin corresponds to an additional degree of freedom, which could be used for information storage and processing. To control electron and spin states, one has to measure different physical quantities. Electrical properties are characterized by electrical conductivity, carrier mobility, voltage profile and electrical current, while spin properties are characterized by magnetization, magnetic resonance frequencies, and spin relaxation rates. There are also different tools that can be used to manipulate electron charge and spin states. Electronic devices are controlled predominantly by applying voltages, while to manipulate a spin state one has to use magnetic field. In contrast to voltages, magnetic field cannot be applied locally. For these reasons, spintronics needs sophisticated solutions for the various classes of spintronic materials. In this paper, we discuss the properties of novel spintronic materials and classic, non-magnetic semiconductors, and the possibility of their use in electronic devices.

2. Magnetic materials

Ferromagnetic metals owe their great career as spintronic materials to the spin effects they display. The most popular in practical applications are giant magnetoresis-

*Corresponding author, e-mail: wilamz@ifpan.edu.pl

tance and tunnel magnetoresistance in devices built of ferromagnetic metals. The resistance of layered structures depends on the mutual orientations of magnetization in neighbouring layers. Such elements are already commonly applied as reader heads for magnetic memories. The weak spot of ferromagnetic metals is that it is hard to modify their properties with applied electric field.

The possibility of changing physical properties with the applied electric field is the feature of semiconducting materials. Materials of the greatest interest to technology are diluted magnetic semiconductors (DMS). To make a typical DMS, such as (Cd,Mn)Te, we need to substitute a part of the diamagnetic atoms in a classic semiconductor with atoms of a transition metal [1]. Such a highly diluted material is paramagnetic. In the absence of external field, DMS acts like a semiconductor. The application of external field results in a strong spin splitting of the conduction and valence bands. The origin of spin splitting is the exchange coupling $sp-d$ between delocalised carriers and core spins.

The most characteristic feature of DMS is a giant spin splitting, which increases the spin polarization of carriers (usually present in small numbers). It is easy to achieve 100% polarization in laboratory conditions. Since the onset of spintronics, there have been attempts to use this property of DMS to build spintronic elements. The first idea was to build a giant magnetoresistance (GMR) structure. Attempts to build a hybrid ferromagnetic metal–semiconductor–ferromagnetic metal structure failed, due to the fact that small semiconductor conductance suppresses the spin current [2], but enhances spin accumulation.

Efforts to inject spins from semi-magnetic semiconductors, however, were much more successful. As Fiederling et al. [3] have shown, the injection efficiency from DMS to GaAs is near 100%. Spin polarization was estimated from the circular polarization ratio of GaAs. It is also possible to build spin transistors [4] based on DMS.

Increasing carrier concentration in DMS may lead to the appearance of ferromagnetic phase. Given sufficiently large band filling, not only do local spins cause the spin polarization of carriers, but conversely, the polarized carrier band may, through the same $p-d$ exchange, cause the polarization of local spins. Munekata and Ohno [5–8] gave the first evidence of ferromagnetism in (In,Mn)As and (Ga,Mn)As materials. The first theoretical description is attributed to Dietl [6].

(Ga,Mn)As is a canonical semiconductor. The critical temperature of currently manufactured layers exceeds 170 K, and the alloy retains all semiconducting properties. The electrical control of ferromagnetism is possible. In particular, the critical temperature can be changed by applying electric field [6, 7]. (Ga,Mn)As is also a very good source of polarized electrons, which allows spins to be injected into normal semiconductors [8]. Due to spontaneous magnetization in ferromagnets, it is not necessary to apply external magnetic field in order to achieve a stream of spin-polarized carriers. Structures similar to the GMR structures built on (Ga,Mn)As show very large magnetoresistance [9] and tunnel anisotropic magnetoresistance [10]. In the tunnelling transport regime, magnetoresistance exceeds 2000%. Yamanouchi et al. demonstrated that current controls domain wall motion [11]. Astakhov et al. [12] demonstrated spin

switching between two metastable magnetization states in materials that possess uniaxial anisotropy. It may be induced not only by applying magnetic field, but also by a laser pulse [13, 14].

3. Spin in classic semiconductors

In non-magnetic metals and semiconductors, magnetism plays a secondary role. Due to the Pauli principle, the equal filling of up and down spin subbands leads to the cancellation of magnetic momenta. In external magnetic field, a weak carrier magnetization appears, but the Pauli susceptibility is very low. In most metals and semiconductors, the dependence of electrical properties on spin properties is negligible. The connection between electrical and magnetic properties is visible only in exceptional cases. One of them is the dependence of the resistance of two-dimensional electron gas on its spin polarization. The only mechanism linking electrical and magnetic properties is the existence of spin-orbit coupling, which leads to a band spin splitting.

The zero field splitting of spin subbands occurs only in semiconductor structures with sufficiently low symmetry. In general, there is a distinction between the Dresselhaus field [15] and the Rashba field [16, 17]. Spin splitting is equivalent to an effective spin-orbit field. The Dresselhaus field is the consequence of the lack of crystal inversion symmetry. It occurs, e.g. in zinc blend structures, i.e. in all II–VI and III–V semiconductor compounds, but it is forbidden by symmetry conditions in bulk silicon. The Bychkov–Rashba field is the consequence of the lack of mirror symmetry in 2D structures. It also occurs in silicon 2D structures. The direction of the spin-orbit field, H_{so} , is perpendicular to the carrier \mathbf{k} -vector. In the case of the Bychkov–Rashba field, it is oriented in-plane. Generally, the inversion of the \mathbf{k} -vector leads to the inversion of H_{so} . As a consequence, in thermal equilibrium the sum of all spin-orbit fields acting on a carrier system vanishes. It follows that most spintronic effects (dependent on both magnetic and electrical properties) vanish in thermal equilibrium. Therefore, we need to search for phenomena engaging both spin and electron properties only in systems in thermodynamic non-equilibrium. Below we shall review the class of spin effects induced by electron current, namely spin Hall, spin manipulation by electrical current, and the class of spin photovoltaic effects.

When electric current is applied and the Fermi sphere is moved from the centre, the total spin-orbit (SO) field acting on the ensemble of electron spins is not zero anymore. Electron spins begin a precession and the tendency to create additional spin polarization appears. Both effects are diminished by spin relaxation. When the frequency of the RF current is much higher than the spin relaxation rate, however, spin polarization is not affected by electric current and the effective RF magnetic field is the main consequence of the current. As has been demonstrated by Wilamowski and Jantsch [18], such an SO field can play the role of a microwave magnetic field, leading to an additional resonance absorption. As a consequence, three different ESR signals are observed in a 2D electron gas: classic absorption caused by the magnetic

component of the microwave field, the SO field caused by electric current, and an additional, so-called polarization signal, resulting from the change in electrical conductivity under resonance conditions. This effect reflects the dependence of the conductivity of high-mobility 2D electrons on spin polarization and allows for electrical measurements of spin structure.

When a DC or low frequency current is applied to a semiconducting layered structure, two additional processes have to be considered: the possible precession of spin polarization around the total magnetic field, including the effective SO field, and spin relaxation leading to an additional spin polarization caused by the SO field. The interference of these effect leads to the spin Hall effect [19–22]. Spin accumulation at the edges of non-magnetic semiconducting samples has been demonstrated experimentally [19, 20]. The effect can also occur in the absence of any external magnetic field, reflecting its intrinsic character and indicating that the SO field is responsible for the effect.

Since in a 2D electron gas the SO field is oriented only in-plane, the resulting magnetization is oriented the same way. Moreover, the spin polarizations of individual electrons are parallel to individual SO fields. Thus, such a SO field does not cause any precession that would lead to a perpendicular component of carrier magnetization, which seems to be a necessary condition for the Hall effect. For these reasons, modeling of spin Hall effect requires the simultaneous discussion of momentum scattering, which allows the SO field and spin directions to be tilted, and of spin precession and relaxation, which could lead to a perpendicular component of carrier magnetization [21, 22].

It is well known that circularly polarized light, due to spin dependent transition probabilities, causes the spin polarization of excitons and carrier spins. The occurrence of spin polarization means that up and down spin sub-bands are differently occupied. Consequently, the Fermi \mathbf{k} -vectors for up and down spins are different. For symmetry reasons, however, spin polarization not only does not lead to any macroscopic current, but to symmetry changes when external magnetic field is additionally applied. As has been shown by Ganichev et al. [23, 24], sample illumination leads to an electric current. Such a spin galvanic effect (the Hanle effect) is ruled by a velocity and spin-dependent momentum relaxation and by the precession of magnetization in an external magnetic field. The complex direction dependence of the Dresselhaus SO field results in a complex dependence of the spin galvanic effect on the direction of light illumination, and of the magnetic field on crystallographic directions [24].

Also, the reversed galvanic effect has been observed. In this case, the electric current causes non-equilibrium spin polarization. The idea of such an effect was proposed by Edelstein 15 years ago [25]. Experimental evidence was presented in 2004 by Silov et al. [26], who showed that for the proper experimental geometry the electric current results in circular photoluminescence. Kato et al. [27] also established current-induced spin polarization predictions by measuring Faraday rotation.

4. Summary

To summarise, the present fast development of spintronics shows that spintronic elements can be built of not only magnetic materials such as ferromagnetic metals or ferromagnetic semiconductors. A wide spectrum of spintronic effects can also be found in classic, non-magnetic semiconductors.

Acknowledgement

This work supported by PBZ-KBN-044/P03/2001.

References

- [1] FURDYNA J.K., *J. Appl. Phys.*, 64 (1988), R29.
- [2] SCHMIDT G., RICHTER G., GRABS P., GOULD C., FERRAND D., MOLENKAMP L.W., *Phys. Rev. Lett.*, 87 (2001), 227203.
- [3] FIEDERLING R., KEIM M., REUSCHER R., OSSAU W., SCHMIDT G., WAAG A., MOLENKAMP L.W., *cond-mat/0302477* (2003).
- [4] ZUTIC I., FABIAN J., DAS SARMA S., *Rev. Mod. Phys.*, 76 (2004), 323.
- [5] MUNEKATA H., OHNO H., VON MOLNAR S., SEGMÜLLER A., CHANG L.L., ESAKI L., *Phys. Rev. Lett.*, 63 (1989), 1849.
- [6] DIETL T., OHNO H., MATSUKURA F., *Phys. Rev. B*, 63 (2001), 195205.
- [7] OHNO H., CHIBA D., MATSUKURA F., OMIYA T., ABE E., DIETL T., OHNO Y., OHTANI N., *Nature*, 408 (2000), 994.
- [8] OHNO Y., YOUNG D.K., BESCHOTEN B., MATSUKURA F., OHNO H., AWSCHALOM D.D., *Nature*, 402 (1999), 790.
- [9] RÜSTER C., BORZENKO T., GOULD C., SCHMIDT G., MOLENKAMP L.W., LIU X., WOJTOWICZ T.J., FURDYNA J.K., YU Z.G., FLATTÉ M.E., *Phys. Rev. Lett.*, 91 (2003), 216602.
- [10] GOULD C., RÜSTER C., JUNGWIRTH T., GIRGIS E., SCHOTT G.M., GIRRAUD R., BRUNNER K., SCHMIDT G., MOLENKAMP L.W., *Phys. Rev. Lett.*, 93 (2004), 117203.
- [11] YAMANOUCHI M., CHIBA D., MATSUKURA F., OHNO H., *Nature*, 428 (2004), 539.
- [12] ASTAKHOV G.V., KIMEL A.V., SCHOTT G.M., TSVETKOV A.A., KIRILYUK A., YAKOVLEV D.R., KARCZEWSKI G., OSSAU W., SCHMIDT G., MOLENKAMP L.W., RASING TH., *Appl. Phys. Lett.*, 86 (2005), 152506.
- [13] TANG H.X., KAWAKAMI R.K., AWSCHALOM D.D., ROUKES M.L., *Phys. Rev. Lett.*, 90 (2003), 107201.
- [14] WELP U., VLASKO-VLASOV V.K., LIU X., FURDYNA J.K., WOJTOWICZ T., *Phys. Rev. Lett.*, 90 (2003), 167206.
- [15] DRESSELHAUS G., *Phys. Rev.*, 100 (1955), 580.
- [16] RASHBA E.I., *Fiz. Tverd. Tela (Leningrad)* 2 (1969), 1224 (*Sov. Phys. Solid State*, 2 (1960), 1109).
- [17] BYCHKOV YU.L., RASHBA E.I., *J. Phys. C*, 17 (1984), 6039.
- [18] WILAMOWSKI Z., JANTSCH W., *Phys. Rev. B*, 69 (2004), 035328.
- [19] NIKOLIC B.K., SOUMA S., ZARBO L.P., SINOVA J., *cond-mat/0412595* (2004).
- [20] KATO Y.K., MYERS R.C., GOSSARD A.C., AWSCHALOM D.D., *Science*, 306 (2004), 1910.
- [21] SINOVA J., CULCER D., NIU Q., SINITSYN N.A., JUNGWIRTH T., MACDONALD A.H., *Phys. Rev. Lett.*, 92 (2004), 126603.
- [22] HANKIEWICZ E.M., MOLENKAMP L.W., JUNGWIRTH T., SINOVA J., *Phys. Rev. B*, 70 (2004), 241301 R.
- [23] GANICHEV S.D., IVCHENKO E.L., BEL'KOV V.V., TARASENKO S.A., SELLINGER M., WEISS D., WEGSCHEIDER W., PRETTL W., *Nature*, 417 (2002), 153.

- [24] GANICHEV S.D., BEL'KOV V.V., GOLUB L.E., IVCHENKO E.L., SCHNEIDER P., GIGLBERGER S., EROMS J., DE BOECK J., BORGHIS G., WEGSCHEIDER W., WEISS D., PRETTL W.. Phys. Rev. Lett., 92 (2004), 256601.
- [25] EDELSTEIN V.M., Sol. State. Comm., 73 (1990), 233.
- [26] SILOV A.YU., BLIANOV P.A., WOLTER J.H., HEY R., PLOG K.H., AVIERKIEV N.S., Appl. Phys. Lett., 85 (2004), 5929.
- [27] KATO Y., MYERS R.C., MYERS A.C., GOSSRD A.C., AWSCHALOM D.D., Phys. Rev. Lett., 93 (2004), 176601.

Received 1 June 2005
Revised 10 October 2005

Photoluminescence in EuS–PbS–EuS semiconductor structures with a double ferromagnetic barrier

L. KOWALCZYK¹, M. CHERNYSHOVA¹, T. STORY^{1*}, A. YU. SIPATOV²

¹Institute of Physics, Polish Academy of Sciences, al. Lotników 32/46, 02-668 Warsaw, Poland

²National Technical University KPI, 21 Frunze Street, 310002 Kharkov, Ukraine

The temperature, magnetic field, and laser excitation power dependences of photoluminescence (PL) were studied in 5×(EuS (5.5 nm)–PbS (17.5 nm)) semiconductor ferromagnetic multilayers grown epitaxially by high vacuum deposition on a BaF₂ (111) substrate. In EuS–PbS heterostructures, ferromagnetic layers of EuS form electron barriers for both electrons and holes in nonmagnetic quantum wells of PbS. PL was observed in the near infrared due to electronic transitions in PbS quantum wells with narrow energy gaps. Measurements carried out at 4.2 and 77 K (i.e., below and above the Curie temperature of EuS layers, which is about 14 K) showed characteristic PL spectra consisting of one or two lines with a strongly non-linear response upon increasing the YAG laser excitation power. Below the Curie temperature, the application of a weak magnetic field of 200 Oe results in a change of the PL intensity as well as a small red shift in the PL energy of about 1 meV. These observations are discussed in terms of the model taking into account the magnetization-dependent height of the EuS potential barrier for electrons in a PbS quantum well.

Key words: *spintronics; magnetic semiconductor; europium chalcogenide; IV–VI semiconductor*

1. Introduction

EuS–PbS multilayers are ferromagnetic–nonmagnetic heterostructures built only of semiconductor materials. EuS is a well-known ferromagnetic semiconductor with the Curie temperature of bulk crystals $T_c = 16.5$ K [1]. It is considered to be a model example of a Heisenberg ferromagnet. PbS is a diamagnetic material from the IV–VI group of semiconductor compounds [2]. Both materials crystallize in a rock salt lattice and have very well matching lattice parameters, $\Delta a/a = 0.5\%$. Employing high vacuum deposition techniques permits epitaxial growth of high-quality multilayer structures [3, 4]. A ferromagnetic transition in EuS–PbS multilayers is observed even for structures with ultrathin EuS layers of only 0.6 nm, i.e. just about two monolayers [3, 4]. In EuS–PbS multilayers grown along the

*Corresponding author, e-mail: story@ifpan.edu.pl

[001] crystal direction with ultrathin (about 1 nm) PbS nonmagnetic spacer layers, the effect of antiferromagnetic interlayer coupling is observed [5, 6]. In EuS–PbS multilayers, wide-energy-gap ($E_g = 1.65$ eV) ferromagnetic layers of EuS form electron barriers, whereas narrow-energy-gap ($E_g = 0.3$ eV) nonmagnetic layers of PbS constitute quantum wells for both electrons and holes (Fig. 1) [4, 7–9]. These semiconductor heterostructures exhibit good luminescence properties in the near infrared, related to the direct-gap electronic band structure of PbS (also exploited in PbS bulk crystals and thin films near infrared lasers and detectors) [2].

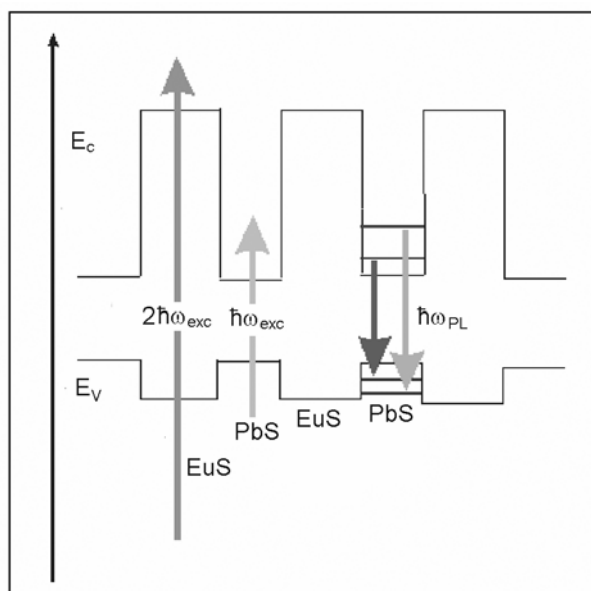


Fig. 1. The energy scheme of a EuS–PbS multilayer with PbS nonmagnetic quantum wells and EuS ferromagnetic barriers. The arrows labelled $2\hbar\omega_{\text{exc}}$ and $\hbar\omega_{\text{exc}}$ depict two optical excitation modes employed. The arrows labelled $\hbar\omega_{\text{PL}}$ show photoluminescence radiation due to electronic transitions between the conduction and valence band states in the PbS well

Due to the ferromagnetic character of EuS barriers which exhibit strong exchange splitting of conduction band states below the Curie temperature, the height of the potential barrier for electrons in a PbS well depends on the magnetization of the EuS layers. This effect is particularly strong in EuS with a total exchange splitting (corresponding to full magnetic saturation) of 0.36 eV as compared to the average (observed in the paramagnetic state) height of the potential barrier of about 1.2 eV. Such a change in the potential barrier influences the energies of size-quantised electronic states in a PbS well. An additional control mechanism may also be related to the influence of the mutual orientation of the magnetization vectors of two EuS barriers, as modelled theoretically in Ref. [9]. Therefore, EuS–PbS multilayers form a new spin optoelectronic semiconductor system, in which the electronic states and optical proc-

esses can be controlled by low external magnetic fields needed to magnetically saturate EuS barriers. In this work, we experimentally examine a new spin optoelectronic idea of controlling the wavelength and other characteristics of PL emission in a semiconductor magnetic heterostructure of EuS–PbS multilayers by changing the height of the ferromagnetic barriers induced by low magnetic fields.

2. Experimental results and discussion

Photoluminescence (PL) was studied in a $5 \times (\text{EuS (5.5 nm)} - \text{PbS (17.5 nm)})$ multilayer grown by high-vacuum deposition on a BaF_2 (111) substrate. EuS was evaporated using an electron gun, whereas for PbS a standard thermal source (tungsten boat) was used.

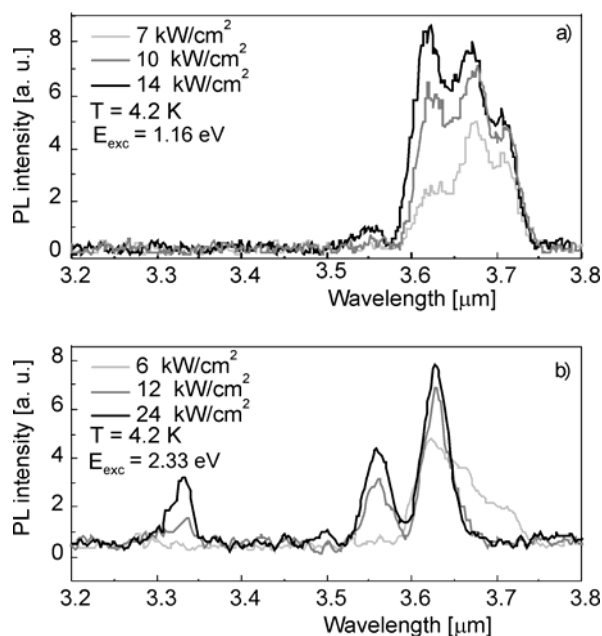


Fig. 2. Dependence of the photoluminescence spectra of a $5 \times (\text{EuS (5.5 nm)} - \text{PbS (17.5 nm)})/\text{BaF}_2$ (111) multilayer on laser excitation power as indicated in the Figure. The experimentally observed minimum at a wavelength of about $3.6 \mu\text{m}$ is due to the absorption of the atmosphere. The spectra were detected in the backscattering optical geometry of the experiment

The analysis of the crystalline structure as well as the magnetic and optical properties of this multilayer showed its high crystal and excellent optical quality. This multiple quantum well showed a very strong, relatively well resolved PL spectrum which is a necessary pre-condition for our experiment. We did not observe such a strong PL in EuS–PbS multilayers with narrower PbS wells. The ferromagnetic transition temperature of the multilayer, $T_c = 14 \text{ K}$, was determined from the analysis of the tem-

perature dependence of magnetization. The PL was excited by YAG:Nd laser pulses with 1.16 eV photon energy (absorbed only in PbS wells) or pulses with 2.33 eV photon energy (absorbed in both the quantum wells and barriers, as shown in Fig. 1). The measurements were carried out at 4.2 and 77 K (i.e., below and above the Curie temperature of EuS layers). The pulse duration was 6 ns, which is much longer than the recombination time of the material, hence the excitation was quasi-steady. Both back-scattering and edge emission optical experimental geometries were employed, with the PL emission collected along the normal to the layer or from the side of the layer, respectively. A weak external magnetic field was applied in the plane of the layer.

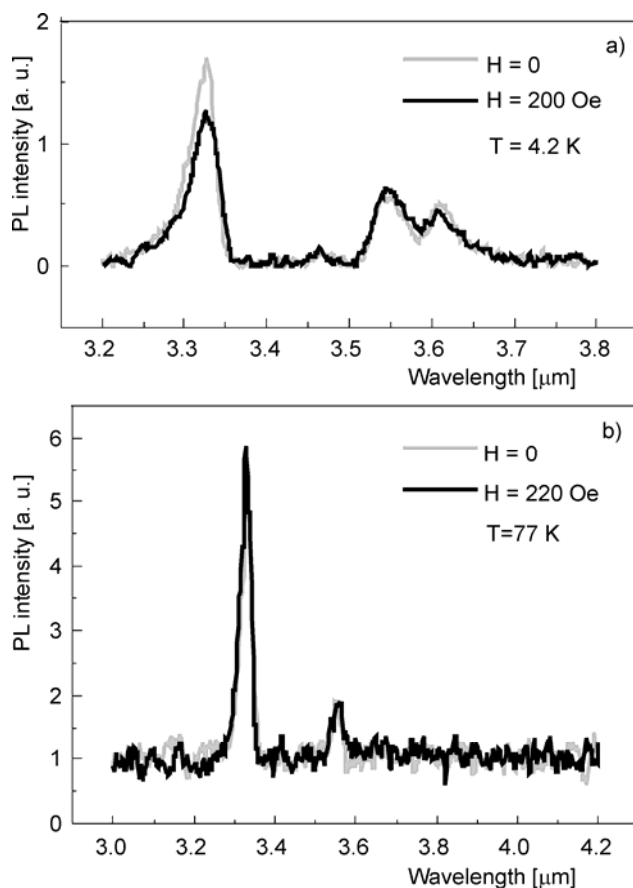


Fig. 3. The effect of a weak magnetic field on the photoluminescence of a $5 \times (\text{EuS} (5.5 \text{ nm})\text{-PbS} (17.5 \text{ nm})/\text{BaF}_2 (111))$ multilayer below (a) and above (b) its Curie temperature ($T_c = 14 \text{ K}$). The spectra were detected in the edge emission geometry, with a 2.33 eV laser excitation and pumping power of 6 kW/cm^2

The PL spectra of the PbS-EuS multilayer are presented in Fig. 2. The spectra are attributed to the allowed optical transitions between PbS well states of the first and the second size-quantization sub-bands (see Fig. 1). The PL spectra presented in

Fig. 2 were recorded as a function of an increasing power density of the laser excitation. For pumping by laser pulses with 1.16 eV photon energy we observed only PL radiation related to the first size-quantised sub-band (Fig. 2a), while for PL excitation by laser pulses with 2.33 eV photon energy radiation related to both the first and the second sub-bands was observed for high density power pumping (Fig. 2b). One can notice a strongly non-linear dependence of the intensity of the PL line related to the second sub-band with increasing laser pumping power density. This indicates the importance of the transfer of photo-excited electrons between ferromagnetic EuS barriers and nonmagnetic PbS wells. Figure 3a presents the effect of a weak external magnetic field on the PL spectra of the PbS–EuS multilayer at 4.2 K. A red shift (of about 1 meV) of the higher energy line is observed in a field of 200 Oe. Above the Curie temperature of the EuS–PbS multilayer, no shift of the PL lines is experimentally found (Fig. 3b). The application of a weak external field also substantially reduces the intensity of the PL line below the Curie temperature, with practically no effect above the Curie temperature.

The estimated Zeeman splitting of electron states in the nonmagnetic PbS well induced by an external field of 200 Oe is about 0.02 meV and can be neglected. This conclusion is supported by PL spectra measurements in the paramagnetic region ($T=77$ K, Fig. 3b). Therefore, it is likely that the mechanism responsible for the experimental observations discussed above is related to magnetization-dependent changes in the EuS potential barrier. As a consequence of a rather wide PbS well used in our multilayers (optical limit of the experiment), however, the expected red shift is barely resolved experimentally. We believe that the other effect (the change of PL intensity) is also related to the same mechanism. No theoretical model for this effect, however, is known yet.

3. Summary

In conclusion, we have experimentally studied the photoluminescence excited by a YAG laser in EuS–PbS ferromagnetic semiconductor heterostructures. The PL spectra were studied both above and below the Curie temperature of EuS, applying low magnetic fields and using two laser excitation energies. The PL spectra observed in the near infrared range were attributed to electronic transitions between size-quantised electronic states in the conduction and valence bands of the PbS well. In the ferromagnetic state, an external field of 200 Oe (magnetically saturating EuS layers) substantially influenced the intensity of the PL as well as produced a small red shift in the position of the higher energy PL line. This effect can be understood in terms of the influence of magnetization-dependent ferromagnetic EuS potential barriers on the electronic states in PbS wells.

Acknowledgements

The work was supported by the KBN research projects PBZ-KBN-044/P03/2001 and 1P03B05426.

References

- [1] MAUGER A., GODART C., Phys. Rep., 141 (1986), 51.
- [2] *Lead Chalcogenides – Physics and Applications*, D.R. Khokhlov (Ed.), Taylor and Francis, New York, 2003.
- [3] STACHOW-WÓJCIK A., STORY T., DOBROWOLSKI W., ARCISZEWSKA M., GALĄZKA R.R., KREIJVELD M.W., SWUSTE C.H.W., SWAGTEN H.J.M., DE JONGE W.J.M., TWARDOWSKI A., SIPATOV A.YU., Phys. Rev. B, 60 (1999), 15220.
- [4] STORY T., Phys. Stat. Sol. (b), 236 (2003), 3 10.
- [5] KĘPA H., KUTNER-PIELASZEK J., BLINOWSKI J., TWARDOWSKI A., MAJKRZAK C.F., STORY T., KACMAN P., GALĄZKA R.R., HA K., SWAGTEN H.J.M., DE JONGE W.J.M., SIPATOV A.YU., VOLOBUEV V.V., GIEBULTOWICZ T., Europhys. Lett., 56 (2001), 54.
- [6] SMITS C.J.P., FILIP A.T., SWAGTEN H.J.M., KOOPMANS B., DE JONGE W.J.M., CHERNYSHOVA M., KOWALCZYK L., GRASZA K., SZCZERBAKOW A., STORY T., PALOSZ W., SIPATOV A.YU., Phys. Rev. B, 69 (2004), 224410.
- [7] KOLESNIKOV I.V., LITVINOV V.A., SIPATOV A.YU., FEDORENKO A.I., YUNOVICH A.E., Sov. Phys. JETP, 67 (1988), 1431.
- [8] KOWALCZYK L., SADOWSKI J., GALĄZKA R.R., STACHOW-WÓJCIK A., SIPATOV A.YU. AND VOLOBUEV V.V., Acta Phys. Polon., A, 94 (1998), 397.
- [9] ZORCHENKO V.V., SIPATOV A.YU. AND VOLOBUEV V.V., Low Temp. Phys., 29 (2003), 1208 (in Russian).

Received 1 June 2005

Revised 10 October 2005

Torque due to spin-polarized current in ferromagnetic single-electron transistors

M. KOWALIK^{1*}, J. WIŚNIEWSKA¹, J. BARNAŚ^{1, 2}

¹Department of Physics, Adam Mickiewicz University, Umultowska 85, 61-614 Poznań, Poland

²Institute of Molecular Physics, Polish Academy of Sciences,
M. Smoluchowskiego 17, 60-179 Poznań, Poland

A theoretical analysis of current-induced torque acting on the magnetic moment of the central part (island) of a ferromagnetic single-electron transistor has been carried out in the regime of sequential tunnelling. The island is assumed to be ferromagnetic and attached to two leads (electrodes). One of the leads is ferromagnetic, and the corresponding magnetic moment is oriented arbitrarily. The torque is calculated from the spin current absorbed by the magnetic moment of the island, and calculations are carried out in the limit of fast spin relaxation on the island (no spin accumulation).

Key words: *single electron transistor; spin-polarized transport; current-induced magnetic switching*

1. Introduction

It is well known that spin-polarized current in magnetic multilayers or nanopilars can switch the magnetic configuration from a parallel to antiparallel one and/or *vice versa*. The switching is a result of angular momentum transfer from a conduction electron system to the local magnetization, and takes place when the electric current exceeds a certain critical density [1]. Current-induced magnetic switching is of great importance, mainly because it offers a possibility of manipulating magnetic moment orientation without an external magnetic field. The switching phenomenon in all-metal magnetic structures has already been observed experimentally in various systems [2, 3].

Recently, magnetic switching has also been reported in simple planar tunnel junctions [4], where the current density is much smaller than in metallic devices. In this paper, we consider the possibility of current-induced switching in ferromagnetic double-barrier tunnel junctions with a Coulomb blockade, i.e. in ferromagnetic single-electron transistors (SETs). We calculate the torque exerted on the magnetic moment

*Corresponding author, e-mail: kowalik@amu.edu.pl

of the central electrode (island) and on the magnetic moment of the external ferromagnetic lead. It is worth noting that a significantly different mechanism of the switching phenomenon due to spin-polarized current in ferromagnetic SETs has been recently predicted by Inoue and Brataas [5]. This mechanism is based on spin accumulation in the nonmagnetic island. In our case, however, we consider the limit of fast spin relaxation, so there is no spin accumulation on the island. Such an approximation is justified, since spin relaxation time in ferromagnetic systems is usually significantly smaller (due to a stronger spin-orbit coupling) than in nonmagnetic ones. Apart from this, we consider the torque acting on both the island and external lead, whereas in Ref. [5] only the torque acting on the magnetic leads was studied.

2. Model and method

We consider a SET whose one external electrode and island are ferromagnetic, whereas the second external electrode is nonmagnetic. The magnetic moments of the lead and island can be oriented arbitrarily, as shown in Fig. 1. The island is assumed to be sufficiently large to neglect level quantisation, but small enough to have a charging energy $e^2/2C$ significantly larger than the thermal energy $k_B T$, $e^2/2C \gg k_B T$, where C is the island capacitance. Moreover, we consider only the case where the charge on the island is well localized, which takes place when the resistances $R_{l(r)}$ of the two barriers separating the island from the external electrodes are much larger than the quantum resistance, $R_{l(r)} \gg R_Q = h/e^2$. The indices l and r refer to the left and right barriers, respectively. As a consequence, orthodox tunnelling theory based on second-order perturbation theory (Fermi golden rule) and on the master equation is applicable. This theory describes electronic transport in the sequential tunnelling regime relatively well. Finally, as already stated in the Introduction, we restrict ourselves to the situation with no spin accumulation on the island. Therefore, the energy change associated with the tunnelling process can be entirely determined from the change in the electrostatic energy.

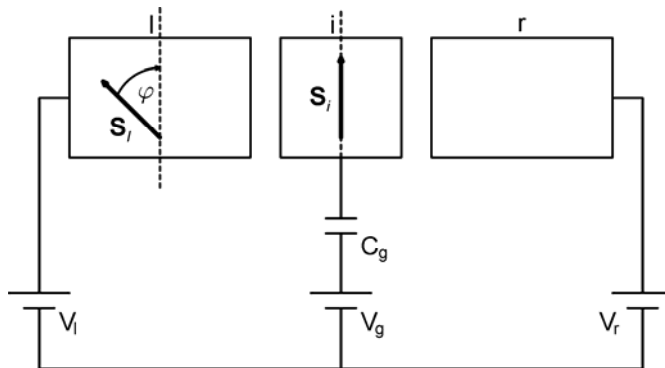


Fig. 1. A schematic diagram of the ferromagnetic single-electron transistor. The vectors S_l and S_i indicate the net spin moments of the left external electrode and the island, respectively

A detailed description of the method used to calculate the tunnelling current and transport characteristics is presented elsewhere [6]. This method allows us to calculate the tunnelling current across each barrier. The total charge current I_0 in each ferromagnetic component of the device can be written as $I_0 = I_+ + I_-$, where I_+ and I_- are the currents flowing in the spin-majority and spin-minority channels, respectively. The corresponding spin current I_s may then be defined as $I_s = I_+ - I_-$.

Electrons in the ferromagnetic components of the device have spin orientations either parallel (spin-majority) or antiparallel (spin-minority) to the net local spin polarizations (local spin quantization axis). When the magnetic moments of the island and left electrode are non-collinear, electrons from the spin-majority (or spin minority) channel of the left electrode can tunnel with some probability to the spin-majority (spin-minority) channel of the island and *vice versa*. An electron tunnelling through the barrier between the magnetic electrode and island adjusts its spin orientation in an atomically thin interfacial layer [7, 8]. Thus some angular momentum is transferred to the local magnetization of the island and also to the magnetic moment of the left electrode, giving rise to the corresponding spin transfer torques. The torques can be then calculated as the difference between spin currents incoming and leaving the interfacial region [7].

The angular momentum absorbed by the island is equivalent to the torque. The absolute value of angular momentum carried by a single electron is $\hbar/2$, hence the total angular momentum transferred to the magnetic moment of the island can be calculated by counting the contributions from individual electrons. As a result, the torque τ_i acting on the island due to the tunnelling current flowing through the left barrier is given by

$$\tau_i = \frac{\hbar}{2e} \left[(I_{l+} - I_{l-}) - (I_{i+}^< - I_{i-}^<) \cos \varphi \right] \frac{1}{\sin \varphi} \quad (1)$$

where $I_{l+(-)}$ and $I_{i+(-)}^<$ denote currents in the spin-majority (spin-minority) channel of the left electrode and island, respectively, taken at a certain atomic distance from the left barrier. φ is the angle between the spin moments of the left electrode and island, as defined in Fig. 1, whereas e denotes the electron charge ($e > 0$). According to our definition, the torque is positive when it tends to a clockwise rotation of the magnetic moment. A similar formula can be derived for the torque τ_l exerted on the magnetic moment of the left electrode

$$\tau_l = -\frac{\hbar}{2e} \left[(I_{l+} - I_{l-}) \cos \varphi - (I_{i+}^< - I_{i-}^<) \right] \frac{1}{\sin \varphi} \quad (2)$$

The currents $I_{l+(-)}$, flowing when a bias voltage V is applied can be calculated from the formula

$$I_{l\sigma} = -e \sum_{\sigma'=\pm, -} \sum_n \left[\Gamma_{l \rightarrow i}^{\sigma, \sigma'}(n, V) - \Gamma_{i \rightarrow l}^{\sigma', \sigma}(n, V) \right] P(n, V) \quad (3)$$

where $\Gamma_{l \rightarrow i}^{\sigma, \sigma'}(n, V)$ is the electron tunnelling rate from the spin channel σ in the left electrode to the spin channel σ' on the island when there are already n excess electrons on the island. Similarly, $\Gamma_{i \rightarrow l}^{\sigma, \sigma'}(n, V)$ is the tunnelling rate from the island back to the left electrode. Apart from this, $P(n, V)$ is the probability of having n excess electrons on the island, which can be calculated from the relevant master equation [6].

3. Numerical results and discussion

The results of numerical calculations of the angular variation of the torque τ_i acting on the magnetic moment of the island are shown in Fig. 2, for two values of spin polarization of the density of states at the Fermi level in the ferromagnetic components of the device (we assume that the ferromagnetic electrode and island are made of the same material). The corresponding spin asymmetry of the resistance of the left barrier is then $R_l^{p,+}/R_l^{p,-} = 1/p^2$, where $R_l^{p,+(-)}$ is the resistance of the left barrier in the parallel configuration for the spin-majority (spin-minority) channel. Similarly, the spin asymmetry of the resistance of the right barrier is $R_r^+/R_r^- = 1/p$, where $R_r^{+(-)}$ is the resistance of the right barrier for the spin-majority (spin-minority) channel.

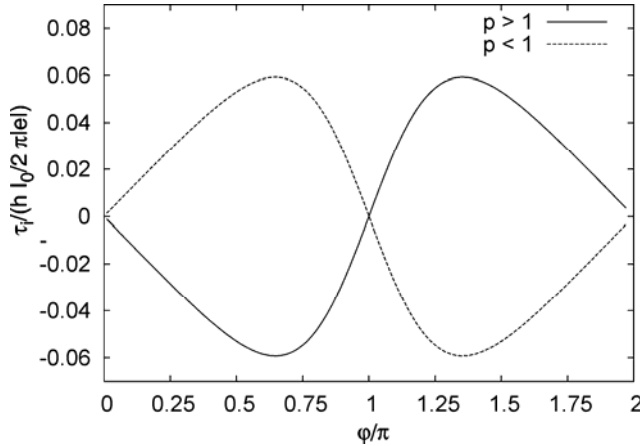


Fig. 2. Normalized torque acting on the island as a function of the angle φ , calculated for $R_l^{p,+} = 25 \text{ M}\Omega$ (1 M Ω), $R_l^{p,-} = 1 \text{ M}\Omega$ (25 M Ω), $R_r^+ = 0.5 \text{ M}\Omega$ (0.1 M Ω), and $R_r^- = 0.1 \text{ M}\Omega$ (0.5 M Ω), corresponding to

$$p = 0.2 \text{ (} p = 5 \text{)}. \text{ In the antiparallel configuration we used } R_l^{ap,+} = R_l^{ap,-} = \sqrt{R_l^{p,+} R_l^{p,-}}.$$

The other parameters were: $V_l = 0.043 \text{ V}$, $V_r = 0.043 \text{ V}$, $V_g = 0$, $T = 4.3 \text{ K}$ and $C_l = C_g = C_r = 1 \text{ aF}$

The torque shown in Fig. 2 is normalized to the electric current I_0 , and thus changes sign when the current I_0 is reversed. For $p > 1$, the parallel configuration may become unstable for sufficiently large positive currents, $I_0 > 0$, whereas the antiparallel configuration is stable. The situation changes for $p < 1$, for which the parallel con-

figuration is stable for $I_0 > 0$ and the antiparallel configuration becomes unstable. For a negative current, $I_0 < 0$, the torque changes sign and therefore all possible switching phenomena are also reversed. Similar curves also correspond to the torque acting on the magnetic electrode.

The curves presenting the torque normalized to I_0 are universal in the sense that they are independent of the gate and bias voltages. This means that the torque is proportional to the current I_0 . Thus, to find the magnitude of the torque one needs to know the magnitude of the current flowing through the system due to the applied bias voltage V . In Figure 3, we show the current as a function of the bias and gate V_g voltages. The curves show typical Coulomb steps and Coulomb oscillations. Thus, the torque τ_i exerted on the magnetic moment of the island reveals similar features as a function of bias and gate voltages.

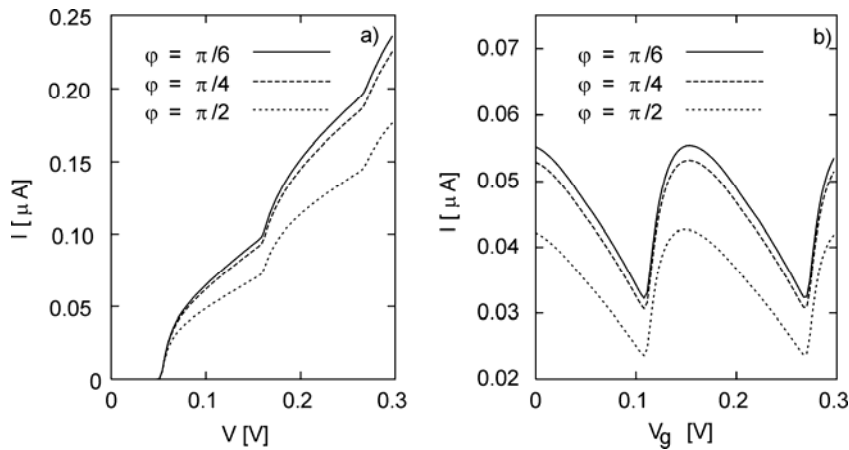


Fig. 3. Electric current as a function of the bias (a) and gate (b) voltages, calculated for $p = 0.2$ and $V_g = 0$ (a), and $V_l = 0.043$ V, $V_r = 0.043$ V (b). The other parameters the same as in Fig. 2

In conclusion, we have calculated the torque exerted by a spin-polarized current on the magnetic moment of the island in a ferromagnetic SET, with the island and one electrode being ferromagnetic. The results of numerical calculations show the possibility of normal and inverse current-induced magnetic switching, similarly as in all-metal layered structures [8]. Numerical calculations have been performed for the situation where the density of states in the ferromagnetic components for one spin orientation is 5 times larger than that for the opposite spin orientation, which is of the order of the corresponding values in ferromagnetic metals. The corresponding ratio may be even significantly larger in half-metallic ferromagnets, where the density of states for one spin orientation is negligibly small.

Acknowledgements

The authors acknowledge support by the Polish State Committee for Scientific Research through the project No. PBZ/KBN/044/P03/2001.

References

- [1] SLONCZEWSKI J.C., J. Magn. Magn. Mater., 159 (1996), L1.
- [2] KATINE J.A., ALBERT F.J., BUHRMAN R.A., MYERS E.B., RALPH D.C., Phys. Rev. Lett., 84 (2000), 3149.
- [3] GROLLIER J., CROS V., HAMZIC A., GEORGE J.M., JAFFRES H., FERT A., FAINI G., BEN YOUSSEF J., LEGALL H., Appl. Phys. Lett., 78 (2001), 3663.
- [4] HUAI Y., ALBERT F., NGUYEN P., PAKALA M., VALET T., Appl. Phys. Lett., 84 (2004), 3118.
- [5] INOUE J., BRATAAS A., Phys. Rev. B, 70 (2004), 140406.
- [6] WIŚNIEWSKA J., KOWALIK M., BARNAŚ J., Mater. Sci.-Poland, 24 (2006), 761.
- [7] SLONCZEWSKI J.C., Phys. Rev. B, 71 (2005), 24411.
- [8] BARNAŚ J., FERT A., GMITRA M., WEYMANN I., DUGAEV V., Phys. Rev. B, 72 (2005), 024426

Received 1 June 2005
Revised 10 October 2005

Weak interlayer exchange coupling in Fe–Zr and Fe–Ti layered structures

L. SMARDZ^{1*}, K. SMARDZ²

¹Institute of Molecular Physics, Polish Academy of Sciences,
M. Smoluchowskiego 17, 60-179 Poznań, Poland

²Institute of Materials Science and Engineering, Poznań University of Technology,
pl. Skłodowskiej-Curie 5, 60-965 Poznań, Poland

20 nm Fe/ d_{Zr} Zr/20 nm Fe and 20 nm Fe/ d_{Ti} Ti/20 nm Fe trilayers with wedged Zr and Ti sublayers were prepared at room temperature using UHV (5×10^{-10} mbar) RF/DC magnetron sputtering. The results showed that the Fe sublayers are ferromagnetically coupled up to a Zr or a Ti spacer thickness of about 1.5 or 2 nm, respectively. Furthermore, a weak antiferromagnetic (ferromagnetic) coupling of the Fe sublayers was observed for a Zr (Ti) thickness range of 1.5–3 nm (2–3.4 nm). The Fe sublayers are very weakly exchange coupled or decoupled for $d_{\text{Zr}} > 3$ nm and $d_{\text{Ti}} > 3.4$ nm. The small decoupling Ti and Zr thickness can be explained by the spontaneous formation of a quasi-amorphous structure of paramagnetic spacer during the deposition process.

Key words: *magnetic film*; *multilayers*; *exchange coupling*

1. Introduction

In our previous papers, we have shown that polycrystalline Co sublayers are ferromagnetically (FM) coupled up to Ti [1] and Zr [1, 2] spacer thicknesses of about 2 and 2.5 nm, respectively. Furthermore, a weak antiferromagnetic (AFM) coupling of the Co sublayers was observed for a Ti (Zr) thickness range of 2–2.7 nm (2.5–3.2 nm). The Co sublayers were very weakly exchange coupled or decoupled for $d_{\text{Ti}} > 2.7$ nm and $d_{\text{Zr}} > 3.2$ nm. The rapid decrease of interlayer exchange coupling with Ti and Zr spacer thickness could be explained by its strong damping due to the spontaneous formation of a non-magnetic quasi-amorphous Ti–Co and Zr–Co alloy layer at the interface during the deposition process. The above behaviour is also in agreement with experimental results for interlayer coupling studies across amorphous metallic Cu₆₅Zr₃₅ spacers [3].

*Corresponding author, e-mail: smardz@ifmpan.poznan.pl

In this paper, we report on the magnetic exchange coupling of polycrystalline ($d_{\text{Fe}} > d_{\text{crit}}$) Fe sublayers across a paramagnetic noncrystalline spacer in Fe/Zr/Fe and Fe/Ti/Fe trilayers. Very recently we have shown that iron sublayers grow on sufficiently thick zirconium [4, 5] ($d_{\text{Zr}} > 0.7$ nm) and titanium [6] ($d_{\text{Ti}} > 0.6$ nm) sublayers in the soft magnetic nanocrystalline phase up to a critical thickness of $d_{\text{crit}} \sim 2.3$ nm. For thicknesses greater than d_{crit} , the Fe sublayers undergo a structural transition to the polycrystalline phase with a much higher coercivity. On the other hand, it is well known that suitable annealing of Fe/Zr and Fe/Ti MLs leads to the formation of an amorphous phase due to a solid state reaction [7, 8]. Therefore, the spontaneous formation of an amorphous or nanocrystalline nonmagnetic Zr–Fe and Ti–Fe spacer between Fe sublayers is very likely to proceed during the deposition of the Fe/Zr(Ti)/Fe trilayer or Fe/Zr (Fe/Ti) multilayers.

2. Experimental

Fe/Zr/Fe and Fe/Ti/Fe trilayers with wedged Zr and Ti sublayers were prepared on glass substrates at room temperature using UHV (5×10^{-10} mbar) DC/RF magnetron sputtering [1]. The Fe layers ($d_{\text{Fe}} = 20$ nm) were deposited using a DC source. RF source was used to prepare the wedged Zr and Ti layers ($0 < d_{\text{Zr(Ti)}} < 10$ nm). Typical deposition rates for the Fe and Zr sublayers were 0.1 and 0.05 nm/s, respectively. After outgassing the glass substrate at 500 K for 30 minutes, we first deposited a Fe layer. A wedged Zr or Ti spacer layer was then grown immediately on the Fe layer. Finally, a 3 nm Au cap layer was deposited to prevent the oxidation of the top Fe sublayer. The chemical composition and the purity of all layers was checked *in situ* immediately after deposition, after transferring the samples to an UHV (4×10^{-11} mbar) analysis chamber equipped with X-ray photoelectron spectroscopy (XPS). The structures of the samples with step-like wedge forms (areas with Fe and Zr sublayers of constant thickness) was examined *ex situ* by standard θ – 2θ X-ray diffraction using CuK_α radiation. The magnetic characterisation of the wedged Fe/Zr MLs was carried out at room temperature using the magneto-optical Kerr effect and a vibrating sample magnetometer.

3. Results and discussion

Results of systematic high-angle X-ray diffraction studies as a function of Fe and Zr sublayer thickness for 20 nm Fe/ d_{Zr} Zr/20 nm Fe, and 20 nm Fe/ d_{Ti} Ti/20 nm Fe trilayers with d_{Zr} (d_{Ti}) greater than ~ 3 nm showed only (110) and (002) reflections of bcc Fe and hcp Zr (Ti) in the patterns, respectively. Only a broad peak related to Fe sublayers was observed for trilayers with d_{Zr} (d_{Ti}) $< \sim 3$ nm, in agreement with the X-ray diffraction studies for Co/Zr, Co/Ti, and Fe/Ti multilayers reported in Refs.

[4–6]. The absence of Zr and Ti reflections for $d_{\text{Zr}}(d_{\text{Ti}}) < \sim 3$ nm is consistent with UHV STM images [9] which showed randomly oriented nanocrystalline grains with an average size D of ~ 3 –5 nm.

In situ XPS analyses of freshly deposited Fe and Zr layers revealed no contamination elements such as oxygen and carbon. In the XPS experiment, we have also studied Fe layer growth on a 10 nm Zr underlayer and Zr layer growth on a 10 nm Fe underlayer. From the exponential variation of the XPS Fe-2p and Ti-2p and Zr-3d integral intensities with increasing layer thickness, we conclude that the Fe, Ti, and Zr sublayers grow homogeneously during the deposition of the trilayers [9, 10].

In the case of wedged trilayers, the bottom Fe layer was deposited on a rather rough glass substrate. Such a layer showed a greater coercivity compared to the top Fe layer, which was deposited on a quasi-amorphous Zr–Fe (Ti–Fe) interlayer, formed spontaneously during the deposition process [1, 2]. For a sufficiently small Zr–Fe (Ti–Fe) thickness, however, the FM exchange coupling energy of the Fe layers across the paramagnetic spacer is large enough for the simultaneous magnetisation reversal process of the bottom and top sublayers. On the other hand, for a weaker interlayer exchange coupling ($d_{\text{Zr}} > \sim 1.5$ nm, $d_{\text{Ti}} > \sim 2$ nm), we have observed step-like hysteresis loops due to different coercivities of the bottom and top Fe layers.

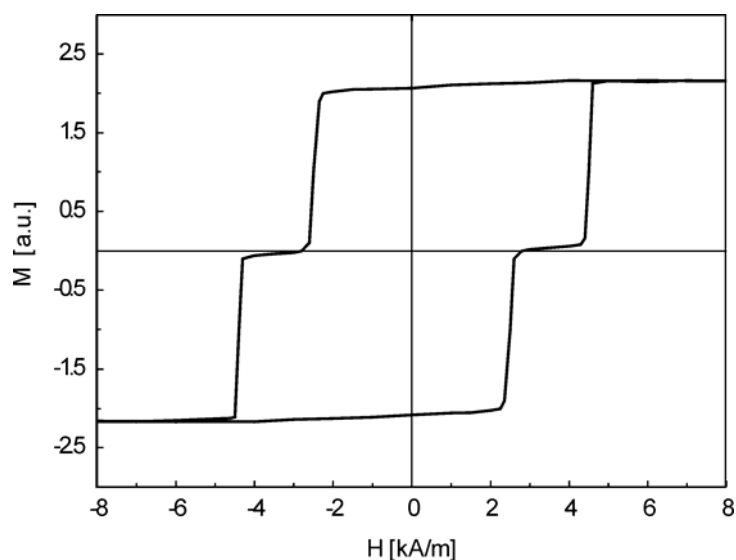


Fig. 1. A hysteresis loop of the 20 nm –Fe/2 nm –Zr/20 nm –Fe trilayer

Figure 1 shows an example of a step-like hysteresis loop measured for the Fe/Zr/Fe trilayer with $d_{\text{Zr}} = 2$ nm. In the intermediate case between fully coupled and independent (i.e. fully decoupled) Fe layers, the exchange field felt by each layer due to the presence of the second layer decreases (increases) the observed switching field of the soft (hard) magnetic layer in the case of AFM coupling, and vice versa for FM

coupling [1]. The two observed significantly different coercive fields in Fig. 1, H_{c1} and H_{c2} , originate from the soft and hard magnetic Fe layers, respectively [1, 2].

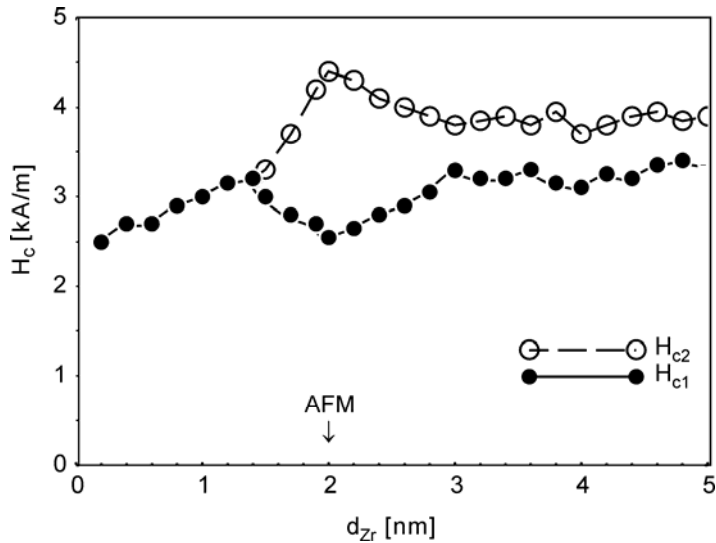


Fig. 2. Two different coercive fields H_{c1} and H_{c2} as functions of Zr interlayer thickness for a wedged 20 nm Fe/ d_{Zr} Zr/20 nm Fe trilayer

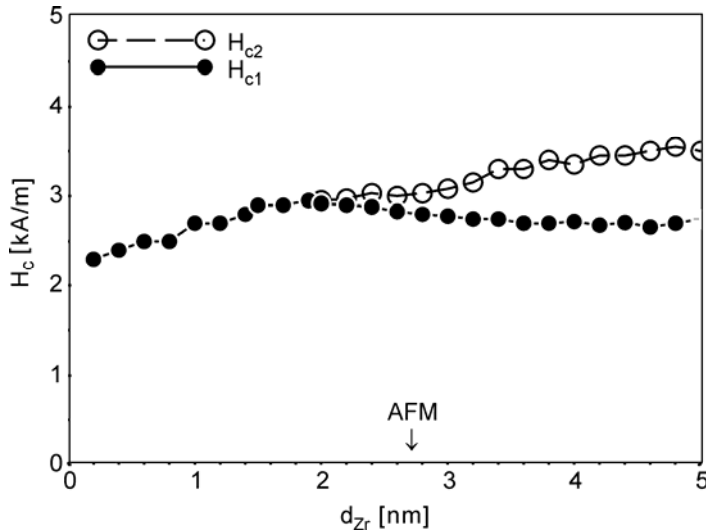


Fig. 3. Two different coercive fields H_{c1} and H_{c2} as functions of Ti interlayer thickness for a wedged 20 nm Fe/ d_{Ti} Ti/20 nm Fe trilayer

The results of systematic studies of coercivity as a function of Zr and Ti interlayer thickness are presented in Figs. 2 and 3, respectively. The spacer thickness dependence of coercivity for wedged trilayers allows us to characterise the weak interlayer

exchange coupling of Fe sublayers [1, 2]. For $d_{Zr} \approx 2$ nm (Fig. 2), we observe a weak minimum and maximum for H_{c1} and H_{c2} , respectively. The above behaviour possibly indicates weak AFM coupling between Fe layers, with a maximum near $d_{Zr} \approx 2$ nm. The difference between H_{c1} and H_{c2} determined for the Fe/Ti/Fe trilayer (Fig. 3) is rather small for Ti layer thickness between ~ 2 and ~ 3.4 nm. The above behaviour could indicate a weak FM coupling between Fe layers for Ti spacer thickness ~ 2 – 3.4 nm. The absence of weak AFM coupling for the Fe/Ti/Fe trilayer could be associated with a low density of the ferromagnetic “bridges” between Fe sublayers. Furthermore, coercivity measurements show that Fe layers are very weakly exchange coupled or decoupled for $d_{Zr} > 3$ nm ($d_{Ti} > 3.4$ nm). The small decoupling Zr and Ti thicknesses could be explained by a spontaneous formation of a quasi-amorphous structure in the paramagnetic spacer during deposition [1–3]. In the case of the Fe/Zr/Fe (Fe/Ti/Fe) trilayer, the spacer interlayer consists of a Fe_xZr_{1-x} (Fe_xTi_{1-x}) alloy and pure Zr (Ti) layer. For the ultrathin spacer ($d_{Zr} < 2$ nm), the Fe_xZr_{1-x} (Fe_xTi_{1-x}) alloy layer remains practically quasi-amorphous, with a variable concentration (x) in the direction perpendicular to the substrate. This is consistent with the results of our XRD and magnetisation studies for Fe/Zr and Fe/Ti [4–6] MLs. In the case of such a quasi-amorphous structure of the spacer, a strong damping of the interlayer exchange coupling is to be expected from the theory based on the RKKY interaction [3]. The above effect could explain our results of the studies of coercivity as a function of Zr and Ti spacer thickness, shown in Figs. 2 and 3. Furthermore, amorphous Fe–Ti and Fe–Zr alloys approximately fulfil the Nagel–Tauc criterion [1–3] ($2k_F = k_p$), where k_F and k_p denote the Fermi k -vector and ion correlation radius, respectively. Therefore, for Fe–Zr alloy spacers the location of the first weak AFM maximum was detected at $d_{Zr} \approx 2$ nm, in agreement with the large oscillation period of the exchange coupling ($\lambda \approx 1/|2k_F - k_p|$) expected from the theory [3].

In summary, the planar growth of Fe and Zr (Ti) sublayers was confirmed *in situ* by X-ray photoelectron spectroscopy. Furthermore, a weak AFM (FM) coupling of the Fe sublayers was observed for Zr (Ti) thickness between 1.5 and 3 nm (2 and 3.4 nm). The Fe layers are very weakly exchange coupled or decoupled for $d_{Zr} > 3$ nm ($d_{Ti} > 3.4$ nm). The rapid decrease in exchange coupling could be explained by its strong damping due to the formation of a non-magnetic quasi-amorphous alloy layer at the interfaces.

Acknowledgements

This work was financially supported by the Polish Committee for Scientific Research under grant No. PBZ KBN 044/P03/02 2001.

References

- [1] SMARDZ L., Sol. State Comm., 112 (1999), 693.
- [2] SMARDZ L., Czech. J. Phys., 52 (2002), 209.
- [3] BÜRGLER D.E., SCHALLER D.M., SCHMIDT C.M., MEISINGER F., KROHA J., MCCORD J., HUBERT A., GÜNTHERODT H.J., Phys. Rev. Lett., 80 (1998), 4983.

- [4] SMARDZ L., SMARDZ K., Mol. Phys. Rep., 40 (2004), 137.
- [5] SMARDZ L., J. All. Comp., 389 (2005), 17.
- [6] SMARDZ K., SMARDZ L., Mater. Sci.-Poland, 24 (2006), 827.
- [7] SAMWER K., Phys. Reports ,161 (1988), 3.
- [8] STOBIECKI T., KOPCEWICZ M., CASTAÑO F.J., Chaos, Solitons and Fractals, 10 (1999), 2031.
- [9] SMARDZ K., PhD Thesis, Institute of Molecular Physics, Polish Acad. Sci., Poznań (Poland), 1999.
- [10] BRIGGS D., [in:] *Handbook of X-ray and Ultraviolet Photoelectron Spectroscopy*, D. Briggs (Ed.), Heyden & Son Ltd., London, 1977, p. 153 and references therein.

Received 1 June 2005
Revised 10 October 2005

Structure and electronic properties of Fe–Ti thin films

K. SMARDZ¹, L. SMARDZ^{2*}

¹Institute of Materials Science and Engineering, Poznań University of Technology,
pł. M. Skłodowskiej-Curie 5, 60-965 Poznań, Poland

²Institute of Molecular Physics, Polish Academy of Sciences,
M. Smoluchowskiego 17, 60-179 Poznań, Poland

Fe/Ti multilayers (MLs) were prepared on glass substrates using UHV RF/DC magnetron sputtering. The results showed a significant drop in coercivity measured for the Fe/Ti MLs with decreasing Fe layer thickness, typically from $H_c \approx 2.2$ kA/m to $H_c \approx 0.2$ kA/m, observed at a critical Fe thickness of $d_{\text{crit}} \approx 2.3$ nm. Structural studies showed that the deposition of a 0.18 nm Fe/0.22 nm Ti ML at 285 K leads to the formation of a uniform amorphous Fe–Ti alloy thin film due to strong interdiffusion during growth. On the other hand, *in situ* annealing of this ML at 750 K for 2 h resulted in the creation of a nanocrystalline phase. Furthermore, *in situ* XPS studies showed that the valence band of the nanocrystalline Fe–Ti alloy film is broader than that measured for the amorphous phase with the same average composition.

Key words: *magnetic multilayers; electronic structure*

1. Introduction

Metallic multilayers (MLs) composed of alternating sublayers of ferromagnetic and non-magnetic metals exhibit interesting magnetic properties which can be tailored by varying the compositions and thicknesses of the sublayers. In previous papers [1–4], we have shown that below the critical Co or Fe thickness (d_{crit}), Co/Zr ($d_{\text{crit}} \approx 2.8$ nm) [1], Co/Ti ($d_{\text{crit}} \approx 3$ nm) [2, 3], and Fe/Zr ($d_{\text{crit}} \approx 2.3$ nm) [4] MLs are magnetically soft and exhibit a saturation magnetisation higher than that observed in conventional soft magnetic films. It has been found that Co (Fe) sublayers grow in the soft magnetic nanocrystalline structure up to d_{crit} [1–4]. Above d_{crit} , Co (Fe) sublayers grow in the polycrystalline structure with an average grain size greater than the magnetic exchange length [5]. On the other hand, it is well known that a suitable annealing of

*Corresponding author, e-mail: smardz@ifmpan.poznan.pl

Fe/Ti MLs leads to the formation of an amorphous phase due to a solid-state reaction [6]. Therefore, the spontaneous formation of a quasi-amorphous or nanocrystalline interface Fe–Ti alloy layer is very likely to proceed during the deposition of the Fe/Ti/Fe trilayer and especially Fe/Ti MLs. This is also consistent with the results of our structural and magnetisation studies for very similar systems Co/Ti, Co/Zr, and Fe/Zr MLs [1–4]. In this paper, we study the stability range of the polycrystalline and soft magnetic nanocrystalline iron phase as a function of the sublayer thickness. Furthermore, we study the valence band of *in situ* prepared amorphous and nanocrystalline Fe–Ti alloy thin films.

2. Experimental

Fe/Ti MLs were prepared on glass substrates at 285 K using computer-controlled ultra high vacuum (UHV) magnetron co-sputtering. Fe and Ti targets were sputtered using the DC and RF modes, respectively. The base pressure before deposition was lower than 5×10^{-10} mbar. The chemical composition and the purity of all layers was checked *in situ*, immediately after deposition, after transferring the samples to an UHV (4×10^{-11} mbar) analysis chamber equipped with X-ray photoelectron spectroscopy (XPS). The XPS spectra were recorded with AlK_{α} radiation (1486.6 eV) at room temperature using a SPECS EA 10 PLUS energy spectrometer. All emission spectra were recorded immediately after *in situ* sample transfer to a vacuum of 8×10^{-11} mbar. The deposition rates of Fe and Ti were checked individually with a quartz thickness monitor. The thicknesses of individual sublayers were controlled mainly by varying their deposition times. The number of repetitions was increased with decreasing Fe and Ti sublayer thicknesses, so as to keep the total thickness of the samples at about 50 nm and 500 nm for magneto-optical measurements and X-ray diffraction studies, respectively.

The Fe/Ti MLs were prepared with either wedged Fe or wedged Ti sublayers. Wedge-shaped Fe or Ti sublayers with a slope of 0.05–0.125 nm/mm were grown by moving a shutter linearly or step-wise in front of the substrate during deposition. The structures of the samples with step-like wedge forms (areas with Fe and Ti sublayers of constant thickness) were examined *ex-situ* by standard θ – 2θ X-ray diffraction (XRD) using CuK_{α} radiation. The modulation wavelength was determined from the spacing between satellite peaks in low-angle XRD patterns. The results were consistent with the values obtained by dividing the total thickness by the number of repetitions. The thicknesses of the individual Fe and Ti sublayers were also determined using X-ray fluorescence analysis (XRF). The magnetic characterisation of the wedged Fe/Ti MLs was carried out utilizing the magneto-optical Kerr effect at room temperature. The coercive fields (H_c) were determined from in-plane hysteresis loop measurements.

3. Results and discussion

The composition modulation of Fe/Ti MLs was confirmed in low-angle XRD measurements. We have observed from two to six satellite peaks for MLs with the thinner and the thicker sublayers, respectively. The wavelengths of modulation calculated from these peaks were in agreement with values determined from XRF measurements. Figure 1a shows an example of a low-angle XRD pattern for the 1.8 nm Fe/2.2 nm Ti ML. The intense satellite peaks up to the 4th order revealed the good quality of the multilayered sample. For the Fe/Ti MLs with $d_{\text{Fe}} > 2.3$ nm and $d_{\text{Ti}} > 2.3$ nm, high-angle X-ray diffraction patterns show the (110) and (002) reflections of bcc Fe and hcp Ti, respectively. The average Fe and Ti crystallite sizes in directions perpendicular to the substrates, as determined from the Scherer equation, are comparable to their respective sublayer thicknesses. Only very weak and broad peaks related to Fe and Ti sublayers were observed for MLs with $d_{\text{Fe}} < 2.3$ nm and $d_{\text{Ti}} = 2.2$ nm, in agreement with the X-ray diffraction studies reported in Ref. [3]. We have previously observed a very similar growth mode for Co sublayers in Co/Zr MLs [1]. The very broad and weak Fe and Ti reflections observed for $d_{\text{Fe}} < \sim 2.3$ nm can be explained by the nanocrystalline growth of the sublayers (average grain size $D \ll 10$ nm), similar to that observed earlier for Co [1–3] and Fe [4] sublayers.

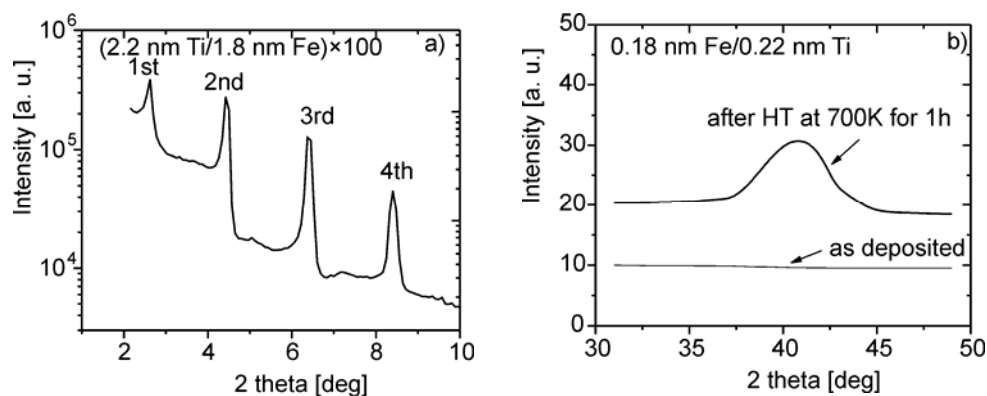


Fig. 1. Low-angle X-ray diffraction patterns ($\text{CuK}\alpha$) for the 2.2 nm Ti/1.8 nm Fe multilayer (a) and high-angle X-ray diffraction patterns ($\text{CuK}\alpha$) for the as deposited and annealed 0.18 nm Fe/0.22 nm Ti multilayer (b)

The above behaviour was revealed by UHV STM measurements of the average in-plane grain sizes, similar to the effect observed earlier for Co/Ti MLs [3]. Furthermore, the deposition of a 0.18 nm Fe/0.22 nm Ti ML at 285 K leads to the formation of a uniform amorphous Fe–Ti alloy thin film due to strong interdiffusion during growth. On the other hand, *in situ* annealing of the 0.18 nm Fe/0.22 nm Ti ML at 700 K for 1 h resulted in the creation of a nanocrystalline phase. The corresponding XRD patterns are shown in Fig. 1a. The average crystallite size of the FeTi alloy film,

as determined from the FWHM of the peak shown in Fig. 1b using the Scherer equation, was about 8 nm.

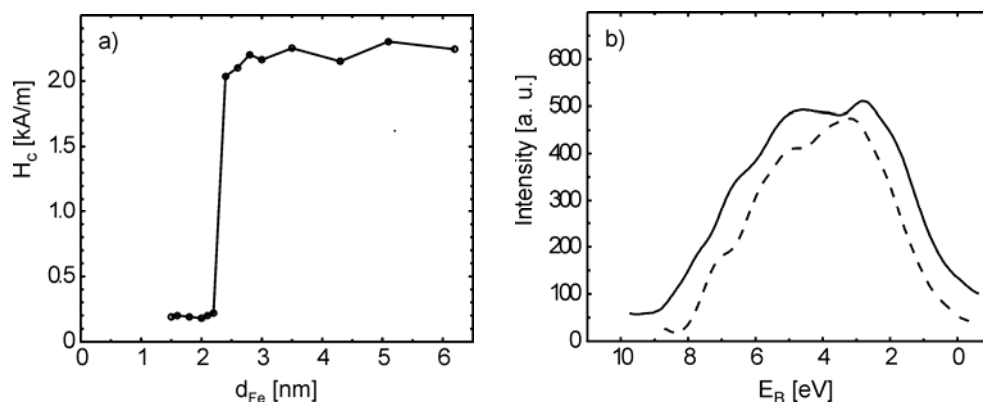


Fig. 2. Coercive field (H_c) as a function of the Fe sublayer thickness for wedged Fe/Ti multilayers with $d_{\text{Ti}} = 2.2$ nm (a) and XPS spectra of the as deposited (broken line) and *in situ* annealed, at 700 K for 1 h (solid line), 0.18 nm Fe/0.22 nm Ti multilayer (b)

Figure 2a shows the H_c values measured at room temperature as function of Fe sublayer thickness for wedged Fe/Ti MLs with $d_{\text{Ti}} = 2.2$ nm. A significant drop in coercivity with decreasing Fe layer thickness – typically from $H_c \approx 2.2$ kA/m to $H_c \approx 0.2$ kA/m – can be observed at a critical Fe thickness of $d_{\text{crit}} \approx 2.3$ nm. The behaviour of coercivity shown in Fig. 2a can be associated with structural properties of the Fe layer grown on Ti, similarly to the transition observed earlier for Co/Zr [2] and Co/Ti [3] MLs. According to the above interpretation, iron sublayers grow in the soft magnetic nanocrystalline phase ($D \ll 10$ nm) for thicknesses lower than the critical one. In this case, the average Fe grain size is significantly smaller than the magnetic exchange length [5] for the iron layer ($L_{\text{ex}} \approx 15$ nm) [5]. For thicknesses larger than d_{crit} , Fe sublayers undergo a structural transition to the polycrystalline phase with an average grains size $D > 15$ nm [5].

Figure 2b shows the XPS valence bands of the as prepared (amorphous phase) and annealed (nanocrystalline phase) 0.18 nm Fe/0.22 nm Ti MLs. XPS measurements were performed *in situ* on freshly prepared samples with thicknesses of about 500 nm. The results showed that the valence band of the “as prepared” amorphous Fe–Ti alloy film (broken line) is broader than that measured for the polycrystalline bulk material [7]. On the other hand, the valence band of the nanocrystalline Fe–Ti alloy (solid line) is even broader than the valence band of the amorphous alloy (broken line). This is probably due to a strong deformation of the nanocrystals. Normally, the interior of the nanocrystal is constrained and the distances between atoms located at grain boundaries expanded [1, 7]. Strong modifications of the electronic structure of nanocrystalline Fe–Ti alloy films could also significantly influence their hydrogenation properties [7]. According to existing semi-empirical models [8, 9] which can explain the

maximum hydrogen absorption capacity of the metallic matrices, the significant broadening of their valence bands is a very important factor, leading to an increase in hydrogen absorption. Such behaviour has already been observed in the case of mechanically alloyed nanocrystalline FeTi- [7] and LaNi₅-type[10] bulk alloys.

In the XPS experiment, we have also studied the growth of a Fe layer on a 10 nm Ti underlayer and the growth of a Ti layer on a 10 nm Fe underlayer. The freshly deposited 10 nm Ti/*d*₀ Fe or 10 nm Fe/*d*₀ Ti bilayer was transferred *in situ* from the preparation chamber to the analysis chamber, where the XPS Fe-2p_{3/2} and Ti-3d_{5/2} core level spectra were immediately recorded in a vacuum of 8×10⁻¹¹ mbar. The bilayer was then transferred back to the preparation chamber and the deposition process of the overlayer was continued. From the exponential variation of the XPS Fe-2p and Ti-3d integral intensities with increasing layer thickness, we conclude that the Fe and Ti sublayers grow homogeneously [11, 12].

In conclusion, the planar growth of Fe and Ti sublayers was confirmed *in situ* by XPS. Iron sublayers grow on sufficiently thick titanium sublayers in the soft magnetic nanocrystalline phase up to a critical thickness of *d*_{crit} ≈ 2.3 nm. *In situ* XPS studies showed that the valence band of the Fe–Ti alloy thin film strongly depends on its microstructure.

Acknowledgements

This work was financially supported by the Polish Committee for Scientific Research under grant No. PBZ KBN 044/P03/02 2001.

References

- [1] SMARDZ L., LE DANG K., NIEDOBA H., CHRZUMNICKA K., J. Magn. Magn. Mater., 140–144 (1995), 569.
- [2] SMARDZ L., Sol. State Comm., 112 (1999), 693.
- [3] SMARDZ L., SMARDZ K., CZAJKA R., Cryst. Res. Technol., 36 (2001), 1019.
- [4] SMARDZ L., J. All. Comp., 395 (2005), 17.
- [5] HERZER G., J. Magn. Magn. Mater., 157/158 (1996), 133.
- [6] STOBIECKI T., KOPCEWICZ M., CASTAÑO F. J., Chaos, Solitons and Fractals, 10 (1999), 2031.
- [7] SMARDZ K., SMARDZ L., JURCZYK M., JANKOWSKA E., Phys. Stat. Sol. A, 196 (2003), 263.
- [8] BOUTEN P. C., MIEDEMA A. R., J. Less Common Metals, 71 (1980), 147.
- [9] GRIESSEN R., Phys. Rev., B38 (1988), 3690.
- [10] SMARDZ L., SMARDZ K., NOWAK M., JURCZYK M., Cryst. Res. Technol., 36 (2001), 1385.
- [11] SMARDZ L., SMARDZ K., Mol. Phys. Rep., 40 (2004), 137.
- [12] BRIGGS D., [in:] *Handbook of X-ray and Ultraviolet Photoelectron Spectroscopy*, D. Briggs (Ed.), Heyden and Son Ltd., London, 1977, p. 153 and references therein.

Received 1 June 2005
Revised 10 October 2005

Ni₈₀Fe₂₀/Au/Co/Au multilayers as magnetic field sensors

F. STOBIECKI*, M. URBANIAK, B. SZYMAŃSKI,
T. LUCIŃSKI, M. SCHMIDT, J. ALEKSIEJEW

Institute of Molecular Physics, Polish Academy of Sciences, 60-179 Poznań, Poland

Sputter-deposited (Ni₈₀Fe₂₀/Au/Co/Au)_N multilayers characterized by alternating easy-plane (Permalloy) and perpendicular (cobalt) anisotropy were investigated. Such films can be used as giant magnetoresistance (GMR) sensors with linear $R(H)$ dependences in a broad range of magnetic fields. The influence of the thicknesses of the NiFe, Au and Co layers, and of the repetition number N on the GMR effect is discussed. We have optimised the multilayer parameters for application purposes.

Key words: *magnetic multilayers; alternating anisotropy; GMR sensors*

1. Introduction

Magnetic field sensors based on the giant magnetoresistance effect (GMR) are widely used in computer hard drives as reading heads. This application requires large changes of electrical resistance $\Delta R/R$ with small changes of the magnetic field H . Magnetic field measurements in industrial applications, on the other hand, often require sensors capable of measuring fields of up to several kOe. Magnetoresistive sensors used for such applications should exhibit linear $R(H)$ characteristics in a broad field range as well as high values of $\Delta R/R$. It has been previously shown [1, 2] that these requirements are fulfilled in layered structures of the $F_{\parallel}/S/F_{\perp}$ type, where F_{\parallel} and F_{\perp} are ferromagnetic layers with in-plane and perpendicular anisotropy, respectively. F_{\parallel} and F_{\perp} are separated by a nonmagnetic metallic spacer S . In this new kind of GMR-based spin valves (SV), the external magnetic field H perpendicular to the layer rotates the magnetization of the F_{\parallel} layer and leaves the magnetization of the F_{\perp} layer unchanged. If we neglect anisotropic magnetoresistance (AMR), the $R(H)$ dependence can be expressed as $R(\varphi) = R_p + (R_{AP} - R_p)(1 - \cos\varphi)/2$, where R_p and R_{AP} are the electrical resistances of the system with parallel and antiparallel magnetization configurations, respectively, and φ is the angle between the magnetizations of the ferromagnetic

*Corresponding author, e-mail: sfeliks@ifmpan.poznan.pl

layers. For $F_{\parallel}/S/F_{\perp}$ structures with no coupling between ferromagnetic layers, changes in $\cos\phi(H)$ are related only to the rotation of magnetization in F_{\parallel} layers and can be described by: $\cos(H_{\perp}) \propto H_{\perp}$ for $|H| < H_S$. This assures a linear $R(H_{\perp})$ dependence.

Spin valves reported by Mancoff [1] used a magnetically hard Pt/Co/Pt/Pd multilayer ($H_C = 5$ kOe) as F_{\perp} . As a result, the magnetoresistance $R(H_{\perp})$ was an odd function and linear for H_{\perp} in the ± 5 kOe range. These valves, however, exhibit a small change in resistance of $\Delta R/R = 1.5\%$ and a hysteresis of $R(H_{\perp})$ for $H_{\perp} > H_C$.

We propose multilayer sensors with the $(\text{Ni}_{80}\text{Fe}_{20}/\text{Au}/\text{Co}/\text{Au})_N$ structure, where N is the number of repetitions, $F_{\perp} = \text{Co}$ (Co layers with thickness $t_{\text{Co}} < 1.2$ nm sandwiched between Au have perpendicular anisotropy), and $F_{\parallel} = \text{Ni}_{80}\text{Fe}_{20}$ (Permalloy). Such structures display high changes of resistance ($\Delta R/R = 9\%$ at room temperature) and linear, non-hysteretic $R(H)$ characteristics even in H for the $H_S^{\text{Co}} < |H_{\perp}| < H_S^{\text{NiFe}}$ field range. H_S^{Co} and H_S^{NiFe} are the saturation fields (in perpendicular configurations) of the Co and NiFe layers respectively. It is worth noting that it is possible to obtain an odd dependence for $R(H)$ by applying a bias field [3].

In this paper, we discuss the influence of the thicknesses of constituent layers of the NiFe/Au/Co/Au multilayer sensor on its properties, important from the application point of view.

2. Experimental

$(\text{Ni}_{80}\text{Fe}_{20}/\text{Au}/\text{Co}/\text{Au})_N$ multilayers (MLs) were deposited on Si(100) wafers using UHV magnetron sputtering [2, 4]. The periodic structure of MLs was controlled using LAXRD. Magnetoresistance (four-point measurements with current in the plane configuration) and magnetization reversal (vibrating sample magnetometer – VSM) were studied at room temperature for a magnetic field applied perpendicular to the sample plane ($|H_{\perp}| \leq 2$ T) (from this point we will refer to H_{\perp} simply as H). The $\Delta R/R(H)$ dependence was calculated using the formula

$$\frac{\Delta R}{R}(H) = \frac{R(H) - R(H = 2 \text{ T})}{R(H = 2 \text{ T})} \times 100\%$$

where $\Delta R/R$ denotes the maximum value determined from the $\Delta R/R(H)$ dependence.

3. Results and discussion

Figure 1 shows the magnetization reversal $M(H)$ and the magnetoresistance $R(H)$ curves typical of the $(\text{Ni}_{80}\text{Fe}_{20}/\text{Au}/\text{Co}/\text{Au})_N$ system. There are three distinctive field ranges in the magnetization curves: (i) $|H| > H_S^{\text{NiFe}} = 0.6 \text{ T} = 4\pi M_S^{\text{NiFe}}$, corresponding to a parallel magnetization configuration of Co and $\text{Ni}_{80}\text{Fe}_{20}$ layers, (ii) H_N^{Co}

(H_S^{Co}) < $|H|$ < H_S^{NiFe} (H_N^{Co} and H_S^{Co} are the domain nucleation and annihilation fields of Co, respectively), which is related to the coherent rotation of magnetization in Ni₈₀Fe₂₀ layers, and (iii) $|H|$ < H_N^{Co} (H_S^{Co}), related mainly to magnetization reversal in Co layers. Magnetic structure in the third range is dominated by strong ferromagnetic dipolar magnetostatic coupling (caused by a dense stripe domain structure) between NiFe and Co layers [5]. From the application point of view, the second field range, in which for H_S^{Co} < $|H|$ < H_S^{NiFe} a linear and non-hysteretic $R(H)$ dependence can be obtained, is the most interesting.

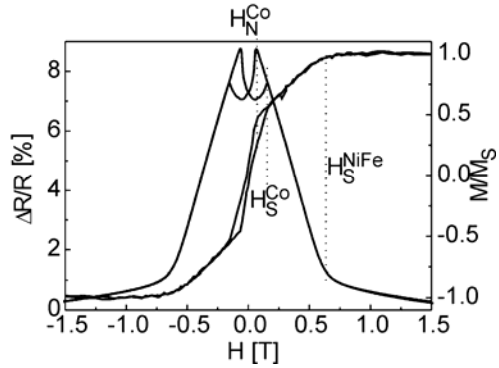


Fig. 1. Magnetoresistance and hysteresis loop of the (NiFe 2 nm/Au 1.5 nm/Co 0.6 nm/Au 1.5 nm)₁₅ multilayer, measured with the magnetic field applied perpendicular to the sample surface. The characteristic magnetic fields H_N^{Co} , H_S^{Co} , and H_S^{NiFe} denote the nucleation, annihilation (saturation) of stripe domains of Co layers, and saturation of Permalloy layers, respectively

The magnetization reversal and magnetoresistance of our structures are influenced by coupling between ferromagnetic layers and their magnetic properties (mainly anisotropy). This behaviour is similar to other SVs [6]. In order to determine the influence of Au, Co, and NiFe layer thickness on the magnetoresistive properties of (Ni₈₀Fe₂₀/Au/Co/Au)_N MLs, we investigated three series of samples:

- (Ni₈₀Fe₂₀ 2 nm/Au t_{Au} /Co 0.6 nm/Au t_{Au})₁₅ ($0.5 \leq t_{Au} \leq 3$ nm),
- (Ni₈₀Fe₂₀ 2 nm/Au 3 nm/Co t_{Co} /Au 3 nm)₁₅ ($0.2 \leq t_{Co} \leq 1.5$ nm),
- (Ni₈₀Fe₂₀ t_{NiFe} /Au 2 nm/Co 0.6 nm/Au 2 nm)₁₅ ($1 \leq t_{NiFe} \leq 4$ nm).

The dependence of $\Delta R/R$ on t_{Au} (Fig. 2a) is related to changes in effective coupling. The $H_S^{Co}(t_{Au})$ dependence, with a kink at $t_{Au} \approx 1.5$ nm, suggests that two different mechanisms are responsible for the observed changes in interlayer coupling. The first one is the relatively weak magnetostatic coupling (Néel's coupling), important in the whole range of t_{Au} . The second one, dominating for $t_{Au} < 1.5$ nm, is much stronger and probably originates from pinholes. The role of relatively weak ($t_{Au} > 1.5$ nm) RKKY-like coupling can be neglected. As a consequence of such changes in coupling, a strong degradation of GMR for $t_{Au} < 1.5$ nm is observed. The slow decrease of the magnetoresistance $\Delta R/R(t_{Au})$ for $t_{Au} > 1.5$ nm can be attributed to the shunting effect [7].

The $\Delta R/R(t_{Co})$ dependence (Fig. 2b) exhibits a maximum at $t_{Co} = 0.6$ nm, which corresponds to the transition from a discontinuous to continuous Co layer. In the $0.6 < t_{Co} < 1.2$ nm range, magnetoresistance decreases slowly. This change can be attrib-

uted to the diminishing influence of interface spin scattering compared to that within the Co layer [8]. The sudden drop in magnetoresistance at $t_{Co} > 1.2$ nm is related to the transition from perpendicular to in-plane anisotropy in Co layers. The monotonic increase of H_S^{Co} with t_{Co} is typical of ferromagnetic layers with stripe domains [9].

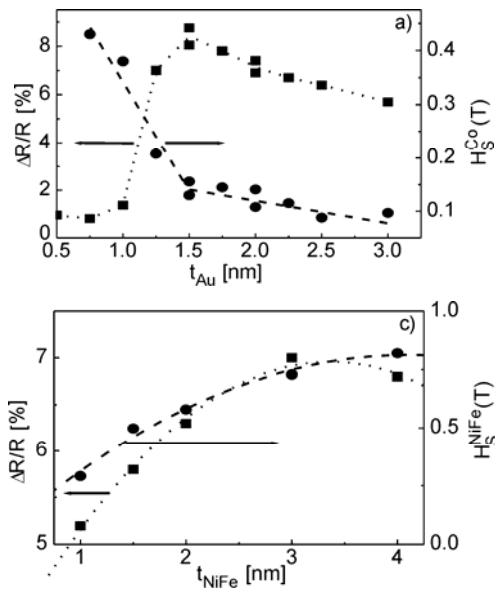


Fig. 2. Changes in magnetoresistance as functions of t_{Au} , t_{Co} , and t_{NiFe} determined for (NiFe 2 nm/Au t_{Au} /Co 0.6 nm/Au t_{Au})₁₅ (a), (NiFe 2 nm/Au 3 nm/Co t_{Co} /Au 1.5 nm)₁₅ (b), and (NiFe t_{NiFe} /Au 2 nm/Co 0.6 nm/Au 2 nm)₁₅ (c) MLs, respectively. The saturation fields of Co layers (H_S^{Co}) and Permalloy (H_S^{NiFe}) are also plotted in panels a, b and c, respectively

Magnetoresistance as a function of Permalloy layer thickness (Fig. 2c) exhibits a maximum at much higher values ($t_{NiFe} \approx 3$ nm) than that observed for Co. This can be explained by the predominant contribution of volume spin scattering in Ni₈₀Fe₂₀ to the magnetoresistance effect [8].

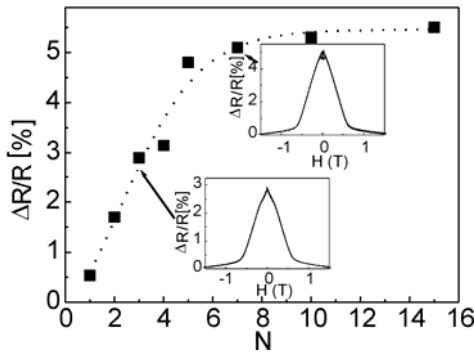


Fig. 3. The magnetoresistance of (NiFe 2 nm/Au 3 nm/Co 0.8 nm/Au 3 nm)_{*N*} MLs vs. repetition number N . The insets show the field dependences of resistance for MLs with $N = 3$ and $N = 7$

The increase of H_S^{NiFe} with t_{NiFe} is similar to that observed for NiFe/Cu multilayers [10] and in the first approximation can be interpreted as a result of a magnetically inactive NiFe/Au interface layer. The strong $H_S^{NiFe}(t_{NiFe})$ dependence observed for

small values of t_{NiFe} offers a simple way of tailoring the saturation fields of $\Delta R/R(H)$ in our structures. Larger values of t_{NiFe} , however, lead to an increase of the anisotropic magnetoresistance effect (AMR) and deteriorates the linearity of $R(H)$.

Our investigation proved that (NiFe/Au/Co/Au)₁₅ MLs with $1.5 \leq t_{\text{Au}} \leq 0.8$ nm, $0.6 \leq t_{\text{Co}} \leq 0.8$ nm, and $2 \leq t_{\text{NiFe}} \leq 3$ nm can be used as sensors with linear $R(H)$ characteristics in a broad field range and for relatively large $\Delta R/R$.

The number of repetitions, N , is the next parameter that greatly influences the magnetoresistance of layered structures (Fig. 3). The increase of $\Delta R/R$ with N is mainly the result of the diminishing role of electron scattering at the sample surfaces. We believe that low magnetoresistance for low N is most likely caused by imperfections in the first period and subsequent lack of perpendicular anisotropy in Co. This interpretation is corroborated by the low $\Delta R/R$ value (0.5%) observed for $N = 1$ and the distinct kink in $\Delta R/R(H)$ for $N = 3$. For $N \geq 7$, the dependence of $\Delta R/R(H)$ saturates and the influence of the first layer becomes negligible.

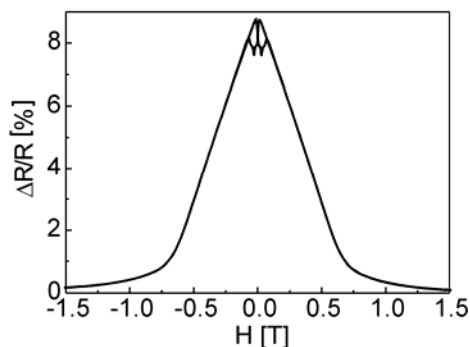


Fig. 4. The magnetoresistance of (Co 3.2 nm/Au 2 nm/Co 0.8 nm/Au 2 nm)₃ MLs deposited on a Si(100) substrate with a (Au 2 nm/Si 1 nm)₃ buffer layer

In order to increase GMR, the NiFe layers were replaced by 3.2 nm thick Co layer. Cobalt displays a higher spin polarization than NiFe, and for that t_{Co} the effective anisotropy is in-plane and the saturation field $H_s^{\text{Co}}(3.2 \text{ nm}) \approx 0.7$ T. In (Co 3.2 nm/Au 2 nm/Co 0.8 nm/Au 2 nm)₃ structures deposited on high-resistance (Au 2 nm/Si 1 nm)₃ buffer layers, the $\Delta R/R(H)$ dependences (Fig. 4) are similar to those observed for (NiFe/Au/Co/Au) MLs with $N > 7$ (Fig. 1). The low total thickness of MLs ($N = 3$) results in high R/\square (sheet resistance), which is very desirable for sensor applications.

4. Conclusions

We have studied the magnetoresistance of (Ni₈₀Fe₂₀/Au/Co/Au)_N multilayers as functions of the repetition number and Ni₈₀Fe₂₀, Au, and Co thickness. We have identified a set of parameters for which the $R(H)$ dependence is linear and non-hysteretic in the range $0.2 \leq |H| \leq 0.6$ T and displays $\Delta R/R \approx 6\%$ at RT. For structures in which Ni₈₀Fe₂₀ layers were replaced by 3.2 nm thick Co, a broader range of linearity

($0.1 \leq |H| \leq 0.6$ T) and higher GMR values ($\Delta R/R \approx 6.5\%$) were observed. The presented structures are promising candidates for magnetic field sensors.

Acknowledgements

Supported by the State Committee for Scientific Research with Grant 3 T08A 03127 and by the Center of Excellence for Magnetic and Molecular Materials for Future Electronics within EC Contract G5MA-CT-2002-04049.

References

- [1] MANCOFF F.B., HUNTER DUNN J., CLEMENS B.M., WHITE R.L., *Appl. Phys. Lett.*, 77 (2000), 1879.
- [2] STOBIECKI F., SZYMAŃSKI B., LUCIŃSKI T., DUBOWIK J., URBANIAK M., SCHMIDT M., RÖLL K., *J. Magn. Magn. Mater.*, 272–276 (2004), e1751.
- [3] HILL E.W., NOR A.F., BIRTWISTLE J.K., PARKER M.R., *Sensors Act. A*, 59 (1997), 30.
- [4] STOBIECKI F., SZYMAŃSKI B., LUCIŃSKI T., DUBOWIK J., URBANIAK M., RÖLL K., *J. Magn. Magn. Mater.*, 282 (2004), 32.
- [5] URBANIAK M., STOBIECKI F., SZYMAŃSKI B., *Phys. Stat. Sol. A*, 202 (2005), 2013.
- [6] RIJKS T.G.S.M., COEHOORN R., DAEMEN J.T.F., DE JONGE W.J.M., *J. Appl. Phys.*, 76 (1994), 1092.
- [7] MATHON J., [in:] *Spin Electronics*, M. Ziese, M.J. Thornton (Eds.), Springer-Verlag, Berlin, 2001.
- [8] DIENY B., *J. Magn. Magn. Mater.*, 136 (1994), 335.
- [9] HUBERT A., SCHÄFER R., *Magnetic Domains*, Springer-Verlag, Berlin, 1998.
- [10] LUCIŃSKI T., STOBIECKI F., ELEFANT D., ECKERT D., REISS G., SZYMAŃSKI B., DUBOWIK J., SCHMIDT M., ROHRMANN H., RÖLL K., *J. Magn. Magn. Mater.*, 174 (1997), 192.

Received 1 June 2005
Revised 10 October 2005

Calculated magnetic moments and electronic structures of the compounds $R_{n+1}Co_{3n+5}B_{2n}$, $R = Gd, Tb$, $n = 0, 1, 2, 3$, and ∞

A. SZAJEK, J. A. MORKOWSKI*

Institute of Molecular Physics, Polish Academy of Sciences,
M. Smoluchowskiego 17, 60-179 Poznań, Poland

The compounds of the $R_{n+1}Co_{3n+5}B_{2n}$ family crystallize in a hexagonal structure with the $P6/mmm$ space group. *Ab initio* spin-polarized band structure calculations have been performed based on the tight-binding linear muffin-tin orbitals method (TB LMTO) for the following five representatives: RCO_5 , RCO_4B , $R_3CO_{11}B_4$, $R_2CO_7B_3$, and RCO_3B_2 , where $R = Gd$ or Tb . The cobalt atoms in these compounds occupy distinct sites having different types and numbers of neighbouring atoms, and as a consequence their magnetic moments are different. The calculated values are compared with bulk measurements.

Key words: rare earth compounds; electronic structure; magnetic moments

1. Introduction

Lanthanide compounds $R_{n+1}Co_{3n+5}B_{2n}$ are interesting as they allow systematic studies of the dependence of magnetic moments on local environment, not to mention their relevance to the search for high performance permanent magnets. The compounds crystallize in a hexagonal $CaCu_5$ -type structure, belonging to the $P6/mmm$ space group. Their structure is generated from RCO_5 ($n = 0$) by replacing Co atoms by B atoms, until saturation ($n = \infty$) is reached in RCO_3B_2 [1]. Systematic studies of electronic structure have been performed for the series $Y_{n+1}Co_{3n+5}B_{2n}$ [2–4]. Some calculations have been done for the representatives of the Gd series [5–11]. In the present paper, the results of systematic studies of the band structure for $R = Gd$ and Tb are given.

*Corresponding author, e-mail: jmorkows@ifmpan.poznan.pl

2. Computational details

Band structures and magnetic moments were calculated using the spin-polarized tight-binding linear muffin-tin orbital (TB LMTO) method in the atomic sphere approximation (ASA) [12, 13]. The overlap volumes of the muffin-tin spheres for both structures are in the range 7.7–8.7%. The standard [12] combined corrections for overlapping were used to compensate for errors due to the ASA. Spin-orbit interactions were taken into account in the form proposed by Min and Jang [14]. The Perdew–Wang [15] exchange-correlation potential with non-local corrections was used. The input electronic configurations were taken as: core(Xe + 4f⁷) + 5d¹6s² for Gd, core(Xe + 4f⁸) + 5d¹6s² for Tb, core(Ar) + 3d⁷4s² for Co, and core(He) + 2s²2p¹ for the B atom. Due to difficulties related to the band structure treatment of the localized 4f electrons of rare-earth metals and the itinerant magnetism of spd conduction electrons, the scheme proposed by Brooks et al. [16] was used. In this approach, the 4f states of Gd and Tb are treated as open core states that do not hybridise with conduction electron states. The number of 4f electrons of Gd was fixed to seven and to eight for Tb, and experimental values of lattice constants [1] were used in the calculations. Self-consistent calculations were carried out for 259 *k*-points in the irreducible wedge (1/24) of the Brillouin zone. For integration over the Brillouin zone, the tetrahedron method was used [17]. Iterations were repeated until the total energies of the consecutive iteration steps were the same within an error of 0.01 mRy.

3. Results

The results of the band structure calculations are summarized in Fig. 1 as the total densities of electronic states for up and down spins. The shift of the up valence band with respect to the down band is an indication of the ferromagnetic ground state of the studied compounds. The shift is the largest for $n = 0$ (i.e., for RCo₅), decreases for increasing n , and at $n = \infty$ (i.e. for RCo₃B₂) is quite small.

The calculated saturation magnetic moments are collected in Table 1. The large moments on Gd and Tb obviously come from the core 4f states. The calculated moments, however, are higher than the values from Hund's rule for the free ions Gd³⁺ and Tb³⁺ – 7μ_B and 9μ_B, respectively. A plausible explanation of this difference can be the contribution of the valence d-electrons of Gd or Tb. The magnetic moments on Co atoms are sensitive to the number of cobalt ions in the local environment and vary from ~1.8μ_B to ~0.1μ_B. As is typical of rare earth compounds with transition metals, the calculated magnetic moments on Gd and Tb are antiparallel to the ones on Co. For the Tb compounds, the calculated magnetic moments can be compared with experimental data available from neutron scattering [18], quoted (in the 5th and 10th columns) in Table 1. Except for $n = 3$, at least qualitative agreement with measurements [18] can be claimed.

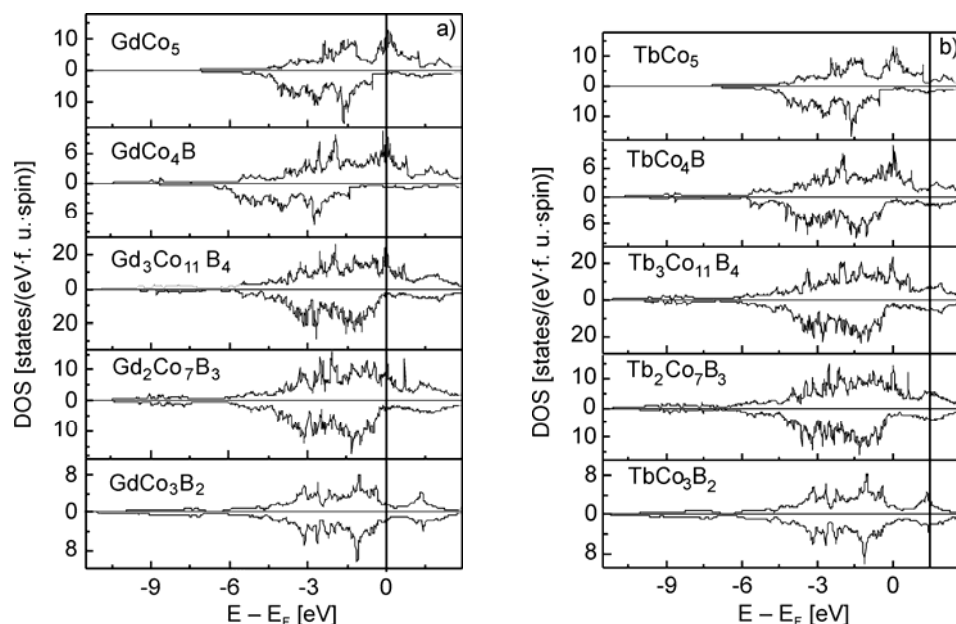


Fig. 1. The densities of states (DOS) of RCo_5 , RCo_4B , $R_3Co_{11}B_4$, $R_2Co_7B_3$, and RCo_3B_2 compounds, where $R = Gd$ (a) or Tb (b)

Table 1. The calculated and measured [18] local magnetic moments of $R_{n+1}Co_{3n+5}B_{2n}$ compounds, where $n = 0, 1, 2, 3$, and ∞ , and $R = Gd$ or Tb . For $n = 3$, only the “raw” data from [18] are quoted, not the ones from a specific refinement procedure

Compound	Atoms	m [μ_B /atom]			Compound	Atoms	m [μ_B /atom]		
		R = Gd	R = Tb	R = Tb [4]			R = Gd	R = Tb	R = Tb [4]
$n = 0$ RCo_5	R (1a)	-7.580	-9.530	-8.35(55)	$n = 3$ $R_2Co_7B_3$	R (1a)	-7.457	-9.423	-11(4)
	Co (2c)	1.514	1.575	1.55(20)		R (1b)	-7.236	-9.219	-6(3)
	Co (3g)	1.517	1.519	1.7(1)		R (2e)	-7.366	-9.309	-10(3)
$n = 1$ RCo_4B	R (1a)	-7.442	-9.394	-7(1)	Co (2c)	1.776	1.760	-0.5(10)	
	R (1b)	-7.556	-9.508	-7.3(7)	Co (6i ₁)	0.795	0.744	1.6(7)	
	Co (2c)	1.521	1.619	1.6(3)	Co (6i ₂)	0.164	0.184	-0.4(8)	
	Co (6i)	0.778	0.863	0.6(1)	B (2d)	-0.014	-0.016	0	
$n = 2$ $R_3Co_{11}B_4$	B (2d)	-0.048	-0.056	0	B (4h)	-0.034	-0.031	0	
	R (1a)	-7.500	-9.439	-8.5(7)	$n = \infty$ RCo_3B_2	R (1a)	-7.227	-9.183	-5.4(2)
	R (2e)	-7.377	-9.349	-7.9(7)		Co (2c)	0.106	0.086	-0.13(7)
	Co (2c)	1.648	1.749	1.3(5)		B (3g)	-0.005	-0.003	0
Co (3g)	0.171	0.126	0.5(4)						
	Co (6i)	0.792	0.787	0.5(2)					
	B (4h)	-0.035	-0.032	0					

The densities of states at the Fermi level are predominantly due to d-electrons, as is evident from Table 2.

Table 2. Spin projected (\uparrow , \downarrow) densities of electronic states at the Fermi energy, DOS (E_F) in states/(eV \times spin formula unit). The numbers in parentheses are the partial contributions from d-electrons, DOS_d(E_F)

Compound	R = Gd		R = Tb	
	\uparrow	\downarrow	\uparrow	\downarrow
RCo ₅	13.98 (13.63)	1.14 (1.10)	11.95 (11.57)	1.22 (0.76)
RCo ₄ B	3.38 (3.24)	0.46 (0.34)	3.53 (3.40)	0.52 (0.38)
R ₃ Co ₁₁ B ₄	22.82 (21.76)	2.66 (2.04)	20.53 (19.53)	2.53 (1.96)
R ₂ Co ₇ B ₃	5.05 (4.73)	1.09 (0.84)	5.90 (5.50)	1.32 (1.06)
RCo ₃ B ₂	1.86 (1.59)	1.76 (1.39)	1.84 (1.84)	1.70 (1.38)

The following conclusions can be drawn from the calculations: the magnetic moments on Gd and Tb are antiparallel to Co moments, the moments on Co are sensitive to the type of the crystallographic site, i.e. to the symmetry of the environment, the band structure near the Fermi energy is dominated by d-electrons.

References

- [1] KUZ'MA Y.B., BILONIZHKO N.S., *Kristallografia*, 18 (1973), 710.
- [2] SZAJEK A., *J. Magn. Magn. Mater.*, 185 (1998), 322.
- [3] KITAGAWA I., SUZUKI N., *J. Magn. Magn. Mater.*, 177–181 (1998), 1357.
- [4] YAMADA H., TERAOKA K., NAKAZAWA H., KITAGAWA I., SUZUKI N., IDO H., *J. Magn. Magn. Mater.*, 183 (1998), 94.
- [5] KOWALCZYK A., JEZERSKI A., *J. Magn. Magn. Mater.*, 182 (1998), 137.
- [6] JEZERSKI A., KOWALCZYK A., MAEHL S., NEUMANN M., BORSTEL G., *J. Phys. Cond. Matter*, 10 (1998), 6277.
- [7] KOWALCZYK A., JEZERSKI A., *J. Magn. Magn. Mater.*, 188 (1998), 361.
- [8] KOWALCZYK A., SMARDZ L., JEZERSKI A., BASZYŃSKI J., KOVAČ J., *Acta Phys. Slov.*, 48 (1998), 619.
- [9] KOWALCZYK A., SMARDZ L., JEZERSKI A., *J. Magn. Magn. Mater.*, 190 (1998), 205.
- [10] KOWALCZYK A., CHELKOWSKA G., SZAJEK A., *Solid State Commun.*, 120 (2001), 407.
- [11] SZAJEK A., MALINOWSKI W.L., *Acta Phys. Polon. A*, 101 (2002), 525.
- [12] ANDERSEN O.K., JEPSEN O., ŠOB M., [in:] M.S. Yussouff (Ed.), *Electronic Structure and Its Applications*, Springer-Verlag, Berlin, 1987, p. 2.
- [13] KRIER G., JEPSEN O., BURKHARDT A., ANDERSEN O.K., The TB-LMTO-ASA program, source code, version 4.7, available upon request from the authors of the program.
- [14] MIN B.I., JANG Y.-R., *J. Phys.: Cond. Matter*, 3 (1991), 5131.
- [15] PERDEW J.P., CHEVARY J.A., VOSKO S.H., JACKSON K.A., PEDERSON M.R., SINGH D.J., FIOLETTI C., *Phys. Rev. B*, 46 (1992), 6671.
- [16] BROOKS M.S.S., NORDSTROM L., JOHANSSON B., *Physica B*, 172 (1991), 95.
- [17] BLÖCHL P., JEPSEN O., ANDERSEN O.K., *Phys. Rev. B*, 49 (1994), 16223.
- [18] CASPI E.N., PINTO H., MELAMUD M., *J. Appl. Phys.*, 87 (2000), 416.

Received 1 June 2005
Revised 10 October 2005

Electronic and magnetic properties of $\text{Nd}_5\text{Co}_{19}\text{B}_6$ and $\text{Nd}_5\text{Co}_{21}\text{B}_4$

A. SZAJEK *

Institute of Molecular Physics, Polish Academy of Sciences,
ul. Smoluchowskiego 17, 60-179 Poznań, Poland

The compounds $\text{Nd}_5\text{Co}_{19}\text{B}_6$ and $\text{Nd}_5\text{Co}_{21}\text{B}_4$ were manufactured as promising systems suitable for the fabrication of permanent magnets. They belong to the $\text{R}_{m+n}\text{Co}_{5m+3n}\text{B}_{2n}$ family and have the $P6/mmm$ space group. Band structure calculations are performed by the tight binding version of the linear muffin-tin orbital method in the atomic sphere approximation (TB-LMTO ASA). The calculated magnetic moments on Co atoms depend on their local environment. The calculated values are compared with bulk measurements.

Key words: *rare earth compounds; electronic structure; magnetic moment*

1. Introduction

Boron substitution for Co in RCo_5 Haucke compounds (R = rare earth element) leads to the formation of a series of systems expressed by the general formula $\text{R}_{1+n}\text{Co}_{5+3n}\text{B}_{2n}$, $n = 0, 1, 2, \dots, \infty$ [1]. Unit cells of these systems have an interesting crystallographic regularity (see Fig. 1 in [2]); they are formed by the alternate stacking of one layer of RCo_5 and n layers of RCo_3B_2 . A partial substitution of Co atoms by boron in the $\text{R}_{1+n}\text{Co}_{5+3n}\text{B}_{2n}$ system causes a decrease in the Curie temperature (T_C), saturation magnetization (M_S), and effective inter-sublattice exchange interaction ([3] and references therein). Although the systems have uniaxial symmetry, their T_C and M_S are too low to be suitable for permanent magnet applications [4–6]. In order to overcome this drawback, a new series of compounds, $\text{R}_{m+1}\text{Co}_{5m+3}\text{B}_2$, with high Co content, was proposed [7–9]. The above-mentioned two homologous series can be expressed by the general formula $\text{R}_{m+n}\text{Co}_{5m+3n}\text{B}_{2n}$.

It has been shown that the magnetic moments of Co atoms depend on their local environment in $\text{R}_{1+n}\text{Co}_{5+3n}\text{B}_{2n}$. This observation was confirmed by *ab initio* calculations [2, 10–12] as well as by neutron diffraction measurements [13, 14]. In this pa-

* E-mail: szajek@ifmpan.poznan.pl

per, a study of the electronic structure of hexagonal $\text{Nd}_5\text{Co}_{19}\text{B}_6$ and $\text{Nd}_5\text{Co}_{21}\text{B}_4$ systems is presented.

2. Method of calculations and results

The electronic structures and magnetic moments were calculated using the spin-polarized tight-binding linear muffin-tin orbital (TB LMTO) method in the atomic sphere approximation (ASA) [15, 16], where the unit cell is filled by Wigner–Seitz spheres with the same total volumes

$$\frac{4\pi}{3} \sum_{j=1}^{N_A} S_j^3 = V$$

where j is the index of the atom in the unit cell, N_A is number of atoms in the cell, S_j is the Wigner–Seitz radius of the j -type atom, and V is the volume of the unit cell. In our case, the unit cells contain one formula unit each ($N_A = 30$ for $\text{Nd}_5\text{Co}_{19}\text{B}_6$ and $\text{Nd}_5\text{Co}_{21}\text{B}_4$). The structures of the unit cells of the considered compounds are presented in Fig. 1.

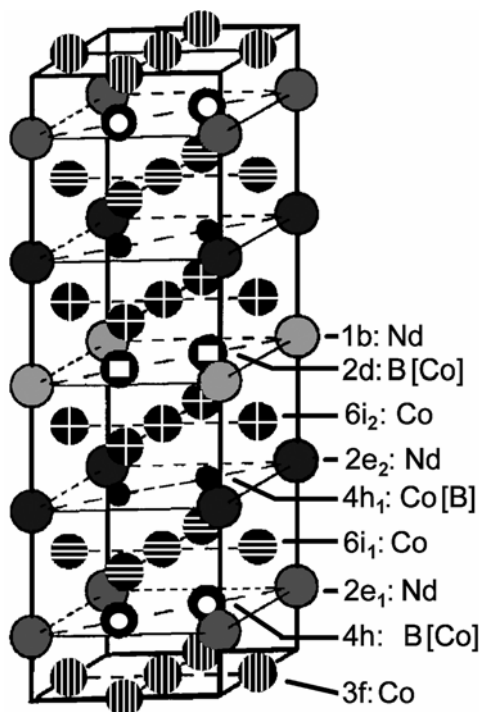


Fig. 1. Crystal structure of $\text{Nd}_5\text{Co}_{19}\text{B}_6$ [$\text{Nd}_5\text{Co}_{21}\text{B}_4$]

The overlap volumes of the muffin-tin spheres for both structures are about 7.3%. The standard combined corrections [15] for overlapping were used to compensate for errors due to the ASA. The experimental values of the lattice constants [8, 9] were used in the calculations. Spin-orbit interactions were taken into account in the form proposed by Min and Jang [17]. The Perdew–Wang [18] potential with non-local corrections was used. The input electronic configurations were taken as: core (Xe+4f³) + 5d¹6s² for Nd, core(Ar) + 3d⁷4s² for Co, and core(He) + 2s²2p¹ for B atom. Due to difficulties with the band structure treatment of the localized 4f electrons of rare-earth metal and the itinerant magnetism of spd conduction electrons, the scheme proposed by Brooks et al. [19] was used.

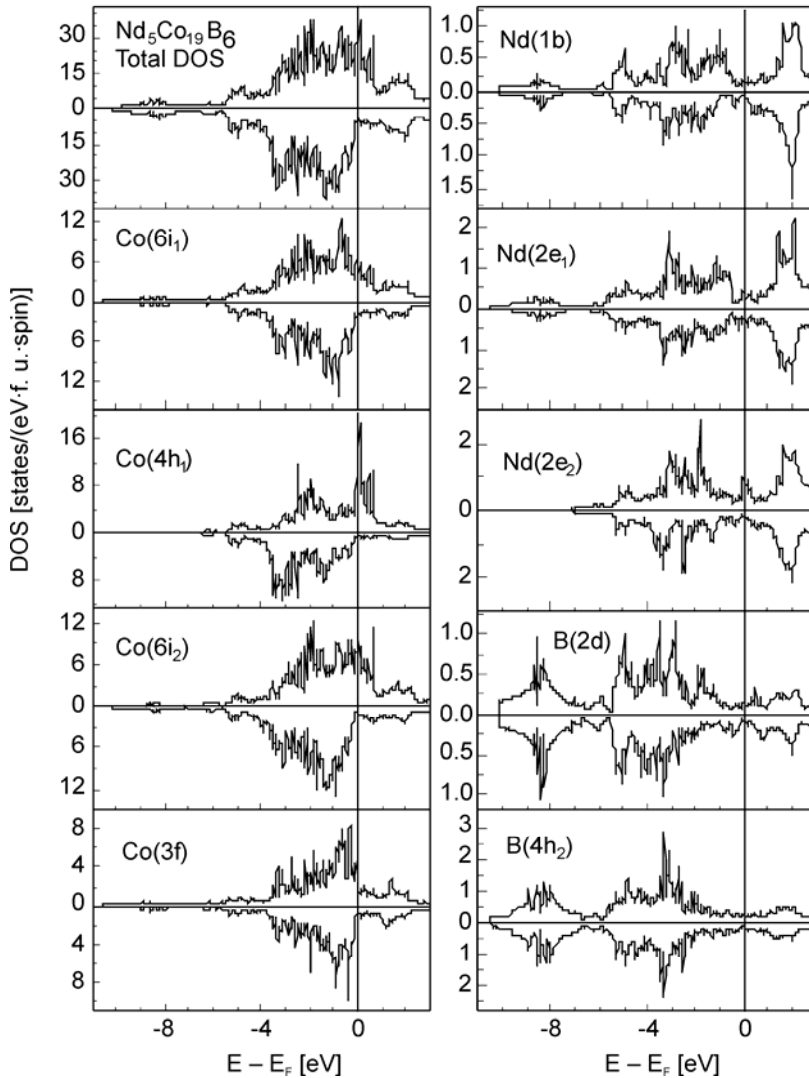


Fig. 2. Total and local DOS functions for the Nd, Co, and B atoms of $Nd_5Co_{19}B_6$

In this approach, the 4f states of Nd are treated as open core states that do not hybridise with conduction electron states. The number of 4f electrons in Nd was fixed to three. Self-consistent calculations were carried out for 259 k -points in the irreducible wedge (1/24) of the Brillouin zone. The tetrahedron method was used to integrate over the Brillouin zone [20]. Iterations were repeated until the total energies of the consecutive iteration steps were the same within an error of 0.01 mRy.

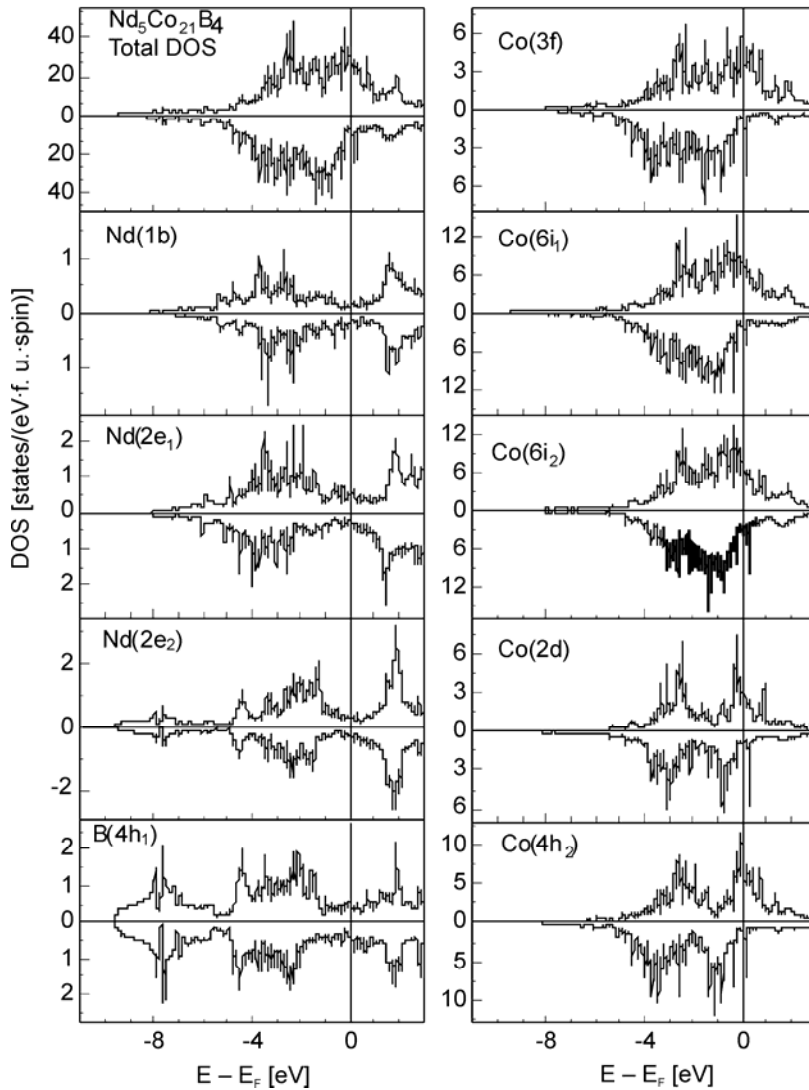


Fig. 3. Total and local DOS functions for the Nd, Co, and B atoms of $\text{Nd}_5\text{Co}_{21}\text{B}_4$

The densities of states (DOS) are presented in Fig. 2 for $\text{Nd}_5\text{Co}_{19}\text{B}_6$ and in Fig. 3 for $\text{Nd}_5\text{Co}_{21}\text{B}_4$. In both cases, the widths of the valence bands are similar. The bottoms

of the valence bands are formed foremost by s-type electrons, localized mainly on B atoms and their neighbours: (1b), (2e₂) for Nd and (6i₁), (6i₂) for Co in $\text{Nd}_5\text{Co}_{21}\text{B}_4$, and (1b), (2e₁) for Nd and (6i₁), (6i₂), (3f) for Co in $\text{Nd}_5\text{Co}_{19}\text{B}_6$. The rest of the atoms provide essential contributions to the DOS above 3.5 eV from the bottom of the valence band. The main contribution to the DOS at the Fermi level (E_F) is provided by Co atoms, especially d-type electrons localized close to the E_F (above 90% of the contributions to the total DOS on Co atoms, see Table I). The values of the total DOS at the Fermi level are 36.60 and 5.00 states/(eV·spin·f. u.) for $\text{Nd}_5\text{Co}_{19}\text{B}_6$ with spin up and down, respectively. The corresponding values for $\text{Nd}_5\text{Co}_{21}\text{B}_4$ are: 27.58 and 7.69 states/(eV·spin·f. u.).

Table 1. Spin projected (\uparrow , \downarrow) densities of electronic states (DOS [states/(eV·spin·f. u.)]) at the Fermi level and calculated local magnetic moments (m [μ_B /atom]) for $\text{Nd}_5\text{Co}_{19}\text{B}_6$ and $\text{Nd}_5\text{Co}_{21}\text{B}_4$

Compound	Atoms	DOS \uparrow	DOS \downarrow	m	Compound	Atoms	DOS \uparrow	DOS \downarrow	m
$\text{Nd}_5\text{Co}_{19}\text{B}_6$	Nd(1b)	0.152	0.070	2.92	$\text{Nd}_5\text{Co}_{21}\text{B}_4$	Nd(1b)	0.189	0.212	2.98
	Nd(2e ₁)	0.550	0.279	3.07		Nd(2e ₁)	0.431	0.333	2.84
	Nd(2e ₂)	0.901	0.184	2.98		Nd(2e ₂)	0.287	0.321	2.93
	Co(6i ₁)	5.288	1.702	0.40		Co(6i ₁)	7.198	1.613	0.88
	Co(6i ₂)	9.468	0.908	0.80		Co(6i ₂)	6.303	2.632	0.46
	Co(4h ₁)	16.647	0.651	1.65		Co(4h ₂)	5.488	0.827	1.18
	Co(3f)	3.180	0.956	0.21		Co(3f)	4.379	0.570	0.63
	B(2d)	0.177	0.078	-0.05		Co(2d)	2.877	0.765	1.17
	B(4h ₂)	0.235	0.175	-0.02		B(4h ₁)	0.432	0.412	-0.08

The magnetic moments of Co atoms are strongly dependent on local environment. Their values vary between 0.2 and 1.65 μ_B /atom (Table 1). The mean magnetic moment calculated per Co atom is slightly larger for $\text{Nd}_5\text{Co}_{21}\text{B}_4$ (0.81 μ_B /Co atom) than for $\text{Nd}_5\text{Co}_{19}\text{B}_6$ (0.79 μ_B /Co atom). This results in a larger magnetic moment per formula unit. The experimental values of saturation magnetization μ_s are 23.7 μ_B /f. u. and 31.1 μ_B /f. u. for $\text{Nd}_5\text{Co}_{19}\text{B}_6$ and $\text{Nd}_5\text{Co}_{21}\text{B}_4$, respectively [13, 14]. The corresponding calculated values are equal to 29.46 and 31.53 μ_B /f. u.

3. Conclusions

In this paper, the electronic structures of $\text{Nd}_5\text{Co}_{19}\text{B}_6$ and $\text{Nd}_5\text{Co}_{21}\text{B}_4$ have been calculated by the TB-LMTO method. The results were compared with experimental bulk measurements of saturation magnetization. Electronic structure calculations showed that $\text{Nd}_5\text{Co}_{19}\text{B}_6$ and $\text{Nd}_5\text{Co}_{21}\text{B}_4$ are ferromagnetically ordered. The Co bands dominate the densities of states near the Fermi level. Nd and B atoms provide very small contributions to the DOS at the Fermi level. The values of magnetic moments on Co atoms are strongly dependent on the local environment. The largest magnetic moments of Co

atoms were found for the ($4h_1$) site of $\text{Nd}_5\text{Co}_{19}\text{B}_6$ ($1.65\mu_B/\text{atom}$) and for the ($4h_2$) and ($2d$) sites of $\text{Nd}_5\text{Co}_{21}\text{B}_4$ (1.18 and $1.17\mu_B/\text{atom}$, respectively).

References

- [1] KUZ'MA Y.B., BILONIZHKO N.S., *Kristallografiya*, 18 (1973), 710.
- [2] SZAJEK A., *J. Magn. Magn. Mat.*, 185 (1998), 322.
- [3] KOWALCZYK A., *J. Magn. Magn. Mat.*, 175 (1997), 279.
- [4] PEDZIWIATR A.T., JIANG S.Y., WALLECE W.E., BURZO E., POP V., *J. Magn. Magn. Mat.*, 66 (1987), 69.
- [5] TETEAN R., BURZO E., *J. Magn. Magn. Mat.*, 157/158 (1996), 633.
- [6] ITO T., ASANO H., IDO H., YAMADA M., *J. Appl. Phys.*, 79 (1996), 5507.
- [7] CHEN Y., LIU Q.L., LIANG J.K., CHEN X.L., SHEN B.G., HUANG F., *Appl. Phys. Lett.*, 74 (1999), 856.
- [8] CHEN Y., LIANG J.K., CHEN X.L., LIU Q.L., SHEN B.G., SHEN Y.P., *J. Phys. Cond. Matter*, 11 (1999), 8251.
- [9] CHU W.G., RAO G.H., YANG H.F., LIU G.Y., LIANG J.K., *J. Appl. Phys.*, 90 (2001), 1931.
- [10] JEZIERSKI A., KOWALCZYK A., MAEHL S., NEUMANN M., BORSTEL G., *J. Phys. Cond. Matter*, 10 (1998), 6277.
- [11] KOWALCZYK A., SZAJEK A., CHELKOWSKA G., TOLIŃSKI T., *Solid State Commun.*, 132 (2004), 225.
- [12] SZAJEK A., KOWALCZYK A., *Czech. J. Phys.*, 54, Suppl. D (2004), D343.
- [13] CASPI E.N., PINTO H., KUZNIETZ M., ETTEDGUI H., MELAMUD M., FELNER I., SHAKED H., *J. Appl. Phys.*, 83 (1998), 6733.
- [14] CASPI E.N., PINTO H., MELAMUD M., *J. Appl. Phys.*, 87 (2000), 416.
- [15] ANDERSEN O.K., JEPSEN O., ŠOB M., [in:] *Electronic Structure and Its Applications*, M.S. Yussouff (Ed.), Springer-Verlag, Berlin, 1987, p.2.
- [16] KRIER G., JEPSEN O., BURKHARDT A., ANDERSEN O.K., The TB-LMTO-ASA program, source code, version 4.7, available upon request from the authors of the program.
- [17] MIN B.I., JANG Y.-R., *J. Phys. Cond. Matter*, 3 (1991), 5131.
- [18] PERDEW J.P., CHEVARY J.A., VOSKO S.H., JACKSON K.A., PEDERSON M.R., SINGH D.J., FIOLEHAI S., *Phys. Rev. B*, 46 (1992), 6671.
- [19] BROOKS M.S.S., NORDSTROM L., JOHANSSON B., *Physica B*, 172 (1991), 95.
- [20] BLÖCHL P., JEPSEN O., ANDERSEN O.K., *Phys. Rev. B*, 49 (1994), 16223.

Received 1 June 2005
Revised 10 October 2005

Temperature dependence of magnetization reversal in $\text{Ni}_{80}\text{Fe}_{20}/\text{Au}/\text{Co}/\text{Au}$ multilayers

B. SZYMAŃSKI*, F. STOBIECKI, M. URBANIAK

Institute of Molecular Physics, Polish Academy of Sciences,
M.. Smoluchowskiego 17, 60-179 Poznań, Poland

The results are presented concerning the temperature changes of the magnetic properties of $[\text{Ni}_{80}\text{Fe}_{20}$ (2 nm)/Au(t_{Au})/Co(t_{Co})/Au(t_{Au})]₁₀ multilayers (MLs) with $t_{\text{Au}} = 1.5, 2.2$ nm and $t_{\text{Co}} = 0.6, 0.8$ nm. The hysteresis loops of the investigated MLs were measured using a vibrating sample magnetometer in the temperature range 175–423 K. The saturation field H_S^{Co} of Co layers, determined from loops taken with a field applied in-plane, increases with decreasing temperature. The H_S^{Co} field is directly related to the perpendicular magnetic anisotropy of the Co layer. It was also found that the shape of the central parts of the hysteresis loops, taken with the magnetic field applied perpendicular to the sample plane, is characteristic of samples with large perpendicular anisotropy and a stripe domain structure. The shape of the hysteresis loops is preserved in the whole temperature range of measurements, indicating the presence of stable stripe domains. The magnetization reversal of Co layers can be described by nucleation (H_N), annihilation (H_A), and coercive fields (H_C). The temperature dependences of these parameters are presented.

Key words: *magnetic multilayers; perpendicular magnetic anisotropy*

1. Introduction

There is currently much interest in the investigation of multilayered structures composed of layers with alternating out-of-plane and in-plane magnetic anisotropy, because of their potential applications [1–3]. Examples of such structures are sputter-deposited $[\text{NiFe}/\text{Au}/\text{Co}/\text{Au}]_N$ MLs [3]. $\text{Ni}_{80}\text{Fe}_{20}$ (Permalloy = Py) layers exhibit distinct in-plane anisotropy, while ultrathin Co layers ($t_{\text{Co}} < 1.4$ nm), sandwiched between Au, have strong perpendicular anisotropy [4]. A detailed study of magnetization reversal and GMR effects enabled us to show that an Au spacer with a thickness of $t_{\text{Au}} \geq 1.5$ nm assures small interlayer coupling [5]. Therefore, we consider the magnetization reversal of Co and Py layers to be nearly independent. This allows us to

*Corresponding author, e-mail: szyman@ifmpan.poznan.pl

determine the magnetic properties of Co (separately of Py) layers from $M(H)$ (as well as $R(H)$) curves taken with magnetic fields applied perpendicular (H_{\perp}) and parallel (H_{\parallel}) to the layer plane. In this contribution, we have investigated the temperature dependence of the magnetic properties of Py/Au/Co/Au MLs which are important from the point of view of possible applications. Our particular goal was to determine the temperature dependence of the magnetic anisotropy of ultrathin Co layers, sandwiched between Au. Despite the vast literature on the anisotropy of the Co layers, data on its temperature dependence are scarce [6].

2. Experimental

A set of [Py(2 nm)/Au(t_{Au})/Co(t_{Co})/Au(t_{Au})]₁₀ MLs with $t_{\text{Co}} = 0.6, 0.8$ nm and $t_{\text{Au}} = 1.5, 2.2$ nm were deposited in an Ar atmosphere using UHV magnetron sputtering [5]. The samples were deposited at room temperature on a Si(100) substrate. A very good periodic structure of the MLs was confirmed by low- and high-angle X-ray diffraction. Magnetization reversal $M(H)$ was measured in the temperature range 175–423 K, both in the perpendicular and parallel configurations (H_{\perp} , $H_{\parallel} \leq 1.5$ T). The $M(H)$ loops were recorded with a vibrating sample magnetometer.

3. Results and discussion

The measured hysteresis loops are characteristic of a system composed of weakly coupled layers with two mutually perpendicular easy axes (Fig. 1), as mentioned in the Introduction. Apart from the region of small magnetic fields (i.e. $|H|$ smaller than the saturation field of layers magnetized along the easy direction), the magnetization of NiFe (Co) layers is always parallel to H_{\parallel} (H_{\perp}), but the magnetization of Co (NiFe) rotates from perpendicular (in-plane) to the field direction.

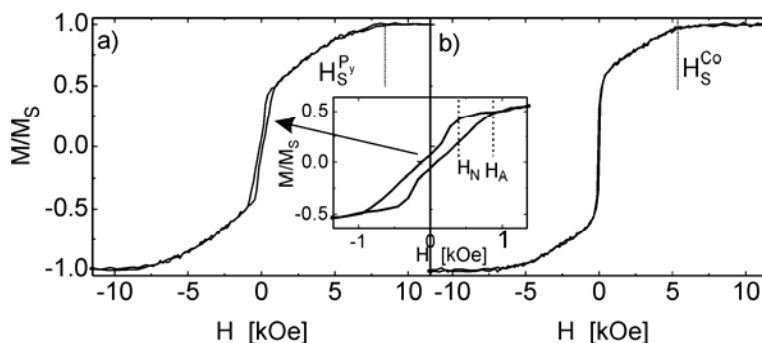


Fig. 1. Exemplary hysteresis loops of MLs with $t_{\text{Co}} = 0.8$ nm and $t_{\text{Au}} = 2.2$ nm, at room temperature in perpendicular (a) and parallel (b) configurations of the applied field

The shape of the central parts of loops, taken with H_{\perp} (Fig. 1a), which is related to the magnetization reversal of Co layers, strongly suggests the existence of a stripe domain structure. The latter was confirmed by magnetic force microscopy [7]. We characterize the $M(H_{\perp})$ loops by the nucleation (H_N), annihilation (H_A), and coercive (H_C) fields (Fig. 1a and its inset), which are related to the stripe domain structure in the Co layer and saturation field H_S^{Co} of the Permalloy layers. The most important parameter of the loop shown in Fig. 1b is H_S^{Co} , which is directly related to the effective perpendicular anisotropy of Co layers, $H_S = 2K_{eff}/M_S$. In further discussion, we will concentrate on the temperature changes of Co layer magnetic properties because they are crucial for applications.

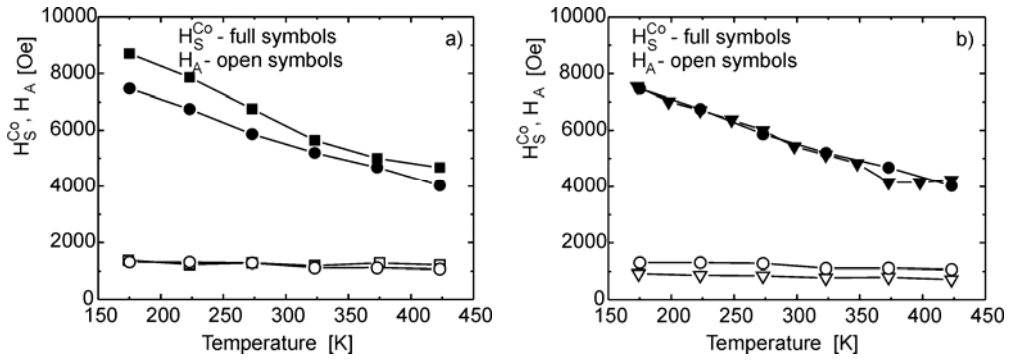


Fig. 2. Temperature dependence of the H_S^{Co} and H_A fields in the MLs:

- a) with constant $t_{Au} = 1.5$ nm and various Co thicknesses: 0.6 nm (squares) and 0.8 nm (circles),
 b) with constant $t_{Co} = 0.8$ nm and various Au thicknesses: 1.5 nm (circles) and 2.2 nm (triangles)

Figure 2 presents the temperature dependences of the saturation and annihilation fields of Co layers, measured in both configurations. H_S^{Co} values clearly diminish when the temperature increases. The values determined for the thinner Co layer, with $t_{Co} = 0.6$ nm, are systematically higher than for $t_{Co} = 0.8$ nm, which reflects the enhanced role of surface anisotropy in the former Co layer (Fig. 2a). Moreover, H_S^{Co} has exactly the same value and temperature dependence for samples with different values of t_{Au} and the same t_{Co} (Fig. 2b). This confirms our assumption of weak coupling between ferromagnetic layers, and additionally indicates a very good reproducibility of the parameters of our sputtered MLs. A slight decrease in H_A with temperature is negligible in comparison to H_S^{Co} changes. It should be stressed that, despite perpendicular anisotropy diminishing with T , the difference between H_S^{Co} and H_A is large enough to preserve the Co easy axis perpendicular to the sample plane over the whole T range.

Figure 3 shows the temperature dependence of H_N and H_C for MLs, (i) with different t_{Co} (Fig. 3a) and constant $t_{Au} = 1.5$ nm, and (ii) with different t_{Au} (Fig. 3b) and

constant $t_{\text{Co}} = 0.8\text{ nm}$. In all cases, H_{N} slightly increases with T . Thus, considering the weak decrease of $H_{\text{A}}(T)$ (Fig. 2), the difference ΔH between these fields, at which the nucleation (H_{N}) and annihilation (H_{A}) of stripe domains in Co layers takes place ($\Delta H = H_{\text{A}} - H_{\text{N}}$), diminishes with increasing temperature.

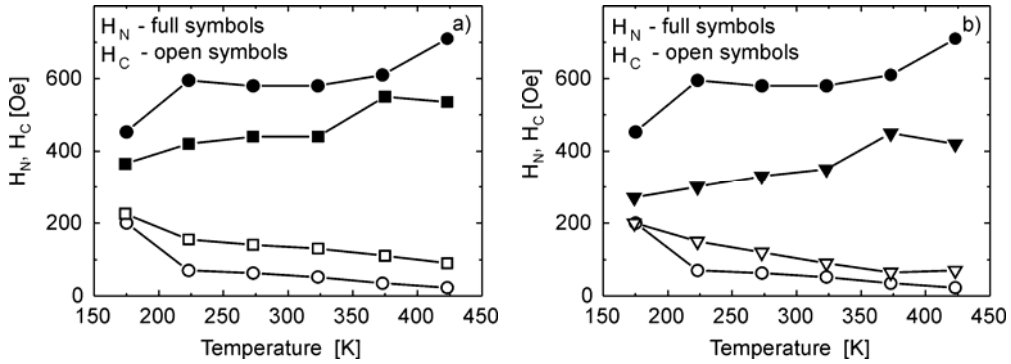


Fig. 3. Temperature dependences of the H_{N} and H_{C} fields in the same MLs as in Fig. 2

For instance, ΔH decreases from 1000 to 700 Oe when T increases from 175 to 425 K for MLs with $t_{\text{Co}} = 0.6\text{ nm}$ and $t_{\text{Au}} = 1.5\text{ nm}$. This tendency (as well as the decrease of $H_{\text{C}}(T)$) is related mainly to the temperature dependence of Co perpendicular anisotropy. The influence of other effects, however, such as the diminishing role of domain wall pinning centres at higher T , can also be substantial. It should also be noted that both the decrease of Co thickness (compare results for MLs with $t_{\text{Au}} = 1.5\text{ nm}$ and $t_{\text{Co}} = 0.8, 0.6\text{ nm}$) and increase of Au spacer thickness (compare MLs with $t_{\text{Co}} = 0.8\text{ nm}$ and different values of t_{Au} : 1.5 and 2.2 nm) leads to diminishing H_{N} values in the entire T range. This effect, in our opinion, is related mainly to magnetostatic (dipolar) coupling originating from the dense domain structure [8]. For the studied MLs, the values of H_{N} and H_{A} indicate the presence of stable stripe domains up to 425 K, which is important from the application point of view.

4. Conclusions

The temperature dependences of magnetic properties in sputtered $[\text{Ni}_{80}\text{Fe}_{20}(2\text{nm})/\text{Au}(t_{\text{Au}})/\text{Co}(t_{\text{Co}})/\text{Au}(t_{\text{Au}})]_{10}$ MLs with $t_{\text{Au}} = 1.5, 2.2\text{ nm}$ and $t_{\text{Co}} = 0.6$ and 0.8 nm was investigated in the range 175–425 K. It was shown that the effective perpendicular anisotropy of Co layers, which is the most important parameter for applications, diminishes almost linearly with increasing T . It remains sufficiently high in the investigated T range, however, to ensure that the easy axis of Co is perpendicular to the sample plane. This implies a good stability of stripe domain structure. Thus the studied MLs are promising candidates for applications such as magnetic storage media with perpendicular arrangements of bit cells.

Acknowledgements

Supported by the State Committee for Scientific Research through Grant 3 T08A 03127 and by the Centre of Excellence for Magnetic and Molecular Materials for Future Electronics within the European Commission Contract G5MA-CT-2002-04049.

References

- [1] WANG S.X., TARATORIN A.N., *Magnetic Information Storage Technology*, Academic Press, New York, 1999.
- [2] MANCOFF F.B., HUNTER DUNN J., CLEMENS B.M., WHITE R.L., *Appl. Phys. Lett.*, 77 (2000), 1879.
- [3] STOBIECKI F., SZYMAŃSKI B., LUCIŃSKI T., DUBOWIK J., URBANIAK M., SCHMIDT M., RÖLL K., *J. Magn. Mater.*, 272–276 (2004), E1751.
- [4] CHAPPERT C., LE DANG K., BEAUVILLAIN P., HURDQUINT H., RENARD D., *Phys. Rev. B*, 34 (1986), 3192.
- [5] STOBIECKI F., SZYMAŃSKI B., LUCIŃSKI T., DUBOWIK J., URBANIAK M., RÖLL K., *J. Magn. Mater.*, 282 (2004), 32.
- [6] DUBOWIK J., STOBIECKI F., GOŚCIAŃSKA I., *Phys. Stat. Sol. (a)*, 196 (2003), 41.
- [7] URBANIAK M., STOBIECKI F., ENGEL D., SZYMAŃSKI B., EHRESMANN A., KIM J.B., *Phys. Stat. Sol. (c)*, 3 (2006), 57.
- [8] URBANIAK M., STOBIECKI F., SZYMAŃSKI B., *Phys. Stat. Sol. (a)*, 202 (2005), 2013.

Received 1 June 2005
Revised 10 October 2005

Electronic and magnetic properties of metastable $\text{Fe}_{22}\text{PdB}_6$ and $\text{Fe}_{22}\text{PtB}_6$ compounds

A. SZAJEK, S.A. KOSTYRYA, B. IDZIKOWSKI*

Institute of Molecular Physics, Polish Academy of Sciences,
M. Smoluchowskiego 17, 61-179 Poznań, Poland

Nanostructured soft magnets are examples of materials that are made by the partial crystallization of amorphous precursors. $\text{Fe}_{22}(\text{Pt},\text{Pd})\text{B}_6$ compounds, which crystallize in the Cr_{23}C_6 -type structure and have four inequivalent sites (4a, 8c, 48h, 32f) for Fe, Pd, and Pt atoms, can form grains of several nanometers in diameter in a residual amorphous matrix. Band structure calculations show that the local magnetic moments of Fe atoms depend on their local environments, and for 4a and 8c sites the resultant moments are enhanced up to about $2.5\text{--}3\mu_{\text{B}}/\text{atom}$. Pd and Pt atoms prefer to be located in the 4a and 8c positions, respectively. Magnetic moments induced on the substituted atoms are equal to $0.45\mu_{\text{B}}/\text{atom}$ on the Pt atom and $0.39\mu_{\text{B}}/\text{atom}$ on Pd.

Key words: *amorphous alloy; electronic structure; magnetic moment*

1. Introduction

Amorphous Fe-based alloys are subject to intensive investigations, because of their interesting properties. Many of them exhibit excellent soft magnetic properties [1] and are very promising materials from the practical point of view. High saturation induction and low coercivity combined with good corrosion resistance [2] make amorphous Ni-based alloys (or with Ni additions) very attractive for a variety of applications. For instance, melt-spun $(\text{Fe}_{100-x}\text{Ni}_x)_{93-y}\text{Zr}_7\text{B}_y$ alloys can be used as shape memory materials [3] based on the martensitic transformation from γ -austenite to α -martensite recently studied in this system.

Annealing Ni-based amorphous precursors, e.g. with a chemical composition of $\text{Ni}_{64}\text{Fe}_{16}\text{Zr}_7\text{B}_{12}\text{Au}$, favours the emergence of cubic $\text{Fe}_x\text{Ni}_{23-x}\text{B}_6$ nanocrystalline grains, the metastable phase of which does not exist as a bulk material. The grains are isostructural with Cr_{23}C_6 (space group $Fm\bar{3}m$), revealing rather high values of saturation magnetization in the amorphous as well as nanocrystalline states [4].

* Corresponding author, e-mail: idzi@ifmpan.poznan.pl

Nanocrystalline soft magnetic samples can be prepared from fully amorphous alloys with special compositions. As a general rule, introducing a so-called inhibitor of grain growth into the alloy is necessary. Controlled annealing in a protective atmosphere favours the emergence of the nanocrystalline phase or phases. The phases can be identified by X-ray diffraction, transmission electron microscopy, or by Mössbauer spectrometry [4]. Various contents of nanocrystals are easily obtained by varying the temperature of isochronal annealing (usually 1 hour) or by special combinations of time/temperature annealing and heating rates.

The temperature dependences of magnetic parameters corresponding to nanosized grains deviate from those of bulk alloys with the same composition. Two mechanisms responsible for the observed effects are proposed: (i) the influence of impurities in nanograins, and (ii) grain surface contribution. The latter plays a non-negligible role, especially when the grain size is of the order of tens of nanometres. The former effect seems to be of minute importance. Different magnetic behaviours may be observed for low, medium, and high volumetric fractions of crystallites.

Band structure calculations showed that the local magnetic moments of Fe, Ni, and Co atoms in $(\text{FeNiCo})_2\text{B}_6$ compounds depend on their local environments (see Ref. [6] and references therein). Investigations of $\text{Fe}_{22}(\text{Pd,Pt})\text{B}_6$ alloys are a part of our studies of the magnetic properties of Fe_{23}B_6 -type alloys. In this paper, we determine the magnetic behaviour of Pd and Pt additions and their site preference based on *ab initio* band structure calculations.

2. Method of calculation

Band structures and magnetic moments were calculated using the spin-polarized tight-binding linear muffin-tin orbital (TB LMTO) method in the atomic sphere approximation (ASA) [7, 8]. The overlap volumes of the muffin-tin spheres for both structures were equal to 9.8%. Standard combined corrections for overlapping [7] were used to compensate for errors due to the ASA. Spin-orbit interactions were taken into account in the form proposed by Min and Jang [9]. The von Barth–Hedin [10] potential and experimental values of the lattice constants were used in the calculations. Self-consistent calculations were carried out for 4096 k -points in the Brillouin zone. The tetrahedron method was used to integrate over the Brillouin zone [11]. Iterations were repeated until the energy eigenvalues change for consecutive steps was below 0.01 mRy.

3. Results and discussion

The results of the band structure calculations are summarized in Fig. 1 as the total densities of electronic states (DOS) for up and down spins. The shapes of local DOS plots depend on the type of atom, its localization, and local environment. The values

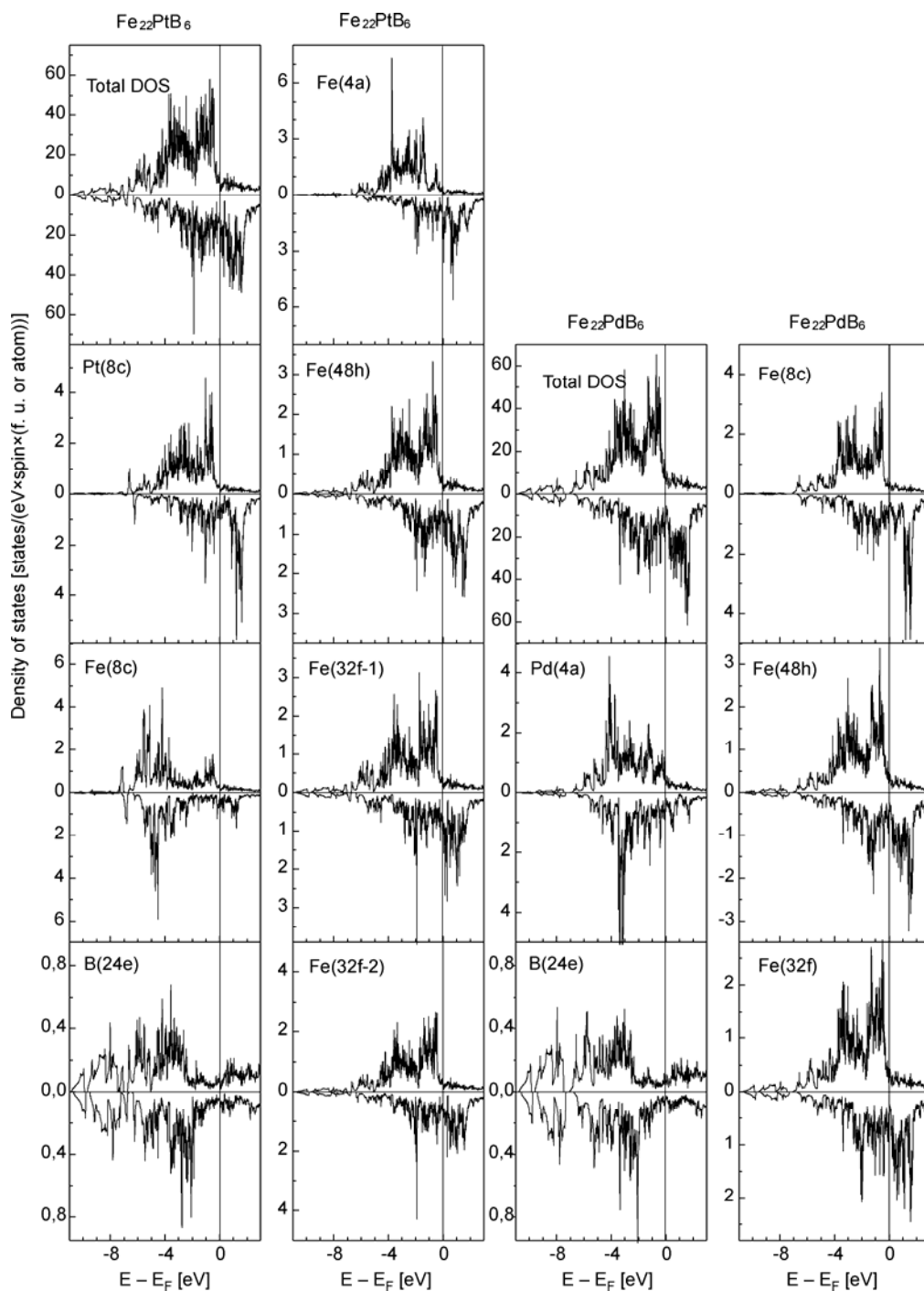


Fig. 1. The total (calculated per f. u.) and local DOS functions for $Fe_{22}(Pt,Pd)B_6$ systems

of the total DOS at the Fermi level (E_F) are equal to 14.99 and 22.76 states/(eV·f. u.) for $\text{Fe}_{22}\text{PdB}_6$ and $\text{Fe}_{22}\text{PtB}_6$, respectively. Fe(3d), Pd(4d), and Pt(5d) electrons provide the main contribution to the DOS($E = E_F$), about 90%. The site and spin projected values are collected in Table 1, which also contains the calculated saturation magnetic moments.

Table 1. Spin projected (\uparrow , \downarrow) DOS [states/(eV·spin·atom)] at the Fermi level and calculated local magnetic moments m for Fe, Pd, Pt, and B atoms [μ_B /atom] in $\text{Fe}_{22}(\text{Pt,Pd})\text{B}_6$

Compound	Atoms	DOS \uparrow	DOS \downarrow	m	Compound	Atoms	DOS \uparrow	DOS \downarrow	m	
$\text{Fe}_{22}\text{PtB}_6$	Fe(4a)	0.340	1.466	3.02	$\text{Fe}_{22}\text{PdB}_6$	Pd(4a)	0.262	0.459	0.39	
	Fe(8c)	0.294	0.500	2.53		Fe(8c)	0.183	0.407	2.53	
	Pt(8c)	0.285	0.262	0.45		Fe(48h)	0.215	0.414	2.23	
	Fe(48h)	0.394	0.501	2.27		Fe(32f)	0.204	0.422	1.91	
	Fe(32f-1)	0.351	0.743	2.00		B(24e)	0.048	0.041	-0.17	
	Fe(32f-2)	0.365	0.543	1.95						
	B(24e)	0.093	0.051	-0.17						
	Total (per f. u.)	9.069	13.690	48.02		Total (per f. u.)	5.128	9.863	46.47	

Note that since Pd atoms are located in the 8c site, broken symmetry causes the appearance of additional inequivalent atoms in the 32f position, marked as 32f-1 and 32f-2.

Especially high values of magnetic moments are located on Fe(4a) and Fe(8c) atoms, higher than for bulk bcc-Fe. The magnetic moments depend on local environment, namely (i) the types of neighbours and (ii) interatomic distances. In the case of the 4a and 8c positions, interatomic distances are larger than for bcc-Fe and lead to larger Wigner–Seitz (WS) radii and consequently larger magnetic moments. These data can be interpreted qualitatively as showing a tendency toward the localization of d electrons [12]. With increasing WS radii, the magnetic moments approach values closer to the moment of an isolated Fe atom. An increasing number of neighbouring boron atoms reduces the magnetic moment of iron. Band structure calculations were performed for all possible configurations of Pd and Pt impurities in the unit cell. A direct comparison of the calculated total energies gave the site preference of impurities. Table 1 contains values for the positions of the impurities that minimize the total energies. Pd and Pt atoms prefer 4a and 8c positions, respectively. Although metallic palladium and platinum are nonmagnetic, in this case quite large magnetic moments are induced on these additions, $0.45\mu_B$ /atom on Pt atoms and $0.39\mu_B$ /atom on Pd. The WS radius used in calculations for Pd in the 4a site was about 1.7 Å, 8.6% larger than for the Pd-fcc metallic system. The influence of the lattice constant on the magnetic moment of Pd has been considered by other researchers [13–15]. In their calculations, sudden phase transitions from a nonmagnetic to a ferromagnetic state were observed for lattice constants larger than the equilibrium value by about 5.5–10%.

4. Conclusions

Nanocrystalline $Fe_{22}(Pt,Pd)B_6$ grains created by devitrification in soft magnets could be the reason for the enhancement of their magnetic properties (e.g., saturation and/or remanence magnetization) which is useful in applications. Band structure calculations showed that the local magnetic moments of Fe atoms in $Fe_{22}(Pt,Pd)B_6$ depend on their local environments. In 4a and 8c sites, the resultant Fe moments are enhanced up to about $2.5\text{--}3\mu_B/\text{atom}$. Pd and Pt atoms prefer, in the $Cr_{23}C_6$ type structure, the 4a and 8c positions, respectively. The magnetic moments induced on the substituted atoms are equal to $0.45\mu_B/\text{atom}$ for Pt and $0.39\mu_B/\text{atom}$ for Pd.

References

- [1] HASEGAWA R., Mater. Sci. Eng., A 375-377 (2004), 90.
- [2] BOZORTH R.M., *Ferromagnetism*, IEEE Press, New York, 1993, p. 102.
- [3] GRRER A.L., WALKER I.T., J. Non-Cryst. Solids., 317 (2003), 78.
- [4] IDZIKOWSKI B., SZAJEK A., GRENECHE J.-M., KOVAČ J., Appl. Phys. Lett., 85 (2004), 1392.
- [5] KOSTYRYA S.A., ŚNIADECKI Z., IDZIKOWSKI B., phys. stat. sol. (b), 242 (2005), 621.
- [6] IDZIKOWSKI B., SZAJEK A., Czech. J. Phys. 54 Suppl. D (2004), D59.
- [7] ANDERSEN O.K., JEPSEN O., ŠOB M., in *Electronic Structure and Its Applications*, M.S. Yussouff (Ed.), Springer-Verlag, Berlin, 1987, p. 2.
- [8] KRIER G., JEPSEN O., BURKHARDT A., ANDERSEN O.K., *The TB-LMTO-ASA program* (source code, version 4.7).
- [9] MIN B.I., JANG Y.-R., J. Phys. Cond. Matter, 3 (1991), 5131.
- [10] VON BARTH U., HEDIN L., J. Phys. C, 5 (1972), 1629.
- [11] BLÖCHL P., JEPSEN O., ANDERSEN O.K., Phys. Rev. B, 49 (1994), 16223.
- [12] BAGAYOKO D., CALLAWAY J., Phys. Rev. B, 28 (1983), 5419.
- [13] CHEN H., BRENER N.E., CALLAWAY J., Phys. Rev. B, 40 (1989), 1443.
- [14] MORUZZI V.L., MARCUS P.M., Phys. Rev. B, 39 (1989), 471.
- [15] FRITSCHÉ L., NOFFLKE J., ECKARDT H., J. Phys. F, 17 (1987), 943.

Received 1 June 2005
Revised 10 October 2005

Influence of Ge on antiferromagnetic coupling in Fe/Si multilayers

P. WANDZIUK^{1*}, T. LUCIŃSKI¹, M. KOPCEWICZ²

¹Institute of Molecular Physics, Polish Academy of Sciences,
M. Smoluchowskiego 17, 60-179 Poznań, Poland

²Institute of Electronic Materials Technology, Wólczyńska 133, Warsaw, Poland

Magnetic and structural properties of sputtered Fe/Ge, Fe/Ge/Si/Ge and Fe/Si/Ge/Si multilayers were studied. Magnetization measurements revealed the absence of antiferromagnetic coupling for the Ge spacer. It was found that during multilayer deposition, a 0.5 nm thick Fe layer at each Fe/Ge interface became non-ferromagnetic, leading to the formation of antiferromagnetic structures. Mössbauer spectra showed the existence of ferro- and/or antiferromagnetic structures at Fe/Ge interfaces, and ferromagnetic and paramagnetic structures at Fe/Si interfaces. We have found that the substitution of Si by at least 0.5 nm of Ge in the 1.1 nm thick Si spacer led to the disappearance of antiferromagnetic coupling in Fe/Si multilayers.

Key words: *magnetic multilayers; antiferromagnetic coupling; Mössbauer spectroscopy*

1. Introduction

In recent years, a lot of scientific attention has been paid to ferromagnet/semiconductor (FM/SC) layered structures, because of their potential application in spintronics [1–3]. One of the most interesting systems in this field seem to be Fe/Si multilayers (MIs), due to their strong antiferromagnetic (AF) interlayer coupling [1, 3]. Despite many efforts, the origin of AF coupling in this system has not been clarified. Another FM/SC system is Fe/Ge. One could expect that these very similar systems exhibit comparable properties, but experiments revealed no AF coupling at room temperature (RT) in the second structure [1]. In both systems, Fe diffuses into the spacer layer [1, 2]. Therefore, we can surmise that different magnetic and paramagnetic Fe–Si and Fe–Ge phases can be formed. The formation of these phases may play a vital role in the presence or absence of the AF coupling. In this paper, we compare the results of Fe/Si MIs reported previously [3, 4] with Fe/Ge MIs prepared by the same method, and the influence of substituting Si by Ge is discussed.

*Corresponding author, e-mail: wandziuk@ifmpan.poznan.pl

2. Experimental

Four series of samples were deposited by magnetron sputtering at RT on oxidized Si substrates: (i) $[\text{Fe} (3 \text{ nm})/\text{Ge} (d_{\text{Ge}})]_{15}$ with the Ge layer thickness of $0.5 \leq d_{\text{Ge}} \leq 3 \text{ nm}$, (ii) $[\text{Fe} (d_{\text{Fe}})/\text{Ge} (2 \text{ nm})]_{15}$ with the Fe layer thickness of $0.5 \leq d_{\text{Fe}} \leq 4 \text{ nm}$, (iii) $[\text{Fe} (3 \text{ nm})/(\text{Ge}/\text{Si}/\text{Ge})(d_{\text{S}})]_{15}$, and (iv) $[\text{Fe} (3 \text{ nm})/(\text{Si}/\text{Ge}/\text{Si})(d_{\text{S}})]_{15}$ MIs. For series (iii) and (iv), d_{S} denotes $d_{\text{Ge}} + d_{\text{Si}} + d_{\text{Ge}}$ and $d_{\text{Si}} + d_{\text{Ge}} + d_{\text{Si}}$, respectively. The total spacer thickness, $d_{\text{S}} = 1.1 \text{ nm}$, corresponding to strong AF coupling for Fe/Si MIs,

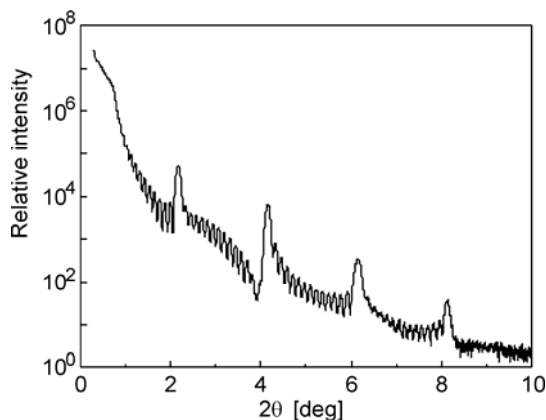


Fig. 1. An example of SAXRD spectrum recorded at room temperature for $[\text{Fe}(3 \text{ nm})/\text{Ge}(2 \text{ nm})]_{15}$ MIs

was kept constant and the partial thicknesses of both components were varied. Magnetic and structural properties were investigated at RT by a vibrating sample magnetometer (VSM) and by conversion electron Mössbauer spectroscopy (CEMS), respectively. Well-defined multilayered structures for the investigated MIs were confirmed by small-angle X-ray diffraction (SAXRD), an example spectrum of which is shown in Fig. 1.

3. Results and discussion

The dependence of the saturation field (H_{S}) on the spacer thickness (d_{S}), measured at RT for $[\text{Fe} (3 \text{ nm})/\text{Ge} (d_{\text{Ge}})]_{15}$ and $[\text{Fe} (3 \text{ nm})/\text{Si} (d_{\text{Si}})]_{15}$ MIs is shown in Fig. 2. As can be seen, in contrast to Fe/Si MIs, Fe/Ge reveals no AF coupling in the entire range of examined Ge spacer thicknesses. Figure 3 shows the Fe thickness dependence of magnetic moment per surface area (m/S) for $[\text{Fe} (d_{\text{Fe}})/\text{Ge} (2 \text{ nm})]_{15}$ and $[\text{Fe} (d_{\text{Fe}})/\text{Si} (2.5 \text{ nm})]_{15}$ MIs (see also [3]). From the interception of the straight line with the d_{Fe} axis we conclude that about 1 nm (0.5 nm at each interface) of sputtered Fe intermixes with Ge and that non-ferromagnetic Fe–Ge structures are formed. As can be seen, this value is twice as large as that found in Fe/Si MIs.

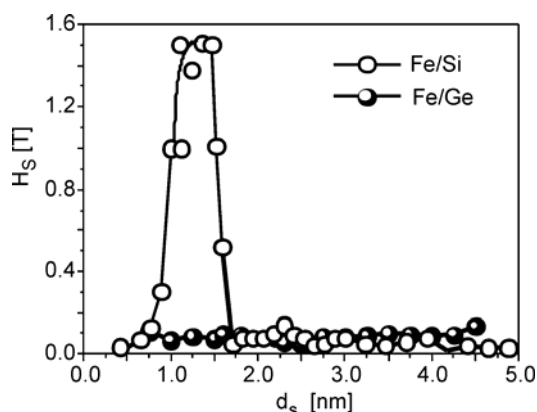


Fig. 2. The saturation field (H_S) of Fe(3 nm)/Si(d_s) and Fe(3 nm)/Ge(d_s) vs. the spacer thickness of Si and Ge, respectively, at room temperature

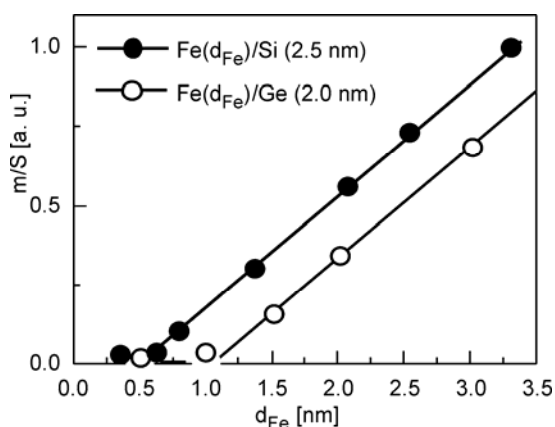


Fig. 3. Magnetic moment per surface area (m/S) at room temperature for Fe(d_{Fe})/Ge (2 nm) and Fe(d_{Fe})/Si (2.5 nm) MLs as a function of Fe thickness

Since, as was already shown, no AF coupling through the Ge spacer occurs, therefore in order to find the influence of Ge on AF coupling in Fe/Si MLs, Fe/(Ge/Si/Ge) and Fe/(Si/Ge/Si) MLs are studied. Magnetic measurements (Fig. 4) reveal that, independently of the position of Ge in the Si spacer, the saturation field decreases with increasing Ge thickness. In the case of the Fe/(Ge/Si/Ge) MLs, due to interdiffusion, the Fe–Ge layer is progressively formed and prevents further diffusion of Fe into the Si layer, which, as we have shown [4, 5], plays a crucial role in the appearance of AF coupling in Fe/Si MLs. For the Fe/(Si/Ge/Si) system, the gradual formation of a continuous Ge layer may occur, leading to the reduction of AF coupling. This process is complete for $d_{Ge} > 0.5$ nm and AF coupling disappears. This reasoning seems to be reflected in the CEMS spectra (Fig. 5).

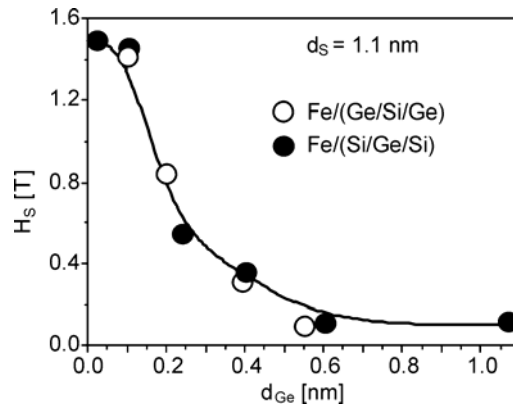


Fig. 4. The influence of Ge sublayer thickness on the value of H_S at room temperature

All the recorded spectra contain two magnetic components:

- The Zeeman sextet with a hyperfine field $H_{\text{hf}} \approx 32.8$ T characteristic of the bcc-Fe phase of Fe layers. This value is a little lower than that characteristic of α -Fe, and this reduction can be induced by stress in the Fe layers.
- The magnetic broadened sextet with a hyperfine field $H_{\text{hf}} \approx 30$ T and isomer shift $\delta = 0.05$ mm/s, which can be assigned to ferro- or/and antiferromagnetic Fe-Ge phases.

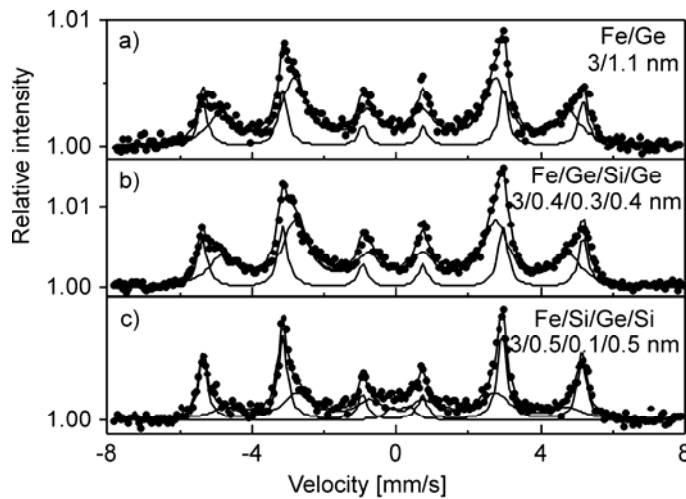


Fig. 5. Room temperature CEMS spectra for: a) Fe/Ge, b) Fe/(Si/Ge/Si) and c) Fe/(Ge/Si/Ge) MLs. Sublayer thicknesses are indicated

In contrast to Fe/Si MLs [3, 4], however, in Fe/Ge MLs no nonmagnetic quadrupole splitting (QS) doublet is found (Fig. 5a). This may suggest that Fe diffuses into the Ge spacer and only ferromagnetic and/or antiferromagnetic Fe-Ge phases can be formed.

Since all CEMS spectra for Fe/Si Mls contain a pronounced QS doublet due to the appearance of nonmagnetic Fe silicides at Fe/Si interfaces [3, 4], we expect that the introduction of Ge between Fe and Si will prevent the formation of paramagnetic Fe–Si phases, which can be responsible for the observed AF coupling in this system. Indeed, as can be seen from Fig. 5b, for Fe/(Ge/Si/Ge) Mls, a diffusive Fe/Ge interface gives rise to a broadened sextet and no QS doublets are observed. Since all existing Fe–Ge phases are ferro- and antiferromagnetic [6], they are represented by sextets. Our CEMS investigations, however, cannot determine which phases are present in the spacer, and cannot distinguish between ferro- and antiferromagnetic structures. Therefore, the absence of the paramagnetic doublet in Fe/Ge and Fe/(Ge/Si/Ge) suggests that 0.5 nm of Fe diffuses into Ge (Fig. 3) and forms an antiferromagnetic interfacial layer. Thus antiferromagnetic structures similar to FeGe and FeGe₂ phases may be formed. In the case of Fe/(Si/Ge/Si) Mls (Fig. 5c), however, both ferro- and paramagnetic structures are present at Fe/Si interfaces. They are represented by a broadened sextet and paramagnetic QS doublet.

4. Conclusions

The absence of AF coupling in Fe/Ge Mls is established. It was shown that during multilayer deposition 0.5 nm of Fe intermixes with Ge and antiferromagnetic structures are formed. Independently of Ge position in the Si spacer, the progressive substitution of Si by Ge leads to a gradual reduction of AF coupling. In Fe/(Si/Ge/Si) Mls, the formation of a continuous Ge layer is responsible for the absence of AF coupling, whereas in Fe/(Ge/Si/Ge) Mls the formation of antiferromagnetic and/or ferromagnetic Fe-Ge structures disables further diffusion of Fe into the Si layer.

Acknowledgements

One of the authors (P. W.) is grateful to professor F. Stobiecki for discussions. Supported by the State Committee for Scientific Research under grant PBZ/KBN/044/P03/2001, and by the Centre of Excellence for Magnetic and Molecular Materials for Future Electronics within the European Commission Contract G5MA-CT-2002-04049.

References

- [1] DE VRIES J.J., KOHLHEPP J., DEN BROEDER F.J.A., VERHAEGH P.A., JUNGBLUT R., REINDERS A., DE JONGE W.J.M., *J. Magn. Magn. Matter.*, 165 (1997), 435.
- [2] SCHLEBERGER M., WALSER P., HUNZIKER M., LANDOLT M., *Phys. Rev. B*, 60 (1999), 14360.
- [3] LUCIŃSKI T., KOPCEWICZ M., HÜTTEN A., BRÜCKL H., HEITMANN S., HEMPEL T., G. REISS, *J. Appl. Phys.*, 93 (2003), 6501.
- [4] WANDZIUŁ P., KOPCEWICZ M., SZYMAŃSKI B., LUCIŃSKI T., *Mol. Phys. Rep.*, 40 (2004), 182.
- [5] LUCIŃSKI T., WANDZIUŁ P., BASZYŃSKI J., STOBIECKI F., ZWECCK J., to appear in *J. Alloy Compd.*, 2006.
- [6] KANEMATSU K., OHYAMA T., *J. Phys. Soc. Japan*, 20 (1965), 236.

Received 1 June 2005
Revised 10 October 2005

Magnetic properties and electronic structure of $Y_xGd_{1-x}Ni_5$ compounds

A. BAJOREK^{1*}, D. STYSIAK¹, G. CHEŁKOWSKA¹,
J. DENISZCZYK², W. BORGIEL¹, M. NEUMANN³

¹A. Chełkowski Institute of Physics, University of Silesia, Uniwersytecka 4, 40-007 Katowice, Poland

²Institute of Material Science, University of Silesia, Bankowa 12, 40-007 Katowice, Poland

³Fachbereich Physik, Universität Osnabrück, Germany

Measurements of the magnetic susceptibility, crystal and electronic structure for $Y_xGd_{1-x}Ni_5$ ($x = 0.0, 0.2, 0.5, 0.8, 1.0$) compounds with a $CaCu_5$ -type crystal structure are reported. The substitution of Y for Gd atoms results in a decrease of the unit cell volume and Curie temperature. In the paramagnetic range (300–650 K), the DC susceptibility follows the Curie–Weiss law for all investigated compounds. The effective moment deduced from the Curie constant decreases rapidly with Y concentration. The saturation magnetic moment for $GdNi_5$ exhibits a negative polarization of the Ni3d band, induced by interactions with Gd5d states. Both valence band and core level X-ray photoelectron spectra are analysed. The presence of satellite structure in the Ni2p core level suggests that the magnetic polarisation of Ni3d states, which dominates the valence band in all investigated compositions. The experimental investigations were complemented by the band structure calculations. In all cases, the calculations were based on the KKR and KKR–CPA methods. Satisfactory agreement between the recorded spectra and those obtained from the calculated electronic structure was achieved.

Key words: *rare earth–nickel intermetallics; magnetic properties; XPS; electronic structure*

1. Introduction

Intermetallic compounds RM_5 show interesting magnetic properties associated with both the localized moments of rare earth (R) and the itinerant electrons of 3d atoms (M). These compounds crystallize in a hexagonal $CaCu_5$ -type crystal structure (space group $P6/mmm$) [1–4]. In this structure, the R atoms are located at 1a positions, and Ni atoms can occupy two positions, 2c and 3g [5]. Magnetic properties as studied by Gignoux [1] show that $GdNi_5$ is a ferromagnet with $T_C = 32$ K and a satura-

*Corresponding author, e-mail: ankabaj@poczta.onet.pl

tion magnetic moment of $6.2\mu_B/\text{f.u.}$ This value is lowered with increasing yttrium concentration for $\text{Gd}_x\text{Y}_{1-x}\text{Ni}_5$, and the magnetic properties correlate with negative Ni d-band polarization which is induced by interactions with Gd atoms [1, 2]. It has been reported that YNi_5 is a strong Pauli paramagnet exhibiting an effect of spin fluctuations in the temperature variation of susceptibility [6, 7].

In this work, we focus on the influence of the partial substitution of Gd by Y atoms on the magnetic properties and electronic structure of the $\text{Y}_x\text{Gd}_{1-x}\text{Ni}_5$ system ($x = 0.0, 0.2, 0.5, 0.8, 1.0$). We report electronic structure analysis using experimental X-ray photoemission spectroscopy (XPS) and theoretical *ab initio* calculations.

2. Experimental and computing method

Polycrystalline samples of $\text{Y}_x\text{Gd}_{1-x}\text{Ni}_5$ with $x = 0.0, 0.2, 0.5, 0.8$, and 1.0 were prepared by arc melting of high purity elements under an argon atmosphere. The purity of phases was checked by X-ray diffraction using a Siemens D5000 diffractometer. AC magnetic susceptibility measurements were done in the temperature range $4.2\text{--}300\text{ K}$ at the frequency of 1 kHz . The DC susceptibility was measured in the paramagnetic range $300\text{--}800\text{ K}$ using the Faraday method in the magnetic field of 0.38 T .

XPS measurements were performed with a PHI 5700/660 Physical Electronics spectrometer. The spectra were analysed at room temperature using monochromatised AlK_α radiation (1486.6 eV). The samples were fractured and measured in a vacuum of $6 \times 10^{-10}\text{ Torr}$. After breaking in high vacuum, we observe only small amounts of carbon and oxygen. Band structure calculations were carried out using the spin-polarized relativistic Korringa-Kohn-Rostoker (SPR-KKR) band structure program [8]. The Local Spin Density Approximation (LSDA) exchange-correlation potential (XC) was used in the form given by Vosko et al. [9]. The crystal volume is divided into overlapping Wigner–Seitz (WS) spheres, with the volume equal to the volume of a unit cell. The radii of the constituents were $r_{\text{Gd}} = 1.798$, $r_{\text{Y}} = 1.798$, $r_{\text{Ni}2c} = 1.508$, and $r_{\text{Ni}3g} = 1.328\text{ \AA}$. XPS was simulated by convoluting the partial density of states with a Lorentzian (0.35 eV HW) and multiplying by the corresponding cross-section taken from [10].

3. Results and discussion

The X-ray powder diffraction measurements show the presence of only a hexagonal CaCu_5 -type crystal structure for all the investigated $\text{Y}_x\text{Gd}_{1-x}\text{Ni}_5$ compounds. The decrease of both lattice parameters and the volume unit cell with increasing yttrium concentration (Fig. 1) was observed. The Curie temperatures T_c (Fig. 1) obtained from AC measurements decrease from 34 K ($x = 0.0$) to about 5.5 K ($x = 0.8$) as a function of Y concentration.

The temperature dependence of reciprocal DC susceptibility exhibits the Curie–Weiss type behaviour in the paramagnetic range $300\text{--}650\text{ K}$ for all the investigated

compounds. The effective moments deduced from the Curie constant decrease rapidly with Y concentration from $8.35\mu_B/f.u.$ ($x = 0.0$) to $3.90\mu_B/f.u.$ ($x = 1.0$). As has been previously reported for $GdNi_5$ [3] and YNi_5 [7], the value of the effective moment is higher above the characteristic temperature T^* in the paramagnetic range, where the system behaves as having local moments. Such behaviour was already analysed using the theory of spin fluctuations [3, 7]. For $GdNi_5$, the effective magnetic moment obtained up to 300 K is about $7.7\mu_B/f.u.$, the same as that obtained by Gignoux [1]. The field dependence of magnetization for $GdNi_5$ obtained at 4.2 K saturates at the field of 9 T and the value of the saturation magnetic moment is equal to $6.77\mu_B/f.u.$ [11].

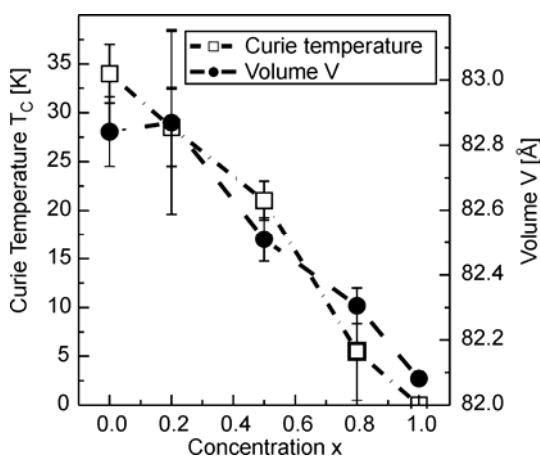


Fig. 1. Volume unit cell V and Curie temperature T_C for the $Y_xGd_{1-x}Ni_5$ system

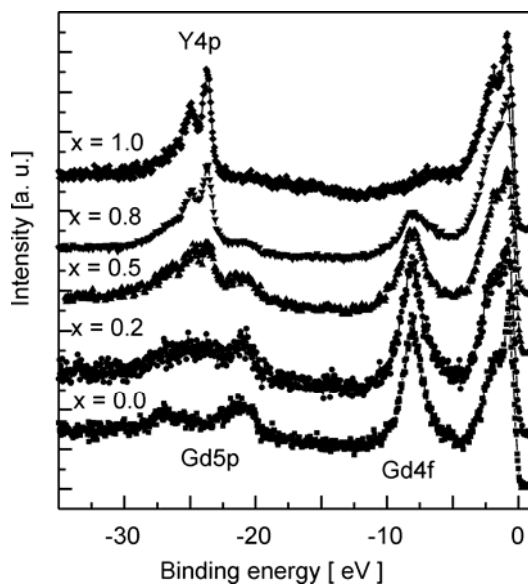


Fig. 2. XPS valence bands for a broad range for $Y_xGd_{1-x}Ni_5$ compounds

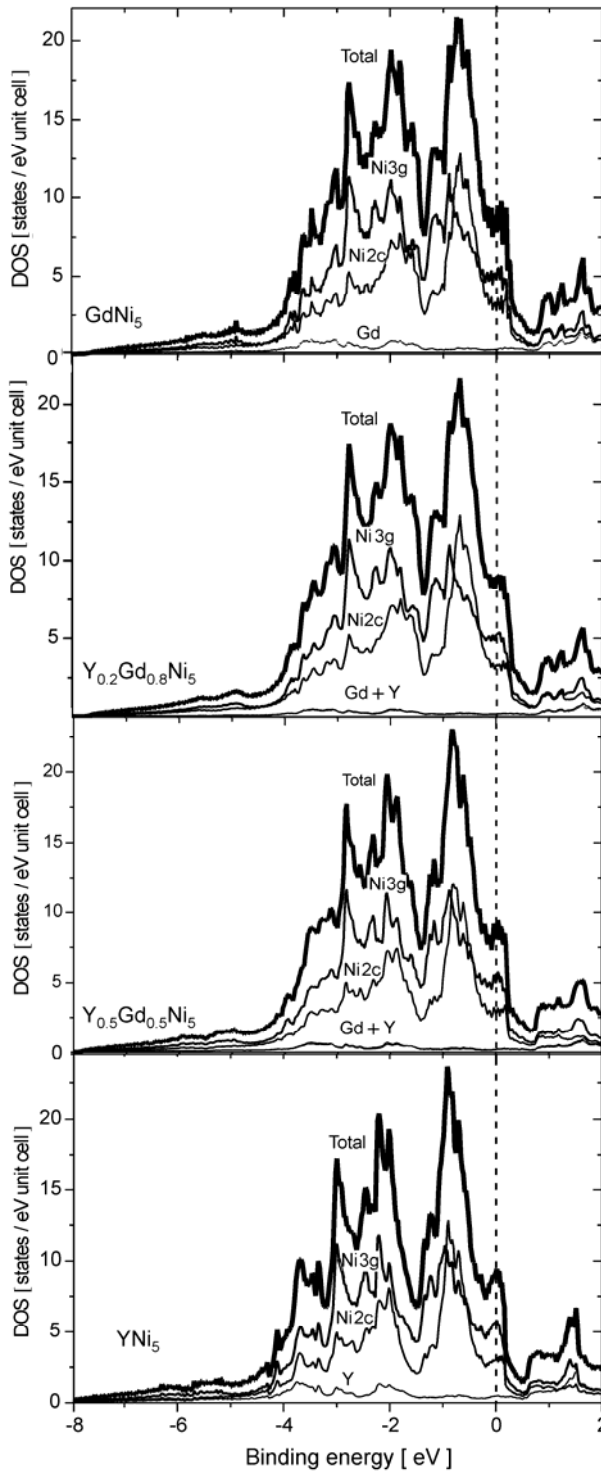


Fig. 3. Total density of states – thick solid lines (the highest density of states) and contributions coming from different types of atoms in the unit cell: Ni – solid lines (medium density of states), Y, Gd – solid lines (the smallest density of states). The vertical dashed line denotes the E_F level

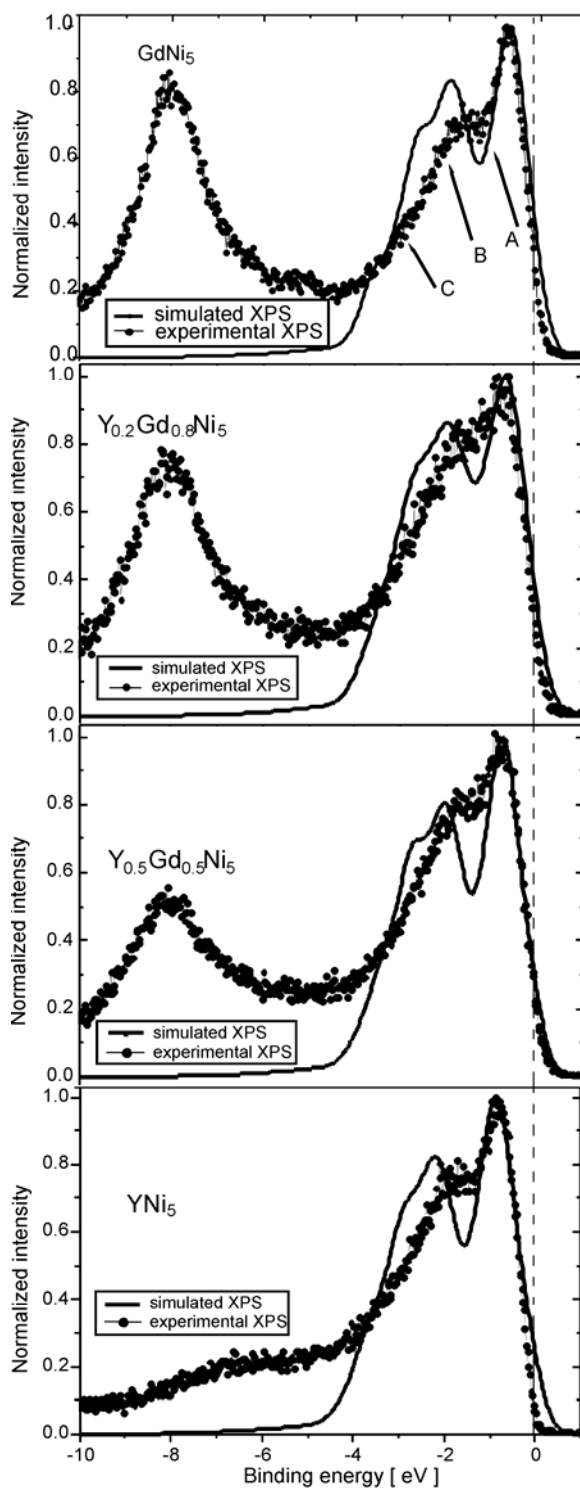


Fig. 4. Experimental (dotted lines) and simulated (solid lines) XPS valence bands. The vertical dashed line denotes the E_F level

In the valence bands (Fig. 2), we have observed the contribution of Gd5p states located at about 26 eV (Gd5p_{3/2}) and 21 eV (Gd5p_{1/2}). When replacing Gd by Y, a gradual vanishing of Gd5p peaks and appearance of Y4p peaks is observed. Y4p lines are located at about 23.7 eV (Y4p_{3/2}) and 24.8 eV (Y4p_{1/2}). The position of the Gd4f states is almost the same as in pure Gd. A gradual decrease of the Gd4f intensities with increasing Y content is observed.

From the valence bands near the Fermi level (Fig. 4) we conclude that Ni3d are dominant at E_F for all the investigated compounds. The main line located in the valence band spectrum consists of two visible peaks at about 0.7 eV (peak A) and 1.8 eV (peak B). One can also see a small contribution at 2.9 eV (peak C). When increasing Y concentration, a small shift in those peaks by about 0.11 eV towards higher binding energies is observed. The separation between peaks A and B is larger for GdNi₅ and YNi₅ than for the other compounds. This behaviour may be related to hybridization effects between Ni3d, Gd5d, and Y4d. About 6 eV below E_F one can observe a small satellite structure related to two-hole nickel final states: 3d⁹4s (main line) and 3d⁸4s² (satellite line). A similar satellite structure at about 6 eV below the main line is observed for the core level spectra of Ni2p (not shown here). The existence of these satellites is usually associated with an incompletely filled Ni3d band. In our compounds, we have not observed these satellites vanish with an increasing number of Y atoms, contrary to other Ni compounds [3]. Therefore, we conclude that the Ni d band in Y_xGd_{1-x}Ni₅ is not completely filled.

In Figure 3, the total density of states (DOS) and contributions coming from different crystallographic positions of each atom are shown. Their partial densities of states are multiplied by their number in the unit cell. The dominating features of the total DOS plots have their counterparts in the simulated XPS spectrum (Fig. 4).

The contributions from Ni atoms in the inequivalent positions 2c and 3g are significantly different due to different environments. The contribution from Ni atoms is dominant, and it originates mainly from 3d states. This is simply due to the fact that there are 5 times as many Ni atoms than Gd or Y atoms in the unit cell. E_F is located at the top of the Ni3d band. The 4f bands of Gd give relatively high and unphysical peaks at -4 eV and 1.5 eV. Their binding energies are twice smaller than the measured binding energy, which is a well known deficiency of the local density approximation. This deficiency can be corrected by using the LDA + U or SIC (self interaction corrected) method. The Gd4f states were removed for clarity and the remaining states were used to obtain the XPS spectra.

These simulated and measured XPS spectra are very similar, except for the Gd4f bands positions noted above. The positions of other peaks are in a good agreement with the experimental ones. The slight shift of the peak at 1 eV in the direction of higher binding energies with increasing yttrium concentration is reflected in both experimental and simulated spectra. This peak originates from Ni3d bands and is caused mainly by Ni atoms in 2c positions. The next peaks, at 2 and 4 eV, also arise from Ni3d bands, but from Ni atoms in the 3g positions. The widths of the peaks are in good agreement with the experimental data.

The magnetic moments of Ni in 2c and 3g positions are oriented antiparallel to Gd and Y moments in all samples (Table 1). Quite interesting is the fact that the value of Gd5d moments, equal to $0.132\mu_B/\text{f.u.}$ for $GdNi_5$, is larger than Ni3d moments at both lattice positions. Ni polarization is very small due to its almost fully filled 3d band. The substitution of Gd atoms by Y is reflected in the slight growth of the Ni moment, which can be correlated with the arrangement of Gd5d moments, oriented parallel to Gd4f moments. Very small changes in Gd4f moments with Y concentration were also observed. The total magnetic moment decreases rapidly with increasing Y concentration, from $6.75\mu_B$ for $x = 0.0$ to $0.181\mu_B$ for $x = 1.0$.

Table 1. Total and partial magnetic moments obtained from band structure calculations for $Y_xGd_{1-x}Ni_5$

x	M_Y [μ_B/atom]	M_{Gd} [μ_B/atom]	M_{Ni2c} [μ_B/atom]	$M_{Ni(3g)}$ [μ_B/atom]	Total M [$\mu_B/\text{f.u.}$]
0.0	–	6.97	–0.02	–0.06	6.75
0.2	0.02	6.97	–0.02	–0.05	5.39
0.5	0.01	6.98	–0.01	–0.02	3.42
1.0	–0.01	–	0.03	0.04	0.17

4. Conclusions

From the results of our measurements for $Y_xGd_{1-x}Ni_5$ compounds, the following conclusions can be drawn. The decrease of the Curie temperature and effective magnetic moment with increasing Y concentration were observed. From the analysis of XPS valence band spectra, the domination of Ni3d states at E_F is observed. Hybridization effects between Ni3d, Gd5d, and Y4d states are evident from the experimental spectra as well as from the band structure calculations. In addition, the Ni3d band remains almost unchanged for all $Y_xGd_{1-x}Ni_5$ compounds. The observed satellite structure in Ni2p core level lines can be correlated with the incompletely filled Ni3d bands. The agreement found between the experimental and simulated XPS valence bands is quite good. The calculations have shown three visible contributions coming from Ni2c and Ni3g states near the Fermi level. The positions of these contributions are almost the same in the experimental spectra (peaks A, B, and C). The different values for Ni2c and Ni3g magnetic moments obtained from band structure calculations can be attributed to different local environments.

References

- [1] GIGNOUX D., GIVORD D., DEL MORAL A., *Solid State Commun.*, 19 (1976), 891.
- [2] BURZO E., CHEŁKOWSKI A., KIRCHMAYR H.R., *Landolt Börnstein Handbook*, Vol. III/19d2, Springer-Verlag, Berlin, 1990.

- [3] COLDEA M., CHIUZBAIAN S.G., NEUMANN M., TODORAN D., DEMETER M., TETEAN R., POP V., Acta Phys. Polon. A, 98 (2000), 629.
- [4] UEBAYASHI K., TERAOKA K., YAMADA H., J. Alloys Comp., 346 (2002), 47.
- [5] BALKIS AMEEN K., BHATIA M.L., J. Alloys Comp., 374 (2002), 165.
- [6] COLDEA M., ANDREICA D., BITU M., CRISAN V., J. Magn. Magn. Mater., 157/158 (1996), 627.
- [7] BURZO E., POP V., COSTINA I., J. Magn. Magn. Mater., 157/158 (1996), 615.
- [8] ERBERT H., Lecture Notes in Physics, 535 (2000), 191.
- [9] WILK L., VOSKO S.H., NUSSAIR M., Can. J. Phys., 58 (1980), 1200.
- [10] YEH J., LINDAU I., At. Data. Nucl. Data Tables, 32 (1985), 1.
- [11] BAJOREK A., CHELKOWSKA G., ANDRZEJEWSKI B., sent to Physica B.

Received 1 June 2005
Revised 10 October 2005